DISSERTATION

Search for the top squark in semileptonic final states in compressed scenarios with the ATLAS detector

Vakhtang Tsiskaridze

Fakultät für Mathematik und Physik
Albert-Ludwigs-Universität Freiburg

Search for the top squark in semileptonic final states in compressed scenarios with the ATLAS detector

DISSERTATION

zur Erlangung des Doktorgrades der
Fakultät für Mathematik und Physik der

ALBERT-LUDWIGS-UNIVERSITÄT
Freiburg im Breisgau

vorgelegt von
Vakhtang Tsiskaridze

June 2016

Dekan:	Prof. Dr. Dietmar Kröner
Betreuer der Arbeit:	Prof. Dr. Karl Jakobs
Referent:	Prof. Dr. Karl Jakobs
Koreferent:	Prof. Dr. Horst Fischer
Prüfer:	Prof. Dr. Karl Jakobs
	Prof. Dr. Stefan Dittmaier
	Prof. Dr. Markus Schumacher

Datum der mündlichen Prüfung:
29 August 2016

Contents

Introduction

The Standard Model of particle physics is a theory which describes all known particles together with the electromagnetic, weak and strong interactions. The Higgs particle was discovered in 2012 at the European Organisation for Nuclear Research (CERN) by the ATLAS and CMS experiments [1, 2].

With the observation of the Higgs particle, the particle content of the Standard Model is complete. In spite of the big success of the Standard Model to describe elementary particles and their interactions, it is considered as an approximation ("effective theory") to a more fundamental theory.

There are some questions which remain open:

- Why are there exactly three generations of fermions which have the same properties, but such different masses?
- The observation of neutrino oscillations implies, that at least some of the neutrinos have a mass, which so far is not included in the Standard Model.
- Cosmology is hinting for dark matter, for which the Standard Model does not have a good explanation.
- Why is the Higgs boson mass so much smaller than the Planck mass (*hierarchy problem*).
- It is expected that the new theory would unify electromagnetic, weak and strong interactions at a high scale, the so-called *Grand Unification Theory* (GUT).
- Gravitation is not included in the Standard Model, moreover – the attempts to create a quantum theory of gravity is facing technical problems. The final theory should unify the gravitational force, too, such a theory is mentioned as a *Theory of Everything* (TOE).

Supersymmetry provides a solution for some of these problems:

- The hierarchy problem can be solved by the introduction of supersymmetric partners, which removes divergences in a natural way.
- The electromagnetic, weak and strong interactions can be unified at a high energy scale (the above mentioned Grand Unification Theory).
- The neutralino is a good candidate for the dark matter particle.

The high interest in supersymmetry searches at the ATLAS and CMS experiments, especially for top-squark ($\tilde{t}_1$) searches, is dictated by the hierarchy problem. To solve this problem, the top-squark mass should be in the 1 TeV range, which is reachable at the LHC. For the presented searches, R-parity conservation is assumed. This implies the stability of the *Lightest Supersymmetric Particle* (LSP), which is assumed to be the neutralino ($\tilde{\chi}_1^0$).

All presented analyses search for the top-squark pair production in final states one lepton (electron or muon), jets and large missing transverse momentum. The analysis has been performed with the data recorded by the ATLAS experiment at $\sqrt{s} = 7$ TeV and $\sqrt{s} = 8$ TeV. The thesis is organised as follows:

Chapter 1 contains a theory overview of the Standard Model, the motivation for Supersymmetry, a theory overview of the Minimal Supersymmetric extension of the Standard Model, and a brief discussion on some open questions. A short description of the LHC and the ATLAS detector is given in Chapter 2. General explanations for object definitions and reconstruction used in the ATLAS experiment are described in Chapter 3.

The general search strategy used in the reported analyses is presented in Chapter 4. This chapter also contains a short overview and a brief discussion on mathematical methods and software frameworks and tools used for the analysis.

Searches for the light top squark at $\sqrt{s} = 7$ TeV for the $\tilde{t}_1 \to b\tilde{\chi}_1^{\pm}$, $\tilde{\chi}_1^{\pm} \to W^{\pm(*)}\tilde{\chi}_1^0$ decay mode are presented in Chapter 5.

Chapter 6 presents the $\tilde{t}_1 \to b\tilde{\chi}_1^{\pm}$ analysis at $\sqrt{s} = 8$ TeV which was published in Ref. [3]. The contribution in the published paper is the analysis, where $m(\tilde{t}_1) \approx m(b) + m(\tilde{\chi}_1^{\pm})$.

Background reweighting strategies for the $t\bar{t}$ process are discussed in Chapter 7. First the default 4-bin reweighting approach is described, which is used in the zero- and one-lepton analyses. Then an exponential reweighting approach is presented, which is smoothing the reweighting function based on the default 4-bin strategy. The difference and improvement from using exponential reweighting are highlighted.

Chapter 8 presents the $\tilde{t}_1 \to t\tilde{\chi}_1^0$ analysis at $\sqrt{s} = 8$ TeV to cover the phase-space region where $m(\tilde{t}_1) \approx m(t) + m(\tilde{\chi}_1^0)$, which remained uncovered during the ATLAS and CMS top-squark pair production searches at $\sqrt{s} = 8$ TeV. The presented analysis covers this gap in the $200 - 300$ GeV interval. The strategy for searches targeting the diagonal and the variables sensitive for this region of a mass plane are discussed.

An alternative approach for a multijet background estimation is presented in Chapter 9. It also provides a detailed validation for this approach and a cross-check with the Matrix Method.

The summary of the work is presented in Chapter 10.

The results obtained in Chapter 6 of this thesis were included in a journal publication of the ATLAS Collaboration [3]. The search presented in Chapter 8 is a pioneering study, which was done for the first time in the course of this thesis. It provides the basis for further publications on this topic in future analyses by the ATLAS Collaboration. In addition, an independent cross-check was performed during the early phase of this thesis in Chapter 5 for the results published by the ATLAS Collaboration on the light top-squark pair production searches with $\sqrt{s} = 7$ TeV data [4].

CHAPTER 1

Theory Overview

1.1 The Standard Model of particle physics

The *Standard Model* (SM) of particle physics is a theory, which describes elementary particles together with the electromagnetic, weak and strong interactions. It is considered as an approximation ("effective theory") to a more fundamental global theory. For a more detailed description of the Standard Model see, for example, Ref. [5]. The description given in the following is closely based on this reference.

The Standard Model of particle physics is based on a local gauge symmetry:

$$G_{\text{SM}} = SU(3)_C \otimes SU(2)_L \otimes U(1)_Y \tag{1.1}$$

It consists of three generations of fermions with spin $\frac{1}{2}$, which are divided into quarks and leptons. Quarks transform as $SU(3)_C$ triplets. There exist three generations of quarks:

$$\begin{pmatrix} u \\ d \end{pmatrix} \quad \begin{pmatrix} c \\ s \end{pmatrix} \quad \begin{pmatrix} t \\ b \end{pmatrix}$$

Leptons transform as $SU(3)_C$ singlets. They also appear in three generations:

$$\begin{pmatrix} \nu_e \\ e^- \end{pmatrix} \quad \begin{pmatrix} \nu_\mu \\ \mu^- \end{pmatrix} \quad \begin{pmatrix} \nu_\tau \\ \tau^- \end{pmatrix}$$

The gauge group is presented by eight generators L_a for $SU(3)_C$, three generators T_a for $SU(2)_L$ and one generator Y for $U(1)_Y$. The commutation relations between these generators are:

$$[L_a, L_b] = i f_{abc} L_c, \quad [T_a, T_b] = i\epsilon_{abc} T_c, \qquad [L_a, T_b] = [L_a, Y] = [T_b, Y] = 0, \tag{1.2}$$

where ϵ_{abc} and f_{abc} are the structure constants for the $SU(2)$ and $SU(3)$ groups, respectively, retaining standard notations.

Table 1.1 presents the Standard Model fermions with the corresponding representations. The notation $(3, 2, +1/3)$ indicates a triplet of the $SU(3)_C$ colour, a doublet of $SU(2)_L$ isospin with hypercharge $Y = 2(Q - T_3) = +1/3$, where Q is the electric charge.

Fermions	Notation	$SU(3)_C \otimes SU(2)_L \otimes U(1)_Y$		
Quarks	$Q_{L_i} = \begin{pmatrix} u_i \\ d_i \end{pmatrix}_L$	3	2	$+\frac{1}{3}$
$u_i = (\ u,\ c,\ t\ )$	$u_{R_i} = (u_i)_R$	3	1	$+\frac{4}{3}$
$d_i = (\ d,\ s,\ b\ )$	$d_{R_i} = (d_i)_R$	3	1	$-\frac{2}{3}$
Leptons	$L_{L_i} = \begin{pmatrix} \nu_i \\ \ell_i \end{pmatrix}_L$	1	2	-1
$\nu_i = (\nu_e, \nu_\mu, \nu_\tau)$	$\nu_{R_i} = (\nu_i)_R$	1	1	0
$\ell_i = (\ e,\ \mu,\ \tau\ )$	$\ell_{R_i} = (\ell_i)_R$	1	1	-2

Table 1.1: List of Standard Model fermionic particles with the corresponding representations.

Gauge Fields	Notation	$SU(3)_C \otimes SU(2)_L \otimes U(1)_Y$		
Colour Charge	G_a^μ	8	1	0
Weak Isospin	W_a^μ	1	3	0
Weak Hypercharge	B^μ	1	1	0

Table 1.2: List of Standard Model gauge fields with corresponding representations.

The local symmetry is presented with the following gauge fields: the G_a^μ are the gauge fields for the $SU(3)_C$ of colour, the W_a^μ are for the $SU(2)_L$ of the weak isospin and the B^μ are for the $U(1)_Y$ of weak hypercharge. The gauge fields are listed in Table 1.2 with the corresponding representations. The L and R indices represent the left- and right-handed components of the Dirac field and are described in Section 1.1.4.

The fields strengths are:

$$\begin{aligned} G_a^{\mu\nu} &= \partial^\mu G_a^\nu - \partial^\nu G_a^\mu - g_s f_{abc} G_b^\mu G_c^\nu, \qquad && a,b,c = 1,\dots,8 \\ W_a^{\mu\nu} &= \partial^\mu W_a^\nu - \partial^\nu W_a^\mu - g\epsilon_{abc} W_b^\mu W_c^\nu, && a,b,c = 1,2,3 \\ B^{\mu\nu} &= \partial^\mu B^\nu - \partial^\nu B^\mu. \end{aligned} \tag{1.3}$$

The Standard Model Lagrangian can be expressed as follows:

$$\mathcal{L}_{\text{SM}} = \mathcal{L}_{\text{Gauge}} + \mathcal{L}_{\text{Fermion}} + \mathcal{L}_{\text{Higgs}} + \mathcal{L}_{\text{Yukawa}}. \tag{1.4}$$

The $\mathcal{L}_{\text{Gauge}}$ describes the free propagation of the gauge fields and their self-interaction and can be presented as

$$\mathcal{L}_{\text{Gauge}} = -\frac{1}{4}G_a^{\mu\nu}G_{\mu\nu}^a - \frac{1}{4}W_b^{\mu\nu}W_{\mu\nu}^b - \frac{1}{4}B^{\mu\nu}B_{\mu\nu}. \tag{1.5}$$

The term $\mathcal{L}_{\text{Fermion}}$ describes the interaction of the gauge fields with the fermions and can be presented as

$$\mathcal{L}_{\text{Fermion}} = i\overline{\Psi}_{Q_L}\not{D}\Psi_{Q_L} + i\overline{\psi}_{u_R}\not{D}\psi_{u_R} + i\overline{\psi}_{d_R}\not{D}\psi_{d_R} + i\overline{\Psi}_{L_L}\not{D}\Psi_{L_L} + i\overline{\psi}_{\ell_R}\not{D}\psi_{\ell_R} + i\overline{\psi}_{\nu_R}\not{D}\psi_{\nu_R}, \tag{1.6}$$

where the three gauge coupling constants g_s, g and g' are used for $SU(3)_C$, $SU(2)_L$ and $U(1)$ groups.

The interaction itself is encapsulated in the covariant derivative

$$D^\mu = \partial^\mu + ig_s G_a^\mu L_a + igW_b^\mu T_b + ig'\frac{Y}{2}B^\mu, \tag{1.7}$$

where for the $SU(3)_C$ quark triplets $L_a = \lambda_a/2$, with λ_a as the Gell-Mann matrices for $SU(3)_C$, for the $SU(3)_C$ lepton singlets $L_a = 0$. For the $SU(2)_L$ doublets $T_a = \sigma_a/2$, with σ_a as Pauli matrices, while for the $SU(2)_L$ singlets $T_a = 0$.

1.1.1 Spontaneous symmetry breaking

The $\mathcal{L}_{\text{Gauge}} + \mathcal{L}_{\text{Fermion}}$ terms of the Standard Model Lagrangian do not include any mass terms. A naive introduction of mass terms like the $W_\mu^a W_a^\mu$ for gauge bosons will break the gauge invariance. A fermionic mass term $\bar{\psi}_{f_L}\psi_{f_R} + \bar{\psi}_{f_R}\psi_{f_L}$ for a fermion f also breaks gauge invariance, since left- and right-handed fermions transform differently under $SU(2)_L \otimes U(1)_Y$ gauge transformations.

A gauge invariant introduction of mass terms for particles is based on a *Spontaneous Symmetry Breaking* (SSB) approach and requires an extension of the theory.

The theory is extended by an introduction of a new complex scalar $SU(2)_L$ doublet of the weak hypercharge, a so-called Higgs field

$$\Phi = \begin{pmatrix} \varphi^+ \\ \varphi^0 \end{pmatrix} \tag{1.8}$$

and the potential

$$V(\Phi) = -\mu^2(\Phi^\dagger\Phi) + \lambda(\Phi^\dagger\Phi)^2. \tag{1.9}$$

The Higgs term in the Lagrangian is described as

$$\mathcal{L}_{\text{Higgs}} = (D_\mu\Phi)^\dagger(D^\mu\Phi) - V(\Phi). \tag{1.10}$$

The form of the potential for the model fulfils the gauge invariance and renormalisability requirements. For a stable vacuum, the condition $\lambda > 0$ is necessary, while to get a nontrivial *vacuum expectation value* (*vev*) $\mu^2 > 0$ has to be chosen. In this case the minimum Φ_0 should fulfil the conditions

$$\Phi_0^\dagger\Phi_0 = \frac{v^2}{2}, \qquad v \equiv \sqrt{\frac{\mu^2}{\lambda}}. \tag{1.11}$$

Requiring the vacuum expectation value to be electrically neutral, Φ_0 can, up to a phase, be presented as

$$\Phi_0 = \frac{1}{\sqrt{2}}\begin{pmatrix}0\\ v\end{pmatrix}. \tag{1.12}$$

This breaks the $SU(2)_L \otimes U(1)_Y$ symmetry to the $U(1)_Y$ group. The scalar doublet $\Phi(x)$ can be rewritten with the splitt-off Φ_0 in the form

$$\Phi(x) = \exp\left(i\frac{\sigma_a}{2}\theta_a(x)\right)\frac{1}{\sqrt{2}}\begin{pmatrix}0\\ v+H(x)\end{pmatrix}. \tag{1.13}$$

The local $SU(2)_L$ symmetry allows to vanish the $\theta^a(x)$ dependence. This is mentioned as the three Goldstone bosons are "eaten" by three gauge bosons. The non-vanished real scalar degree of freedom $H(x)$ is called the *Higgs boson*.

The charged $W^\pm$ bosons are defined as

$$W^\pm_\mu = \frac{W^1_\mu \mp iW^2_\mu}{\sqrt{2}}. \tag{1.14}$$

After substitution, the mass contribution to the Lagrangian is

$$\begin{aligned}\mathcal{L}_{\text{mass}} = &-\frac{v}{\sqrt{2}}(g_{u_i}\overline{\psi}_{u_i}\psi_{u_i} + g_{d_i}\overline{\psi}_{d_i}\psi_{d_i} + g_{\ell_i}\overline{\psi}_{\ell_i}\psi_{\ell_i}) + \left(\frac{vg}{2}\right)^2 W^+_\mu W^\mu_- \\ &+\frac{v^2}{8}\left(W^3_\mu, B_\mu\right)\begin{pmatrix}g^2 & -gg'\\ -gg' & g'^2\end{pmatrix}\begin{pmatrix}W^3_\mu\\ B_\mu\end{pmatrix}.\end{aligned} \tag{1.15}$$

The charged W-boson mass corresponds to

$$m_W = \frac{gv}{2}. \tag{1.16}$$

The mass matrix for W^3_μ and B_μ is not diagonal, therefore the neutral gauge bosons are mixed. Diagonalisation of the matrix can be done by a rotation about the weak mixing angle θ_W, which is defined by

$$\tan\theta_W = \frac{g'}{g}. \tag{1.17}$$

The transformation to the new basis of the photon and Z boson, A_μ and Z_μ respectively is defined as

$$\begin{pmatrix}Z_\mu\\ A_\mu\end{pmatrix} = \begin{pmatrix}\cos\theta_W & -\sin\theta_W\\ \sin\theta_W & \cos\theta_W\end{pmatrix}\begin{pmatrix}W^3_\mu\\ B_\mu\end{pmatrix}. \tag{1.18}$$

In this basis, the mass terms for the γ photon and Z boson are

$$m_\gamma = 0 \quad \text{and} \quad m_Z = \frac{v}{2}\sqrt{g^2+g'^2}. \tag{1.19}$$

One can see, that the mass ratio of massive gauge-bosons is fixed by

$$\frac{m_W}{m_Z} = \cos\theta_W. \tag{1.20}$$

Rewriting the Higgs potential (equation 1.9) in terms of the Higgs field H and v, one can get

$$V = -\frac{\mu^2 v^2}{4} + \mu^2 H^2 + \lambda v H^3 + \frac{\lambda}{4} H^4. \tag{1.21}$$

The Higgs mass determined by the quadratic term, taking into account equation 1.13, can be expressed as

$$m_H = \sqrt{2\mu^2} = \sqrt{2\lambda} v. \tag{1.22}$$

Interaction vertices of the Higgs boson with the fermions, $W^{\pm}$, Z^0 and Higgs bosons are shown in Figure 1.1. The strength of the Higgs boson coupling with f fermion is proportional to the mass m_f of the particle.

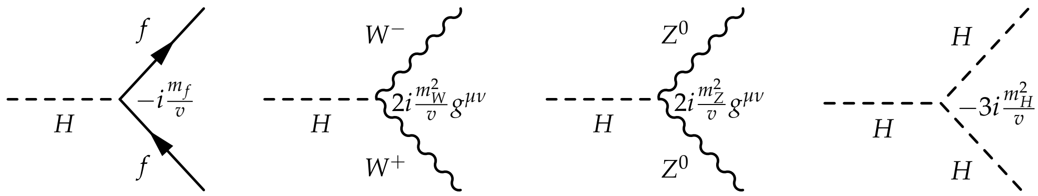

Figure 1.1: Interaction vertices for the Higgs boson with the (from left to right) fermions and $W^{\pm}$, Z^0 and Higgs bosons.

1.1.2 Fermion masses

The masses for fermions are added ad-hoc by Yukawa coupling terms of fermions to the Higgs doublet Φ.

$$\mathcal{L}_{\text{Yukawa}} = -\overline{\Psi}_{L_L} G_\ell \psi_{\ell_R} \Phi - \overline{\Psi}_{Q_L} G_u \psi_{u_R} \widetilde{\Phi} - \overline{\Psi}_{Q_L} G_d \psi_{d_R} \Phi + \text{h.c.}, \tag{1.23}$$

where "h.c." means hermitian conjugate and $\widetilde{\Phi}$ is the charge-conjugate Higgs doublet which is defined as

$$\widetilde{\Phi} = i\sigma_2 \Phi^* = \begin{pmatrix} \varphi^{0*} \\ -\varphi^- \end{pmatrix}. \tag{1.24}$$

The matrices $G_f(f = \ell, u, d)$ are arbitrary complex 3×3 matrices. The non-diagonal elements of the G_f matrices mix left- and right-handed fermions of different flavours, which causes oscillations during a free propagation.

To avoid oscillations, one can transform from the "flavour basis" $(\psi_{f_{1\mathcal{T}}}, \psi_{f_{2\mathcal{T}}}, \psi_{f_{3\mathcal{T}}})$ to the "mass basis" $(\psi'_{f_{1\mathcal{T}}}, \psi'_{f_{2\mathcal{T}}}, \psi'_{f_{3\mathcal{T}}})$ by means of a unitary matrix $U_{f_\mathcal{T}}$ for left- and right-handed fields:

$$\psi'_{f_{i\mathcal{T}}} = U_{f_\mathcal{T}} \psi_{f_{i\mathcal{T}}}, \quad f = \ell, u, d \quad \mathcal{T} = L, R \quad i = 1, 2, 3. \tag{1.25}$$

In the mass basis the corresponding G_f' matrices take a diagonal form:

$$G_f' = U_{f_L} G_f U_{f_R}^\dagger = \frac{\sqrt{2}}{v} \begin{pmatrix} m_{f_1} & & \\ & m_{f_2} & \\ & & m_{f_3} \end{pmatrix}. \tag{1.26}$$

The diagonal value m_{f_i} corresponds to the mass of the fermion f_i. By convention all fermion masses are chosen non-negative. This can always be achieved, since U_{f_L} and U_{f_R} are different operators and can be, up to some extent, selected separately. In case of negative m_f, the sign can always be changed by flipping the corresponding component of the "mass basis" to the opposite for only left- or right-handed basis, keeping G_f' diagonal and making m_f non-negative.

After the substitution of $\psi \to \psi'$ in the Standard Model Lagrangian, all coupling matrices G_f are transformed to a diagonal form. The effect of the substitution to the whole Standard Model Lagrangian is discussed in Section 1.1.5.

By default it is assumed, that the Standard Model Lagrangian is written in the mass basis and hats over fermionic fields are omitted. If the unitary gauge is used, where the Goldstone fields are "eaten", the $\mathcal{L}_{\text{Yukawa}}$ term can be represented in the form

$$\mathcal{L}_{\text{Yukawa}} = -\sum_f m_f (\bar{\psi}_{f_L}\psi_{f_R} + \bar{\psi}_{f_R}\psi_{f_L}) \left(1 + \frac{H}{v}\right), \tag{1.27}$$

where the sum is taken over all fermions. From the Yukawa terms one can see, that the Higgs boson couplings to fermions f are proportional to their masses

$$g_f = \frac{\sqrt{2}}{v} m_f. \tag{1.28}$$

1.1.3 Strong interaction

Quantum Chromodynamics (QCD) is the $SU(3)_C$ non-abelian gauge theory of strong interactions. It describes the interactions between *quarks* and *gluons*.

There are two important properties of QCD:

- ***Confinement***
  The force between quarks increases with distance. An attempt to separate two quarks from each other, increases the energy between them, until it will be enough to create another quark pair. From the newly created pair, one quark stays with the first and the second comes with the second quark. Therefore quarks do not exist in an isolated state, they are always bound into the hadrons.
- ***Asymptotic freedom***
  At high energies, or at very small distances, the interaction between quarks and gluons is very weak, i.e. they are asymptotically free.

The Lagrangian for quantum chromodynamics without a mass term is defined as

$$\mathcal{L}_{\text{QCD}} = -\frac{1}{4}G_a^{\mu\nu}G_{\mu\nu}^a + \sum_f i\bar{\psi}_f \not{D}\psi_f \tag{1.29}$$

where $G_a^{\mu\nu}$ is defined in equation 1.3 and D^μ is defined as follows

$$D^\mu = \partial^\mu + ig_s G_a^\mu L_a. \tag{1.30}$$

1.1.4 Electroweak interaction

In the Standard Model only left-handed fermions are involved in the weak interaction. The Dirac field ψ can be projected on left- and right-handed components using P_L and P_R projection operators

$$\begin{aligned} \psi_L &= P_L\psi = \tfrac{1}{2}(1-\gamma_5)\psi, \\ \psi_R &= P_R\psi = \tfrac{1}{2}(1+\gamma_5)\psi, \end{aligned} \qquad \psi = \begin{pmatrix} \psi_L \\ \psi_R \end{pmatrix}, \tag{1.31}$$

where γ^5 is a Dirac gamma matrix. For the fermion f the left- and right-handed components of the Dirac field ψ_f are denoted accordingly as ψ_{f_L} and ψ_{f_R}.

By substitution of equations 1.14 and 1.18, the interaction term of the electroweak Lagrangian can be rewritten as

$$\mathcal{L}_{\text{int}}^{\text{EW}} = -\frac{g}{2\sqrt{2}}(W_\mu^+ J_+^\mu + W_\mu^- J_-^\mu) - eA_\mu J_{\text{em}}^\mu - \frac{g}{\cos\theta_W} Z_\mu J_0^\mu. \tag{1.32}$$

The total charged weak currents $J_\pm^\mu$ have the form

$$J_\pm^\mu = \sum_i \left[j_\pm^\mu(\ell_i \to \nu_i) + j_\pm^\mu(d_i \to u_i) \right], \tag{1.33}$$

where the charged weak currents for quarks, without the quark mixing term, are defined as

$$j_\mu^+ = j_\mu(d \to u) = \bar{\psi}_{u_L}\gamma_\mu\psi_{d_L} = \bar{\psi}_u\gamma_\mu\tfrac{1}{2}(1-\gamma_5)\psi_d, \tag{1.34}$$

$$j_\mu^- = j_\mu^\dagger(d \to u) = \bar{\psi}_{d_L}\gamma_\mu\psi_{u_L} = \bar{\psi}_d\gamma_\mu\tfrac{1}{2}(1-\gamma_5)\psi_u. \tag{1.35}$$

Here $j_\pm^\mu$ and $j_\mu^\pm$ are a contravariant and the corresponding covariant tensors. For leptons the weak currents are defined in a similar way.

The electromagnetic current J_{em}^μ and the neutral current J_0^μ are defined, respectively, as

$$J_{\text{em}}^\mu = \sum_f Q^f \bar{\psi}_f \gamma^\mu \psi_f, \tag{1.36}$$

and

$$J_0^\mu = \sum_f \bar{\psi}_f \gamma^\mu \tfrac{1}{2}(c_v^f - c_a^f\gamma^5)\psi_f, \tag{1.37}$$

$$c_v^f = T_3^f - 2Q^f \sin^2\theta_W, \quad c_a^f = T_3^f. \tag{1.38}$$

The coupling coefficients for the neutral weak interaction are listed in Table 1.3.

Fermions	c_v^f	c_a^f
ν_e, ν_μ, ν_τ	$+\frac{1}{2}$	$+\frac{1}{2}$
e, μ, τ	$-\frac{1}{2} + 2\sin^2\theta_W$	$-\frac{1}{2}$
u, c, t	$+\frac{1}{2} - \frac{4}{3}\sin^2\theta_W$	$+\frac{1}{2}$
d, s, b	$-\frac{1}{2} - \frac{2}{3}\sin^2\theta_W$	$-\frac{1}{2}$

Table 1.3: Neutral current vector and axial-vector couplings for fermions.

Due to $\sin^2\theta_W \approx 0.23$, the vector coupling constants for leptons are suppressed $c_v^{e,\mu,\tau} \approx -0.04$ with respect to the axial-vector couplings. In case of a no mixing angle θ_W, the weak interaction would be dependent only in the term T_3^f.

Interaction vertices for the weak interaction with a γ photon, a neutral current Z^0 boson and a charged current W^+ boson with fermions are shown in Figure 1.2.

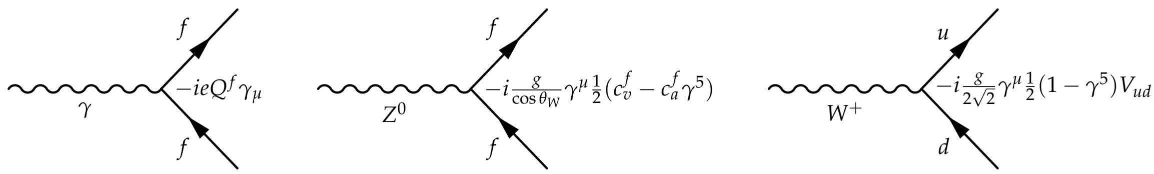

Figure 1.2: Weak interaction vertices with fermions for γ photon (left), neutral current Z^0 boson (middle) and charged current W^+ boson (right).

1.1.5 Fermion mixing

In this paragraph the "mass basis" is noted as ψ, while the "flavour basis" is referred to as ψ'. The transformation from the mass basis to the flavour basis has the form

$$\psi'_{\vec{f}_\mathcal{T}} = U^f_\mathcal{T}\psi_{\vec{f}_\mathcal{T}} \qquad U^{f\dagger}_\mathcal{T}U^f_\mathcal{T} = I, \quad \mathcal{T} = L, R, \quad f = u, d, \nu, \ell. \tag{1.39}$$

After substitution of $\psi \to \psi'$ in the Standard Model Lagrangian, all the coupling matrices G_f are transformed to the diagonal form. The substitution affects only the weak interaction, as described in the following.

The electromagnetic j_μ^{em} and the neutral weak j_μ^0 currents can be broken down to terms like $\bar{\psi}'_{\vec{f}_\mathcal{T}}\gamma_\mu\psi'_{\vec{f}_\mathcal{T}}$, where the summation over $\vec{f}$ family index $i = 1, 2, 3$ (like in scalar product) is assumed. This term is invariant under the flavour-to-mass basis transformation, as it follows from

$$\bar{\psi}'_{\vec{f}_\mathcal{T}}\gamma_\mu\psi'_{\vec{f}_\mathcal{T}} = (\bar{\psi}_{\vec{f}_\mathcal{T}}U^{f\dagger}_\mathcal{T})\gamma_\mu(U^f_\mathcal{T}\psi_{\vec{f}_\mathcal{T}}) = \bar{\psi}_{\vec{f}_\mathcal{T}}\gamma_\mu(U^{f\dagger}_\mathcal{T}U^f_\mathcal{T})\psi_{\vec{f}_\mathcal{T}} = \bar{\psi}_{\vec{f}_\mathcal{T}}\gamma_\mu\psi_{\vec{f}_\mathcal{T}}. \tag{1.40}$$

Due to this invariance *Flavour Changing Neutral Currents* (FCNC) do not exist in the Standard Model, which gives room for beyond the Standard Model searches in this direction.

The charged weak currents $j_\mu^\pm$ can be broken down to terms like $\overline{\psi}'_{\vec{u}_L}\gamma_\mu\psi'_{\vec{d}_L}$ and $\overline{\psi}'_{\vec{d}_L}\gamma_\mu\psi'_{\vec{u}_L}$, which after substitution convert to terms like

$$\begin{aligned}\overline{\psi}'_{\vec{u}_L}\gamma_\mu\psi'_{\vec{d}_L} &= \overline{\psi}_{\vec{d}_L}\gamma_\mu(U_L^{u\dagger}U_L^d)\psi_{\vec{u}_L} = \overline{\psi}_{\vec{d}_L}\gamma_\mu V^q\psi_{\vec{u}_L},\\ \overline{\psi}'_{\vec{d}_L}\gamma_\mu\psi'_{\vec{u}_L} &= \overline{\psi}_{\vec{d}_L}\gamma_\mu(U_L^{d\dagger}U_L^u)\psi_{\vec{u}_L} = \overline{\psi}_{\vec{d}_L}\gamma_\mu V^{q\dagger}\psi_{\vec{u}_L},\end{aligned} \qquad V^q = U_L^{u\dagger}U_L^d = \begin{pmatrix} V_{ud} & V_{us} & V_{ub} \\ V_{cd} & V_{cs} & V_{cb} \\ V_{td} & V_{ts} & V_{tb}\end{pmatrix}. \tag{1.41}$$

The V^q is called the *Cabibbo-Kobayashi-Maskawa* (*CKM*) matrix.

Similarly for leptonic terms $\overline{\psi}'_{\vec{\nu}_L}\gamma_\mu\psi'_{\vec{\ell}_L}$ and $\overline{\psi}'_{\vec{\ell}_L}\gamma_\mu\psi'_{\vec{\nu}_L}$ and after substitution one obtains

$$\begin{aligned}\overline{\psi}'_{\vec{\nu}_L}\gamma_\mu\psi'_{\vec{\ell}_L} &= \overline{\psi}_{\vec{\nu}_L}\gamma_\mu(U_L^{\nu\dagger}U_L^\ell)\psi_{\vec{\ell}_L} = \overline{\psi}_{\vec{\nu}_L}\gamma_\mu V^\nu\psi_{\vec{\ell}_L},\\ \overline{\psi}'_{\vec{\ell}_L}\gamma_\mu\psi'_{\vec{\nu}_L} &= \overline{\psi}_{\vec{\ell}_L}\gamma_\mu(U_L^{\ell\dagger}U_L^\nu)\psi_{\vec{\nu}_L} = \overline{\psi}_{\vec{\ell}_L}\gamma_\mu V^{\nu\dagger}\psi_{\vec{\nu}_L},\end{aligned} \qquad V^\nu = U_L^{\nu\dagger}U_L^\ell = \begin{pmatrix} V_{e1} & V_{e2} & V_{e3} \\ V_{\mu1} & V_{\mu2} & V_{\mu3} \\ V_{\tau1} & V_{\tau2} & V_{\tau3}\end{pmatrix}. \tag{1.42}$$

The V^ν is called the *Pontecorvo-Maki-Nakagawa-Sakata* (PMNS) matrix and is responsible for neutrino mixing.

Both V^q and V^ν matrices are unitary. Due to the unitarity, the parameters of each matrix can be reduced to three mixing angles θ_{12}, θ_{23}, θ_{13} and one phase factor δ. The matrices can be represented as sequential rotations in corresponding planes

$$V = \begin{pmatrix} 1 & 0 & 0 \\ 0 & c_{23} & s_{23} \\ 0 & -s_{23} & c_{23}\end{pmatrix}\begin{pmatrix} c_{13} & 0 & s_{13}e^{-\delta} \\ 0 & 1 & 0 \\ -s_{13}e^{i\delta} & 0 & c_{13}\end{pmatrix}\begin{pmatrix} c_{12} & s_{12} & 0 \\ -s_{12} & c_{12} & 0 \\ 0 & 0 & 1\end{pmatrix}, \qquad \begin{aligned} s_{\alpha\beta} &\equiv \sin\theta_{\alpha\beta},\\ c_{\alpha\beta} &\equiv \cos\theta_{\alpha\beta}.\end{aligned} \tag{1.43}$$

In case of the CKM matrix, the $\theta_{\alpha\beta}$ angle is called Cabibo mixing angle and the phase factor δ represents a source of CP-violation.

1.2 Supersymmetry

Despite all success of the Standard Model, as it was mentioned earlier, there are many open questions, which are left unanswered. Searches for *Physics Beyond the Standard Model* (BSM) are very intensive. Supersymmetric theories have an internal beauty and coherence to a much larger extent, than many other BSM proposals.

In this section, some of these arguments and the open problems, which could be solved by the supersymmetry are briefly discussed. In addition, a short general overview of the supersymmetry and the *Minimal Supersymmetric Extension of the Standard Model* (MSSM) is given.

1.2.1 Open questions

If supersymmetry is considered, it may solve some open problems of the Standard Model.

Hierarchy problem

In particle physics, the hierarchy problem can be formulated as the question: why is the Higgs-boson mass much lighter than the Planck mass M_P, which is an order of 10^{19} GeV.

If coupling to the Higgs field by a fermion f is present in the Lagrangian as the term $-g_f\,\bar{\psi}_f H \psi_f$, the Feynman diagram from Figure 1.3 (top) gives the correction:

$$\Delta m_H^2 = -\frac{|g_f|^2}{8\pi^2}\Lambda_{\mathrm{UV}}^2 + \ldots, \tag{1.44}$$

where Λ_{UV} is an ultraviolet cut-off for the loop integral regularisation and f denotes leptons or quarks. In case of quarks, each colour has to be counted separately. In general, each fermion

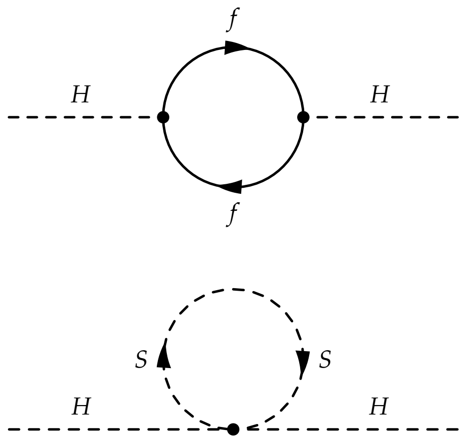

Figure 1.3: One-loop quantum corrections for the Higgs-boson mass from a fermion f (top) and a scalar particle S (bottom).

from the Standard Model is adding its contribution, but the largest correction comes from the top quark with $g_f \approx 1$. Assuming, that Λ_{UV} has an order of magnitude of the Planck mass M_P, the quantum correction to m_H^2 is about 30 orders of magnitude higher than m_H^2, which is about 10^4 GeV^2.

Assuming also, that there exists a complex scalar particle S with a mass m_S, which is present in the Lagrangian as a term $-\lambda_S\,|H|^2\,|S|^2$, the Feynman diagram from Figure 1.3 (bottom) gives a correction:

$$\Delta m_H^2 = \frac{\lambda_S}{16\pi^2}\left[\Lambda_{\mathrm{UV}}^2 - 2m_S^2 \ln(\Lambda_{\mathrm{UV}}/m_S) + \ldots\right]. \tag{1.45}$$

Comparing these two equations, one can see, that if for each fermion there exist two particles whith $\lambda_S = |g_f|^2$, then Λ_{UV}^2 will vanish from each fermion correction.

Supersymmetry introduces a symmetry between fermions and bosons and provides a natural way to cancel the Λ_{UV}^2 term.

Grand Unified Theory

After the unification of electromagnetic and weak interactions in the electroweak force, the next natural step would be to unify strong and electroweak interactions. The running coupling constants for the Standard Model are coming close to each other, but do not intersect at one point, see Figure 1.4 (left), while for the Minimal Supersymmetric Extension of the Standard Model (MSSM), this unification is achievable at about 10^{16} GeV (right).

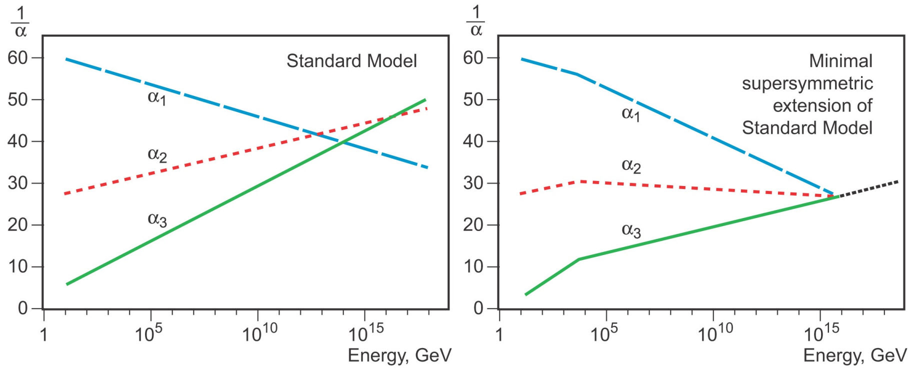

Figure 1.4: Running coupling constants for the Standard Model (left) and the Minimal Supersymmetric Extension of the Standard Model (right) [6].

Dark matter

Evidence for the existence of dark matter comes from astronomical measurements. Some disagreements between the expected and the observed results, pointing to dark matter are:

– ***Galaxy rotation curves***
  The measured velocity of rotation as a function of the distance from the galactic centre. The observed rotational curves for spiral galaxies have flatness, which cannot be explained by the visible matter only. The existence of an additional invisible mass (the dark matter) can explain the experimental observations of the velocity curves.

– ***Galaxies velocity dispersions***
  By measuring the radial velocities of a group of objects (clusters, galaxies, . . .), the cluster mass can be estimated from the *virial theorem*. The observations show a difference of about ten times. These measurements have pushed the fraction of the dark matter to about 95%.

– ***Gravitational lensing***
  This is an effect, when the light from a background source, which is located on a larger distance is "bent" by a massive object placed between the source and the observer. Based on this lensing it is possible to estimate the mass of the object and compare this with the visible mass. The comparisons show, that for lensing an extra mass is needed.

These and many other arguments are pointing to *Weakly Interacting Massive Particles* (WIMP). A natural candidate for such a particle does not exist in the Standard Model, while for supersymmetric models this can be a neutralino.

1.2.2 Superspace and superalgebra

In this section the mathematical background for the supersymmetry is shortly presented. The description follows Refs.[7, 8].

Superspace

Consider a vector space V over the field $\mathbb{F}$ with characteristic 0. In physics cases, the $\mathbb{F}$ is either the real $\mathbb{R}$ or the complex $\mathbb{C}$ field.

A vector space V over $\mathbb{F}$ is called a *supervector space* or *superspace* if it is $\mathbb{Z}_2$-graded, i.e., it may be composed as a direct sum of two vector spaces:

$$V = V_0 \oplus V_1, \quad 0, 1 \in \mathbb{Z}_2, \tag{1.46}$$

where $\mathbb{Z}_2$ is two-element finite field $\mathbb{Z}_2 = \mathbb{Z}/2\mathbb{Z}$. The elements of V_0 and V_1 are called *even* and *odd*, respectively. The dimension of V is defined as $d_0|d_1$, where d_i is the dimension of V_i. The elements from V_0 and V_1 are called *pure* vectors. The *parity* function p can be defined for a non-zero pure vector x as the $p(x) = 0$ for an even and $p(x) = 1$ for an odd vector.

The $V = \mathbb{F}^{p|q}$ super vector space is defined as vector space $\mathbb{F}^{p+q}$ with an even and odd spaces defined as $V_0 = \mathbb{F}^p$ and $V_1 = \mathbb{F}^q$.

The *super homomorphism* $T : U \to V$ of superspaces U and V is defined as homomorphism of corresponding vector spaces, that preserve grading, i.e. $T(U_i) \in V_i$, for $i = 0, 1$.

The direct sum of U and V superspaces is defined as superspace $W = U \oplus V$, with

$$W_0 = (U_0 \oplus V_0) \quad \text{and} \quad W_1 = (U_1 \oplus V_1), \tag{1.47}$$

while the tensor product is defined as superspace $W = U \otimes V$, with

$$W_0 = (U_0 \otimes V_0) \oplus (U_1 \otimes V_1) \quad \text{and} \quad W_1 = (U_0 \otimes V_1) \oplus (U_1 \otimes V_0). \tag{1.48}$$

Superalgebra

A *superalgebra* A is a vector superspace $A = A_0 \oplus A_1$ which is an associative algebra with a unity element $\mathbb{1}$. The multiplication is a morphism, and for pure vectors

$$p(xy) = p(x) + p(y) \pmod 2, \quad \forall x, y \in A_0 \cup A_1. \tag{1.49}$$

It is easy to check, that the unity element is always even $p(\mathbb{1}) = 0$, the subalgebra A_0 is purely even $A_0 A_0 \subseteq A_0$, and that $A_0 A_1 \subseteq A_1$ and $A_1 A_1 \subseteq A_0$.

A superalgebra A is called *supercommutative*, if for all pure vectors

$$xy = (-1)^{p(x)p(y)} yx, \quad \forall x, y \in A_0 \cup A_1. \tag{1.50}$$

For odd vectors x and y of commutative superalgebra A following conditions hold:

$$xy + yx = 0, \quad x^2 = 0, \quad \forall x, y \in A_1. \tag{1.51}$$

An important example of a supercommutative algebra is the *exterior algebra* (or *Grassmann algebra*). The exterior algebra $\wedge(V)$ of a vector space V is defined as *quotient algebra* of the *tensor algebra* $T(V)$ by the two-sided ideal I

$$\wedge(V) = T(V)/I. \tag{1.52}$$

The ideal I is generated by all elements of the form $x \otimes x$, such that $x \in V$, i.e. is the vector subspace of $T(V)$ spanned by elements of the form

$$a_i \otimes (x_i \otimes x_i) \otimes b_i, \quad x_i \in V, \ a_i, b_i \in T(V). \tag{1.53}$$

The $\wedge$ operation induced from the tensor product $\otimes$ and defined as:

$$x \wedge y = x \otimes y \pmod{I}. \tag{1.54}$$

The following important relations fulfil:

$$x \wedge y + y \wedge x = 0, \quad x \wedge x = 0, \quad \forall x, y \in \wedge(V). \tag{1.55}$$

The k-th exterior power of V, referred to as $\wedge^k(V)$, is the vector subspace of $\wedge(V)$ spanned by elements of the form

$$x_1 \wedge x_2 \wedge \cdots \wedge x_k, \quad x_i \in V, \ i = 1, 2, \ldots, k. \tag{1.56}$$

By convention $\wedge^0(V) = \mathbb{F}$ and $\wedge^1(V) = V$.

The $\wedge(V)$ can be presented as sum of only even and only odd powers k of $\wedge^k(V)$ spaces, which are called the *even* (*commutative*) and the *odd* (*anti-commutative*) elements of the $\wedge(V)$. It is easy to check, that even elements are commute between each other and with odd elements, while odd elements are anticommute between each other.

A *super Lie algebra* is defined as a vector superspace A with a bracket $[\cdot, \cdot]$, which is a supermorphism from $A \oplus A \to A$ and fulfils the following properties:

$$[x, y] + (-1)^{p(x)p(y)}[y, x] = 0 \tag{1.57}$$

and the *super Jacobi identity*

$$(-1)^{p(x)p(z)}[x, [y, z]] + (-1)^{p(y)p(x)}[y, [z, x]] + (-1)^{p(z)p(y)}[z, [x, y]] = 0. \tag{1.58}$$

Poincare superalgebra

The *Poincare superalgebra* $G = G_0 \oplus G_1$ extends the Poincare Lie algebra with odd generators. According to the Coleman-Mandula theorem [9], an even G_0 part of the superalgebra G contains Poincare Lie group generators P_μ and $M_{\mu\nu}$ which are in direct sum with other semisimple compact Lie group generators T_i. The following relations fulfil:

$$\begin{aligned}
\left[M_{\mu\nu}, M_{\rho\sigma}\right] &= i\eta_{\mu\sigma}M_{\nu\rho} - i\eta_{\mu\rho}M_{\nu\sigma} + i\eta_{\nu\rho}M_{\mu\sigma} - i\eta_{\nu\sigma}M_{\mu\rho}, \\
\left[M_{\mu\nu}, P_\rho\right] &= i\eta_{\nu\rho}P_\mu - i\eta_{\mu\rho}P_\nu, \qquad \left[P_\mu, P_\nu\right] = 0, \\
\left[T_i, T_j\right] &= ic_{ij}^k T_k, \qquad \left[T_i, P_\mu\right] = 0, \qquad \left[T_i, M_{\mu\nu}\right] = 0.
\end{aligned} \tag{1.59}$$

The metric in the *Minkowski space* is defined as

$$\eta_{\mu\nu} = \mathrm{diag}(1, -1, -1, -1), \tag{1.60}$$

while the generators are defined using the following representations of the Lorentz group:

$$P_\mu = (\tfrac{1}{2}, \tfrac{1}{2}), \qquad M_{\mu\nu} = (1,0) \oplus (0,1), \qquad T_i = (0,0). \tag{1.61}$$

For an odd G_1 part of the superalgebra G any unitary representation can be generated by a Lorenz spinors Q_α^I and $\overline{Q}_{\dot\alpha}^I$, where $I = 1, \ldots, n$ [8]. The dimension of the supersymmetry is defined depending on the number of indices of I, for example, in case of only one index, it is called $N = 1$ supersymmetry.

Considering the case for $N = 1$ supersymmetry, and leaving only Q_α and $\overline{Q}_{\dot\alpha}$, one can obtain the following equations:

$$\begin{aligned}
\left\{Q_\alpha, \overline{Q}_{\dot\beta}\right\} &= 2\sigma^\mu_{\alpha\dot\beta}P_\mu, \\
\left\{Q_\alpha, Q_\beta\right\} &= \left\{\overline{Q}_{\dot\alpha}, \overline{Q}_{\dot\beta}\right\} = 0, \\
\left[P_\mu, Q_\alpha\right] &= \left[P_\mu, \overline{Q}_{\dot\alpha}\right] = 0,
\end{aligned} \tag{1.62}$$

and for the rest of the generators:

$$\begin{aligned}
\left[M_{\mu\nu}, Q_\alpha\right] &= i(\sigma_{\mu\nu})_\alpha{}^\beta Q_\beta, \qquad \left[Q_\alpha, T_i\right] = b_i Q_\alpha, \\
\left[M_{\mu\nu}, \overline{Q}^{\dot\alpha}\right] &= i(\bar\sigma_{\mu\nu})^{\dot\alpha}{}_{\dot\beta}\overline{Q}^{\dot\beta}, \qquad \left[\overline{Q}_{\dot\alpha}, T_i\right] = -\overline{Q}_{\dot\alpha} b_i,
\end{aligned} \tag{1.63}$$

where $b_i = \bar{b}_i$ are Hermitian matrices realising the representation of the T_i Lie algebra:

$$\left[b_i, b_j\right] = ic_{ij}^k b_k. \tag{1.64}$$

The generators Q_α and $\overline{Q}_{\dot\alpha}$ are described by the following representations of the Lorentz group:

$$Q_\alpha = (\tfrac{1}{2}, 0), \qquad \overline{Q}_{\dot\alpha} = (0, \tfrac{1}{2}). \tag{1.65}$$

The σ^μ are the Pauli matrices. The $\bar\sigma^\mu$ and commutators $\sigma_{\mu\nu}$ and $\bar\sigma_{\mu\nu}$ are defined as:

$$\bar\sigma^\mu_{\dot\beta\alpha} = \sigma^\mu_{\alpha\dot\beta}, \qquad \sigma_{\mu\nu} = -\tfrac{1}{4}(\sigma_\mu\bar\sigma_\nu - \sigma_\nu\bar\sigma_\mu), \qquad \bar\sigma_{\mu\nu} = -\tfrac{1}{4}(\bar\sigma_\mu\sigma_\nu - \bar\sigma_\nu\sigma_\mu). \tag{1.66}$$

Taking into account commutational relations, one can check, that the first Casimir operator for the Poincare Lie group:

$$C_1 = -P^\mu P_\mu \tag{1.67}$$

commutes with Q_α and $\overline{Q}_{\dot{\alpha}}$ generators and therefore is a Casimir operator for the Poincare superalgebra. For an irreducible representation of Poincare superalgebra all particles have equal masses $C_1 = m^2$, therefore for realistic theories supersymmetry has to be broken.

1.2.3 The Minimal Supersymmetric Standard Model

The *Minimal Supersymmetric Standard Model* (MSSM) is a supersymmetric extension of the Standard Model which adds the minimal number of new particles with interactions consistent with those of the Standard Model. The MSSM is the $N = 1$ supersymmetry. The chiral supermultiplet fields are presented in Table 1.4. The gauge supermultiplet fields before symmetry breaking are shown in Table 1.5.

Particle Names		Spin-$\frac{1}{2}$	Spin-0	$SU(3)_C \otimes SU(2)_L \otimes U(1)_Y$		
quarks, squarks	Q_i	$\begin{pmatrix} u_{L_i} \\ d_{L_i} \end{pmatrix}$	$\begin{pmatrix} \tilde{u}_{L_i} \\ \tilde{d}_{L_i} \end{pmatrix}$	3	2	$+\frac{1}{3}$
	$\bar{u}_i$	$u^\dagger_{R_i}$	$\tilde{u}^*_{R_i}$	$\bar{3}$	1	$-\frac{4}{3}$
	$\bar{d}_i$	$d^\dagger_{R_i}$	$\tilde{d}^*_{R_i}$	$\bar{3}$	1	$+\frac{2}{3}$
leptons, sleptons	L_i	$\begin{pmatrix} \tilde{\nu}_{Li} \\ \tilde{\ell}_{Li} \end{pmatrix}$	$\begin{pmatrix} \nu_{Li} \\ \ell_{Li} \end{pmatrix}$	1	2	-1
	$\bar{\ell}_i$	$\ell^\dagger_{R_i}$	$\tilde{\ell}^*_{R_i}$	1	1	$+2$
higgsinos, higgs	H_u	$\begin{pmatrix} \widetilde{H}^+_u \\ \widetilde{H}^0_u \end{pmatrix}$	$\begin{pmatrix} H^+_u \\ H^0_u \end{pmatrix}$	1	2	-1
	H_d	$\begin{pmatrix} \widetilde{H}^0_d \\ \widetilde{H}^-_d \end{pmatrix}$	$\begin{pmatrix} H^0_d \\ H^-_d \end{pmatrix}$	1	2	$+1$

Table 1.4: Chiral supermultiplet fields in the MSSM.

Particle Names	Spin-$\frac{1}{2}$	Spin-1	$SU(3)_C \otimes SU(2)_L \otimes U(1)_Y$		
gluinos, gluons	$\tilde{g}$	g	8	1	0
winos, W-bosons	$\widetilde{W}^0, \widetilde{W}^\pm$	$W^0, W^\pm$	1	3	0
bino, B-boson	$\widetilde{B}^0$	B^0	1	1	0

Table 1.5: Gauge supermultiplet fields in the MSSM before symmetry breaking.

The MSSM Lagrangian can be described as follows:

$$\mathcal{L}_{\text{MSSM}} = \mathcal{L}_{\text{Gauge}} + \mathcal{L}_{\text{Yukawa}} + \mathcal{L}_{\text{Scalar}} + \mathcal{L}_{\text{Soft}}. \tag{1.68}$$

For the MSSM the superpotential W which conserves the baryon and lepton number (R-parity conservation) is defined similarly to the Standard Model:

$$W = QG_u\bar{u}\cdot H_u + QG_d\bar{d}\cdot H_d + LG_\ell\bar{\ell}\cdot H_d + \mu H_u\cdot H_d \tag{1.69}$$

In the MSSM all coupling constants and G_f matrices (Yukawa couplings) are exactly the same as those used in the Standard Model, the only new coupling appears in the μ-term ($\mu H_u\cdot H_d$). The corresponding dot product is defined as

$$H_u\cdot H_d = H_u^+ H_d^- - H_u^0 H_d^0. \tag{1.70}$$

R-parity conservation

The gauge-invariant and renormalisable superpotential may also include terms which violate the baryon and lepton number. Three terms which violate the lepton number are:

$$W_{\Delta L=1} = \epsilon_i L_i H_u + \lambda_{ijk} L_i L_j \bar{\ell}_k + \lambda'_{ijk} L_i Q_j \bar{d}_k, \tag{1.71}$$

while the baryon number violating term is:

$$W_{\Delta B=1} = \lambda''_{ijk}\bar{u}_i\bar{d}_j\bar{d}_k. \tag{1.72}$$

The presence of both of them (i.e. baryon violating term and any of the lepton violating terms) in the Lagrangian will lead to proton decay. Since the proton is quite stable, with a lifetime larger than 10^{33} years, the coupling constants, which lead to the decay should be very small. One possibility is to set these couplings to zero. This can be done by postulating R-parity conservation.

The R-parity is defined as:

$$R = (-1)^{3(B-L)+2s}, \tag{1.73}$$

where B and L are baryon and lepton numbers, respectively, and s corresponds to the spin of the particle.

The R-parity conservation implies that:

- The *Lightest Supersymmetric Particle* (LSP) is stable;
- The decay cascade of any supersymmetric particle must finish with an odd number of LSPs;
- At the LHC, supersymmetric particles can be produced only in pairs.

Soft supersymmetry breaking

Since supersymmetry is not yet observed, if it exists, it should be spontaneously broken, to allow for high masses of the superpartners. Different possible terms for a soft supersymmetry breaking are listed below:

- ***Gaugino mass terms***: related to three vector superfields ($\widetilde{B}$, $\widetilde{W}$ and $\widetilde{G}$), the corresponding mass terms are $M_1\widetilde{B}\widetilde{B}$, $M_2\widetilde{W}\widetilde{W}$ and $M_3\widetilde{G}\widetilde{G}$.

– ***Scalar mass term***: for each scalar superfield $m\phi_i^*\phi_j$ can be added. If the generation indices i and j are different, this term leads to flavour violation.

– ***Trilinear scalar couplings***: three trilinear couplings $A^u_{ij}\widetilde{Q}_i\bar{u}_jH_d$, $A^d_{ij}\widetilde{Q}_i\bar{d}_jH_u$ and $A^\ell_{ij}\widetilde{L}_i\bar{\ell}_jH_u$.

– ***Bilinear scalar couplings***: this term can be defined as BH_uH_d. This is the only gauge invariant bilinear scalar coupling, after the scalar mass term.

The soft supersymmetry breaking terms mentioned above do not include the part, related to the $SU(2)_L \otimes U(1)_Y \to U(1)_Y$ symmetry breaking. The Standard Model-like spontaneous symmetry breaking is discussed below.

Electroweak symmetry breaking

Both neutral Higgs fields H_u^0 and H_d^0 are getting non-zero vacuum expectation values:

$$< H_u^0 >= \frac{v_u}{\sqrt{2}}, \quad < H_d^0 >= \frac{v_d}{\sqrt{2}}. \tag{1.74}$$

One constraint on these values can be fixed from experiment, in particular, from Z^0 and $W^\pm$ boson masses, since

$$\begin{aligned} m_W^2 &= \tfrac{1}{4}g^2(v_u^2+v_d^2), \\ m_Z^2 &= \tfrac{1}{4}(g^2+g'^2)(v_u^2+v_d^2), \\ v_u^2+v_d^2 &= v^2 = \frac{4m_W^2}{g^2}, \quad v \approx 246 \text{ GeV}, \end{aligned} \tag{1.75}$$

here v is the vacuum expectation value (*vev*) for the Standard Model Higgs field.

The ratio between *vev*s is chosen as a second constraint

$$\tan\beta \equiv \frac{v_u}{v_d}, \tag{1.76}$$

the value of $\tan\beta$ is not fixed experimentally, but can be calculated from the other MSSM parameters. Since both $v_u = v\sin\beta$ and $v_d = v\cos\beta$ are positive, it is required by convention that $0 < \beta < \pi/2$.

After electroweak symmetry breaking the two Higgs doublets are converted to three massive $W^\pm$ and Z^0 bosons and five Higgs particles:

– two CP-even neutral scalar particles h^0 and H^0 (by convention $m_{h^0} < m_{H^0}$);

– one CP-odd neutral scalar particle A^0;

– two charged scalar particles H^+ and H^- with charge $+1$ and -1, respectively.

At tree level the mass of the h^0 can be constrained as

$$m_{h^0} < m_Z\,|\cos 2\beta| < m_Z. \tag{1.77}$$

From this constraint $m_{h^0} < 91$ GeV, but after one-loop corrections, the constraint is weakened up to $m_{h^0} < 135$ GeV, which is consistent to the observed Higgs particle at 125 GeV.

Particle spectrum

The list of MSSM particles after symmetry breaking is shown in Table 1.6. It is assumed, that for the first two generations of sfermions the mixing is negligible.

Particle Names	Spin	P_R	Gauge Eigenstates	Mass Eigenstates
Higgs bosons	0	+1	$H_u^0, H_d^0, H_u^+, H_d^-$	h^0, H^0, A^0, H^+, H^-
squarks 3-rd gen.	0	-1	$\tilde{t}_L, \tilde{t}_R, \tilde{b}_L, \tilde{b}_R$	$\tilde{t}_1, \tilde{t}_2, \tilde{b}_1, \tilde{b}_2$
sleptons 3-rd gen.	0	-1	$\tilde{\tau}_L, \tilde{\tau}_R, \tilde{\nu}_\tau$	$\tilde{\tau}_1, \tilde{\tau}_2, \tilde{\nu}_\tau$
neutralinos	$\frac{1}{2}$	-1	$\widetilde{B}^0, \widetilde{W}^0, \widetilde{H}_u^0, \widetilde{H}_d^0$	$\tilde{\chi}_1^0, \tilde{\chi}_2^0, \tilde{\chi}_3^0, \tilde{\chi}_4^0$
charginos	$\frac{1}{2}$	-1	$\widetilde{W}^+, \widetilde{W}^-, \widetilde{H}_u^+, \widetilde{H}_d^-$	$\tilde{\chi}_1^+, \tilde{\chi}_1^-, \tilde{\chi}_2^+, \tilde{\chi}_2^-$
gluino	$\frac{1}{2}$	-1	$\tilde{g}$	$\tilde{g}$

Table 1.6: The gauge and mass eigenstates for the Minimal Supersymmetric Standard Model. It is assumed, that sfermion mixing for the first and second families is negligible [10].

1.3 Hadron-hadron interactions

Hadron-hadron collisions at high energies create events with a much more complex structure, than, for example, for the lepton colliders. The complexity of the structure makes it necessary to use multiparticle simulation to get valuable results [11, 12]. In this section a short overview of challenges for the simulation of hadron-hadron collisions and Monte Carlo generators [13, 14] used in the analysis is given.

Due to the high density of the colliding beams, each bunch contains about 10^{11} protons. Together with a hard scattering process, many soft elastic and inelastic scatterings are produced. The inelastic scatterings at $\sqrt{s} = 8$ TeV have very large cross section about 70 mb. The processes, involved at high-momentum transfer may be described with perturbative QCD, which is not the case for the soft scattering.

1.3.1 Parton Distribution Function

An attempt to avoid a detailed simulation of processes and to encapsulate all non-perturbative problems in a set of functions measurable on the experiment is used. With a good approximation, a decay cross section for the $AB \to X$ can be described based on *Parton Distribution Functions* (PDF). Considered, that the probability to find a parton a in the object A with a momentum fraction x_a of the total momentum of object A at the energy scale of the hard interaction μ^2 can be expressed by the function $f_{a/A}(x_a, \mu^2)$, where $f_{a/A}$ is mentioned as a distribution of density of the parton a in the A object. Accordingly, for parton b and object B the corresponding function will be $f_{b/B}(x_b, \mu^2)$. The cross section of the $AB \to X$ decay can be expressed as:

$$\sigma_{AB\to X} = \sum_{a,b} \int f_{a/A}(x_a, \mu^2)\, f_{b/B}(x_b, \mu^2)\, \hat{\sigma}_{ab\to X}\, dx_a dx_b \tag{1.78}$$

where $\hat{\sigma}_{ab\to X}$ is a partonic cross section, which can be computed using the perturbative approach. Following this approach, all non-perturbative parts are encapsulated inside the experimental measurements of the $f_{a/A}$ and $f_{b/B}$ functions.

The *Dokshitzer-Gribov-Lipatov-Altarelli-Parisi* (DGLAP) equation [15, 16, 17] is playing an important role for PDF studies. It describes the evolution of the PDF when varying the μ^2 parameter:

$$\frac{\partial f_q(x,\mu^2)}{\partial \log \mu^2} = \frac{\alpha_s}{2\pi} \int_x^1 \frac{dy}{y} f_q(y,\mu^2) P\left(\frac{x}{y}\right), \tag{1.79}$$

where P is the regularised splitting function ($P_{q\to qg}, P_{q\to gq}, P_{g\to gg}, P_{g\to q\bar{q}}$) and α_s is the coupling constant for the strong interaction. This equation is widely used for PDF analyses, since it allows to calculate $f_q(x,\mu^2)$ from the known values at a reference scale μ_0 and to compare the measurements of $f_q(x,\mu^2)$ from different experiments for different scales.

Different groups CTEQ [18, 19], MSTW [20], NNPDF [21, 22], HeraPDF [23] are using the DGLAP equation to calculate PDFs based on measurements, which are carried out by different experiments for different μ^2. An example of PDFs computed by the NNPDF collaboration for $\mu^2 = 10$ GeV^2 and $\mu^2 = 10^4$ GeV^2 is shown in Figure 1.5.

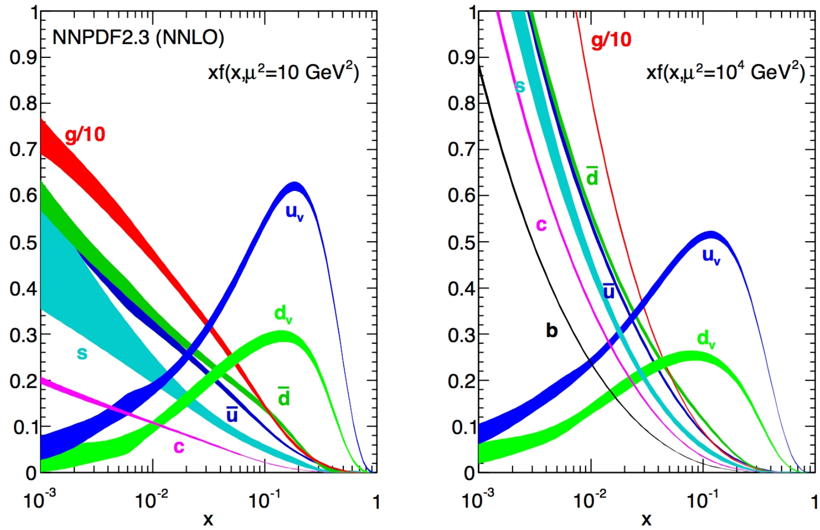

Figure 1.5: Distributions of PDFs at NNLO for $\mu^2 = 10$ GeV^2 (left) and $\mu^2 = 10^4$ GeV^2 (right) computed by the NNPDF collaboration [24].

The scale μ^2 used for cross section calculations in equation 1.79 is called factorisation scale μ_F. Since the equation also includes the $\hat{\sigma}_{ab\to X}$ calculation, which is done using a perturbative approach, it depends on the renormalisation scale μ_R. Since the results depend on the choice of the μ_F and μ_R scales, in the analysis, corresponding uncertainties have to be taken into account. Often for calculations a scale $\mu_F = \mu_R = \mu$, which is relevant for the considered hard interactions, is used.

1.3.2 Monte Carlo generators

The simulation of a hard interaction leads to the creation of a large number of 100-1000 particles with a large momentum spread. The most challenging problem is to make accurate predictions for QCD processes, which are out of computational reach for the complex final states. The two main problems are the evolution of the QCD states from short to long distances and the proper modelling of hadronic states.

The Monte Carlo generators [13, 14] should take care about multi parton scattering and re-scattering processes, as well as to convert partonic final states into colour-neutral hadrons. A sketch for a generated event is shown in Figure 1.6. Different modelling steps are shown with different colours.

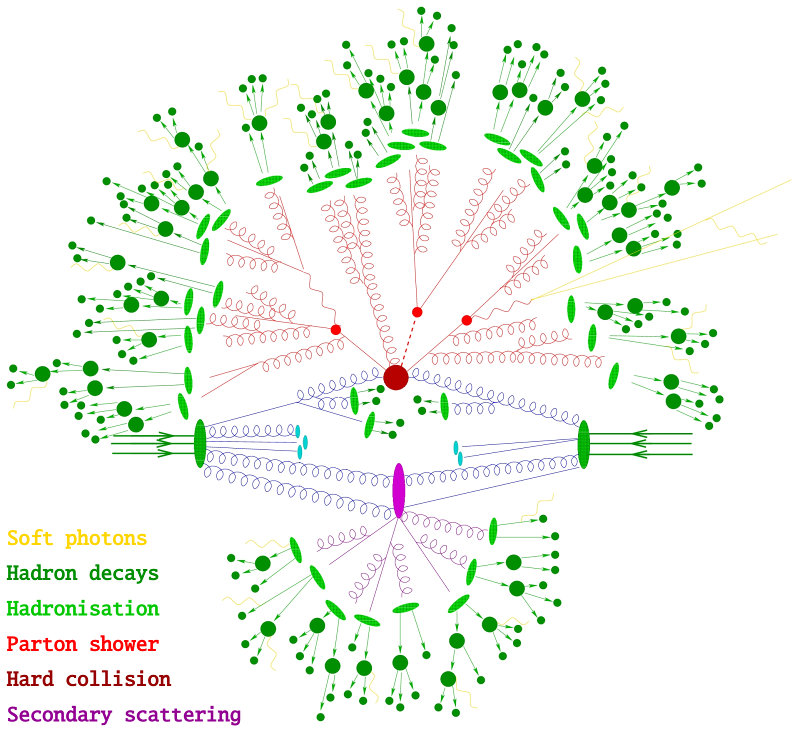

Figure 1.6: Sketch of a simulated event from a hadron-hadron collision. The dark red spot represents the hard collision, the purple blob corresponds to secondary hard scattering, the three structures around blobs are QCD radiation simulated by parton showers. The hadronisation of partons is shown as light green blobs, whereas dark green shows hadron decays, yellow lines are soft photon radiation [25].

The generation process can be divided into the following steps:

- ***Hard scattering*** is an interaction of the partons of the protons with a high momentum transfer with an annihilation or a scattering channel. It can be calculated using the matrix element based calculations, which are based on the perturbation approach.

- ***Parton shower*** simulates the shower of partons. Partons which are involved in the hard interaction emit gluons. Since gluons carry colour charges, they can emit other softer gluons. This shower propagates to produce more radiation with lower momentum, as long as perturbation theory can be applicable.

– ***Hadronisation*** models are used when perturbation theory cannot be used, for example due to low momentum of particles. It is responsible to group partons into colourless hadrons taking into account confinement.

– ***Underlying event*** is created from secondary hard interactions of the proton remnants. This produces soft objects everywhere in the event and contaminates the initial hard scattering process.

– ***Hadron decays*** models a decay of unstable hadrons, which was produced in one of the previous steps. This is usually done based on decay tables and decay channels, which are measured for different hadrons.

A more detailed explanation for each step is described in the following.

Hard scattering

The generation of the event starts from the computation of the hard scattering cross section. Calculations are performed at *Leading Order* (LO) or for more precision at *Next-to-Leading Order* (NLO). The calculation involves PDFs which are measured at lower energies and transferred to higher scales using the DGLAP equation 1.79. The generator uses tree-level matrix elements, usually to generate a $2 \to n$ process, while extra m partons are added later by the parton shower algorithm. Since this step may count some configurations twice, algorithms to resolve a double counting have to be used.

In cases, when NLO calculations are not available, one can use LO calculations for analysis, but with corrected cross section to the NLO prediction. This correction factor is called K-factor and is defined as a ratio between the next-to-leading order and the leading order inclusive cross sections:

$$K = \frac{\sigma_{NLO}}{\sigma_{LO}}. \tag{1.80}$$

The K-factor depends on the process, the factorisation scale as well as on the selection criteria used in the analysis. Nevertheless, under the assumption, that the leading order calculations model relative quantities well enough, one can improve the leading order predictions by applying the corresponding K-factors.

This approach is used for some leading order simulations for current analysis.

Parton showering

Partons involved in the hard scattering processes have large momenta and emit gluons. Since gluons carry colour charges, they also can emit other gluons or quarks. The shower propagates and produces more and more radiation with lower momenta. It constitutes part of the higher order corrections to the hard process, but due to its complexity, for calculations approximate approach is used, which takes into account only dominant contributions.

The parton shower algorithm introduces a parameter Q_0, which describes a minimal momentum $k_\perp$, below which the splitted results cannot be resolved. For $k_\perp > Q_0$ splitted partons are considered as *resolvable* and perturbation theory is applicable, otherwise they are considered *unresolvable*.

The probability, that a parton a will not split during the evolution from scale q_1^2 to q_2^2 is described by the *Sudakov Form Factor* (SFF), which is defined as:

$$\Delta_a(q_1^2, q_2^2) = \exp\left\{ -\int_{q_2^2}^{q_1^2} \frac{dq^2}{q^2} \frac{\alpha_s}{2\pi} \int_{Q_0^2/q^2}^{1-Q_0^2/q^2} P_{ba}(z)dz \right\}, \tag{1.81}$$

where P_{ba} is a function used in the DGLAP equation.

The algorithm of a parton shower generation can be described as follows:

– Starting with parton a at initial scale Q^2, by taking a random number R_1 uniformly distributed in the interval $[0, 1]$ and solving the equation $\Delta_a(Q^2, q_1^2) = R_1$, one can obtain the first splitting scale q_1^2.

– If $q_1 < Q_0^2$ the splitting is unresolvable and the showering of parton a is terminated, otherwise parton is split $a \to b + c$ and the procedure is repeated for partons b and c.

– These steps are repeated until all splittings will be below the resolvable scale Q_0^2.

Important parameters for parton shower algorithms are the Λ_{QCD} scale and the cut-off parameter Q_0. The Q_0 parameter is responsible for the termination of the parton shower and regularises the soft gluon singularity. To use perturbative QCD calculations $Q_0 \gg \Lambda_{\text{QCD}}$ should hold. Since Λ_{QCD} is about 200 MeV, the cut-off parameter Q_0 is taken to be about 1 GeV.

Since fixed order calculations are combined to the parton showering, double counting is possible. To avoid this dedicated algorithms are used, for example CKKW [26] or MLM [27].

Hadronisation

The hadronisation process is not calculable neither based on perturbative QCD techniques, nor with currently available non-perturbative approaches. Therefore the hadronisation is based on different models, which encapsulate general features of QCD. Two models are explained in the following:

– The ***string model*** uses an approach that at large distances the potential energy of colour sources increase linearly. This approach is based on the observation from lattice simulations of QCD. In this approach the colour field collapses into a string. When due to distance the potential energy between two partons increases up to the level of hadron masses, it is energetically favorable to break a string and to produce quark-antiquark pairs. This string segments will stretch again and produce more quark-antiquark pairs. This process will continue, until the whole energy will not be converted into pairs with short string segments. These segments can be identified as hadrons.

– The ***cluster model*** is based on the *preconfinement* property of QCD, which means, that for $q \ll Q$ partons are grouped in colourless clusters with an invariant mass distribution which depends only on q and Λ_{QCD} and does not depend on the scale or mode of initial hard process. For $Q_0 \approx 1$ GeV most clusters have masses below 3 GeV. Figure 1.7 shows, that for colour singlets the mass distribution does not depend on Q. Since masses are mainly below 3 GeV an isotropic quasi-two-body phase space model is used to decay into hadrons. For the higher-mass tail of the distribution a string-like model is used.

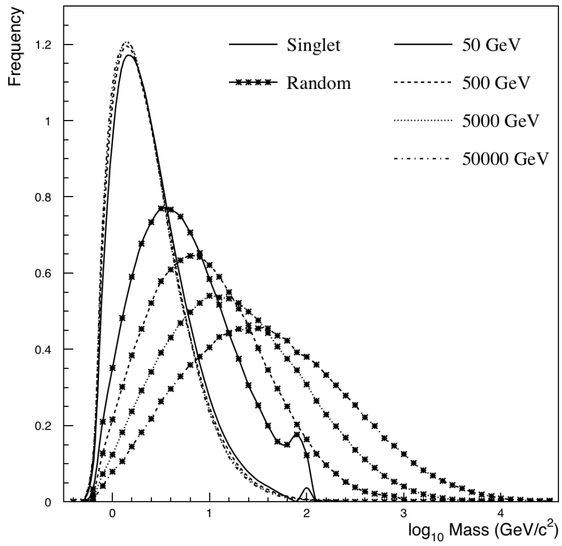

Figure 1.7: Distribution of colour singlet masses and random quark-antiquark combinations [28].

Hadron decays

This part of generation is modelling decays of all unstable hadrons produced on the hadronisation stage. Most decay modes and states are listed in the Review of Particle Physics [29]. In addition, generators should properly deal with many details, which are not listed in the list. The total sum of branching fractions should be unity, since the list may not contain all relevant decays, missing modes may need to be modelled by the generator. For hadronisation of heavy-flavour quarks, complete flavour multiplets must be included for proper modelling. In case of multiparticle decays, momentum distribution and spin correlations also have to be taken into account.

Underlying event and pile-up

Parts of the protons, which do not participate in the hard interaction, can also collide and contaminate existing events. The part of the event produced from collisions of proton remnants is called *underlying event*. The collisions, which are not associated to hard interactions are called *minimum-bias events*. Underlying and minimum-bias events contain soft interactions and cannot be calculated based on perturbative approach. Therefore different phenomenological models are used. These models contain different parameters, which are “tuned” based on the experimental data. For a better description of the underlying event and minimum-bias events, Monte Carlo generators were tuned using published data from the ATLAS and other (Tevatron, LEP) experiments [30, 31].

Independent proton-proton collisions, which superimposed on the main event are mentioned as a *pile-up*. Proton-proton collisions from the same bunch crossing are called *in-time pile-up*, while from different bunch crossings they are mentioned as *out-of-time pile-up*. The pile-up is modelled by taking into account an average number of interactions per bunch crossing $\langle \mu \rangle$ and a distance between bunches.

General-purpose event generators

For SUSY analyses samples are produced with different Monte Carlo generators. To produce samples the following leading-order (LO) generators are used:

- The PYTHIA is a program to generate high-energy physics events [32, 33], for the current analysis used for parton showering.
- The HERWIG++ is a general-purpose event generator for hard lepton-lepton, lepton-hadron and hadron-hadron processes [34]. In the current analysis it is used to simulate signal models.
- The SHERPA is a general purpose tool to simulate particle collisions for high energies [35]. For current $\sqrt{s} = 8$ TeV analyses, W+jets and Z+jets processes are generated using the SHERPA.
- The ALPGEN is used to generate hard multiparton processes in pp collisions [36]. For the current study it is used to generate W+jets and Z+jets samples at $\sqrt{s} = 7$ TeV.
- The ACERMC is used to generate background processes for pp collisions at the LHC [37]. In the current analysis this generator is used to estimate the theoretical uncertainty of *Initial and Final State Radiation* (ISR/FSR) for $t\bar{t}$ production.
- The MADGRAPH is a matrix element generator [38], for this analysis it is used for diboson sample production, for signal models and to study different theory uncertainties related to signal modelling.

For the current analysis the following next-to-leading-order (NLO) [39] generators are used:

- The MC@NLO is the NLO generator [40], which matched to HERWIG or HERWIG++ generators for parton showering. Since the parton shower generator adds terms, which are already present in the NLO generation, to avoid double counting for some events negative weights are assigned. For the current analysis the MC@NLO is used for $t\bar{t}$ and single top sample production at $\sqrt{s} = 7$ TeV.
- The POWHEG (positive-weight hardest emission generator) is the NLO generator [41], which generates the hardest radiation, while for softer radiations a parton shower generator is used. For the current analysis for parton showering it is matched to PYTHIA generator and used for $t\bar{t}$ and single top sample production at $\sqrt{s} = 8$ TeV.

Events generated with the Monte Carlo generators on this level do not include any detector effects. These events are referred to in the following as *true* or *particle level* events.

CHAPTER 2

The LHC and the ATLAS Detector

2.1 The Large Hadron Collider

The *Large Hadron Collider* (LHC) is a particle accelerator, used to accelerate protons and heavy ions [42]. Up to the moment, it is the largest and the most powerful accelerator in the world.

The accelerator is located about 100 m under ground, the main ring of the collider is 26659 m long. The LHC accelerates two beams, which travel in opposite directions, close to the speed of light. Superconducting magnets are used to produce the high magnetic field 8.3 T to keep the protons on their orbit. The magnets operate at 1.9 K. To cool down to this temperature liquid helium is used.

Four detectors are located on the LHC ring:

- ALICE (A Large Ion Collider Experiment)
- ATLAS (A Toroidal LHC ApparatuS)
- CMS (Compact Muon Solenoid)
- LHCb (The Large Hadron Collider beauty experiment)

ATLAS and CMS are general purpose detectors to study Standard Model processes and to perform searches for new particles. ALICE is used to study the properties of the quark-gluon plasma in Pb-Pb collisions. LHCb was built to study b-quark physics, to answer such questions as why e.g. our universe consists mainly of matter and almost not antimatter.

2.2 The ATLAS detector

The ATLAS Detector is the largest detector on the LHC with a length of 46 m, a diameter of 25 m and a weight of about 7000 tons. A cutaway view of the detector is shown in Figure 2.2 It is a general purpose detector for searches for heavy particles like the Higgs boson or super-symmetric particles.

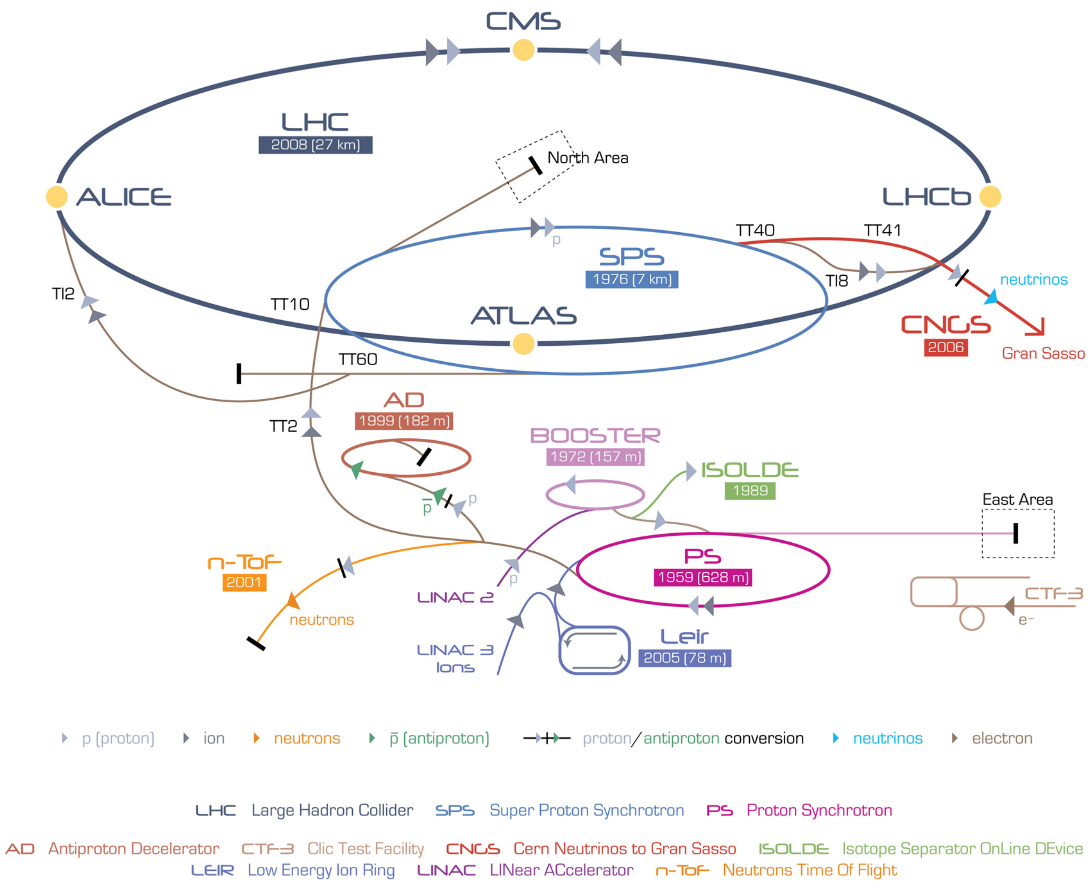

Figure 2.1: The CERN accelerator complex [43]. The four main experiments ALICE, ATLAS, CMS and LHCb and the pre-accelerators Linac2, Booster, PS and SPS are shown.

The ATLAS detector was designed to fulfil the following requirements:

- Large pseudorapidity (η) acceptance with almost complete azimuthal angle (ϕ) coverage (variables are described in the following).
- High resolution charged particle tracking system for the very large track density conditions.
- Good electromagnetic calorimeter for electron and photon identification and measurements.
- Fully covered hadronic calorimeter for accurate missing transverse momentum ($E_{\mathrm{T}}^{\mathrm{miss}}$) measurements.
- High precision muon spectrometer, able to reconstruct muon tracks based on standalone measurements.
- Flexible multilevel trigger system for triggering on particles with low p_{T} and complex reconstructed objects.

In the following, the coordinate system and the related variables are described. The positive direction of the x-axis is pointing to the centre of the LHC, the positive direction of the y-axis

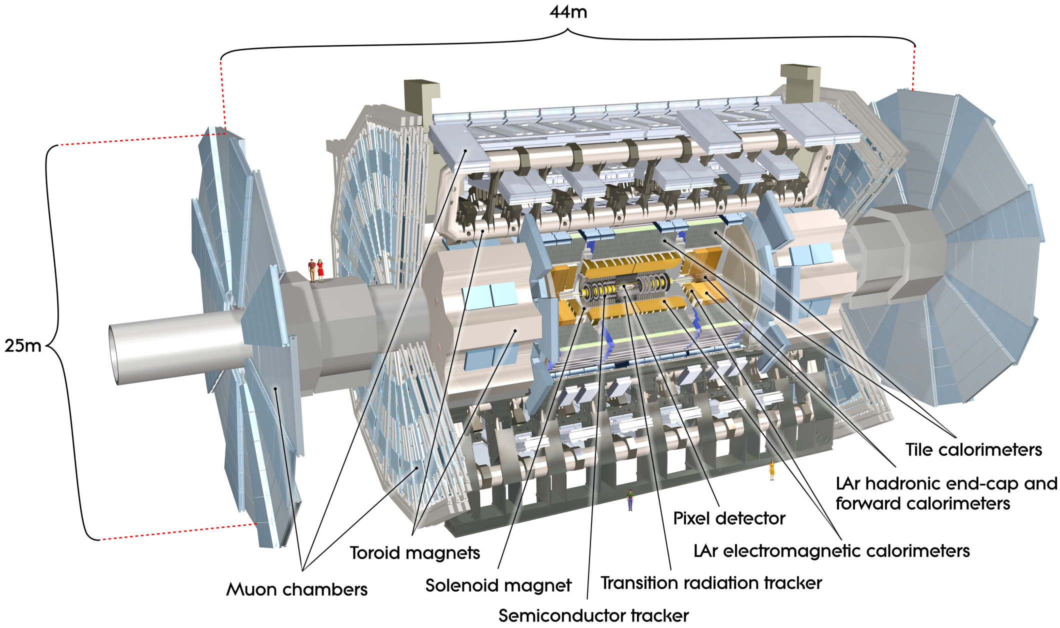

Figure 2.2: A cutaway view of the ATLAS detector. The detector has a length of 46 m, a diameter of 25 m and a weight of about 7000 tons [44].

is pointing upward, the z-axis is defined along the beam direction. The azimuthal angle ϕ is measured in the x-y plane, the polar angle θ is measured from the z-axis. The pseudorapidity is defined as $\eta = -\ln\tan(\theta/2)$. For LHC physics, this variable is preferable to the polar angle θ, due to the invariance of $\Delta\eta$ under a longitudinal Lorentz boost for massless objects. The transverse momentum p_{T} and the missing transverse energy $E_{\mathrm{T}}^{\mathrm{miss}}$ are defined in the x-y plane. The distance ΔR in the pseudorapidity-azimuth plane is defined as $\Delta R = \sqrt{\Delta\eta^2 + \Delta\phi^2}$.

2.2.1 The Inner Detector

The Inner Detector (ID) is used for charged particle tracks reconstruction (momentum and impact parameter). It consists of three sub-detectors: the pixel, the semiconductor tracker and the transition radiation tracker. To measure the p_{T} of charged particles, the Inner Detector operates in a 2 T axial magnetic field provided by the Central Solenoid (CS). The CS is a superconducting solenoid, which is located between the Inner Detector and the electromagnetic calorimeter. To decrease particle scattering effects, the solenoid has a thickness of 45 mm and shares the cryostat with the electromagnetic calorimeter.

The Inner Detector has a length of 7 m and a radius of of 1.15 m and covers a pseudorapidity range up to $|\eta| < 2.5$. The momentum resolution of the Inner Detector is

$$\frac{\sigma_{p_{\mathrm{T}}}}{p_{\mathrm{T}}} = 0.05\%\ p_{\mathrm{T}} \oplus 1\%. \tag{2.1}$$

A cutaway view of the ID with all sub-detectors is shown in Figure 2.3. The ID sub-detectors with distances from the interaction point are shown in Figure 2.4.

A detailed description of sub-detectors of the Inner Detector is given below.

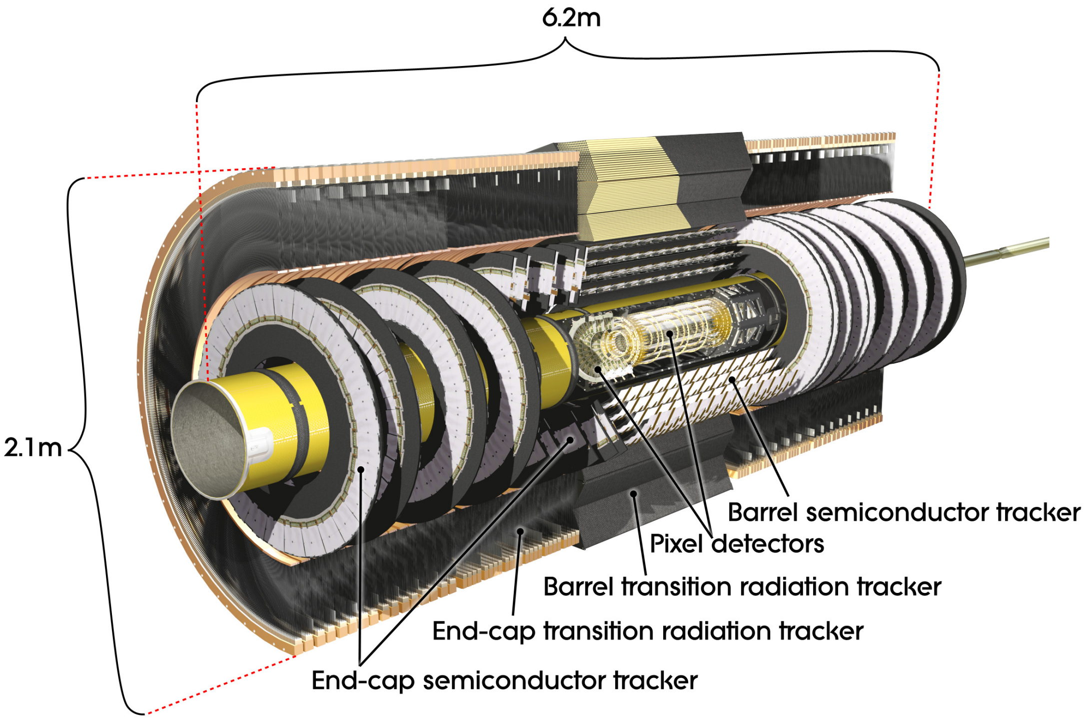

Figure 2.3: A cutaway view of the Inner Detector [44].

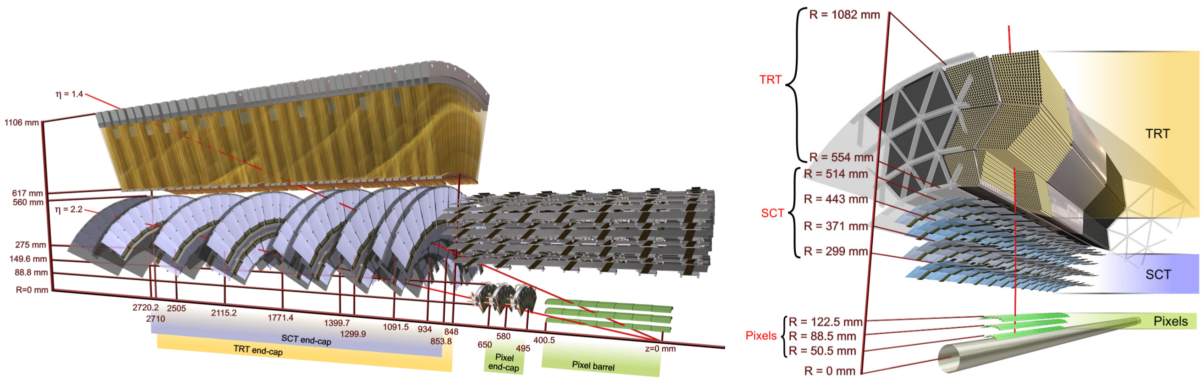

Figure 2.4: ID sub-detectors with distances from the interaction point in the end-cap region (left) and from the beam axis in the barrel region (right) [44].

Pixel detector

The pixel detector consists of three barrel layers (pixel barrel) with radii of 50.5 mm, 88.5 mm and 122.5 mm and three disks with radii 88.8 mm till 149.6 mm from each side of the barrel (pixel end-cap). It operates in a high magnetic field 2 T at a temperature of about -10°C. It is designed in such a way, that in general, each track crosses three pixel layers. The barrel consists of 1456 modules, the end-caps of 288 modules. Each pixel module has a length of

62.4 mm and a width of 21.4 mm, it contains $46\,080 = 288 \times 160$ pixels, which are read out by 16 chips, each chip reading out an array of 18×160 pixels. Most of the pixels have a size of $40 \times 400\ \mu\text{m}^2$. Overall there are 80 million pixels covering an area of 1.7 m^2.

The increasing luminosity in Run-II may cause significant radiation damage of the existing B-layer (first layer of the Pixel detector). To decrease the effect from radiation damage, an additional Insertable B-Layer (IBL) was installed during the 2013-2014 shutdown. Adding the fourth layer improves the tracking accuracy as well as the tagging efficiency for b-quark decays.

Semiconductor Tracker

The Semiconductor Tracker (SCT) is a silicon microstrip detector which is placed around the Pixel detector and contributes to momentum and vertex position measurements. The SCT consists of four barrel layers and nine end-cap disks on each side of the barrel. The barrel consists of 2112 modules, the end-caps of 1976 modules. Each module consists of two silicon microstrip sensors, which are aligned back-to-back with a stereo angle of 40 mrad. The sensors have p-strips on n-type silicon, the strips have a pitch of 80 μm and a length of 12.8 cm. Each sensor has 768 channels. The detector is designed to have eight measurements for each track (which corresponds to four space points). The space point resolution is $\delta(r_\phi) \approx 16\ \mu$m, $\delta(z) \approx 580\ \mu$m. The pseudorapidity coverage of the SCT is $|\eta| < 2.5$, the same as for the Pixel detector. The detector is cooled down to $-8°$C to decrease the noise and the radiation damage of the sensors. Overall, 6.2 million readout channels are covering the area of 61 m^2.

Transition Radiation Tracker

The Transition Radiation Tracker (TRT) is the outermost part of the Inner Detector. Measurements are done by straw tubes, which have a diameter of 4 mm. The detector is configured into a barrel and two end-cap segments. The barrel contains 50 000 straws with a length of 144 cm, which are placed along the z-axis. Each barrel is divided into two equal parts, the information is read out from both ends. The end-caps consist of 320 000 straws which are placed radially in the x-y plane, the length of the straw tubes is 37 cm, the readout is connected to the outer ends. Transition radiation photons are created from the radiator material between the straws. Xenon gas, which is filled inside tubes, is used to increase the measured signal. Each channel measures the drift time. Two thresholds allow to discriminate between tracking hits, which pass only a low threshold and transition radiation hits, which pass a higher one. The pseudorapidity coverage of the TRT is $|\eta| < 2.0$, the measured track precision is about 200 μm, a low precision is compensated by a high number of measured hits (about 30 hits).

2.2.2 The Calorimetry System

The calorimetry system is used for electrons, photons and jets identification, and energy measurements, and plays a leading role in missing transverse energy measurements. It consists of electromagnetic and hadronic parts, and is placed around the Inner Detector and the solenoid, see Figure 2.5. All calorimeters are using the *sampling* approach, where the material used to produce particle showers differs from that, which is used for energy measurements. The calorimetry system has a large pseudorapidity coverage of $|\eta| < 4.9$. The performance requirement for the electromagnetic calorimeter is driven by two decay channels, $H \rightarrow \gamma\gamma$ and $H \rightarrow 4e^{\pm}$. The electromagnetic calorimeter has a very fine granularity in the $|\eta| < 2.5$ region to be able to measure electrons and photons with the precision, which allows to separate $\pi^0 \rightarrow \gamma\gamma$ from $H \rightarrow \gamma\gamma$ decays. To address the large dynamic range (from 30 MeV to 3 TeV) of energy measurements, calorimeters have several gains for each channel. The important property of the calorimeter is to completely prevent hadronic showers and to protect the muon system from punch-through particles. This is achieved by a ≈ 22 radiation length of electromagnetic and ≈ 10 interaction length of hadronic calorimeters.

A more detailed description of the different calorimetry detectors is given below.

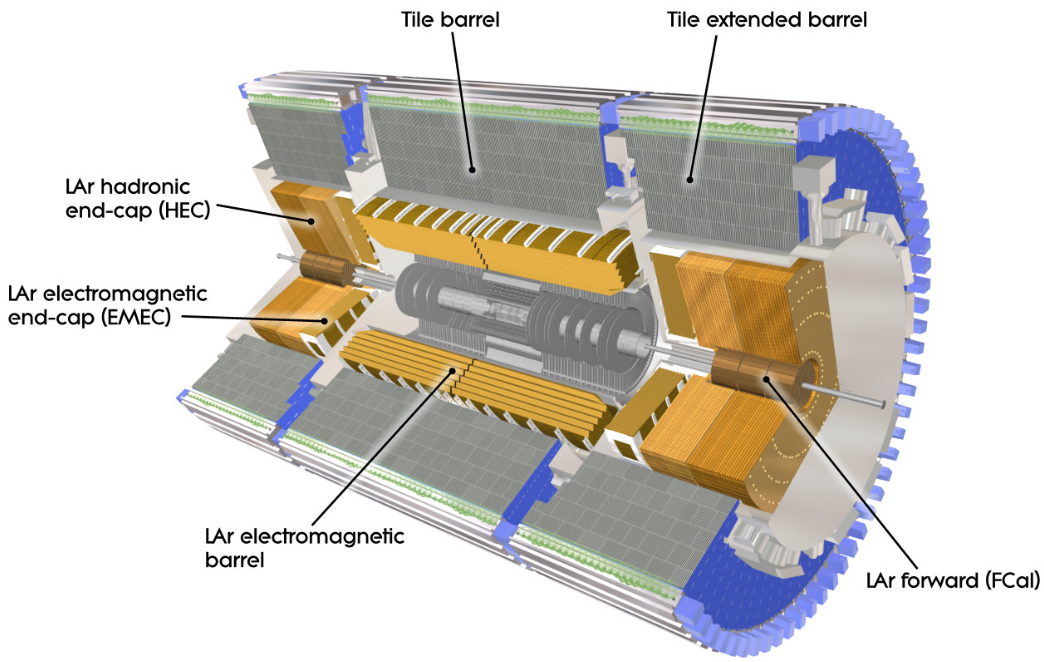

Figure 2.5: A cutaway view of the ATLAS calorimetry system [44].

Electromagnetic Calorimeter

The electromagnetic (EM) calorimeter consists of a barrel and two end-caps (EMEC). All of them are using liquid argon as an active medium because of its radiation hardness and speed. The shower passing through liquid argon liberates electrons, which are later collected and measured by electronics. The EM barrel covers a pseudorapidity range of $|\eta| < 1.475$,the electromagnetic end-caps extend this to $1.375 < |\eta| < 3.2$. The EM barrel detector consists of three radial layers, the first layer has fine $\Delta\eta$ granularity $\Delta\eta \times \Delta\phi = 0.003 \times 0.1$, the second layer has $\Delta\eta \times \Delta\phi = 0.025 \times 0.025$, while the third layer has $\Delta\eta \times \Delta\phi = 0.1 \times 0.1$. The fine granularity of the first layer is due to the requirement of angular separation of photons to identify π^0 decay. Presamplers are used to correct an energy loss due to dead materials in front of the calorimeter, they have a granularity of $\Delta\eta \times \Delta\phi = 0.025 \times 0.1$ and cover a range of $|\eta| < 1.8$.

The energy resolution of the electromagnetic calorimeter is

$$\frac{\sigma_E}{E} = \frac{10\%}{\sqrt{E(\mathrm{GeV})}} \oplus 0.7\%. \tag{2.2}$$

Hadronic Calorimeter

The hadronic tile calorimeter (TileCal) consists of a long barrel and two extended barrels. The long barrel has a length of 5.64 m and covers a rapidity range of $|\eta| < 1.0$. Itl consists of two parts, LBA and LBC, according to sides A and C. The extended barrels (EBA and EBC) each have a length of 2.9 m and a rapidity range of $0.8 < |\eta| < 1.7$. Each part of the long barrel and of each extended barrel are divided into 64 modules. Each of these 256 modules consists of scintillating tiles and steel plates serving as absorbers. Particles passing through the scintillator tiles are producing a light, which is collected by wavelength-shifting fibers and is measured by photomultipliers. These tiles are grouped by cells. To provide redundancy, each cell is measured by two photomultipliers, which are connected to fibers from the left and the right side of the cells. Tile calorimeter has three layers of cells, the granularity for the first two inner layers is $\Delta\eta \times \Delta\phi = 0.1 \times 0.1$, while the outer one has a granularity of $\Delta\eta \times \Delta\phi = 0.2 \times 0.1$.

The hadronic end-cap calorimeter (HEC) is a liquid argon-sampling calorimeter with copper plates as absorber. The HEC consists of two wheels, HEC1 and HEC2, which are installed after the EMEC wheel. Each wheel has a diameter of 4 m and consists of 32 identical modules. The length of the HEC1 and HEC2 wheels is 0.82 m and 0.96 m, respectively. The detector covers a range of $1.5 < |\eta| < 3.2$ and has a granularity of $\Delta\eta \times \Delta\phi = 0.1 \times 0.1$ for $1.5 < |\eta| < 2.5$ and of $\Delta\eta \times \Delta\phi = 0.2 \times 0.2$ for $2.5 < |\eta| < 3.2$.

The combined energy resolution of the electromagnetic and the hadronic sections of the calorimeter is

$$\frac{\sigma_E}{E} = \frac{50\%}{\sqrt{E(\mathrm{GeV})}} \oplus 3\%. \tag{2.3}$$

Forward Calorimeter

The forward calorimeter (FCal) is situated in the end-cap cryostat together with the electromagnetic and the hadronic end-cap calorimeters (EMEC and HEC). The FCal covers a very forward region of $3.1 < |\eta| < 4.9$ where energies and densities of oncoming particles are very high. The calorimeter improves the missing transverse energy reconstruction and the measurement of forward jets, the first being important for SUSY searches, while the latter is needed for the analysis of vector boson fusion (VBF) processes. The FCal consists of three layers – FCal1, FCal2 and FCal3, the first layer closest to the interaction point being an electromagnetic calorimeter, while the second and the third layers are hadronic calorimeters. After the third layer an absorber is installed to stop the rest of the hadronic showers that punch through. All three layers are using liquid argon as an active medium, whereas copper is used as absorber in the electromagnetic calorimeter and tungsten in the hadronic ones. The granularity of FCal is $\Delta\eta \times \Delta\phi = 0.1 \times 0.1$.

The energy resolution for the hadronic component is

$$\frac{\sigma_E}{E} = \frac{100\%}{\sqrt{E(\mathrm{GeV})}} \oplus 10\%. \tag{2.4}$$

2.2.3 The Muon Spectrometer

The muon spectrometer (MS) shown in Figure 2.6 is the outermost detector with a length of 44 m and a diameter of 22 m. It consists of three superconduction air-core toroids, precision tracking chambers and triggering chambers with fast response. Muons are the only particles, which can pass through the whole calorimeter without being absorbed. The design of the muon spectrometer allows to carry out precise stand-alone measurements of muon tracks over the large range of p_{T} from 3 GeV to 3 TeV.

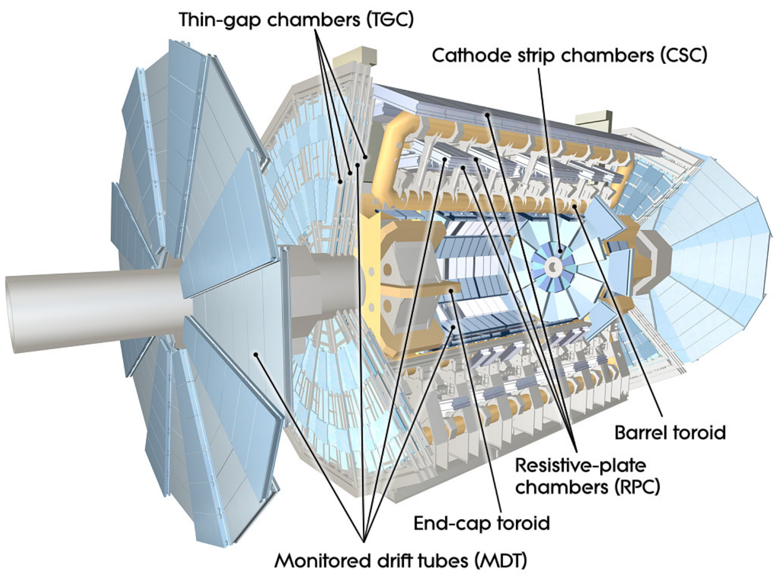

Figure 2.6: A cutaway view of the ATLAS muon system [44].

The three superconducting toroids, one for barrel and two for end-caps are providing a magnetic field of 0.5 T in the central region and of 1 T in the end-caps. The end-cap toroids are located inside the barrel toroid. Each of the toroids consists of eight coils and is assembled symmetrically around the beam axis.

The *Monitored Drift Tubes* (MDT) are used for precision measurements of tracks for barrel and end-caps. They cover a pseudorapidity range of $|\eta| < 2.7$, except for the innermost end-cap layer, where the coverage is $|\eta| < 2.0$. For precision measurements in the innermost tracking layer the Cathode Strip Chambers (CSC) are used, to cover the range of $2.0 < |\eta| < 2.7$. The momentum resolution for the $|\eta| < 1.05$ region is 2% at 100 GeV and 8% at 1 TeV.

For fast triggering, the muon spectrometer has two different trigger systems, the Resistive

Plate Chambers (RPC) for the barrel region and the Thin Gap Chambers (TGC) for the end-caps. The RPC have a time resolution of 1.5 ns and cover $|\eta| < 1.05$, the TGC have a time resolution of 4 ns and cover $1.05 < |\eta| < 2.4$. The triggering system therefore allows to identify bunch crossing with an accuracy of 99%.

2.2.4 Trigger and Data Acquisition

The *Trigger and Data Acquisition* (TDAQ) system is responsible for collecting the event data from the detector, selecting potentially interesting data for physics events and storing them on the disk for further offline analysis.

The trigger system consists of three levels: *Level-1* (L1), *Level-2* (L2) and the *Event Filter* (EF), see Figure 2.7. The last two levels are also called *High Level Triggers* (HLT).

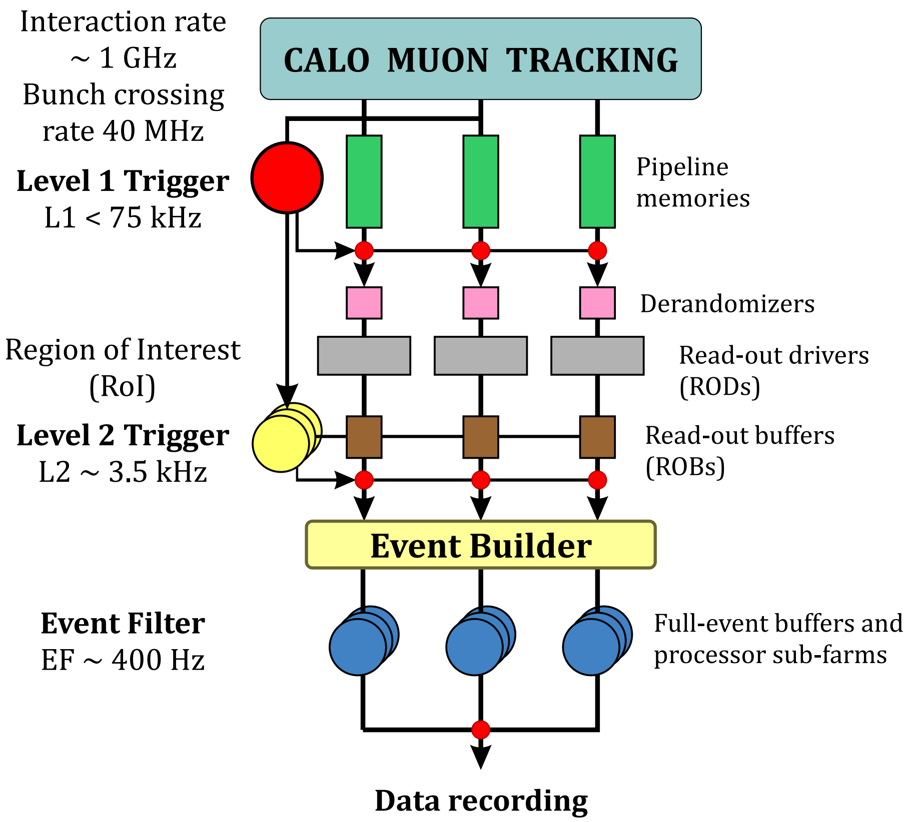

Figure 2.7: The ATLAS Trigger System from Ref. [45].

The design event rate of the ATLAS detector is 40 MHz, (during the 2012 data taking it worked at a rate of 20 MHz). The responsibility of the Level-1 trigger is to decrease this rate down to 75 KHz. The decision whether to accept the event or not, has to be taken by the Level-1 trigger in 2.5 μs. Due to this time constraint, the Level-1 trigger is based on custom hardware, which uses the information only from the calorimeter and the muon detectors. Therefore the L1 can trigger only on electrons, photons, jets, muons, and a simplified version of missing transverse energy. Tracking of the information is not available at this level, therefore triggering, for example on b-tagged jets, is not possible. Until the L1 trigger has taken the decision, events, that are coming at a rate of 40 MHz with corresponding timestamps are being buffered in each sub-detector. In case the event is accepted, it is retrieved by the timestamp through the Read Out System (ROS) and passed on to the Level-2 trigger. The event information itself is distributed between several computers. Since gathering the event information in one place takes some time, the Level-2 trigger analyses the data from the “Region of Interest” (RoI) only, which usually is made up by just a few percent of data. The L2 trigger decreases the event rate to about 3.5 KHz. An event accepted by Level-2 trigger is then sent to the Event Filter. On the Event Filter level the whole information on the event is collected in one place. The EF runs its own offline-like software, which takes the final decision. If the event is accepted by EF, it is stored in one of the “streams” according to the trigger signature. The four main physics streams are used: `Egamma`, `Muon`, `JetTauEtmiss` and `MinBias`. The EF output rate during the 2012 data taking was up to 700 Hz.

CHAPTER 3

Objects reconstruction

The ATLAS physics analyses use reconstructed objects, which are presenting the characteristics of the particles created from the proton-proton collisions. In this chapter the reconstruction of physics objects and the performance of the ATLAS detector are presented [46].

Track and vertex reconstruction, electron and muon identification, jet reconstruction, *b*-tagging algorithm, and the missing transverse momentum reconstruction are briefly discussed. All these objects are playing an important role in the analysis.

3.1 Tracks and vertices

The reconstruction of track parameters is based on the hit position measurements performed by the Inner Detector. Due to a high pile-up environment the reconstruction of tracks for the primary vertices is quite challenging [47]. The particles from the pile-up creating hits, pose significant problems for reconstruction algorithms.

3.1.1 Track reconstruction

The tracks in the inner detector are reconstructed using different algorithms [48] in the following order:

– The ***inside-out*** algorithm represents a baseline algorithm for the charged particles reconstruction. The reconstruction starts from creation of *space points* the three-dimensional representations of the Pixel and SCT detectors measurements. The algorithm starts from three space point hits and extend the track moving away from the interaction point by adding hits using a combinatorial Kalman filter. Reconstructed tracks are extended into the TRT. The inside-out algorithm is only used for tracks with $p_{\mathrm{T}} > 0.4$ GeV.

  The particles are defined as *primary particles* if they have a lifetime greater than 3×10^{-11} s and are produced from a decay of particles, whose lifetime is less than 3×10^{-11} s.

– The ***back-tracking*** algorithm detects a track in the TRT and extends it inside the silicon tracker by adding hits. This algorithm is responsible for the reconstruction of secondary tracks, which are produced from the decay products of the primary particles, having their origin not close to the primary interaction point.

– The ***TRT-standalone*** algorithm reconstructs the tracks, left unreconstructed with the first two algorithms, due to the absence of corresponding hits in the silicon detector.

Figure 3.1 illustrates the difference between the default track reconstruction approach, used for the 2011 data taking with low pile-up and the more "robust" one, with tighter requirements tuned for the high pile-up environment. A missing measurement, which is expected from the track, is called a *hole*. The default approach requires at least 7 silicon hits and not more than two holes in the Pixel detector. The robust selection requires 9 hits in the silicon detector (Pixel and SCT) and no holes in the Pixel detector.

Figure 3.1 represent the primary reconstruction track efficiency as a function of p_T and η. The plots show this dependency for various pile-up conditions.

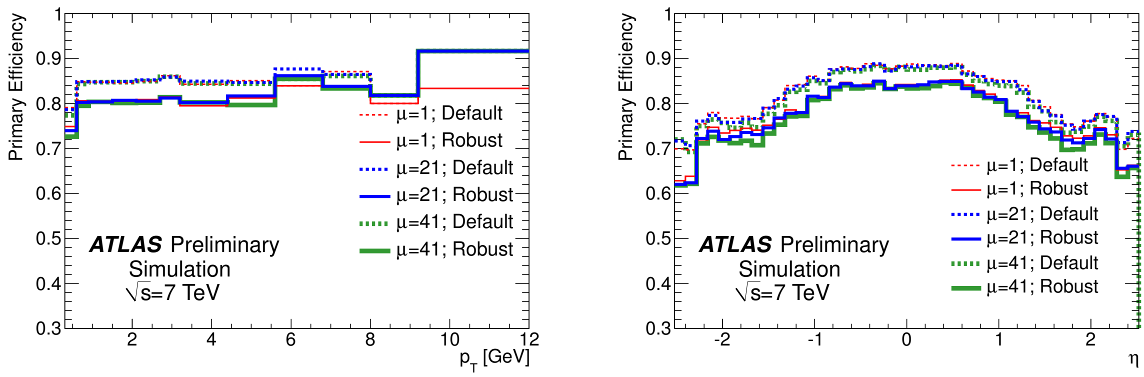

Figure 3.1: The p_T (left) and η (right) distributions of the primary track reconstruction efficiency for the minimum bias Monte Carlo samples with average number of interactions per bunch-crossing $\mu = 1, 21, 41$. Tracks passing the default (dashed) and robust (solid) selection are shown [47].

One can see, that robust requirements reduce the efficiency by around 5%, but improve another important property of the tracking algorithm, the fraction of reconstructed non-primary tracks. The plots in Figure 3.2 show, that this fraction for the robust algorithm is reduced by a factor of $2 - 5$ and is almost pile-up independent.

The transverse momentum resolution of the Inner Detector is

$$\frac{\sigma_{p_T}}{p_T} = 0.05\%\ p_T \oplus 1\%, \tag{3.1}$$

while the resolution of the transverse impact parameter for high momentum particles in the central η region is $10\,\mu$m.

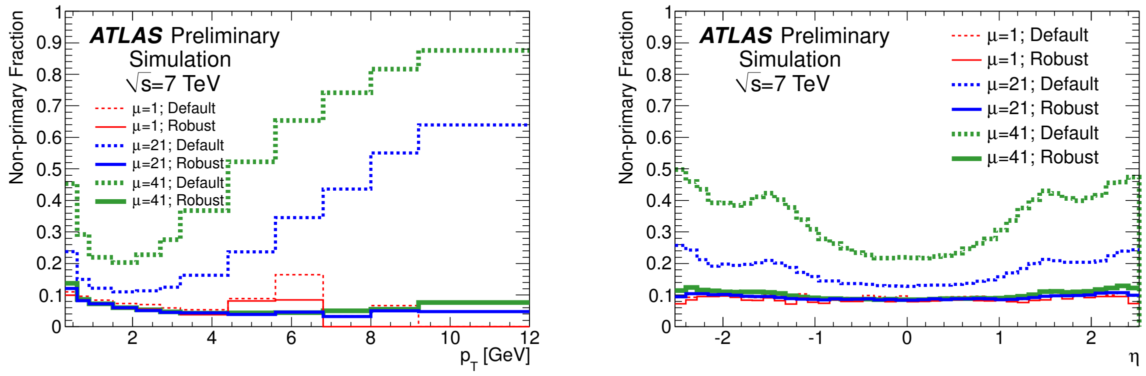

Figure 3.2: The p_T (left) and η (right) distributions of the non-primary track fraction in the minimum bias Monte Carlo samples with average interactions per bunch-crossing $\mu = 1, 21, 41$. Tracks passing the default (dashed) and robust (solid) selection are shown [47].

3.1.2 Primary vertex reconstruction

The primary vertices reconstruction is based on the *Iterative Vertex Finding* algorithm [49]. This algorithm works in the following way:

- A preselection from the tracks, that are candidates to come from the interaction region.
- The vertex seed is selected as the global maximum of the distribution of z coordinates of the tracks, at the point of closest approach to the interaction point.
- The vertex position is fitted using an *adaptive vertex fitting* algorithm [50]. The fit algorithm considers only tracks around the seed position. It is down-weighting tracks based on their contribution to the overall χ^2.
- The tracks associated with the fitted vertex compatible less than approximately 7σ are removed from the subsequent considerations. The tracks are not associated to any vertex are used to seed the next vertex. These steps are repeated, until no more vertex can be found.

3.2 Electrons

For the one-lepton analysis the electrons are playing an important role. The requirement the presence of exactly one electron in the analysis significantly suppresses other backgrounds, especially the multijet background, therefore it is important to have a good rejection against misidentified hadronic jets. It is also important to have a high tagging efficiency. In this section, a brief description of the electron trigger, reconstruction, identification, and performance is given. The performance studies are based on the *tag-and-probe* approach and $Z \to ee$, $J/\psi \to ee$ and $W \to e\nu$ processes are used for these analyses.

3.2.1 Trigger

The electron trigger works as follows:

- The ***Level 1*** (L1) EM trigger considers the EM calorimeter as a grid with granularity $\Delta\eta \times \Delta\phi = 0.1 \times 0.1$, called *trigger towers*. A sliding-window algorithm searches for seeds within a 4×4 window of trigger towers and identifies the so-called *Region of Interest* (RoI). It sends a trigger request, when the central 2×2 trigger towers contain one pair of neighbouring towers with a total energy above the threshold.
- The ***Level 2*** (L2) trigger uses the e/γ algorithm and builds cell clusters within the RoI of a $\Delta\eta \times \Delta\phi = 0.4 \times 0.4$ window, found by the L1 trigger. Some offline-like corrections are applied, to improve the energy and cluster position.
- The ***Event Filter*** (EF) level retrieves the cell information from a region slightly larger than the RoI. It uses the offline sliding-window algorithm for cluster reconstruction and applies all offline based corrections.

Further details about the trigger studies can be found in Ref. [51].

3.2.2 Reconstruction and identification

Electrons and photons are reconstructed for the $|\eta| < 2.47$ region using energy deposits in the electromagnetic calorimeter. The $\eta - \phi$ space of the EM calorimeter is divided into a grid of $N_\eta \times N_\phi = 200 \times 256$, each grid cell with a size of $\Delta\eta \times \Delta\phi = 0.025 \times 0.025$. The cells along the longitudinal layers of the EM calorimeter with the same $\eta \times \phi$ grid cell are forming a tower. The tower energy is the total energy deposited in the tower cells.

The *sliding-window* algorithm [52] searches with window size of 3×5 towers for the total cluster transverse energy above 2.5 GeV. Monte Carlo simulations show, that the cluster reconstruction is very efficient: for electrons with $E_T = 7$ GeV the efficiency is about 95%, while for $E_T = 15$ GeV it reaches 99%.

A cluster in the EM calorimeter is classified as an electron, if it matches a well-reconstructed track from the ID. If the track is consistent with a photon conversion and the conversion vertex has also been reconstructed, the corresponding electrons are matched as converted photons. Depending on the number of assigned electron tracks, a converted photon is classified as a single- or double-track conversion. If a cluster does not have any matched track, it is classified as an unconverted photon.

The electron clusters are rebuilt with different sizes depending on the barrel and end-cap calorimeter regions. The cluster sizes are optimised to minimize pile-up and noise contributions. Corresponding Monte Carlo simulation-based correction factors are applied to the cluster energies.

The relative energy resolution for electromagnetic objects can be expressed as:

$$\frac{\sigma_E}{E} = \frac{a}{\sqrt{E}} \oplus \frac{b}{E} \oplus c, \tag{3.2}$$

where a is the sampling term, by design expected to be about 10%, b corresponds to the noise term, while c is a constant term, which, by design, is expected to be about 0.7% at high energies. All parameters are considered to be η dependent.

The clusters considered as electron or photon candidates should have longitudinal and transverse profiles consistent with the response of the EM calorimeter for the corresponding particle.

For the analysis, three different cut-based selections *loose*, *medium* and *tight* are defined for electrons, with increasing background rejection power, but decreasing efficiency [53]. Shortly they can be described as follows:

– The ***Loose identification*** uses requirements on the hadronic leakage, lateral shower and shower related parameters, the number of hits in the Pixel and SCT detectors, and track-cluster matching.

– The ***Medium identification*** adds requirements on hits related to the TRT detector, the transverse impact parameter, hits in the B-layer and on the ratio of the energy in the back layer and EM calorimeter.

– The ***Tight identification*** adds additional requirements on the track-cluster matching, on the cluster energy over the track momentum ratio E/p, and imposes a veto on electrons matched as from photon conversions.

In addition to the above selections, identifications based on multivariate techniques are also developed. They were designed to have similar electron identification efficiencies, but better jets and converted photons rejection power. For one-lepton analyses, as well as for the current analysis, the cut-based identification is used.

In addition to the identification criteria described above, different analyses use isolation requirements to further suppress jets, which are misidentified as electrons. Two different types of isolation variables are used:

– The ***Calorimetric isolation*** variable $E_T^{\text{cone}\Delta R}$ is defined as transverse energy deposited in the calorimeter in a cone of size ΔR around the electron, excluding the energy deposited in the cluster. Corresponding pile-up and energy leakage corrections are applied.

– The ***Track isolation*** variable $p_T^{\text{cone}\Delta R}$ is defined as the sum of the transverse momenta of the tracks within a cone of the ΔR around the electron and with $p_{\mathrm{T}} > 0.4$ GeV. The electron track itself is excluded from the sum. Tracks included in the sum are required to meet certain quality criteria and come from the same primary vertex as the electron.

Identification and reconstruction efficiencies are measured using a tag-and-probe approach. It uses $Z \to ee$ and $J/\psi \to ee$ signatures and tags one of the two decay electrons based on strict selection criteria (mentioned as "tag"), while another electron (mentioned as "probe") is used to measure the identification and reconstruction efficiency [54].

The total efficiency to detect an electron $\varepsilon_{\text{total}}$ can be decomposed on different components:

$$\varepsilon_{\text{total}} = \varepsilon_{\text{reco}} \cdot \varepsilon_{\text{id}} \cdot \varepsilon_{\text{trig}} \cdot \varepsilon_{\text{other}}. \tag{3.3}$$

The reconstruction efficiency $\varepsilon_{\text{reco}}$ is related to the electromagnetic cluster reconstruction, the ε_{id} corresponds to the efficiency of the identification, with respect to the reconstructed electrons, the $\varepsilon_{\text{trig}}$ accounts for the trigger efficiency, with respect to the electrons passing the identification criteria, while the other efficiency $\varepsilon_{\text{other}}$ is related to the analysis specific requirements, for example on isolation variables.

Combined reconstruction and identification efficiencies for different criteria, are based on the $Z \to ee$ decay tag-and-probe approach are shown in Figure 3.3.

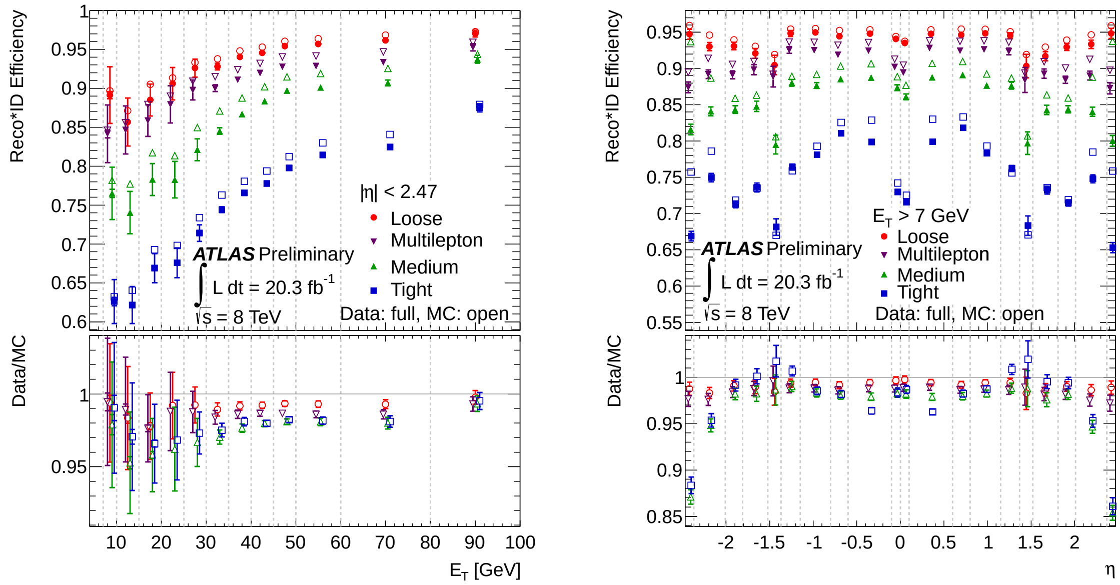

Figure 3.3: Combined reconstruction and identification efficiencies for lose, multilepton, medium and tight criteria as a function of $E_{\mathrm{T}}^{\mathrm{miss}}$ (left) and η (right) [53]. Data/MC comparisons are done for electrons from $Z \to ee$ decay. Uncertainties related to the statistics are shown as inner error bars, while total (statistical and systematic) uncertainty are shown as outer error bars.

3.2.3 Energy scale and resolution

The energy scale and resolution is determined using $Z \to ee$ decays.

The energy correction is defined as:

$$E^{\text{data}} = E^{\text{MC}}(1 + \alpha_i), \tag{3.4}$$

where E_{data} and E_{MC} denote the electron energy in data and simulation, respectively. The α_i corresponds to the relative difference from the simulated value in the i-th bin.

The α_i coefficients depend on η and are estimated as:

$$m_{ij}^{\text{data}} = m_{ij}^{\text{MC}}(1 + \alpha_{ij}), \qquad \alpha_{ij} \approx \frac{\alpha_i + \alpha_j}{2}. \tag{3.5}$$

Here it is taken into account, that the α_i are small, therefore higher order terms may be neglected and the angle between electrons is well modelled. m_{ij}^{data} and m_{ij}^{MC} are invariant masses, respectively, for the data and the Monte Carlo simulation, of the electron pair reconstructed for pseudorapidity bin (η_i, η_j), where α_{ij} corresponds to the relative shift of the mass peak for this bin.

To estimate electron resolution corrections, it is assumed, that the Monte Carlo simulation is well modelling the resolution curve up to some Gaussian smearing term c:

$$\left(\frac{\sigma_E}{E}\right)^{\text{data}} = \left(\frac{\sigma_E}{E}\right)^{\text{MC}} \oplus c. \tag{3.6}$$

It is considered that c_i also depends on η. Therefore, the resolution of the invariant mass for the (η_i, η_j) bin can be written as:

$$\left(\frac{\sigma_m}{m}\right)_{ij}^{\text{data}} = \left(\frac{\sigma_m}{m}\right)_{ij}^{\text{MC}} \oplus c_{ij} = \frac{1}{2} \cdot \left[\left(\frac{\sigma_E}{E}\right)_i^{\text{MC}} \oplus c_i\right] \oplus \left[\left(\frac{\sigma_E}{E}\right)_j^{\text{MC}} \oplus c_j\right], \quad c_{ij} = \frac{c_i \oplus c_j}{2}. \tag{3.7}$$

Finally the α_i and c_i coefficients are obtained by solving the equations above, where α_{ij} and c_{ij} are involved.

The energy scale corrections α_i and effective constant term corrections c_i as functions of η are shown in Figure 3.4. Both correction coefficients are derived from the $Z \to ee$ events [54]. The plots in the bottom row show statistical and total uncertainties as functions of η.

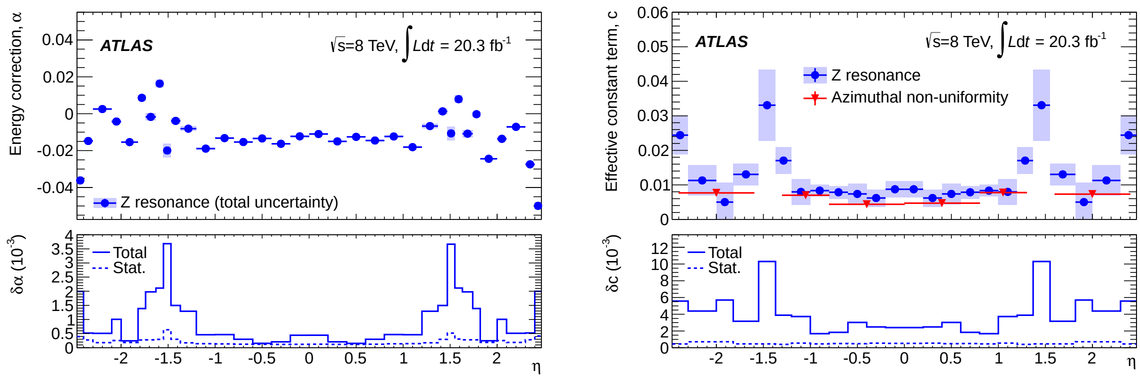

Figure 3.4: Energy scale corrections α_i (left) and effective constant term correction c_i (right) as functions of η [54]. Both correction coefficients are derived from the $Z \to ee$ events. The plots in the bottom row show statistical and total uncertainties as functions of η.

The left plot in Figure 3.5 shows the invariant mass distribution after applying all corrections. The data/MC agreement is at the level of 2% in the mass range $80 < m_{ee} < 100$ GeV.

The resolution can be measured from the Z resonance width. The right plot in Figure 3.5 shows the resolution curve as a function of E_T for $|\eta| = 0.2$. A minimal relative uncertainty of 5% is achieved for electrons with $E_T = 40$ GeV.

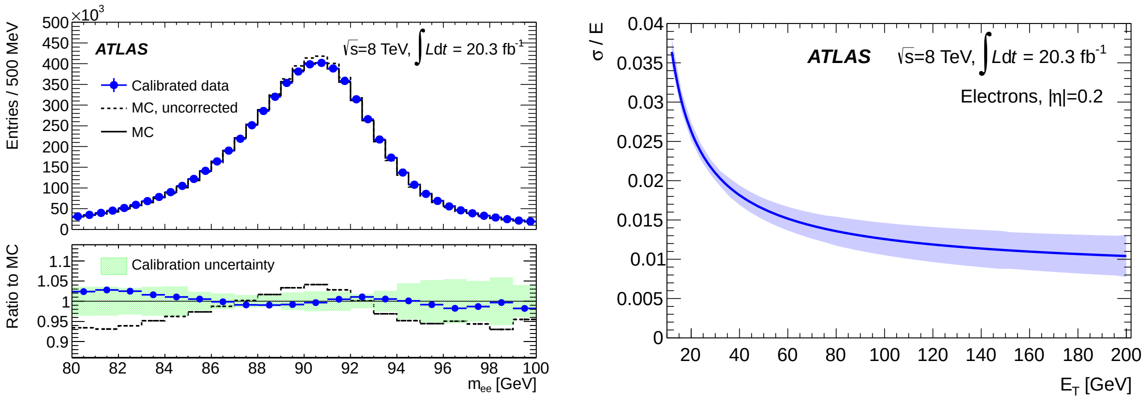

Figure 3.5: Invariant mass distribution for the $Z \to ee$ decay, before and after energy scale corrections are applied is shown in the left plot. Distributions are normalised to the number of events in the data. The right plot shows the resolution curve as a function of E_T for $|\eta| = 0.2$ [54].

3.3 Muons

Muons are playing an important role in the one-lepton analysis, they have an even cleaner signature than electrons. In this section a brief description of the muon trigger, reconstruction, identification and performance is given. The performance studies are based on the *tag-and-probe* approach and use $J/\psi \to \mu\mu$, $\Upsilon \to \mu\mu$ and $Z \to \mu\mu$ processes for the analysis [55].

3.3.1 Trigger

The muon trigger works as follows:

– The ***Level 1*** (L1) trigger identifies muons by hits coincidences in the RPCs or TGCs, which are pointing to the beam interaction region. The L1 muon trigger system has six programmable p_{T} thresholds. The global L1 trigger uses information about the number of muon candidates passing each threshold. If an event is accepted by the L1 trigger, the information about the corresponding detector *Region of Interest* (RoI) and p_{T} thresholds is sent to the L2 trigger. The size of the RoI is $\Delta\eta \times \Delta\phi = 0.1 \times 0.1$ for RPCs and 0.03×0.03 for TGCs. The L1 trigger covers about 80% of the barrel and 99% of the end-cap regions.

– The ***Level 2*** (L2) trigger reconstructs a *stand-alone muon* by adding information from the MDT chambers to get a more precise track estimation. To fit in the time constraints, a simplified reconstruction algorithm is used. The reconstructed stand-alone muon information is then combined with a track measured by the ID detector. The closest track in the $\eta - \phi$ plane is used to create a *L2 combined muon* by taking the weighted average of the transverse momenta of the track and the stand-alone muon.

– The ***Event Filter*** (EF) trigger uses two methods to define a muon: one method is based on the RoI defined at L1 and L2 level, the other one uses a full-scan of the detector. Muons candidates found by the RoI method are called *EF stand-alone muons*, while the muons found by the full-scan method are referred to as *EF full-scan muons*.

Further details about the trigger studies can be found in Ref. [56].

3.3.2 Reconstruction and identification

Muons are reconstructed for $|\eta| < 2.7$ based on the information from the Muon Spectrometer (MS) and the Inner Detector (ID). In some cases, when the information from the ID is not sufficient, the calorimeter information is also taken into consideration. Muon measurements are provided by *Monitored Drift Tube Chambers* (MDT) or *Cathode Strip Chambers* (CSC).

Four different types of muons can be encountered:

– ***Stand-alone*** (SA) muons are reconstructed based on the MS information only. The parameters of the muon track are determined by an extrapolation of the track information from the MS to the interaction point, taking into account energy losses in the detector material before the MS. These muons are mainly used for the $2.5 < |\eta| < 2.7$ range, where the ID does not have any coverage.

– ***Combined*** (CB) muons are reconstructed by combining independently reconstructed tracks from the MS and from the ID. In the analysis mainly this type of muons is used.

– ***Segment-tagged*** (ST) muons present a case, when a complete track from the MS cannot be reconstructed, but there still exists information from at least one segment of the MDT or CSC chambers. In this case the track of the muon candidate from the ID is combined with the available information from these segments.

– ***Calorimeter-tagged*** (CaloTag) muons for which the track from the ID can be associated to the region of the calorimeter with deposited energy compatible with a minimum ionising particle. This type of muons has the lowest purity, but it recovers acceptance in the uninstrumented region of the MS for $|\eta| < 0.1$ and is optimised for the momentum range of $25 < p_T < 100$ GeV.

Reconstruction efficiencies for various types of muons as functions of p_T and η are shown in Figure 3.6. Efficiencies are measured using $Z \to \mu\mu$ events for muons with $p_T > 10$ GeV.

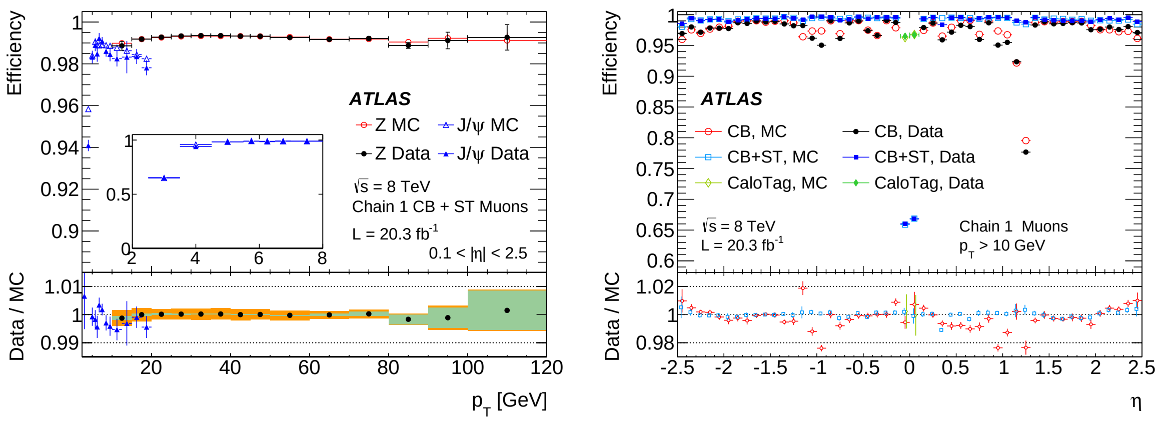

Figure 3.6: Efficiency of the muon reconstruction as a function of p_T (left) and η (right) measured using $Z \to \mu\mu$ events for muons with $0.1 < |\eta| < 2.5$ and $p_T > 10$ GeV, respectively [55]. Efficiencies are shown for different reconstruction types. The error bars represent the total uncertainty.

3.3.3 Energy scale and resolution

The energy scale and resolution corrections for muons in Monte Carlo simulation are defined as functions in the $\eta - \phi$ plane. Corrections for the muon momenta p_{T} are considered separately for tracks measured in the ID and MS. The following equation is used for p_{T} corrections in Monte Carlo simulation:

$$p_{\mathrm{T}}^{\mathrm{corr}} = \frac{p_{\mathrm{T}} + s_0 + s_1 \cdot p_{\mathrm{T}}}{1 + G(\Delta r_0/p_{\mathrm{T}}) + G(\Delta r_1) + G(\Delta r_2 \cdot p_{\mathrm{T}})}. \tag{3.8}$$

The $G(\sigma)$ is a random variable distributed as a Gaussian with the mean equal to zero and the width σ. The $p_{\mathrm{T}} = p_{\mathrm{T}}^{\mathrm{MC,\ det}}$ is a momenta from the Monte Carlo simulation, where "det" denotes the ID or MS sub-detector. Terms $s_i = s_i^{\mathrm{det}}(\eta, \phi)$ and $\Delta r_i = \Delta r_i^{\mathrm{det}}(\eta, \phi)$ correspond to the scale corrections and momentum resolution smearing, respectively.

For the muon momentum resolution the following empirical parametrisation is used:

$$\frac{\sigma_{p_{\mathrm{T}}}}{p_{\mathrm{T}}} = \frac{r_0}{p_{\mathrm{T}}} \oplus r_1 \oplus r_2 \cdot p_{\mathrm{T}}, \tag{3.9}$$

where the first term r_0/p_{T} corresponds to the resolution for energy loss in the material. The second term r_1 does not depend on p_{T} and accounts for multiple scattering, inhomogenity of the local magnetic field, etc., whereas the last term $r_2 \cdot p_{\mathrm{T}}$ accounts for intrinsic effects due to the spatial resolution of hit measurements and residual misalignment.

Assumed, that energy loss and it's fluctuation between the interaction point and the ID are negligible, the corresponding corrections s_0^{ID} and Δr_0^{ID} set to zero.

It is considered, that the corrected CB muon momentum reconstruction $p_{\mathrm{T}}^{\mathrm{corr,\ CB}}$ can be presented as the weighted average of the corrected p_{T} for each of the ID and MS components:

$$p_{\mathrm{T}}^{\mathrm{corr,\ CB}} = f \cdot p_{\mathrm{T}}^{\mathrm{corr,\ ID}} + (1-f) \cdot p_{\mathrm{T}}^{\mathrm{corr,\ MS}}, \tag{3.10}$$

where the weight f is derived from the Monte Carlo event before the corrections by solving the following linear equation

$$p_{\mathrm{T}}^{\mathrm{MC,\ CB}} = f \cdot p_{\mathrm{T}}^{\mathrm{MC,\ ID}} + (1-f) \cdot p_{\mathrm{T}}^{\mathrm{MC,\ MS}}. \tag{3.11}$$

The ID and MS corrections are extracted from the data using a template fit to $J/\psi \to \mu\mu$ and $Z \to \mu\mu$ events. For the ID track the scale corrections are below 0.1% with an uncertainty of about 0.02% for $|\eta| < 1.0$ and up to 0.2% for $|\eta| > 2.3$. Corrections for the MS scale are mainly below 0.1%, except for some specific regions, where they increase up to 0.4%.

The muon momentum resolution is studied by using $J/\psi \to \mu\mu$, $\Upsilon \to \mu\mu$ and $Z \to \mu\mu$ events.

Presumed that the angles between muons are modelled properly, one can estimate the invariant mass resolution as:

$$\frac{\sigma_{m_{\mu\mu}}}{m_{\mu\mu}} = \frac{1}{2} \cdot \frac{\sigma_{p_1}}{p_1} \oplus \frac{\sigma_{p_2}}{p_2}, \tag{3.12}$$

where p_1 and p_2 are the momenta of the muons.

Assuming that momentum resolution is similar for both muons, this can be rewritten as:

$$\frac{\sigma_{m_{\mu\mu}}}{m_{\mu\mu}} = \frac{1}{\sqrt{2}} \frac{\sigma_p}{p}. \tag{3.13}$$

The plots in Figure 3.7 show the data/MC comparison for the fitted mean invariant mass $\langle m_{\mu\mu} \rangle$ and it's resolution $\sigma_{m_{\mu\mu}}/m_{\mu\mu}$. The data are compared with the corrected Monte Carlo samples as functions of the $\langle p_{\mathrm{T}} \rangle$ for various $|\eta|$ regions for CB muons. For J/ψ and Υ an

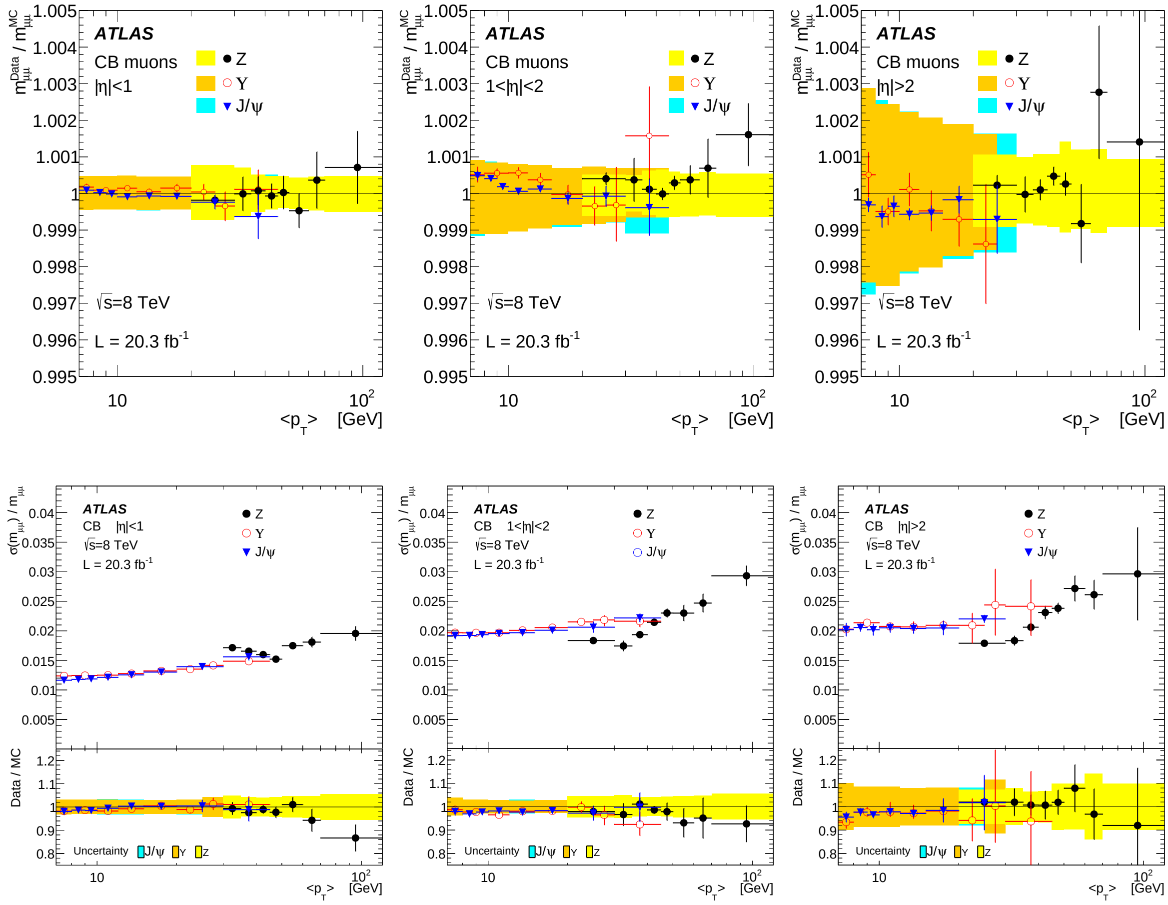

Figure 3.7: Data/MC agreement for the fitted mean invariant mass $\langle m_{\mu\mu} \rangle$ (top row) and it's resolution $\sigma_{m_{\mu\mu}}/m_{\mu\mu}$ (bottom row) with the corrected Monte Carlo samples [55]. Corrections are calculated from $J/\psi \to \mu\mu$, $\Upsilon \to \mu\mu$ and $Z \to \mu\mu$ events as functions of the average $\langle p_{\mathrm{T}} \rangle$ for various $|\eta|$ ranges. It is required, that both muons are within the same $|\eta|$ range. For J/ψ and Υ it is $\langle p_{\mathrm{T}} \rangle = \bar{p}_T$, while for Z it is $\langle p_{\mathrm{T}} \rangle = p_{\mathrm{T}}^*$. Error bars represent the total uncertainty. The bands show uncertainties on the Monte Carlo corrections separately for each process.

average momentum $\langle p_{\mathrm{T}} \rangle$ is defined as:

$$\bar{p}_T = \frac{1}{2}(p_{\mathrm{T}_1} + p_{\mathrm{T}_2}), \tag{3.14}$$

while, in case of Z decay, the definition is:

$$p_{\mathrm{T}}^{*} = m_Z \sqrt{\frac{\sin\theta_1 \sin\theta_2}{2(1-\cos\alpha_{12})}}, \tag{3.15}$$

where m_Z denotes the mass of a Z-boson, θ_1, θ_2 are polar angles of the muons and α_{12} denotes the angle between the muons. This definition of p_{T}^{*} depends on angular variables only and removes the correlation between $\langle m_{\mu\mu}\rangle$ and the average p_{T}.

Figure 3.8 shows the data/MC agreement for distributions of the invariant mass $m_{\mu\mu}$ for $J/\psi \to \mu\mu$, $\Upsilon \to \mu\mu$ and $Z \to \mu\mu$ reconstructed with the combined (CB) muons for MC simulation before and after corrections. One can see, that the data/MC agreement has significantly improved after MC corrections were applied.

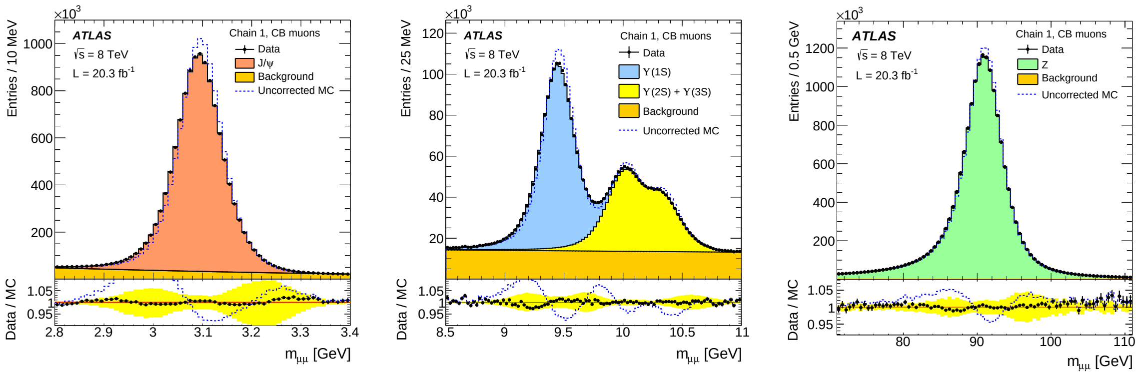

Figure 3.8: Distribution of the invariant mass $m_{\mu\mu}$ for $J/\psi \to \mu\mu$ (left), $\Upsilon \to \mu\mu$ (middle) and $Z \to \mu\mu$ (right) decays reconstructed with the combined (CB) muons [55]. The dashed blue line represents Monte Carlo simulations before any momentum correction is applied. The yellow band represents the systematic uncertainties for the momentum corrections.

3.4 Jets

Jets are playing a key role in many analyses for hadron-hadron collisions. In this chapter the "anti-k_t" algorithm – a default jet finding and reconstruction algorithm – is discussed, together with the determination of the *Jet Energy Scale* (JES) and *Jet Energy Resolution* (JER).

3.4.1 Reconstruction

The "anti-k_t" jet clustering algorithm is the default jet reconstruction algorithm used in the ATLAS experiment [57]. This algorithm can be described by a generalised approach, which includes other well known sequential recombination algorithms, the k_t algorithm [58], and the Cambridge/Aachen algorithm [59].

The generalised approach can be described as follows:

The distance d_{ij} between objects (particles or pseudojets) i and j and the distance d_{iB} between two object i and the beam axis B are defined as:

$$\begin{aligned} d_{ij} &= \min(k_{t_i}^{2p}, k_{t_j}^{2p}) \frac{\Delta_{ij}^2}{R^2}, \\ d_{iB} &= k_{t_i}^{2p}, \end{aligned} \tag{3.16}$$

where:

- $k_{t_i}^{2p}$, y_i and ϕ_i are the transverse momentum, rapidity and azimuthal angle of the particle i, respectively;
- $\Delta_{ij}^2 = (y_i - y_j)^2 + (\phi_i - \phi_j)^2$ is the distance between the objects i and j in the $y - \phi$ plane;
- R denotes the radius parameter; for jets used in the current analysis, it is taken as $R = 0.4$;
- p is a parameter, allowing to generalise the algorithm.

The clustering algorithm searches for the smallest distance between the objects. There are two cases:

- The distance d_{ij} is the smallest. In this case, objects i and j are combined in one object;
- The distance d_{iB} is the smallest. In this case, the object i is called a jet and removed from the list of objects.

After each iteration, the distances are recalculated and the procedure repeated until the list of objects is empty.

An important property, which is required from a jet clustering algorithm, is *Infrared and Collinear* (IRC) safety. Collinear safety means, that the results should not be changed by collinear splitting of objects, while infrared safety means, that soft emission should not change the properties of the jet.

Different values of the parameter p correspond to different algorithms:

- $p = 1$ corresponds to the k_t algorithm. It is shown, that the behaviour of the algorithm with respect to soft radiation for $p > 0$ is similar to that of the case $p = 1$.
- $p = 0$ represents the Cambridge/Aachen algorithm.
- $p = -1$ is the anti-k_t algorithm. Its behaviour for $p < 0$ with respect to the soft radiation is similar to that of the case $p = -1$. The anti-k_t algorithm is IRC safe.

An example of how differently the jet clustering algorithms behave, in the case when many random soft objects are produced together with jets, is shown in Figure 3.9. One can see that the anti-k_t algorithm generates approximately circular regions around hard jets. The SISCone algorithm is not used in the following, for the description of the algorithm one can see Ref. [60].

The active jet area A measures the susceptibility of the jet to the diffuse radiation. A comparison between anti-k_t and other algorithms is shown in Figure 3.10. The deviations from πR^2 are measured as functions of p_{T}. Small deviations from πR^2 mean, that the anti-k_t algorithm is quite stable against soft radiation [61].

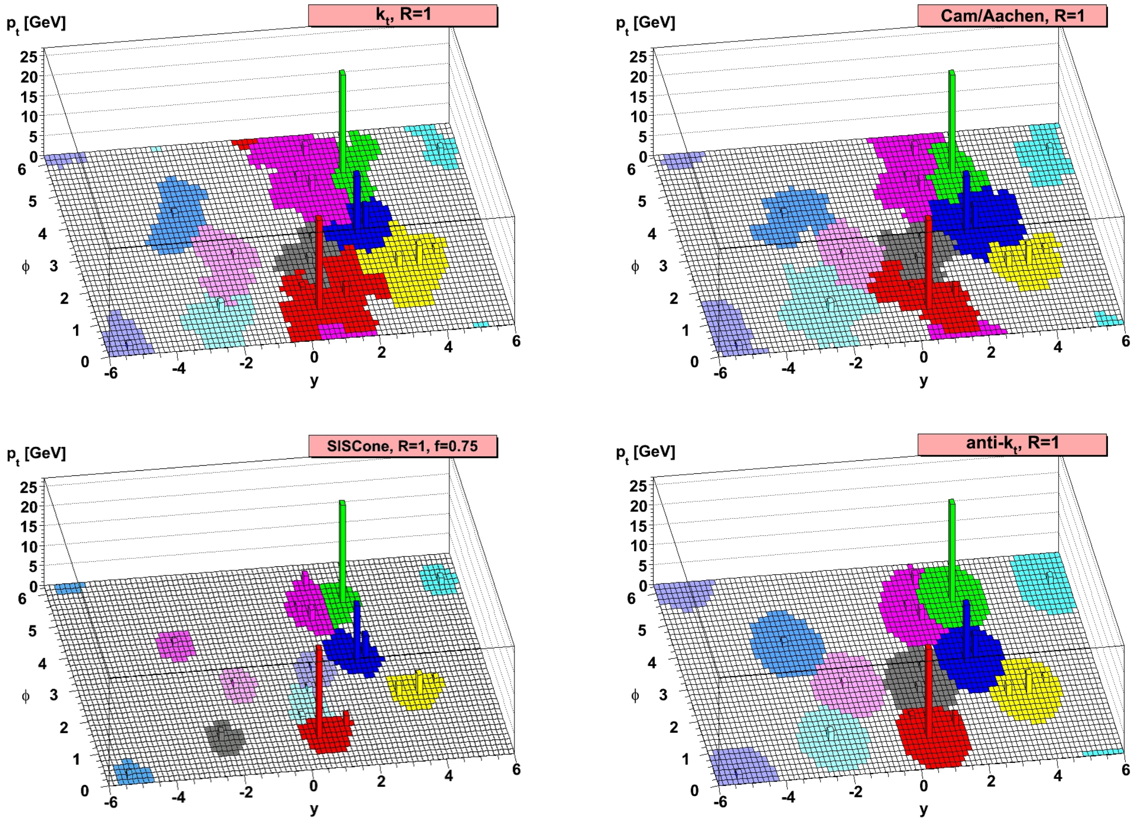

Figure 3.9: A jet clustering using Cambridge/Aachen (top left), SISCone (top right), k_t (bottom left) and anti-k_t (bottom right) algorithms. Each colour corresponds to the area for each hard jet. The presence of many random soft components change the areas for k_t and Cambridge/Aachen algorithms [57].

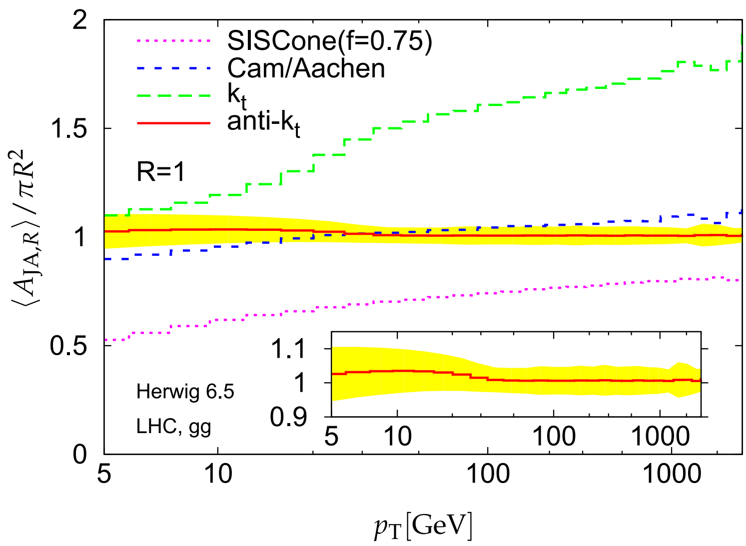

Figure 3.10: Dependence of the average jet area $\langle A_{\mathrm{JA},R} \rangle$ on the jet p_{T}. A comparison is done for various jet algorithms. The ratio is close to unity only for the anti-k_t algorithm [57].

For a better identification of the calorimeter jet origin, tracks measured in the Inner Detector are associated to jets [61], which allows the estimation of the pile-up contribution to the jet based on the *Jet Vertex Fraction* (JVF) approach [62].

The JVF is defined as follows:

$$\mathrm{JVF}(\mathrm{jet}, \mathrm{PV}_k) = \frac{\sum\limits_i p_\mathrm{T}(\mathrm{track}_i^{\mathrm{jet}}, \mathrm{PV}_k)}{\sum\limits_m \sum\limits_i p_\mathrm{T}(\mathrm{track}_i^{\mathrm{jet}}, \mathrm{PV}_m)}. \tag{3.17}$$

where PV_k is the k-th primary vertex, while $\mathrm{JVF}(jet, \mathrm{PV}_k)$ is the ratio of contributions of tracks associated with the k-th primary vertex to all tracks associated with the jet. Setting requirements on the JVF variable allows to efficiently discard jets from pile-up interactions.

3.4.2 Energy scale and resolution

The energy deposited in the ATLAS calorimeter cells is grouped into *topological clusters* (topo-clusters). Two different calibrations can be applied to a topocluster: an electromagnetic scale (EM) calibration and *Local Cluster Weights* (LCW) for the hadronic scale calibration, which corrects the response for the non-compensating nature of the calorimeter.

Depending on the origin, jets are calibrated using EM-or LCW-scales. The calibration consists of the following steps:

– The direction of the jet is adjusted to point to the interaction vertex, rather than to the detector centre, as described in Ref. [63].

– The pile-up contribution is subtracted from jets [62]. For the 2011 dataset, the correction can be described as a function of N_{PV} and $\langle\mu\rangle$, while for the 2012 dataset the pile-up subtraction is based on a jet area approach [60]. An advantage of this approach is that it deals with pile-up on event-by-event basis and relies less on the tracks and vertices identification, which is affected by the pile-up.

– The jet is corrected on particle level using calibration factors as functions of the energy and pseudorapidity [63]. The *Global Sequential* (GS) set of multiplicative corrections, which are based on global jet observables, are applied [64].

– After applying all calibrations, jets are clustered based on EM- and LCW-scale topo-clusters. Reconstructed jets are mentioned as EM+JES and LCW+JES accordingly.

Jet energy scale calibration

The *in-situ* jet energy scale is calibrated using as reference well calibrated objects. For different p_T and η of jets a different in-situ methodology is used. Different approaches cover the same calibration region give the possibility to cross-check and improve the calibration.

The $p_\mathrm{T}^{\mathrm{ref}}$ of reference object, which can be γ, Z and jet and is well-calibrated based on other techniques, is compared to the $p_\mathrm{T}^{\mathrm{jet}}$ of a jet, which has to be calibrated. The ratio between data and Monte Carlo

$$\frac{\Re_{\mathrm{data}}}{\Re_{\mathrm{MC}}} = \frac{\langle \mathcal{R}_{\mathrm{data}} \rangle}{\langle \mathcal{R}_{\mathrm{MC}} \rangle}, \qquad \mathcal{R} = p_{\mathrm{T}}^{\mathrm{jet}} / p_{\mathrm{T}}^{\mathrm{ref}} \tag{3.18}$$

is used to define the correction, which is applied to the jets reconstructed in the data.

For the central rapidity region $|\eta| < 0.8$ the jet scale calibration is based on the *Direct Balance* (DB) and *Multijet balance* (MJB) methods [65].

Briefly, both methodologies can be described as follows:

Direct balance method

The direct balance (DB) method is based on the transverse momentum balance between a Z-boson or a photon γ and a jet [66]. To reduce the effect of additional parton radiation, $p_{\mathrm{T}}^{\mathrm{jet}}$ is compared to the reference transverse momentum $p_{\mathrm{T}}^{\mathrm{ref}}$, which is calculated as:

$$p_{\mathrm{T}}^{\mathrm{ref}} = p_{\mathrm{T}}^{Z/\gamma} \times |\cos \Delta\varphi| \,, \tag{3.19}$$

where $p_{\mathrm{T}}^{Z/\gamma}$ is the transverse momentum of the Z/γ and $\Delta\varphi$ is the azimuthal angle between the Z/γ and the leading jet. Due to the p_{T}^{Z} spectrum, the Z-jet direct balance approach covers only $20 < p_{\mathrm{T}}^{\mathrm{jet}} < 200$ GeV transverse momentum range. To extend this range, the γ-jet analysis is used, which covers the range $30 < p_{\mathrm{T}}^{\mathrm{jet}} < 800$ GeV. For the jet energy scale calibration, a combination of these two analyses is used.

Dijet balance method

The dijet balance method is based on the approximation, that, at leading order in QCD, for dijet events the transverse momenta should balance each other [67]. The imbalance of the transverse momenta can be characterised by the asymmetry:

$$\mathcal{A} = \frac{p_{\mathrm{T}}^{\mathrm{jet}} - p_{\mathrm{T}}^{\mathrm{ref}}}{p_{\mathrm{T}}^{\mathrm{avg}}}, \qquad p_{\mathrm{T}}^{\mathrm{avg}} = \frac{1}{2}(p_{\mathrm{T}}^{\mathrm{jet}} + p_{\mathrm{T}}^{\mathrm{ref}}), \tag{3.20}$$

where $p_{\mathrm{T}}^{\mathrm{ref}}$ is the transverse momentum of the reference jet and $p_{\mathrm{T}}^{\mathrm{jet}}$ is the transverse momentum of the jet under investigation.

The calorimeter response can be described as:

$$\mathcal{R}^{\mathrm{dijet}} = \frac{p_{\mathrm{T}}^{\mathrm{jet}}}{p_{\mathrm{T}}^{\mathrm{ref}}} = \frac{2 + \langle \mathcal{A} \rangle}{2 - \langle \mathcal{A} \rangle}, \tag{3.21}$$

where $\langle \mathcal{A} \rangle$ is the mean value of the asymmetry, which depends on $p_{\mathrm{T}}^{\mathrm{avg}}$ and η_{det}.

Multijet balance method

The multijet balance (MJB) method is used to calibrate high p_{T} jets [67]. The high p_{T} jet is calibrated to the recoil system of jets with lower p_{T}. This approach requires to have well calibrated low p_{T} jets, which may be achieved by other in-situ methods.

$$\mathcal{R}^{\mathrm{MJB}} = \frac{p_{\mathrm{T}}^{\mathrm{leading}}}{p_{\mathrm{T}}^{\mathrm{recoil}}}, \tag{3.22}$$

where $p_{\mathrm{T}}^{\mathrm{leading}}$ corresponds to the transverse momentum of the leading jet and $p_{\mathrm{T}}^{\mathrm{recoil}}$ denotes the vectorial sum of transverse momenta of all sub-leading jets. To estimate the response of high p_{T} jets, the ratio $\langle \mathcal{R}_{\mathrm{data}}^{\mathrm{MJB}} \rangle / \langle \mathcal{R}_{\mathrm{MC}}^{\mathrm{MJB}} \rangle$ is used. The MJB method covers the range of $300 < p_{\mathrm{T}} < 1700$ GeV.

Figure 3.11 shows the ratio of the response $\Re_{\mathrm{data}}/\Re_{\mathrm{MC}}$ for the Z+jet, γ+jet and multijet balance in-situ methods for EW+JES and LCW+JES. In the $20 < p_{\mathrm{T}} < 2000$ GeV range, the agreement between data and Monte Carlo simulation is at the 1% level. The black line represents the combined correction from all three methods.

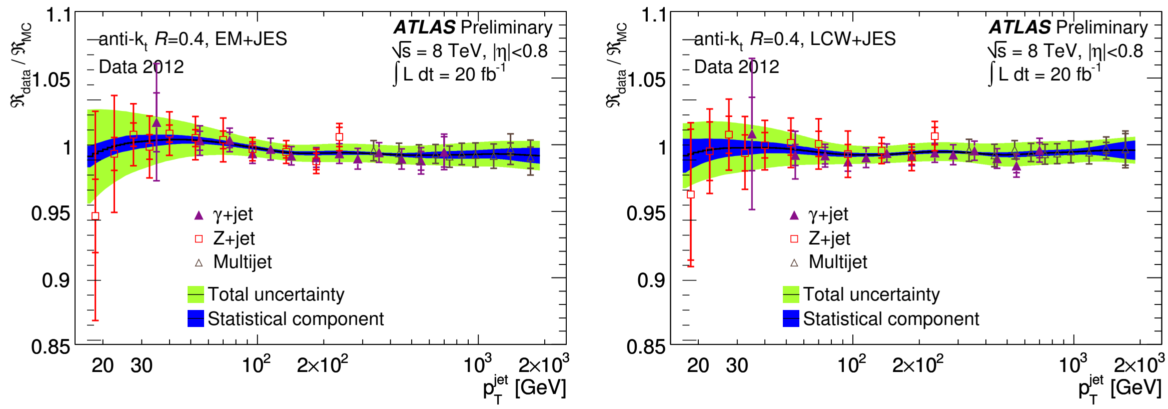

Figure 3.11: Ratio of $\Re_{\mathrm{data}}/\Re_{\mathrm{MC}}$ measured for Z+jet, γ+jet and multijet balance in-situ methods for EW+JES (left) and LCW+JES (right). The black line represents the combined correction from all three methods [65].

The jet energy scale uncertainty includes 65 different parameters related to uncertainty sources from in-situ methods, η-intercalibration and pile-up correction uncertainties.

The plots in Figure 3.12 show the total jet energy scale uncertainty for LCW+JES calibrated

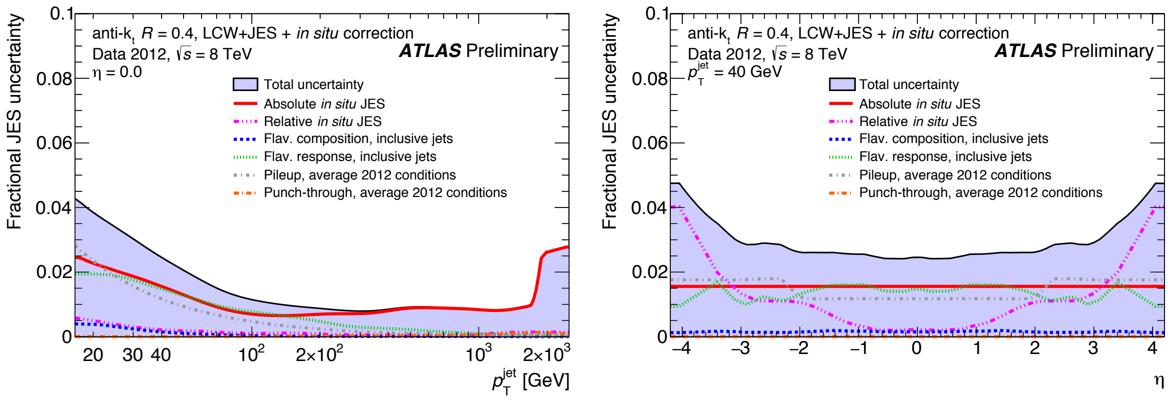

Figure 3.12: The total jet energy scale uncertainty for LCW+JES calibration is shown as a function of $p_{\mathrm{T}}^{\mathrm{jet}}$ for $\eta = 0$ (left) and as a function of η for $p_{\mathrm{T}}^{\mathrm{jet}} = 40$ GeV (right). Distributions are shown for dijet events. "Absolute *in situ* JES" corresponds to V+jet and multijet measurements, "Relative *in situ* JES" corresponds to dijet η-intercalibration, and "Punch-through" is related to the uncertainty on the muon-based stage of the global sequential corrections [65].

jets with in-situ calibration as a function of $p_{\mathrm{T}}^{\mathrm{jet}}$ for $\eta = 0$ (left) and as a function of η for $p_{\mathrm{T}}^{\mathrm{jet}} = 40$ GeV (right). Uncertainties for EM+JES jets with in-situ calibration are similar.

Jet energy resolution

The jet energy resolution is estimated using data-driven techniques based on the transverse momentum balance in dijet, multijet and Z/γ-jet events. It can be parametrised as [63]:

$$\frac{\sigma_{p_{\mathrm{T}}}}{p_{\mathrm{T}}} = \frac{a}{p_{\mathrm{T}}} \oplus \frac{b}{\sqrt{p_{\mathrm{T}}}} \oplus c, \tag{3.23}$$

where a represents a contribution from the external noise (electronics and detector noise and pile-up), b is related to the sampling nature of the calorimeter, and c accounts for fluctuations, which do not depend on p_{T}.

Different methods described above for the jet energy scale calibration can also be used to estimate the jet energy resolution. Two methods are listed below:

Direct balance method

The direct balance method for Z/γ-jet events can be used to estimate the jet energy resolution. The in-situ resolution $\sigma_{\text{in-situ}}$ is obtained as difference in quadrature between detector and particle level resolutions:

$$\sigma_{\text{in-situ}} = \sqrt{\sigma^2(\mathcal{R}_{\mathrm{data}}) - \sigma^2(\mathcal{R}_{\mathrm{truth}})}, \tag{3.24}$$

where $\mathcal{R}_{\mathrm{data}} = p_{\mathrm{T}}^{\mathrm{jet}}/p_{\mathrm{T}}^{\mathrm{ref}}$, $\mathcal{R}_{\mathrm{truth}} = p_{\mathrm{T}}^{\text{truth-jet}}/p_{\mathrm{T}}^{\mathrm{ref}}$, and $p_{\mathrm{T}}^{\text{truth-jet}}$ is the transverse momentum of the true jet, which is matched to the corresponding detector level probe jet.

Dijet balance method

The width of the asymmetric distribution of the dijet balance method can be used to estimate the jet energy resolution:

$$\sigma(\mathcal{A}) = \frac{\sigma(p_{\mathrm{T}}^{\mathrm{jet}}) \oplus \sigma(p_{\mathrm{T}}^{\mathrm{ref}})}{p_{\mathrm{T}}^{\mathrm{avg}}}, \tag{3.25}$$

where $\sigma(p_{\mathrm{T}}^{\mathrm{jet}})$ and $\sigma(p_{\mathrm{T}}^{\mathrm{ref}})$ are energy resolutions for the reference and probe jets, respectively.

Combining dijet measurements with Z/γ-jet measurements, the jet energy resolution as a function of p_{T} for different $|\eta|$ regions ($[0, 0.8]$, $[0.8, 1.2]$, $[1.2, 2.1]$ and $[2.1, 2.8]$) is obtained for EM+JES and LCW+JES calibrations [65].

The plots in Figure 3.13 show the jet energy resolution as a function of p_{T} for $|\eta| < 0.8$ measured with dijet, Z-jet and γ-jet in-situ methods. For $|\eta| > 0.8$ the jet energy resolution is estimated based only on dijet approach, the resolution obtained as a function of p_{T} is similar to that shown in Figure 3.13.

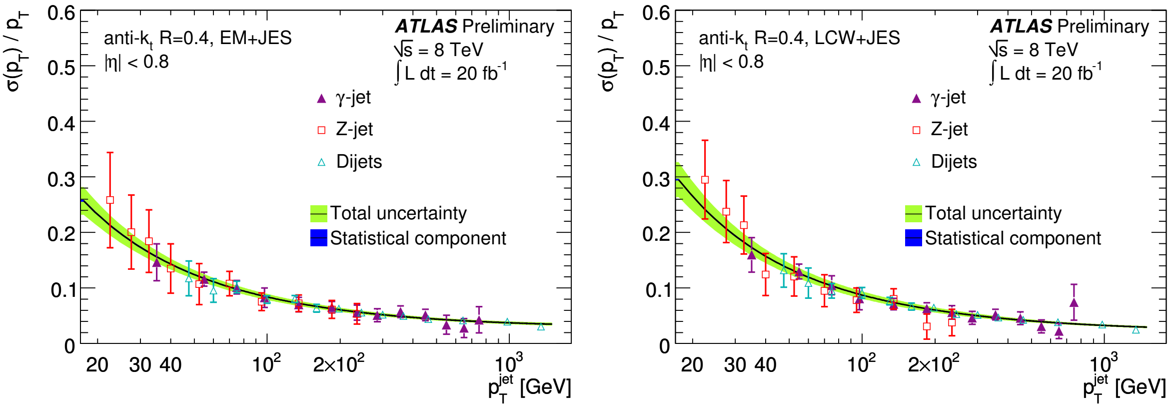

Figure 3.13: Jet energy resolution (JER) for EM+JES (left) and LCW+JES (right) calibrated jets as a function of the jet p_T for $|\eta_{det}| < 0.8$ detector pseudorapidity region [65].

There are alternative techniques which are also used to estimate the jet energy and resolution, for example the *Missing Projection Fraction* (MPF) method [66] or the *Dijet bisector* method [67].

3.5 Heavy flavour tagging

The identification of jets coming from b quarks plays an important role to reject the vector boson background processes (W+jets, Z+jets and diboson). For the b-quark identification, the relatively long lifetime of b hadrons is used. With $p_T \approx 50$ GeV, they are able to travel about half a centimeter from the beam axis before decaying. The secondary vertex created by this decay can be detected by the inner detector. Since the inner detector plays a major role in b-tagging, jets can only be tagged for $|\eta| < 2.5$, due to the inner detector pseudorapidity coverage. A schematic view of a b-hadron decay is shown in Figure 3.14

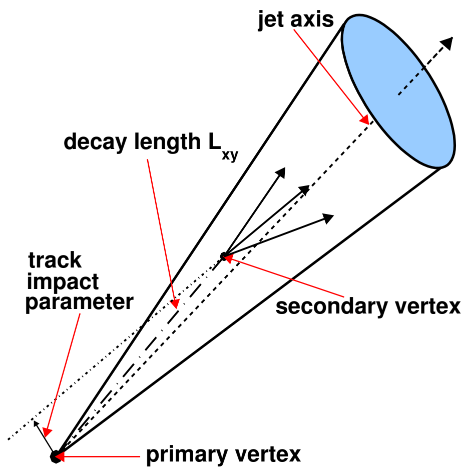

Figure 3.14: Schematic view of a b-hadron decay [68].

The following b-tagging algorithms were developed within the ATLAS experiment:

- The ***IP3D*** is an algorithm based on the transverse d_0 and longitudinal z_0 impact parameters. The tagging algorithm compares impact parameters with smoothed distribution of b- and light-jet hypotheses obtained from the Monte Carlo simulation using a likelihood ratio technique [69].
- The ***SV1*** is a secondary vertex-based algorithm. It uses a likelihood technique to combine the invariant mass of all tracks associated with the vertex, the number of vertices with two tracks and the ratio of the sum of energies for tracks associated with the vertex over the sum of all tracks in the jet [69].
- The ***JetFitter*** is an algorithm using the topology of the b- and c-hadron decays inside the jet. The discrimination is based on a likelihood approach using kinematical and topological variables [69].

The following two algorithms are using a neural network approach to increase the separation between b-, c- and light jets:

- The ***JetFitterCombNN*** is a combination of the JetFitter and IP3D [69]. This algorithm was used for the b-tagging for the 2011 $\sqrt{s} = 7$ TeV data analysis.
- The ***MV1*** algorithm is using as input quantities the output from the IP3D, SV1 and JetFitterCombNN algorithms [70]. This algorithm was used for b-tagging for the 2012 $\sqrt{s} = 8$ TeV data analysis.

An efficiency of the MV1 tagging algorithm to select the b-, c- and light-jet as a function of the p_{T} (left) and η (right) is shown in Figure 3.15.

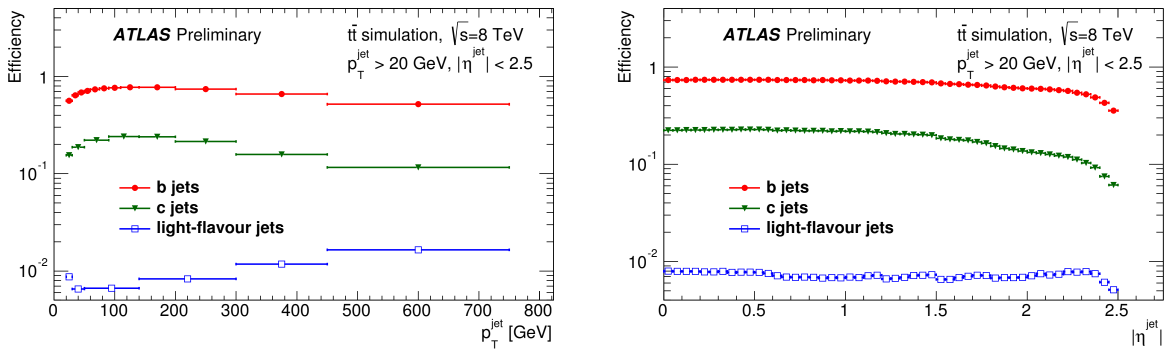

Figure 3.15: Efficiency of the MV1 tagging algorithm to select the b-, c- and light-jet as a function of p_{T} (left) and η (right). The MV1 working point is 70% for b-jets with $p_{\mathrm{T}} > 20$ GeV and $|\eta| < 2.5$, estimated on a sample of $t\bar{t}$ events [71].

3.6 Missing transverse energy

One of the most important objects for supersymmetry searches is *missing transverse energy* ($E_{\mathrm{T}}^{\mathrm{miss}}$) [72]. Due to the presence of neutralinos, the $E_{\mathrm{T}}^{\mathrm{miss}}$ for signal events is higher than for Standard Model processes. This makes it a powerful separation variable to reject background events. A description of the trigger, reconstruction and performance of $E_{\mathrm{T}}^{\mathrm{miss}}$ is given below.

3.6.1 Trigger

The transverse-momentum trigger is designed to select events with weakly interacting particles passing through the detector. The trigger system works as follows:

- The ***Level 1*** (L1) trigger only uses information from calorimeter "trigger towers". Each trigger tower corresponds to an analogue sum of (η, ϕ) calorimeter cells with a size of 0.1×0.1. Analogue signals are digitised, the results of four adjacent trigger towers are summed up to create a jet element. The E_x and E_y quantities are calculated using the coarse information available for jet elements. At this level the $E_{\mathrm{T}}^{\mathrm{miss}}$ is not calculated and the decision to accept or reject events is taken based on the measured (x, y) components of the energies, by mean of look-up tables.
- The ***Level 2*** (L2) trigger recalculates quantities calculated at L1 level based on the objects in the *Region of Interest* (RoI) using the full granularity of the detector. The L2 algorithm improves the $E_{\mathrm{T}}^{\mathrm{miss}}$ calculation by including the muons, reconstructed at L2 level.
- The ***Event Filter*** (EF) trigger recalculates all quantities using the full available event information and full granularity of both calorimeters and muon spectrometers. To suppress noise, for $E_{\mathrm{T}}^{\mathrm{miss}}$ calculations only calorimeter energies above 3 σ of the noise are considered.

Further details related to the transverse-momentum trigger performance can be found in Refs. [73, 74].

3.6.2 Reconstruction

In this section all p_{T} and $E_{\mathrm{T}}^{\mathrm{miss}}$ are considered as vectors in the $x - y$ plane. The missing transverse energy of a set of objects X is defined as the vector in the $x - y$ plane, opposite to the vectorial sum of all measured objects in X:

$$E_{\mathrm{T}}^{\mathrm{miss},\,X} = - \sum_{\mathrm{obj} \in X} p_{\mathrm{T}}^{\mathrm{obj}}. \tag{3.26}$$

The $E_{\mathrm{T}}^{\mathrm{miss}}$ is reconstructed as missing energy from the calorimeter and muon systems:

$$E_{\mathrm{T}}^{\mathrm{miss}} = E_{\mathrm{T}}^{\mathrm{miss,\,calo}} + E_{\mathrm{T}}^{\mathrm{miss,\,muon}} \tag{3.27}$$

The $E_{\mathrm{T}}^{\mathrm{miss,\,calo}}$ consists of the following components:

- $E_{\mathrm{T}}^{\mathrm{miss},\,e}$, $E_{\mathrm{T}}^{\mathrm{miss},\,\gamma}$, $E_{\mathrm{T}}^{\mathrm{miss},\,\tau}$ – reconstructed based on calorimeter cells, which were identified as electron, photon and hadronically decaying τ lepton;
- $E_{\mathrm{T}}^{\mathrm{miss,\,jets}}$ – LCW+JES calibrated anti-k_t $R = 0.4$ jets with $p_{\mathrm{T}} > 20$ GeV;
- $E_{\mathrm{T}}^{\mathrm{miss,\,soft\text{-}jets}}$ – LCW calibrated anti-k_t $R = 0.4$ jets with $10\ \mathrm{GeV} < p_{\mathrm{T}} < 20$ GeV;
- $E_{\mathrm{T}}^{\mathrm{miss,\,calo}\text{-}\mu}$ – energy loss of muons in the calorimetry system;
- $E_{\mathrm{T}}^{\mathrm{miss,\,CellOut}}$ – includes all cells, which are not associated to any reconstructed objects.

The calibration of these objects is done independently, taking into account their physical nature.

The muon term is computed as:

$$E_{\mathrm{T}}^{\mathrm{miss,\,muon}} = -\sum_{\mu} p_{\mathrm{T}}^{\mu}, \tag{3.28}$$

where all muons with $|\eta| < 2.5$ are included in the sum.

To improve the calculation of the $E_{\mathrm{T}}^{\mathrm{miss,\,CellOut}}$ term, the energy-flow approach is used. The track based information is used in order to recover the contribution from low-p_{T} objects which did not reach the calorimeter. If a track associated to a topocluster with a low deposited energy exists, the track based calculation of the momentum is preferred over the calorimeter information.

For the $E_{\mathrm{T}}^{\mathrm{miss}}$ affected by pile-up, two different approaches to pile-up suppression are used:

In the first approach the *Soft Term Vertex Fraction* is calculated:

$$\mathrm{STVF} = \sum_{\mathrm{track}\in\mathrm{soft\text{-}term,PV}} p_{\mathrm{T}}(\mathrm{track,PV}) \Big/ \sum_{\mathrm{track}\in\mathrm{soft\text{-}term}} p_{\mathrm{T}}(\mathrm{track}). \tag{3.29}$$

The correction to the $E_{\mathrm{T}}^{\mathrm{miss,\,soft\text{-}term}}$ is applied by scaling with the STVF factor.

Another pile-up subtraction approach is based on considering the jet area A^{jet}. The energy for topoclusters entering into the $E_{\mathrm{T}}^{\mathrm{miss,\,soft\text{-}term}}$ is reclustered based on the k_t algorithm, which reconstructs jets down to $p_{\mathrm{T}} = 0$. To define a contribution from pile-up in the jet area, the event transverse momentum density ρ is used. Jets are corrected as:

$$p_{\mathrm{T}}^{\mathrm{jet,\,corr}} = p_{\mathrm{T}}^{\mathrm{jet}} - \rho \times A^{\mathrm{jet}}, \tag{3.30}$$

where A^{jet} is the jet area. Finally the JVF > 0.25 filter is applied. Details about the jet-area corrections can be found in Refs. [61, 62].

Two different ways to estimate ρ are considered:

- ***Extrapolated Jet Area Filtered***
  The ρ is calculated as the median of $p_{\mathrm{T}}^{\mathrm{jet}} / A^{\mathrm{jet}}$, where the jet is clustered by the k_t algorithm with $R = 0.4$ from the soft term in the $|\eta| < 1.8$ region. The value of ρ is then extrapolated to the forward region. The soft term jets are clustered using the k_t algorithm with $R = 0.6$ and corrected and filtered as described above.

– ***Jet Area Filtered***
  The ρ is calculated as the median of $p_{\mathrm{T}}^{\mathrm{jet}} / A^{\mathrm{jet}}$, where the jet is clustered by the k_t algorithm with $R = 0.8$ from the soft term in the $|\eta| < 5$ region. The soft term jets are clustered using the k_t algorithm with $R = 0.4$ and corrected and filtered as described above.

3.6.3 Performance

Performance of the $E_{\mathrm{T}}^{\mathrm{miss}}$ reconstruction is measured using minimum bias, dijet, $Z \to \ell\ell$ and $W \to \ell\nu$ events. For all these processes, the simulated samples are compared with the observed data distributions [75, 76].

Apart from the $W \to \ell\nu$ process, three other processes can be used to investigate the $E_{\mathrm{T}}^{\mathrm{miss}}$. It can be done almost without relying on the simulation, since they do not have a direct source of $E_{\mathrm{T}}^{\mathrm{miss}}$, apart from some semileptonic decays which will have a much smaller contribution. Therefore, the measured $E_{\mathrm{T}}^{\mathrm{miss}}$ will be mainly due to reconstruction or detector effects.

The response of $E_{\mathrm{T}}^{\mathrm{miss}}$ is studied for two different cases: for the $Z \to \ell\ell$ decay, where no genuine $E_{\mathrm{T}}^{\mathrm{miss}}$ is expected, and for the $W \to \ell\nu$, where genuine $E_{\mathrm{T}}^{\mathrm{miss}}$ is produced from the neutrino.

An important variable, used in performance measurements, is the total scalar sum of all objects

$$\sum E_T = \sum_{\mathrm{obj}} \left| p_{\mathrm{T}}^{\mathrm{obj}} \right| . \tag{3.31}$$

The resolutions of the E_x^{miss} and E_y^{miss} distributions as a function of $\sum E_T$ before (left) and after (right) pile-up suppression with the STVF approach for various Monte Carlo samples are shown in Figure 3.16.

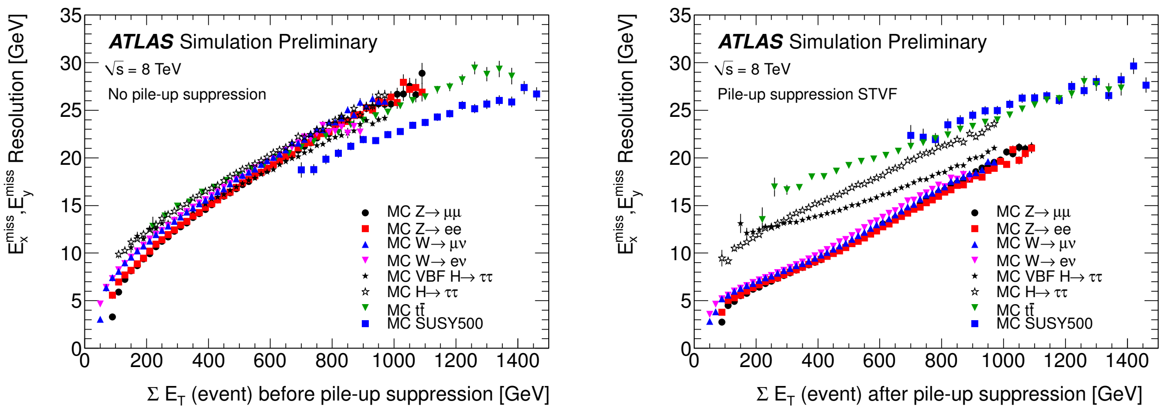

Figure 3.16: The E_x^{miss} and E_y^{miss} distributions as a function of $\sum E_T$ before (left) and after (right) pile-up suppression with the STVF approach for various Monte Carlo samples [76].

For the $Z \to \ell\ell$ decay, a projection of $E_{\mathrm{T}}^{\mathrm{miss}}$ to the direction of the Z boson in the transverse plane is defined as:

$$\text{Projection} = \langle E_{\mathrm{T}}^{\mathrm{miss}} \cdot A_Z \rangle, \qquad A_Z = \frac{p_{\mathrm{T}}^{\ell^+} + p_{\mathrm{T}}^{\ell^-}}{\left|p_{\mathrm{T}}^{\ell^+} + p_{\mathrm{T}}^{\ell^-}\right|}, \tag{3.32}$$

where $p_{\mathrm{T}}^{\ell^\pm}$ are transverse momentum vectors of the lepton anti-lepton pair, which is forming the Z-boson, and A_Z is the direction of the Z-boson in the transverse plane. Figure 3.17 shows distributions of the mean value of $E_{\mathrm{T}}^{\mathrm{miss}}$ (left) and the mean value of the projection of $E_{\mathrm{T}}^{\mathrm{miss}}$ on the transverse momentum direction of the Z boson p_{T}^{Z} (right) as functions of p_{T}^{Z}.

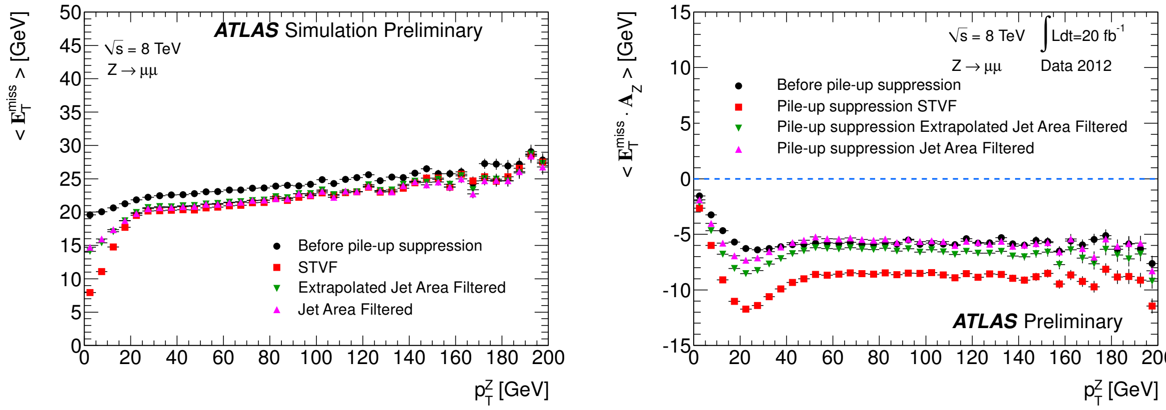

Figure 3.17: Distributions of the mean value of $E_{\mathrm{T}}^{\mathrm{miss}}$ (left) and the mean value of the projection of $E_{\mathrm{T}}^{\mathrm{miss}}$ on the transverse momentum direction of the Z boson p_{T}^{Z} (right) [76]. Both distributions are shown for the $Z \to \mu\mu$ selection as functions of p_{T}^{Z}.

Another important distribution is the hadronic recoil in the $Z \to \ell\ell$ decay, which is defined as the vectorial difference $\left|E_{\mathrm{T}}^{\mathrm{miss}} - p_{\mathrm{T}}^{Z}\right|$. The plots in Figure 3.18 show the ratio of the projection

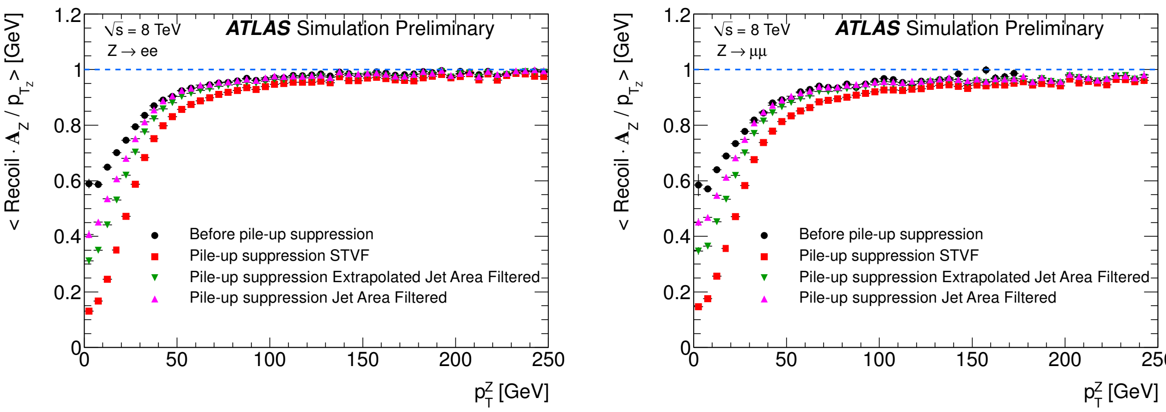

Figure 3.18: Distribution of the mean value of the hadronic recoil $\langle (E_{\mathrm{T}}^{\mathrm{miss}} - p_{\mathrm{T}}^{Z}) \cdot A_z / p_{\mathrm{T}}^{Z} \rangle$ as function of p_{T}^{Z} [76]. Left plot shows the distribution for the $Z \to ee$ decay, the right plot for the $Z \to \mu\mu$ decay.

of the hadronic recoil on the transverse direction A_Z to the p_{T}^{Z} of the Z boson. Distributions are shown for the $Z \to ee$ and $Z \to \mu\mu$ processes.

Correct modelling of the recoil is very important for the presented $\sqrt{s} = 8$ TeV analyses, since both of them significantly benefit from the radiated jet. The variable, similar to the projection, but based on the recoil jet is used to improve the signal to background separation.

For the $W \to \ell\nu$ decay, the measured parameter is the $E_{\mathrm{T}}^{\mathrm{miss}}$ linearity, which is defined as:

$$\text{Linearity} = \left\langle \frac{E_{\mathrm{T}}^{\mathrm{miss}} - E_{\mathrm{T}}^{\mathrm{miss,\,True}}}{E_{\mathrm{T}}^{\mathrm{miss,\,True}}} \right\rangle, \tag{3.33}$$

and the resolution of $E_{\mathrm{T}}^{\mathrm{miss}}$, which is defined as:

$$\text{Resolution} = \frac{\sigma(E_{\mathrm{T}}^{\mathrm{miss}} / E_{\mathrm{T}}^{\mathrm{miss,\,True}})}{\langle E_{\mathrm{T}}^{\mathrm{miss}} / E_{\mathrm{T}}^{\mathrm{miss,\,True}} \rangle}. \tag{3.34}$$

The plots in Figure 3.19 show distributions of the resolution of $E_{\mathrm{T}}^{\mathrm{miss}}$ (left) and $E_{\mathrm{T}}^{\mathrm{miss}}$ linearity (right) as functions of the true $E_{\mathrm{T}}^{\mathrm{miss,\,True}}$ for $W \to \mu\nu$ based on the Monte Carlo simulation.

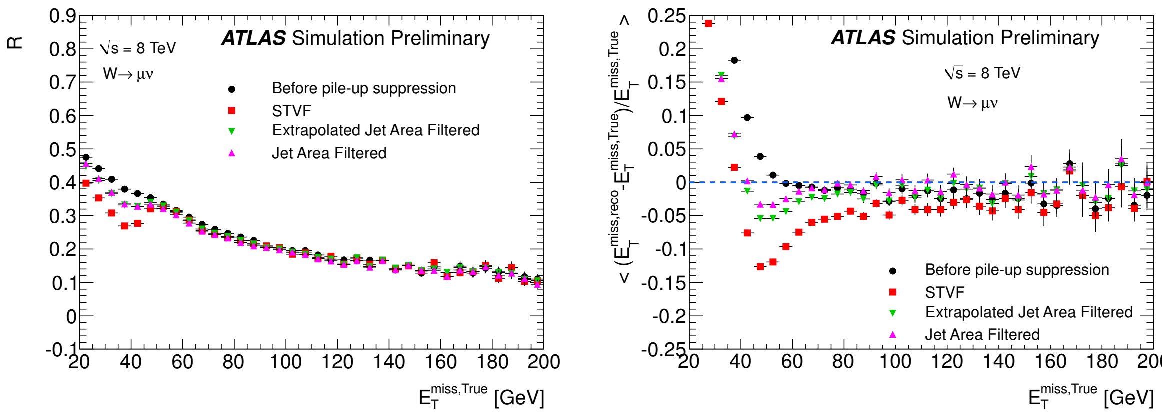

Figure 3.19: Distributions of the resolution of $E_{\mathrm{T}}^{\mathrm{miss}}$ (left) and $E_{\mathrm{T}}^{\mathrm{miss}}$ linearity (right) as functions of the true $E_{\mathrm{T}}^{\mathrm{miss,\,True}}$ for $W \to \mu\nu$ based on the Monte Carlo simulation [76].

The following approach is used to study the balance between $E_{\mathrm{T}}^{\mathrm{miss,\,soft}}$ and hard objects. The total transverse momentum of the hard objects is defined as:

$$p_{\mathrm{T}}^{\mathrm{hard}} = \sum_{\mu} p_{\mathrm{T}}^{\mu} + \sum_{e} p_{\mathrm{T}}^{e} + \sum_{\mathrm{jet}} p_{\mathrm{T}}^{\mathrm{jet}} + \sum_{\gamma} p_{\mathrm{T}}^{\gamma} + \sum_{\nu} p_{\mathrm{T}}^{\nu}. \tag{3.35}$$

Following this definition, the $p_{\mathrm{T}}^{\mathrm{hard}}$ is calculable only for Monte Carlo events, since it contains invisible objects. It is expected, that the difference between $E_{\mathrm{T}}^{\mathrm{miss}}$ and $p_{\mathrm{T}}^{\mathrm{hard}}$ would be equal to $E_{\mathrm{T}}^{\mathrm{miss,\,soft}}$. To evaluate the scale and the resolution of $E_{\mathrm{T}}^{\mathrm{miss,\,soft}}$, it is decomposed into two components, along and perpendicular to the $p_{\mathrm{T}}^{\mathrm{hard}}$ direction. The mean longitudinal component corresponds to the scale of $E_{\mathrm{T}}^{\mathrm{miss,\,soft}}$, while the resolution is estimated from the longitudinal and perpendicular components distributions on the $p_{\mathrm{T}}^{\mathrm{hard}}$ bins fitted by a Gaussian.

Distributions of $E_{\mathrm{T}}^{\mathrm{miss}}$ for the $Z \to \mu\mu$ process before and after pile-up suppression with STVF approach are shown in Figure 3.20. Variations of $E_{\mathrm{T}}^{\mathrm{miss,\,soft}}$ are done according to the scale

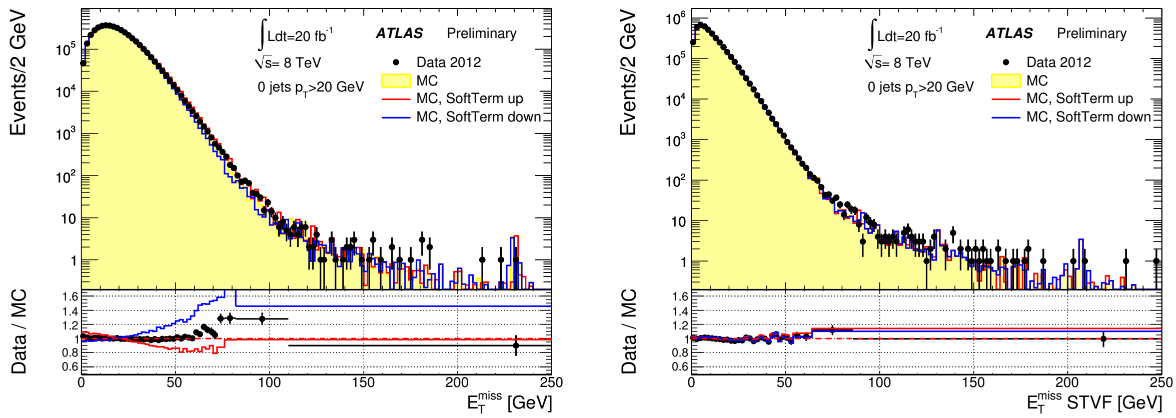

Figure 3.20: Distributions of $E_{\mathrm{T}}^{\mathrm{miss}}$ before (left) and after (right) pile-up suppression with STVF approach [76]. Distributions show a data/MC comparison for the $Z \rightarrow \mu\mu$ process. Variations of $E_{\mathrm{T}}^{\mathrm{miss,\,soft}}$ are done according to the scale and resolution uncertainties estimated for the $E_{\mathrm{T}}^{\mathrm{miss,\,soft}}$ term.

and resolution uncertainties estimated for the $E_{\mathrm{T}}^{\mathrm{miss,\,soft}}$ term. The uncertainty on $E_{\mathrm{T}}^{\mathrm{miss,\,soft}}$ is significantly reduced after pile-up suppression, due to the strong reduction of the $E_{\mathrm{T}}^{\mathrm{miss,\,soft}}$ term.

Distributions of $E_{\mathrm{T}}^{\mathrm{miss}}$ and m_{T} for the $W \rightarrow e\nu$ process are shown in Figure 3.21 for different pile-up suppression methods. The true $E_{\mathrm{T}}^{\mathrm{miss}}$ and m_{T} reconstructed with true $E_{\mathrm{T}}^{\mathrm{miss}}$ are also shown for comparison. Many analyses which estimate theory uncertainties are based on

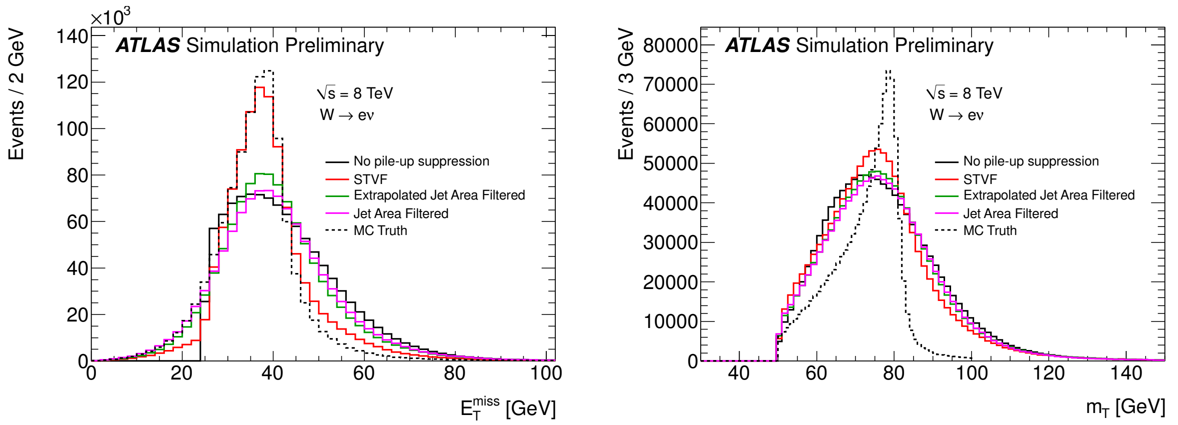

Figure 3.21: Distribution of $E_{\mathrm{T}}^{\mathrm{miss}}$ (left) and m_{T} (right) for the $W \rightarrow e\nu$ process for different pile-up suppression methods [76]. The true $E_{\mathrm{T}}^{\mathrm{miss}}$ and m_{T} reconstructed with true $E_{\mathrm{T}}^{\mathrm{miss}}$ are also shown for comparison.

particle level studies. The m_{T} distribution (right plot) shows, that if a selection with a hard m_{T} requirement (above 100 GeV) is used, it cannot be applied directly to particle level objects without relaxing the m_{T} requirement or applying a smearing of the true $E_{\mathrm{T}}^{\mathrm{miss}}$.

CHAPTER 4

Search strategy

The strategy for searches for supersymmetry in the one-lepton channel, the statistical methods and the tools used for the analysis are briefly discussed in this chapter.

For all searches presented in this thesis, R-parity conservation is assumed. A consequence is the stability of the *Lightest Supersymmetric Particle* (LSP). Since the LSP has not been observed so far by any experiment, it should be neutral and weakly interacting. It is assumed, that the LSP is the lightest neutralino $\tilde{\chi}_1^0$.

4.1 Decay modes

The mass difference between two particles X and Y is denoted as $\Delta m(X, Y) = m(X) - m(Y)$. In the presented work the following decay modes are considered:

- The $\tilde{t}_1 \to t\tilde{\chi}_1^0$ decay, with a branching ratio ($\mathcal{BR}$) of 100%, where the top quark decays on-shell: $m(t) < \Delta m(\tilde{t}, \tilde{\chi}_1^0)$. This mode is denoted as the top-neutralino decay and to refer to it, the acronym "tN" (for "top-Neutralino") is used in the following.
- The $\tilde{t}_1 \to bW\tilde{\chi}_1^0$ decay, with a $\mathcal{BR} = 100\%$; this corresponds to a top quark off-shell decay, where the W-boson decays on-shell: $m(b) + m(W) < \Delta m(\tilde{t}, \tilde{\chi}_1^0) < m(t)$. This decay mode is denoted as 3-body decay and is referred to with the acronym "bWN" (for "bottom-W-Neutralino") in the following.
- The $\tilde{t}_1 \to b\tilde{\chi}_1^\pm$ decay, with the subsequent decay of $\tilde{\chi}_1^\pm \to W^{\pm(*)}\tilde{\chi}_1^0$, where both decays proceed with a $\mathcal{BR} = 100\%$, and $m(b) < \Delta m(\tilde{t}, \tilde{\chi}_1^\pm)$ and $m(\tilde{\chi}_1^0) < m(\tilde{\chi}_1^\pm)$, while the W boson decays either on its mass shell $m(W) < \Delta m(\tilde{\chi}_1^\pm, \tilde{\chi}_1^0)$ or as a virtual particle $m(W) > \Delta m(\tilde{\chi}_1^\pm, \tilde{\chi}_1^0)$. This mode is called the bottom-chargino decay and to refer to it, the acronym "bC" (for "bottom-Chargino") is used.

The Feynman diagrams for these decay modes for the semileptonic decay channel are shown in Figure 4.1.

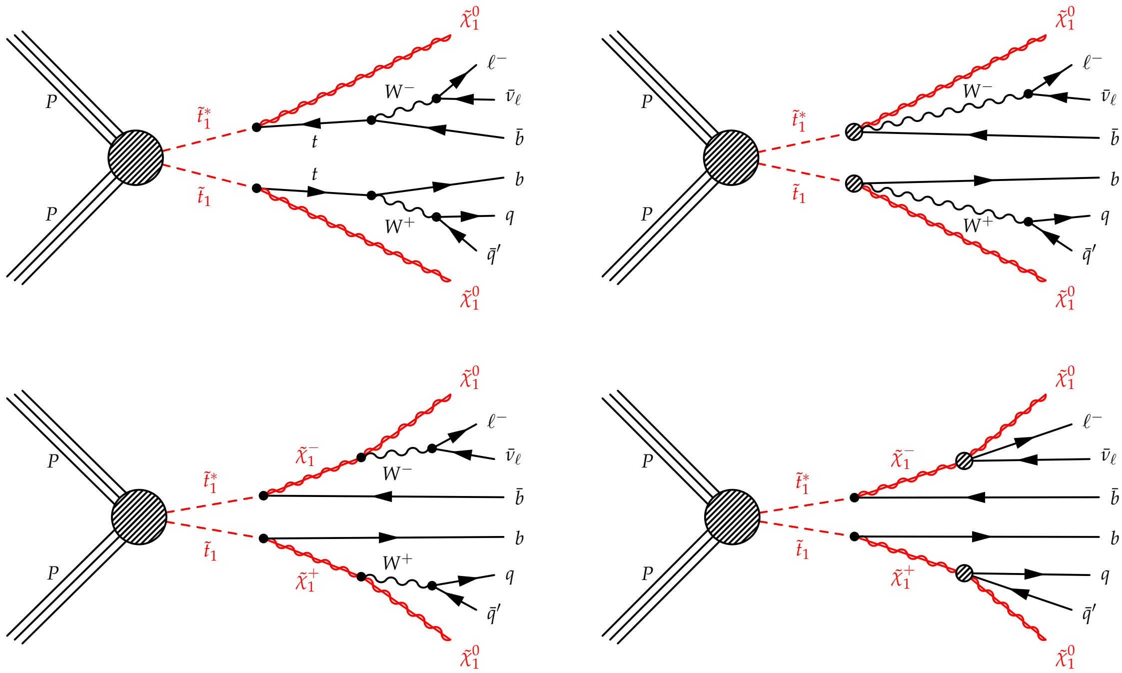

Figure 4.1: The Feynman diagrams for top-squark pair production followed by semileptonic decay channels, where both top squarks decay via: on-shell top quark and neutralino $\tilde{t}_1 \to t\tilde{\chi}_1^0$ (top left), off-shell top quark (3-body decay) via bottom quark, W boson and neutralino $\tilde{t}_1 \to bW\tilde{\chi}_1^0$ (top right) and bottom quark and chargino $\tilde{t}_1 \to b\tilde{\chi}_1^\pm \to bW^{\pm(*)}\tilde{\chi}_1^0$ with W-boson decay either on-shell (bottom left) or off-shell (bottom right).

4.2 Simplified models

Since the SUSY partners do not have the same masses as the corresponding Standard Model particles, supersymmetry has to be broken.

In general, the masses of SUSY particles, if there are no other assumptions, enter the model as input parameters. To decrease the number of input parameters, *simplified models* are considered, meaning that all supersymmetric particles, which are not included in the decay, are considered to be very heavy (above 3 TeV) and are neglected.

This simplification allows to generate a model-dependent set of signal samples for different masses of the particles in the decay mode. The produced set of signal samples for the $\tilde{t}_1 \to t\tilde{\chi}_1^0$ on-shell and off-shell decay modes are referred to as “tN grid” and “bWN grid”, respectively. Since these decays include only two supersymmetric particles, each signal model can be presented as a point in the $(\tilde{t}, \tilde{\chi}_1^0)$ mass plane.

For the $\tilde{t}_1 \to b\tilde{\chi}_1^\pm \to bW^{\pm(*)}\tilde{\chi}_1^0$ decay mode, three particles are involved, therefore each signal model is represented as a point in the $(\tilde{t}, \tilde{\chi}_1^\pm, \tilde{\chi}_1^0)$ mass space. Since a three-dimensional space is difficult to present, the signal points are generated for different mass planes and are referred to as “bC grids”. The *gaugino universality* grid, which assumes $m(\tilde{\chi}_1^\pm) = 2 \cdot m(\tilde{\chi}_1^0)$, is presented in the $(\tilde{t}, \tilde{\chi}_1^0)$ mass plane. The motivation for this assumption is that for supersymmetry the gauge coupling constants are unified at a high scale. Assuming that the gaugino masses are also unified at the same scale, one can get the relation

$$m(\tilde{\chi}_1^{\pm}) \approx 2 \cdot m(\tilde{\chi}_1^0) \tag{4.1}$$

for the lightest chargino and neutralino.

4.3 Compressed scenarios

A *Compressed Scenario* refers to signal models where mass differences between some supersymmetric particles are small or some masses are degenerated. Usually in these regions the standard analysis does not have enough sensitivity and dedicated analyses have to be developed. The presented work targets different compressed scenarios for both $\tilde{t}_1 \to t\tilde{\chi}_1^0$ and $\tilde{t}_1 \to b\tilde{\chi}_1^{\pm}$ decays.

For the $\tilde{t}_1 \to t\tilde{\chi}_1^0$ decay mode the compressed scenario corresponds to $\Delta m(\tilde{t}, \tilde{\chi}_1^0) \approx m(t)$, the so-called *tN diagonal* region. This region consists of two parts:

– Below the diagonal, $\Delta m(\tilde{t}, \tilde{\chi}_1^0) > m(t)$; with on-shell top-quark decay $\tilde{t}_1 \to t\tilde{\chi}_1^0$;

– Above the diagonal, $\Delta m(\tilde{t}, \tilde{\chi}_1^0) < m(t)$; with off-shell (3-body) decay $\tilde{t}_1 \to bW\tilde{\chi}_1^0$.

The analysis covers the region which is left uncovered after top-squark pair production SUSY searches at $\sqrt{s} = 8$ TeV. This analysis uses the $\sqrt{s} = 8$ TeV data and allows to cover the tN diagonal region of $m(\tilde{t}_1)$ from 200 GeV up to 300 GeV on both sides of the diagonal for on- and off-shell top-quark decays.

For the $\tilde{t}_1 \to b\tilde{\chi}_1^{\pm}$ decay mode, the compressed scenario targets the so-called *bC diagonal* region of the gaugino universality grid, where $\Delta m(\tilde{t}, \tilde{\chi}_1^{\pm})$ is small, less than about 25 GeV. In this region the p_{T} of the produced *b*-jets is small and mainly below the acceptance threshold. Therefore the standard analysis does not have enough sensitivity. Analyses for this compressed scenario are developed for the $\sqrt{s} = 7$ TeV and $\sqrt{s} = 8$ TeV data. The analyses cover the bC diagonal region of $m(\tilde{t}_1)$ from 125 GeV up to 300 GeV.

4.4 Variable definition

In this section the variables used in the analysis are defined. For the tN diagonal analysis, additional specific variables are defined in Section 8.3.

$E_{\mathrm{T}}^{\mathrm{miss}}$ is defined as the magnitude of the transverse momentum vector $|p_{\mathrm{T}}^{\mathrm{miss}}|$.

The H_{T} variable is defined as the scalar sum of the leading three jets $H_{\mathrm{T}} = \sum_{i=1}^{3} p_{\mathrm{T}}(j_i)$. This variable is used for the bC analysis, where the jet selection requires at least three jets.

The $E_{\mathrm{T}}^{\mathrm{miss}}/\sqrt{H_{\mathrm{T}}}$ variable represents an approximation to the $E_{\mathrm{T}}^{\mathrm{miss}}$ significance.

The rapidity y is defined as:

$$y = \frac{1}{2}\ln\left(\frac{E+p_z}{E-p_z}\right). \tag{4.2}$$

The pseudorapidity η is defined as:

$$\eta = \frac{1}{2}\ln\left(\frac{p+p_z}{p-p_z}\right) = \text{artanh}\left(\frac{p_z}{p}\right), \tag{4.3}$$

where p is the magnitude of the three-momentum of the particle. In the limit $m \ll p$, one obtains $E \approx p$ and $\eta \approx y$.

The invariant mass of a particle X with the four-momentum $p^\mu(X)$ is defined as

$$m(X) = m(p^\mu(X)) = p^\mu(X)p_\mu(X). \tag{4.4}$$

In case of the system of particles, to improve the readability, the following notation is used:

$$m(X_1 + \cdots + X_n) = m(p^\mu(X_1) + \cdots + p^\mu(X_n)), \tag{4.5}$$

where $X_1, \ldots, X_n$ are arbitrary particles.

The m_T variable

Since for proton-proton collisions at the LHC, the boost along the z-axis is not known, the *transverse mass* (m_T) variable, which is invariant under this boost, is defined. This is the key variable for the one-lepton searches for supersymmetry.

The projection of the four-momentum for the particle with mass m on the transverse $x-y$ plane is defined as:

$$P_T(E, p_x, p_y, p_z) = (E_T, p_x, p_y, 0), \tag{4.6}$$

where

$$p^2 = p_x^2 + p_y^2 + p_z^2, \quad p_T^2 = p_x^2 + p_y^2, \quad E = \sqrt{m^2 + p^2}, \quad E_T = \sqrt{m^2 + p_T^2}. \tag{4.7}$$

In this notation, the *transverse mass* m_T of two particles a and b can be defined as:

$$m_\mathrm{T}(a, b) = m(P_T(a) + P_T(b)). \tag{4.8}$$

The more standard, equivalent definition is

$$m_\mathrm{T}(a, b) = \sqrt{m_a^2 + m_b^2 + 2(E_T^a E_T^b - p_x^a p_x^b - p_y^a p_y^b)}. \tag{4.9}$$

The following assertions hold:

$$m_\mathrm{T}(a, b) \leq m(a+b), \quad m_\mathrm{T}(a, b) = m(a+b) \iff y(a) = y(b), \tag{4.10}$$

where y is the rapidity. In the $m \ll p$ approximation this can be written as $\eta(a) = \eta(b)$, where η is the pseudorapidity.

4.5 Multivariate analysis

The *Toolkit for Multivariate Analysis* (TMVA) is used for the tN diagonal analysis [77]. It provides a machine learning environment and is integrated inside the ROOT package [78]. For the training a *Boosted Decision Trees* (BDT) algorithm is used. Using an automated multivariate tool allows to improve the sensitivity of the analysis, but in general, the main challenge is to define variables, which have a good signal-to-background separation power.

4.6 Background estimate

For analyses, which study some physics models, the region of phase space where a signal model predicts a significant excess over the Standard Model background is important. Such a region is referred to as a *signal regions* (SR). It is possible that the analysis has several signal regions.

To decrease the influence from different systematic variations, the dominant backgrounds in the signal region are usually normalised using a semi-data-driven approach. For this purpose *control regions* (CRs) enriched with the dominant background processes are defined. It is assumed that control regions have a high number of background events to decrease the statistical uncertainty and a low signal contamination, to be nearly independent on the signal model. The normalisation of the background processes is performed using the observed data.

To validate the modelling of the Standard Model background in the signal regions, so called *validation regions* (VRs) are defined. Usually they have selection requirements similar to those used for the signal regions.

The signal and control regions have to be statistically independent. Therefore, it is important that they do not overlap. Since validation regions are used for validation purposes, it is important that they do not overlap with the signal and control regions, but they may overlap with each other.

To normalise n background processes, one should define at least n control regions. The control regions should be optimised to minimise the uncertainties of the fit, therefore it is desirable, that each background process p_i dominates in a dedicated control region CR_i.

The background processes, for which a semi-data-driven approach for the normalisation is not used, are normalised to the Monte Carlo prediction.

The background process p in the signal region SR can be estimated as:

$$N_{\mathrm{SR}}^{p,\,\mathrm{est}} = N_{\mathrm{CR}}^{p,\,\mathrm{obs}} \cdot \frac{\mathrm{MC}_{\mathrm{SR}}^{p}}{\mathrm{MC}_{\mathrm{CR}}^{p}} = N_{\mathrm{CR}}^{p,\,\mathrm{obs}} \cdot \mathrm{TF}_{\mathrm{CR}\to\mathrm{SR}}^{p} = \mu^{p} \cdot \mathrm{MC}_{\mathrm{SR}}^{p}, \tag{4.11}$$

where:

$N_{\mathrm{SR}}^{p,\,\mathrm{est}}$ is the background estimate for the SR;

$N_{\mathrm{CR}}^{p,\,\mathrm{obs}}$ is the number of observed events in the CR;

$\mathrm{MC}^p_{\mathrm{SR}}$ and $\mathrm{MC}^p_{\mathrm{CR}}$ are the unnormalised Monte Carlo predictions in the SR and the CR;

μ^p is the normalisation for process p, as obtained from the fit;

$\mathrm{TF}^p_{\mathrm{CR}\to\mathrm{SR}} = \dfrac{\mathrm{MC}^p_{\mathrm{SR}}}{\mathrm{MC}^p_{\mathrm{CR}}}$ is the *transfer factor* (TF) for a process p from the CR to the SR.

An important benefit of the estimation of the $N^{p,\mathrm{est}}_{\mathrm{SR}}$ based on the transfer factor is that part of the systematic uncertainties may cancel. For example, the b-tagging uncertainty, without using the normalisation in the CR, is about $\pm 20\%$, while with a correct normalisation, it can be reduced to a few percent.

In the current analysis, the dominant backgrounds are $t\bar{t}$ and $W+$jets production. Therefore, at least two control regions are needed. For the current analysis, one control region is dominated by the main background process ($t\bar{t}$ or $W+$jets, depending on tN or bC analysis), while for the second one it is difficult to define a region where it dominates. Therefore, for other control region both background processes have significant contributions.

4.7 Likelihood function

The likelihood function that is considered for the analysis is the product of the Poisson probabilities of event counts in the signal and control regions, and distributions, which represent systematic uncertainties. The function is defined as:

$$\begin{aligned} L(n,\theta^0|\mu_{\mathrm{sig}},\mu^p,\theta) &= \mathcal{P}_{\mathrm{SR}} \times \mathcal{P}_{\mathrm{CR}} \times \mathcal{C}_{\mathrm{syst}} = \\ &= \prod_i P(n_i|\lambda_i(\mu_{\mathrm{sig}},\mu^p,\theta)) \times C_{\mathrm{syst}}(\theta^0,\theta), \end{aligned} \tag{4.12}$$

where:

P is the Poisson distribution;

n_i is the number of observed events in i-th bin of signal and control regions;

λ_i is the prediction in the i-th bin, depends on $\mu_{\mathrm{sig}}, \mu^p, \theta$ parameters;

$\theta = (\theta_1, \ldots, \theta_k)$ are nuisance parameters for systematic uncertainties;

$\theta^0 = (\theta^0_1, \ldots, \theta^0_k)$ are central value for auxiliary measurements;

$\mu^p = (\mu^p_1, \ldots, \mu^p_m)$ are normalisation factors for background processes;

μ_{sig} is the signal strength ($\mu_{\mathrm{sig}} = 0$ corresponds to background only, while $\mu_{\mathrm{sig}} = 1$ corresponds to the nominal signal).

The $\mathcal{P}_{\mathrm{SR}}$ and $\mathcal{P}_{\mathrm{CR}}$ are the Poisson distributions for signal and control regions. In the likelihood definition there is no difference between signal and control regions.

For independent nuisance parameters, C_{syst} can be described by a product of Gaussian probability distributions with unit width:

$$C_{\text{syst}}(\theta^0, \theta) = \prod_i G(\theta_i^0 - \theta_i), \tag{4.13}$$

where:

G is the Gaussian distribution with the mean 0 and variance 1;

$\theta = (\theta_1, \ldots, \theta_k)$ are nuisance parameters for systematic uncertainties;

$\theta^0 = (\theta_1^0, \ldots, \theta_k^0)$ are central values for auxiliary measurements, typically fixed to zero.

4.8 Systematic uncertainties

Any systematic uncertainty used in the analysis is estimated from the nominal V_{nom} and two variations, an upwards variation V_{up} and a down downwards variation V_{dn}.

The following basic methods are used for the estimation of the uncertainties:

- ***Normalisation systematic uncertainty***
  The uncertainty on the global normalisation of the sample. It does not affect the shape of the distribution, and uses a Gaussian constraint to model the uncertainty.
- ***Shape systematic uncertainty***
  Uncertainty related to the systematic variation of a shape. Both the shape and normalisation may changed. To model the uncertainty a Gaussian constraint is used.
- ***Shape statistical uncertainty***
  Uncertainty on the shape due to statistical fluctuations in the bins. Used to model a limited number of Monte Carlo events.

Some modifications of the basic methods are used, when the process is normalised in the control regions, or when some variations are not available. The modifications are described as follows:

- ***Normalised uncertainty***
  For the $t\bar{t}$ and $W+$jets processes, which are normalised in dedicated control regions, it is required to keep the total number of events in the normalisation regions for the up and down uncertainty variations invariant. This approach allows to describe the systematic uncertainties on the *Transfer Factors* (TF).
- ***Symmetrised uncertainty***
  This is the main type of uncertainty used for different scale variations, where an asymmetric behaviour of up and down variations can be neglected, or when the nominal value is modelled with a different generator. The relative uncertainty is estimated as:

  $$\frac{V_{up} - V_{dn}}{V_{up} + V_{dn}}. \tag{4.14}$$

  The result is symmetrised, i.e. treated as a symmetric uncertainty.

An example of an uncertainty without a nominal value is an ISR/FSR uncertainty for the $t\bar{t}$ process. It is estimated using ACERMC samples with higher and lower parton shower activity, while the nominal sample is generated using POWHEG+PYTHIA.

– ***Symmetrised full difference***
This type of uncertainty is used to estimate the difference between generators or between parton shower models, i.e. for uncertainties, where the up and down variations do not exist by definition. The relative uncertainty is estimated as:

$$\frac{V_{var} - V_{nom}}{V_{nom}}, \tag{4.15}$$

where V_{var} and V_{nom} are the variation and the nominal. The result is symmetrised.

4.9 Fit strategies

To obtain the final results for the analyses, the HistFitter framework [79] is used. All signal, control and validation regions, as well as the corresponding systematic uncertainties are defined within the HistFitter framework. The framework allows to perform the following common fit strategies:

– ***Background-only fit***
This fit is used to estimate the total number of events in the signal regions (SRs) without any assumption on the signal model. Since the fit is model independent, the control regions (CRs) do not include any signal contamination. During the fit, the likelihood function (equation 4.12) includes only control regions, i.e. $\mathcal{P}_{\mathrm{SR}}$ is removed from the likelihood. The background-only fit can be used for the transfer factor validation.

– ***Model-dependent signal fit***
This fit strategy is used to study a specific signal model. It is also often mentioned as *Exclusion Fit*. In case of no significant event excess in signal regions, one can set exclusion limits for the signal models under study. In this case the likelihood fit uses both signal and control regions. To perform the fit properly, the signal sample is included in all regions which are used in the fit (all SRs and CRs).

The signal strength parameter μ_{sig} is used by default for the signal sample. To gain sensitivity, one can use the distribution of the signal-sensitive variable, and perform a so-called “shape-fit”. In the tN diagonal analysis presented in this thesis, the shape-fit is used for the output variables from the multivariate analysis tool trained with the *Boosted Decision Tree* (BDT) algorithm. This approach allows to improve the sensitivity and to reach better exclusion limits.

– ***Model-independent signal fit***
This strategy is used for the analysis, which searches for new physics. It is usually referred to as *Discovery Fit*. Since the fit is model independent, it is assumed, that the signal contamination in control regions is negligible. For this fit, it is assumed, that the signal region consists of only one bin with a “dummy signal”. Using more than one bin needs additional information about the signal distribution. The number of signal events in the

signal region bin is added as a parameter to the fit. Model-independent limits are set for the bC diagonal analysis, since there is only one signal region. For the tN diagonal analysis, to achieve exclusion power, the shape fit is used, therefore no model-independent limit is given.

4.10 The CL_s method

The CL_s method is based on the conditional probability calculation [80, 81]. It is considered, that a signal hypothesis (signal and background, denoted as $s + b$) has to be tested with respect to a null hypothesis (background only, denoted as b). The test statistics q is constructed based on Monte Carlo generated samples. The CL_s value is defined as the ratio of the confidence level of the signal hypothesis to the background-only hypothesis:

$$\mathrm{CL}_s = \frac{\mathrm{CL}_{s+b}}{\mathrm{CL}_b} = \frac{P_{s+b}(q \leq q_{\mathrm{obs}})}{P_b(q \leq q_{\mathrm{obs}})}, \tag{4.16}$$

where q_{obs} is the value observed in the experiment and P_{s+b} and P_b are probability functions for the signal and background-only hypotheses.

A signal model is considered as excluded at a confidence level CL, if

$$\mathrm{CL}_s < 1 - \mathrm{CL}. \tag{4.17}$$

For supersymmetry searches, a confidence level of 95% is used for the exclusion, which means, that a signal model is considered as excluded for $\mathrm{CL}_s < 0.05$.

CHAPTER 5

Searches for the top squark at $\sqrt{s} = 7$ TeV

In this chapter searches for direct top-squark pair production are presented for an integrated luminosity of $\mathcal{L}_{\text{int}} = 4.7\ \text{fb}^{-1}$ of data recorded at $\sqrt{s} = 7$ TeV. The analysis is focused on the light top-squark scenario, where $m(\tilde{t}_1) < m(t)$ and the decay is assumed to proceed via a chargino $\tilde{t}_1 \rightarrow b\tilde{\chi}_1^{\pm}$, with the subsequent decay of $\tilde{\chi}_1^{\pm} \rightarrow W^{(*)}\tilde{\chi}_1^0$. It is further assumed, that both decays proceed with a branching ratio $(\mathcal{BR})$ of 100%.

The Feynman diagram for the semileptonic decay channel is shown in Figure 5.1. One can see that this decay exactly mimics semileptonic decays of top-quark pairs. The two neutralinos are not detected and contribute to the missing transverse energy.

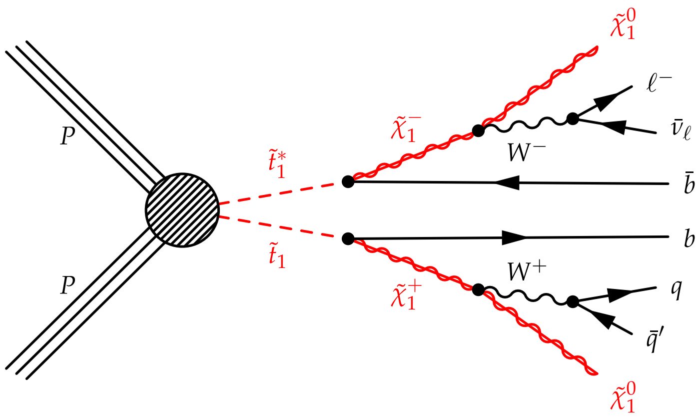

Figure 5.1: Feynman diagram for semileptonic decays for the $\tilde{t}_1 \rightarrow b\tilde{\chi}_1^{\pm}$, $\tilde{\chi}_1^{\pm} \rightarrow W^{\pm(*)}\tilde{\chi}_1^0$ channel.

A general approach for SUSY searches relies on large $E_{\text{T}}^{\text{miss}}$ or higher transverse momenta of the reconstructed objects. The difficulty for light stop searches is, that, since the top squark is lighter than the top quark, there is no large contribution to the missing transverse momentum. The objects are soft, in some cases they are even below the threshold to be reconstructed. This makes it much more difficult to perform the analysis.

In this case the standard approach to push the $E_{\text{T}}^{\text{miss}}$ or $m_{\text{eff}} = \sum |p_{\text{T}}|$ thresholds to higher values is not successful. A refined and more sophisticated analysis based on differences on kinematic variables has to be performed.

The published one- and two-lepton analyses [4] targeted this decay mode by performing searches with one and two leptons. The preselection was:

- One lepton, at least two b-tagged jets and large $E_{\mathrm{T}}^{\mathrm{miss}}$;
- Two leptons, at least one b-tagged jet and large $E_{\mathrm{T}}^{\mathrm{miss}}$.

In order not to interfere with these analyses, the analysis developed and described here requires to have exactly one lepton and exactly one b-tagged jet. The analysis targets the region with $\Delta m(\tilde{t}_1, \tilde{\chi}_1^{\pm}) \approx 20\text{–}40$ GeV. The restriction to one b-tagged jet does not allow to target regions with $\Delta m(\tilde{t}_1, \tilde{\chi}_1^{\pm}) > 50$ GeV, where both b-jets are reconstructed in the majority of cases. Targeting the region with $\Delta m(\tilde{t}_1, \tilde{\chi}_1^{\pm}) < 10$ GeV appears difficult, since for a large fraction of events both b-jets are below the detection threshold of 20 GeV. This leads to a significant drop of the sensitivity to this decay mode.

5.1 Analysis strategy

The published one- and two-lepton analyses [4] are based on the reconstruction of the $t\bar{t}$ system and use the variable $\sqrt{s}_{\mathrm{min}}^{\mathrm{sub}}$ [82]. The reconstruction strategy used for the published one-lepton analysis is described in the following.

5.1.1 Published one-lepton analysis

Two main discriminant variables are used in the published one-lepton analysis, the mass of the hadronically decaying top quark $m(t_{\mathrm{had}})$ and the minimum invariant mass compatible with the $t\bar{t}$ subsystem $\sqrt{s}_{\mathrm{min}}^{\mathrm{sub}}$.

Reconstruction of the $t\bar{t}$ system

The published one-lepton analysis requires exactly one lepton, at least two b-tagged jets and at least two light jets. The reconstruction of the $t\bar{t}$ system is done by reconstructing the decayed top quarks. It is assumed, that one top quark decays via $t_{\mathrm{had}} \to b_{\mathrm{had}} + W_{\mathrm{had}}$, with a subsequent hadronic decay of $W_{\mathrm{had}} \to q_1 + q_2$, where b_{had} is a b-tagged jet, while q_1 and q_2 are light jets. The other top quark decays via $t_{\mathrm{lep}} \to b_{\mathrm{lep}} + W_{\mathrm{lep}}$, with the subsequent leptonic decay of $W_{\mathrm{lep}} \to \ell + \nu$, where b_{lep} is a b-tagged jet, ℓ is a lepton (e or μ) and ν is a neutrino.

The transverse component of the neutrino $p_{\mathrm{T}}(\nu)$ is taken as $p_{\mathrm{T}}^{\mathrm{miss}}$, while the longitudinal component $p_z(\nu)$ is reconstructed by solving the equation $m(W_{\mathrm{lep}}) = m(W)$. Usually, there are two solutions for $p_z(\nu)$. Both candidates are considered. In the case when the equation is not solvable, the solution which minimises the difference $\left|m(W_{\mathrm{lep}}) - m(W)\right|$ is taken.

The top quarks (t_{had} and t_{lep}) are reconstructed based on the four jets (two b-tagged and two light jets), the lepton ℓ and the reconstructed neutrino ν. The ambiguity in the reconstruction is resolved by maximising the total decay probability, which is defined as

$$\mathcal{P}_{\text{total}} = \mathcal{P}_{t_{\text{had}}}(m_{t_{\text{had}}}) \times \mathcal{P}_{W_{\text{had}}}(m_{W_{\text{had}}}) \times \mathcal{P}_{t_{\text{lep}}}(m_{t_{\text{lep}}}) \times \mathcal{P}_{W_{\text{lep}}}(m_{W_{\text{lep}}}), \tag{5.1}$$

where $\mathcal{P}_X(m)$ is the probability to reconstruct the mass m for particle $X = t_{\text{had}}$, t_{lep}, W_{had} and W_{lep}. The probabilities are approximated by Gaussian probability density functions. The mean values and the widths for the Gaussian distributions are obtained from the corresponding $m(X)$ distributions, where the particle X is reconstructed using detector level objects, which are matched to the corresponding decay products of the particle X at particle level.

The $\sqrt{s}^{\,\text{sub}}_{\,\text{min}}$ variable

The four-momentum of the subsystem p^{μ}_{sub} is defined as the sum of the four-momenta of the visible components from the $t\bar{t}$ decay:

$$p^{\mu}_{\text{sub}} = p^{\mu}(\ell) + p^{\mu}(b_{\text{had}}) + p^{\mu}(b_{\text{lep}}) + p^{\mu}(q_1) + p^{\mu}(q_2). \tag{5.2}$$

The transverse component of the subsystem is defined as:

$$p^{\text{sub}}_{\text{T}} = (E^{\text{sub}}_T, p^{\text{sub}}_x, p^{\text{sub}}_y, 0), \qquad E^{\text{sub}}_T = \sqrt{m^2_{\text{sub}} + (p^{\text{sub}}_x)^2 + (p^{\text{sub}}_y)^2}, \tag{5.3}$$

where m_{sub} is the invariant mass of the subsystem.

The invisible component is defined as:

$$p^{\text{inv}}_T = (E^{\text{inv}}_T, p^{\text{miss}}_x, p^{\text{miss}}_y, 0), \qquad E^{\text{inv}}_T = \sqrt{m^2_{\text{miss}} + (p^{\text{miss}}_x)^2 + (p^{\text{miss}}_y)^2}, \tag{5.4}$$

where the m_{miss} is a sum of the masses of all invisible particles in the system, while the $p^{\text{miss}}_{\text{T}}$ is the missing transverse momentum vector.

In these notations, the minimum invariant mass, which is compatible with the subsystem can be defined as:

$$\sqrt{s}^{\,\text{sub}}_{\,\text{min}} = \sqrt{(p^{\text{sub}}_{\text{T}} + p^{\text{inv}}_{\text{T}})^2}, \tag{5.5}$$

or in the equivalent notations:

$$\sqrt{s}^{\,\text{sub}}_{\,\text{min}} = \sqrt{\left(\sqrt{m^2_{\text{sub}} + (p^{\text{sub}}_{\text{T}})^2} + \sqrt{m^2_{\text{miss}} + (p^{\text{miss}}_{\text{T}})^2}\right)^2 - \left(p^{\text{sub}}_{\text{T}} + p^{\text{miss}}_{\text{T}}\right)^2}. \tag{5.6}$$

Since the subsystem is defined for the $t\bar{t}$ system, the invisible component accounts only for one or two neutrinos, therefore the $m_{\text{miss}} = 0$.

The one-lepton selection

The default one-lepton analysis employs two main discriminant variables: the mass of the hadronically decaying top quark $m(t_{\text{had}})$ and the minimum invariant mass compatible with the $t\bar{t}$ subsystem $\sqrt{s}^{\,\text{sub}}_{\,\text{min}}$, as discussed above.

The signal selection for the one-lepton analysis with two b-jets is defined as:

- Exactly one signal lepton (e or μ) with $p_{\mathrm{T}}(e) > 25$ GeV or $p_{\mathrm{T}}(\mu) > 20$ GeV;
- Al least four signal jets ($N_{\mathrm{jets}} \geq 4$) with $p_{\mathrm{T}} > 20$ GeV and $|\eta| < 2.5$;
- At least two b-tagged jets;
- $E_{\mathrm{T}}^{\mathrm{miss}} > 40$ GeV;
- $m_{\mathrm{T}}(\ell, E_{\mathrm{T}}^{\mathrm{miss}}) > 30$ GeV;
- $m(t_{\mathrm{had}}) < 158$ GeV;
- $\sqrt{s}_{\mathrm{min}}^{\mathrm{sub}} < 250$ GeV.

For this signal selection, both the $E_{\mathrm{T}}^{\mathrm{miss}}$ and m_{T} variables are mainly used to reject the multijet background. For $t\bar{t}$ events, the hadronically decaying top quark t_{had} can be well reconstructed, therefore $m(t_{\mathrm{had}}) \approx m(t)$, while the distribution of $\sqrt{s}_{\mathrm{min}}^{\mathrm{sub}}$ is expected to peak around $m(t\bar{t}) \approx 2 \cdot m(t) \approx 345$ GeV. This is not the case for the signal events, since the top quark is not involved in the $\tilde{t}_1 \to b\tilde{\chi}_1^{\pm} \to bW^{\pm(*)}\tilde{\chi}_1^0$ decay. Therefore, selections requiring $m(t_{\mathrm{had}}) < 158$ GeV and $\sqrt{s}_{\mathrm{min}}^{\mathrm{sub}} < 250$ GeV suppress $t\bar{t}$ background events.

5.1.2 Improved one-lepton analysis

Contrary to the approach discussed above, the analysis developed in this thesis does not reconstruct the $t\bar{t}$ system. However, it targets to exploit kinematic differences between the signal and $t\bar{t}$ background events.

To suppress the W+jets and semileptonic $t\bar{t}$ backgrounds, a tight requirement on the m_{T} variable is applied. The selection of $m_{\mathrm{T}} > 110$ GeV significantly suppresses all backgrounds where the missing transverse momentum comes only from $W \to e\nu, \mu\nu$ decays. An upper requirement $m_{\mathrm{T}} < 180$ GeV suppresses backgrounds from dileptonic $t\bar{t}$ decays, where a lepton from the second $W \to e\nu, \mu\nu$ decay is missing (for example not identified or lost), or where the second W boson decays via $W \to \tau\nu$ and the τ lepton undergoes a hadronic decay.

An important variable for the analysis is the transverse momentum of the b-jet. From the $t \to bW$ decay $p_{\mathrm{T}}(b) \approx 50$ GeV, therefore, if the second b-jet is below the detection threshold of 20 GeV, the requirement of exactly one b-tagged jet with $p_{\mathrm{T}}(b) < 50$ GeV can be rewritten as $p_{\mathrm{T}}(b_1) < 50$ GeV and $p_{\mathrm{T}}(b_2) < 20$ GeV, which suppresses the $t\bar{t}$ background.

Another important variable is the invariant mass of the system of the b-jet and the lepton ℓ, denoted as $m(b+\ell)$. If a b-jet comes from a leptonic top-quark decay $t \to bW \to b\ell\nu$, the corresponding invariant mass $m(b+\ell+\nu)$ is equivalent to the top-quark mass. This is not the case for $\tilde{t}_1 \to b\tilde{\chi}_1^{\pm} \to bW\tilde{\chi}_1^0 \to b\ell\nu\tilde{\chi}_1^0$ decays, where a massive neutralino takes some momentum. Since $m(b+\ell)$ does include neither the neutralino nor the neutrino, the distribution of this variable peaks around 80 GeV, while for signal models with $\Delta m(\tilde{t}_1, \tilde{\chi}_1^{\pm}) < 40$ GeV the same distribution peaks around 40 GeV. This difference makes this variable very powerful for the $t\bar{t}$ background rejection.

The use of these variables allows to significantly improve the exclusion limits.

5.2 Data set and Monte Carlo samples

5.2.1 The data set

The analysis uses data recorded by the ATLAS experiment at $\sqrt{s} = 7$ TeV in 2011. The integrated luminosity, after data quality requirements, corresponds to 4.7 ± 0.2 fb^{-1}.

5.2.2 Trigger selection

Different electron and muon triggers are used for different data taking periods. All used triggers are required to be unprescaled, therefore, due to the constantly increasing instantaneous luminosity, the p_{T} threshold and the isolation requirements for the triggers are tightened. For electrons with $p_{\mathrm{T}}(e) > 25$ GeV a trigger efficiency of $\approx 97\%$ is achieved, while for muons with $p_{\mathrm{T}}(\mu) > 20$ GeV a trigger efficiency of $\approx 75\%$ and $\approx 90\%$ is achieved for the barrel and end-caps, respectively.

5.2.3 Monte Carlo samples

The production of the Monte Carlo background samples was performed using the ATLAS full detector simulation[83] based on GEANT4 [84]. Signal samples and additional $t\bar{t}$ samples used for studies of systematic uncertainties, were simulated using the ATLAS fast simulation package ATLFAST-II [85].

Background samples

For all NLO Monte Carlo generations the CTEQ6.6 [86] PDF set was used. The top-quark NLO production was simulated with the MC@NLO generator [40] using a top-quark mass $m(t) = 172.5$ GeV. The W+jets and Z+jets background production are simulated using the ALPGEN [36] with the CTEQL1 [19] set of PDF. Signal samples for the one-lepton analysis were simulated using HERWIG [87] with MRST2007 [88] leading order PDF set. For the ALPGEN and MC@NLO generators the modelling of the fragmentation and hadronisation was done with the HERWIG which employes the JIMMY to simulate the underlying event. Generator-related systematic uncertainties for the production of the $t\bar{t}$ events are taken as the difference between the ALPGEN and POWHEG samples. For the initial and final state radiations (ISR/FSR) different variations of samples generated with the ACERMC [37] are used. The list of the background samples used in the analysis is shown in Table 5.1.

Signal samples

The direct top-squark pair production samples for the one-lepton analysis were produced using the HERWIG++ and PYTHIA generators [34, 32]. The signal cross sections are calculated at NLO precision, where the resummation of the soft gluon emission is considered at the next-to-leading-logarithmic (NLL) accuracy.

Sample ID	Name	Equivalent $\mathcal{L}$ [fb^{-1}]
ttbar	MC@NLO	
105200	T1_McAtNlo_Jimmy	165.4
single top	MC@NLO	
108340–108342	st_tchan_[e,mu,tau]nu_McAtNlo_Jimmy	42.8
108343–108345	st_schan_[e,mu,tau]nu_McAtNlo_Jimmy	641
108346	st_Wt_McAtNlo_Jimmy	69.2
ttbar+W/Z	MadGraph	
119353–119356	PythiaMadgraph_ttbar[W,Wj,Z,Zj]	0.62, 0.92, 0.81, 0.94
119583	PythiaMadgraph_ttbarWW	61.6
W+jets	Alpgen	
107680–107685	AlpgenJimmyWenuNp[0-5]_pt20	[0.42, 1.61, 8.34, 8.34, 8.24, 8.46]
107690–107695	AlpgenJimmyWmunuNp[0-5]_pt20	[0.42, 1.61, 8.34, 8.34, 8.41, 8.46]
107700–107705	AlpgenJimmyWtaunuNp[0-5]_pt20	[0.41, 1.61, 8.30, 8.35, 8.24, 7.86]
107280–107283	AlpgenJimmyWbbFullNp[0-3]_pt20	[8.37, 4.79, 8.39, 8.80]
117284–117287	AlpgenWccFullNp[0-3]_pt20	[8.33, 8.36, 8.40, 8.35]
117293–117297	AlpgenWcNp[0-4]_pt20	[12.6, 10.8, 10.2, 9.68, 10.9]
Z+jets	Alpgen	
107650–107655	AlpgenJimmyZeeNp[0-5]_pt20	[7.97, 8.03, 16.1, 15.8, 16.6, 21.2]
107660–107665	AlpgenJimmyZmumuNp[0-5]_pt20	[7.97, 8.03, 8.05, 7.90, 8.30, 10.6]
107670–107675	AlpgenJimmyZtautauNp[0-5]_pt20	[12.8, 20.1, 20.0, 36.6, 40.1, 47.8]
107710–107715	AlpgenJimmyZnunuNp[0-5]_pt20_filt1jet	[1.53, 1.66, 0.69, 1.94, 16.7, 14.1]
109300–109303	AlpgenJimmyZeebbNp[0-3]_nofilter	[18.4, 35.6, 36.4, 20.5]
109305–109308	AlpgenJimmyZmumubbNp[0-3]_nofilter	[18.4, 35.6, 36.4, 20.5]
109310–109313	AlpgenJimmyZtautaubbNp[0-3]_nofilter	[18.4, 35.6, 36.4, 18.5]
118962–118965	AlpgenJimmyZnunubbFullNp[0-3]_pt20	[14.4, 15.2, 15.2, 15.3]
diboson	Herwig	
105985–105987	[WW,ZZ,WZ]_Herwig	[142.7, 197.6, 180.1]
systematic uncertainties		
105205	AcerMCttbar	22.1
117209, 117210	AcerMCttbar_[More,Less]PS	110
117255–117258	AcerMCttbar_[isr,fsr]_[up,down]	11.0
117259	AcerMCttbar_isr_down_fsr_down	10.4
117260	AcerMCttbar_isr_up_fsr_up	10.2
105860, 105861	TTbar_PowHeg_[Jimmy,Pythia]	33.1

Table 5.1: List of the Monte Carlo samples used in the $\sqrt{s} = 7$ TeV analysis. An equivalent luminosity is defined as N/σ, where N is the total number of generated events and σ is the cross section (including the K-factor and the filter efficiency).

The ATLAS SUSY searches at $\sqrt{s} = 7$ TeV for the $\tilde{t}_1 \to b\tilde{\chi}_1^{\pm} \to bW^{\pm(*)}\tilde{\chi}_1^0$ decay channel are performed based on simplified models, as explained in Section 4.2. The parameter space for the generated signal models is a three dimensional $(\tilde{t}, \tilde{\chi}_1^{\pm}, \tilde{\chi}_1^0)$ mass space. In the following, the triple (m_1, m_2, m_3) refers to the signal model with $m(\tilde{t}_1) = m_1$, $m(\tilde{\chi}_1^{\pm}) = m_2$ and $m(\tilde{\chi}_1^0) = m_3$, where masses are given in GeV. The list of the produced signal samples for the one- and two-lepton analyses is shown in Table 5.2. The first two grids `ch2nt` and `st180` were produced

Grid	Sample ID	Constraint	Mass Plane	Filter	Generator
`ch2nt`	139175–139229 144747–144765	$m(\tilde{\chi}_1^{\pm}) = 2 \cdot m(\tilde{\chi}_1^0)$	$(\tilde{t}_1, \tilde{\chi}_1^0)$	1-lepton	HERWIG++
`st180`	144766–144790	$m(\tilde{t}_1) = 180$ GeV	$(\tilde{\chi}_1^{\pm}, \tilde{\chi}_1^0)$	1-lepton	HERWIG++
`ch106`	144025–144052	$m(\tilde{\chi}_1^{\pm}) = 106$ GeV	$(\tilde{t}_1, \tilde{\chi}_1^0)$	2-lepton	POWHEG

Table 5.2: List of signal samples used for the analysis of the $\tilde{t}_1 \to b\tilde{\chi}_1^{\pm}$, $\tilde{\chi}_1^{\pm} \to W^{\pm(*)}\tilde{\chi}_1^0$ decay channel at $\sqrt{s} = 7$ TeV.

with the HERWIG++ generator with a 1-lepton filter, while the third one `ch106` was produced using POWHEG with a 2-lepton filter. For the presented analysis only the gaugino universality (`ch2nt`) and the fixed top-squark mass (`st180`) grids are used.

5.3 Object definitions and event cleaning

5.3.1 Object definitions

Electrons

Electrons are identified using a cut-based selection [89]. *Baseline electrons* are defined with requirements to have `medium` identification, $p_{\mathrm{T}} > 20$ GeV and $|\eta| < 2.47$, see Section 3.2. For *signal electrons* additionally the `tight` criteria and $p_{\mathrm{T}}^{\mathrm{cone}\,0.2}/p_{\mathrm{T}} < 0.1$ isolation is required. The $p_{\mathrm{T}}^{\mathrm{cone}\,0.2}$ is the sum of p_{T} of all tracks in a $\Delta R < 0.2$ cone around the electron (where the electron track itself is not included). The overlap removal procedure first removes all jets, which are within $\Delta R < 0.2$ of an electron, it than removes all electrons which are within $\Delta R < 0.4$ of jets. A summary of the electron selection criteria is given in Table 5.3.

Electron baseline selection	
Acceptance	$p_{\mathrm{T}} > 10$ GeV, $|\eta| < 2.47$
Quality	`medium`
Overlap	$\Delta R(e, \mathrm{jet}) < 0.2$ or $\Delta R(e, \mathrm{jet}) > 0.4$
Electron signal selection	
Acceptance	$p_{\mathrm{T}} > 20$ GeV, $|\eta| < 2.47$
Quality	`tight`
Isolation	$p_{\mathrm{T}}^{\mathrm{cone}\,0.2}/p_{\mathrm{T}} < 0.1$

Table 5.3: Summary of the selection criteria for an electron in the baseline and signal selections.

Muons

Muons are reconstructed by combining tracks from the Inner Detector and the Muon Spectrometer into *Combined Muons* (CB), see Section 3.3. *Baseline muons* are defined as combined muons with $p_{\mathrm{T}} > 10$ GeV and $|\eta| < 2.4$. Quality requirements based on the number of hits for Pixel, SCT and TRT detectors are applied as listed in Table 5.4. The $N^{\mathrm{hits}}_{\mathrm{TRT}}$ is the total number of TRT hist including outliers. For *signal muons* additionally the $p_{\mathrm{T}}^{\mathrm{cone}\,0.2} < 1.8$ GeV isolation criterion is applied and a suppression against cosmic muons, $|z_{\mu} - z_{PV}| < 1$ mm and $|d_0| < 0.2$ mm. A summary of the muon selection criteria is given in Table 5.4.

Muon baseline selection	
Algorithm	`combined muon`
Acceptance	$p_{\mathrm{T}} > 10$ GeV, $\lvert\eta\rvert < 2.4$
Quality	≥ 1 B-layer hits, ≥ 2 Pixel hit, ≥ 6 SCT hits
	$\lvert\eta\rvert \leq 1.9:\ N^{\mathrm{hits}}_{\mathrm{TRT}} \geq 5,\ N^{\mathrm{outliers}}_{\mathrm{TRT}} < 0.9 \times N^{\mathrm{hits}}_{\mathrm{TRT}}$
	$\lvert\eta\rvert > 1.9$ and $N^{\mathrm{hits}}_{\mathrm{TRT}} \geq 5:\ N^{\mathrm{outliers}}_{\mathrm{TRT}} < 0.9 \times N^{\mathrm{hits}}_{\mathrm{TRT}}$
Overlap	$\Delta R(\mu, jet) > 0.4$
Muon signal selection	
Acceptance	$p_{\mathrm{T}} > 10$ GeV, $\lvert\eta\rvert < 2.4$
Isolation	$p_{\mathrm{T}}^{\mathrm{cone}\,0.2} < 1.8$ GeV
Cosmic	$\lvert z_{\mu} - z_{PV}\rvert < 1$ mm, $\lvert d_0\rvert < 0.2$ mm

Table 5.4: Summary of the selection criteria for a muon in the baseline and signal selections.

Jets

Jets are reconstructed using the anti-k_t jet algorithm, with a distance parameter $R = 0.4$, see Section 3.4. They are calibrated to correct the lower response to hadrons than electrons or photons. To increase the robustness against pileup, the jet vertex fraction requirement is also applied, see Section 3.4. *Baseline jets* are defined as calibrated jets with $p_{\mathrm{T}} > 20$ GeV and $|\eta| < 4.5$. Baseline jets are used for the overlap removal procedure. Jets which are close to the electron within $\Delta R(e, \mathrm{jet}) < 0.2$ cone are removed. *Signal jets* are defined as baseline jets with an additional jet vertex fraction requirement `JVF` > 0.75. A summary of the jets selection criteria is given in Table 5.5.

Jet baseline selection	
Algorithm	anti-k_t, $R = 0.4$
Acceptance	$p_{\mathrm{T}} > 20$ GeV, $\lvert\eta\rvert < 4.5$
Overlap	$\Delta R(e, \mathrm{jet}) > 0.2$
Jet signal selection	
Acceptance	$p_{\mathrm{T}} > 20$ GeV, $\lvert\eta\rvert < 2.5$
Quality	`JVF` > 0.75

Table 5.5: Summary of the selection criteria for a jet in the baseline and signal selections.

b-jets

The b-tagging algorithm [69] is based on a multivariate approach and uses the `JetCombNN` as output, see Section 3.5. A jet is considered b-tagged, if `JetCombNN` > 1.8, which corresponds to a b-tagging efficiency of 60% estimated on a sample of $t\bar{t}$ event, with a misidentification rate for c- and light-quarks of less than 10%.

Missing transverse momentum

The missing transverse momentum is calculated as the negative vectorial sum of the p_{T} of the identified objects (electrons, muons and jets) and calorimeter clusters within $|\eta| < 4.9$ which are not associated to any object, see Section 3.6.

$$E_{\mathrm{T}}^{\mathrm{miss}} = -\sum p_{\mathrm{T}}^{e} - \sum p_{\mathrm{T}}^{\mu} - \sum p_{\mathrm{T}}^{\mathrm{jet}} + E_{\mathrm{T}}^{\mathrm{miss,\,CellOut}}. \tag{5.7}$$

5.3.2 Overlap removal

The overlap removal procedure resolves overlaps between leptons and jets. It is based on the distance between the lepton and the jet $\Delta R = \sqrt{\Delta\phi^2 + \Delta\eta^2}$. The overlap removal is applied in the following order:

- If an electron lies within $\Delta R < 0.2$ of a jet, then the jet is considered as "fake" and is removed;
- If an electron is within $0.2 < \Delta R < 0.4$ of a jet, it is considered, that the electron "belongs" to the jet, and the electron is removed;
- If a muon is within $\Delta R < 0.4$ of a jet, it is considered, that the muon "belongs" to the jet, and the muon is removed.

5.3.3 Event cleaning

Basic cleaning requirements are applied for the whole one-lepton analysis. In addition, common preselection requirements for all signal, control and validation regions used in the current analysis are applied. A list of cleaning requirements is given in the following:

- The standard ATLAS Data Quality requirements are applied.
- The electron or muon trigger requirement.
- At least five tracks have to be associated to the primary vertex.
- Events which contain a baseline muon tagged as "bad" or a cosmic muon candidate, are rejected.
- Events which contain "very loose bad" baseline jets, are rejected.
- Events with mismeasured $E_{\mathrm{T}}^{\mathrm{miss}}$ due to jets pointing to the LAr hole region, are rejected.

5.4 Signal selection

The selection for the signal region (SR) consists of the preselection and a series of requirements. In the following, each selection requirement is referred to as a “cut”. Figure 5.2 shows distributions of the discriminant variables for successively applied selection requirements. For each requirement, the distribution of the corresponding discriminant variable is shown, before the requirement is applied. Three signal models $m(\tilde{t}_1, \tilde{\chi}_1^{\pm}, \tilde{\chi}_1^0) = (190, 160, 80)$, $(200, 180, 90)$ and $(230, 200, 100)$ GeV are shown for comparison.

Preselection:

- One-lepton cleaning requirements, as described in Section 5.3.3;
- Exactly one signal lepton (e or μ) with $p_{\mathrm{T}}(e) > 20$ GeV or $p_{\mathrm{T}}(\mu) > 10$ GeV and no other baseline leptons;
- There, four or five jets with $p_{\mathrm{T}} > 20$ GeV;
- Exactly one b-tagged jet at 60% working point (to avoid overlap with the SUSY one-lepton two b-jet analysis, exactly one b-tagged jet is required);

Cut1: $E_{\mathrm{T}}^{\mathrm{miss}} > 60$ GeV

This requirement is used to reject multijet background as well as backgrounds from other processes, which do not have missing transverse momentum.

Cut2: $110 \text{ GeV} < m_{\mathrm{T}} < 180$ GeV

This requirement is applied against $W \to \ell\nu$ decays. In the case of $W \to e\nu$ or $W \to \mu\nu$, the distribution of m_{T} should drop above $m(W) \approx 82$ GeV. Due to detector resolution effects the distribution of m_{T} is broadened. Therefore, the requirement is applied at $m_{\mathrm{T}} > 110$ GeV. This significantly reduces the W+jets as well as the semileptonic $t\bar{t}$ background. An upper restriction of $m_{\mathrm{T}} < 180$ GeV is applied against the dileptonic $t\bar{t}$ background, where one of the W-boson decays via $W \to \tau\nu$, and the τ lepton decays hadronically.

Cut3: $m(b + j_1 + j_2 + \ell + E_{\mathrm{T}}^{\mathrm{miss}}) < 400$ GeV

This is the invariant mass of visible objects, under the assumption, that z-component of the neutrino momentum is zero $p_z(\nu) = 0$.

Cut4: $p_{\mathrm{T}}(b) < 50$ GeV

This requirement suppresses the $t\bar{t}$ background. In case of the $t \to bW$ decay, the average transverse momentum $p_{\mathrm{T}}(b)$ is about 60 GeV, while for signal models with small $\Delta m(\tilde{t}_1, \tilde{\chi}_1^{\pm}) < 40$ GeV, the distribution of $p_{\mathrm{T}}(b)$ is much softer.

Cut5: $m(b + \ell) < 50$ GeV

This requirement almost completely rejects the W+jets events and significantly reduces the $t\bar{t}$ background.

Cut6: $\Delta R(b, E_{\mathrm{T}}^{\mathrm{miss}}) < 2.8$

This requirement further improves the signal to background ratio. It is mainly needed for signal models with higher top-squark masses.

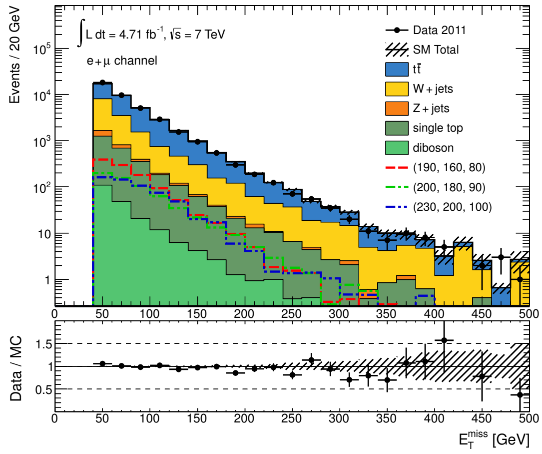

Cut1: $E_{\mathrm{T}}^{\mathrm{miss}} > 60$ GeV

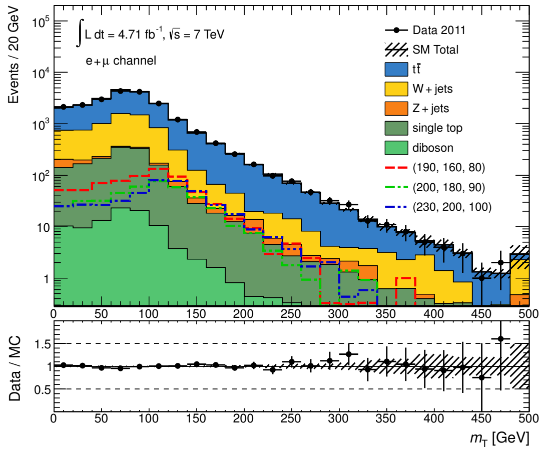

Cut2: 100 GeV $< m_{\mathrm{T}}(\ell, E_{\mathrm{T}}^{\mathrm{miss}}) < 180$ GeV

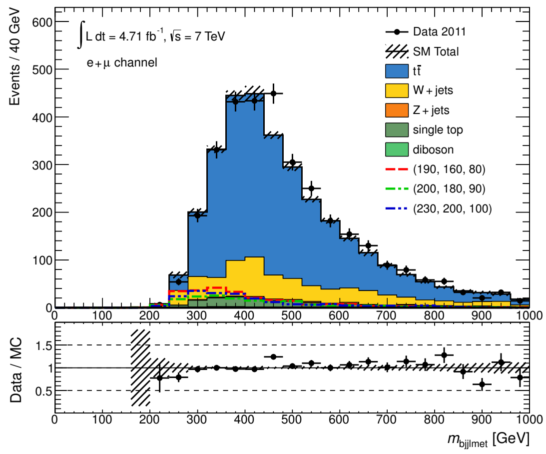

Cut3: $m(b + j_1 + j_2 + \ell + E_{\mathrm{T}}^{\mathrm{miss}}) < 400$ GeV

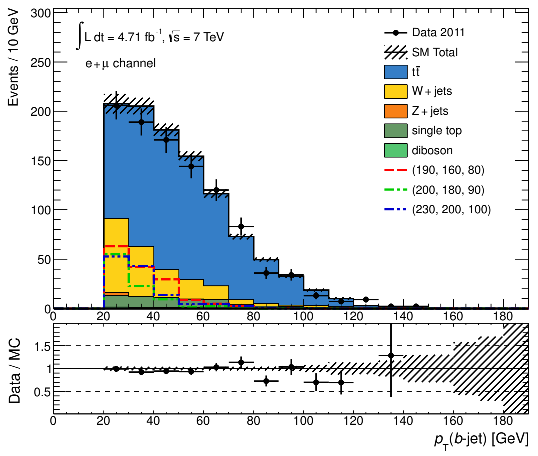

Cut4: $p_{\mathrm{T}}(b) < 50$ GeV

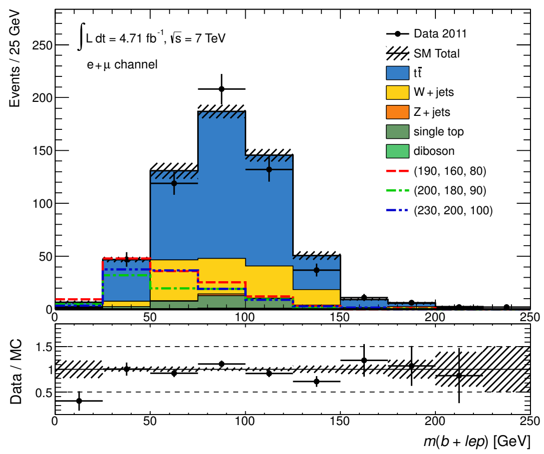

Cut5: $m(b + \ell) < 50$ GeV

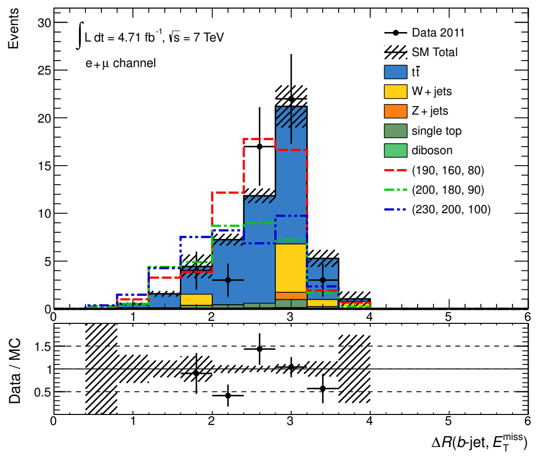

Cut6: $\Delta R(b, E_{\mathrm{T}}^{\mathrm{miss}}) < 2.8$

Figure 5.2: Distributions of the discriminant variables for successively applied selection requirements ("cuts"). For each cut, the distribution of the corresponding discriminant variable is shown, before the requirement is applied. The error bars include only the Monte Carlo statistical uncertainties. Three signal models for the $(\tilde{t}_1, \tilde{\chi}_1^{\pm}, \tilde{\chi}_1^0)$ mass plane are shown for comparison. The masses of $\tilde{t}_1$, $\tilde{\chi}_1^{\pm}$ and $\tilde{\chi}_1^0$ are given in GeV.

5.5 Background estimation

The dominant backgrounds are normalised in control regions. In this section the definition of control regions and the estimation of the main backgrounds are discussed.

The dominant background for the analysis is the $t\bar{t}$ process, which amounts to around 90% of the total background. The sub-dominant background is the W+ jets process with a contribution of about 5%. Normalisation scale factors for these processes are estimated by normalising the $t\bar{t}$ and W+ jets background to the observed data in the control regions. Control regions should not overlap with each other and with the signal region. They should have a low signal contamination and a large number of events, to decrease the uncertainty of the normalisation scale factors.

Normalisation of backgrounds

In the analysis the $t\bar{t}$ and W+ jets backgrounds are normalised simultaneously. To calculate the $\omega_{t\bar{t}}$ and ω_W normalisation scale factors for the $t\bar{t}$ and W+ jets processes, the corresponding $t\bar{t}$ and W+ jets control regions (T-CR and W-CR, respectively) have to be defined. Using these control regions, scale factors can be obtained by solving the following linear equation:

$$\begin{bmatrix} N_{t\bar{t}}^{\text{T-CR}} & N_{W}^{\text{T-CR}} \\ N_{t\bar{t}}^{\text{W-CR}} & N_{W}^{\text{W-CR}} \end{bmatrix} \begin{bmatrix} \omega_{t\bar{t}} \\ \omega_W \end{bmatrix} + \begin{bmatrix} N_{\text{other}}^{\text{T-CR}} \\ N_{\text{other}}^{\text{W-CR}} \end{bmatrix} = \begin{bmatrix} D^{\text{T-CR}} \\ D^{\text{W-CR}} \end{bmatrix} \tag{5.8}$$

where:

$N_{t\bar{t}}^{\text{CR}}$ and N_{W}^{CR} are number of Monte Carlo events for the $t\bar{t}$ and W+ jets processes in the CR control region, where CR is T-CR or W-CR;

$N_{\text{other}}^{\text{CR}}$ is all other (except the $t\bar{t}$ and W+ jets) Monte Carlo backgrounds in the CR;

D^{CR} is a number of observed data events in the CR.

Multijet background

The multijet background has not been estimated, but due to the requirements of one lepton, one b-tagged jet and high $m_{\text{T}} > 110$ GeV it is expected to be negligible.

5.5.1 Control regions

The T-CR and W-CR control regions are defined by omission of the $m(b+\ell)$ and $\Delta R(b, E_{\text{T}}^{\text{miss}})$ and by altering the m_{T} and $p_{\text{T}}(b\text{-jet})$ requirements of the SR selection. The event selection requirements for these variables are shown for each region in Table 5.6. A schematic illustration for the signal and control regions after the application of the ***Preselection*** + ***Cut1*** + ***Cut3*** requirements is shown in Figure 5.3.

A breakdown of the expected event yields together with the observed numbers of events for the control regions are shown in Table 5.7. The W+ jets and $t\bar{t}$ production is normalised to the Monte Carlo cross section. The purity for the $t\bar{t}$ events in the T-CR is about 85%, while for the

Variable	W-CR	T-CR	SR
m_{T} [GeV]	$[80, 110]$	$[110, 180]$	$[110, 180]$
$p_{\mathrm{T}}(b\text{-jet})$ [GeV]	–	> 60	< 50
$m(b+\ell)$ [GeV]	–	–	< 50
$\Delta R(b, E_{\mathrm{T}}^{\mathrm{miss}})$	–	–	< 2.8

Table 5.6: The event selection requirements which differ for the signal and control regions. The regions differ only in these variables, therefore other selection requirements are not shown.

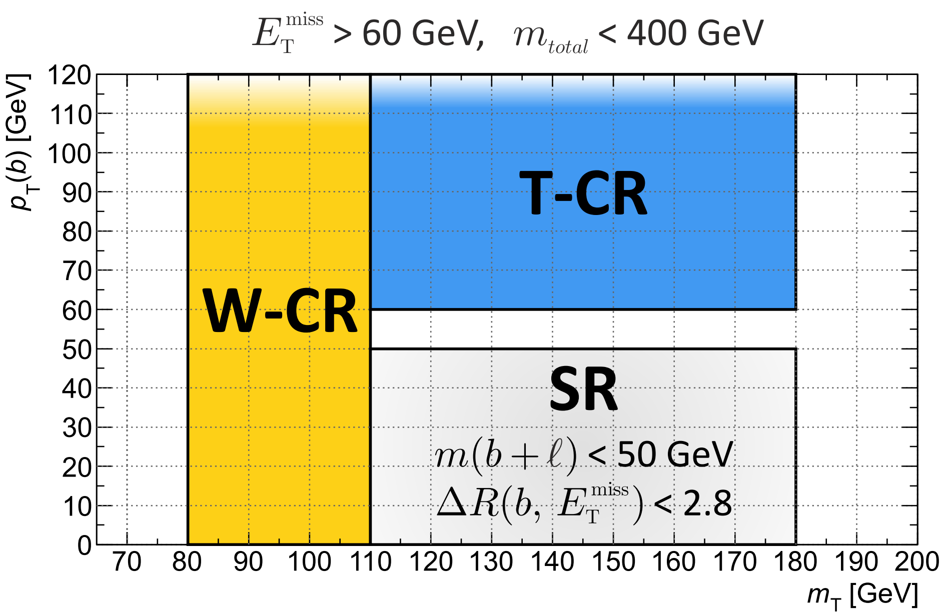

Figure 5.3: A schematic illustration of the signal and control regions. The $(m_{\mathrm{T}}, p_{\mathrm{T}}(b))$ plane is shown after the application of the ***Preselection*** + ***Cut1*** + ***Cut3*** requirements.

	1 electron		1 muon		1 lepton	
Process	T-CR	W-CR	T-CR	W-CR	T-CR	W-CR
$t\bar{t}$	137.5	608.9	114.7	549.8	252.2 ± 3.4	1158.7 ± 7.5
single top	7.7	65.2	8.5	63.5	16.3 ± 1.3	128.8 ± 4.4
W+jets	8.9	250.5	16.0	261.1	24.9 ± 4.7	511.6 ± 30.3
Z+jets	0.7	1.8	0.7	9.0	1.4 ± 0.6	10.8 ± 2.1
diboson	0.5	5.6	0.4	6.5	0.9 ± 0.2	12.1 ± 0.6
SM Total	155.4	932.0	140.3	889.9	295.7 ± 6.0	1822.0 ± 31.6
Observed	153	970	153	919	306	1889

Table 5.7: A breakdown of the expected yields together with the observed numbers of events for the control regions. The W+jets and $t\bar{t}$ production are normalised to the Monte Carlo cross section. Only the Monte Carlo statistical uncertainties are shown. The numbers are normalised to an integrated luminosity of 4.7 fb^{-1}.

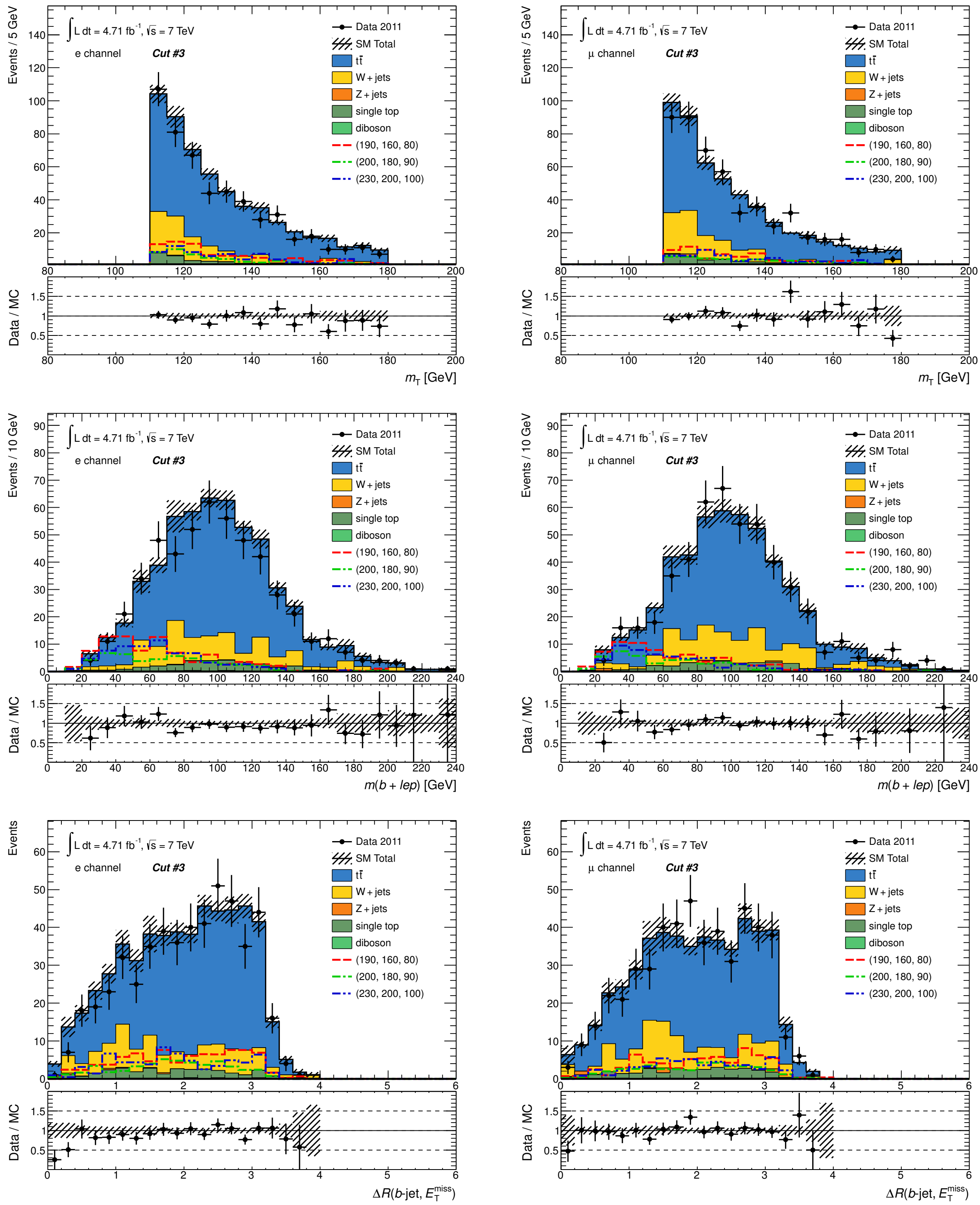

Figure 5.4: Distributions of the $m_{\mathrm{T}}(\ell, E_{\mathrm{T}}^{\mathrm{miss}})$ (top), $m(b+\ell)$ (middle) and $\Delta R(b, E_{\mathrm{T}}^{\mathrm{miss}})$ (bottom) after the application of the ***Preselection*** + ***Cut1*** + ***Cut2*** + ***Cut3*** requirements for the electron (left) and muon (right) channel. Only the Monte Carlo statistical uncertainties are shown. Three signal models for the $(\tilde{t}_1, \tilde{\chi}_1^{\pm}, \tilde{\chi}_1^0)$ mass plane are shown for comparison. The masses of $\tilde{t}_1$, $\tilde{\chi}_1^{\pm}$ and $\tilde{\chi}_1^0$ are given in GeV.

W+jets events in the W-CR it is about 28%. The low purity of the W-CR does not play a significant role due to the small contribution of the W+jets (about 5%) in the signal region.

Distributions of the data to Monte Carlo comparison for the electron and muon channel after the application of ***Preselection*** + ***Cut1*** + ***Cut2*** + ***Cut3*** requirements are shown in Figure 5.4. Three signal models for the $(\tilde{t}_1, \tilde{\chi}_1^{\pm}, \tilde{\chi}_1^0)$ mass plane are shown for comparison. The masses of $\tilde{t}_1$, $\tilde{\chi}_1^{\pm}$ and $\tilde{\chi}_1^0$ are given in GeV. One can see a good agreement for all presented variables for both channels.

The normalisation scale factors for the $t\bar{t}$ and W+jets production are estimated by solving the equation 5.8. The results of the estimation are:

$$\omega_{t\bar{t}} = 1.03 \pm 0.09, \qquad \omega_W = 1.05 \pm 0.26. \tag{5.9}$$

One can see, that the scale factors are consistent with unity withing the uncertainty.

The signal contamination for the control regions is shown in Figure 5.5. One can see, that the signal contamination for different signal models for the gaugino universality grid (left) for both control regions is below 10%. For the fixed top-squark mass grid (right) for some signal models the T-CR control region have a high signal contamination, while for the W-CR control region, contamination is below 14%.

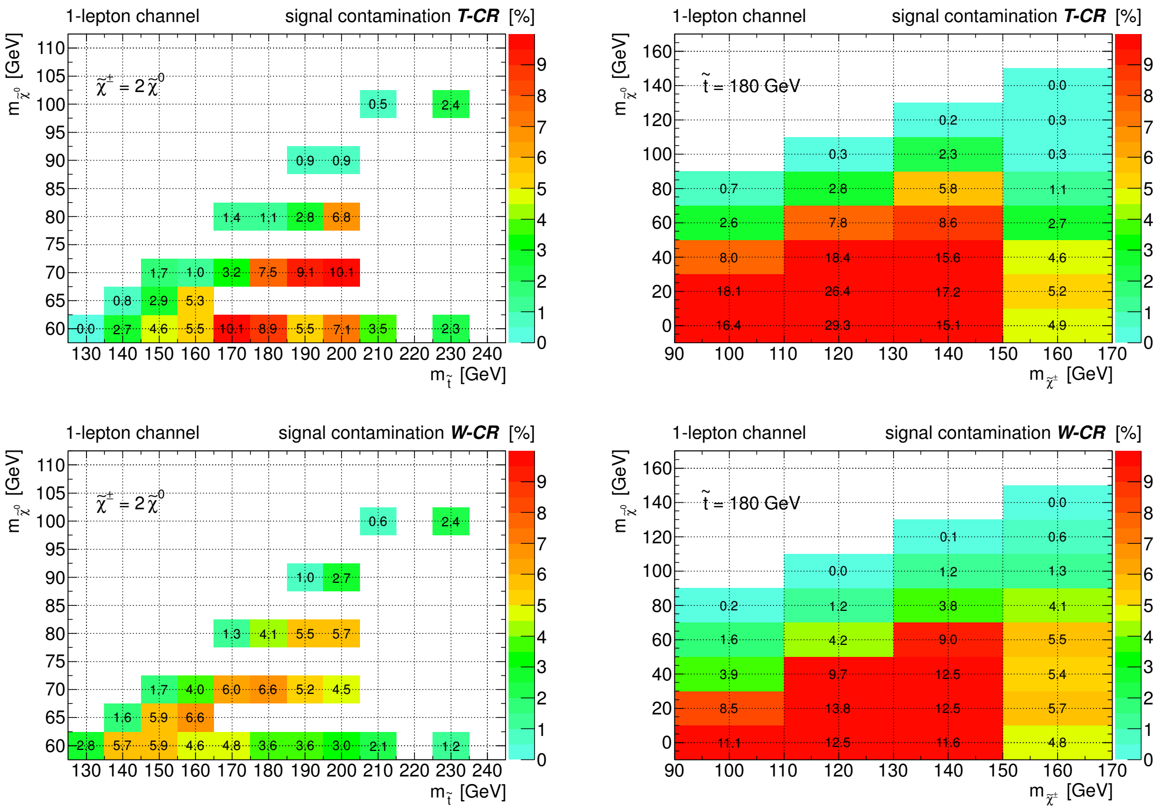

Figure 5.5: Signal contaminations in the T-CR (top) and W-CR (bottom) control region for the gaugino universality (left) and fixed top-squark mass (right) grid. Values are shown in percents.

The signal yields and values for acceptance times efficiency for the gaugino universality grid and for the fixed top-squark mass grid are shown in Figure 5.6.

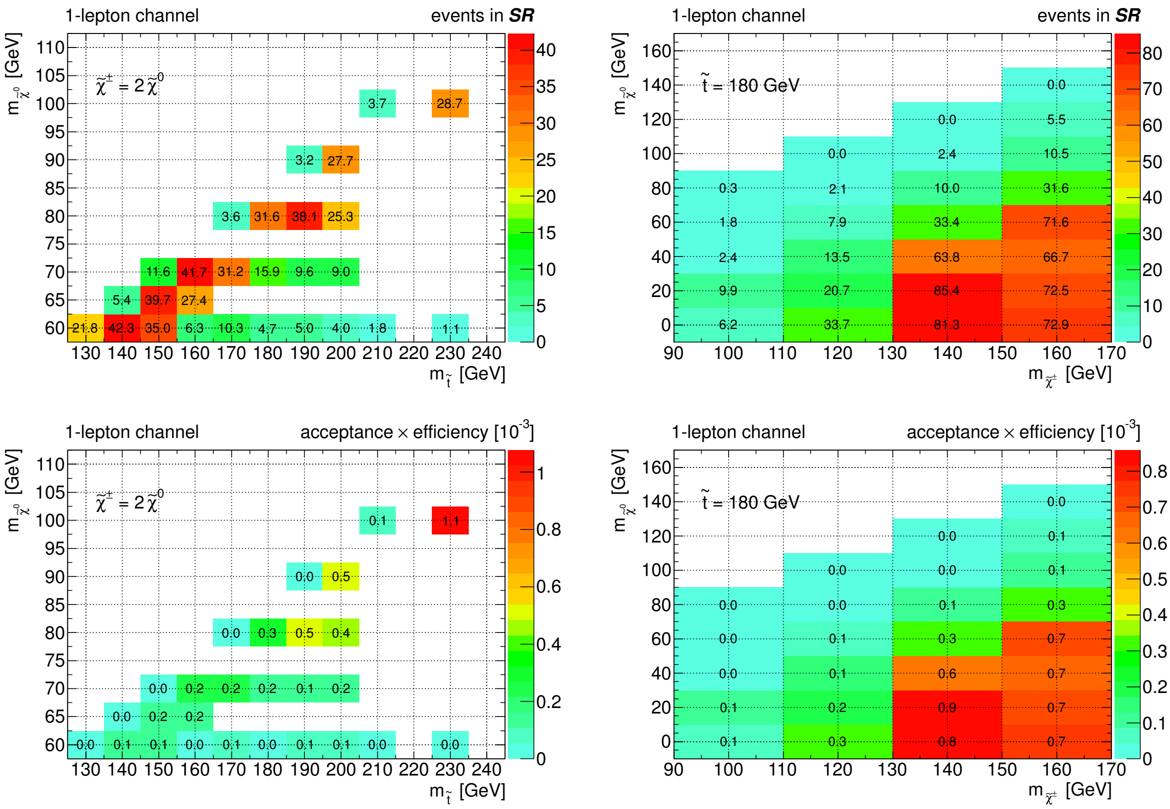

Figure 5.6: Signal yields (top) and acceptance times efficiency (bottom) for the signal region for the gaugino universality (left) and fixed top-squark mass (right) grid.

5.6 Systematic uncertainties

5.6.1 Experimental uncertainties

The following dominant detector uncertainties have been considered.

- The jet energy scale (JES) is estimated by varying jet energy scale within $\pm 1\sigma$ of the uncertainty coherently for all jets in the event.
- The jet energy resolution (JER) is obtained by applying an additional smearing to jets according to their p_{T} and η parameters.
- The uncertainty on the b-tagging is estimated by varying b-tagging efficiency and mis-tagging rates within the measured uncertainty.
- The uncertainties on the $E_{\mathrm{T}}^{\mathrm{miss}}$ due to the energy scale of the clusters, which are not associated to any object (CellOut) are estimated based on the uncertainties on calorimeter energy clusters involved in $E_{\mathrm{T}}^{\mathrm{miss}}$ calculation.

5.6.2 Theoretical uncertainties

Around 95% of the background is composed of $t\bar{t}$ and $W+$jets events, therefore, theoretical uncertainties are estimated for these processes only.

$t\bar{t}$ production

The total theoretical uncertainty for the $t\bar{t}$ production is estimated by summing in quadrature the following uncertainties:

- **Generator uncertainty**
  The uncertainty related to the choice of the generator is estimated as a difference between the baseline MC@NLO and POWHEG generated samples. Both generators are interfaced with HERWIG for parton showering.
- **Initial and final state radiation**
  The uncertainty on the initial and final state radiations is estimated as the difference between the nominal ACERMC and the same samples generated with higher and lower parton shower activity.
- **Parton shower**
  The difference between HERWIG and PYTHIA parton showering is taken as a parton shower uncertainty. For this, samples generated with POWHEG are interfaced either with HERWIG or with PYTHIA for parton showering. The difference between these two samples is symmetrised.

$W+$jets production

The total theoretical uncertainty for the $W+$jets production is estimated by summing in quadrature generator and scale variation uncertainties:

- **Generator uncertainty**
  The difference between the baseline ALPGEN and HERWIG samples is estimated as a Monte Carlo generator uncertainty.
- **Scale variations**
  The factorisation and renormalisation scale uncertainties were estimated by varying corresponding parameters in the ALPGEN generator by factors of 0.5 and 2.0 from the nominal value. The following approach [90] is used: since variations mainly affect the number of generated partons N_{parton}, instead of generating samples with different variations, the corresponding reweighting of the nominal samples according to the number of generated partons ($N_{\text{parton}} = 0, \ldots, 5$) is used.

5.6.3 Summary

The summary of the experimental and theoretical systematic uncertainties and statistical uncertainties of the Monte Carlo events is presented in Table 5.8. One can see, that the dominant detector uncertainties are the jet energy scale (JES) and resolution (JER) uncertainties. For the theoretical uncertainty, the main (about ±7%) uncertainty is associated to the $t\bar{t}$ production. The total uncertainty related to the number of Monte Carlo events in signal region also have a sizable contribution of 6%.

	Detector				Theory		
Process	JES	JER	b-tagging	CellOut	ttbar	W+jets	MC stat.
$t\bar{t}$	6%	1%	3.0%	1.8%	7%	0.3%	5%
single top	2%	19%	0.6%	4.2%	4%	0.3%	27%
W+jets	43%	194%	1.2%	51%	11%	19%	100%
Z+jets	–	–	–	–	–	–	–
diboson	21%	18%	0.8%	12%	–	–	36%
Total SM	7.2%	7.8%	2.6%	2.6%	7%	1%	6.3%

Table 5.8: The summary of the experimental and theoretical systematic uncertainties and statistical uncertainties of the Monte Carlo events

5.7 Results

The final event yields of the Monte Carlo prediction and of the observed number of events in the data separated for the electron and muon channels and for their combination are shown in Table 5.9. The numbers are normalised to an integrated luminosity of 4.7 fb^{-1}. The $t\bar{t}$ and W+jets backgrounds are normalised in control regions, as described in Section 5.5. The Monte Carlo predictions before normalisation are shown in brackets.

Process	1 electron	1 muon	1 lepton
$t\bar{t}$	12.3 ± 1.9 (11.9)	10.7 ± 1.7 (10.4)	23.0 ± 3.1 (22.3)
single top	0.6 ± 0.3 (0.6)	0.6 ± 0.3 (0.6)	1.2 ± 0.4 (1.2)
W+jets	1.2 ± 1.5 (1.1)	0.0 ± 0.0	1.2 ± 1.5 (1.1)
Z+jets	0.0 ± 0.0	0.0 ± 0.0	0.0 ± 0.0
diboson	0.1 ± 0.1	0.2 ± 0.1	0.3 ± 0.1
Total SM	14.2 ± 2.4	11.4 ± 1.7	25.6 ± 3.5
Observed	13	11	24

Table 5.9: Breakdown of the expected yields and the observed numbers of events in the signal region. The Monte Carlo prediction before normalisation is reported in parentheses. Only the statistical uncertainties are shown. The numbers are normalised to an integrated luminosity of 4.7 fb^{-1}.

The final distributions for the signal region (SR), after the application of all selection requirements are shown separately for the electron and muon channels for N_{jets}, $E_{\text{T}}^{\text{miss}}$ and m_{T} in Figure 5.7 and for the p_{T} of the leading light jet, b-jet and lepton in Figure 5.8. Three signal models for the $(\tilde{t}_1, \tilde{\chi}_1^{\pm}, \tilde{\chi}_1^0)$ mass plane are shown for comparison. The masses of $\tilde{t}_1$, $\tilde{\chi}_1^{\pm}$ and $\tilde{\chi}_1^0$ are given in GeV.

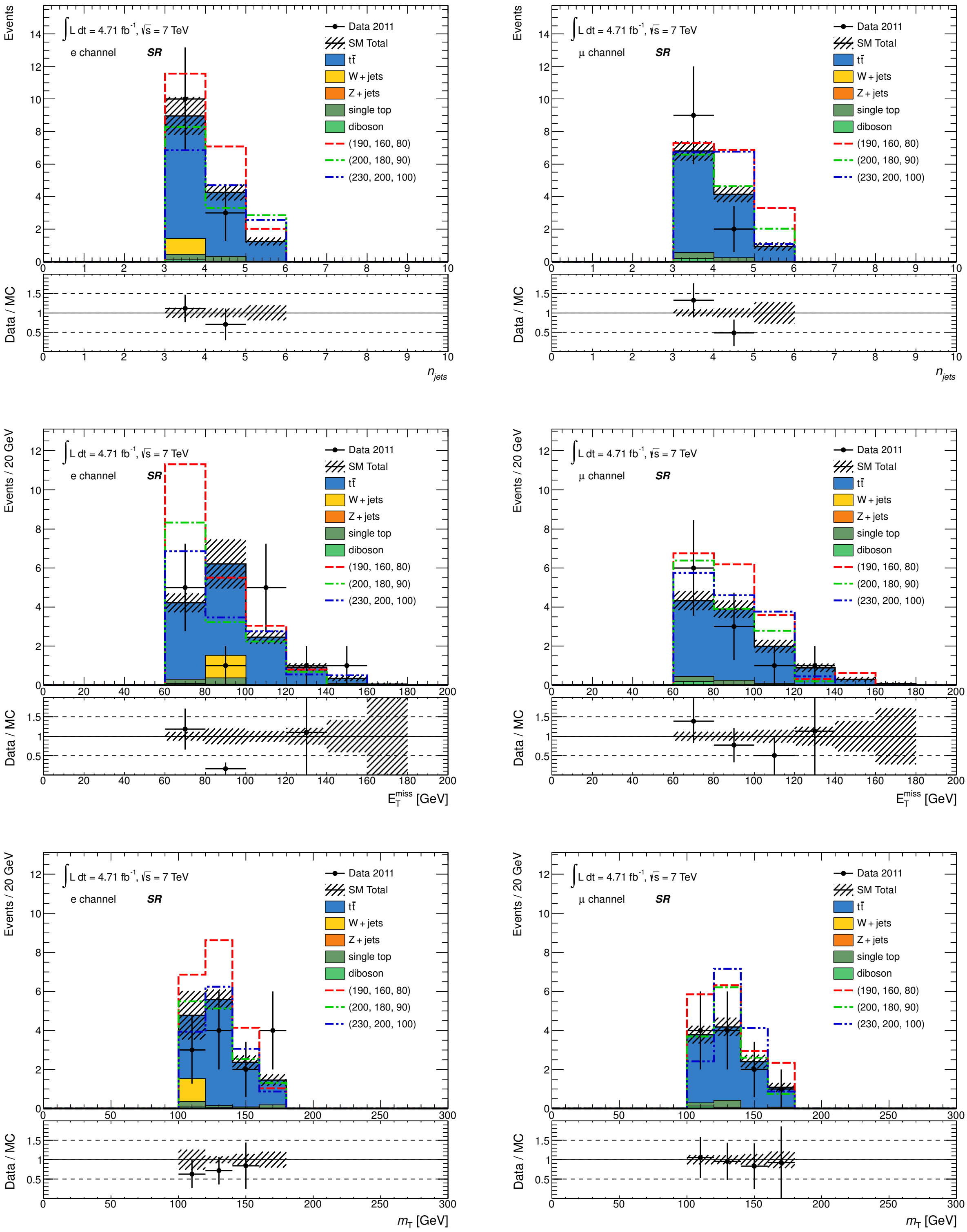

Figure 5.7: Distributions of the number of selected jets N_{jets} (top), $E_{\text{T}}^{\text{miss}}$ (middle) and m_{T} (bottom) for the electron (left) and muon (right) channel for the signal region (SR) after applying all selection requirements. The error bars include only the Monte Carlo statistical uncertainties. Three signal models for the $(\tilde{t}_1, \tilde{\chi}_1^{\pm}, \tilde{\chi}_1^0)$ mass plane are shown for comparison. The masses of $\tilde{t}_1$, $\tilde{\chi}_1^{\pm}$ and $\tilde{\chi}_1^0$ are given in GeV.

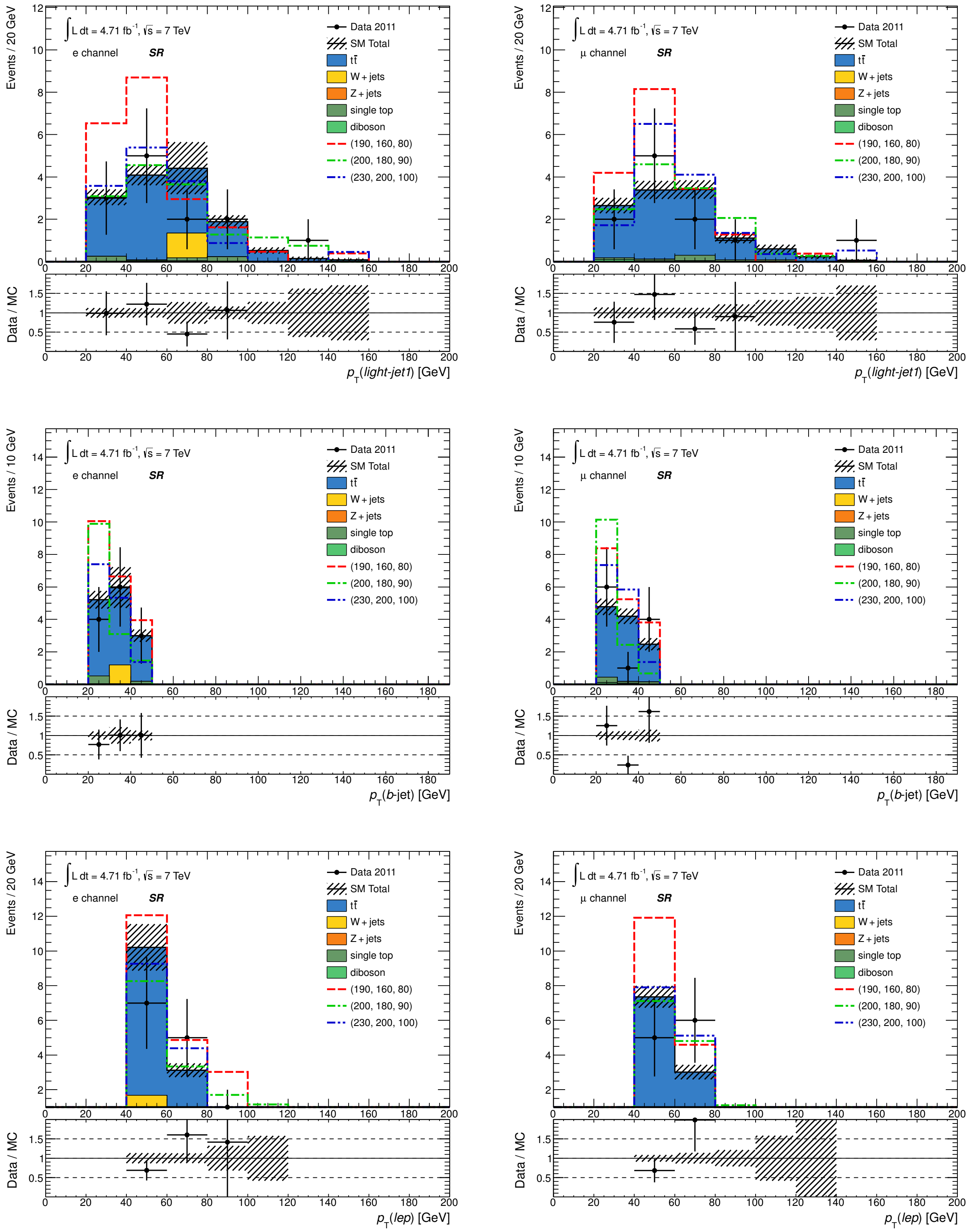

Figure 5.8: Distribution of p_{T} of the leading light jet (top), b-jet (middle) and lepton (bottom) for the electron (left) and muon (right) channels for the signal region (SR) after applying all selection requirements. The error bars include only the Monte Carlo statistical uncertainties. Three signal models for the $(\tilde{t}_1, \tilde{\chi}_1^{\pm}, \tilde{\chi}_1^0)$ mass plane are shown for comparison. The masses of $\tilde{t}_1$, $\tilde{\chi}_1^{\pm}$ and $\tilde{\chi}_1^0$ are given in GeV.

5.7.1 Interpretation

The 95% CL exclusion limits for the gaugino universality $m(\tilde{\chi}_1^{\pm}) = 2 \cdot m(\tilde{\chi}_1^0)$ grid and for the fixed top-squark mass $m(\tilde{t}) = 180$ GeV grid for the presented analysis are shown in Figure 5.9. The limits include only the relevant experimental and theoretical uncertainties, as described in Section 5.6. The solid red line represents the expected limits. The yellow band shows the $\pm 1\sigma$ uncertainty variations, which include all uncertainties except the signal cross-section uncertainty. The green line shows the observed limits for the one/two-lepton combined analysis for the ATLAS SUSY searches at $\sqrt{s} = 7$ TeV. The dashed lines (green and red) show variations of the signal cross section within $\pm 1\sigma$ of the theoretical uncertainty. The current analysis was re-optimised towards the diagonal of the gaugino universality (left) grid and was performed for the $\sqrt{s} = 8$ TeV data.

The limits obtained in this thesis show a significant improvement with respect to those obtained in the existing ATLAS SUSY one/two-lepton combined analysis based on the $\sqrt{s}\,^{\text{sub}}_{\text{min}}$ variable for the $\tilde{t}_1 \to b\tilde{\chi}_1^{\pm}$, $\tilde{\chi}_1^{\pm} \to W^{\pm(*)}\tilde{\chi}_1^0$ SUSY searches. The low sensitivity of the analysis in the region around $m(\tilde{t}) = 180$ GeV, $m(\tilde{\chi}_1^0) = 60$ GeV for the gaugino universality grid (left) is caused by the requirement of exactly one b-tagged jet, which was applied to avoid overlap with the one/two-lepton SUSY searches. The same is the case for the fixed top-squark mass grid (right). Here the sensitivity drops down above the exclusion contour in the region around $m(\tilde{\chi}_1^{\pm}) = 140$ GeV, $m(\tilde{\chi}_1^0) = 80$ GeV. Requiring exactly one b-tagged jet suppresses the sensitivity in these regions, where two b-jets are dominating.

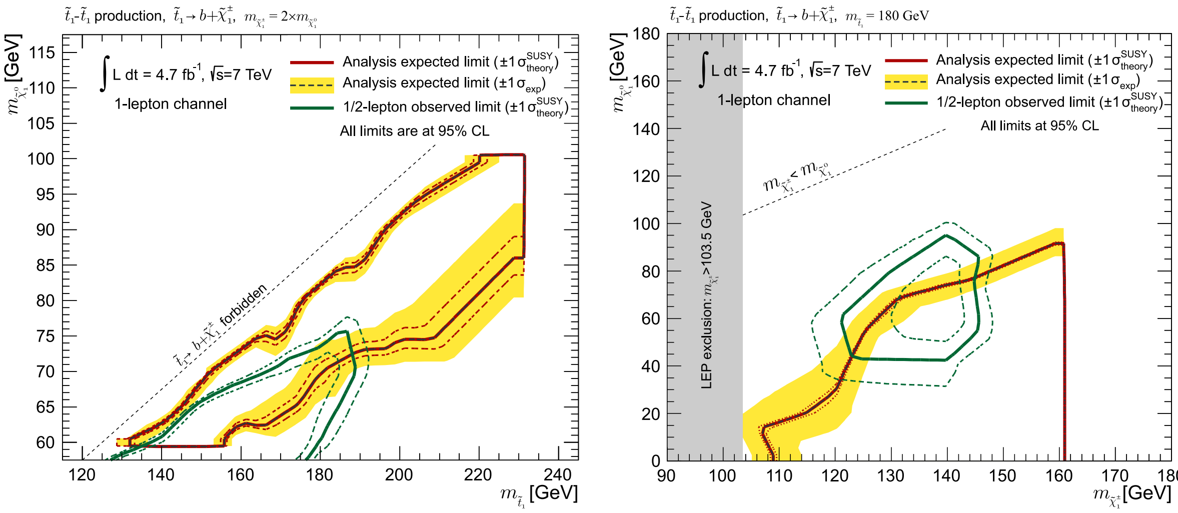

Gaugino universality grid　　　　Fixed top-squark mass grid

Figure 5.9: Preliminary 95% exclusion limits for the analysis performed in this thesis in comparison to those obtained in previous ATLAS analyses. The limits are shown for the gaugino universality grid ($m(\tilde{\chi}_1^{\pm}) = 2 \cdot m(\tilde{\chi}_1^0)$, left) and the fixed top-squark mass grid ($m(\tilde{t}) = 180$ GeV, right). The solid red line represents the expected limits, the yellow band shows the $\pm 1\sigma$ uncertainty variations, which include all uncertainties except the signal cross-section uncertainty. The green line shows the observed limits for the one/two-lepton combined analysis for the ATLAS SUSY searches at $\sqrt{s} = 7$ TeV. The dashed lines (green and red) show variations of the signal cross section within $\pm 1\sigma$ of the theoretical uncertainty.

CHAPTER 6

Searches for the top squark at $\sqrt{s} = 8$ TeV, $\tilde{t}_1 \to b\tilde{\chi}_1^{\pm}$, $\Delta m(\tilde{t}_1, \tilde{\chi}_1^{\pm}) \approx m(b)$

In this chapter the search for top-squark pair production in the $\tilde{t}_1 \to b\tilde{\chi}_1^{\pm}$, $\tilde{\chi}_1^{\pm} \to W^{(*)}\tilde{\chi}_1^0$ decay mode is presented. This analysis is part of the published ATLAS top-squark searches in semileptonic final states at $\sqrt{s} = 8$ TeV [3]. A Feynman diagram for the corresponding semileptonic decay is shown in Figure 6.1. It is assumed, that both decay channels have a $\mathcal{BR} = 100\%$ and all other supersymmetric particles are assumed to have masses above 3 TeV and not to be involved in interactions.

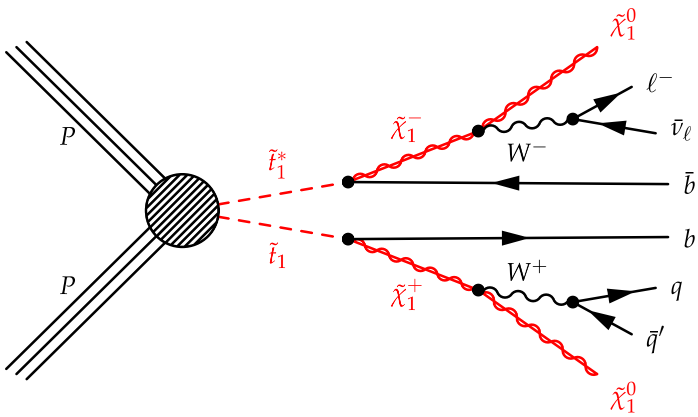

Figure 6.1: Feynman diagram for the $\tilde{t}_1 \to b\tilde{\chi}_1^{\pm}, \tilde{\chi}_1^{\pm} \to W^{(*)}\tilde{\chi}_1^0$ semileptonic decay channel.

Exclusion limits at 95% CL for the gaugino universality grid $m(\tilde{\chi}_1^{\pm}) = 2 \cdot m(\tilde{\chi}_1^0)$ are shown in Figure 6.2. These limits have been derived from the ATLAS searches for supersymmetry in final states with one lepton for $\mathcal{L}_{\text{int}} = 20.3\ \text{fb}^{-1}$ at $\sqrt{s} = 8$ TeV [91] before the analysis presented here. One can see, that a region along the diagonal $m(\tilde{t}_1) = m(b) + m(\tilde{\chi}_1^{\pm})$ (dashed gray line) is not excluded. Signal models above the diagonal are kinematically impossible.

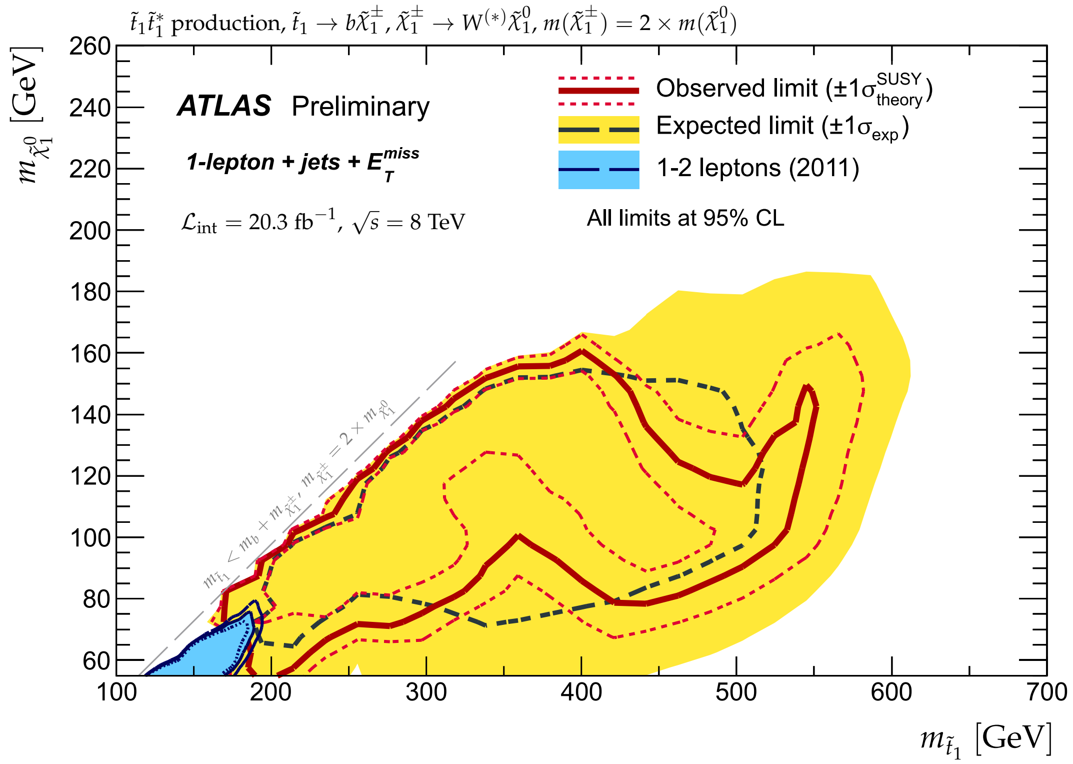

Figure 6.2: The expected (black dashed line) and observed (red solid line) 95% CL exclusion limits for $\tilde{t}_1 \to b\tilde{\chi}_1^{\pm}, \tilde{\chi}_1^{\pm} \to W^{(*)}\tilde{\chi}_1^0$ decays for the gaugino universality grid [91]. It is assumed, that both decays have a $\mathcal{BR} = 100\%$ and $m(\tilde{\chi}_1^{\pm}) = 2 \cdot m(\tilde{\chi}_1^0)$. The yellow band corresponds to the $\pm 1\sigma$ uncertainty on the expected limit and includes all uncertainties except the signal cross-section theoretical uncertainties. The dashed red line represents the change of the observed exclusion, when the signal cross section is varied by $\pm 1\sigma$ of the signal theoretical uncertainty. The non-excluded area within about 20 GeV below the gray dashed line is referred to as "bC diagonal" region. Signal models above the diagonal are kinematically non-accessible.

This analysis is targeting a compressed scenario, where the mass difference $\Delta m(\tilde{t}_1, \tilde{\chi}_1^{\pm})$ is below 40 GeV, the so-called "bC diagonal" region. For signal models with a small Δm, the p_{T} of the b-jets from the $\tilde{t}_1 \to b\tilde{\chi}_1^{\pm}$ decay are below the detection threshold of 25 GeV. Due to this, there are no b-tagged jets in the reconstructed events. This significantly decreases the acceptance of the standard one-lepton analyses, which require at least one b-tagged jet. Therefore, for this compressed scenario, a dedicated analysis was developed.

6.1 Data set and Monte Carlo samples

6.1.1 The data set

For this analysis, the data recorded by the ATLAS detector between April and December 2012 are used. After applying various ATLAS data-quality requirements, the integrated luminosity is 20.3 fb^{-1} with an uncertainty of $\pm 2.8\%$ [92, 93].

6.1.2 Trigger selection

For the one-lepton analysis single electron and muon triggers are used in combination with a trigger for large missing transverse energy.

For the electron channel, two different triggers are used: The `EF_e24vhi_medium1` is triggering at the high level trigger (HLT) on the energy deposited in the calorimeter $E_T > 24$ GeV with an isolation requirement $p_T^{\mathrm{cone}\,0.2}/E_T < 0.1$, see Section 3.2. To partially recover inefficiencies caused by isolation requirements, the `EF_e60_medium1` trigger with an increased HLT threshold up to $E_T > 60$ GeV, but without isolation requirements, is used in addition.

A similar approach is used for the muon channel. The `EF_mu24i_tight` is triggering at the HLT on the muons with $p_{\mathrm{T}} > 24$ GeV and applies isolation requirements $p_T^{\mathrm{cone}\,0.2}/p_{\mathrm{T}} < 0.12$, see Section 3.3. As for electrons, to recover inefficiencies of this trigger, the muon trigger `EF_mu36_tight` is used, which has an increased $p_{\mathrm{T}} > 36$ GeV threshold and no isolation requirement.

Two similar triggers, `EF_xe80T_tclcw_loose` and `EF_xe80_tclcw_loose`, are used for a missing transverse momentum selection. Both triggers have the HLT threshold at $E_{\mathrm{T}}^{\mathrm{miss}} > 80$ GeV and are fully efficient (efficiency is more then 99%) for the offline-calibrated $E_{\mathrm{T}}^{\mathrm{miss}} > 150$ GeV, see Section 3.6. The first trigger is available during the whole data taking, but omits events from the first three bunch crossings in a bunch train, which causes a 10% efficiency loss. Therefore, it is used only up to an integrated luminosity of 2.077 fb^{-1}. After that it became available a second trigger, which worked for all bunches and used for the rest of the data taking.

The combined trigger efficiency is measured for $W \to \mu\nu$ and $Z \to \ell\ell$ events and is found to be more than 98% for both electron and muon channels.

6.1.3 Monte Carlo samples

All Monte Carlo samples are simulated using either ATLAS full simulation GEANT4 or the fast simulation ATLFAST-II package.

Background samples

The following background samples are used for the analysis:

– The $t\bar{t}$ process is generated with a top-quark mass $m_t = 172.5$ GeV. The same top-quark mass is used in all other samples. The $t\bar{t}$ samples are generated with POWHEG with NLO accuracy. The inclusive cross section for the $t\bar{t}$ process is calculated at next-to-next-to-leading-order (NNLO) with the resummation of soft gluon terms at next-to-next-to-leading-logarithmic (NNLL) order [94, 95].

– Single top production samples are simulated using two different generators: for the Wt- and the s-channel processes the POWHEG generator is used, while the t-channel process is generated with ACERMC. The interference of the Wt-channel with the $t\bar{t}$ channel at NLO level is resolved by the *diagram removal* (DR) approach [96]. Cross sections for single top production channels are calculated at NLO+NNLO accuracy [97, 98].

Sample ID	Name	Simulation	Equivalent $\mathcal{L}$ [fb^{-1}]
ttbar	POWHEG + PYTHIA		
117050	`PowhegPythia_P2011C`	AF2	545.6
single top	ACERMC + PYTHIA, POWHEG + PYTHIA		
110101	`AcerMCPythia_P2011CCTEQ6L1_singletop_tchan_l`	FS	316.0
110119, 110140	`PowhegPythia_P2011C_st_[schan_lep,Wtchan_incl_DR]`	FS	[3299, 891.3]
ttbar+W/Z	MADGRAPH + PYTHIA		
119353, 119355	`MadGraphPythia_AUET2BCTEQ6L1_ttbar[W,Z]`	FS	[3284, 4377]
174830, 174831	`MadGraphPythia_AUET2BCTEQ6L1_ttbarW[jExcl,jjIncl]`	FS	[6404, 8237]
174832, 174833	`MadGraphPythia_AUET2BCTEQ6L1_ttbarZ[jExcl,jjIncl]`	FS	[6532, 7446]
119583	`MadgraphPythia_AUET2B_CTEQ6L1_ttbarWW`	FS	[10870]
W+jets	SHERPA		
167740–167748	`W[enu,munu,taunu]MassiveCBPt0_BFilter`	AF2	[96.4, 96.0, 95.8]
	`W[enu,munu,taunu]MassiveCBPt0_CJetFilterBVeto`	AF2	[16.7, 19.3, 17.8]
	`W[enu,munu,taunu]MassiveCBPt0_CJetVetoBVeto`	AF2	[4.14, 4.33, 3.49]
167761–167769	`W[enu,munu,taunu]MassiveCBPt70_140_BFilter`	AF2, FS	[156.6, 155.7, 156.5]
	`W[enu,munu,taunu]MassiveCBPt70_140_CJetFilterBVeto`	AF2, FS	[53.6, 54.2, 54.2]
	`W[enu,munu,taunu]MassiveCBPt70_140_CJetVetoBVeto`	AF2, FS	[23.9, 23.7, 23.8]
167770–167778	`W[enu,munu,taunu]MassiveCBPt140_280_BFilter`	AF2, FS	[457.8, 457.2, 458.2]
	`W[enu,munu,taunu]MassiveCBPt140_280_CJetFilterBVeto`	AF2, FS	[260.3, 266.5, 262.6]
	`W[enu,munu,taunu]MassiveCBPt140_280_CJetVetoBVeto`	AF2, FS	[81.0, 80.0, 80.7]
167779–167787	`W[enu,munu,taunu]MassiveCBPt280_500_BFilter`	FS	[590.3, 591.2, 590.9]
	`W[enu,munu,taunu]MassiveCBPt280_500_CJetFilterBVeto`	FS	[418.0, 428.8, 420.9]
	`W[enu,munu,taunu]MassiveCBPt280_500_CJetVetoBVeto`	FS	[358.4, 355.1, 358.5]
167788–167796	`W[enu,munu,taunu]MassiveCBPt500_BFilter`	FS	[887.3, 886.1, 885.5]
	`W[enu,munu,taunu]MassiveCBPt500_CJetFilterBVeto`	FS	[364.9, 369.9, 366.9]
	`W[enu,munu,taunu]MassiveCBPt500_CJetVetoBVeto`	FS	[136, 668, 669]
180534–180542	`W[enu,munu,taunu]MassiveCBPt40_70_BFilter`	FS	[44.0, 43.8, 43.9]
	`W[enu,munu,taunu]MassiveCBPt40_70_CJetFilterBVeto`	FS	[7.25, 7.48, 7.34]
	`W[enu,munu,taunu]MassiveCBPt40_70_CJetVetoBVeto`	FS	[29.6, 29.3, 29.5]
Z+jets	SHERPA		
167749–167760	`Z[ee,mumu,tautau,nunu]MassiveCBPt0_BFilter`	AF2	[115, 115, 116, 127]
	`Z[ee,mumu,tautau,nunu]MassiveCBPt0_CJetFilterBVeto`	AF2	[8.52, 8.50, 8.50, 10.6]
	`Z[ee,mumu,tautau,nunu]MassiveCBPt0_CJetVetoBVeto`	AF2	[5.85, 5.83, 3.49, 4.86]
167797–167808	`Z[ee,mumu,tautau,nunu]MassiveCBPt70_140_BFilter`	AF2, FS	[513, 511, 513, 382]
	`Z[ee,mumu,tautau,nunu]MassiveCBPt70_140_CJetFilterBVeto`	AF2, FS	[85.3, 85.4, 85.2, 45.6]
	`Z[ee,mumu,tautau,nunu]MassiveCBPt70_140_CJetVetoBVeto`	AF2, FS	[108, 108, 108, 47.5]
167809–167820	`Z[ee,mumu,tautau,nunu]MassiveCBPt140_280_BFilter`	AF2, FS	[470, 470, 467, 410]
	`Z[ee,mumu,tautau,nunu]MassiveCBPt140_280_CJetFilterBVeto`	AF2, FS	[243, 241, 242, 216]
	`Z[ee,mumu,tautau,nunu]MassiveCBPt140_280_CJetVetoBVeto`	AF2, FS	[251, 251, 252, 222]
167821–167832	`Z[ee,mumu,tautau,nunu]MassiveCBPt280_500_BFilter`	FS	[681, 679, 695, 1211]
	`Z[ee,mumu,tautau,nunu]MassiveCBPt280_500_CJetFilterBVeto`	FS	[477, 478, 481, 429]
	`Z[ee,mumu,tautau,nunu]MassiveCBPt280_500_CJetVetoBVeto`	FS	[365, 364, 364, 1303]
167833–167844	`Z[ee,mumu,tautau,nunu]MassiveCBPt500_BFilter`	FS	[5596, 5947, 5856, 5186]
	`Z[ee,mumu,tautau,nunu]MassiveCBPt500_CJetFilterBVeto`	FS	[1666, 1662, 1706, 1536]
	`Z[ee,mumu,tautau,nunu]MassiveCBPt500_CJetVetoBVeto`	FS	[6920, 5530, 6920, 5024]
180543–180551	`Z[ee,mumu,tautau]MassiveCBPt40_70_BFilter`	AF2, FS	[107.6, 107.3, 107.1]
	`Z[ee,mumu,tautau]MassiveCBPt40_70_CJetFilterBVeto`	AF2, FS	[22.2, 22.2, 22.2]
	`Z[ee,mumu,tautau]MassiveCBPt40_70_CJetVetoBVeto`	AF2, FS	[30.2, 30.1, 30.2]
diboson	SHERPA		
183734–183739	`WWto[enu,munu,taunu]qq_MassiveCB`	FS	[102.3, 102.1, 102.5]
	`WZto[enu,munu,taunu]qq_MassiveCB`	FS	[105.1, 104.9, 104.4]
183585–183590	`ZWto[ee,mumu,tautau]qq_MassiveCB`	FS	[114.4, 114.5, 115.4]
	`ZZto[ee,mumu,tautau]qq_MassiveCB`	FS	[121.6, 121.2, 124.1]
179974, 179975	`[lllnu,lnununu]_WZ_MassiveCB`	FS	[263.8, 244.1]
177997, 177999	`llnunu_[WW,ZZ]_MassiveCB`	FS	[1407, 1734]

Table 6.1: The Monte Carlo samples used in the $\sqrt{s} = 8$ TeV analysis. An equivalent luminosity is defined as N/σ, where N is the total number of generated events and σ is the cross section (including K-factor and filter efficiency). The labels `AF2` and `FS` indicate whether fast (`AF2`) or full (`FS`) simulation is used.

– The $W+$jets and $Z+$jets samples are generated with SHERPA with up to four additional partons taking into account the correct masses of the b and c quarks. The corresponding cross sections are calculated at NNLO including the $\gamma - Z$ interference, finite-width effects, leptonic decays of W/Z and spin correlations [99].

– The $t\bar{t} + W/Z$ and $t + Z$ samples are generated with MADGRAPH with up to two additional partons. Cross sections are calculated at NLO [100, 101] and LO [102] precision, respectively.

– The diboson samples WW, WZ, ZZ are generated with SHERPA with massive b and c quarks. Cross sections are calculated at NLO precision [103].

Cross sections for $t\bar{t}$, $W+$jets, $Z+$jets and diboson processes are calculated using the `MSTW2008` PDF set. For the $t\bar{t} + W$ and $t\bar{t} + Z$ cross section calculations, the `MSTW2008` and `CTEQ6.6M` PDF sets are used. A detailed list of the background Monte Carlo samples used by the SUSY Working Group for the $\sqrt{s} = 8$ TeV analysis are shown in Table 6.1.

Signal samples

Signal samples for the process $\tilde{t}_1 \to b\tilde{\chi}_1^{\pm} \to bW^{\pm(*)}\tilde{\chi}_1^0$ are generated with MADGRAPH, which is interfaced to PYTHIA. The detector effects are modelled with the ATLAS fast simulation ATLFAST-II program. Each signal model can be represented as a point in three-dimensional mass space $(\tilde{t}_1, \tilde{\chi}_1^{\pm}, \tilde{\chi}_1^0)$. In the following the triple (m_1, m_2, m_3) refers to the signal model with $m(\tilde{t}_1) = m_1$, $m(\tilde{\chi}_1^{\pm}) = m_2$ and $m(\tilde{\chi}_1^0) = m_3$, where masses are given in GeV.

Results are presented on different two-dimensional plots. The signal models shown in each plot are selected by adding a linear constraint on the masses of the $\tilde{t}_1$, $\tilde{\chi}_1^{\pm}$ and $\tilde{\chi}_1^0$ particles. Signal models for each linear constraint are often called "grid". The same signal model may belong to different grids. The list of signal models used for the one-lepton analysis is shown in Table 6.2.

Grid	Sample ID	Constraint	Mass Plane	Filter	Generator
`ch2nt`	166418–166500 173278–173294 173473–173485	$m(\tilde{\chi}_1^{\pm}) = 2 \cdot m(\tilde{\chi}_1^0)$	$(\tilde{t}_1, \tilde{\chi}_1^0)$	1-lepton	MADGRAPH
`stch10`	172689–172725	$m(\tilde{t}_1) = m(\tilde{\chi}_1^{\pm}) + 10$ GeV	$(\tilde{t}_1, \tilde{\chi}_1^0)$	1-lepton	MADGRAPH
`nt001`	172648–172688	$m(\tilde{\chi}_1^0) = 1$ GeV	$(\tilde{t}_1, \tilde{\chi}_1^{\pm})$	1-lepton	MADGRAPH
`st300`	172726–172737	$m(\tilde{t}_1) = 300$ GeV	$(\tilde{\chi}_1^{\pm}, \tilde{\chi}_1^0)$	1-lepton	MADGRAPH
`st150`	172738–172744	$m(\tilde{t}_1) = 150$ GeV	$(\tilde{\chi}_1^{\pm}, \tilde{\chi}_1^0)$	1-lepton	MADGRAPH
`ch150`	172745–172769 174849–174853 177080–177089	$m(\tilde{\chi}_1^{\pm}) = 150$ GeV	$(\tilde{t}_1, \tilde{\chi}_1^0)$	1-lepton	MADGRAPH
`ch106`	175708–175766	$m(\tilde{\chi}_1^{\pm}) = 106$ GeV	$(\tilde{t}_1, \tilde{\chi}_1^0)$	1-lepton	MADGRAPH

Table 6.2: List of signal samples used for the $\tilde{t}_1 \to b\tilde{\chi}_1^{\pm} \to bW^{\pm(*)}\tilde{\chi}_1^0$ analysis at $\sqrt{s} = 8$ TeV.

The current analysis is mainly sensitive to the $m(\tilde{\chi}_1^{\pm}) = 2 \cdot m(\tilde{\chi}_1^0)$ – gaugino universality grid and the $\Delta m(\tilde{t}_1, \tilde{\chi}_1^{\pm}) = 10$ GeV – compressed scenario grid. The motivation for the gaugino universality grid is explained in Section 4.2.

For the presented compressed scenario an extra radiation jet is required, therefore a proper estimation of systematic uncertainties related to *Initial and Final State Radiation* (ISR/FSR) is very important. For this reason, for each signal sample of the two grids mentioned above, additional samples using different scale choices are generated with a high number of events on particle level.

6.2 Object definitions and event cleaning

6.2.1 Object definitions

Object definitions are based on the standard tool set used in the ATLAS SUSY Working Group.

Jets

Jets are reconstructed using an anti-k_t clustering algorithm, with $R = 0.4$ as distance parameter, see Section 3.4.

Baseline jets are calibrated jets with $p_{\mathrm{T}} > 20$ GeV, $|\eta| < 2.8$. These jets are used for overlap removal (see Section 6.2.2). For jets, which pass the overlap removal, additional quality checks are applied. Events containing very loose bad jets (i.e. jets from non-collision background, from Hadronic Endcap Calorimeter noise spikes or jets that fail the Electromagnetic Calorimeter energy reconstruction quality/noise check) are rejected.

Signal jets are defined as baseline jets with $p_{\mathrm{T}} > 25$ GeV and $|\eta| < 2.5$.

A summary of the jet selection criteria is shown in Table 6.3.

Baseline jet	
Algorithm	`AntiKt4LCTopo`
Acceptance	$p_{\mathrm{T}} > 20$ GeV, $\|\eta\| < 2.8$
Overlap	$\Delta R(e, \text{non } b\text{-jet}) > 0.2$
Quality	`VeryLoose` bad jet: reject event
Signal jet	
Acceptance	$p_{\mathrm{T}} > 25$ GeV, $\|\eta\| < 2.5$

Table 6.3: Summary of the jet definition criteria.

b-jets

The definition of b-tagged jets uses the `MV1` jet tagger at a 80% operation point, see Section 3.5. To correct the b-tagging rate from the Monte Carlo to the data, a weight is applied for each jet.

The weight is defined based on the efficiencies for the data and Monte Carlo, $\epsilon_f^{\text{data}}(p_{\text{T}}, \eta)$ and $\epsilon_f^{\text{MC}}(p_{\text{T}}, \eta)$, where f is the jet flavour [70]. If a jet is tagged, the weight is calculated as:

$$w_{\text{jet}} = \frac{\epsilon_f^{\text{data}}}{\epsilon_f^{\text{MC}}} = \text{SF}_f. \tag{6.1}$$

If a jet is not tagged, the weight is:

$$w_{\text{jet}} = \frac{1 - \epsilon_f^{\text{data}}}{1 - \epsilon_f^{\text{MC}}} = \frac{1 - \text{SF}_f \epsilon_f^{\text{MC}}}{1 - \epsilon_f^{\text{MC}}}. \tag{6.2}$$

The b-tagging efficiencies ϵ_f^{data} and ϵ_f^{MC} and scale factors SF_f are determined by the ATLAS Flavour Tagging Working Group. It is assumed, that the b-tagging weights can be applied independently for each jet. Therefore, the final b-tagging weight for the event is obtained by miltiplication of the w_{jet} weights for each jet from the event.

Electrons

Electrons are reconstructed using energy clusters in the electromagnetic calorimeter matched to tracks from the inner detector, see Section 3.2.

Baseline electrons are defined as `loose++` type with $p_{\text{T}} > 10$ GeV and $|\eta| < 2.47$. The *Electromagnetic Fraction* (EMF) – the fraction of energy deposited in the electromagnetic calorimeter – is required to be more than 0.8. The overlap removal is done between baseline electrons and jets. In case of an overlap with b-tagged jets with $\Delta R(e, b\text{-jet}) < 0.2$, the electron is removed. In case of non b-tagged jets, the electron is removed only if $0.2 < \Delta R(e, \text{non } b\text{-jet}) < 0.4$.

Signal electrons are additionally required to have `tight++` type, $p_{\text{T}} > 25$ GeV and an isolation requirement $p_{\text{T}}^{\text{cone}\,0.2}/p_{\text{T}} < 0.1$.

A summary of the electron selection is shown in Table 6.4.

Baseline electron	
Algorithm	combined track+cluster electron
Acceptance	$p_{\text{T}} > 10$ GeV, $|\eta| < 2.47$
Quality	`loose++` and `EMF` > 0.8 requirement on quality flag
Overlap	$\Delta R(e, \text{non } b\text{-jet}) < 0.2$ or $\Delta R(e, \text{jet}) > 0.4$
Signal electron	
Acceptance	$p_{\text{T}} > 25$ GeV, $|\eta| < 2.47$
Quality	`tight++`
Isolation	$p_{\text{T}}^{\text{cone}\,0.2}/p_{\text{T}} < 0.1$

Table 6.4: Summary of the electron definition criteria.

Muons

Two types of muons are used: `combined` and `segment-tagged`, see Section 3.3.

Baseline muons are defined as muons with $p_\mathrm{T} > 10$ GeV, $|\eta| < 2.4$ and are requited to fulfil quality requirements for tracks, see Table 6.5. $N^{\mathrm{hits}}_{\mathrm{TRT}}$ is the total number of TRT hits including outliers. Baseline muons are used for the overlap removal with jets. If a muon overlaps with a jet with $\Delta R(\mu, \mathrm{jet}) < 0.4$, the muon is removed.

Signal muons are additionally required to fulfil $p_\mathrm{T} > 25$ GeV, $|\eta| < 2.4$ and an isolation requirement $p_\mathrm{T}^{\mathrm{cone}\,0.2} < 1.8$ GeV. A suppression against cosmic muon candidates $|z_\mu - z_{PV}| < 1$ mm and $|d_0| < 0.2$ mm is also applied.

A summary of the muon selection is shown in Table 6.5.

Baseline muon	
Algorithm	`combined` or `segment-tagged` muon
Acceptance	$p_\mathrm{T} > 10$ GeV, $|\eta| < 2.4$
Quality	≥ 1 Pixel hit, ≥ 5 SCT hits, Pixel + SCT holes < 3
	$0.1 < |\eta| < 0.9$: $N^{\mathrm{hits}}_{\mathrm{TRT}} \geq 6$, $N^{\mathrm{outliers}}_{\mathrm{TRT}} < 0.9 \times N^{\mathrm{hits}}_{\mathrm{TRT}}$
Overlap	$\Delta R(\mu, \mathrm{jet}) > 0.4$
Signal muon	
Acceptance	$p_\mathrm{T} > 25$ GeV, $|\eta| < 2.4$
Isolation	$p_\mathrm{T}^{\mathrm{cone}\,0.2} < 1.8$ GeV
Cosmics veto	$|z_\mu - z_{PV}| < 1$ mm, $|d_0| < 0.2$ mm

Table 6.5: Summary of the muon definition criteria.

Missing transverse momentum

The missing transverse momentum $E_\mathrm{T}^{\mathrm{miss}}$ is calculated as the vectorial sum of the transverse momenta of identified objects (electrons, muons and jets) and calorimeter clusters, not assigned to any object:

$$E_\mathrm{T}^{\mathrm{miss}} = E_\mathrm{T}^{\mathrm{miss},\, e\gamma} + E_\mathrm{T}^{\mathrm{miss,\, muon}} + E_\mathrm{T}^{\mathrm{miss,\, soft\text{-}jets}} + E_\mathrm{T}^{\mathrm{miss,\, jets}} + E_\mathrm{T}^{\mathrm{miss,\, CellOut}}, \tag{6.3}$$

for more details, see Section 3.6.

For the $E_\mathrm{T}^{\mathrm{miss}}$ calculation a looser object definition is used: jets are included with $p_\mathrm{T} > 10$ GeV and $|\eta| < 4.9$, electrons are taken with `medium` type and $p_\mathrm{T} > 10$ GeV, for muons the overlap requirements with jets are loosened to $\Delta R(\mu, jet) > 0.3$. The "CellOut" term is calculated from the topological clusters, which are not assigned to any physical object.

6.2.2 Overlap removal

Some jets may contain leptons, which "belong" to the jet, but they also can appear in a lepton collection. On the other side, some leptons may be identified as jets, and they may appear in a jet collection as extra jets. To resolve such cases, an overlap removal is needed. It is based on performance studies [46] and uses the $\Delta R = \sqrt{\Delta\phi^2 + \Delta\eta^2}$ variable between the lepton and the jet.

The overlap removal is applied in the following order:

- If an electron lies within $\Delta R < 0.2$ of a jet then:
  – If the jet is b-tagged, the electron is removed,
  – Otherwise, the jet is considered as "fake" and is removed;
- If an electron is within $0.2 < \Delta R < 0.4$ of a jet, it is considered, that the electron "belongs" to the jet, and the electron is removed;
- If a muon is within $\Delta R < 0.4$ of a jet, it is considered, that the muon "belongs" to the jet, and the muon is removed.

6.2.3 Event cleaning

The basic cleaning requirements are applied for all SUSY one-lepton analyses. The so-called "cleaning cuts" are listed in the following:

- The *Good Run List* (GRL) – official ATLAS Data Quality (DQ) requirements – is applied. These requirements are applied only on data.
- A combination of the electron, muon and missing transverse momentum trigger is applied.
- Incompletely recorded events and events with an error flag set from the calorimetry system (LAr or TileCal) or events for which TileCal module power supplies had tripped, are rejected. This requirement is applied only on data.
- Event with mismeasured $E_{\mathrm{T}}^{\mathrm{miss}}$, due to non-operational cells in the TileCal or Hadronic Endcap Calorimeter, are rejected.
- Event with a cosmic muon candidate or with a bad muon are rejected.
- The primary vertex is required to have at least 5 tracks.
- Event with "bad" jets, i.e. jets from non-collision background and cosmics, jets from Hadronic Endcap Calorimeter spikes or Electromagnetic Calorimeter noise, are rejected.

6.3 Background reweighting

The Monte Carlo generated samples for the $\sqrt{s} = 8$ TeV analysis show some discrepancies with data. Examples are the distributions of the leading jet p_{T}, the jet multiplicity N_{jets} and m_{T}, for the 2 b-jet selection. These distributions are shown in Figure 6.3.

The mismodelling causes a slope in the data-to-Monte-Carlo ratio for the leading jet p_{T} and N_{jets} distributions, while the m_{T} distribution is not sensitive to the mismodelling and has a good data vs Monte Carlo agreement.

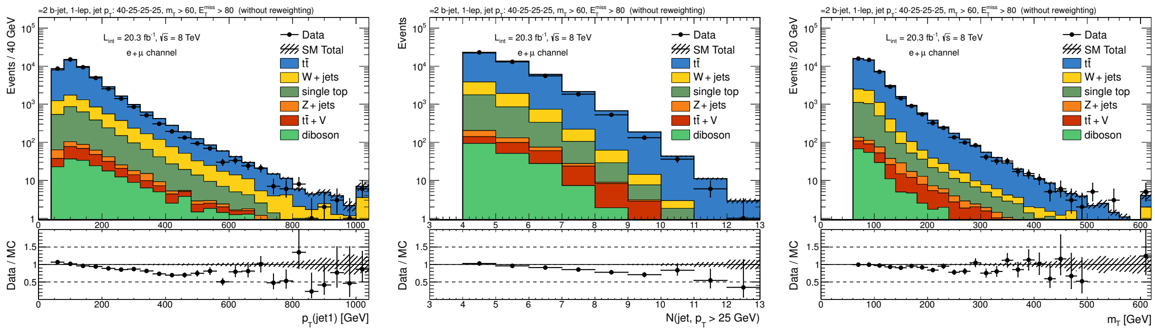

Figure 6.3: The data-MC comparison for the 2 b-jet selection before any reweighting is applied for the variables: p_{T} of the leading jet (left), jet multiplicity N_{jets} (middle), and m_{T} (right). The distributions are shown for the selection: 1 lepton, exactly 2 b-tagged jets, 4 jets with p_{T} values above 40, 25, 25, and 25 GeV, $E_{\mathrm{T}}^{\mathrm{miss}} > 80$ GeV, $m_{\mathrm{T}} > 60$ GeV. The $t\bar{t}$ and W+jets production are normalised to the Monte Carlo cross sections. The error bands include only the Monte Carlo statistical uncertainties.

Any attempt to correct the slope based on the N_{jets} distribution in a control region may introduce an opposite slope in the signal region. One exercise which highlights this problem was done during a background reweighting study. This example shows why the reweighting of the jet multiplicity distribution is dangerous and how it may introduce an opposite slope. A detailed description of this example is presented in Appendix A.

Since for the one-lepton analysis the dominant backgrounds are $t\bar{t}$ and W+jets production, the needs for corresponding reweightings are studied separately for each process.

The W+jets reweighting

After requiring a high $E_{\mathrm{T}}^{\mathrm{miss}}$ and m_{T}, the regions dominated by the W+jets background have a good data-MC agreement for key variables within the systematic uncertainties. A detailed data-MC comparison for different kinematic variables for control and validation regions can be found in Appendix B. Based on this comparison it was decided to not apply any reweighting for the W+jets background in the one-lepton analysis.

The $t\bar{t}$ reweighting

While for the W+jets background, the data-MC agreement was good, this is not the case for the $t\bar{t}$ production. After checking different reweightings strategies, it was decided to use a reweighting based on the true p_{T} of the $t\bar{t}$ system.

A measurement of the top-quark pair production differential cross section [104] shows a mismodelling of the unfolded distributions of the p_{T} of the $t\bar{t}$ system. Based on the measurements, the weights are defined as a 4-bin function of the true p_{T} of the $t\bar{t}$ system. The electron and muon weights are averaged. The reweighting coefficients are shown in Table 6.6.

The scale factors to reweight the distribution of the true p_{T} of the $t\bar{t}$ system are derived for the POWHEG+PYTHIA samples simulated at $\sqrt{s} = 7$ TeV. The same generator is used as default for the $t\bar{t}$ process modelling at $\sqrt{s} = 8$ TeV.

truth $p_{\mathrm{T}}(t\bar{t})$ [GeV]	e - channel	μ - channel	average
$p_{\mathrm{T}} \in [0, 40)$	0.988	1.006	0.997
$p_{\mathrm{T}} \in [40, 170)$	0.912	0.967	0.940
$p_{\mathrm{T}} \in [170, 340)$	0.710	0.758	0.734
$p_{\mathrm{T}} \in [340, \infty)$	0.556	0.584	0.570

Table 6.6: Reweighting factors as a function of the true $p_{\mathrm{T}}(t\bar{t})$ extracted from the ATLAS top-quark differential cross-section measurement [104].

The approach considered has the following advantages:

- It does not depend on the analysis (zero- or one-lepton);
- It does not depend on a semileptonic $t\bar{t}$ decay channel (e, μ, τ);
- It does not use the jet multiplicity for the reweighting.

The reweighting significantly improves the data-MC agreement for key variables. In Figure 6.4 the same distributions as discussed above are shown after the reweighting is applied. One can see, that the data-MC agreement is significantly improved. This 4-bin $t\bar{t}$ reweighting is used for both the zero- and one-lepton SUSY analyses. For the presented bC diagonal analysis, the default 4-bin $t\bar{t}$ reweighting is applied.

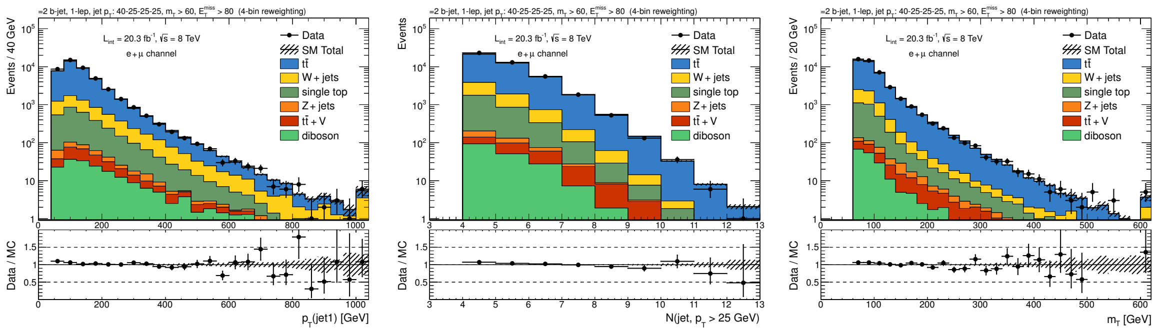

Figure 6.4: The data-MC comparison for the 2 b-jet selection after the default 4-bin $t\bar{t}$ reweighting for the variables: p_{T} of the leading jet (left), jet multiplicity N_{jets} (middle), and m_{T} (right). The distributions are shown for the selection: 1 lepton, exactly 2 b-tagged jets, 4 jets with p_{T} values above 40, 25, 25, and 25 GeV, $E_{\mathrm{T}}^{\mathrm{miss}} > 80$ GeV, $m_{\mathrm{T}} > 60$ GeV. The $t\bar{t}$ and W+jets production are normalised to the Monte Carlo cross sections. The error bands include only the Monte Carlo statistical uncertainties.

Distributions for various kinematical variables before any reweighting is applied and after the default 4-bin $t\bar{t}$ reweighting for the 1 b-jet and 2 b-jets selections are presented in Chapter 7. In the same chapter an improved, smooth exponential $t\bar{t}$ reweighting is also presented.

6.4 Signal selection

For signal points near the diagonal, where the mass difference $\Delta m = m(\tilde{t}_1) - m(\tilde{\chi}_1^{\pm})$ is small, in a large fraction of the events both b-jets have $p_{\mathrm{T}} < 25$ GeV, which is below the detector acceptance. The distribution of the number of true b-jets with $p_{\mathrm{T}} > 25$ GeV is shown in Figure 6.5 for several signal points. Since most $t\bar{t}$ events have at least one b-tagged jets, by vetoing b-jets one can suppress the $t\bar{t}$ background. One can see, that the rejection power increases towards the diagonal.

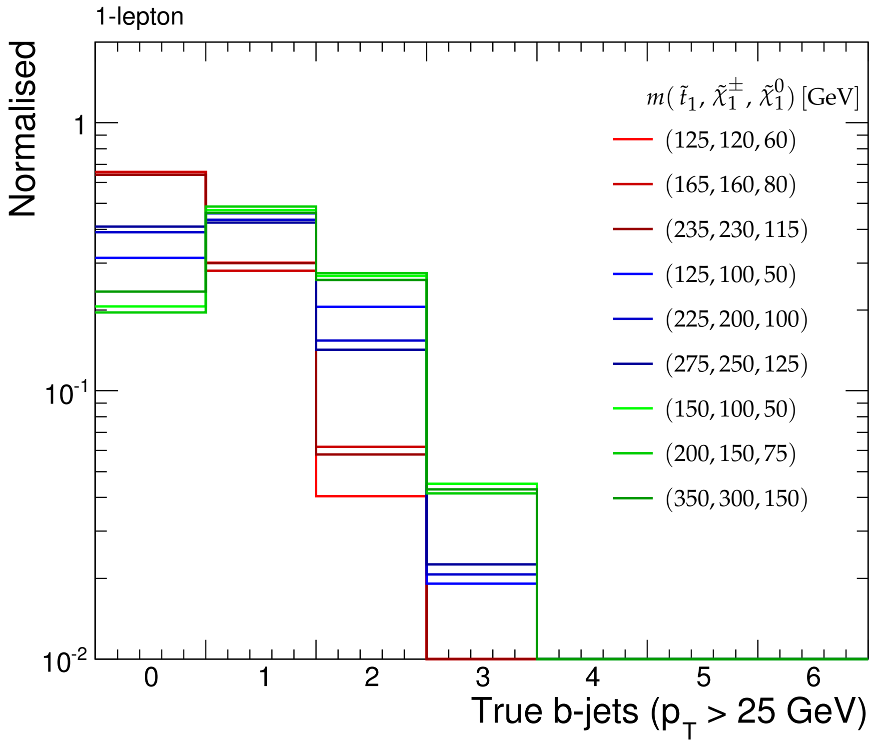

Figure 6.5: Distributions of the number of true b-jets after the preselection requirements. The colours correspond to different $\Delta m = m(\tilde{t}_1) - m(\tilde{\chi}_1^{\pm})$ values: 5 GeV (red), 25 GeV (blue), and 50 GeV (green).

The signal region for the bC diagonal analysis (SR-bC) is defined by the preselection and the following selection requirements, referred to as "cuts":

Preselection:

- The one-lepton event cleaning cuts as described in Section 6.2.3;
- Exactly one signal lepton with $p_{\mathrm{T}} > 25$ GeV and no other baseline leptons;
- At least three jets with $p_{\mathrm{T}}(j_{1,2,3}) > 80,\ 40,\ 30$ GeV;
- $\Delta\phi(j_{1,2}, E_{\mathrm{T}}^{\mathrm{miss}}) > 0.8$ – minimal azimuthal (transverse) separation between the leading two jets and the missing transverse momentum;
- $E_{\mathrm{T}}^{\mathrm{miss}} / \sqrt{H_{\mathrm{T}}} > 5\ \sqrt{\mathrm{GeV}}$ – cut on the $E_{\mathrm{T}}^{\mathrm{miss}}$ significance. It is not relevant for the current analysis, but is kept for consistency with other selections of the one-lepton analysis.

Cut1: $E_{\mathrm{T}}^{\mathrm{miss}} > 140$ GeV
This requirement suppresses the multijet and other backgrounds, where high $E_{\mathrm{T}}^{\mathrm{miss}}$ is not expected.

Cut2: b-jet veto
Veto on b-tagged jets among the leading four jets with $p_{\mathrm{T}} > 25\,\mathrm{GeV}$. This selection is introduced mainly against the $t\bar{t}$ background. For signal models near the diagonal, both b-jets are below the detector acceptance, while b-jets from $t \to bW$ decays typically have $p_{\mathrm{T}}(b) \approx 60$ GeV. Therefore, a veto on b-tagged jets significantly suppresses the $t\bar{t}$ background.

Cut3: $m_{\mathrm{T}} > 120\,\mathrm{GeV}$
A high m_{T} requirement is introduced against background from $W \to e\nu$ and $W \to \mu\nu$ decays. Therefore, it suppresses the W+jets background as well as the semileptonic $t\bar{t}$ background, with W decay to $e\nu$ or $\mu\nu$.

Cut4: $\Delta\phi(j_1, E_{\mathrm{T}}^{\mathrm{miss}}) > 2.0$
If b-jets are vetoed and at least three light jets are required, for $t\bar{t}$ events one jet should come from initial or final state radiation (ISR/FSR). This selection requires, that the leading light jet recoils against the $E_{\mathrm{T}}^{\mathrm{miss}}$.

Cut5: $0.8 < \Delta R(j_1, \ell) < 2.4$
A requirement on the distance ΔR between the leading jet and the lepton improves the signal-to-background separation.

Cut6: $|\eta(\ell)| < 1.2$
This selection requires centrality of the lepton. Due to a high m_{T} requirement the $\eta(\ell)$ correlates with the $\eta(\nu)$ of the neutrino. In case of a supersymmetric signal this correlation is less expressed. The requirement improves the signal-to-background separation.

The breakdown of the expected yields together with the observed numbers of events for the signal region SR-bC are presented in Table 6.7. The default 4-bin $t\bar{t}$ reweighting is applied, see

Process	SR-bC
$t\bar{t}$	145.6 ± 2.7
W+jets	276.8 ± 10.5
single top	12.1 ± 0.8
$t\bar{t} + W/Z$	3.3 ± 0.1
diboson	58.9 ± 2.2
Z+jets	5.2 ± 1.2
MC expected SM Total	501.9 ± 11.2
Observed events	493
$m(\tilde{t}_1, \tilde{\chi}_1^{\pm}, \tilde{\chi}_1^0) = (180, 174, 87)$	397.5 ± 41.8
$m(\tilde{t}_1, \tilde{\chi}_1^{\pm}, \tilde{\chi}_1^0) = (250, 240, 120)$	331.7 ± 8.5
$m(\tilde{t}_1, \tilde{\chi}_1^{\pm}, \tilde{\chi}_1^0) = (350, 340, 170)$	172.5 ± 2.4

Table 6.7: Breakdown of the expected yields together with the observed numbers of events for the signal region SR-bC. The default 4-bin $t\bar{t}$ reweighting is applied, see Section 6.3. The $t\bar{t}$ and W+jets production is normalised to the Monte Carlo cross section. The numbers are normalised to an integrated luminosity of 20.3 fb^{-1}. Only the statistical uncertainties are shown. Three signal models for the $(\tilde{t}_1, \tilde{\chi}_1^{\pm}, \tilde{\chi}_1^0)$ mass plane are shown for comparison. The masses of $\tilde{t}_1$, $\tilde{\chi}_1^{\pm}$ and $\tilde{\chi}_1^0$ are given in GeV.

Section 6.3. The $t\bar{t}$ and W+jets production is normalised to the Monte Carlo cross section. The numbers are normalised to an integrated luminosity of 20.3 fb^{-1}.

Figure 6.6 shows the distributions for the successively applied selection requirements ("cuts"), starting from ***Cut3***. For each cut, the distribution of the discriminant variable is shown befor the selection is applied. The cut values are indicated by black vertical lines. The arrow points towards events which pass the selection. Signal models $m(\tilde{t}_1, \tilde{\chi}_1^{\pm}, \tilde{\chi}_1^0) = (180, 174, 87)$, $(250, 240, 120)$ and $(350, 340, 170)$ GeV are shown for comparison. The masses of $\tilde{t}_1$, $\tilde{\chi}_1^{\pm}$ and $\tilde{\chi}_1^0$ are given in GeV.

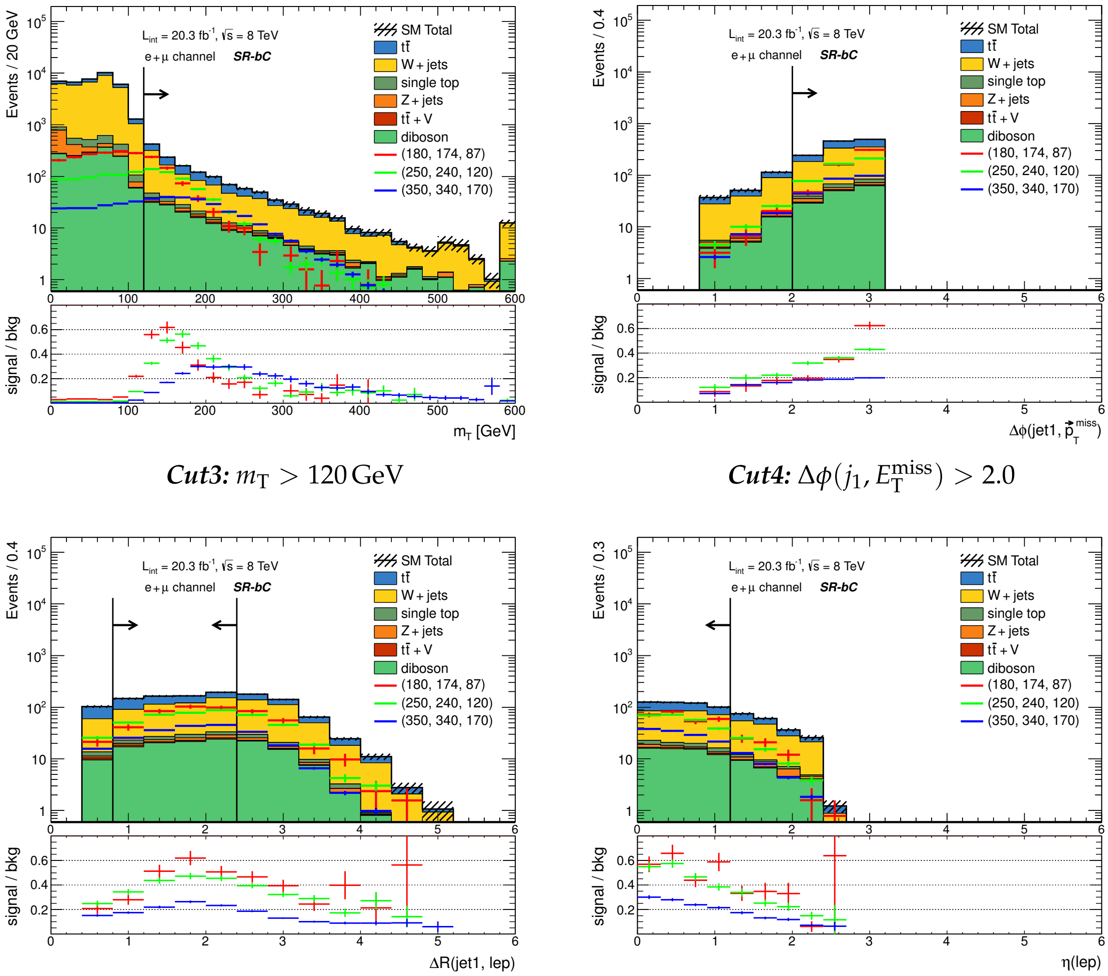

Cut3: $m_{\mathrm{T}} > 120\,\mathrm{GeV}$ ***Cut4:*** $\Delta\phi(j_1, E_{\mathrm{T}}^{\mathrm{miss}}) > 2.0$

Cut5: $0.8 < \Delta R(j_1, \ell) < 2.4$ ***Cut6:*** $|\eta(\ell)| < 1.2$

Figure 6.6: Distributions of the discriminant variables for successively applied selection requirements ("cuts"), starting from ***Cut3***. For each cut, the distribution of the corresponding discriminant variable is shown before the requirement is applied. The cut values are indicated by black vertical lines. The arrow points towards events which pass the selection. The error bars include only the Monte Carlo statistical uncertainties. Three signal models for the $(\tilde{t}_1, \tilde{\chi}_1^{\pm}, \tilde{\chi}_1^0)$ mass plane are shown for comparison. The masses of $\tilde{t}_1$, $\tilde{\chi}_1^{\pm}$ and $\tilde{\chi}_1^0$ are given in GeV.

6.5 Background estimation

6.5.1 Control and validation regions

The dominant and sub-dominant background for the bC diagonal analysis is the W+jets and $t\bar{t}$ production, respectively. The normalisation of the W+jets and $t\bar{t}$ process for the SR-bC signal region is based on the semi-data-driven approach, described in Section 4.6.

The control region for the W+jets (WCR-bC) and $t\bar{t}$ (TCR-bC) background, is defined by altering the m_{T} and b-jet requirement of the signal region. Following the common approach used in the one-lepton analysis [3], for both control regions the m_{T} selection is altered to 60 GeV $< m_{\mathrm{T}} <$ 90 GeV. In addition, for TCR-bC region, the b-jet veto selection is inverted, requiring at least one b-tagged jet.

The validation region for the $t\bar{t}$ process (TVR-bC) is defined by inverting the b-jet veto selection for the SR-bC signal region, while the validation region for the W+jets process (WVR-bC) is defined by altering the m_{T} selection to 100 GeV $< m_{\mathrm{T}} <$ 120 GeV.

The event selection requirements for the signal, control and validation regions differ only for the m_{T} and the number of b-tagged jets variables. The selection requirements of these variables are shown for each region in Table 6.8.

Variable	WCR-bC	TCR-bC	WVR-bC	TVR-bC	SR-bC
m_{T} [GeV]	$[60, 90]$	$[60, 90]$	$[100, 120]$	> 120	> 120
b-jet/veto	veto b-jet	≥ 1 b-jet	veto b-jet	≥ 1 b-jet	veto b-jet

Table 6.8: Differences in selection requirements for the m_{T} and number of b-tagged jets variables between the signal, control and validation regions of the bC analysis. Since these regions differ only for these variables, no requirements on other selection variables are shown.

A schematical illustration for the signal, control and validation regions of the bC analysis is shown in Figure 6.7.

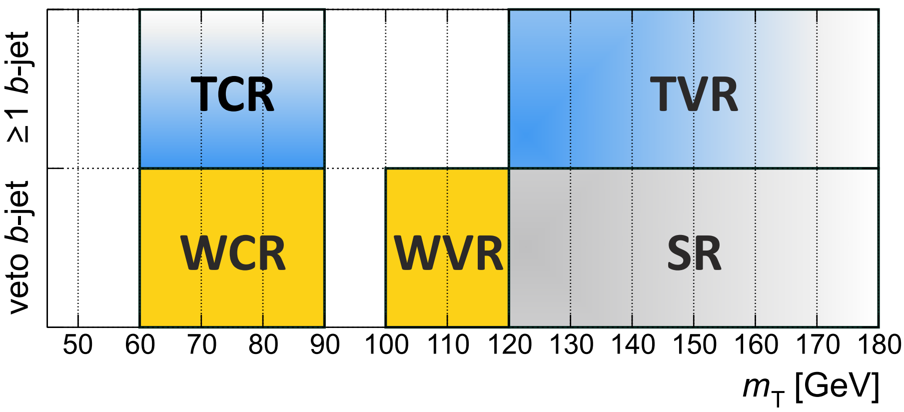

Figure 6.7: A schematic illustration for the signal, control and validation regions of the bC analysis.

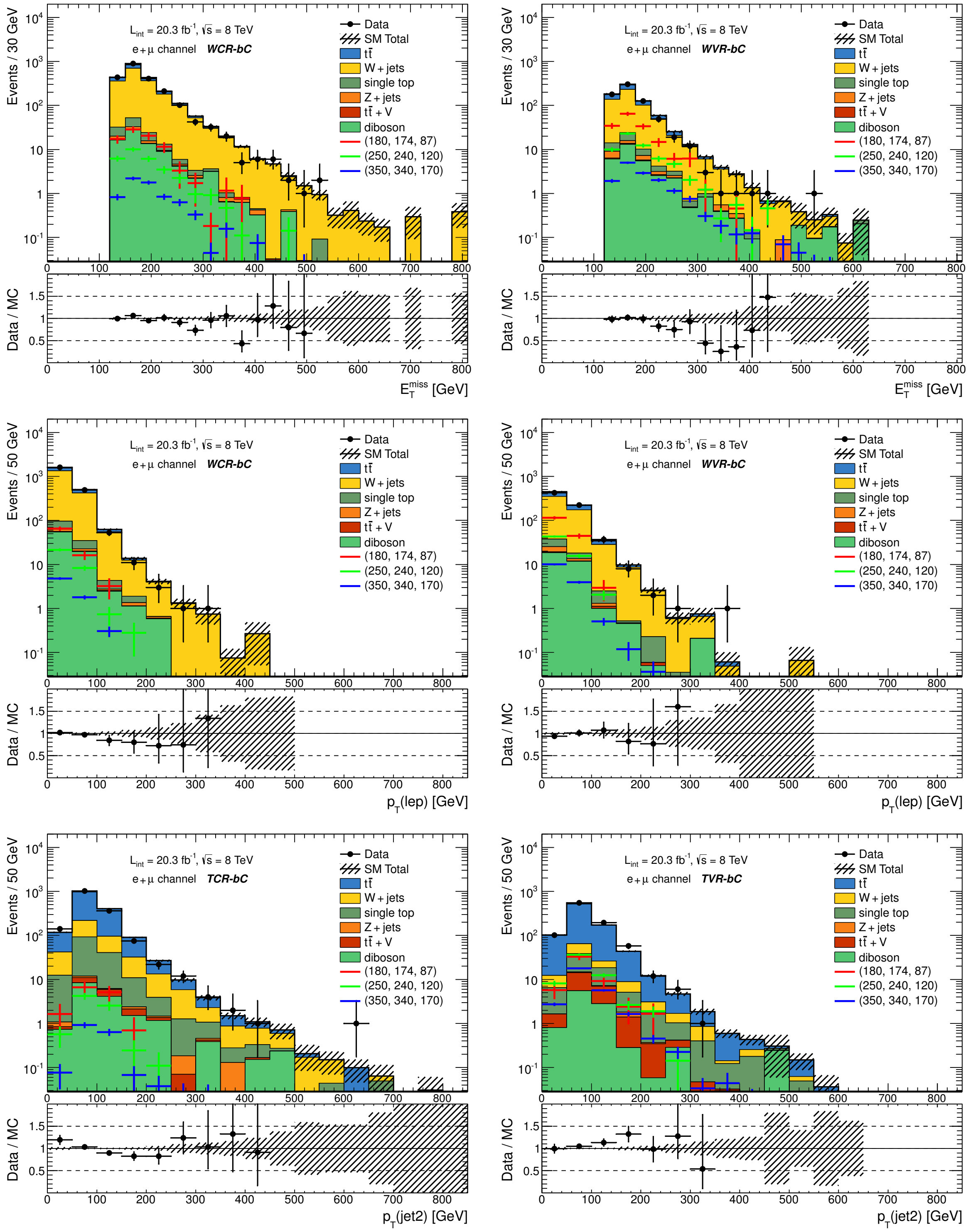

Figure 6.8: A comparison of the data and Monte Carlo for the bC diagonal analysis. Top: distribution of the $E_{\mathrm{T}}^{\mathrm{miss}}$ for the WCR-bC (left) and WVR-bC (right), middle: distribution of the $p_{\mathrm{T}}(\ell)$ for the WCR-bC (left) and WVR-bC (right), bottom: distribution of the $p_{\mathrm{T}}(j_2)$ for the TCR-bC (left) and TVR-bC (right). The $t\bar{t}$ and $W+$jets production is normalised in the control regions. Three signal models for the $(\tilde{t}_1, \tilde{\chi}_1^{\pm}, \tilde{\chi}_1^0)$ mass plane are shown for comparison. The masses of $\tilde{t}_1$, $\tilde{\chi}_1^{\pm}$ and $\tilde{\chi}_1^0$ are given in GeV.

A comparison between the data and Monte Carlo for some kinematic variables is shown in Figure 6.8. Comparison plots for additional variables for the control and validation regions are presented in Appendix B.

The breakdown of the expected yields together with the observed numbers of events for the control and validation regions are shown in Table 6.9. The W+jets and $t\bar{t}$ production is normalised to the Monte Carlo cross section.

Process	WCR-bC	TCR-bC	WVR-bC	TVR-bC
$t\bar{t}$	333.8 ± 4.2	1246.5 ± 8.0	154.7 ± 2.8	752.0 ± 6.0
W+jets	1890.3 ± 22.6	278.2 ± 6.8	567.3 ± 14.1	51.4 ± 5.3
single top	46.5 ± 1.7	140.2 ± 2.9	18.3 ± 1.1	46.0 ± 1.3
$t\bar{t} + W/Z$	1.6 ± 0.1	5.5 ± 0.2	1.2 ± 0.1	15.3 ± 0.3
diboson	78.5 ± 3.8	16.8 ± 1.9	32.2 ± 2.2	10.1 ± 1.1
Z+jets	10.4 ± 1.1	1.9 ± 0.4	7.7 ± 1.0	1.3 ± 0.3
MC exp. SM Total	2361.2 ± 23.4	1689.1 ± 11.0	781.2 ± 14.7	876.1 ± 8.2
Observed events	2162	1650	693	925
$(180, 174, 87)$	138.4 ± 25.1	13.0 ± 6.7	227.2 ± 31.8	101.4 ± 21.0
$(250, 240, 120)$	42.6 ± 3.1	11.1 ± 1.6	85.6 ± 4.3	86.3 ± 4.5
$(350, 340, 170)$	9.5 ± 0.6	2.6 ± 0.3	19.8 ± 0.8	40.2 ± 1.2

Table 6.9: The breakdown of the expected yields together with the observed numbers of events for the W+jets and $t\bar{t}$ control and validation regions. The $t\bar{t}$ production is reweighted according to the procedure described in Section 6.3. The $t\bar{t}$ and W+jets production is normalised to the Monte Carlo cross section. The numbers are normalised to the integrated luminosity of 20.3 fb^{-1}. Only the Monte Carlo statistical uncertainties are shown. Three signal models for the $(\tilde{t}_1, \tilde{\chi}_1^{\pm}, \tilde{\chi}_1^0)$ mass plane are shown for comparison. The masses of $\tilde{t}_1$, $\tilde{\chi}_1^{\pm}$ and $\tilde{\chi}_1^0$ are given in GeV.

6.5.2 Multijet background

Events from the multijet background may pass the lepton identification requirements due to jet misidentification, heavy flavour decays or photon conversions. Events with such a type of leptons are referred to as a fake lepton background. The fake lepton background is estimated separately for the electron and muon channel. The estimation is based on the *Exponential Extrapolation* (EE) approach. For fake electrons, additionally, the Matrix Method is used for a cross-check. For a detailed description of both approaches, as well as for definitions used in the following, the reader is referred to Chapter 9.

Estimation of fake electrons

To employ the fake electron estimation approach (see Section 9.2) an isolation variable ξ and a loose and tight electron have to be defined.

The isolation variable ξ is defined as $p_{\mathrm{T}}^{\mathrm{cone}\,0.2}/p_{\mathrm{T}}$, where the $p_{\mathrm{T}}^{\mathrm{cone}\,0.2}$ is the track isolation variable with $\Delta R = 0.2$ GeV (see Section 3.2). A loose electron is defined as a baseline electron, while for a tight electron a definition of a signal electron without the isolation requirement $\xi < 0.1$ is used (see Section 6.2.1).

The fake electron background is estimated for the FLR-bC region, which is described by the following selection criteria:

- The one-lepton event cleaning cuts as described in Section 6.2.3;
- One electron with $p_{\mathrm{T}}(e) > 25$ GeV, no other baseline leptons;
- $\Delta\phi(j_{1,2}, E_{\mathrm{T}}^{\mathrm{miss}}) > 0.8$;
- At least three jets with $p_{\mathrm{T}}(j_{1,2,3}) > 80, 40, 30$ GeV;
- Veto on b-tagged jets;
- $E_{\mathrm{T}}^{\mathrm{miss}} > 140$ GeV;
- $m_{\mathrm{T}} > 120$ GeV.

This region is similar to the SR-bC signal region and differs from it only by the omission of the last three selection requirements (***Cut4-Cut6***).

Matrix Method for SR-bC

To use the Matrix Method (see Section 9.1) the tight-to-loose coefficient for real ($\varepsilon_{\mathrm{real}}$) and fake ($\varepsilon_{\mathrm{fake}}$) electrons have to be estimated.

Figure 6.9 shows the ratio between tight and loose electrons as a function of the isolation variable ξ. The $\varepsilon_{\mathrm{fake}}$ coefficient is estimated with the data-driven approach as the ratio between the tight and loose electrons in the $[0.1, 0.5]$ interval.

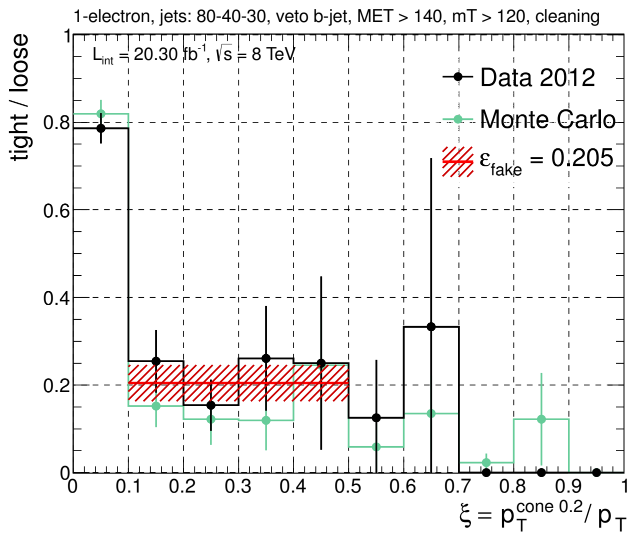

Figure 6.9: The ratio between tight and loose electrons as a function of the isolation variable ξ for the FLR-bC region. The ratio is calculated for data and Monte Carlo simulated samples (simulated samples do not include multijet contributions). The $\varepsilon_{\mathrm{fake}}$ coefficient is estimated as the ratio between tight and loose electrons in the $[0.1, 0.5]$ interval. The error bars show only the statistical uncertainty.

The probability for real loose electrons to pass tight requirements ($\varepsilon_{\mathrm{real}}$) is estimated based on the simulated Monte Carlo events which do not include multijet events. In Figure 6.9 this corresponds to the first bin of the ratio of tight-to-loose electrons for the Monte Carlo simulation. Usually, the electron identification, scale and resolution systematic uncertainties are below 1%. Therefore, in this case they are neglected with respect to the statistical uncertainty of $\pm 4\%$.

The estimate of the $\varepsilon_{\mathrm{real}}$ and $\varepsilon_{\mathrm{fake}}$ coefficients, as well as the number of fake electrons $N_{\mathrm{fake}}^{\mathrm{tight}}$ in the FLR-bC region are presented in Table 6.10. The number of fake electrons is estimated by us-

Region	$\varepsilon_{\mathrm{real}}$	$\varepsilon_{\mathrm{fake}}$	$N_{\mathrm{data}}^{\mathrm{loose}}$	$N_{\mathrm{data}}^{\mathrm{tight}}$	$N_{\mathrm{fake}}^{\mathrm{tight}}$	QCD [%]
FLR-bC	0.82 ± 0.03	0.22 ± 0.04	1155	908	14 ± 14	1.5 ± 1.5

Table 6.10: Results of the Matrix Method estimation for the FLR-bC region. Only the statistical uncertainties are shown.

ing equation 9.2. From the presented results the contribution of the fake electron background with a confidence level of 95% found to be less than 4.0%.

Exponential Extrapolation for SR-bC

The number of fake electrons in the SR-bC signal region ($N_{\mathrm{fake}}^{\mathrm{tight}}$) is also estimated with the Exponential Extrapolation approach (see Section 9.2). Figure 6.10 shows the exponential fit to the distribution of the isolation variable ξ for loose and tight electrons. The corresponding fit results are shown in Table 6.11. The results indicate that the fake electron background with a confidence level of 95% is less then 5.6%.

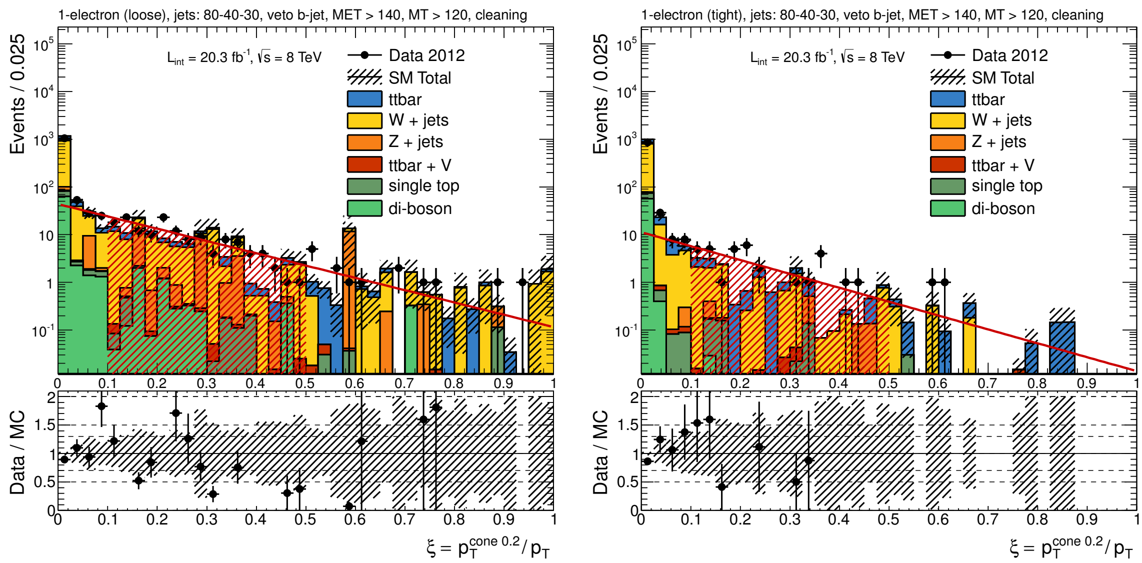

Figure 6.10: Estimation of the number of fake electrons using the Exponential Extrapolation approach. The distribution of the isolation variable ξ for loose (left) and tight (right) electrons is fitted by an exponential function $e^{-\alpha\xi+\beta}$ (red line) in the $[0.1, 0.5]$ interval.

Region	α	β	N_{fake}	N_{data}	QCD [%]
FLR-bC (loose)	5.9 ± 0.7	3.8 ± 0.2	131.6 ± 20.6	1155	11.4 ± 1.8
FLR-bC (tight)	6.7 ± 1.5	2.4 ± 0.4	32.7 ± 11.0	908	3.6 ± 1.2

Table 6.11: Results of the fit and the estimated number of fake electrons for the loose and tight selection criteria for the FLR-bC region. An exponential function $e^{-\alpha\xi+\beta}$ is fitted in the $[0.1, 0.5]$ interval. Only the statistical uncertainties are shown.

The precision can be improved by the use of a combined fit, which fits both distributions with the same α slope. Figure 6.11 shows the results of the combined fit. The fit is performed in the $[0.1, 1.0]$ interval. The distribution of the isolation variable ξ for loose-not-tight electrons (loose electrons which do not pass the tight criteria) is fitted with $e^{-\alpha\xi+\beta'}$, while for tight electrons it is fitted with $e^{-\alpha\xi+\beta}$. The distributions are statistically uncorrelated. The number of fake tight

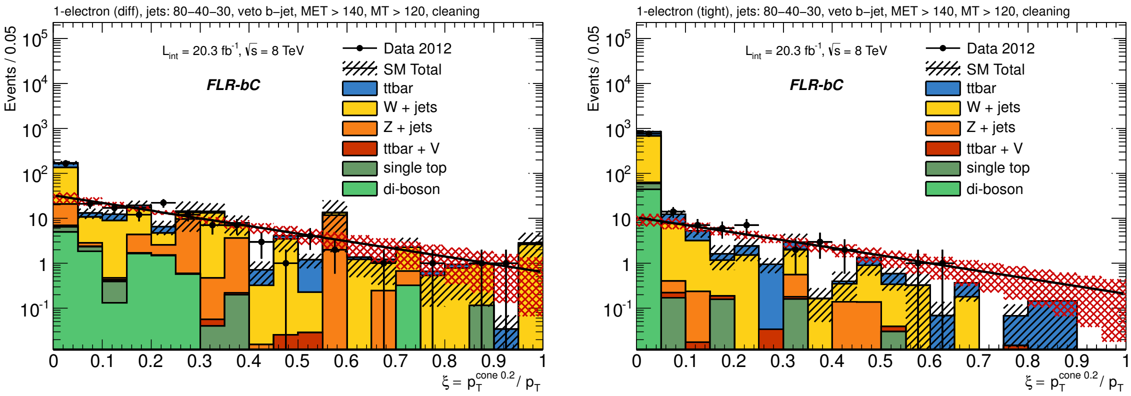

Figure 6.11: A combined fit of the Exponential Extrapolation approach for the FLR-bC region. The distribution of the isolation variable ξ for loose-not-tight electrons is fitted with $e^{-\alpha\xi+\beta'}$ (left), while for tight electrons is fitted with $e^{-\alpha\xi+\beta}$ (right). Both distributions are fitted in the $[0.1, 1.0]$ interval.

electrons is estimated from $e^{-\alpha\xi+\beta}$. The uncertainty on the fake electrons estimation accounts for the uncertainties of the fit parameters α, β and β'.

The results of the combined fit and the estimated number of fake tight electrons are shown in Table 6.12. All values include only the statistical uncertainties. In general, one has to add a systematic uncertainty of the combined fit related to the use of the same α slope for both distributions. Taking into account, that α slopes for loose and tight distributions are consistent within the statistical uncertainty (see Table 6.11), and the difference between the loose and tight slopes is consistent with the statistical uncertainty on the α estimated for the combined

Region	α	β	β'	N_{fake}	QCD [%]
FLR-bC	5.6 ± 0.6	2.7 ± 0.2	3.8 ± 0.2	22 ± 5	2.4 ± 0.6

Table 6.12: Results of the combined fit and the estimated number of fake tight electrons for the FLR-bC region using the Exponential Extrapolation approach. Only the statistical uncertainties are shown.

fit (which is about $\pm 11\%$, see Table 6.12), the systematic uncertainty of the combined fit can be neglected. From the combined fit result, the fake electron background with a confidence level of 95% can be estimated as below 3.4%.

One can see, that the combined fit achieves the same precision as the Matrix Method, but it is fully data-driven and does not rely on the Monte Carlo simulation to estimate the $\varepsilon_{\mathrm{real}}$ coefficient. In both cases, the estimate for the fake electron background in the SR-bC signal region with a confidence level of 95% is less than 4%.

Exponential Extrapolation for WCR-bC and TCR-bC

The contribution of fake electrons is estimated separately for each control region using the combined fit approach. Figure 6.12 shows the distributions of the isolation variable ξ for loose-not-tight and tight electrons for the WCR-bC and TCR-bC control regions. For both regions the fit is performed in the $[0.1, 1]$ interval. The results of the combined fit and the estimated number of fake tight electrons for the WCR-bC and TCR-bC control regions are shown in Table 6.13. Due to a large statistical uncertainty on the α parameter estimate (more than $\pm 20\%$) for both regions, the systematic uncertainty of the combined fit approach is neglected. In both

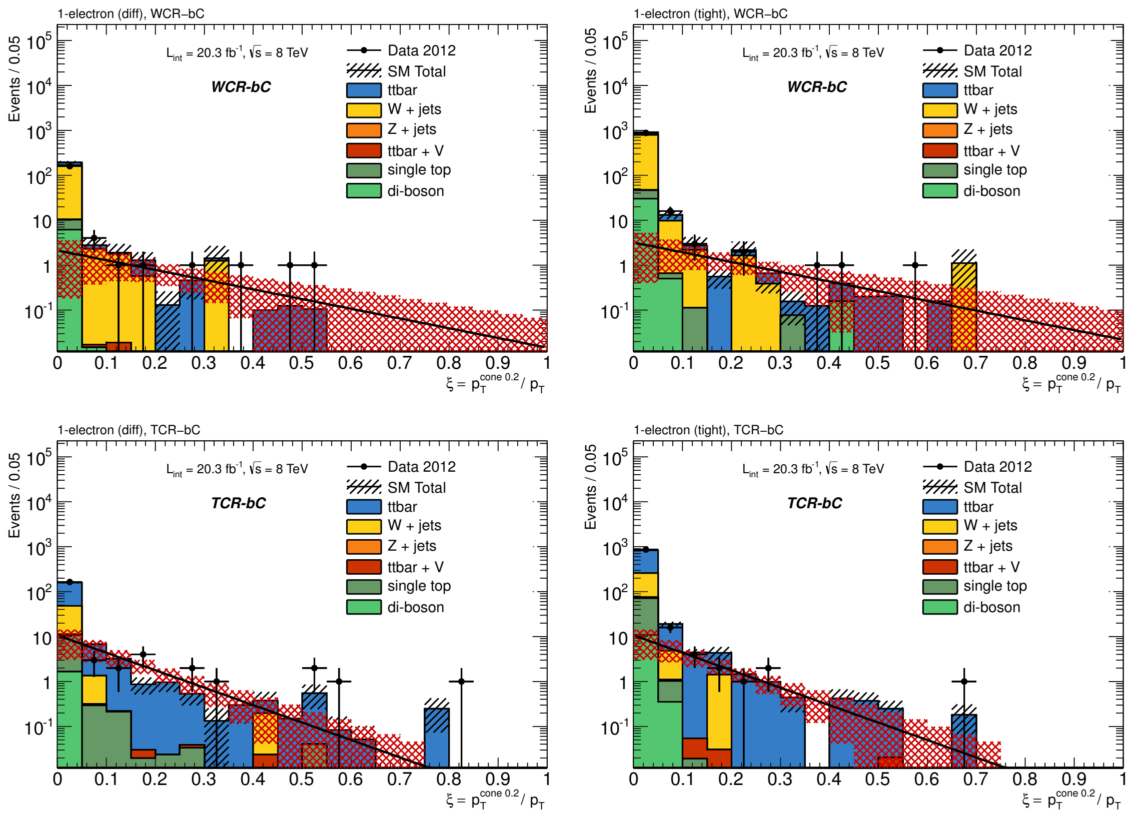

Figure 6.12: Combined fits for the WCR-bC (top) and TCR-bC (bottom) control regions. The distributions of the isolation variable ξ for loose-not-tight electrons, referred to as $h^{\mathrm{diff}}(\xi)$, is fitted by $e^{-\alpha\xi+\beta'}$ (left), while for the tight electrons the $h^{\mathrm{tight}}(\xi)$ is fitted by $e^{-\alpha\xi+\beta}$ (right). The combined fits are performed in the $[0.1, 1.0]$ interval.

Region	α	β	β'	N_{fake}	QCD [%]
WCR-bC	4.8 ± 1.5	1.2 ± 0.6	0.9 ± 0.6	5 ± 3	0.5 ± 0.3
TCR-bC	5.2 ± 1.2	1.5 ± 0.5	1.7 ± 0.4	7 ± 3	0.8 ± 0.4

Table 6.13: Results of the combined fit and the estimated number of fake tight electrons for the WCR-bC and TCR-bC control regions using the Exponential Extrapolation approach. Only the statistical uncertainties are shown.

control regions the estimate for the fake electron background with a confidence level of 95% is less than 1.5%.

Isolated electrons

All fits above are performed under the assumption, that a contamination of isolated electrons (electrons, which are produced from the W-boson decay on a particle level) is negligible for the $\xi > 0.1$ region. The distributions of the isolation variable ξ for the tight isolated electrons for the FLR-bC, WCR-bC and TCR-bC regions are shown in Figure 6.13. The distributions confirm, that in the $\xi > 0.1$ region the contamination from the isolated electrons is negligible.

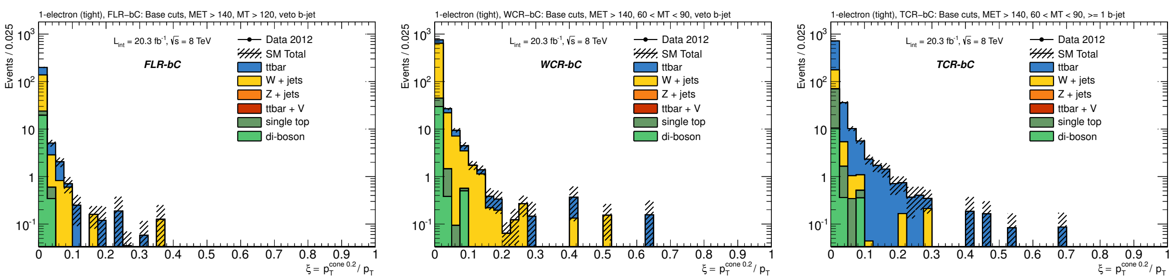

FLR-bC WCR-bC TCR-bC

Figure 6.13: Distributions of the isolation variable ξ for the tight isolated electrons for the FLR-bC (left), WCR-bC (middle) and TCR-bC (right) regions.

Estimation of fake muons

To employ the fake muon estimation approach (see Section 9.3), an isolation variable ξ, a variable ζ, and loose and tight muons have to be defined.

An isolation variable ξ is defined as $p_{\text{T}}^{\text{cone}\,0.2}$, a variable ζ is defined as $p_{\text{T}}^{\text{cone}\,0.4} - p_{\text{T}}^{\text{cone}\,0.2}$, a loose muon is defined as a signal muon without an isolation requirement and with the relaxed overlap removal selection $\Delta R(\mu, \text{jet})$ from 0.4 to 0.2 (see Section 6.2.2), while a tight muon is defined as a signal muon without an isolation requirement $\xi < 1.8\,\text{GeV}$ (see Section 3.3).

Fake muons are estimated for the FLR0-bC (b-jet veto) and FLR1-bC (at least one b-jet) regions.

The regions are described as follows:

- The one-lepton event cleaning cuts, as described in Section 6.2.3;
- One muon with $p_{\mathrm{T}}(e) > 25$ GeV, no other baseline leptons;
- $\Delta\phi(j_{1,2}, E_{\mathrm{T}}^{\mathrm{miss}}) > 0.8$;
- At least three jets with $p_{\mathrm{T}}(j_{1,2,3}) > 80, 40, 30$ GeV;
- Veto on b-tagged jets (FLR0-bC) or at least one b-tagged jet (FLR1-bC);
- $E_{\mathrm{T}}^{\mathrm{miss}} > 140$ GeV;
- $m_{\mathrm{T}} > 60$ GeV.

According to these descriptions, the FLR0-bC region contains the signal region (SR-bC) and the $W+$jets control region (WCR-bC), while the FLR1-bC contains the $t\bar{t}$ control region (TCR-bC).

The distributions of the variable ζ for loose and signal muons for the FLR0-bC and FLR1-bC regions are shown in Figure 6.14. For each region the distribution for loose muons is fitted by an exponential function $e^{-\alpha\zeta+\beta'}$. The estimated slope α is used to fit the distribution for signal muons with an exponential function $e^{-\alpha\zeta+\beta}$. Both functions are fitted in the $[30, 120]$ GeV interval. The fit results with the estimated number of fake signal muons $N_{\mathrm{fake}}^{\mathrm{signal}}$ are shown in Table 6.14. The results include only the statistical uncertainties.

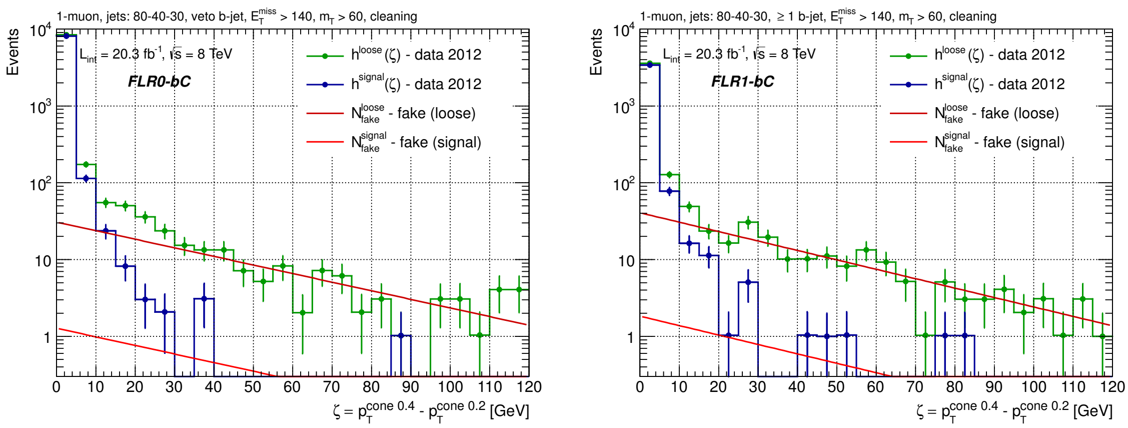

Figure 6.14: Distributions of the variable ζ for loose and signal muons, referred to as the $h^{\mathrm{loose}}(\zeta)$ and $h^{\mathrm{signal}}(\zeta)$, respectively. The distributions are shown for the FLR0-bC (b-jet veto, left) and FLR1-bC (at least 1 b-jet, right) regions. For both regions the $h^{\mathrm{loose}}(\zeta)$ is fitted by an exponential function $e^{-\alpha\zeta+\beta'}$. The estimated slope α is used to fit $h^{\mathrm{signal}}(\zeta)$ with an exponential function $e^{-\alpha\zeta+\beta}$. Both functions are fitted in the $[30, 120]$ GeV interval.

The systematic uncertainties of the approach are estimated as follows. The slope α is estimated by fitting the distribution of ζ for loose muons. This slope is used as a parameter for the exponential fit to the distribution of ζ for tight muons. Following the study performed in Section 9.3.2, the systematic uncertainty on α is taken as $\pm 20\%$. The propagation of this uncertainty to the estimate of the $N_{\mathrm{fake}}^{\mathrm{signal}}$ is giving the systematic uncertainty of about $\pm 20\%$.

The distribution of ζ for fake muons is assumed to be an exponential function. The uncer-

Region	α	β	β'	$N_{\text{fake}}^{\text{signal}}$	QCD [%]
FLR0-bC (veto on *b*-jet)	0.026 ± 0.003	3.4 ± 0.2	0.2 ± 0.2	10 ± 4	0.1 ± 0.1
FLR1-bC (at least 1 *b*-jet)	0.028 ± 0.003	3.7 ± 0.2	0.6 ± 0.3	13 ± 6	0.4 ± 0.2

Table 6.14: Fit results and the estimated number of fake signal muons $N_{\text{fake}}^{\text{signal}}$ for the *b*-jet veto and at least 1 *b*-jet selections. Only the statistical uncertainties are shown.

tainty related to the non-exponentiality of the distribution is estimated for different $E_{\text{T}}^{\text{miss}}$ selections. Figure 6.15 shows the distributions of ζ for loose-not-tight muons, referred to as $h^{\text{diff}}(\zeta)$, for events from the FLR0-bC and FLR1-bC regions with an inverted isolation requirement $p_{\text{T}}^{\text{cone}\,0.2} > 1.8$ GeV.

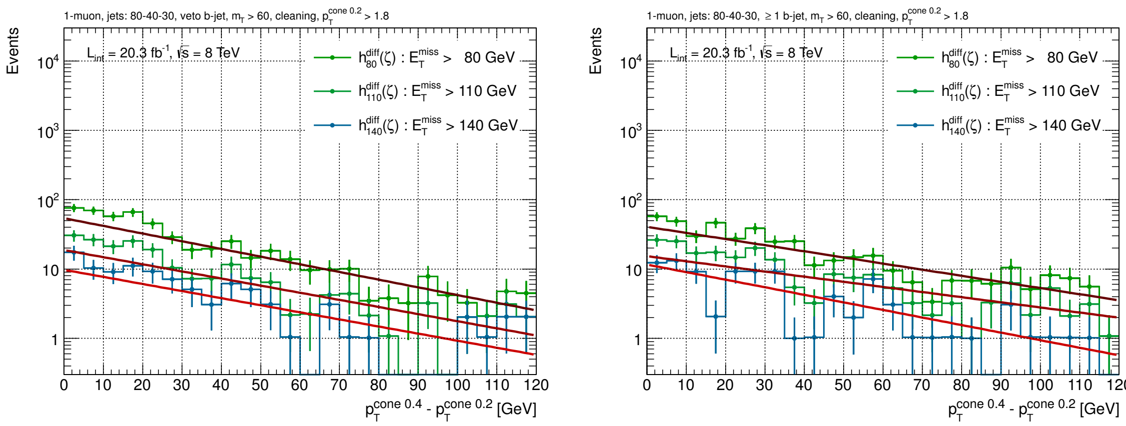

Figure 6.15: Distributions of ζ for loose-not-tight muons for events with an inverted isolation requirement $p_{\text{T}}^{\text{cone}\,0.2} > 1.8$ GeV for the FLR0-bC (*b*-jet veto, left) and FLR1-bC (at least 1 *b*-jet, right) regions. The distributions are shown for different $E_{\text{T}}^{\text{miss}}$ selections.

The systematic uncertainty due to the non-exponentiality is estimated as the relative difference between the integrals from the $h^{\text{diff}}(\zeta)$ and from the fitted exponential function $e^{-\alpha\zeta+\beta}$:

$$N_{\text{diff}} = \int_0^\infty h^{\text{diff}}(\zeta)d\zeta \quad \text{and} \quad N_{\text{fake}} = \int_0^\infty e^{-\alpha\zeta+\beta}d\zeta. \tag{6.4}$$

The results of the estimate are shown in Table 6.15 One can see, that the systematic uncertainty

	FLR0-bC (*b*-jet veto)				FLR1-bC (at least 1 *b*-jet)			
$E_{\text{T}}^{\text{miss}}$ [GeV]	α	β	N^{diff}	Syst.	α	β	N^{diff}	Syst.
> 80	0.026 ± 0.003	4.0 ± 0.2	521	24%	0.020 ± 0.003	3.7 ± 0.2	431	10%
> 110	0.024 ± 0.004	2.9 ± 0.3	202	28%	0.017 ± 0.004	2.7 ± 0.3	205	18%
> 140	0.024 ± 0.006	2.3 ± 0.4	100	22%	0.025 ± 0.006	2.4 ± 0.4	94	3%

Table 6.15: Fit results and the estimate of the systematic uncertainty for fake muons. The results are presented for FLR0-bC (*b*-jet veto) and FLR1-bC (at least 1 *b*-jet) regions.

can be up to ±30%. The total systematic uncertainty is estimated by adding each uncertainty in quadrature and is found to be about ±40%. Even with this systematic uncertainty, the fake muon background for both regions with a confidence level of 95% is less than 1%.

6.6 Systematic uncertainties

Due to the tight selection requirements, the signal regions often have a low number of expected Standard Model events.

Usually, for the nominal Monte Carlo samples the number of generated events is high enough, therefore, even for a low number of expected total Standard Model events in a signal region, the statistical uncertainty of the Monte Carlo estimate is lower than the statistical uncertainty of the observed events in the data. The experimental systematic uncertainties are estimated using the nominal Monte Carlo samples by varying different parameters related to the ATLAS detector modelling and response. The Monte Carlo statistical uncertainty for each variation, is similar to the one for the nominal samples. Therefore, the systematical uncertainty, which is estimated as a difference between the event yields for the variation and nominal samples for some region, usually, has a lower statistical uncertainty, than the total statistical uncertainty of the expected nominal events ($\sqrt{N_{\text{exp}}}$) in the same region.

This is not the case for the theoretical uncertainties. To estimate the theoretical uncertainties, usually, additional Monte Carlo samples with some parameter variations have to be generated. This requires to have a separate production for each parameter variation. Since this process is time consuming, samples used for theory systematic studies often have a lower number of generated events, than the nominal samples. Therefore, theoretical uncertainties are often affected by large statistical fluctuations.

6.6.1 Uncertainty estimation strategy

In the one-lepton analysis, to decrease the contribution of the statistical uncertainty in the estimate of the systematical uncertainty, some selection requirements are relaxed. Uncertainties are estimated for the region selected by the relaxed requirements. The extrapolation uncertainty for each variable is estimated separately for each variable from the region obtained by relaxing only this variable to the signal region. The extrapolation uncertainties are assumed to be uncorrelated. The total systematic uncertainty is obtained by adding in quadrature the systematic uncertainty for the relaxed region and the extrapolation uncertainties for each relaxed variable.

Following the approach employed by the one-lepton analysis, the number of events is increased by relaxing the selection requirements on the $E_{\text{T}}^{\text{miss}}$ and m_{T} variables. The $E_{\text{T}}^{\text{miss}}$ and m_{T} requirements are relaxed to $E_{\text{T}}^{\text{miss}} > 100$ GeV and $m_{\text{T}} > 60$ GeV, respectively. The extrapolation uncertainties for variables are assumed to be uncorrelated. The total systematic uncertainty is estimated by summing up in quadrature the systematic uncertainty in the relaxed region and all extrapolation uncertainties.

Such an approach faces some challenges. One of challenges is that due to a low number of simulated events in the signal region, it is difficult to estimate an extrapolation uncertainty. To make a reasonable extrapolation, an additional assumption is needed, for example about the linear dependency of the uncertainty as a function of the relaxed variable. Usually, such an assumption is difficult to validate due to the lack of events, therefore it is often used without a proper validation.

Another challenge is related to the assumption, that the extrapolation uncertainties are uncorrelated. This assumption allows to sum up all uncertainties in quadrature, but to check this assumption, is even more difficult, than to estimate the extrapolation uncertainties. In case when the systematic uncertainty can be estimated as a linear function of the relaxed variables, the corresponding uncertainties also have to be summed up linearly. By summing up the uncertainties in quadrature one can underestimate the total systematic uncertainty.

To avoid these problems, the presented analysis was optimised to have a high number of events in the signal region, therefore all uncertainties for the presented analysis are estimated without loosening the selection requirements. For some background samples this leads to systematic uncertainties, which are driven by the statistical component, but in all these cases, a contribution of the corresponding background is negligible, and a high systematic uncertainty does not affect the final result.

In the context of the one-lepton analysis [3], both approaches were compared and the estimated uncertainties were found to be consistent within statistical fluctuations. An exception was the $t\bar{t}$ parton shower uncertainty, where the difference was above 3σ, therefore the higher uncertainty from the estimate presented in the following was used.

6.6.2 Experimental uncertainties

Experimental uncertainties are estimated using the package provided by the ATLAS SUSY Working Group. The following sources of experimental uncertainties are considered:

Luminosity uncertainty
: The uncertainty on the total integrated luminosity is taken as $\pm 2.8\%$ (see Section 6.1.1).

Pileup uncertainties
: Following the official recommendation, the uncertainty on the pileup is estimated by scaling the average number of interactions per bunch crossing μ by $\pm 10\%$.

Jet energy scale
: The jet energy is scaled up and down coherently for all jets by the $\pm 1\sigma$ total systematic uncertainty, estimated using the software provided by the ATLAS Jet/Etmiss Working Group. For the current analysis, only the total systematic uncertainty is considered, i.e. the jet energy scale is not broken down into its components.

Jet energy resolution
: The jet resolution systematic uncertainty is estimated by applying an extra smearing of p_{T} of each jet, based on the p_{T} and η parameters of the jet. The difference between event yields with respect to the nominal is considered as the systematic uncertainty, which is treated in a symmetric way.

E_T^{miss} soft term

The scale uncertainty on the E_T^{miss} soft term (see Section 3.6) is estimated by varying the scale up and down. The resolution uncertainty is also included by comparison with the nominal event yields and by treating the uncertainty in a symmetric way.

b-tagging efficiency

The b-tagging efficiency is estimated sepatately for b-, c- and light-jets. The uncertainties are estimated by varying scale factors, which depend on the flavour, on the p_T and η parameters. The scale factors are varied according to the systematic uncertainties on their measured values. These uncertainties are considered to be uncorrelated and added in quadrature.

Lepton uncertainties

Uncertainties related to the lepton identification, energy scale, energy resolution and trigger efficiency are estimated following the recommendations provided by the ATLAS Egamma and Muons Combined Performance Working Groups. These uncertainties are found to be negligible, less than 1–2%, for the one-lepton analysis.

6.6.3 Theoretical uncertainties

All theoretical uncertainties are better to estimate taking into account detector modelling effects, on the so-called "detector" or "reconstruction" level using either ATLAS full or fast simulation software. But, since the modelling of the detector effects is time consuming, and the detector modelling uncertainties are estimated separately as experimental uncertainties, some of theoretical uncertainties are estimated without modelling of detector effects, on the so-called "particle" or "truth" level. In case of the uncertainty estimation on particle level, the analysis selections are approximated on particle level objects. Due to the high number of events in the signal region, all uncertainties are estimated without loosening the selection requirements, as discussed above.

For the bC diagonal analysis, the $W+$jets and $t\bar{t}$ production are the dominant and sub-dominant backgrounds, respectively (see Table 6.7). For the one-lepton analysis all theoretical uncertainties for the $W+$jets production, as well as the factorisation and renormalisation scale uncertainties for the $t\bar{t}$ production are estimated on particle level. The main challenge for these uncertainties is to transfer a high m_T requirement from the reconstruction to particle level. All signal selections in the one-lepton analysis are using the m_T requirement above 120 GeV, which significantly suppresses the $W+$jets and semileptonic $t\bar{t}$ events. Figure 3.21 shows the distribution of the m_T variable evaluated on the particle and detector level for $W \to e\nu$ events. One can see, that by using the $m_T > 120$ GeV requirement on particle level, the $W \to e\nu$ events are significantly suppressed. The same is true for the semileptonic $t\bar{t}$ decay, where the W boson decays via $W \to e\nu, \mu\nu$.

In general, a low number of events is not a big problem for the uncertainty estimate, as long as there are enough events to avoid large statistical fluctuations. The main challenge is the relative composition of decay modes. For example, for the $t\bar{t}$ production, after a suppression of the semileptonic decays on particle level, dileptonic decays with a hadronically decaying τ lepton become dominant. These events have one lepton and three neutrinos on particle level. Therefore, the true m_T variable can easily pass a high m_T selection requirements. This means, that instead of the estimation of the uncertainty for a semileptonic $t\bar{t}$ decay mode, one does estimate it mainly for the dileptonic decay with a hadronically decaying τ lepton.

To avoid this, one can try to relax the m_{T} requirement for selections applied on particle level, but this approach may also create problems, since in this case background events, which pass the control region requirements on the detector level modelling, will pass the relaxed m_{T} requirement on particle level. This can underestimate theoretical uncertainties.

Another approach is to use smearing of particle level jets and to recalculate the missing transverse momentum. This approach can smooth the distribution of the true m_{T} variable and makes it similar to one on detector level.

Since for the presented bC analysis the dominant background is W+jets production, instead of applying a jet smearing approach, it was decided to perform a validation between the factorisation scale uncertainties estimated for the $W \to e\nu$ modelling for the detector and particle level samples.

Validation of the particle vs detector level uncertainties

An uncertainty estimate is validated for the factorisation scale uncertainty for the modelling of the $W \to e\nu$ process. The renormalisation scale is varied by factor 0.5 and 2.0 from the nominal. The same selections are applied for renormalisation scale variation samples generated on the detector and particle level.

The production of all factorisation scale variations for all leptonic decays of $W \to e\nu, \mu\nu, \tau\nu$ is time and resource consuming, therefore the following simplifications were used.

Neglecting the mass difference between electrons and muons, one can consider, that theoretical uncertainties for $W \to e\nu$ and $W \to \mu\nu$ decays are similar. This is not the case for the $W \to \tau\nu$ decay, due to an extra two neutrinos produced from the τ lepton. But, as one can see from Table 6.16, the contribution of this decay in signal and control regions is negligible, below 4%. Therefore, factorisation scale variations were produced only for the $W \to e\nu$ decay.

Process	WCR-bC	TCR-bC	SR-bC
$W \to e\nu$	45.4%	47.6%	44.7%
$W \to \mu\nu$	51.0%	48.7%	51.5%
$W \to \tau\nu$	3.6%	3.7%	3.8%

Table 6.16: Contribution from different $W \to \ell\nu$ decays for the signal and control regions.

Samples for W+jets production are generated in different true $p_{\mathrm{T}}(W)$ slices. To further reduce the number of samples generated on detector level, only the relevant slices are generated. Table 6.17 shows contribution of each $p_{\mathrm{T}}(W)$ slice in the signal and control regions. The corresponding distributions of true $p_{\mathrm{T}}(W)$ are shown in Figure 6.16. For the validation the $[140, 280]$, $[280, 500]$ and $[500, \infty)$ GeV slices are generated on the detector level. One can see, that this covers of about 94% of control regions and more than 70% of a signal region.

$p_T(W)$ [GeV]	WCR-bC	TCR-bC	SR-bC
$[0, 40]$	0.0%	0.1%	0.8%
$[40, 70]$	0.0%	0.0%	1.9%
$[70, 140]$	6.2%	5.6%	28.8%
$[140, 280]$	80.5%	78.7%	54.0%
$[280, 500]$	12.7%	15.0%	13.4%
$[500, \infty)$	0.5%	0.6%	1.1%

Table 6.17: A breakdown of the W+jets production to true $p_T(W)$ slices for the signal and control regions of the bC analysis.

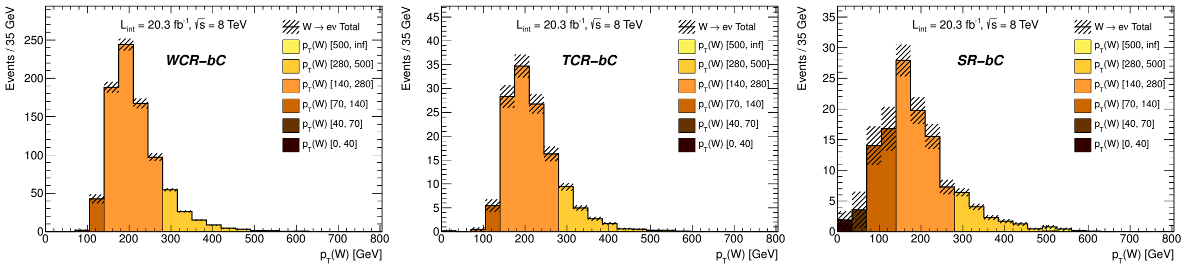

Figure 6.16: Distributions of the $p_T(W)$ for different slices of $W \to e\nu$ production for the WCR-bC (left), TCR-bC (middle) and SR-bC (right) regions.

A validation is done for transfer factor uncertainties, which are estimated only for three generated slices. The results are shown in Table 6.18. A precision of the transfer factor uncertainty estimate for samples generated on particle and detector levels are about of 2% of the transfer factor values. One can see, that the transfer factor uncertainties estimated for the signal and validation regions are consistent within 1–2σ between the estimates on particle and detector levels.

Generated samples	WCR $\leftrightarrow$ TCR	WCR $\leftrightarrow$ WVR	WCR $\leftrightarrow$ TVR	WCR $\leftrightarrow$ SR
Particle level	3%	2%	5%	4%
Detector level	7%	4%	5%	3%

Table 6.18: A comparison of the transfer factor uncertainties of the factorisation scale variation on the $W \to e\nu$ modelling. The transfer factor uncertainties are estimated from the WCR-bC to the associated TCR-bC, WVR-bC, TVR-bC and SR-bC regions for the samples generated on the particle and detector levels.

W+jets production

For the SR-bC signal region the dominant background is W+jets production, at about 55%. Since the W+jets production is normalised in the control regions, uncertainties are estimated on the transfer factors. The validation of the factorisation scale uncertainty with samples which include the detector modelling with ATLAS fast simulation ATLFAST-II showed, that the transfer factor uncertainties can be estimated by applying the analysis selection requirements on the particle level objects (see Table 6.18). All theoretical uncertainties on the W+jets production are estimated on particle level.

The following uncertainties are considered:

- **Scale variations**
  Scale uncertainties are estimated by varying three sources of systematic uncertainty. The systematic uncertainty related to the matrix elements and parton showers matching scheme is estimated by varying the CKKW jet matching parameter from the nominal of 20 GeV to 15 GeV and 30 GeV. The systematic uncertainties related to the factorisation and renormalisation scales are estimated varying the scale by factor of 0.5 and 2.0 from the nominal.
- **Finite number of partons**
  The systematic uncertainty related to the number of partons used in the hard scattering is based on a comparison between the $W \to (e, \mu, \tau)\nu$ with exactly 4 extra partons and with 4-5 extra partons.

The transfer factor uncertainties on the W+jets modelling from the WCR-bC region to the associated TCR-bC, WVR-bC, TVR-bC and SR-bC regions for different sources of systematic uncertainties are presented in Table 6.20.

Systematic uncertainty	WCR $\leftrightarrow$ TCR	WCR $\leftrightarrow$ WVR	WCR $\leftrightarrow$ TVR	WCR $\leftrightarrow$ SR
CKKW jets matching	0.2%	2%	2%	0.1%
Factorisation Scale	3%	1.9%	5%	4%
Renormalisation Scale	6%	3%	6%	3%
Finite number of partons	2%	0.5%	0.3%	4%
Total uncertainty	7%	5%	8%	7%

Table 6.19: Transfer factor uncertainties on the W+jets modelling from the WCR-bC region to the associated TCR-bC, WVR-bC, TVR-bC and SR-bC regions for different sources of systematic uncertainties.

Following the ATLAS SUSY Working Group recommendations, an additional $\pm 24\%$ uncertainty on the Wb cross-section measurements in the 2 jets bin [105] is considered for the W+heavy flavour samples for all regions. For the bC analysis the signal region (SR-bC) and W+jets control and validation regions (WCR-bC and WVR-bC) have the same b-jet veto requirement. Therefore, relative compositions of the light and heavy flavours for the WCR-bC, WVR-bC and SR-bC regions are similar, at 0.48, 0.52 and 0.53, respectively.

Flavour composition	WCR-bC	TCR-bC	WVR-bC	TVR-bC	SR-bC
W+light flavour	54%	3%	48%	1%	36%
W+heavy flavour	26%	13%	25%	5%	19%
Total W+jets	80%	16%	73%	6%	55%

Table 6.20: A composition of the light and heavy flavours of the W+jets background for the signal, control and validation regions of the bC analysis.

$t\bar{t}$ production

For the bC diagonal analysis the $t\bar{t}$ production is a sub-dominant background (at about 29%), which is also normalised in the control regions. Therefore, all theoretical uncertainties are estimated for transfer factors. Theoretical uncertainties for the $t\bar{t}$ production are estimated as follows:

– **Generator uncertainty**
  Studies performed in the context of the one-lepton analysis [3] show, that the $t\bar{t}$ samples modelled with the MC@NLO and ALPGEN generators have a notably worse agreement with data than the nominal samples generated with the POWHEG. Therefore, it was decided to ignore the uncertainty related to the generator choice for the $t\bar{t}$ modelling.

  Just for a comparison, uncertainties on transfer factors for the bC diagonal analysis are shown in Table 6.21. These uncertainties are not included in the analysis.

– **Scale variations**
  The uncertainties on transfer factors for factorisation and renormalisation scale variations are estimated on particle level by varying each scale by factor of 0.5 and 2.0 from the nominal. Figure 6.17 shows distributions of the m_{T} and number of b-tagged jets $N_{b\text{-jet}}$ variables, which are normalised to unity in the $[60, 90]$ GeV interval and the region with at least 1 b-jet, respectively. Distributions of the m_{T} are shown for the WCR-bC and TCR-bC control region selections before the m_{T} requirement is applied, while distributions of the $N_{b\text{-jet}}$ are shown for the TCR-bC and SR-bC region selections before the b-jet requirement is applied.

– **Parton shower**
  The parton shower uncertainty is estimated on detector level as a difference between the samples generated with the POWHEG, interfaced either with PYTHIA or HERWIG for parton showering.

– **ISR/FSR**
  The initial and final state radiation uncertainty is estimated on detector level as a difference between ACERMC samples generated with higher and lower parton shower activity.

Systematic uncertainty	TCR $\leftrightarrow$ WCR	TCR $\leftrightarrow$ WVR	TCR $\leftrightarrow$ TVR	TCR $\leftrightarrow$ SR
POWHEG vs MC@NLO	2%	20%	9%	10%
POWHEG vs ALPGEN	2%	27%	9%	6%

Table 6.21: Transfer factor uncertainties on the $t\bar{t}$ production related to the choice of the generator for the bC analysis. Uncertainties are estimated on transfer factors from the TCR-bC control region to the associated WCR-bC, WVR-bC, TVR-bC and SR-bC regions. These uncertainties are not included in the analysis (for more details see text).

Table 6.22 presents transfer factor uncertainties on the $t\bar{t}$ modelling from the TCR-bC control region to the associated WCR-bC, WVR-bC, TVR-bC and SR-bC regions for different sources of systematic uncertainties.

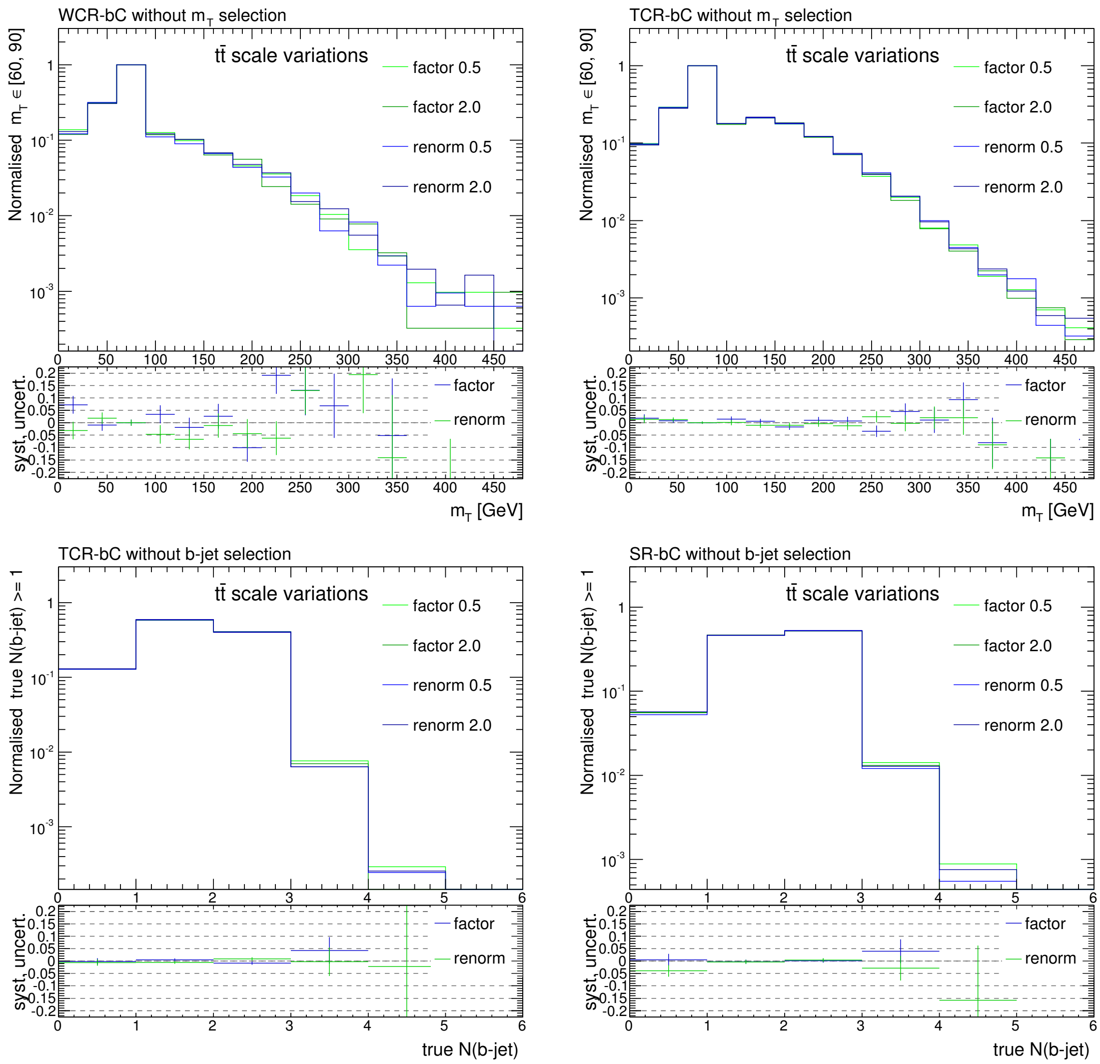

Figure 6.17: Normalised distributions of the m_T and number of b-tagged jets $N_{b\text{-jet}}$ variables for the factorisation (`factor`) and renormalisation (`renorm`) scale variations of the $t\bar{t}$ production. Distributions of the m_T are shown for the WCR-bC (top left) and TCR-bC (top right) control region selections before the m_T requirement is applied, and normalised to unity in the $[60, 90]$ GeV interval. Distributions of the $N_{b\text{-jet}}$ are shown for the TCR-bC (bottom left) and SR-bC (bottom right) region selections before the b-jet requirement is applied, and normalised to unity in the region with at least 1 b-jet.

Systematic uncertainty	TCR $\to$ WCR	TCR $\to$ WVR	TCR $\to$ TVR	TCR $\to$ SR
Factorisation scale	0.2%	3%	0.0%	0.6%
Renormalisation scale	0.6%	6%	0.6%	5%
Parton shower	10%	1%	1.7%	19%
ISR/FSR modelling	5%	8%	6%	18%
Total uncertainty	11%	10%	7%	27%

Table 6.22: Transfer factor uncertainties on the $t\bar{t}$ modelling from the TCR-bC control region to the associated WCR-bC, WVR-bC, TVR-bC and SR-bC regions for different sources of systematic uncertainties.

Single top production

The single top production has a small (less than 3%) contribution in the SR-bC signal region. All uncertainties are estimated on detector level. The following sources of systematic uncertainties are considered:

- **Generator uncertainty**
  The generator uncertainty is estimated by a comparison between the samples generated with MC@NLO and the nominal POWHEG samples;
- **Parton shower**
  The parton shower uncertainty is estimated by a comparison of the nominal POWHEG samples interfaced with either PYTHIA or HERWIG for parton showering;
- **Interference with the $t\bar{t}$ production**
  The uncertainty related to the interference with the $t\bar{t}$ NLO production is estimated by a comparison of the nominal ($t\bar{t} + Wt$) with ACERMC ($WWbb$) samples;
- **ISR/FSR modelling**
  The ISR/FSR uncertainty is evaluated as a difference between the ACERMC samples generated with more and less parton shower activity.

The results for different sources of systematic uncertainties for the single top production are shown in Table 6.23.

Systematic uncertainty	WCR-bC	TCR-bC	WVR-bC	TVR-bC	SR-bC
Generator uncertainty	22%	16%	22%	23%	50%
Parton Shower	10%	6%	17%	9%	28%
Interference with $t\bar{t}$	16%	39%	9%	26%	11%
ISR/FSR modelling	13%	1.1%	8%	0.1%	21%
Total uncertainty	32%	42%	30%	36%	62%

Table 6.23: Uncertainties on the single top production for the signal, control and validation regions for the bC analysis.

Diboson production

The contribution from the diboson production in the SR-bC signal region is about of 12%. All uncertainties are estimated on particle level. The following variations are considered:

- **Scale variations**
  The factorisation and renormalisation scales is varied coherently by factor of 0.5 and 2.0 from the nominal. The uncertainty on the matrix element to parton-shower matching scale for jets is estimated by varying up and down of 10 GeV from the nominal of 20 GeV;
- **Finite number of partons**
  The uncertainty on the finite number of partons is estimated by a comparison of the nominal samples with three extra parton with samples produced with two extra partons.

The results for different sources of systematic uncertainties are shown in Table 6.24.

Systematic uncertainty	WCR-bC	TCR-bC	WVR-bC	TVR-bC	SR-bC
CKKW matching scale	1%	1%	10%	3%	2%
Factorisation scale	5%	3%	7%	2%	8%
Renormalisation scale	13%	11%	18%	4%	5%
Finite number of partons	4%	7%	27%	8%	13%
Total uncertainty	15%	14%	35%	9%	16%

Table 6.24: Uncertainties of the diboson production for the signal, control and validation regions for the bC analysis.

$t\bar{t}W$ and $t\bar{t}Z$ production

The contribution from the $t\bar{t}W$ and $t\bar{t}Z$ production in the SR-bC signal region is negligible, less than 1%. All theoretical uncertainties on the $t\bar{t}W$ and $t\bar{t}Z$ production are estimated on particle level. The following variations are considered:

- **Scale variations**
  The factorisation and renormalisation scales, varied coherently by factor of 0.5 and 2.0 from the nominal; The uncertainty on the matrix element to parton-shower matching scale for jets is estimated by varying up and down of 10 GeV from the nominal of 20 GeV;
- **ISR/FSR modelling**
  The uncertainties on the ISR and FSR modelling are estimated by varying the α_s parameter up and down by factor of 2 and the relevant parameter in the MADGRAPH parton showering model, respectively;
- **Finite number of partons**
  The finite number of partons uncertainty is estimated by a comparison of the nominal two-jet inclusive with the one-jet inclusive samples.

The results for different sources of systematic uncertainties are shown in Table 6.25.

Systematic uncertainty	WCR-bC	TCR-bC	WVR-bC	TVR-bC	SR-bC
Scale variation	3%	0.2%	3%	1.7%	1.0%
Jet matching scale	7%	0.5%	13%	0.6%	1.3%
ISR modelling	1.6%	3%	9%	0.8%	5%
FSR modelling	10%	4%	2%	3%	3%
Finite number of partons	19%	7%	41%	10%	10%
Total uncertainty	23%	9%	44%	11%	12%

Table 6.25: Uncertainties on the $t\bar{t}W$ and $t\bar{t}Z$ modelling for the signal, control and validation regions for the bC analysis.

$Z+$jets production

The contribution from Z+jets in signal and control regions is so small (less than 1%), that the estimation of uncertainties is completely dominated by statistical fluctuations. Therefore, uncertainties for Z+jets process are not estimated. Instead, a systematic uncertainty of ±50% is assigned.

Cross-section uncertainties

Since the $t\bar{t}$ and W+jets processes are normalised to the dedicated control regions (TCR-bC and WCR-bC), the uncertainty on the theoretical cross section of these processes has no effect. The cross-section uncertainties from other backgrounds are estimated as follows:

- **single top production**
  Following Ref. [106], the cross-section uncertainty on the Wt channel is ±6.8%, while for the s- and t-channels it is ±3.9% [97, 98]. Since the contribution of the single top events in the signal region is small anyway, the total cross-section uncertainty for the single top production was conservatively assigned to ±6.8%.
- **$t\bar{t}W$ and $t\bar{t}Z$ production**
  For the $t\bar{t}W$ and $t\bar{t}Z$ processes a cross-section uncertainty of ±22% is assigned, following Ref. [101, 100].
- **diboson production**
  Cross-section uncertainties for the ZZ and WZ samples are taken as ±5% and ±7%, respectively [107].
- **$Z+$ jets production**
  The Z+jets process contribution is almost negligible, therefore, instead of a detailed determination, a cross-section uncertainty of ±50% was conservatively assigned.

PDF uncertainties

PDF uncertainties are estimated following the PDF4LHC recommendations [108] by comparing CT10 NLO, MSTW2008 NNLO and NNPDF [109] PDF error sets. The impact of the PDF uncertainties on the bC analysis is shown in Table 6.26.

Process	WCR-bC	TCR-bC	SR-bC
$t\bar{t}$	$< 0.1\%$	0.1%	0.4%
W+jets	0.1%	0.1%	0.1%
single top	0.1%	0.4%	0.1%
$t\bar{t} + W/Z$	$< 0.1\%$	$< 0.1\%$	$< 0.1\%$
diboson	0.2%	0.1%	0.7%

Table 6.26: Impact of PDF uncertainties on the total background estimate for the signal and control regions of the bC analysis.

Usually, PDF uncertainties for different background processes are about 3–6%, but taking into account, that the $t\bar{t}$ and W+jets background processes are normalised in control regions, the impact due to the PDF uncertainties on the total background estimate is less than 0.4%. The total contribution from all other processes for the signal region is below 15%, therefore, the impact of the PDF uncertainties on the total background estimate in the signal region is less then 0.7%.

6.6.4 Signal uncertainties

Cross-section uncertainties

The direct top-squark pair production cross section as a function of top-squark mass is shown in Figure 6.18. The cross-section uncertainty for top-squark pair-production is calculated following the prescriptions in Ref. [110]. The total cross-section uncertainty includes α_s, factorisation and renormalisation scale variations and PDF uncertainties.

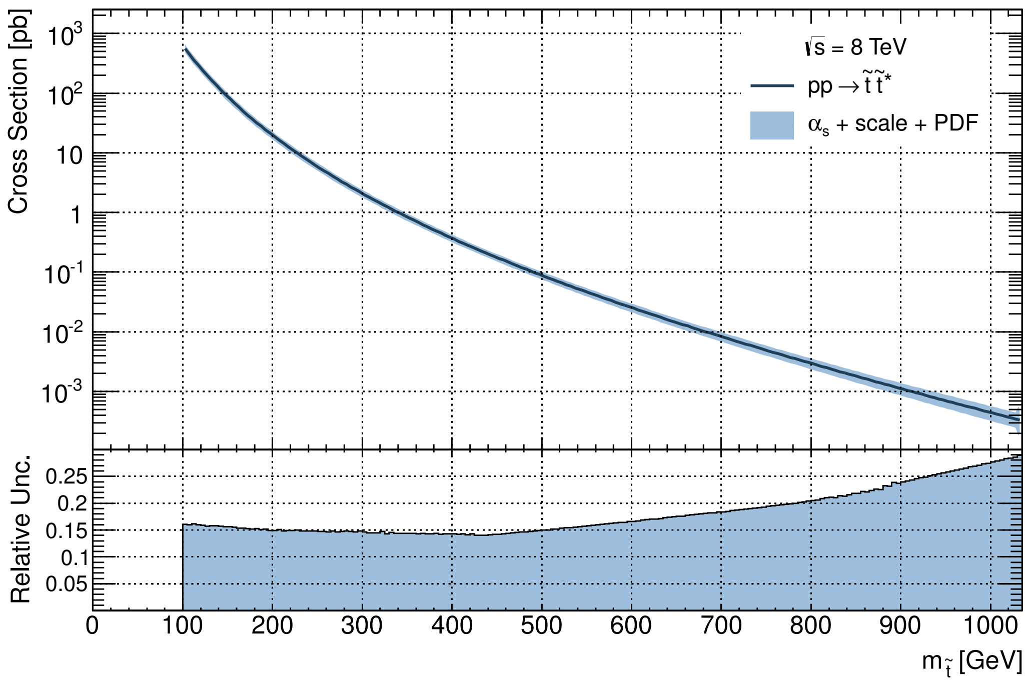

Figure 6.18: Direct top-squark pair production cross section at $\sqrt{s} = 8$ TeV as a function of top-squark mass $m_{\tilde{t}_1}$. The shaded area corresponds to the cross-section uncertainty and includes α_s, factorisation and renormalisation scale variations and PDF uncertainties. The uncertainties are estimated following the prescriptions in Ref. [110].

For the top-squark masses 180 GeV $< m(\tilde{t}_1) <$ 500 GeV the total theoretical cross-section uncertainty, which includes the α_s, factorisation and renormalisation scale variations and PDF uncertainties, is estimated as $\pm$15%.

Theoretical uncertainties

The presented bC analysis significantly benefits from ISR/FSR jets, therefore for each signal model, corresponding scale variations were generated. Systematic uncertainties are estimated on samples generated on particle level. The variation for each bC signal model is done using the MADGRAPH+PYTHIA generator. The following variations are generated:

- **Scale variations**
  The factorisation and renormalisation scales are varied independently by factor of 0.5 and 2.0 from the nominal;
- **ISR/FSR modelling**
  The uncertainty on the ISR modelling is estimated by varying the α_s parameter up and down by a factor of 2, while for FSR modelling by varying the relevant parameter in the MADGRAPH parton showering model by a factor of 0.5 and 1.5.

For each signal model the total theoretical uncertainty is estimated by summing up in quadrature the ISR, FSR and scale variations uncertainties. The total theoretical uncertainties for the SR-bC signal region are shown in Figure 6.19 for the gaugino universality $m(\tilde{\chi}_1^\pm) = 2 \cdot m(\tilde{\chi}_1^0)$ and $\Delta m(\tilde{t}_1, \tilde{\chi}_1^\pm) = 10$ GeV signal model grids. All uncertainties are shown in percent.

One can see, that the uncertainties are not constant and tend to be larger for low top-squark masses. Therefore by estimating the uncertainties for the whole grid using only signal models with $m(\tilde{t}_1) > 250$ GeV, like it was used for dileptonic searches targeting the same bC diagonal region [111], where uncertainties were estimated as 10% for the diagonal region, may lead to significant underestimation of uncertainties for the low top-squark mass region.

6.7 Results

6.7.1 Background-only fit

Results for the background-only fit are shown in Table 6.27. The fit is performed in the control regions only, the signal and validation regions are not included in the fit. To avoid a fit instability due to statistical fluctuations, the detector uncertainties for the negligible Z+jets background are neglected. A visualisation of the fit results is shown in Figure 6.20. The normalisation of the $t\bar{t}$ and W+jets backgrounds is done in the WCR-bC and TCR-bC control regions.

$N - 1$ distributions

Figure 6.21 shows the distributions for various discriminant variables used in the signal region definition. Each distribution is obtained by applying all signal selection requirements except for the discriminant variable shown in the distribution. These distributions are referred to as "$N - 1$" distributions. The requirement is indicated by a black vertical line, the arrow indicates the SR-bC signal region. The error bands include only the Monte Carlo statistical uncertainties. The error bars on the data and data/MC ratio points represent the 68% confidence intervals.

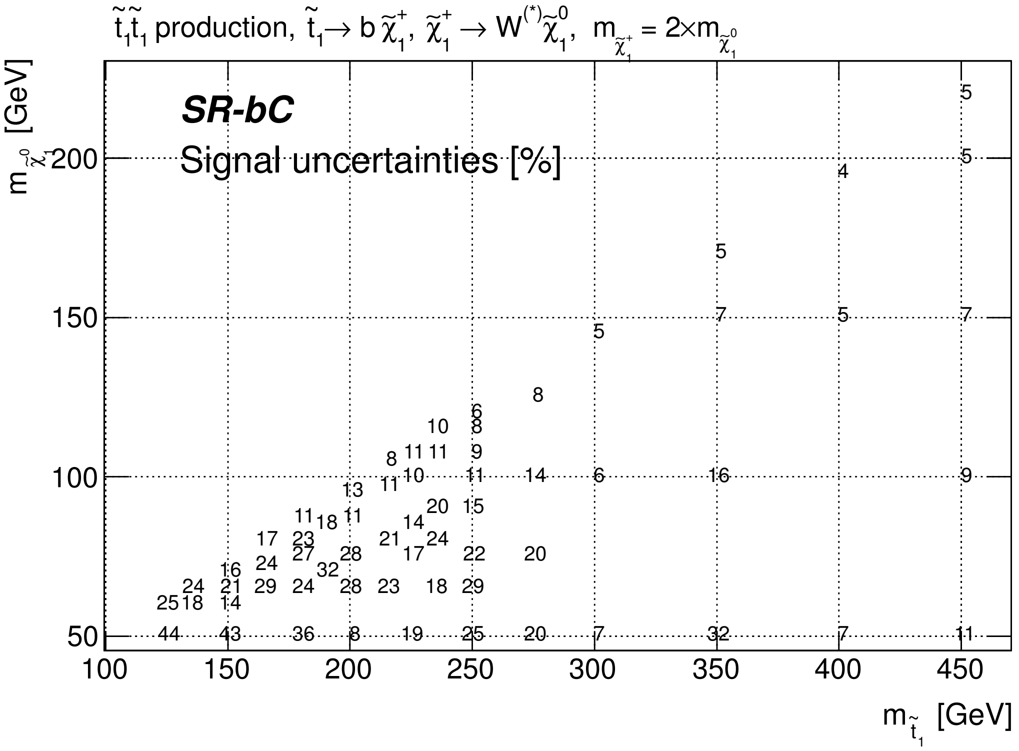

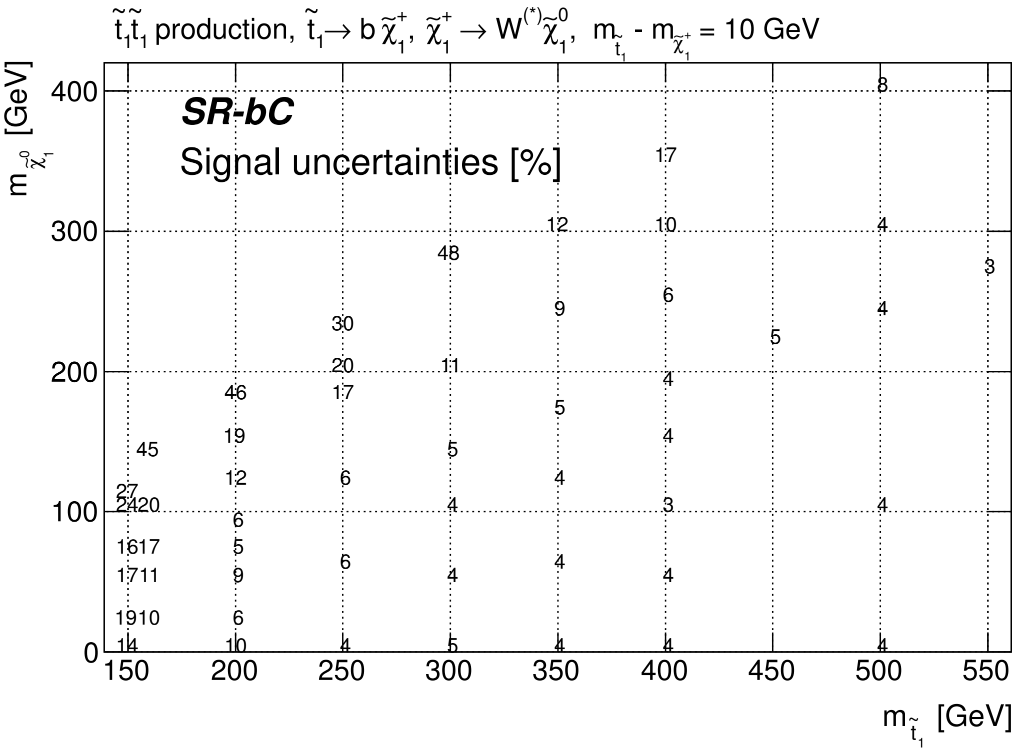

Figure 6.19: The total theoretical uncertainties, estimated by summing up in quadrature the ISR, FSR and scale variations uncertainties, are shown in percent for the SR-bC signal region for the gaugino universality $m(\tilde{\chi}_1^{\pm}) = 2 \cdot m(\tilde{\chi}_1^0)$ and $\Delta m(\tilde{t}_1, \tilde{\chi}_1^{\pm}) = 10$ GeV signal model grids.

SR-bC	WCR-bC	TCR-bC	WVR-bC	TVR-bC	SR-bC
Observed events	2162	1650	693	925	493
Fitted SM Total	2162 ± 47	1650 ± 41	720 ± 160	870 ± 230	472 ± 48
Fitted $t\bar{t}$	331 ± 79	1236 ± 62	153 ± 52	750 ± 230	144 ± 45
Fitted W+jets	1694 ± 99	250 ± 37	510 ± 130	46 ± 9	248 ± 27
Fitted single top	46 ± 10	140 ± 24	18 ± 5	46 ± 15	12 ± 3
Fitted $t\bar{t} + W/Z$	1.6 ± 0.5	5.4 ± 1.6	1.2 ± 0.4	15.3 ± 4.5	3.3 ± 1.1
Fitted diboson	79 ± 23	17 ± 5	32 ± 10	10 ± 3	59 ± 17
Fitted Z+jets	10.4 ± 5.2	1.9 ± 1.0	7.6 ± 3.8	1.2 ± 0.6	5.2 ± 2.6
MC exp. SM Total	2361.2 ± 23.4	1689.1 ± 11.0	781.2 ± 14.7	876.1 ± 8.2	501.9 ± 11.2
MC exp. $t\bar{t}$	333.8 ± 4.2	1246.5 ± 8.0	154.7 ± 2.8	752.0 ± 6.0	145.6 ± 2.7
MC exp. W+jets	1890.3 ± 22.6	278.2 ± 6.8	567.3 ± 14.1	51.4 ± 5.3	276.8 ± 10.5
MC exp. single top	46.5 ± 1.7	140.2 ± 2.9	18.3 ± 1.1	46.0 ± 1.3	12.1 ± 0.8
MC exp. $t\bar{t} + W/Z$	1.6 ± 0.1	5.5 ± 0.2	1.2 ± 0.1	15.3 ± 0.3	3.3 ± 0.1
MC exp. diboson	78.5 ± 3.8	16.8 ± 1.9	32.2 ± 2.2	10.1 ± 1.1	58.9 ± 2.2
MC exp. Z+jets	10.4 ± 1.1	1.9 ± 0.4	7.7 ± 1.0	1.3 ± 0.3	5.2 ± 1.2

Table 6.27: Results of the background-only fit for the bC analysis. The normalisation of the $t\bar{t}$ and W+jets backgrounds is done in the WCR-bC and TCR-bC control regions. The validation regions (WVR-bC and TVR-bC) are not included in the fit.

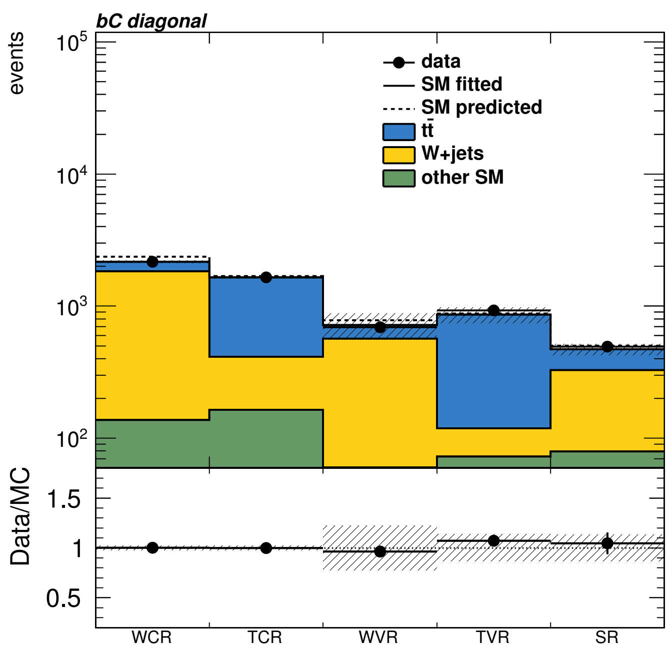

Figure 6.20: Visualisation of the background-only fit results for the bC analysis [3]. The normalisation is done in the WCR-bC and TCR-bC control regions.

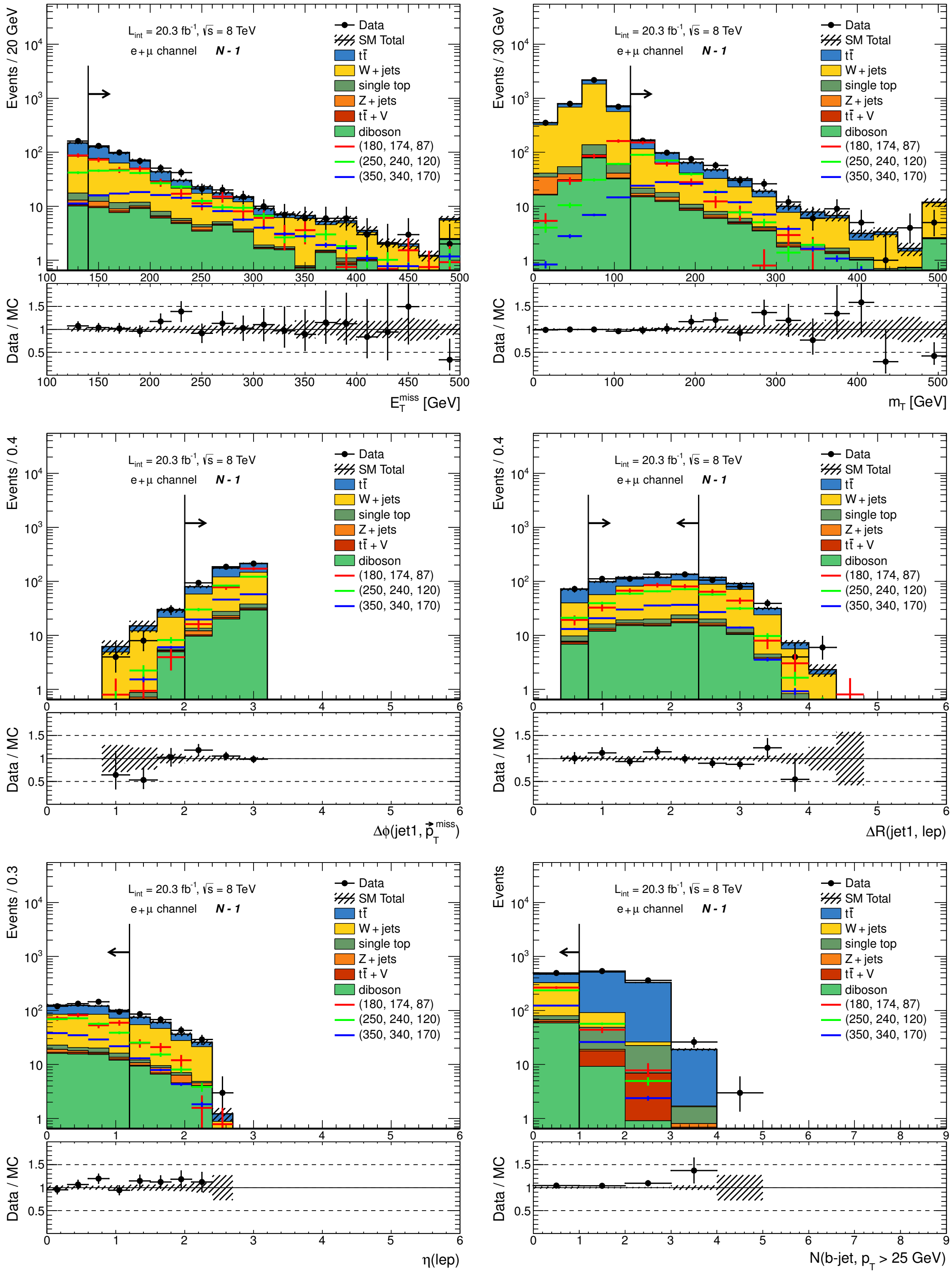

Figure 6.21: The $N-1$ distributions for the SR-bC signal region. Each distribution is obtained by applying all selection requirements except for the discriminant variable shown in the distribution. The requirement is indicated by a black vertical line, the arrow points to the events, which fulfil the requirement. The error bands include only the Monte Carlo statistical uncertainties. The error bars on the data and data/MC ratio points represent the 68% confidence intervals.

6.7.2 Signal-model-independent upper limits

Signal-model-independent limits are determined (see Section 4.9). This is done by varying the number of events in the signal region to determine the highest value $N_{\text{non-SM}}$ for which $\text{CL}_s < 0.05$, i.e. the highest value for which any beyond-the-Standard-Model model contribution can be excluded at a confidence level of 95% (see Section 4.10). This value is stated as the model-independent limit. During the CL_s calculation no signal contamination in control regions is taken into account and all signal-related uncertainties are removed (signal cross section, experimental and theoretical uncertainties related to the signal). All uncertainties related to the Standard Model background are taken into account.

The signal-model-independent limit, as the visible signal cross section σ_{vis}, is obtained by dividing $N_{\text{non-SM}}$ by the integrated luminosity.

The expected and observed signal model independent upper limits for beyond the Standard Model ($N_{\text{non-SM}}$) and the visible signal cross sections ($\sigma_{\text{vis}} = \sigma_{\text{prod}} \times A \times \epsilon$) for the SR-bC signal region at 95% confidence level are shown in Table 6.28.

SR-bC	Expected	Observed
$N_{\text{non-SM}}$	95.1	110.6
σ_{vis} [fb]	4.7	5.7

Table 6.28: Signal-model-independent upper limits for beyond the Standard Model ($N_{\text{non-SM}}$) contribution and the visible signal cross sections ($\sigma_{\text{vis}} = \sigma_{\text{prod}} \times A \times \epsilon$) for the SR-bC signal region. All numbers are given at 95% CL.

6.7.3 Interpretation

The contributions from the presented bC analysis are represented as limits in the $(\tilde{t}_1, \tilde{\chi}_1^0)$ mass plane for the two signal grids considered in Figure 6.22.

For the gaugino universality grid, this analysis is the only ATLAS analysis filling the diagonal gap for the low top-squark mass region in the 125−175 GeV interval.

For the $m(\tilde{t}_1) - m(\tilde{\chi}_1^\pm) = 10$ GeV grid, the bC analysis is the only one-lepton analysis (except the soft-lepton analysis) which has sensitivity. The soft-lepton analysis extends this limit in the region of $m(\tilde{t}_1, \tilde{\chi}_1^0) \approx (200, 150)$ GeV, towards the diagonal $m(\tilde{\chi}_1^\pm) \approx m(\tilde{\chi}_1^0)$. In this region, due to a small mass difference $\Delta m(\tilde{\chi}_1^\pm, \tilde{\chi}_1^0)$, a decay of the chargino $\tilde{\chi}_1^\pm \to W^{(*)}\tilde{\chi}_1^0$ proceed via a virtual W boson. A lepton, produced from the $W^{(*)} \to \ell\nu$ virtual decay is soft and mainly has $p_{\text{T}} < 25$ GeV, which is below the preselection requirement of the one-lepton analysis. Therefore, in this region, the bC analysis has a very low acceptance.

For the $m(\tilde{\chi}_1^\pm) = 150$ GeV and $m(\tilde{t}_1) = 300$ GeV grids presented in Figure 6.23, the bC analysis has some sensitivity, but the exclusion is just slightly extended. It is mainly covered by other one-lepton analysis selections.

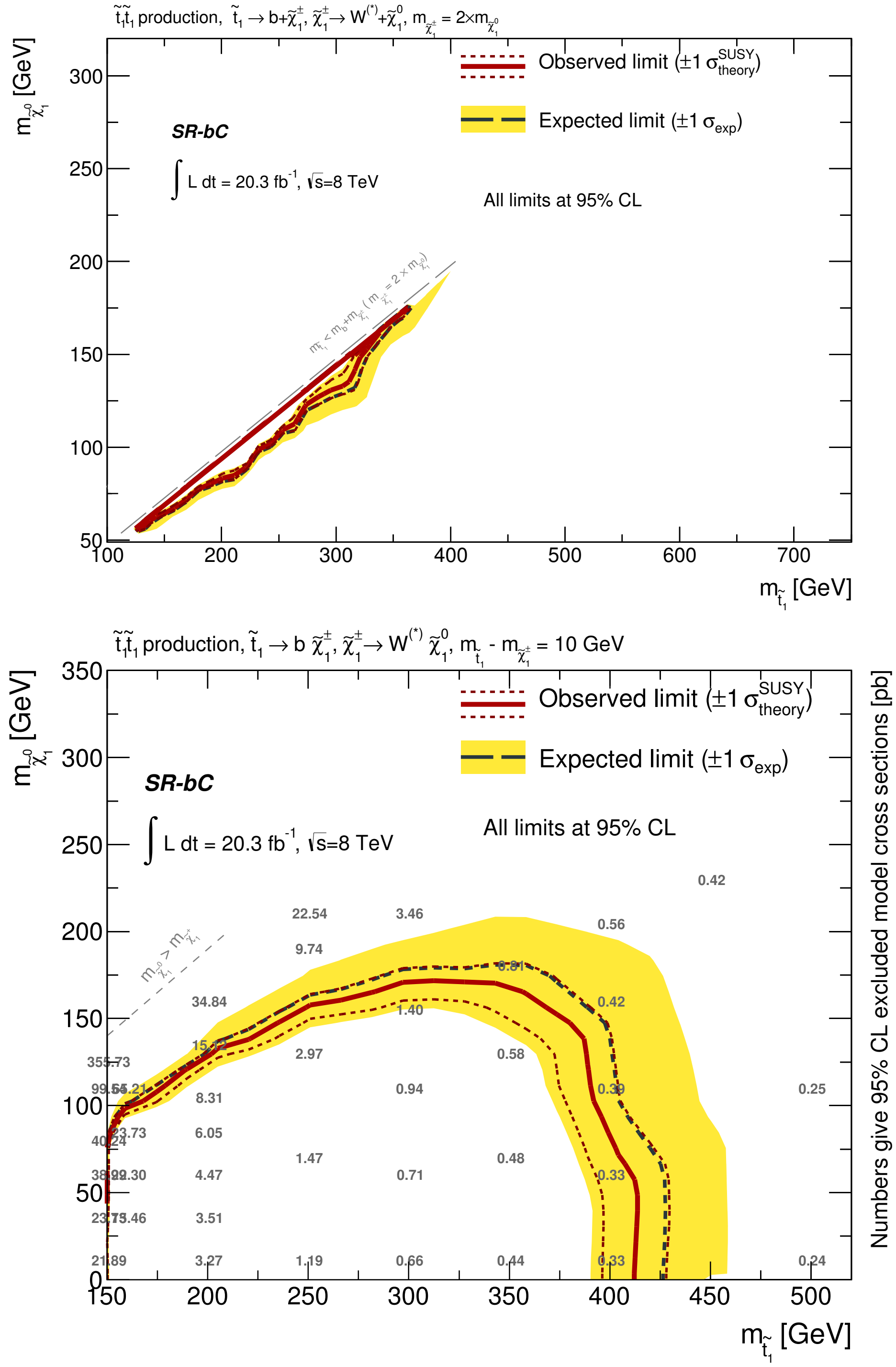

Figure 6.22: Exclusion limits at 95% CL for the gaugino universality grid with $m(\tilde{\chi}_1^{\pm}) = 2 \cdot m(\tilde{\chi}_1^0)$ (top) and for the $m(\tilde{t}_1) - m(\tilde{\chi}_1^{\pm}) = 10$ GeV grid (bottom) for the bC analysis [3]. The limits are shown in the $(\tilde{t}_1, \tilde{\chi}_1^0)$ mass plane. The black dotted line corresponds to the expected limit, the yellow band includes all uncertainties except the uncertainty on the signal cross section. The dark red line corresponds to the observed limit, the dashed red lines are $\pm 1\sigma$ of the signal cross-section uncertainty.

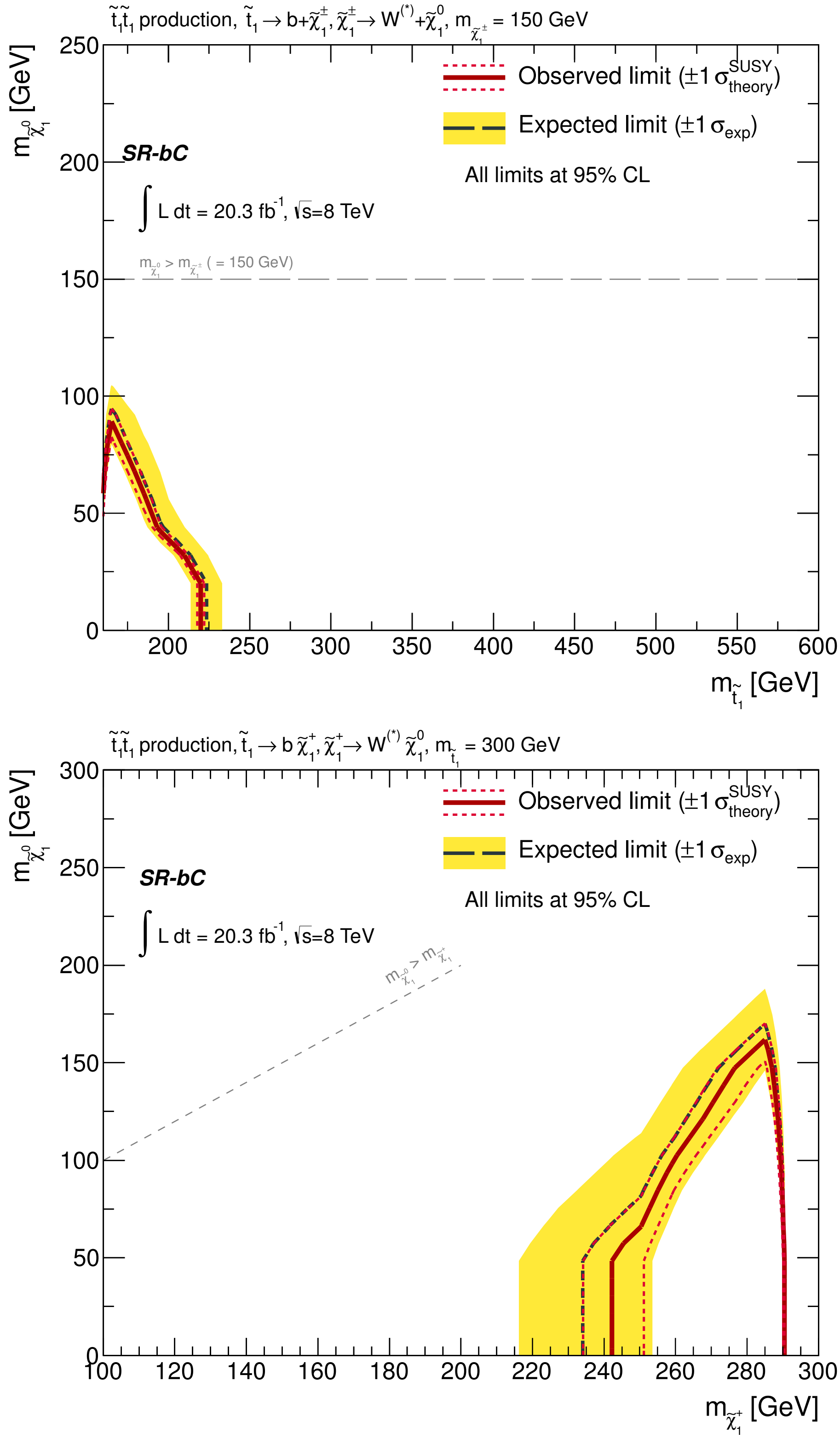

Figure 6.23: Exclusion limits at 95% CL for the $m(\tilde{\chi}_1^{\pm}) = 150$ GeV grid in the $(\tilde{t}_1, \tilde{\chi}_1^0)$ mass plane (top) and for the $m(\tilde{t}_1) = 300$ GeV grid in the $(\tilde{\chi}_1^{\pm}, \tilde{\chi}_1^0)$ mass plane (bottom) for the bC analysis [3]. The black dotted line corresponds to the expected limit, the yellow band includes all uncertainties except the uncertainty on the signal cross section. The dark red line corresponds to the observed limit, the dashed red lines are $\pm 1\sigma$ of the signal cross-section uncertainty.

6.8 ATLAS top-squark searches at $\sqrt{s} = 8$ TeV, $\tilde{t}_1 \rightarrow b\tilde{\chi}_1^{\pm}$

The summary of the ATLAS results on searches for top-squark pair production for the simplified decay scenario, where the top-squark decays via $\tilde{t}_1 \rightarrow b\tilde{\chi}_1^{\pm}$ with subsequent decay of a $\tilde{\chi}_1^{\pm} \rightarrow W^{(*)}\tilde{\chi}_1^0$, is shown in Figure 6.24.

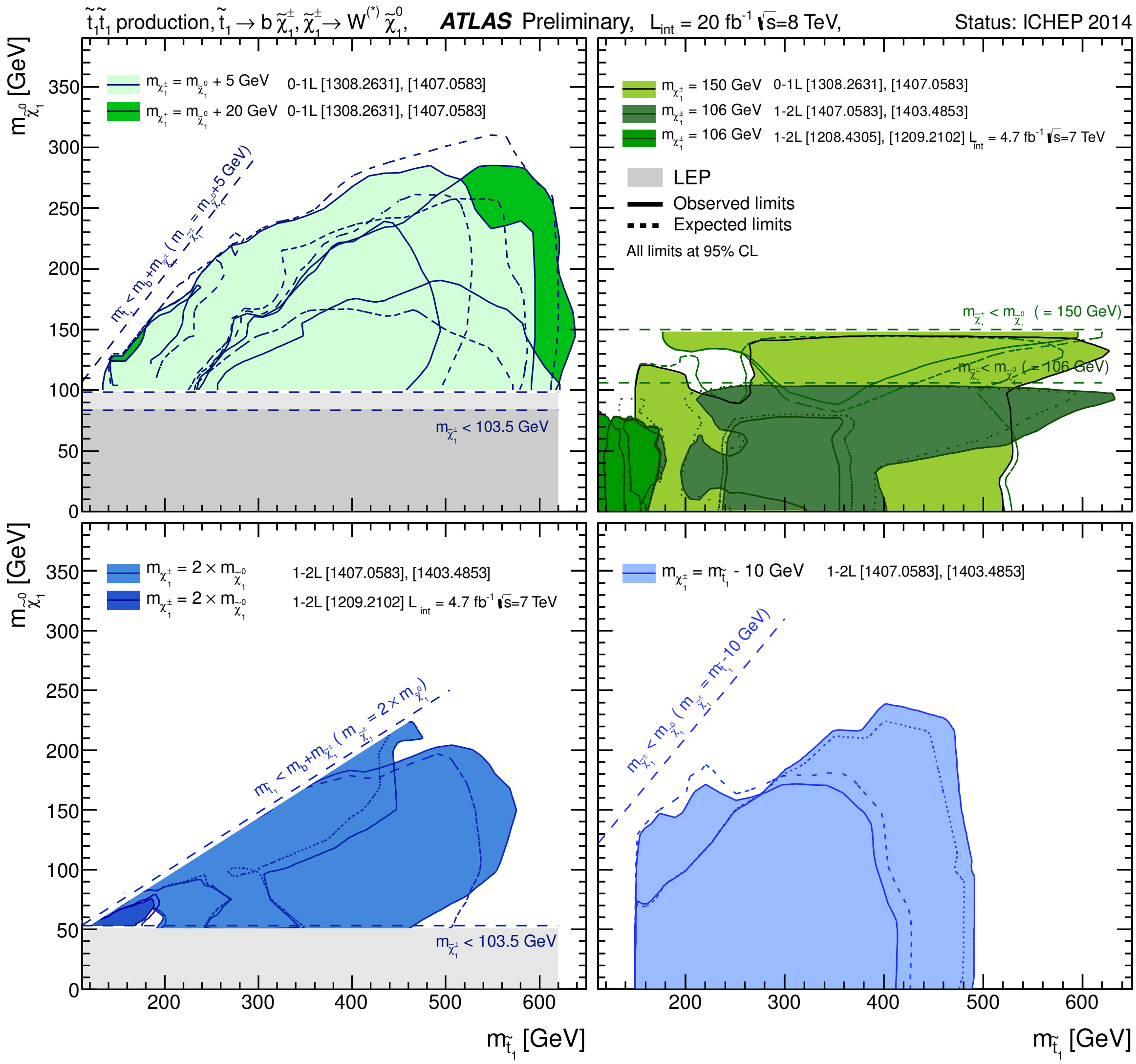

Figure 6.24: The summary of the ATLAS searches for top-squark pair-production for the simplified decay scenario $\tilde{t}_1 \rightarrow b\tilde{\chi}_1^{\pm}, \tilde{\chi}_1^{\pm} \rightarrow W^{(*)}\tilde{\chi}_1^0$ is based on an integrated luminosity of $\mathcal{L}_{\text{int}} = 20.3$ fb^{-1} of data at $\sqrt{s} = 8$ TeV and $\mathcal{L}_{\text{int}} = 4.7$ fb^{-1} of data at $\sqrt{s} = 7$ TeV [112]. It is assumed, that both decays proceed with a branching ratio of 100%. All exclusion limits are shown for the $(\tilde{t}_1, \tilde{\chi}_1^0)$ mass plane at 95% CL. The dashed and solid lines correspond to the expected and observed limits, respectively. The limits include all uncertainties except the uncertainty on the signal cross section. Different grids are presented: $m(\tilde{\chi}_1^{\pm}) - m(\tilde{\chi}_1^0) = 5$ GeV and 20 GeV (top left), $m(\tilde{\chi}_1^{\pm}) = 106$ GeV and 150 GeV (top right), gaugino universality $m(\tilde{\chi}_1^{\pm}) = 2 \cdot m(\tilde{\chi}_1^0)$ (bottom left) and $m(\tilde{t}_1) - m(\tilde{\chi}_1^{\pm}) = 10$ GeV (bottom right).

Both decays are assumed to proceed with a branching ratio of 100%. The results are based on an integrated luminosity of $\mathcal{L}_{\text{int}} = 20.3\ \text{fb}^{-1}$ of data at $\sqrt{s} = 8$ TeV and $\mathcal{L}_{\text{int}} = 4.7\ \text{fb}^{-1}$ of data at $\sqrt{s} = 7$ TeV. All exclusion limits are shown at 95% confidence level.

The following grids are presented:

- $m(\tilde{\chi}_1^{\pm}) - m(\tilde{\chi}_1^0) = 5\,\text{GeV}$ and $20\,\text{GeV}$
  The exclusion contours present the results of the zero- and one-lepton analyses, performed at $\sqrt{s} = 8$ TeV [113, 3]. The LEP limit $m(\tilde{\chi}_1^{\pm}) > 103.5$ GeV is also shown.
- $m(\tilde{\chi}_1^{\pm}) = 106\,\text{GeV}$ and $150\,\text{GeV}$
  The exclusion limits are shown for the zero-, one- and two-lepton analyses, performed at $\sqrt{s} = 8$ TeV [113, 3, 111], and the one- and two-lepton analyses at $\sqrt{s} = 7$ TeV [4, 114].
- Gaugino universality $m(\tilde{\chi}_1^{\pm}) = 2 \cdot m(\tilde{\chi}_1^0)$
  The results are shown for the one- and two-lepton analyses at $\sqrt{s} = 8$ TeV [3, 111], and at $\sqrt{s} = 7$ TeV [4]. The LEP exclusion is also shown.
- $m(\tilde{t}_1) - m(\tilde{\chi}_1^{\pm}) = 10\,\text{GeV}$
  The results are shown for the one- and two-lepton analyses at $\sqrt{s} = 8$ TeV [3, 111].

The summary plot is published in Ref. [112].

CHAPTER 7

The $t\bar{t}$ background reweighting

7.1 Default 4-bin reweighting

A mismodelling of the unfolded distribution of the p_{T} of the $t\bar{t}$ system was observed in the top-quark pair production differential cross-section measurement [104]. This might cause the main disagreement in the Monte Carlo modelling for the regions enriched by the $t\bar{t}$ process.

Based on measurements of $t\bar{t}$ production by the ATLAS Collaboration, weights are determined to correct the disagreement between data and Monte Carlo. The weights are defined as a 4-bin function of the true p_{T} of the $t\bar{t}$ system on particle level. The electron and muon weights are averaged. The reweighting coefficients as determined in Ref. [104] are shown in Table 7.1.

true $p_{\mathrm{T}}(t\bar{t})$ [GeV]	e - channel	μ - channel	average
$p_{\mathrm{T}} \in [0, 40)$	0.988	1.006	0.997
$p_{\mathrm{T}} \in [40, 170)$	0.912	0.967	0.940
$p_{\mathrm{T}} \in [170, 340)$	0.710	0.758	0.734
$p_{\mathrm{T}} \in [340, \infty)$	0.556	0.584	0.570

Table 7.1: Event weights depending on the true $p_{\mathrm{T}}(t\bar{t})$ extracted from the ATLAS top-quark differential cross-section measurements [104].

The considered approach has the following advantages:

- It does not depend on the analysis (zero- or one-lepton);
- It does not depend on a semileptonic $t\bar{t}$ decay channel (e, μ, τ);
- It does not use the jet multiplicity for the reweighting;
- The reweighting coefficients are derived based on the POWHEG+PYTHIA generated samples for $\sqrt{s} = 7$ TeV (equivalent of the nominal $t\bar{t}$ sample), but are applied for $\sqrt{s} = 8$ TeV.

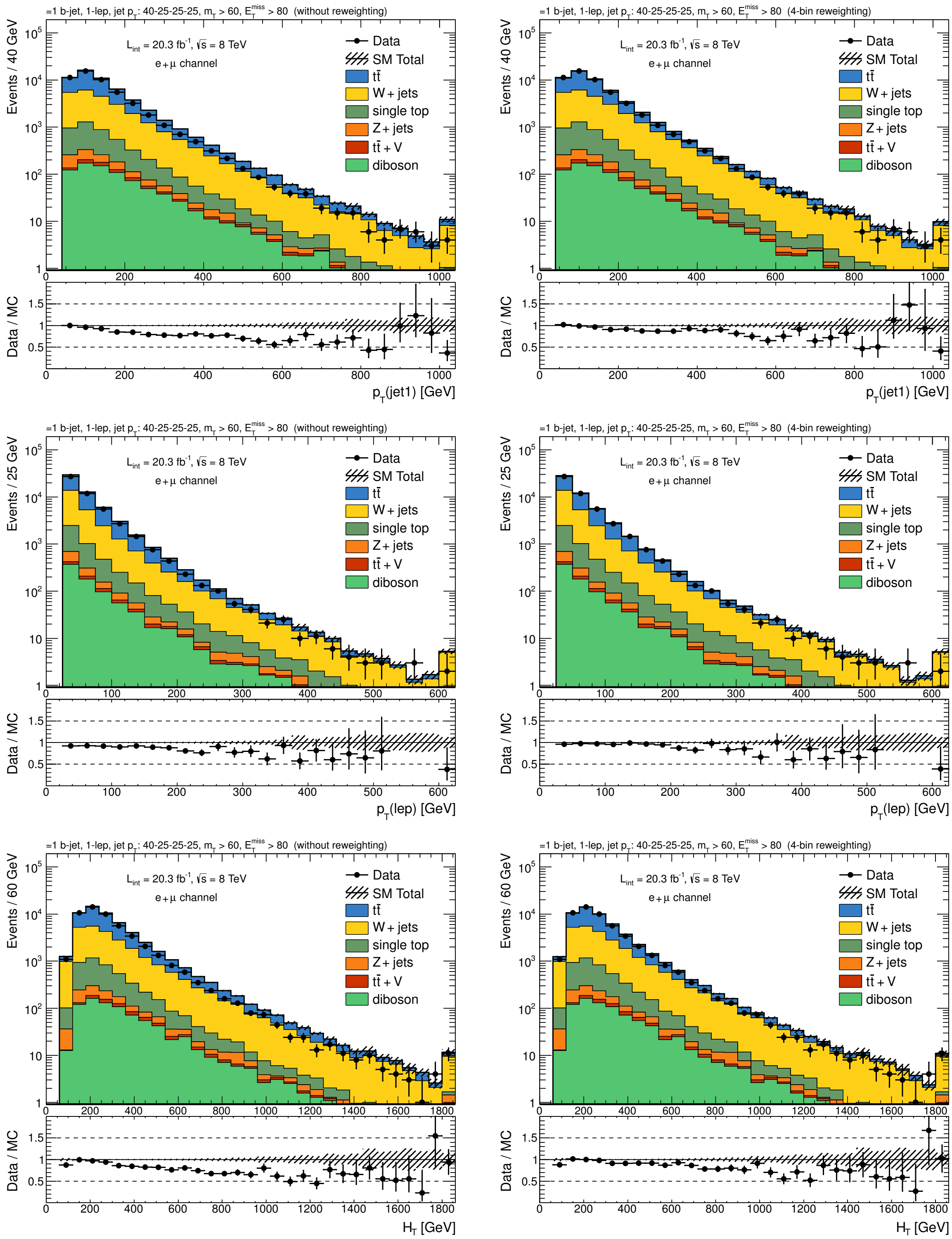

Figure 7.1: The data-MC comparison for the 1 b-jet selection before any reweighting is applied (left) and after the default 4-bin $t\bar{t}$ reweighting (right) for the variables: p_T of the leading jet (top row), p_T of the lepton (middle row) and the H_T (bottom row). The selection: 1 lepton, exactly 2 b-tagged jets, 4 jets with p_T values above 40, 25, 25, and 25 GeV, $E_T^{miss} > 80$ GeV, $m_T > 60$ GeV (for details, see Section 7.1). The $t\bar{t}$ and W+jets production are normalised to the Monte Carlo cross sections. The error bands include only the Monte Carlo statistical uncertainties.

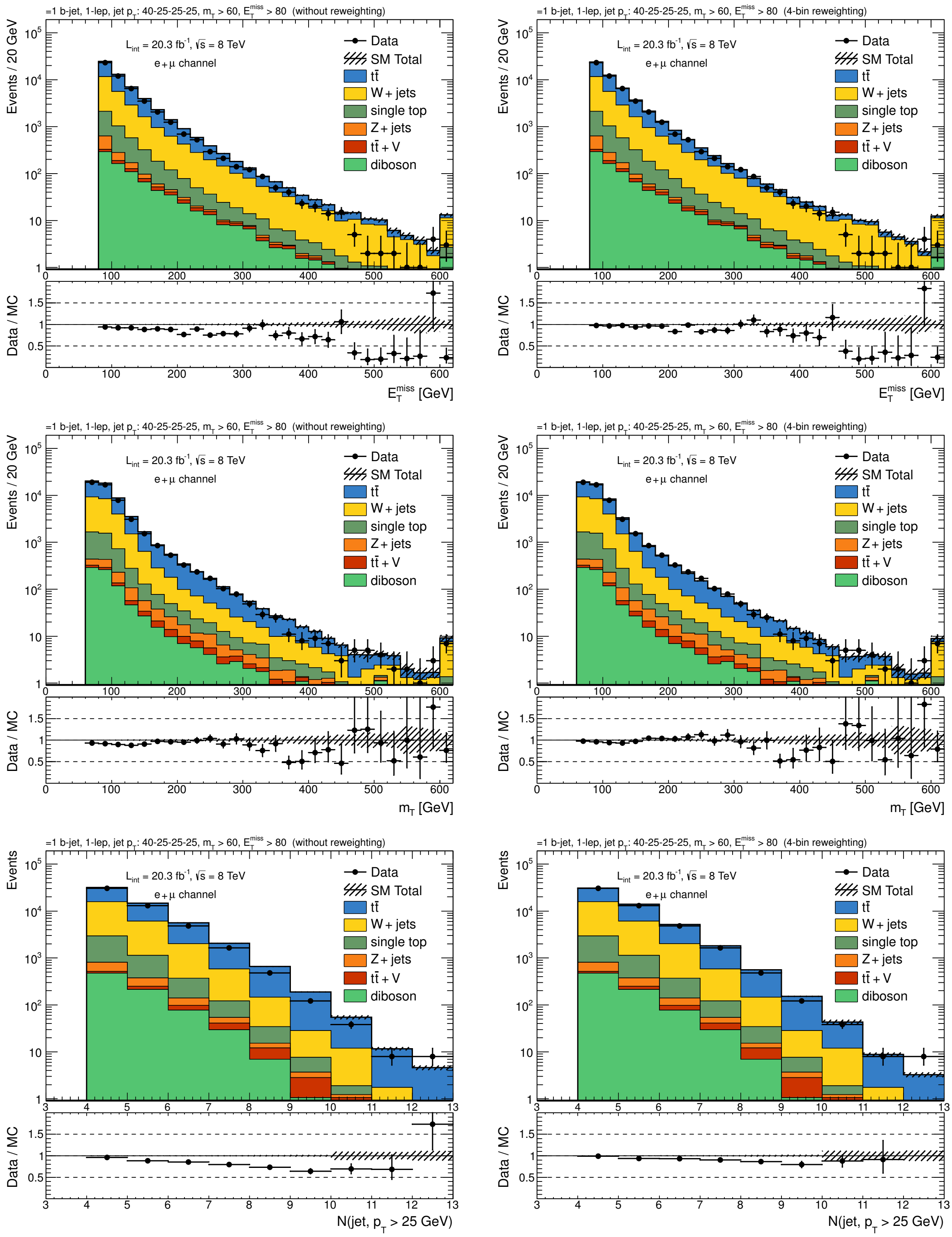

Figure 7.2: The data-MC comparison for the 1 b-jet selection before any reweighting is applied (left) and after the default 4-bin $t\bar{t}$ reweighting (right) for the variables: the $E_{\mathrm{T}}^{\mathrm{miss}}$ (top row), the m_{T} (middle row) and a number of selected jets N_{jet} (bottom row). The selection: 1 lepton, exactly 2 b-tagged jets, 4 jets with p_{T} values above 40, 25, 25, and 25 GeV, $E_{\mathrm{T}}^{\mathrm{miss}} > 80$ GeV, $m_{\mathrm{T}} > 60$ GeV (for details, see Section 7.1). The $t\bar{t}$ and W+jets production are normalised to the Monte Carlo cross sections. The error bands include only the Monte Carlo statistical uncertainties.

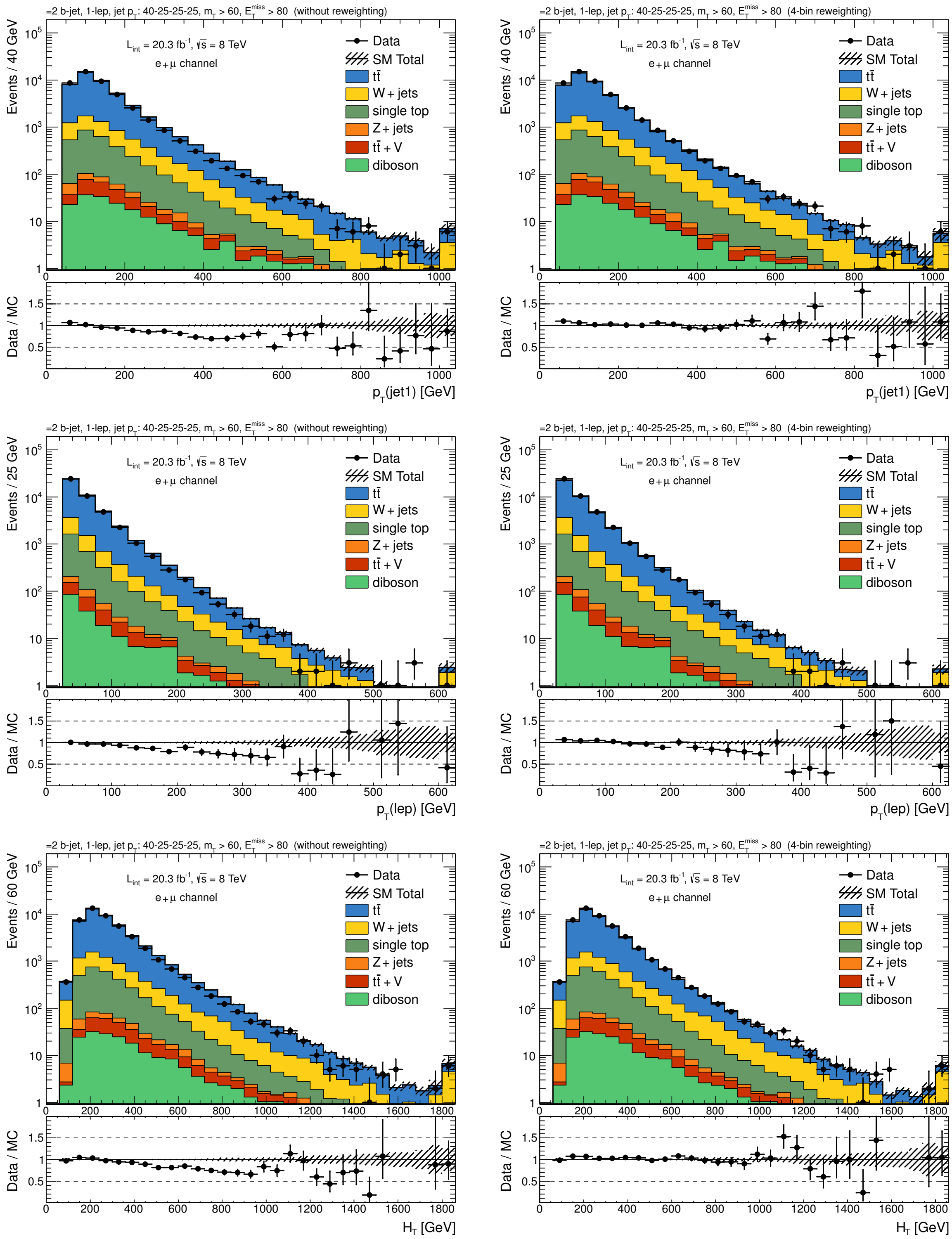

Figure 7.3: The data-MC comparison for the 2 b-jet selection before any reweighting is applied (left) and after the default 4-bin $t\bar{t}$ reweighting (right) for the variables: p_{T} of the leading jet (top row), p_{T} of the lepton (middle row) and the H_{T} (bottom row). The selection: 1 lepton, exactly 2 b-tagged jets, 4 jets with p_{T} values above 40, 25, 25, and 25 GeV, $E_{\mathrm{T}}^{\mathrm{miss}} > 80$ GeV, $m_{\mathrm{T}} > 60$ GeV (for details, see Section 7.1). The $t\bar{t}$ and W+jets production are normalised to the Monte Carlo cross sections. The error bands include only the Monte Carlo statistical uncertainties.

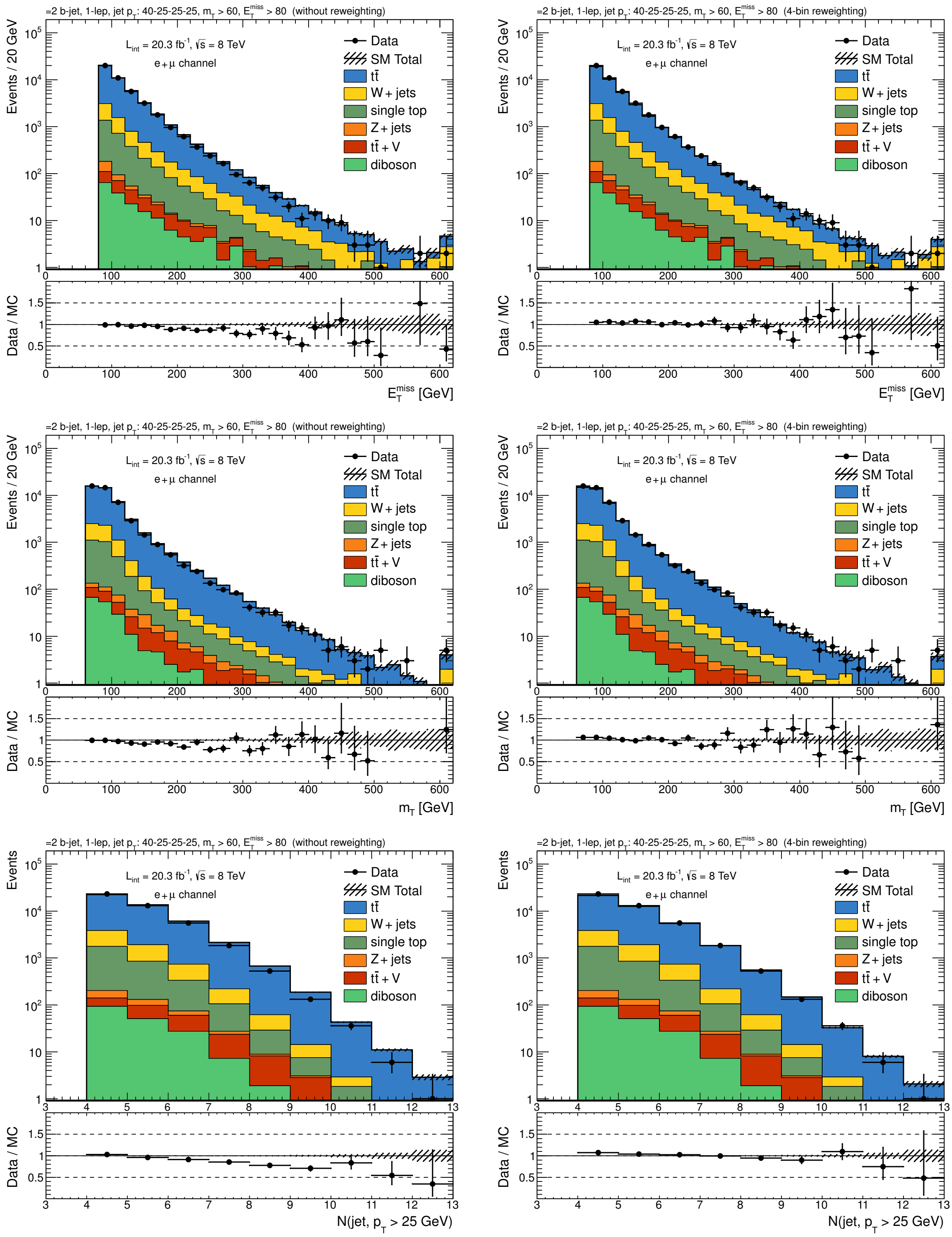

Figure 7.4: The data-MC comparison for the 2 b-jet selection before any reweighting is applied (left) and after the default 4-bin $t\bar{t}$ reweighting (right) for the variables: the $E_{\mathrm{T}}^{\mathrm{miss}}$ (top row), the m_{T} (middle row) and a number of selected jets N_{jet} (bottom row). The selection: 1 lepton, exactly 2 b-tagged jets, 4 jets with p_{T} values above 40, 25, 25, and 25 GeV, $E_{\mathrm{T}}^{\mathrm{miss}} > 80$ GeV, $m_{\mathrm{T}} > 60$ GeV (for details, see Section 7.1). The $t\bar{t}$ and $W+$jets production are normalised to the Monte Carlo cross sections. The error bands include only the Monte Carlo statistical uncertainties.

The selected approach significantly improves the agreement between data and Monte Carlo simulation for key variables in $t\bar{t}$ events. The data-MC comparison is done for two different regions, for events with exactly 1 and exactly 2 b-jets. In the following, these regions are referred to as 1 b-jet and 2 b-jet regions. In the event selection, the following criteria are applied in these regions:

- The one-lepton analysis cleaning cuts, as described in Section 6.2.3;
- Exactly one lepton with $p_{\mathrm{T}} > 25$ GeV, no other background leptons;
- At least four jets with $p_{\mathrm{T}}(j_{1,2,3,4}) > 40,\ 25,\ 25,\ 25$ GeV;
- Exactly 1 b-jet (1 b-jet region) or exactly 2 b-jets (2 b-jet region). The b-jets are tagged using the MV1 tagger for a working point with an efficiency of 80%;
- $\Delta\varphi(j_1, E_{\mathrm{T}}^{\mathrm{miss}}) > 0.4$;
- $E_{\mathrm{T}}^{\mathrm{miss}} > 80$ GeV;
- $m_{\mathrm{T}} > 60$ GeV.

The data-MC comparison before reweighting and after the application of the 4-bin reweighting for the 1 b-jet and 2 b-jet regions is presented in Figures 7.1 – 7.4. From the plots one can see, that the mismodelling does not affect the m_{T} distribution. Therefore, for the one-lepton analysis, the m_{T} variable is used to define control and validation regions (see Section 6.5.1).

7.2 Exponential reweighting

It is clear, that a correct reweighting should have a smooth distribution of weights and should not be a 4-bin step function. Since in Ref.[104] only weights in four bins are provided, some models for smoothing have been considered.

The true $p_{\mathrm{T}}(t\bar{t})$ distribution for the 1 b-jet and 2 b-jet selections, used for the reweighting of the data-MC comparison in Section 7.1, is shown in Figure 7.5. From this plot one can conclude, that in the region $p_{\mathrm{T}}(t\bar{t}) > 170$ GeV the true $p_{\mathrm{T}}(t\bar{t})$ distribution can be approximated by an exponential function. In this region the slope of the exponent does not depend on the 1 b-jet or 2 b-jet selections.

The distribution of the true $p_{\mathrm{T}}(t\bar{t})$ does not exactly follow the exponential function for the $p_{\mathrm{T}}(t\bar{t}) < 170$ GeV. There are several reasons, which may contribute to this disagreement.

One reason is the event selection itself, which applies requirements on the p_{T}, $E_{\mathrm{T}}^{\mathrm{miss}}$ and m_{T} variables. This may distort and suppress the distribution below $p_{\mathrm{T}}(t\bar{t}) < 40$ GeV.

The second lies in different acceptance and scale factors (trigger, lepton, b-tagging, ...), which are applied for the presented distributions and may create some distortion of the shape.

To understand what strategy to use for smoothing, a model for the mismodelling of the true $p_{\mathrm{T}}(t\bar{t})$ distribution has to be considered.

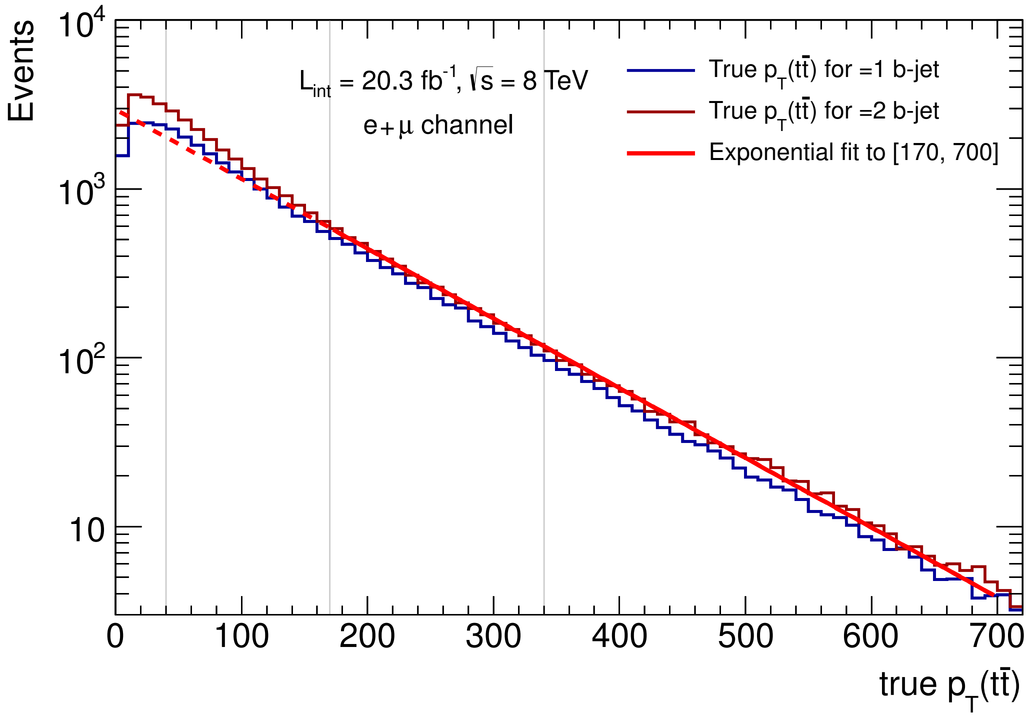

Figure 7.5: Distributions of the true $p_T(t\bar{t})$ before any reweighting is applied for the 1 b-jet and 2 b-jet selections. The 1 b-jet (2 b-jet) selection is: 1 lepton, exactly 1 b-tagged (exactly 2 b-tagged) jets, 4 jets with p_T values above 40, 25, 25, and 25 GeV, $E_T^{miss} > 80$ GeV, $m_T > 60$ GeV (for details, see Section 7.1). An exponential function is fitted to the interval $[170, 700]$ GeV.

Model of $t\bar{t}$ mismodelling

It is assumed, that with a good approximation the normalised distribution of the p_T of the $t\bar{t}$ system is modelled by a normalised exponenential function with some slope α:

$$f_\alpha(x) = \alpha \cdot e^{-\alpha x}, \qquad \int_0^{+\infty} f_\alpha(x)dx = 1. \tag{7.1}$$

It is further assumed that the generator mismodelling affects only the slope of the distribution, i.e. the correct distribution also can be described by an exponential function with a slope β. The normalised function of the generator modelling is assumed to be f_α, while the normalised true function is f_β. It is also assumed, that $\beta > \alpha$, like in the current case.

The reweighting function $w(x)$ can than be defined as:

$$w(x) = \frac{f_\beta(x)}{f_\alpha(x)} = \frac{\beta}{\alpha} \cdot e^{-\Delta\alpha \cdot x}, \qquad \Delta\alpha = \beta - \alpha. \tag{7.2}$$

Experimentally, a reweighting coefficient is measured for an interval $[p, p + \Delta p]$. The integral of $f_\alpha(x)$ for the interval is calculated as:

$$\int_p^{p+\Delta p} f_\alpha(x)dx = \alpha \cdot -\frac{1}{\alpha} \cdot e^{-\alpha \cdot x}\Big|_p^{p+\Delta p} = e^{-\alpha \cdot (p+\Delta p)} - e^{-\alpha \cdot p} = e^{-\alpha \cdot p}(e^{-\alpha \cdot \Delta p} - 1). \tag{7.3}$$

The reweighting coefficient for the interval $[p, p + \Delta p]$ is calculated as:

$$
\begin{aligned}
w(p, p+\Delta p) &= \frac{e^{-\beta\cdot p}(e^{-\beta\cdot\Delta p}-1)}{e^{-\alpha\cdot p}(e^{-\alpha\cdot\Delta p}-1)} = e^{-\Delta\alpha\cdot p}\cdot\frac{e^{-\beta\cdot\Delta p}-1}{e^{-\alpha\cdot\Delta p}-1} = \\
&= e^{-\Delta\alpha\cdot p}\cdot\left(1 + e^{-\alpha\cdot\Delta p}\cdot\frac{1-e^{-\Delta\alpha\cdot\Delta p}}{1-e^{-\alpha\cdot\Delta p}}\right).
\end{aligned}
\tag{7.4}
$$

In the limit of $\Delta p \to +\infty$, one obtains

$$
w = e^{-\Delta\alpha\cdot p}, \quad \Delta\alpha = -\frac{1}{p}\cdot\ln w, \tag{7.5}
$$

where p is the left border of the interval.

The $\Delta\alpha$ parameter is calculated using two different approaches. The first approach estimates $\Delta\alpha$ in the limit of $\Delta p \to +\infty$, where the slope variable α cancels out. Therefore, it is applicable to the fourth bin only. The second approach fits the parameters α and $\Delta\alpha$ based on the true $p_{\mathrm{T}}(t\bar{t})$ distribution and can be applied to all bins. But, to allow for a cross-check with the first approach, it is also applied only to the fourth bin. In this case the systematic uncertainty on the $\Delta\alpha$ parameter can be estimated as the difference between the two approaches.

Another advantage to use only the fourth bin is that the signal region in the tN analysis has a low fraction of events in the region $p_{\mathrm{T}} > 340$ GeV, see Section 8.5. Therefore, it is almost statistically independent with the fourth bin.

The first approach uses equation 7.5 for the fourth bin of the default reweighting. The weight is obtained to be $w_4 = 0.570 \pm 0.014$, with $p_4 = 340$ GeV and $\Delta p_4 = +\infty$. The uncertainty on w_4 is estimated as half the difference between the weights determined for the electron and muon channels. The result of this calculation is

$$
\Delta\alpha_{\mathrm{calc}} = (1.65 \pm 0.07)\cdot 10^{-3}. \tag{7.6}
$$

The second approach is based on equation 7.2, which depends on the two parameters α and $\Delta\alpha$. The slope α is estimated by fitting an exponential in the $[170, 700]$ GeV interval to the true $p_{\mathrm{T}}(t\bar{t})$ distribution for the 2 b-jet selection (see Figure 7.5). The result of the fit is

$$
\alpha = (9.51 \pm 0.12)\cdot 10^{-3}. \tag{7.7}
$$

The slope α is used to fix one parameter for the reweighting function $w(x)$. The second parameter $\Delta\alpha$ is estimated by fitting the integral of the reweighted Monte Carlo distribution in the interval $[340, 700]$ GeV to the experimentally measured value w_4. The fit is performed using the 2 b-jet selection. The result of the fit is

$$
\Delta\alpha_{\mathrm{fit}} = (1.78 \pm 0.08)\cdot 10^{-3}. \tag{7.8}
$$

In general, the 1 b-jet region can also be included in the fit, but to avoid any possible distortion from events where second b-tagged jet is missing, only the 2 b-jet region is used to determine the parameters.

Both results are consistent, but the second approach may account for a non-exponentiality of the true $p_{\mathrm{T}}(t\bar{t})$ distribution, since it is obtained from Monte Carlo. Therefore, the results from the second approach are used. To account for differences between these two approaches, the difference between the two fits is assigned as a systematic uncertainty. The total uncertainty on $\Delta\alpha$ is estimated by summing in quadrature the statistical and systematic uncertainties. Finally, for the exponential reweighting the following parameters are used:

$$\alpha = (9.51 \pm 0.12) \cdot 10^{-3}, \quad \Delta\alpha = (1.78 \pm 0.15) \cdot 10^{-3}. \tag{7.9}$$

The reweighted distributions, based on the exponential reweighting approach for the 1 b-jet and 2 b-jet selection (see Section 7.1 for selection details) are shown in Figures 7.6 and 7.7. More data-MC comparisons after the application of the exponential reweighting for specific variables of the tN analysis are presented in Section 8.5.

7.3 Reweighting comparison

For the comparison to the exponential reweighting approach, the following two smoothing strategies are considered:

– **The "left border" smoothing**
  It is assumed that $\Delta p_i \gg 1$ and using equation 7.5 one can get

$$w_i = e^{-\Delta\alpha \cdot p_i}. \tag{7.10}$$

  The reweighting function $w(x)$ from equation 7.2 can be defined as

$$w(p_i) = \frac{\beta}{\alpha} \cdot e^{-\Delta\alpha \cdot p_i} = \frac{\alpha + \Delta\alpha}{\alpha} \cdot w_i, \tag{7.11}$$

  i.e. w_i is proportional to $w(p_i)$. Therefore the $w(x)$ reweighting function, up to a scale coefficient, can be reconstructed by fitting an exponential function to these points. If the background is normalised in the control region, which is the case for the $t\bar{t}$ process, the scale β/α can be neglected. The benefit of this approach is that it does not need to estimate the α parameter.

  Formally this approach can be formulated such that the bin weights w_i are determined at the left border of each bin interval i.e. $w(p_i) = w_i$. The normalisation of the process is not estimated by this approach and has to be done separately. In the current case, the β/α normalisation coefficient can be estimated to be 1.19 with an uncertainty of $\pm 6\%$ within the $[0, 700]$ GeV interval.

– **The "mean value" smoothing**
  For this approach it is assumed that each weight w_i is determined using the mean value $\bar{p}_i$ of the true $p_{\mathrm{T}}(t\bar{t})$ distribution for the i-th interval, i.e. $w(\bar{p}_i) = w_i$. The $\bar{p}_i$ is calculated for the 2 b-jet selection of the true $p_{\mathrm{T}}(t\bar{t})$ distribution, as shown in Figure 7.5. For smoothing, an exponential function is fitted to these points.

The comparison of the different smoothing strategies is shown in Figure 7.8. The 4-bin re-

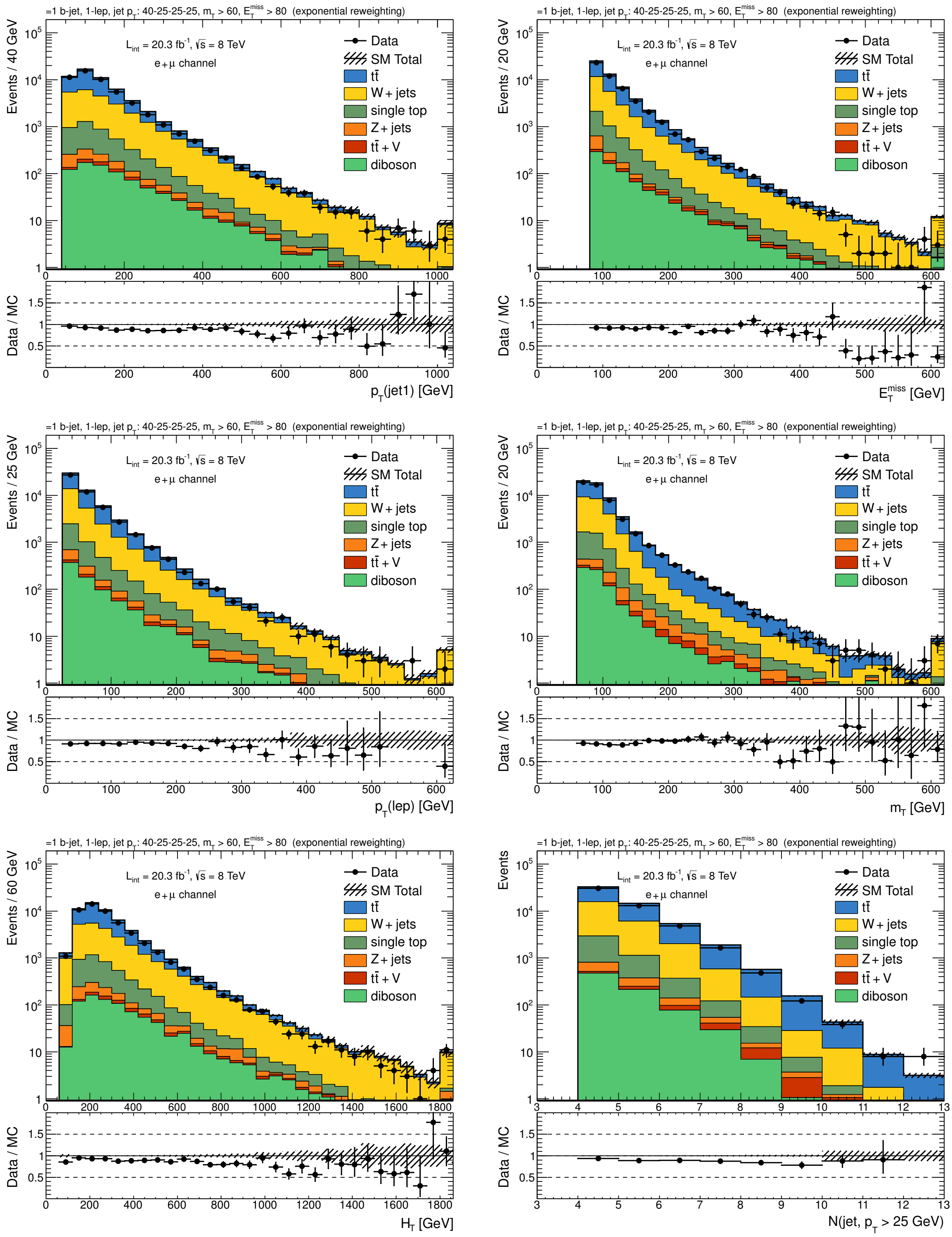

Figure 7.6: The data-MC comparisons for the $t\bar{t}$ reweighting based on the exponential approach for the variables: p_{T} of the leading jet and the $E_{\mathrm{T}}^{\mathrm{miss}}$ (top), p_{T} of the lepton and the m_{T} (middle), and the H_{T} and a number of selected jets N_{jet} (bottom). The selection: 1 lepton, exactly 1 b-tagged jet, 4 jets with p_{T} values above 40, 25, 25, and 25 GeV, $E_{\mathrm{T}}^{\mathrm{miss}} > 80$ GeV, $m_{\mathrm{T}} > 60$ GeV (for details, see the text). The $t\bar{t}$ and W+jets production are normalised to the Monte Carlo cross sections. The error bands include only the Monte Carlo statistical uncertainties.

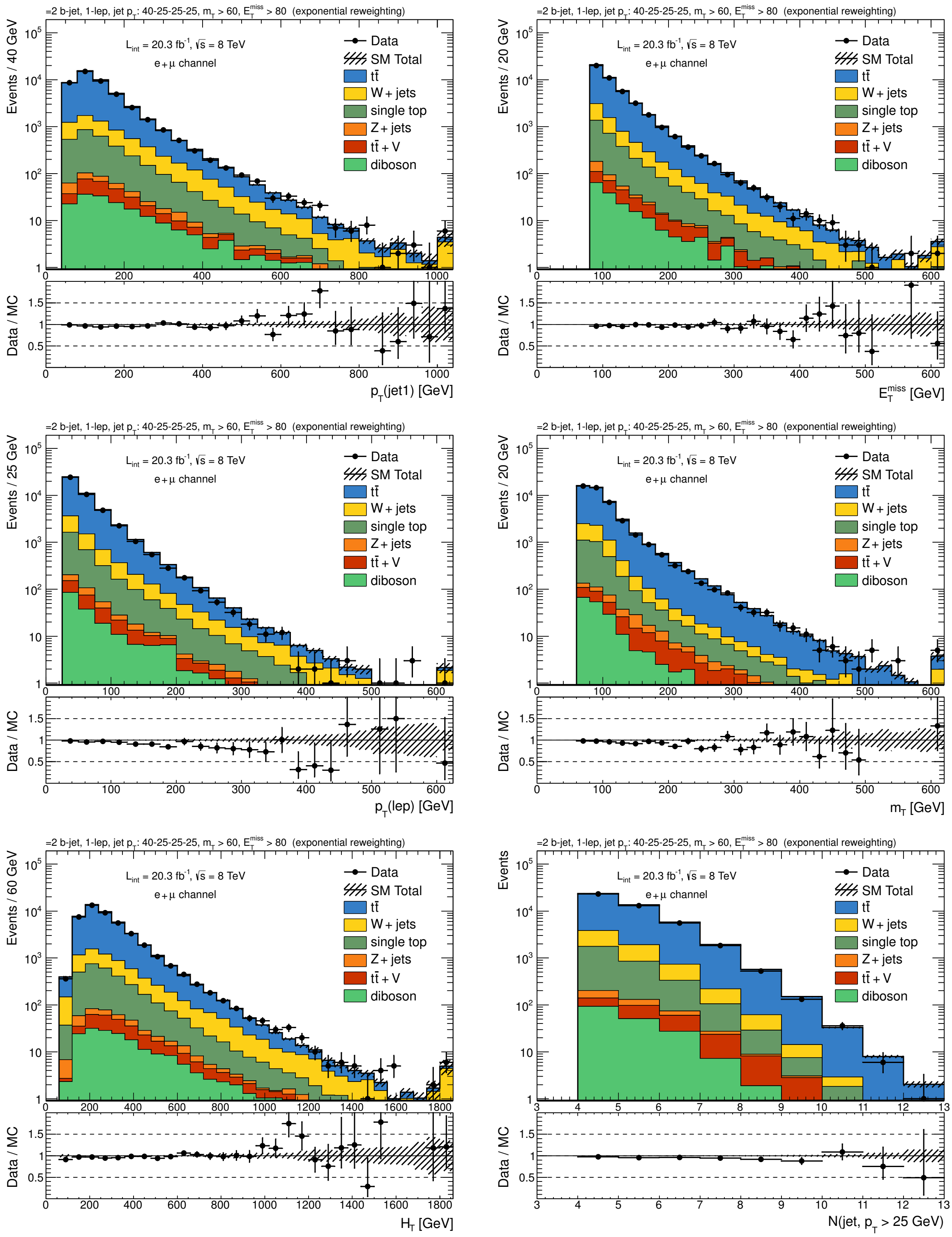

Figure 7.7: The data-MC comparisons for the $t\bar{t}$ reweighting based on the exponential approach for the variables: p_{T} of the leading jet and the $E_{\mathrm{T}}^{\mathrm{miss}}$ (top), p_{T} of the lepton and the m_{T} (middle), and the H_{T} and a number of selected jets N_{jet} (bottom). The selection: 1 lepton, exactly 2 b-tagged jets, 4 jets with p_{T} values above 40, 25, 25, and 25 GeV, $E_{\mathrm{T}}^{\mathrm{miss}} > 80$ GeV, $m_{\mathrm{T}} > 60$ GeV (for details, see the text). The $t\bar{t}$ and $W+$jets production are normalised to the Monte Carlo cross sections. The error bands include only the Monte Carlo statistical uncertainties.

weighting based on the exponential correction method (dashed red line) and the "left border" reweighting – scaled up by a factor 1.19 (dashed green line) are also shown on the same figure. One can see that with a good approximation the "left border" reweighting is proportional to the exponential reweighting. Using the "left border" smoothing, the final result is the same as for the exponential reweighting, but the normalisation of the $t\bar{t}$ process is 1.19 times higher. From the plot it is also clear, that the "mean value" approach gives a different slope.

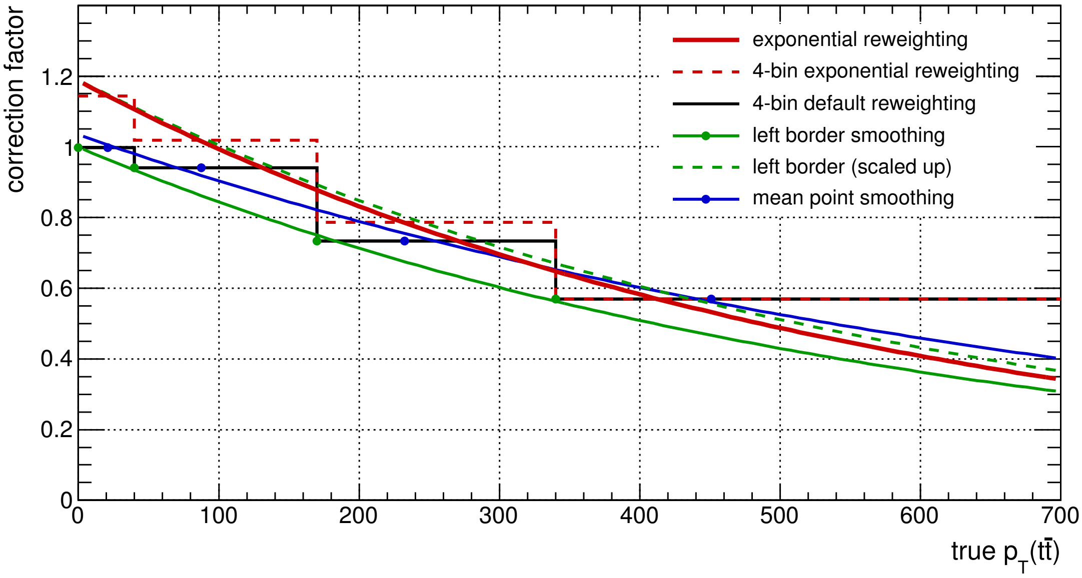

Figure 7.8: Comparison of the different reweightings. The exponential reweighting based on the exponential correction method (red line), the 4-bin reweighting based on the exponential correction method (dashed red line), the default 4-bin reweighting used in the one-lepton analysis (black line), the "left border" smoothing, assuming the w_i weight in the left border of the i-th bin with the fitted exponential function (green line), the "left border" smoothing scaled up for the comparison to the exponential reweighting (dashed green line), the "mean point" smoothing, assuming the w_i weight in the mean point of the p_T distribution of the i-th bin (blue line).

A comparison between the default 4-bin reweighting and the smooth exponential reweighting is presented in Figure 7.9 for the 2 b-jet selection. The exponential reweighting shows an improvement of the normalisation, as well as some improvement in the low p_T region for the H_T and the leading jet p_T distributions.

The underestimation of the data at low H_T, after the 4-bin reweighting points to incorrect weights for the first bin. To improve the normalisation for the 4-bin reweighting, the w_1 reweighting coefficient has to be increased at least by 8%. The N_{jets} distribution shows that the exponential reweighting overweights the $t\bar{t}$ process, but just by about 2%.

The following properties of the exponential reweighting have to be mentioned:

– The important difference between the 4-bin and the exponential reweighting, is that the α slope is measured based on Monte Carlo modelling only, while the $\Delta\alpha$ difference is calculated from w_4 – the fourth bin of the default reweighting for true $p_T(t\bar{t}) > 340$ GeV. The reweighting coefficients for the $p_T < 340$ GeV come from the exponential reweighting model itself.

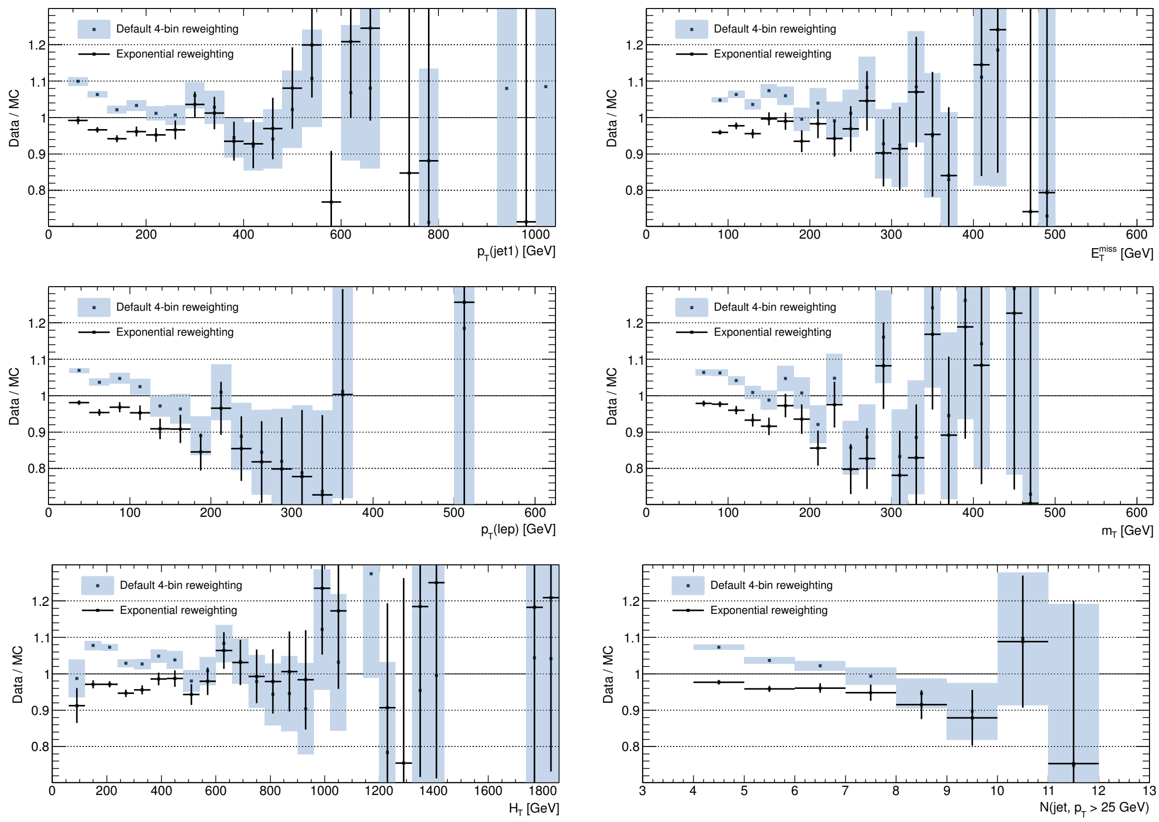

Figure 7.9: The data to Monte Carlo ratio for various kinematical variables for the default 4-bin reweighting and the exponential reweighting for the variables: p_{T} of the leading jet and the $E_{\mathrm{T}}^{\mathrm{miss}}$ (top), p_{T} of the lepton and the m_{T} (middle), and the H_{T} and a number of selected jets N_{jets} (bottom). The selection: 1 lepton, exactly 2 b-tagged jets, 4 jets with p_{T} values above 40, 25, 25, and 25 GeV, $E_{\mathrm{T}}^{\mathrm{miss}} > 80$ GeV, $m_{\mathrm{T}} > 60$ GeV (for details, see Section 7.1). The $t\bar{t}$ and W+jets production are normalised to the Monte Carlo cross sections. The error bands include only the Monte Carlo statistical uncertainties.

– Only one parameter w_4 is used to correct both the slope and the normalisation for the $t\bar{t}$ process. For both reweightings the $t\bar{t}$ and the W+jets processes are normalised to the Monte Carlo cross section. It is therefore plausible, that the proposed model of exponential mismodelling is applicable for this case.

– The exponential reweighting provides a better estimation of the normalisation for the 2 b-jet region, but a worse one for the 1 b-jet region. This can be explained as mismodelling of the W+jets process which is not reweighted. The exponential reweighting is applied to the $t\bar{t}$ process. Therefore, for the 2 b-jet region, where the $t\bar{t}$ background is dominant, this approach provides a better normalisation. One can see from Figure 7.8, that the improvement of the normalisation for the exponential approach comes from the difference between the reweighting coefficients in the low p_{T} region.

– For the 2 b-jet selection, after application of the exponential reweighting approach the slopes for the H_{T} and jet multiplicity N_{jets} distributions are improved.

CHAPTER 8

Searches for the top squark at $\sqrt{s} = 8$ TeV, $\tilde{t}_1 \rightarrow t\tilde{\chi}^0_1$, $\Delta m(\tilde{t}_1, \tilde{\chi}^0_1) \approx m(t)$

In this chapter the search for the top-squark pair production in the $\tilde{t}_1 \rightarrow t\tilde{\chi}^0_1$ decay mode is presented. It is assumed, that decay channel has a branching ratio of 100%, and that the top quark decays either on- or off-shell. A Feynman diagram for the corresponding semileptonic decay is shown in Figure 8.1. One can see that the decay mimics the semileptonic $t\bar{t}$ decay,

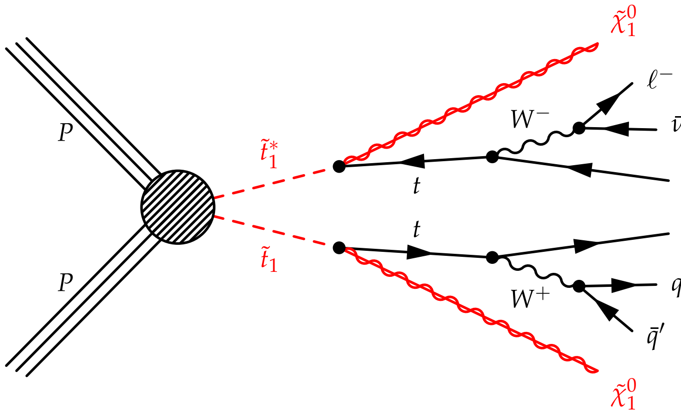

Figure 8.1: Feynman diagram for the $\tilde{t}_1 \rightarrow t\tilde{\chi}^0_1$ semileptonic decay channel.

especially for signal models with $\Delta m(\tilde{t}_1, t) \approx m(\tilde{\chi}^0_1)$, where both neutralinos are soft and have a small contribution in the missing transverse momentum $E_{\mathrm{T}}^{\mathrm{miss}}$.

8.1 Summary of results on top-squark searches

A summary of the ATLAS searches for top-squark pair production in the $(\tilde{t}_1, \tilde{\chi}^0_1)$ mass plane, based on an integrated luminosity of 20.3 fb^{-1} of data recorded at $\sqrt{s} = 8$ TeV, is shown in

Figure 8.2. The results of corresponding searches by the CMS experiment for an integrated luminosity of 19.5 fb^{-1} of data recorded at $\sqrt{s} = 8$ TeV are presented in Figure 8.3.

The existing ATLAS and CMS analyses leave a gap along the mass splitting $\Delta m(\tilde{t}_1, t) = m(\tilde{\chi}_1^0)$ line, the so-called "tN diagonal" region. Near the diagonal, where $\Delta m(\tilde{t}_1, t) \approx m(\tilde{\chi}_1^0)$, two decay modes are present: on- and off-shell top-quark decays (below and above the diagonal), which correspond to $\tilde{t}_1 \to t\tilde{\chi}_1^0$ and $\tilde{t}_1 \to bW\tilde{\chi}_1^0$ (3-body decay), respectively. In this chapter, an analysis covering the gap in the tN diagonal region for top-squark masses of 200–300 GeV is

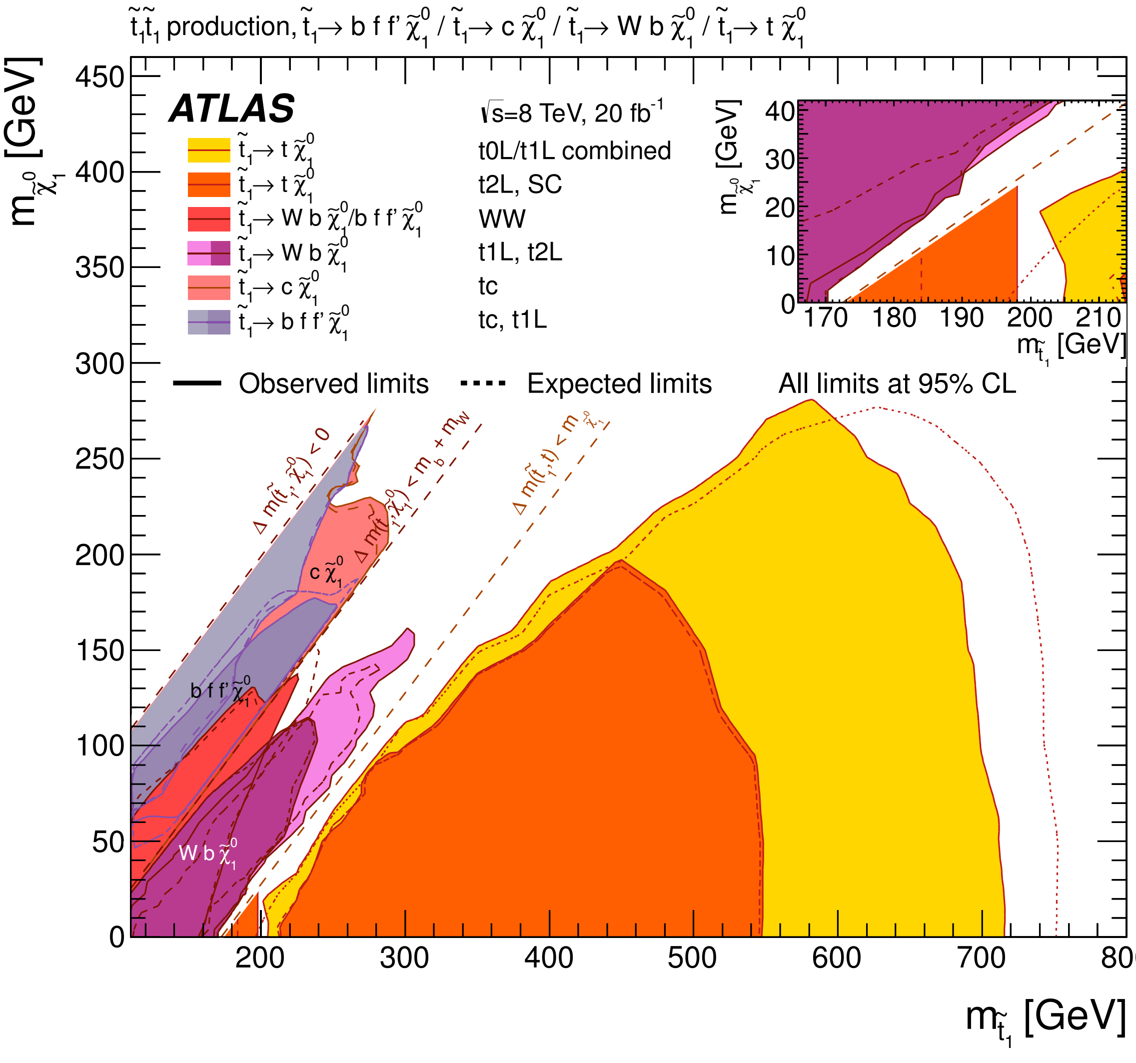

Figure 8.2: A summary of the ATLAS searches for top-squark pair production based on $\mathcal{L}_{\text{int}} = 20.3$ fb^{-1} of data at $\sqrt{s} = 8$ TeV. Exclusion limits are shown for the $(\tilde{t}_1, \tilde{\chi}_1^0)$ mass plane at 95% CL. The dashed and solid lines correspond to the expected and observed limits. The limits include all uncertainties except the uncertainty on the signal cross section. Four different decay modes are considered, each with $\mathcal{BR} = 100\%$: $\tilde{t}_1 \to t\tilde{\chi}_1^0$, $\tilde{t}_1 \to bW\tilde{\chi}_1^0$ (3-body decay), $\tilde{t}_1 \to c\tilde{\chi}_1^0$ and $\tilde{t}_1 \to bff'\tilde{\chi}_1^0$ (4-body decay). The plot corresponds to the simplified decay scenarios and is published in Ref. [112].

presented. This is the first time that a specific analysis is designed to cover this difficult region of phase space.

Two dedicated ATLAS analyses cover the low corner of the diagonal region. An analysis based on $t\bar{t}$ cross-section measurements excludes top-squark masses up to 177 GeV at 95% CL [121], while a spin correlation analysis improves the previous result excluding at 95% CL top-squark masses up to 191 GeV [122].

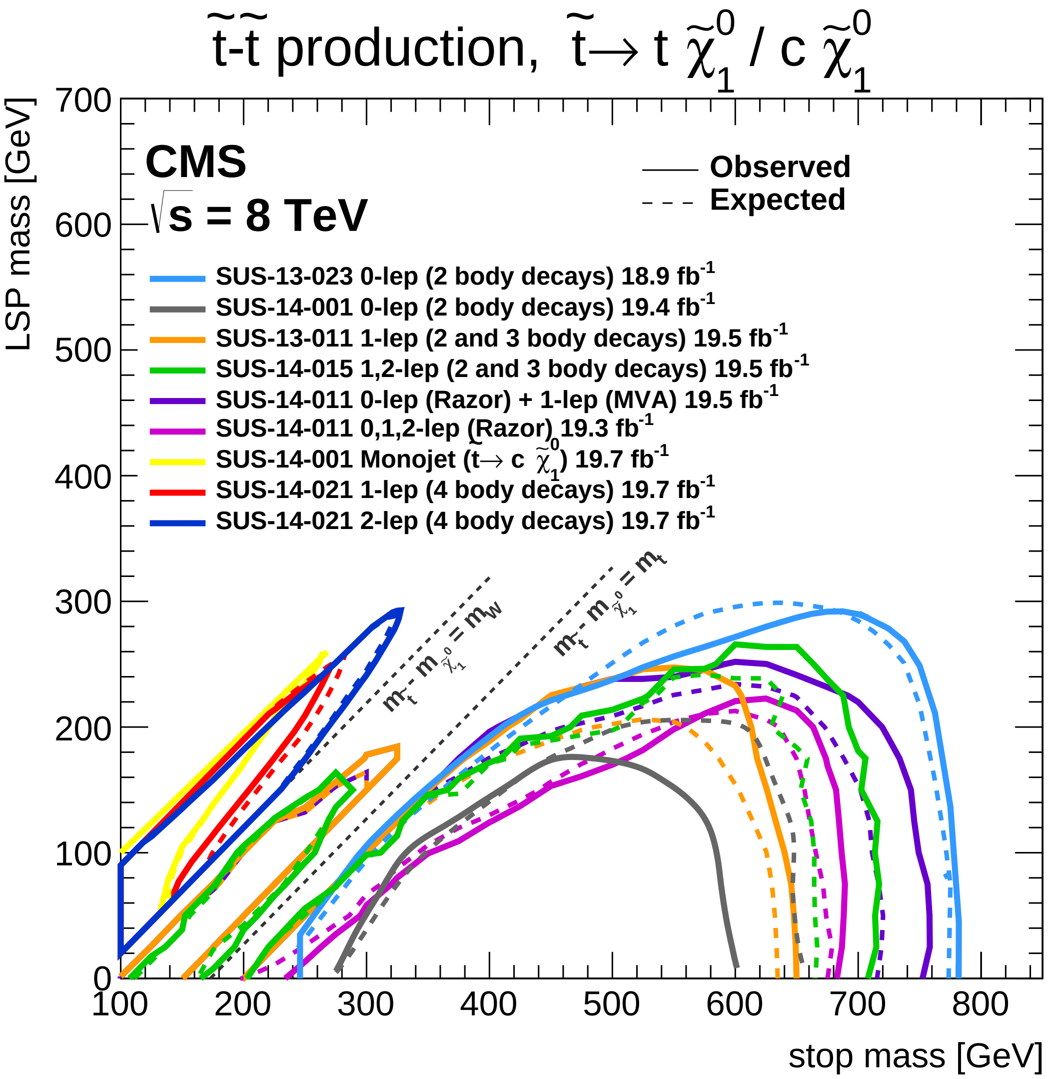

Figure 8.3: A summary of the CMS searches for top-squark pair production based on $\mathcal{L}_{\text{int}} = 19.5$ fb^{-1} of data at $\sqrt{s} = 8$ TeV. Exclusion limits are shown for the $(\tilde{t}_1, \tilde{\chi}_1^0)$ mass plane at 95% CL. The dashed and solid lines correspond to the expected and observed limits. Four different decay modes are considered, each with $\mathcal{BR} = 100\%$: $\tilde{t}_1 \rightarrow t\tilde{\chi}_1^0$, $\tilde{t}_1 \rightarrow bW\tilde{\chi}_1^0$ (3-body decay), $\tilde{t}_1 \rightarrow c\tilde{\chi}_1^0$ and $\tilde{t}_1 \rightarrow bff'\tilde{\chi}_1^0$ (4-body decay). The results correspond to simplified decay scenarios and are published in Refs. [115, 116, 117, 118, 119, 120].

The main challenge in the diagonal region is that in the case of an on-shell top decay, due to the small mass difference $\Delta m = m(\tilde{t}_1) - m(t) - m(\tilde{\chi}_1^0)$ (less than 10 GeV) both neutralinos have low p_{T} and are mainly back-to-back in the transverse plane. Therefore, their total contribution to the $E_{\mathrm{T}}^{\mathrm{miss}}$ is small. This makes signal events very similar to $t\bar{t}$ background events.

Previous ATLAS analyses which target the diagonal region above 200 GeV are hitting problems not only due to a low number of signal events. Some of them do not have enough separation power to reach the diagonal, even assuming an infinite integrated luminosity.

- For the zero-lepton top-squark searches the main constraint is the trigger. Since there is no neutrino in the event and the neutralinos have low p_{T} due to the small Δm, the acceptance of the missing transverse energy trigger is low.
- The one-lepton analysis targeting the diagonal uses a shape fit approach. For the signal model $m(\tilde{t}_1, \tilde{\chi}_1^0) = (350, 150)$ GeV, where $\Delta m \approx 27$ GeV, for each bin the signal-to-background ratio is less than 22%. For this signal region the $t\bar{t}$ background is dominant with a total systematic uncertainty of about $\pm 15\%$. Taking into account, that for smaller Δm the signal acceptance decreases, such an analysis will not be able to reach the diagonal even for a higher integrated luminosity.
- For the two-lepton analysis both W-bosons decay leptonically creating two neutrinos, which contribute to the $E_{\mathrm{T}}^{\mathrm{miss}}$ more than the two neutralinos, which are very soft near the diagonal and mainly back-to-back. Variables used in the two-lepton multivariate analysis become quite similar for the signal and the $t\bar{t}$ background. This makes it challenging to get good separation power to suppress the $t\bar{t}$ background.
- For the $t\bar{t}$ cross-section measurement, an increase of the integrated luminosity will not reach far up along the diagonal, since the top-squark pair production cross section decreases, while the precision of the cross-section measurement is driven by systematic uncertainties.
- The spin-correlation approach may hit the same problem, since it tries to observe a correlation on top of the $t\bar{t}$ background process.

Another challenge are signal points exactly on the diagonal, where on- and off-shell top quarks in the top-squark decay are equally possible. Theoretical predictions of how the branching ratio changes between on- and off-shell decays when crossing the diagonal require additional studies. Therefore, for the current exclusion (see Figure 8.2) in the low mass corner only a region 1–2 GeV below the diagonal is considered excluded, to be sure that the $\mathcal{BR}(\tilde{t}_1 \rightarrow t\tilde{\chi}_1^0)$ is close to 100%.

In general, having two different analyses for on- and off-shell decays raises the problem of a proper modelling of the relative $\mathcal{BR}$ for the process. The ideal would be to have one analysis, which is sensitive to both decay modes. In such a case it is not necessary to have an exact modelling of the relative $\mathcal{BR}$. The decay mode for which the analysis is less sensitive will drive the exclusion. In the Section 8.6 it is shown, that the analysis presented fulfils this requirement and the most challenging scenario appears to be the $\tilde{t}_1 \rightarrow t\tilde{\chi}_1^0$ on-shell decay mode.

8.2 Signal samples

Signal samples for the $\tilde{t}_1 \to t\tilde{\chi}_1^0$ decay mode are generated with HERWIG++ [34]. Detector effects are modelled with the ATLAS fast simulation software ATLFAST-II [85]. Each signal sample can be represented as a point in the $(\tilde{t}_1, \tilde{\chi}_1^0)$ mass plane. In the following, the $m(\tilde{t}_1, \tilde{\chi}_1^0)$ refers to $(m_{\tilde{t}_1}, m_{\tilde{\chi}_1^0})$, and the double (m_1, m_2) refers to the signal model with $m(\tilde{t}_1) = m_1$ and $m(\tilde{\chi}_1^0) = m_2$, where masses are given in GeV.

The list of the signal samples used for the $\tilde{t}_1 \to t\tilde{\chi}_1^0$ analysis for $\sqrt{s} = 8$ TeV is shown in Table 8.1.

Grid	Sample ID	Name	Filter	Generator
tN	118494–118495	Herwigpp_UEEE3_CTEQ6L1_Tt_TXXX_LYYY	no filter	HERWIG++
	127834–127850	Herwigpp_UEEE3_CTEQ6L1_Tt_TXXX_LYYY	no filter	HERWIG++
	144208–144213	Herwigpp_UEEE3_CTEQ6L1_Tt_TXXX_LYYY	no filter	HERWIG++
	164241–164246	Herwigpp_UEEE3_CTEQ6L1_Tt_TXXX_LYYY	no filter	HERWIG++
	164646–164647	Herwigpp_UEEE3_CTEQ6L1_Tt_TXXX_LYYY	no filter	HERWIG++
	179570–179577	Herwigpp_UEEE3_CTEQ6L1_Tt_TXXX_LYYY_noAllHad	1-lepton	HERWIG++
	205196–205202	Herwigpp_UEEE3_CTEQ6L1_Tt_TXXX_LYYY_Lepton10	1-lepton	HERWIG++
bWN	183557–183584	Herwigpp_UEEE3_CTEQ6L1_Tt_bWN_tXXX_nYYY_Lepton20MET60	1-lepton	HERWIG++
	183951–183954	Herwigpp_UEEE3_CTEQ6L1_Tt_bWN_tXXX_nYYY_Lepton20orMET60	1-lepton	HERWIG++
	183955–183957	Herwigpp_UEEE3_CTEQ6L1_Tt_bWN_tXXX_nYYY_MET150	no filter	HERWIG++

Table 8.1: List of signal samples used for the $\tilde{t}_1 \to t\tilde{\chi}_1^0$ analysis (on- and off-shell decay modes) of data collected at $\sqrt{s} = 8$ TeV.

To avoid statistical fluctuations during the analysis optimisation, especially if one wants to use a multivariate approach, signal samples with a high number of events are required. For this reason, along the diagonal $\Delta m(\tilde{t}_1, \tilde{\chi}_1^0) = 175$ GeV extra samples with a large number of events were privately produced with HERWIG++. Overall 10 M events after a 1-lepton filter (filter efficiency ≈ 0.57) were generated. The list of samples of simulated signal events is shown in Table 8.2.

$m(\tilde{t}_1, \tilde{\chi}_1^0)$ [GeV]	Events	Filter	Generator
(210, 35)	2 M	1-lepton	HERWIG++
(230, 55)	2 M	1-lepton	HERWIG++
(240, 65)	1 M	1-lepton	HERWIG++
(250, 75)	2 M	1-lepton	HERWIG++
(260, 85)	1 M	1-lepton	HERWIG++
(270, 95)	2 M	1-lepton	HERWIG++

Table 8.2: Privately generated signal samples for the tN diagonal region with a large number of events.

Additionally, to estimate ISR/FSR signal model uncertainties, samples were generated privately on particle level with a large number of events. The ISR/FSR variations were generated for the $m(\tilde{t}_1, \tilde{\chi}_1^0) = (190, 15)$, $(210, 35)$ and $(230, 55)$ GeV signal models.

8.3 Kinematics on the diagonal

In this section, the kinematical properties of signal models exactly on the diagonal are discussed, under the assumption, that both top squarks decay to an on-shell top quark via the $\tilde{t}_1 \to t\tilde{\chi}_1^0$ decay mode. In this section p^μ refers to a four-momentum, while p_T always refers to a vector in the transverse plane. Furthermore, to improve the readability, the following notations are used:

$$p^\mu(X_1 + \cdots + X_n) = p^\mu(X_1) + \cdots + p^\mu(X_n) \tag{8.1}$$

and

$$p_\mathrm{T}(X_1 + \cdots + X_n) = p_\mathrm{T}(X_1) + \cdots + p_\mathrm{T}(X_n), \tag{8.2}$$

where $X_1, \ldots, X_n$ are arbitrary particles.

8.3.1 Neutralino reconstruction

Consider a top squark in its rest frame for a signal model exactly on the diagonal, where $\Delta m(\tilde{t}_1, t) = m(\tilde{\chi}_1^0)$. In the case of an on-shell top-quark decay, there is no energy to give momentum to the decay products, therefore both the t and $\tilde{\chi}_1^0$ will be produced at rest and the relation between the four-momenta can be presented as:

$$p^\mu_{\tilde{t}_1} = p^\mu_t + p^\mu_{\tilde{\chi}_1^0}, \quad p^\mu_t = \frac{m_t}{m_{\tilde{t}_1}} \cdot p^\mu_{\tilde{t}_1}, \quad p^\mu_{\tilde{\chi}_1^0} = \frac{m_{\tilde{\chi}_1^0}}{m_{\tilde{t}_1}} \cdot p^\mu_{\tilde{t}_1}, \tag{8.3}$$

where $p^\mu_{\tilde{t}_1}$, p^μ_t and $p^\mu_{\tilde{\chi}_1^0}$ are the four-momenta of $\tilde{t}_1$, t and $\tilde{\chi}_1^0$, respectively.

Since the momenta are collinear in the rest frame, this will hold in any boosted frame too. From these equations it follows, that on the diagonal, if the four-momentum of any particle is known, the other one can be calculated by a corresponding scaling. In particular, the four-momentum of the neutralino can be calculated from the four-momentum of the top squark:

$$p^\mu_{\tilde{\chi}_1^0} = \alpha p^\mu_{\tilde{t}_1}, \quad \alpha = \frac{m_{\tilde{\chi}_1^0}}{m_{\tilde{t}_1}}, \tag{8.4}$$

or in case of the top quark

$$p^\mu_{\tilde{\chi}_1^0} = \frac{m_{\tilde{\chi}_1^0}}{m_t} p^\mu_t = \frac{\alpha}{1-\alpha} p^\mu_t. \tag{8.5}$$

As a consequence of this relation, if the neutralino is nearly massless, after the decay it gets a very small momentum and therefore it does not contribute much to the $E_\mathrm{T}^\mathrm{miss}$.

8.3.2 Neutrino p_T reconstruction

The next step is to reconstruct the p_T of the neutrino ν from the semileptonic top-squark decay. Since for signal events not only the neutrino contributes to the $E_\mathrm{T}^\mathrm{miss}$, but also both neutralinos, in general, the reconstruction of the neutrino p_T is not possible. But in the case of the diagonal region one can use the collinearity of the neutralinos to the $t\bar{t}$ system.

In the following, the particles involved in the hadronic and leptonic decay chain, are labeled with "had" and "lep", respectively.

The following assignments are used:

$$\begin{aligned} &\tilde{t}_{1\mathrm{had}} \to t_{\mathrm{had}} + \tilde{\chi}^0_{1\mathrm{had}}, \qquad && t_{\mathrm{had}} \to b_{\mathrm{had}} + W_{\mathrm{had}}, \qquad && W_{\mathrm{had}} \to q_1 + q_2, \\ &\tilde{t}_{1\mathrm{lep}} \to t_{\mathrm{lep}} + \tilde{\chi}^0_{1\mathrm{lep}}, && t_{\mathrm{lep}} \to b_{\mathrm{lep}} + W_{\mathrm{lep}}, && W_{\mathrm{lep}} \to \ell + \nu. \end{aligned} \tag{8.6}$$

where:

b_{had} and b_{lep} are b-tagged jets;

q_1 and q_2 are light jets from the hadronic decay of the W_{had};

ℓ are ν are the lepton and neutrino from the leptonic decay of the W_{lep}.

In these notations, the missing transverse momentum can be defined as:

$$p_{\mathrm{T}}^{\mathrm{miss}} = p_{\mathrm{T}}(\tilde{\chi}^0_{1\mathrm{had}}) + p_{\mathrm{T}}(\tilde{\chi}^0_{1\mathrm{lep}}) + p_{\mathrm{T}}(\nu), \tag{8.7}$$

where p_{T} is considered as a two-dimensional vector.

Taking into account that each neutralino is collinear to the corresponding top squark, the above equation can be rewritten as:

$$p_{\mathrm{T}}^{\mathrm{miss}} = \alpha p_{\mathrm{T}}(\tilde{t}_{1\mathrm{had}}) + \alpha p_{\mathrm{T}}(\tilde{t}_{1\mathrm{lep}}) + p_{\mathrm{T}}(\nu) = \alpha p_{\mathrm{T}}(\tilde{t}_1\tilde{t}_1^*) + p_{\mathrm{T}}(\nu), \tag{8.8}$$

where

$$\tilde{t}_1\tilde{t}_1^* = \tilde{t}_{1\mathrm{had}} + \tilde{t}_{1\mathrm{lep}}. \tag{8.9}$$

The p_{T} of the neutrino can be calculated as:

$$p_{\mathrm{T}}(\nu) = p_{\mathrm{T}}^{\mathrm{miss}} - \alpha p_{\mathrm{T}}(\tilde{t}_1\tilde{t}_1^*). \tag{8.10}$$

Assuming, that the $t\bar{t}$ system is reconstructed from the semileptonic decay

$$p^{\mu}(t\bar{t}) = p^{\mu}(t_{\mathrm{had}} + t_{\mathrm{lep}}) = p^{\mu}(b_{\mathrm{had}} + b_{\mathrm{lep}} + q_1 + q_2 + \ell + \nu), \tag{8.11}$$

and using the equations 8.5 and 8.7 one obtains

$$p_{\mathrm{T}}^{\mathrm{miss}} = \frac{\alpha}{1-\alpha} p_{\mathrm{T}}(t\bar{t}) + p_{\mathrm{T}}(\nu). \tag{8.12}$$

One can split off the neutrino term

$$p_{\mathrm{T}}^{\mathrm{miss}} = \frac{\alpha}{1-\alpha} p_{\mathrm{T}}(b_{\mathrm{had}} + b_{\mathrm{lep}} + q_1 + q_2 + \ell) + \frac{\alpha}{1-\alpha} p_{\mathrm{T}}(\nu) + p_{\mathrm{T}}(\nu). \tag{8.13}$$

From the above equation, the p_{T} of the neutrino for a signal event can be calculated as:

$$p_{\mathrm{T}}(\nu) = (1-\alpha) p_{\mathrm{T}}^{\mathrm{miss}} - \alpha p_{\mathrm{T}}(b_{\mathrm{had}} + b_{\mathrm{lep}} + q_1 + q_2 + \ell). \tag{8.14}$$

8.3.3 Recoil against a jet

An important difference between signal and $t\bar{t}$ background events is the existence of two neutralinos, which can contribute to the $E_{\mathrm{T}}^{\mathrm{miss}}$ and improve the signal separation. The main challenge is, that due to the small mass splitting $\Delta(\tilde{t}_1, t)$ they are mainly back-to-back in the transverse plane and therefore compensate each other.

From equation 8.8 one can see, that the p_{T} of the $\tilde{t}_1\tilde{t}_1^*$ system directly contributes to the $p_{\mathrm{T}}^{\mathrm{miss}}$. Therefore, by boosting the $\tilde{t}_1\tilde{t}_1^*$ system, one can increase the $E_{\mathrm{T}}^{\mathrm{miss}}$, while for the $t\bar{t}$ system, the boost will only indirectly affect the $E_{\mathrm{T}}^{\mathrm{miss}}$ via the neutrino ν.

It is important to mention, that only initial state radiation (ISR) affects the $p_{\mathrm{T}}^{\mathrm{miss}}$. Any radiation of objects after the $\tilde{t}_1 \to t\tilde{\chi}_1^0$ decay does not affect the neutralinos. Therefore, for the analysis, the presence of a hard ISR jet is very important.

The calculation of the $p_{\mathrm{T}}(\nu)$ for signal events plays an important role in the analysis. The approach for the $p_{\mathrm{T}}(\nu)$ calculation, presented in Section 8.3.2, has some disadvantages:

- It is not always clear, which light jets should be taken to reconstruct the hadronic W_{had}. Putting aside, that one can incorrectly select one of the light jets due to combinatorial freedom, one of the light jets may also be missing in the event due to having a p_{T} below the detector acceptance.
- Apart from the $p_{\mathrm{T}}^{\mathrm{miss}}$, which can be the main source of the uncertainty for $p_{\mathrm{T}}(\nu)$, the calculation includes four different jets and one lepton. Each of them add some uncertainty to the $p_{\mathrm{T}}(\nu)$ reconstruction.
- An additional disadvantage can be a final state radiation (FSR). Any jet may radiate for example a gluon, which will not be included in the reconstruction and will produce an additional source of uncertainty for the $p_{\mathrm{T}}(\nu)$.

To improve the $p_{\mathrm{T}}(\nu)$ reconstruction, one can assume, that the boost of the $\tilde{t}_1\tilde{t}_1^*$ system is mainly due to a hard ISR jet (j_{rec}), which recoils against the $\tilde{t}_1\tilde{t}_1^*$ system. The assumption, that only one recoil jet is produced with the p_{T} opposite to the $p_{\mathrm{T}}(\tilde{t}_1\tilde{t}_1^*)$ yields

$$p_{\mathrm{T}}(\tilde{t}_1\tilde{t}_1^*) = -p_{\mathrm{T}}(j_{\mathrm{rec}}). \tag{8.15}$$

Under this assumtion, one can calculate the $p_{\mathrm{T}}(\nu)$ as:

$$p_{\mathrm{T}}(\nu) = p_{\mathrm{T}}^{\mathrm{miss}} - \alpha p_{\mathrm{T}}(\tilde{t}_1\tilde{t}_1^*) = p_{\mathrm{T}}^{\mathrm{miss}} + \alpha p_{\mathrm{T}}(j_{\mathrm{rec}}). \tag{8.16}$$

8.3.4 The m_T^{stop} variable

Based on the calculated $p_{\mathrm{T}}(\nu)$, one can reconstruct the variable $m_{\mathrm{T}}(\ell, p_{\mathrm{T}}(\nu))$, which is the transverse mass of the leptonic W for a signal event. Taking into account, that the reconstruction of $p_{\mathrm{T}}(\nu)$ significantly depends on the top-squark mass $m(\tilde{t}_1)$, it is denoted as $p_{\mathrm{T}}^{m(\tilde{t}_1)}(\nu)$, while the corresponding m_{T} is denoted as $m_{\mathrm{T}}^{m(\tilde{t}_1)}$.

One of the important variables used in the analysis is the difference between the m_{T} variable calculated under the assumption of $t\bar{t}$ or $\tilde{t}_1\tilde{t}_1^*$ semileptonic decays. The variable is defined as:

$$\Delta m_{\mathrm{T}}^{m(\tilde{t}_1)} = m_{\mathrm{T}} - m_{\mathrm{T}}^{m(\tilde{t}_1)} = m_{\mathrm{T}}(\ell, p_{\mathrm{T}}^{\mathrm{miss}}) - m_{\mathrm{T}}(\ell, p_{\mathrm{T}}^{m(\tilde{t}_1)}(\nu)). \tag{8.17}$$

As an example, for $m(\tilde{t}_1) = 250$ GeV the corresponding variable is written as:

$$\Delta m_{\mathrm{T}}^{250} = m_{\mathrm{T}} - m_{\mathrm{T}}^{250} = m_{\mathrm{T}}(\ell, p_{\mathrm{T}}^{\mathrm{miss}}) - m_{\mathrm{T}}(\ell, p_{\mathrm{T}}^{250}(\nu)). \tag{8.18}$$

8.3.5 Estimation of the neutrino p_z

In SUSY searches with semileptonic decays one of the powerful approaches to reject $t\bar{t}$ background is to select events with a high m_{T}. For signal events a contribution from the neutralinos increases the $E_{\mathrm{T}}^{\mathrm{miss}}$, which increases the m_{T} too, while for $t\bar{t}$ events the endpoint of m_{T} is estimated to be the mass of the W boson. Due to detector resolution effects this endpoint is broadened and increased by 20–30 GeV. For the signal selection in the current analysis, mainly events with the $m_{\mathrm{T}} > 110$ GeV are used.

Since m_{T} corresponds to the transverse mass, the following inequality holds

$$m_{\mathrm{T}}(\ell, \nu) \leq m(\ell + \nu). \tag{8.19}$$

From $m_{\mathrm{T}}(\ell, \nu) \approx m(\ell + \nu)$ it follows that $\eta(\ell) \approx \eta(\nu)$, see Section 4.4. This means, that for leptonic W-boson decay with high m_{T} values a good estimation for $\eta(\nu)$ can be $\eta(\nu) \approx \eta(\ell)$. In the current analysis the $p_z(\nu)$ component is estimated based on this approximation.

8.3.6 The η of the recoil jet

The pseudorapidity of the recoil jet $\eta(j_{\mathrm{rec}})$ is found to be a variable with some separation power, after requiring a high momentum of the $t\bar{t}$ system and a centrality of the reconstructed top quarks $\eta(t_{\mathrm{had}}) \approx 0$ and $\eta(t_{\mathrm{lep}}) \approx 0$. The arguments, why the $\eta(j_{\mathrm{rec}})$ variable has separation power, could be the following: If one assumes that the boost of the event along the z-axis is small, it follows from the centrality requirement for the reconstructed top quarks $\eta(t_{\mathrm{had}}) \approx 0$ and $\eta(t_{\mathrm{lep}}) \approx 0$, that for the $t\bar{t}$ event, the recoil jet also should be in the (x, y) plane i.e. $\eta(j_{\mathrm{rec}}) \approx 0$. This is not the case for a signal event, where two neutralinos may compensate the boost of the recoil jet in the z direction, giving the possibility for the recoil jet to have a higher η. Therefore, adding the $\eta(j_{\mathrm{rec}})$, $\eta(t_{\mathrm{had}})$ and $\eta(t_{\mathrm{lep}})$ variables to the multivariate analysis increases the separation power.

8.4 Multivariate analysis

In the current analysis an optimisation was done for the on-shell decay for the signal model with $m(\tilde{t}_1, \tilde{\chi}_1^0) = (250, 75)$ GeV. This corresponds to a mass difference of $\Delta m \approx 3$ GeV below the diagonal. For the $m(\tilde{t}_1, \tilde{\chi}_1^0) = (250, 75)$ GeV signal model a high number of events were produced with ATLFAST-II (equivalent to 2 M events before any filter is applied). The sample was divided into two equal sets A and B.

The analysis uses the *Toolkit for Multivariate Analysis* (TMVA) [77], which is integrated inside the ROOT package [78]. For the training the *Boosted Decision Trees* (BDT) algorithm [123] is used. The BDT algorithm trained on the set A getting output variable BDT_A, and with the same options trained on the set B getting for output BDT_B. To estimate its power and check the overtraining, each BDT is tested against the other set, i.e. BDT_A is tested on set B and BDT_B on set A. All other signal points are used only to test the exclusion reach and not for training.

Finally, both output variables are combined into one BDT output. By definition, for events from the set A, the BDT = BDT_B, while for events from set B, the BDT = BDT_A. This allows to use the full set of events for the analysis.

8.4.1 Variable definitions

In this section a list of variables used for the multivariate analysis is presented. The p_{T} is always considered as a two-dimensional vector in the (x, y) plane. The analysis is optimised for the $m(\tilde{t}_1, \tilde{\chi}_1^0) = (250, 75)$ GeV signal model. The following definitions, assumptions and motivations are used for the tN diagonal analysis:

- The leading tree light jets are referred to as j_1, j_2 and j_3, with $p_{\mathrm{T}}(j_1) > p_{\mathrm{T}}(j_2) > p_{\mathrm{T}}(j_3)$.
- Up to two b-tagged jets in an event, referred to as b_1 and b_2, with $p_{\mathrm{T}}(b_1) > p_{\mathrm{T}}(b_2)$.
- It is assumed, that the recoil jet j_{rec} is the highest p_{T} light jet j_1.
- It is assumed, that one jet from the hadronic W_{had} decay q_1 is the sub-leading light jet j_2.
- Another light jet from the W_{had} decay q_2 is not taken from the reconstructed jets, instead it is constructed under the assumption, that $p_{\mathrm{T}}(q_1 + q_2 + j_{\mathrm{rec}} + p_{\mathrm{T}}^{\mathrm{miss}} + b_1 + b_2 + \ell) = 0$. For the $p_z(q_2)$ component, the assumption $\eta(q_2) = \eta(q_1)$ is made. This approach allows to construct q_2 even if only two light jets are presented in the event.
- The hadronically decaying W_{had} is reconstructed as $p^{\mu}(W_{\mathrm{had}}) = p^{\mu}(q_1 + q_2)$.
- To be sure, that the leading light jet does not come from the W_{had} decay, two invariant masses are computed, $m_{12} = m(j_1 + j_2)$ and $m_{13} = m(j_1 + j_3)$. The multivariate algorithm uses these variables to suppress events, where potentially the j_1 may not be the recoil jet.
- The p_z component of the neutrino is obtained from the assumption $\eta(\ell) = \eta(\nu)$.
- The leptonically decaying W_{lep} is reconstructed as $p^{\mu}(W_{\mathrm{lep}}) = p^{\mu}(\ell + \nu)$.
- If the event contains exactly one b-tagged jet, the second b-jet is assumed to be below the detector acceptance and set to zero, $p^{\mu}(b_2) = 0$.
- The hadronically and leptonically decaying top-quark candidates are reconstructed as $p^{\mu}(t_{\mathrm{had}}) = p^{\mu}(b_{\mathrm{had}} + W_{\mathrm{had}})$ and $p^{\mu}(t_{\mathrm{lep}}) = p^{\mu}(b_{\mathrm{lep}} + W_{\mathrm{lep}})$.
- The choice, which of the two b-tagged jets b_1 or b_2 have to be tagged as hadronic or leptonic is done based on the reconstruction of the leptonic top-quark candidate. The candidate closest to the top-quark mass of 173 GeV from $m(b_1 + W_{\mathrm{lep}})$ and $m(b_2 + W_{\mathrm{lep}})$ defines the corresponding b-jet as the leptonic b_{lep} and the other one as the hadronic b_{had}.

– The neutrino ν^{250} for the signal model exactly on the diagonal with $m(\tilde{t}_1) = 250$ GeV is calculated as described in Section 8.3.2. The $p_z(\nu^{250})$ component of the neutrino is reconstructed under the assumption of $\eta(\nu^{250}) = \eta(\ell)$.

– Based on the reconstructed ν^{250}, the corresponding signal related objects are reconstructed as: $p^\mu(W^{250}_{\rm lep}) = p^\mu(\ell + \nu^{250})$, $p^\mu(t^{250}_{\rm lep}) = p^\mu(b_{\rm lep} + W^{250}_{\rm lep})$, $m^{250}_{\rm T} = m(\ell + \nu^{250})$ and $\Delta m^{250}_{\rm T} = m_{\rm T} - m^{250}_{\rm T}$.

– The difference $|p_{\rm T}(q_2)| - |p_{\rm T}(j_3)|$ is calculated. The third light jet j_3 is expected to be from the hadronic $W_{\rm had}$ decay. If there is no j_3 jet in the event, it is assumed to be zero, $p_{\rm T}(j_3) = 0$. The difference estimates how reasonable is this assumption.

– The difference between the projections of $p^{\rm miss}_{\rm T}$ and $p_{\rm T}(j_{\rm rec})$ in the $p_{\rm T}(j_{\rm rec})$ direction is used: $\Delta{\rm proj}(p^{\rm miss}_{\rm T}, p_{\rm T}(j_{\rm rec})) = (p^{\rm miss}_{\rm T} - p_{\rm T}(j_{\rm rec})) \cdot n_T$, where n_T is a unity vector in the direction of the $p_{\rm T}(j_{\rm rec})$.

The variables passed as input to the multivariate algorithm are the following:

$E^{\rm miss}_{\rm T}, m_{\rm T}, m^{250}_{\rm T}, \Delta m^{250}_{\rm T}, m_{12}, m_{13},$

$|p_{\rm T}(j_{\rm rec})|, |\eta(j_{\rm rec})|, |p_{\rm T}(b_1)|, |p_{\rm T}(q_2)|, |p_{\rm T}(j_3)|,$

$m(W_{\rm had}), m(W_{\rm lep}), m(W^{250}_{\rm lep}), m(t_{\rm had}), m(t_{\rm lep}), m(t^{250}_{\rm lep}), \eta(t_{\rm had}), \eta(t_{\rm lep}),$

$\Delta{\rm proj}(p^{\rm miss}_{\rm T}, p_{\rm T}(j_{\rm rec})), |p_{\rm T}(q_2)| - |p_{\rm T}(j_3)|.$

8.4.2 Training of the BDT

The BDT training was done for the $m(\tilde{t}_1, \tilde{\chi}^0_1) = (250, 75)$ GeV signal model. To increase the exclusion power, the BDT is trained for two different selections: BDT1 for an exclusive 1 b-jet and BDT2 for an exclusive 2 b-jet selection. The common BDT preselection requirements are applied as follows:

– Common one-lepton analysis cleaning cuts are applied, see Section 6.2.3;

– Exactly one signal lepton with $p_{\rm T} > 25$ GeV, no other baseline leptons;

– At least four jets with $p_{\rm T} > 25$ GeV;

– $\Delta\phi(j_1, E^{\rm miss}_{\rm T}) > 0.4$ between the leading jet j_1 and $E^{\rm miss}_{\rm T}$;

– Leading light jet $p_{\rm T}(j_{\rm rec}) > 80$ GeV;

– Sub-leading light jet $p_{\rm T}(j_{1,\rm had}) > 40$ GeV;

– $E^{\rm miss}_{\rm T} > 80$ GeV;

– $m_{\rm T} > 80$ GeV.

The preselection regions PR1-tN and PR2-tN for the 1 b-jet and 2 b-jet selection, respectively, are defined as:

– PR1-tN: Common BDT preselection with exactly 1 b-tagged jet requirement;

– PR2-tN: Common BDT preselection with exactly 2 b-tagged jets requirement.

Both BDTs are trained with the *Gradient Boosting* (`Grad-Boost`) method [123] for the signal model $m(\tilde{t}_1, \tilde{\chi}_1^0) = (250, 75)$ GeV using 150 trees with a maximal depth of 5 variables for each tree. The distributions for the BDT1 and BDT2 output variables are shown in Figure 8.4. The bottom part of each plot shows a signal-to-background ratio for different signal models along the $\Delta m(\tilde{t}_1, \tilde{\chi}_1^0) - m(t) \approx 3$ GeV diagonal (on-shell top-quark decays) for the top-squark masses of $m(\tilde{t}_1) = 190, 210, 230, 250$, and 270 GeV.

One can see that for the BDT output above 0.6 there is no significant difference between the event yields for different signal models, except for the signal model with $m(\tilde{t}_1) = 190$ GeV which has a lower event yield.

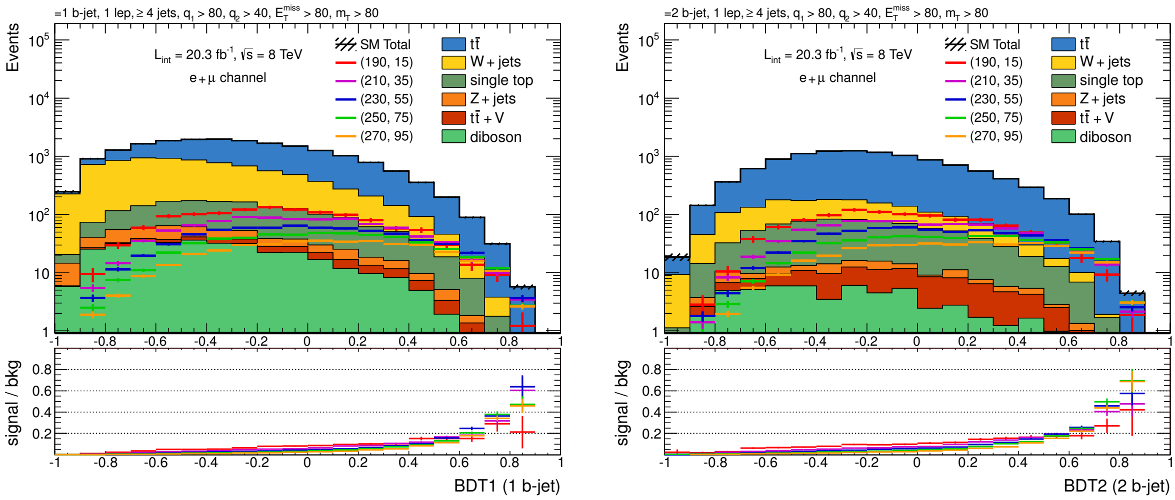

Figure 8.4: Distributions for the BDT1 (1 b-jet selection, left) and BDT2 (2 b-jet selection, right) output variables. The training of the BDTs is done for the $m(\tilde{t}_1, \tilde{\chi}_1^0) = (250, 75)$ GeV signal model. The signal is shown for top-squark masses $m(\tilde{t}_1) = 190, 210, 230, 250$, and 270 GeV, for on-shell top decays at about 3 GeV below the diagonal. One can see that in the BDT > 0.6 region there is no significant difference for the event yields for different signal models.

If one assumes a total systematic uncertainty of $\pm 20\%$ the significance can be estimated as

$$Significance = \frac{S}{\sqrt{S + B + (0.2 \cdot B)^2}}, \tag{8.20}$$

where S and B are the numbers of signal and background events, respectively.

The expected significance for the BDT1 and BDT2 variables under the assumption of a total systematic uncertainty of $\pm 20\%$ is shown in Figure 8.5 for the $m(\tilde{t}_1, \tilde{\chi}_1^0) = (250, 75)$ GeV signal model, which was used to train the BDTs. One can see that the main separation power is expected from the 2 b-jet selection and the optimal point for both BDTs is about 0.7.

There are differences between the significance curves calculated for the test and training samples. This is well visible for the BDT1 output (left plot). The reason for this difference is that the training of the BDT is affected by statistical fluctuations due to a limited number of events in the training samples. In this case, the BDT can separate signal and background events for the

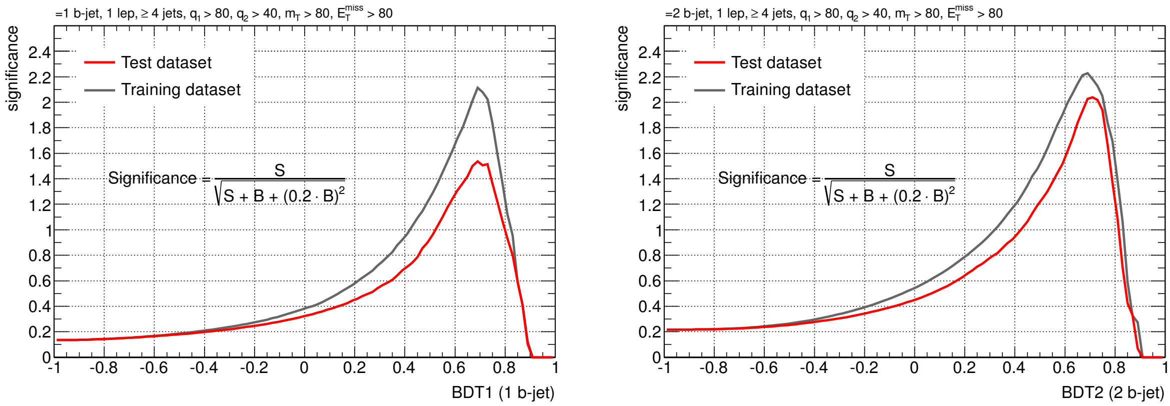

Figure 8.5: The significance assuming a total systematic uncertainty of $\pm 20\%$. The significance is shown for the BDT1 output (1 b-jet selection, left) and BDT2 output (2 b-jet selection, right), as calculated using the test and the training samples.

training samples better, than for an unknown test sample. This effect is called "overtraining" of the BDT.

A comparison of the BDT1 and BDT2 outputs for the test and training samples, the so-called "overtraining plots", for the 1 b-jet and 2 b-jet regions are shown in Figure 8.6. One can see

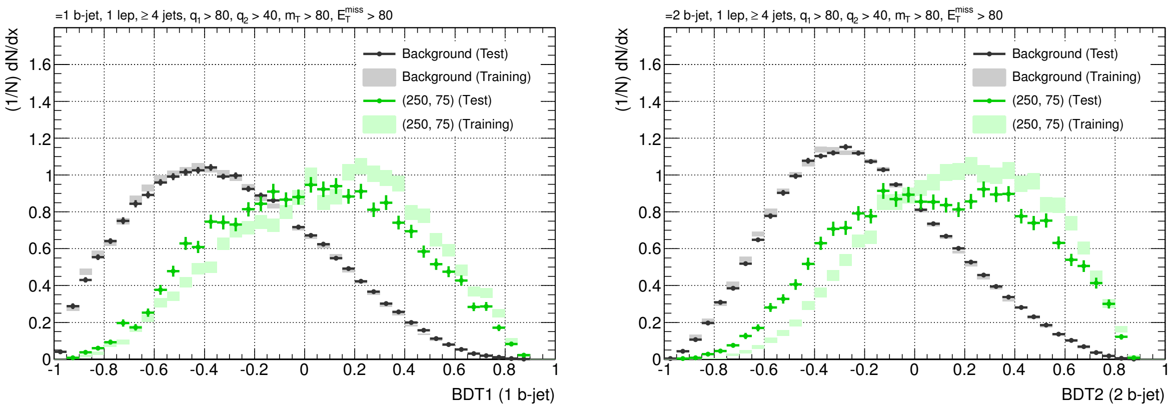

Figure 8.6: A comparison of the BDT1 (1 b-jet selection, left) and BDT2 (2 b-jet selection, right) outputs for the test and training samples. The training of the BDTs is done for the $m(\tilde{t}_1, \tilde{\chi}_1^0) = (250, 75)$ GeV signal model.

that for the 2 b-jet selection the BDT2 is slightly overtrained, but for the BDT output above 0.7 the difference between the training and test datasets is small. In the case of the 1 b-jet selection, there is more overtraining. This is mainly caused by larger contributions of the W+jets and single top processes which pass the preselection. The numbers of Monte Carlo events generated for the W+jets and single top processes are smaller than those for the $t\bar{t}$ process, which results in an overtraining of the BDT1.

One can try to avoid overtraining by increasing the minimal number of events per node (`MinNodeSize` parameter) for the BDT training, but this decreases the separation power for the $t\bar{t}$ process, which dominates for the BDT1 selection. Decreasing the `MinNodeSize` parameter improves the separation, but also leads to overtraining for W+jets and single top samples, due to the low number of trained events for these processes. Removing the single top samples from the training dataset improves the training stability, but decreases the separation power for the analysis, since the BDT is not trained to reject this process.

After several optimisation steps, for both BDT1 and BDT2 output variables, it was found, that independently from this overtraining, the presented BDTs give good results within the instabilities related to the training method. Therefore, it was decided to use the presented BDT outputs for the analysis.

The normalised outputs for the BDT1 and BDT2 selections for different signal points along the diagonal are shown in Figure 8.7. One can see that for BDT > 0.4, an increase of the top-squark mass leads to an increase of the acceptance for the diagonal signal points.

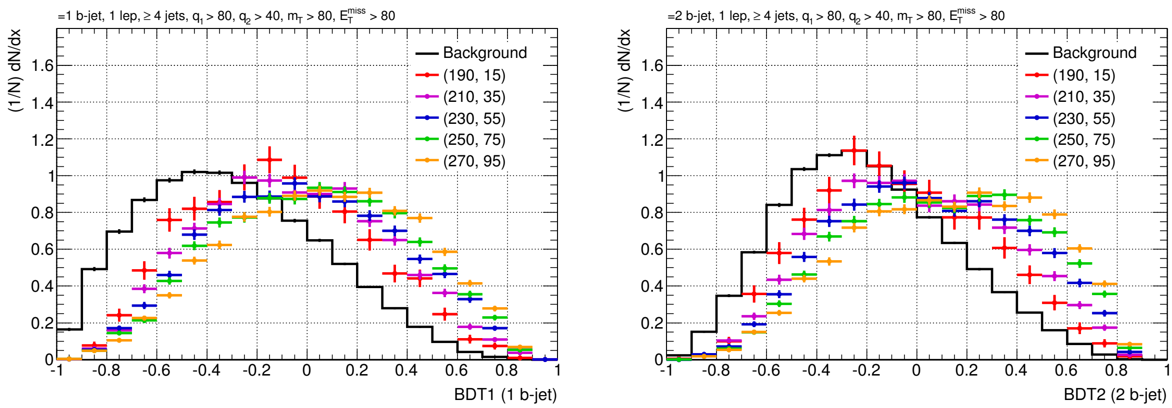

Figure 8.7: Normalised outputs for the BDT1 (left) and BDT2 (right) variables. The BDTs are trained for the $(250, 75)$ signal point. One can see that for BDT > 0.4 an increase of the top-squark mass leads to an increase of the acceptance for diagonal signal points.

Since the 1 b-jet and 2 b-jet regions do not overlap, the BDT1 and BDT2 output variables are simply referred to as the BDT output variable in the following, meaning BDT1 if events are from the 1 b-jet region and BDT2 for events from the 2 b-jet region.

8.5 Background reweighting

The distribution of the p_T of the $t\bar{t}$ system on particle level (true $p_T(t\bar{t})$) for the 1 b-jet and 2 b-jet selection after a BDT > 0.6 requirement is shown in Figure 8.8. The selection is near to the optimal one of ≈ 0.7 for both BDTs (see Figure 8.5).

The gray lines on the plot show the borders of the bins for the default 4-bin reweighting of the true $p_T(t\bar{t})$ used in the one-lepton analysis, see Section 7. One can see, that the peak is located around 170 GeV, i.e. exactly on the border between two bins. The difference between the weights is 0.21, which means, that smoothing the reweighting may have some impact on the data-MC agreement in the signal region. Therefore, for the tN diagonal analysis the exponential reweighting described in Section 7.2 is used.

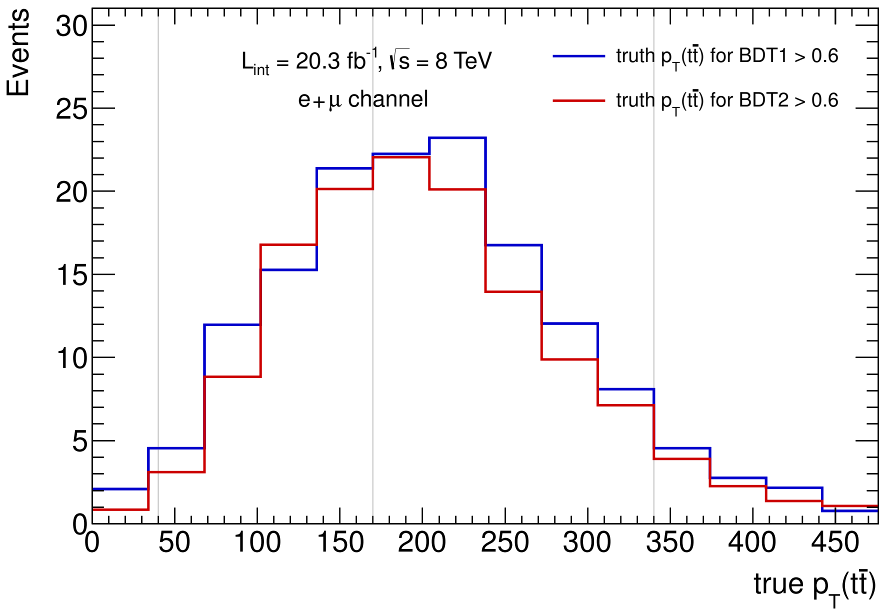

Figure 8.8: Distributions of the true $p_{\mathrm{T}}(t\bar{t})$ for the 1 b-jet and 2 b-jet regions after the BDT > 0.6 requirement. The gray lines show the borders of the bins for the default 4-bin reweighting of the true $p_{\mathrm{T}}(t\bar{t})$ used in the one-lepton analysis. The peaks of the distributions are located around 170 GeV, i.e on the border of the second and third reweighting bin.

Figures 8.9 and 8.10 show the data-MC agreement before any reweighting is applied and after the exponential $t\bar{t}$ reweighting for the variables m_{T}, m_{T}^{250} and $\Delta m_{\mathrm{T}}^{250} = m_{\mathrm{T}} - m_{\mathrm{T}}^{250}$. One can see that m_{T} and m_{T}^{250} show a good agreement even before the reweighting, but their difference is not modelled properly before reweighting. For the $\Delta m_{\mathrm{T}}^{250}$ distribution, the most important region, which includes the signal region, is the $[20, 60]$ GeV interval. Applying the reweighting improves the data-MC agreement.

8.6 Crossing the diagonal

In general, three different scenarios have to be considered:

- Both top squarks are decaying on-shell via $\tilde{t}_1 \rightarrow t\tilde{\chi}_1^0$;
- Both top squarks are decaying off-shell via $\tilde{t}_1 \rightarrow bW\tilde{\chi}_1^0$;
- The mixed decay, where one top squark is decaying on-shell, via $\tilde{t}_1 \rightarrow t\tilde{\chi}_1^0$ and the other one off-shell, via $\tilde{t}_1 \rightarrow bW\tilde{\chi}_1^0$.

Any scenario can be represented as a combination of these three, with the corresponding relative branching ratios $\mathcal{BR}_{\mathrm{on}}$, $\mathcal{BR}_{\mathrm{off}}$ and $\mathcal{BR}_{\mathrm{mix}}$, taking into account, that the total branching ratio should be $\mathcal{BR}_{\mathrm{on}} + \mathcal{BR}_{\mathrm{off}} + \mathcal{BR}_{\mathrm{mix}} = 100\%$.

Under the assumption, that both top squarks decay on-shell independently with probability α, the branching ratios for $\mathcal{BR}_{\mathrm{on}}$, $\mathcal{BR}_{\mathrm{off}}$ and $\mathcal{BR}_{\mathrm{mix}}$ decays will be α^2, $(1-\alpha)^2$ and $2\alpha(1-\alpha)$,

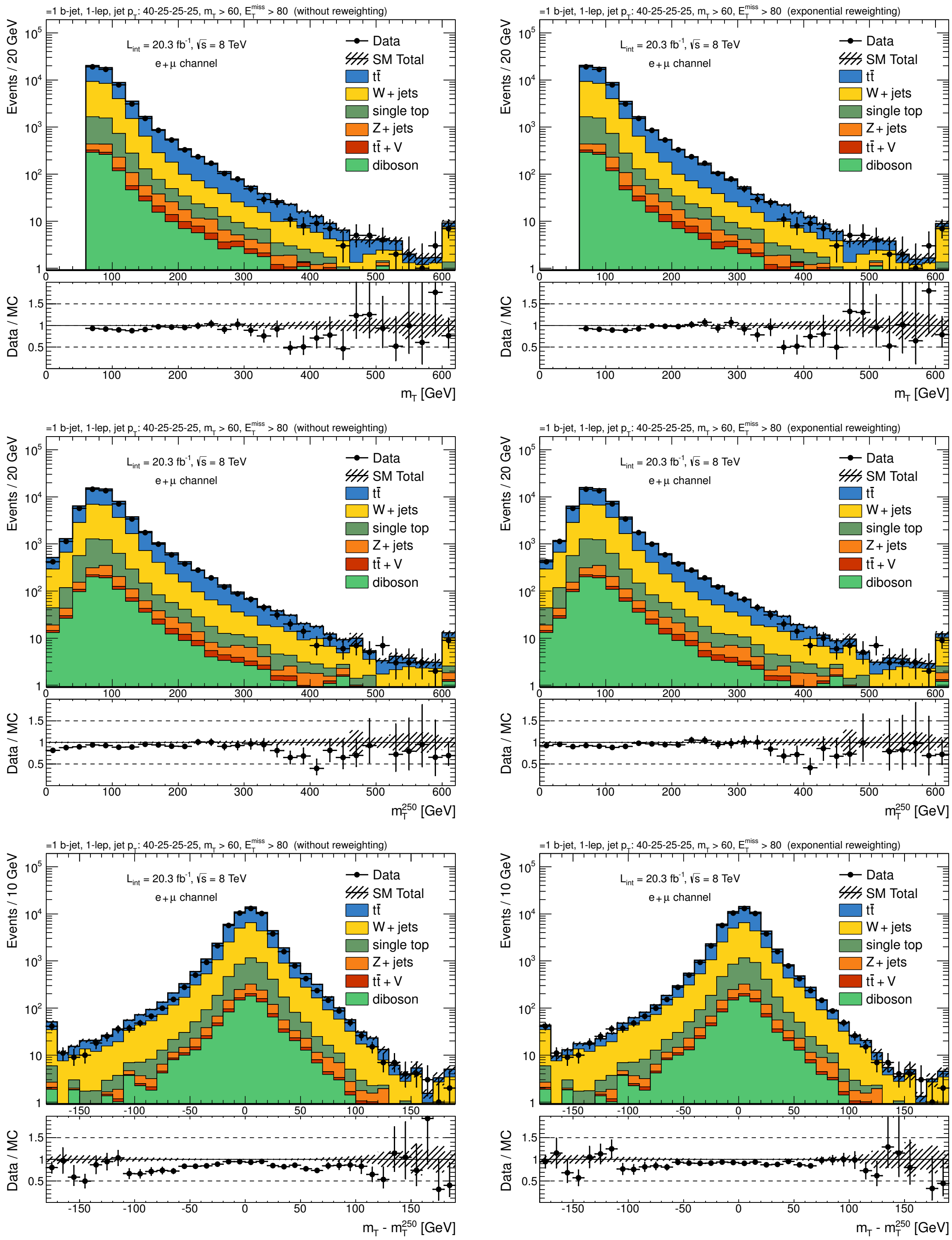

Figure 8.9: The data-MC comparison before any reweighting is applied (left) and after the exponential $t\bar{t}$ reweighting (right) for the m_{T} (top), m_{T}^{250} (middle), and $\Delta m_{\mathrm{T}}^{250}$ (bottom) distributions. The selection: 1 lepton, exactly 1 b-tagged jets, at least 4 jets with $p_{\mathrm{T}}(j_1) > 40$ GeV and $p_{\mathrm{T}}(j_{2,3,4}) > 25$ GeV, $m_{\mathrm{T}} > 60$ GeV, $E_{\mathrm{T}}^{\mathrm{miss}} > 80$ GeV (for the details, see the text). The $t\bar{t}$ and W+jets are normalised to the Monte Carlo cross section. The error bands include only the Monte Carlo statistical uncertainties.

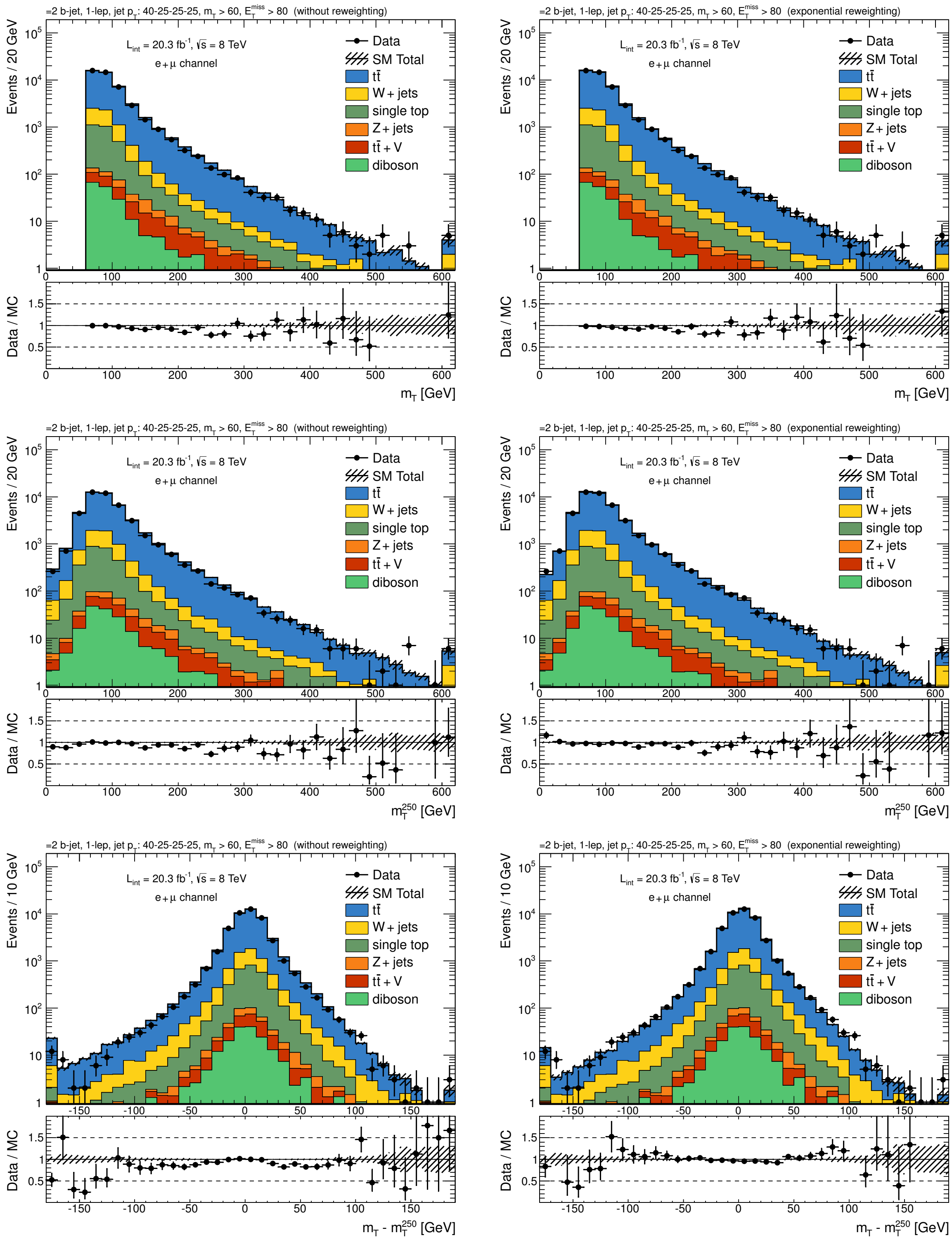

Figure 8.10: The data-MC comparison before any reweighting is applied (left) and after the exponential $t\bar{t}$ reweighting (right) for the m_{T} (top), m_{T}^{250} (middle), and $\Delta m_{\mathrm{T}}^{250}$ (bottom) distributions. The selection: 1 lepton, exactly 2 b-tagged jets, at least 4 jets with $p_{\mathrm{T}}(j_1) > 40$ GeV and $p_{\mathrm{T}}(j_{2,3,4}) > 25$ GeV, $m_{\mathrm{T}} > 60$ GeV, $E_{\mathrm{T}}^{\mathrm{miss}} > 80$ GeV (for the details, see the text). The $t\bar{t}$ and W+jets are normalised to the Monte Carlo cross section. The error bands include only the Monte Carlo statistical uncertainties.

respectively. This means, that while crossing the diagonal, for $\alpha = 0.5$, the branching ratio for the mixed decay mode $\mathcal{BR}_{\text{mix}}$ is 50%.

For signal points further than 3–4 GeV away from the diagonal, both top squarks dominantly decay either on-shell (below the diagonal) or off-shell (above the diagonal). Crossing the diagonal from the on-shell to the off-shell decay region, $\mathcal{BR}_{\text{on}}$ changes from 100% to 0%, while $\mathcal{BR}_{\text{off}}$ changes from 0% to 100%. The mixed decay mode also makes some contribution while crossing the diagonal, but outside the diagonal it can be neglected, $\mathcal{BR}_{\text{mix}} \approx 0\%$.

Having two different analyses for on- and off-shell decays raises a relative branching ratio modelling problem. The analysis presented has the advantage, that it is sensitive to both decay modes. Therefore, instead of calculating the relative branching ratio, one can use a more conservative approach by choosing the worst case in terms of acceptance between the on- and off-shell decay modes.

In general, while crossing the diagonal, signal models for the mixed decay scenario also have to be taken into account, but these samples have not been generated. In the analysis presented it is assumed, that if by swapping the decay mode for one top-quark decay (for example from off-shell to on-shell), the sensitivity decreases, than by swapping the decay mode for the second top quark, the sensitivity should further decrease. Therefore, the sensitivity for the mixed decay cannot be worse than the worst case between the fully on- and fully off-shell decay scenarios.

It is important to mention, that this assumption is only applicable, when the same analysis is sensitive to the fully on- and fully off-shell decay scenario. In this case, for the analysis, the calculation of the relative branching ratio for decay modes is not needed.

The BDT outputs for $m(\tilde{t}_1) = 250$ GeV and $m(\tilde{\chi}_1^0) = 50, 60, 70, 75, 80$, and 100 GeV are shown in Figure 8.11. The signal model exactly on the diagonal has $m(\tilde{\chi}_1^0) \approx 77.5$ GeV. Therefore, $m(\tilde{\chi}_1^0) = 50, 60, 70, 75$ GeV correspond to on-shell, while $m(\tilde{\chi}_1^0) = 80, 100$ GeV to off-shell decay modes. The $m(\tilde{t}_1, \tilde{\chi}_1^0) = (250, 75)$ GeV signal model (green) is generated with about four times more events with respect to the other points on this plot produced by the official ATLAS production.

To improve visibility, the signal-to-background ratio for the $[0.6, 0.7]$, $[0.7, 0.8]$, and $[0.8, 0.9]$ intervals of the BDT outputs are shown in Figure 8.12. One can see, especially for the 2 b-jet selection (right) which is the main contributor in the analysis, that the ratio is quite stable near the diagonal for $m(\tilde{\chi}_1^0) \approx 70$–$80$ GeV.

From the figures one can see, that:

– The shape of the BDT output looks similar for all these points.

– The worst case is realised for the $m(\tilde{t}_1, \tilde{\chi}_1^0) = (250, 75)$ GeV signal model, which is an on-shell decay with less than 2 GeV distance from the diagonal.

– For the 1 b-jet selection, the on-shell decay is more challenging than the off-shell one, since the $m(\tilde{t}_1, \tilde{\chi}_1^0) = (250, 70)$ GeV signal model, which is about 7 GeV below the diagonal, has a signal-to-background ratio similar to the $m(\tilde{t}_1, \tilde{\chi}_1^0) = (250, 80)$ GeV one, which is just about 3 GeV above the diagonal.

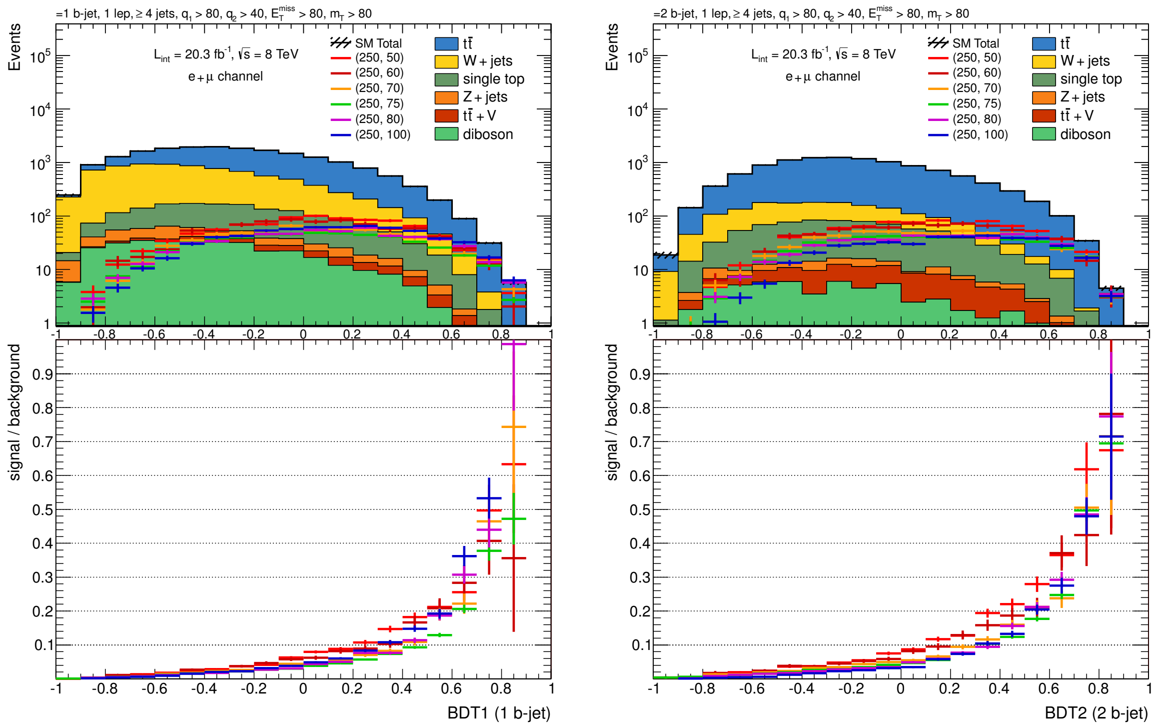

Figure 8.11: Distributions of the BDT1 (left) and BDT2 (right) output for the 1 b-jet and 2 b-jet selection, respectively. Several signal models for the top-squark mass $m(\tilde{t}_1) = 250$ GeV are considered. The diagonal is crossed for $m(\tilde{\chi}_1^0) \approx 77.5$ GeV, therefore $m(\tilde{\chi}_1^0) = 50, 60, 70, 75$ GeV correspond to on-shell, while $m(\tilde{\chi}_1^0) = 80, 100$ GeV to off-shell decay modes. The signal-to-background ratio has the same behaviour for the signal models presented. The worst case appears to be for the $m(\tilde{t}_1, \tilde{\chi}_1^0) = (250, 75)$ GeV signal model, i.e. for an on-shell decay right below the diagonal.

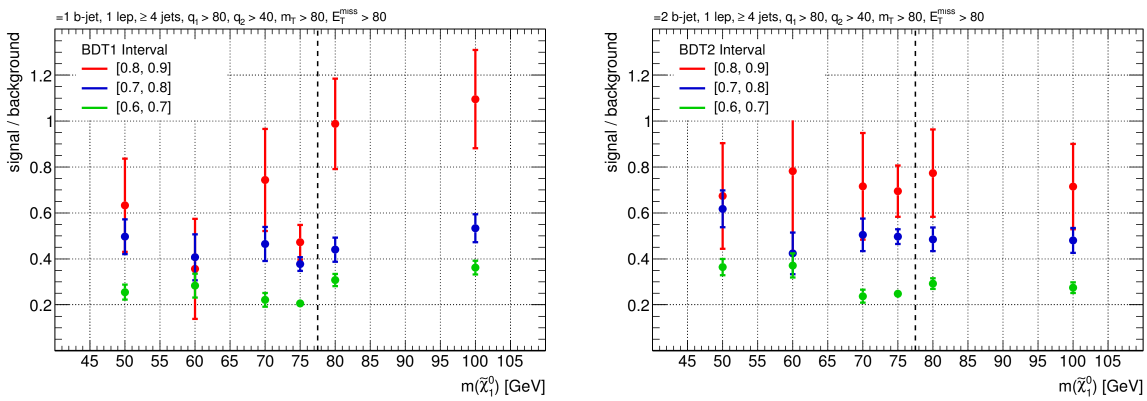

Figure 8.12: Signal-to-background ratio for the $[0.6, 0.7]$, $[0.7, 0.8]$, and $[0.8, 0.9]$ intervals of the BDT1 (left) and BDT2 (right) output for the 1 b-jet and 2 b-jet selection, respectively. Signal models for the top-squark mass $m(\tilde{t}_1) = 250$ GeV with $m(\tilde{\chi}_1^0) = 50, 60, 70, 75, 80$, and 100 GeV are considered. The dashed vertical black line represents the mass $m(\tilde{\chi}_1^0) \approx 77.5$ GeV, where the diagonal is crossed. The signal models with masses below the line $m(\tilde{\chi}_1^0) = 50, 60, 70, 75$ GeV correspond to on-shell, while the masses above the line $m(\tilde{\chi}_1^0) = 80, 100$ GeV to off-shell decay modes.

– The separation power for the 2 b-jets signal region does not depend significantly on the decay mode. The differences for the 2 b-jet selection between ratios for BDT2 > 0.4 are similar within the statistical uncertainty for the signal points.

– The signal point exactly on the diagonal is not produced, but from the signal-to-background ratio for the $[0.6, 0.7]$, $[0.7, 0.8]$, and $[0.8, 0.9]$ intervals of the BDT outputs, shown in Figure 8.12, and taking into account that exactly on the diagonal the worst case is realised for the on-shell decay scenario, one can conclude, that the result is within the 1σ statistical uncertainty of the $m(\tilde{t}_1, \tilde{\chi}_1^0) = (250, 75)$ GeV signal model.

Since the hardest case is the on-shell decay mode, the exclusion on the diagonal, where all three decay modes are available, can be conservatively estimated assuming the on-shell decay mode with $\mathcal{BR} = 100\%$.

8.7 Validation of the BDT

One of the challenges of the BDT analysis is the validation of the BDT output. The data-MC agreement cannot be validated in the signal region before unblinding.

The "default" approach for the one-lepton analysis consists of the following steps:

– Check for different preselection regions, that the m_{T} variable correctly describes the data.

– Define a *Cut Flow* (CF) – the list of selection requirements for the Signal Region (SR) based on the variables used.

– Define the same cut flow but without applying the m_{T} requirement ($\mathrm{CF}_{m_{\mathrm{T}}}$). For the cut-and-count analysis, where regions are defined by sequential application of the requirement ("cut") for each variable, this is always possible. Usually the signal region includes a high m_{T} selection. In this notation, if, for example, for the signal region SR the selection requirement is $m_{\mathrm{T}} > 120$ GeV, the same region can be described as:

$$\mathrm{SR} = \mathrm{CF}(m_{\mathrm{T}}, E_{\mathrm{T}}^{\mathrm{miss}}, \ldots) = \mathrm{CF}_{m_{\mathrm{T}}}(E_{\mathrm{T}}^{\mathrm{miss}}, \ldots) \text{ and } m_{\mathrm{T}} > 120 \text{ GeV}.$$

– Define the control (CR) and validation (VR) regions by relaxing the m_{T} selection:

$$\mathrm{CR} = \mathrm{CF}_{m_{\mathrm{T}}}(E_{\mathrm{T}}^{\mathrm{miss}}, \ldots) \text{ and } 60 \text{ GeV} < m_{\mathrm{T}} < 90 \text{ GeV};$$

$$\mathrm{VR} = \mathrm{CF}_{m_{\mathrm{T}}}(E_{\mathrm{T}}^{\mathrm{miss}}, \ldots) \text{ and } 90 \text{ GeV} < m_{\mathrm{T}} < 120 \text{ GeV}.$$

Usually, after relaxing the m_{T} requirement to the 60 GeV $< m_{\mathrm{T}} <$ 90 GeV, the number of events passing the selection significantly increases due to semileptonic $t\bar{t}$ decays, accordingly the signal contamination is significantly suppressed.

The validation regions for the 1 b-jet (VR1-tN) and 2 b-jet (VR2-tN) selection are defined by altering the $m_{\mathrm{T}} > 80$ GeV requirement of the corresponding preselection regions (PR1-tN and PR2-tN, see Section 8.4.2) to the 60 GeV $< m_{\mathrm{T}} <$ 80 GeV. One can see, that preselection and validation regions do not overlap.

The distributions of the BDT variables for VR1-tN and VR2-tN validation regions are shown in Figure 8.13. They show a good data-MC agreement, but there are almost no events for the BDT > 0.6 region. Therefore, it is impossible to validate the BDT output in this region.

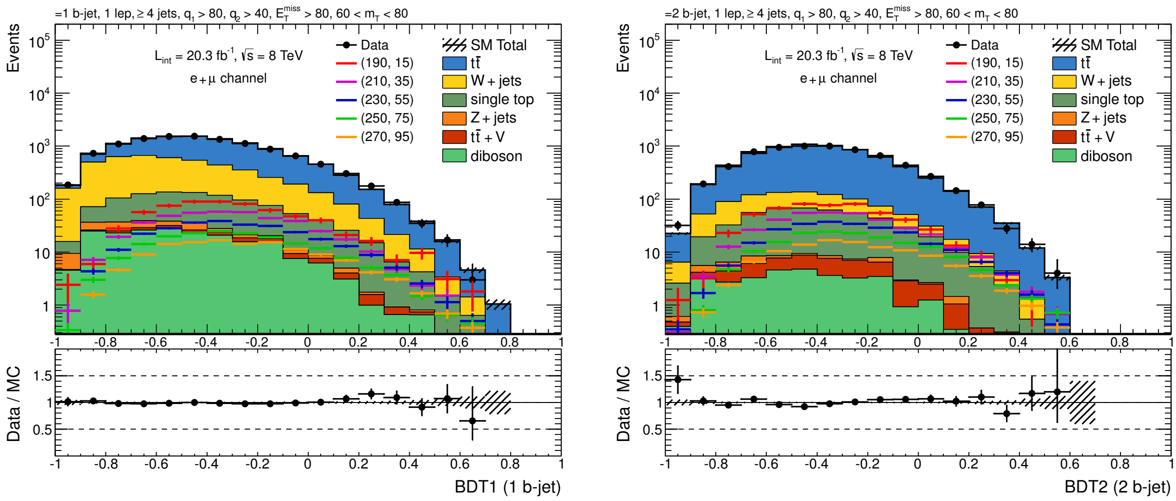

Figure 8.13: Distributions for the BDT1 (left) and BDT2 (right) variable for the VR1-tN (1 b-jet) and VR2-tN (2 b-jet) validation regions. For the validation region the $m_{\mathrm{T}} > 80$ GeV requirement of the corresponding preselection region (PR1-tN and PR2-tN) is altered to the 60 GeV $< m_{\mathrm{T}} <$ 80 GeV. The W+jets process is scaled by a normalisation factor of 0.76 with respect to the Monte Carlo cross section, while for the $t\bar{t}$ process the nominal Monte Carlo cross section is used. The error bands include only the Monte Carlo statistical uncertainties.

Several approaches were checked to construct a control region based on the BDT output:

– The attempt to use the "default" approach mentioned above for the BDT output faces the problem that the m_{T} variable is not detachable from the BDT.

– As an alternative approach one can try to remove the m_{T} variable from the BDT training and apply a separate selection on it, but this decreases the separation power of the BDT, since the m_{T} variable contributes significantly.

One can reinterpret a definition of the control and validation regions as a shift of the m_{T} variable. The definition of CR and VR mentioned above, can de equivalently redefined as:

$$\mathrm{SR} = \mathrm{CF}(m_{\mathrm{T}}, E_{\mathrm{T}}^{\mathrm{miss}}, \ldots);$$

$$\mathrm{CR} = \mathrm{CF}(m_{\mathrm{T}} + 60\ \mathrm{GeV}, E_{\mathrm{T}}^{\mathrm{miss}}, \ldots) \text{ and } m_{\mathrm{T}} < 90\ \mathrm{GeV};$$

$$\mathrm{VR} = \mathrm{CF}(m_{\mathrm{T}} + 30\ \mathrm{GeV}, E_{\mathrm{T}}^{\mathrm{miss}}, \ldots) \text{ and } m_{\mathrm{T}} < 120\ \mathrm{GeV}.$$

Following this strategy, the validation of the BDT output can be performed for the shifted variable $m_{\mathrm{T}} + \Delta m_{\mathrm{T}}$, i.e. for the $\mathrm{BDT}(m_{\mathrm{T}} + \Delta m_{\mathrm{T}}, E_{\mathrm{T}}^{\mathrm{miss}}, \ldots)$ distribution. For validation regions, the m_{T} is about 80 GeV, while for the BDT > 0.6 region, which is the most important region for the analysis, the m_{T} distribution peaks around 120 GeV (see Figure 8.20). Therefore, for the current analysis $\Delta m_{\mathrm{T}} = 40$ GeV is chosen. The BDT output, for the shifted m_{T} parameter, is referred to as $\mathrm{BDT}_{\mathrm{VR}}(m_{\mathrm{T}} + 40\ \mathrm{GeV})$.

Figure 8.14 shows the distributions of the $\mathrm{BDT}_{\mathrm{VR}}(m_{\mathrm{T}} + 40\ \mathrm{GeV})$ output for the validation regions (top row). The comparison shows a good data-MC agreement. For the distributions presented, the $t\bar{t}$ production is normalised to the Monte Carlo cross section, while the W+jets production is scaled by a factor of 0.76 with respect to the Monte Carlo cross section.

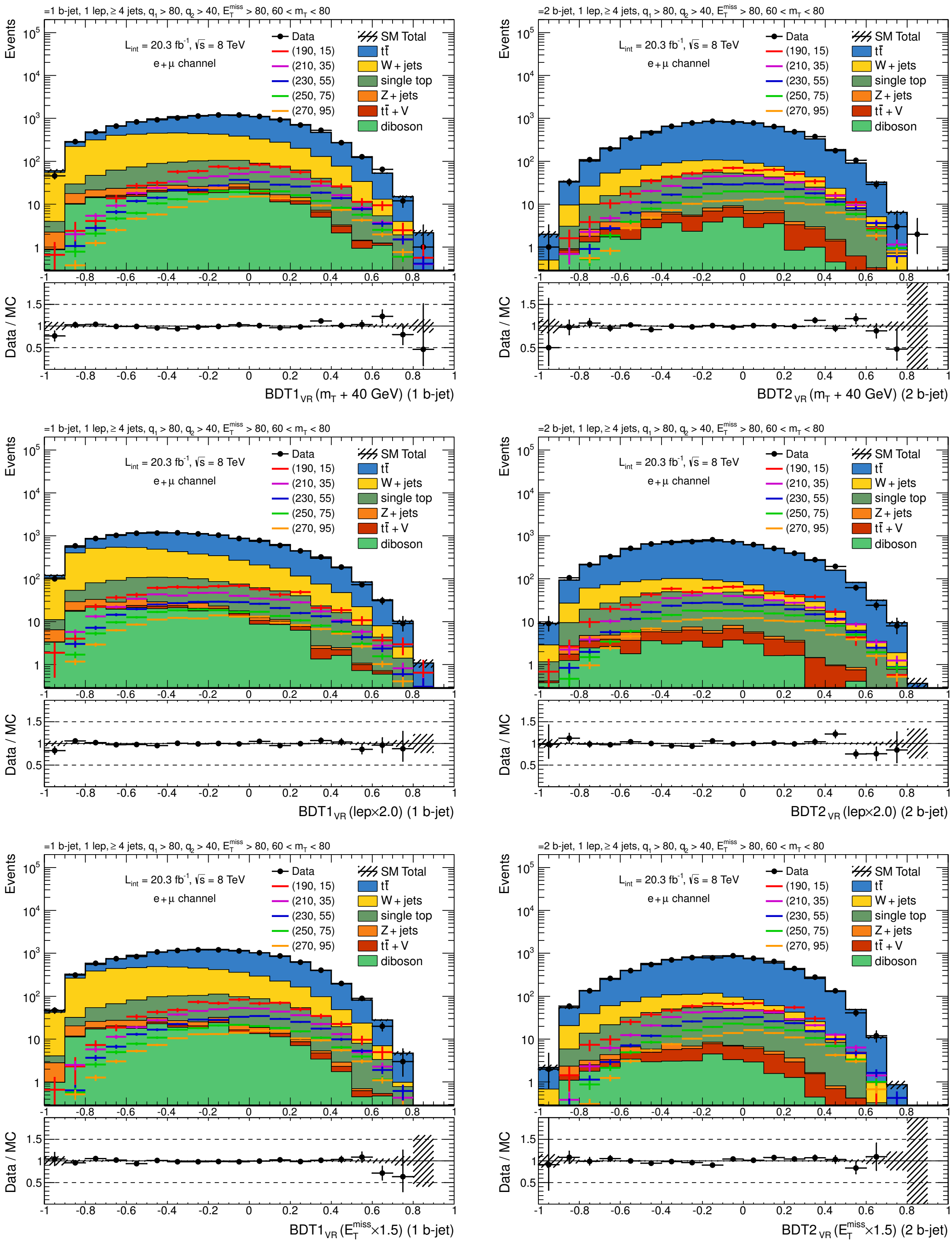

Figure 8.14: Distributions for different $\mathrm{BDT_{VR}}$ variables for the VR1 (left) and VR2 (right) validation regions. The distributions for the $\mathrm{BDT_{VR}}(m_{\mathrm{T}} + 40\ \mathrm{GeV})$ (top), $\mathrm{BDT_{VR}}(\ell \times 2.0)$ (middle), and $\mathrm{BDT_{VR}}(E_{\mathrm{T}}^{\mathrm{miss}} \times 1.5)$ (bottom) outputs are shown (for details, see text). The $t\bar{t}$ and W+jets process is normalised by a factor of 1.0 and 0.76, respectively, to the corresponding Monte Carlo cross section. The error bands include only the Monte Carlo statistical uncertainties.

The approach proposed above has some inconsistency. The input variables used to calculate the BDT output: $E_{\mathrm{T}}^{\mathrm{miss}}$, m_{T}, m_{T}^{250}, $\Delta m_{\mathrm{T}}^{250}$, $m(W_{\mathrm{lep}}^{250})$, $m(t_{\mathrm{lep}}^{250})$, ... are highly correlated. Therefore, when m_{T} is modified, for consistency, the variables which are correlated with m_{T}, for example m_{T}^{250} and $\Delta m_{\mathrm{T}}^{250} = m_{\mathrm{T}}^{250} - m_{\mathrm{T}}$, also have to be modified. Since the m_{T} variable is calculated based on the four-momenta of the lepton $p^{\mu}(\ell)$ and the missing transverse momentum $p_{\mathrm{T}}^{\mathrm{miss}}$, instead of shifting m_{T} one can scale separately each component and recalculate all variables. Two additional validation approaches, based on the scaling of the $p^{\mu}(\ell)$ and $p_{\mathrm{T}}^{\mathrm{miss}}$, are considered.

In the first approach, the four-momenta of the lepton $p^{\mu}(\ell)$ is scaled by a factor of 2, while the $p_{\mathrm{T}}^{\mathrm{miss}}$ variable is not changed. The scaled lepton is defined as $p^{\mu}(\ell') = 2 \cdot p^{\mu}(\ell)$. After scaling, the $m_{\mathrm{T}} = 80$ GeV transforms to the $m'_{\mathrm{T}} = \sqrt{2} \cdot m_{\mathrm{T}} \approx 113$ GeV. All analysis-related variables are recalculated based on the scaled ℓ' lepton. The BDT output which corresponds to the scaled input parameters, is referred to as $\mathrm{BDT_{VR}}(\ell \times 2.0)$.

The second approach scales the $p_{\mathrm{T}}^{\mathrm{miss}}$ vector by a factor of 1.5, while the lepton momentum is not changed. In case of the missing transverse momentum, the multiplication factor is chosen to be smaller, due to the high preselection requirement $E_{\mathrm{T}}^{\mathrm{miss}} > 80$ GeV. The BDT output, which corresponds to the scaled input parameters, is referred to as $\mathrm{BDT_{VR}}(E_{\mathrm{T}}^{\mathrm{miss}} \times 1.5)$.

Validations of a data-MC agreement for these two cases are shown in Figure 8.14 (middle and bottom rows). A good agreement between data and Monte Carlo simulation is found.

8.8 Signal selection

The signal regions SR1-tN and SR2-tN are defined as regions for the 1 b-jet and 2 b-jet selections, respectively, for BDT > 0.4. The distributions of the BDT outputs for values greater that 0.4 are shown in Figure 8.15. One can see, that the signal-to-background ratio increases for higher values of the BDT output.

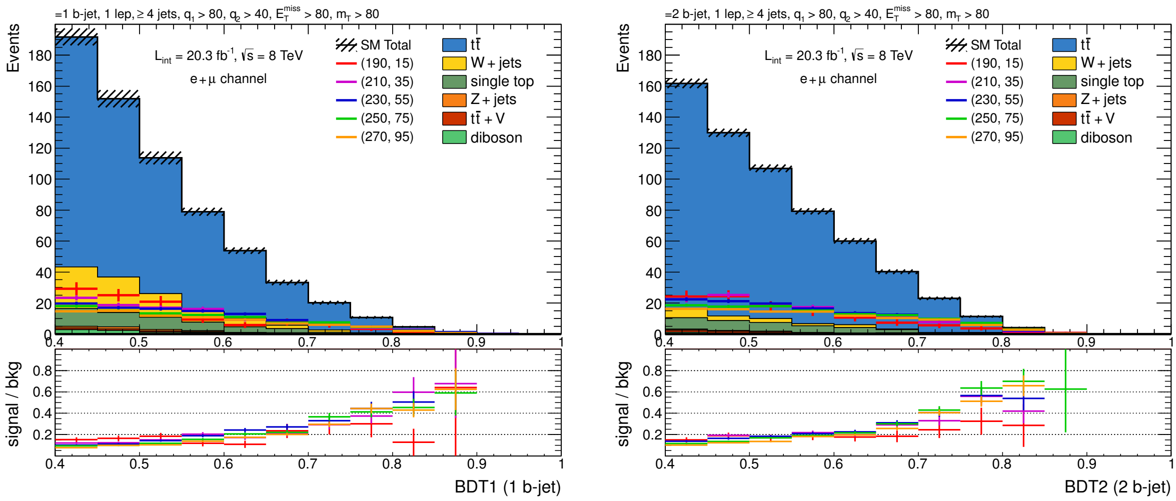

Figure 8.15: Distributions of the BDT output variables for BDT values above 0.4 region for the 1 b-jet (left) and 2 b-jet (right) selections.

To increase the exclusion power of the analysis, a shape-fit strategy is favoured with respect to a cut-and-count approach. Each signal region is divided into nine bins with eight bins for the interval $[0.4, 0.8]$ and one bin covering the $[0.8, 1.0]$ interval.

8.9 Background estimation

Since the dominant Standard Model background of the analysis are $t\bar{t}$ and $W+$jets production, they are normalised in control regions. All other backgrounds are normalised to the predicted cross sections from simulation.

8.9.1 Control regions

The control regions CR1-tN and CR2-tN are defined for the 1 b-jet and 2 b-jet selections based on the BDT1 and BDT2 variables, respectively. Each control region is divided into 17 bins to use a shape-fit approach. The interval $[-0.8, 0]$ is divided into 16 bins, with the same bin width, as used in the signal regions, while the interval $[-1, -0.8]$ is considered as one bin. Taking into account, that the 2 b-jet region is dominated by the $t\bar{t}$ process, the CR2-tN region can be considered a $t\bar{t}$ control region, and CR1-tN as a $W+$jets control region.

8.9.2 Multijet background

The multijet background for the tN diagonal analysis is estimated separately for electrons and for muons. An estimation for the electron channel is performed with two different approaches, with the Exponential Extrapolation approach and with the Matrix Method. For the muon channel only the Exponential Extrapolation approach is used.

For detailed descriptions for both approaches, as well as for the definitions which are used in the following, the reader is referred to Chapter 9.

Fake leptons in the 1 b-jet and 2 b-jet selections are estimated for the FLR1-tN and FLR2-tN regions, respectively. The selection criteria for these regions are defined as follows:

- The one-lepton event cleaning cuts, as described in Section 6.2.3;
- Exactly one signal electron or muon, according to the estimate, with $p_{\mathrm{T}} > 25$ GeV, and no other baseline leptons;
- At least four jets with $p_{\mathrm{T}} > 25$ GeV;
- Exactly 1 b-jet or exactly 2 b-jets (for the FLR1-tN or FLR2-tN selection, respectively);
- Leading and sub-leading light jets: $p_{\mathrm{T}}(q_1) > 80$ GeV, $p_{\mathrm{T}}(q_2) > 40$ GeV;
- $E_{\mathrm{T}}^{\mathrm{miss}} > 80$ GeV;
- $m_{\mathrm{T}} > 60$ GeV;
- BDT1 > 0 or BDT2 > 0 (for the FLR1-tN or FLR2-tN selection, respectively).

The selection uses a missing transverse momentum trigger with an 80 GeV threshold on trigger level without any isolation requirement. This trigger is fully efficient (the efficiency is above 99%) for offline-reconstructed $E_{\mathrm{T}}^{\mathrm{miss}}$ values above 150 GeV. To correct the trigger inefficiencies below 150 GeV for simulated events, correction factors are applied.

Estimation of fake electrons

The multijet background contribution for the electron channel is estimated with two different approaches: with the Exponential Extrapolation and with the Matrix Method.

Exponential Extrapolation estimation

To employ the fake electron estimation approach (see Section 9.2), an isolation parameter ξ and loose and tight electrons have to be defined.

The isolation parameter ξ is defined as $p_{\mathrm{T}}^{\mathrm{cone}\,0.2}/p_{\mathrm{T}}$, where the $p_{\mathrm{T}}^{\mathrm{cone}\,0.2}$ is the track isolation variable with $\Delta R = 0.2$ GeV, see Section 3.2. A loose electron is defined as a baseline electron, while for a tight electron a definition of a signal electron without the isolation requirement $\xi < 0.1$ is used, see Section 6.2.1.

The distribution of the isolation parameter ξ for loose and tight electrons for the 1 b-jet and 2 b-jet selections, for the FLR1-tN and FLR2-tN region, respectively, are shown in Figure 8.16. Each distribution is fitted by an exponential function $e^{-\alpha\xi+\beta}$ in the $[0.1, 0.7]$ region. The fit

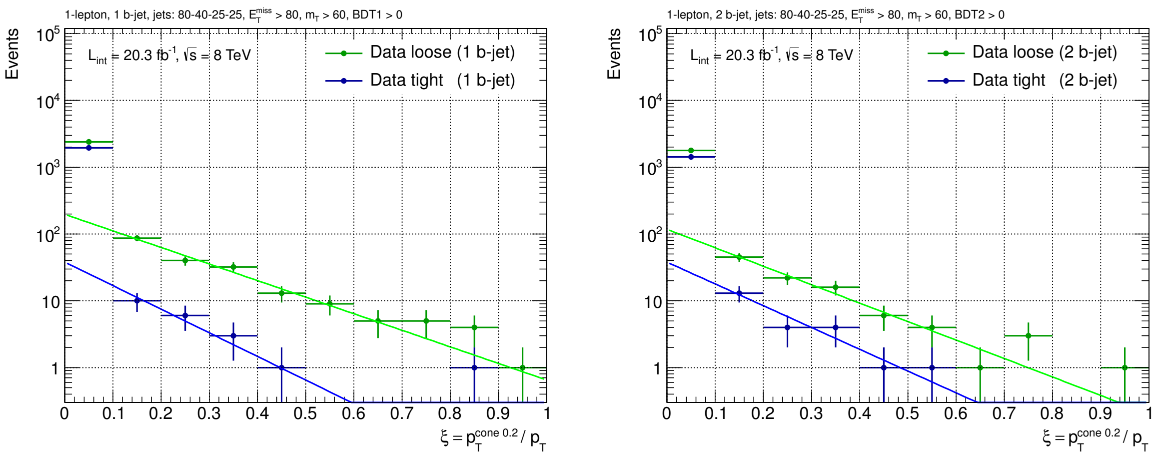

Figure 8.16: Distribution of the $p_{\mathrm{T}}^{\mathrm{cone}\,0.2}/p_{\mathrm{T}}$ isolation parameter for loose and tight electrons for the 1 b-jet (left) and 2 b-jet (right) selection for the FLR1-tN and FLR2-tN regions (for details, see text). Each distribution is fitted by an exponential function $e^{-\alpha\xi+\beta}$ in the $[0.1, 0.7]$ interval.

results with the corresponding extrapolation to the signal electron region ($\xi < 0.1$) are presented in Table 8.3. Only statistical uncertainties are shown. Since the estimate is based only on tight electrons and an exponential function overestimates the fake electrons background, no additional systematic uncertainties are included (see Section 9.2). One can see, that for both the FLR1-tN and the FLR2-tN regions, the contribution of the fake electrons with a confidence

	Loose electrons			Tight electrons				
Region	α	β	$N_{\text{data}}^{\text{loose}}$	α	β	$N_{\text{data}}^{\text{tight}}$	N_{fake}	QCD [%]
FLR1-tN (1 b-jet)	5.7 ± 0.5	5.3 ± 0.1	2398	8.1 ± 1.4	3.6 ± 0.4	1946	26 ± 9	1.3 ± 0.5
FLR1-tN (2 b-jet)	6.4 ± 0.7	4.8 ± 0.2	1783	7.5 ± 1.5	3.6 ± 0.4	1423	27 ± 9	1.9 ± 0.6

Table 8.3: Results of the fit of an exponential function $e^{-\alpha\xi+\beta}$ to the distribution of the isolation parameter $\xi = p_{\mathrm{T}}^{\mathrm{cone}\,0.2}/p_{\mathrm{T}}$ for loose and tight electrons. The fit performed for the FLR1-tN and FLR2-tN regions in the $[0.1, 0.7]$ interval. Only statistical uncertainties are presented.

level of 95% found to be less than 3%.

Matrix Method estimation

To use the Matrix Method, see Section 9.1, the loose-to-tight conversion coefficients for real ($\varepsilon_{\text{real}}$) and fake ($\varepsilon_{\text{fake}}$) electrons have to be estimated.

The $\varepsilon_{\text{real}}$ coefficient is estimated from $t\bar{t}$ Monte Carlo samples, while for the $\varepsilon_{\text{fake}}$ estimation a data-driven approach is used. The coefficients are estimated for the FLR1-tN and FLR2-tN regions.

Figure 8.17 shows a ratio between tight and loose electrons as a function of the isolation parameter ξ for the FLR1-tN and FLR2-tN regions. The value of $\varepsilon_{\text{fake}}$ is estimated as a tight-to-loose ratio from the $[0.1, 0.7]$ interval. The uncertainty on $\varepsilon_{\text{fake}}$ is estimated as the statistical uncertainty of the ratio, taking the correlation between the loose and tight electrons into account.

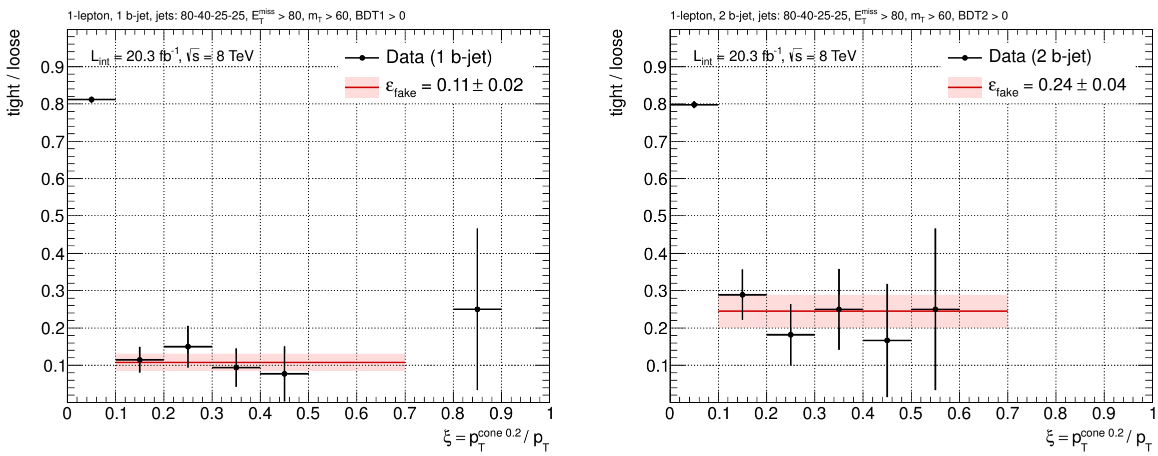

Figure 8.17: The ratio between tight and loose electrons as a function of the isolation parameter ξ for the FLR1-tN (left) and FLR2-tN (right) regions. The value of $\varepsilon_{\text{fake}}$ is estimated from the $[0.1, 0.7]$ interval. The uncertainty corresponds to the statistical uncertainty of the ratio.

The uncertainty on $\varepsilon_{\text{real}}$ is estimated by summing in quadrature the statistical and the electron identification, scale and resolution systematic uncertainties. The results are presented in

Table 8.4.

Region	Stat.	Scale	Resolution	ID efficiency	Total
FLR1-tN (1 b-jet)	0.07%	0.06%	0.02%	0.15%	0.18%
FLR1-tN (2 b-jet)	0.07%	0.11%	0.03%	0.17%	0.22%

Table 8.4: Uncertainties on the $\varepsilon_{\text{real}}$ coefficients. Systematic uncertainties are the electron identification, scale and resolution uncertainties. The total uncertainty is estimated by summing in quadrature the statistical and systematic uncertainties.

The results for $\varepsilon_{\text{real}}$ and $\varepsilon_{\text{fake}}$ with the corresponding matrix method estimation of the real (N_{real}) and fake (N_{fake}) electrons for the FLR1-tN and FLR2-tN regions are presented in Table 8.5. The number of fake electrons N_{fake} is estimated using the equation 9.2. The uncertainty of the N_{fake} takes into account the correlation between $N^{\text{loose}}_{\text{data}}$ and $N^{\text{tight}}_{\text{data}}$.

Region	$\varepsilon_{\text{real}}$	$\varepsilon_{\text{fake}}$	$N^{\text{loose}}_{\text{data}}$	$N^{\text{tight}}_{\text{data}}$	N_{fake}	QCD [%]
FLR1-tN (1 b-jet)	0.831 ± 0.002	0.11 ± 0.02	2398	1946	7 ± 13	0.4 ± 0.7
FLR1-tN (2 b-jet)	0.829 ± 0.002	0.24 ± 0.04	1783	1423	22 ± 9	1.5 ± 0.6

Table 8.5: Results of the Matrix Method for the FLR1-tN and FLR2-tN regions. The total uncertainties are shown.

For both estimates the contamination of the background from the QCD processes is found to be below 3% with a confidence level of 95%.

Estimation of fake muons

To employ the fake muon estimation approach (see Section 9.3), an isolation parameter ζ and loose and tight muons have to be defined.

The isolation parameter ζ is defined as $p_{\text{T}}^{\text{cone}\,0.4} - p_{\text{T}}^{\text{cone}\,0.2}$, where $p_{\text{T}}^{\text{cone}\,0.2}$ and $p_{\text{T}}^{\text{cone}\,0.4}$ are the track isolation variables with $\Delta R = 0.2$ GeV and 0.4 GeV, respectively, see Section 3.3. A loose muon is defined as a signal muon without an isolation requirement and with the relaxed overlap removal selection $\Delta R(\mu, \text{jet})$ from 0.4 to 0.2, see Section 6.2.2. A tight muon is defined as a signal muon without an isolation requirement.

The multijet background contribution for the muon channel in the 1 b-jet and 2 b-jet selection is estimated for the FLR1-tN and FLR2-tN regions, respectively.

The distributions of the parameter ζ for loose and signal muons for FLR1-tN and FLR2-tN regions, denoted as $h^{\text{loose}}(\zeta)$ and $h^{\text{signal}}(\zeta)$, respectively, are shown in Figure 8.18. An exponential function $e^{-\alpha\zeta+\beta'}$ is fitted to the $h^{\text{loose}}(\zeta)$. The estimated fit parameter α is used to fit $e^{-\alpha\zeta+\beta}$ to the $h^{\text{signal}}(\zeta)$. Both functions are fitted in the $[30, 120]$ GeV interval.

The results of the fit and the estimated numbers of fake signal muons $N^{\text{signal}}_{\text{fake}}$ are presented in Table 8.6. For the uncertainty estimation for $N^{\text{signal}}_{\text{fake}}$ the α and β parameters are conservatively

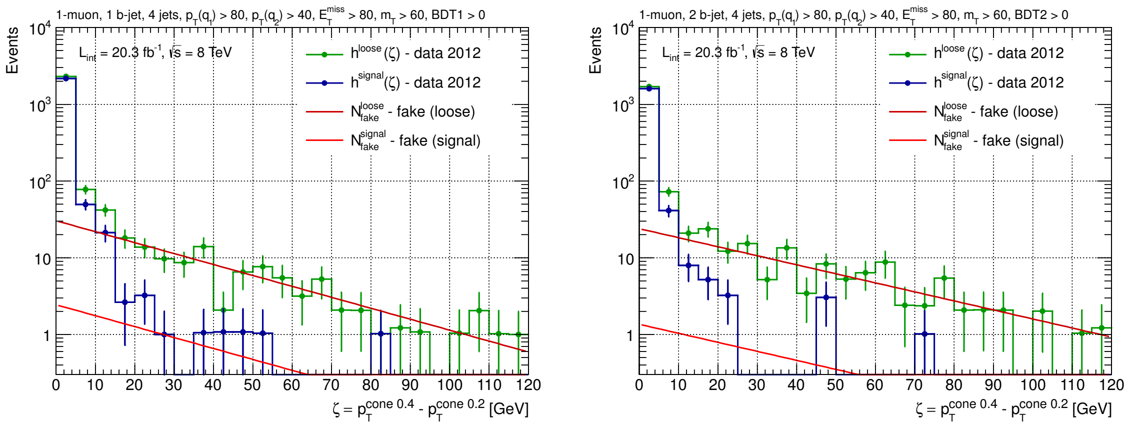

Figure 8.18: Distributions of the parameter ζ for loose and tight muons, denoted as $h^{\text{loose}}(\zeta)$ and $h^{\text{signal}}(\zeta)$, respectively, for the FLR1-tN (1 b-jet, left) and FLR2-tN (2 b-jet, right) regions.

considered to be correlated. Due to the large statistical uncertainty, no additional systematic uncertainties are assigned, but even with an additional uncertainty of 100%, the results show, that for both regions the contribution from the multijet background is negligible, with respect to other uncertainties, see Section 8.10.

Region	α	β	β'	$N_{\text{fake}}^{\text{signal}}$	QCD [%]
FLR1-tN (1 b-jet)	0.033 ± 0.005	0.9 ± 0.3	3.4 ± 0.3	15 ± 8	0.7 ± 0.4
FLR1-tN (2 b-jet)	0.027 ± 0.004	0.3 ± 0.2	3.2 ± 0.3	10 ± 4	0.6 ± 0.3

Table 8.6: Fit results and estimation of fake signal muons $N_{\text{fake}}^{\text{signal}}$ for the FLR1-tN (left) and FLR2-tN1 (right) regions.

8.10 Systematic uncertainties

8.10.1 Strategy to estimate shape-fit uncertainties

The tN diagonal analysis significantly benefits from a shape-fit. Therefore, some challenges related to the estimation of shape-fit uncertainties have to be discussed.

Shape variation

The following model of shape variation is considered. A nominal shape is denoted as $f_0(x)$, while a shape shape variation as $\delta f(x)$. It is assumed, that the variation of the shape $f(x)$ depends on a random parameter α, which is usually distributed according to a Gaussian probability density distribution. The variation $f_\alpha(x)$ is defined as

$$f_\alpha(x) = f_0(x) + \alpha \cdot \delta f(x). \tag{8.21}$$

As an example of such a variation the Jet Energy Scale or the b-tagging systematic uncertainties can be considered. The statistical framework used for the analysis properly handles such variations. It can also take into account an asymmetric behaviour of the shape variations.

Shape uncertainty

Another type of shape uncertainty, which is often also considered as a shape variation, but has a completely different nature, is the uncertainty related to the factorisation or renormalisation scale variations of some process or an uncertainty estimated as a difference between the samples generated with two different Monte Carlo generators.

For example, for the factorisation and renormalisation scale variations of the $t\bar{t}$ production, an official recommendation is to vary the corresponding scales from the nominal by a factor of 0.5 and 2.0. It is assumed, that such an approach will reasonably estimate the uncertainties due to missing higher order contributions.

Often an uncertainty is estimated as a difference between two generators. For example, the uncertainty related to the parton shower modelling for $t\bar{t}$ production is estimated as the difference between the POWHEG+PYTHIA and POWHEG+HERWIG samples. By including this uncertainty in the analysis, the results get independent of the generators are used. However, this does not mean that the results are consistent if another, a third, generator is employed.

A model for this type of uncertainties can be described as follows. A distribution modelled by a Monte Carlo generator is denoted as $f_0(x)$, while the true distribution is denoted as $f(x)$. The shape difference is then defined as

$$\delta f(x) = f(x) - f_0(x). \tag{8.22}$$

The shape uncertainty ΔF is estimated as the difference between distributions $F_1(x)$ and $F_2(x)$ generated using two different generators

$$\Delta F = F_1(x) - F_2(x). \tag{8.23}$$

It is assumed, that the true shape variation $|\delta f(x)|$ can be majorated by $|\Delta F(x)|$:

$$|\delta f(x)| < |\Delta F(x)| \, . \tag{8.24}$$

If the uncertainty depends on a parameter α, it can be rewritten as:

$$|\delta f_\alpha(x)| < |\alpha \cdot \Delta F(x)| \, . \tag{8.25}$$

The main challenge for such a type of uncertainties is, that the true distribution is not known. The approach to use $\Delta F(x)$ as a shape variation, i.e. $\delta f(x) = \Delta F(x)$ may cause a significant underestimation of the uncertainty. An example of such an underestimation is given in the following.

Underestimation of the shape uncertainty

In this section it is shown, that a $|\delta f(x)| < |\Delta F(x)|$ shape uncertainty has to be considered as inequality and cannot be modelled as a $f_\alpha(x) = f_0(x) + \alpha \cdot \Delta F(x)$.

As an example, distributions shown in Figure 8.19 are considered. The goal is to exclude a signal model with the signal-to-background ratio shown as the red line. For the exclusion a shape-fit approach is used. The relative shape uncertainty $\delta f(x)/f_0(x)$ between the true distribution and the background is shown as the blue line.

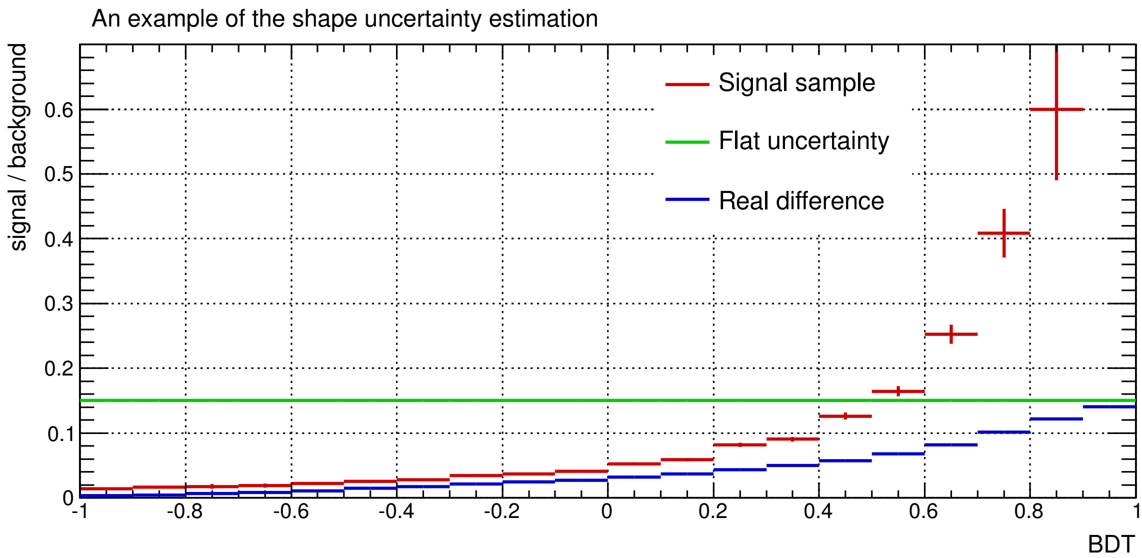

Figure 8.19: An example of a shape uncertainty estimation. The red line shows a signal-to-background ratio, the green line represents a flat $\pm 15\%$ shape variation of the background, and the blue line corresponds to the ratio between the true distribution and the background.

In the first case the shape uncertainty is estimated as a flat uncertainty of $\pm 15\%$. The $+1\sigma$ variation of the background is shown as a green line. The shape uncertainty is considered correlated between bins.

In the second case the shape uncertainty of a $+1\sigma$ variation is assumed to be the difference to the true shape (blue line), which is everywhere less than 15%, but looks similar to the signal shape (red line).

For this example $\delta f(x) < \Delta F = 15\%$. In the $[-1, 0.5]$ interval for the $+1\sigma$ variation the flat uncertainty (green line) is larger than the expected signal. This significantly decreases the CL_{s+b} with respect to the same $+1\sigma$ variation for the ideal shape (blue line). Therefore, the probability to mimic the signal (red line) is much higher for the true uncertainty variation (blue line), than for the simplified flat shape (green line) which overestimates the uncertainty in the whole interval.

The conclusion is that interpreting a shape uncertainty as a shape variation may cause an underestimation of systematic uncertainties.

Estimation approach

It is assumed that the shape difference $\delta f(x)$ between the true distribution and the generated Monte Carlo samples is overestimated $|\delta f(x)| < |\Delta F(x)|$, where $\Delta F(x)$ is the estimated uncertainty.

Since $\delta f(x)$ is not known, one can consider all possible shape variations $|\delta f(x)| < |\Delta F(x)|$ and chose one, which gives the most conservative result.

This approach allows to avoid underestimation of uncertainties, but it has some disadvantages:

- It is difficult to determine, which $\delta f(x)$ variation has to be used;
- The worst shape uncertainty variation scenario may be over-conservative;
- The worst case can be signal model dependent.

One of the reasons, why an increase of an uncertainty improves the result is that in some regions the relative uncertainty δ is higher than the signal-to-background ratio λ. Therefore, by increasing the uncertainty, the difference $|\delta - \lambda|$ also increases, which leads to a decrease of the probability to observe this variation, i.e. the corresponding CL_s value will decrease.

This will allow to improve exclusion limits of the analysis. In case, when $\delta < \lambda$, by increasing the uncertainty, the difference is decreasing, and the probability for this variation is also increasing. This will lead to increase of the CL_s value, therefore the exclusion limits of the analysis will worsened. To avoid cases, where an overestimation of the uncertainty significantly improves the result, one can select only region, where $\lambda > \delta$.

For the current analysis the theoretical uncertainties are estimated as the difference between two generators or scale variations. Therefore, to avoid an underestimation of the uncertainties, only signal regions with a signal-to-background ratio larger than the total theoretical uncertainty are used. For the $m(\tilde{t}_1, \tilde{\chi}_1^0) = (250, 75)$ GeV signal model, and in case of a $\pm 10\%$ uncertainty, this approximately corresponds to the BDT > 0.4 region for both the 1 b-jet and 2 b-jet selections.

The shape of the signal-to-background ratio for all signal models is a monotonic function. It remains similar for signal models along the diagonal, see Figure 8.4. One can see, that the signal-to-background ratio increases, for signal models away from the diagonal, see Figure 8.11. Based on these observations, for all signal models the same signal region is used.

The shape fit is performed under the assumption of $\delta f(x) = \Delta F(x)$. Taking into account, that this may underestimate a theoretical uncertainty, the results are cross-checked for the diagonal signal models near to the exclusion borders for different signal models. A cross-check is performed under the assumption that in the signal region (BDT > 0.4) the total theoretical uncertainty can be estimated by a linear function, which is parametrised as

$$\delta f(x) = \beta(\alpha \cdot x + 1 - \alpha). \tag{8.26}$$

The CL_s values are calculated for uncertainty variations for different positive α slopes, while keeping the same maximal uncertainty $\delta f(1) = \beta$. The results are compared with the one estimated by the nominal analysis.

8.10.2 Experimental uncertainties

The experimental uncertainties are estimated using an official package from the ATLAS SUSY Working Group. The following experimental uncertainties are included:

Luminosity uncertainty
The dominant $t\bar{t}$ and $W+$jets backgrounds are normalised in control regions. For all other backgrounds, the total contribution for each bin is less than 10%. Therefore, the integrated luminosity uncertainty of $\pm 2.8\%$ is added to the cross-section uncertainty of each process.

Pileup uncertainties
An uncertainty on pileup reweighting is obtained by scaling the average number of interactions per bunch crossing μ up and down by $\pm 10\%$.

Jet energy scale and resolution
The systematic uncertainty is estimated by varying the jet energy scale by $\pm 1\sigma$ of the uncertainty on the jet energy scale coherently for all jets in the event. The uncertainty on the jet energy scale is estimated using the software provided by the ATLAS Jet/Etmiss Working Group.

Jet energy resolution
The jet resolution uncertainty is estimated by applying a smearing to the p_{T} of each jet, which depends on the η and p_{T} parameters of the jet. The shape uncertainty is estimated as the difference between the variation and the nominal shapes. The shape variation is symmetrised.

$E_{\mathrm{T}}^{\mathrm{miss}}$ soft term
The uncertainties are estimated by varying the scale and resolution of the $E_{\mathrm{T}}^{\mathrm{miss}}$ soft term (see Section 3.6).

b-tagging efficiency
The systematical uncertainty on the b-tagging efficiency is estimated by varying the b-tagging scale factors, which depends on the η, p_{T}, and the flavour, within the uncertainties of the measured tagging efficiencies and mistagging rates. The uncertainties are estimated separately for b-, c-, and light-jets and treated as uncorrelated.

Lepton uncertainties
For the one-lepton analysis the lepton identification, energy scale and resolution and trigger efficiency uncertainties are usually below $\pm 1\%$, therefore for this analysis they are neglected.

Almost all experimental uncertainties have up and down variations, which are used to model the corresponding shape variation in an asymmetric way. For those uncertainties, which have only one variation, for example the jet energy resolution uncertainty, the shape variation is symmetrised.

8.10.3 Theoretical uncertainties

In this section the estimation of theoretical uncertainties is presented.

The most significant region for the analysis is BDT > 0.7, see Figure 8.5. Due to a lack of events in this region, the theoretical uncertainties on the shape variation are affected by a high statistical uncertainty. To improve the precision of the uncertainty estimate, it is assumed, that the systematic uncertainty as a function of the BDT output can be estimated by a smooth curve. It is further assumed, that over short intervals this curve can be estimated by a second order polynomial $P_2(x) = a_2x^2 + a_1x + a_0$. Since the uncertainty as a function of the BDT output has a shape, which is more complex than the second order polynomial, it cannot be estimated by fitting $P_2(x)$ in the whole $[-1, 1]$ interval.

Therefore, for the current analysis each theoretical uncertainty is estimated by fitting a second order polynomial $P_2(x)$ separately to the $[-1, 0.4]$ and $[-0.2, 1]$ intervals. The corresponding fit results are referred to as $\{a_i\}$ and $\{b_i\}$ coefficients, respectively. The fit regions overlap, but on the plots the corresponding fit results are shown for the $[-1, 0.2]$ and $[0.2, 1]$ intervals, which have no overlap. One can argue, that the uncertainty curve is discontinuous for BDT $= 0.2$. In the analysis, only the $[-1, 0]$ and $[0.4, 1]$ intervals are used, therefore, the curve in the $[0, 0.4]$ interval is not involved in the analysis, and can be replaced by any other smooth curve without affecting the results.

For each systematic uncertainty one of types of uncertainty (normalised uncertainty, symmetrised uncertainty or symmetrised full difference) is used (see Section 4.8).

Since the $t\bar{t}$ and $W+$jets backgrounds are normalised in the TCR1-tN and TCR2-tN control regions, for these processes uncertainties on transfer factors (see Section 4.6) as a function of the BDT output are estimated. For this, all variations are normalised in the $[-1, 0]$ interval.

In addition, in each figure, the distribution of the $\mathrm{BDT_{VR}}(m_\mathrm{T} + 40\ \mathrm{GeV})$ and $\mathrm{BDT_{VR}}(\ell \times 2.0)$ outputs, which are used for the BDT validation, see Section 8.7, are also shown. These distributions have smaller statistical uncertainties in the BDT > 0.6 region. They are not involved in the fit and are shown only for comparison.

Uncertainty estimates on particle level

Some uncertainties are estimated on particle level, without taking into account detector effects. At particle level, a sharp cut-off of the m_T distribution appears around 80 GeV, while when including the detector simulation it is smoothed out and moves to 90−100 GeV, see Figure 3.21. For this analysis, events passing the BDT > 0.6 requirement mainly have the m_T value about 120 GeV, see Figure 8.20. Therefore, the calculation of the BDT output on particle level results in very few events in the signal region. This affects all theoretical uncertainties of the $W+$jets production, which are estimated on particle level.

This problem affects the factorisation and renormalisation scale uncertainties of the $t\bar{t}$ production, which are also estimated on particle level. For the BDT > 0.6 requirement on particle level, most of the semileptonic decays are rejected, and mainly dileptonic decays with a hadronically decaying τ lepton pass the selection. On particle level the latter have one lepton and three neutrinos and can easily give $m_\mathrm{T} \approx 120$ GeV. Therefore, for the $t\bar{t}$ production, the BDT > 0.6 requirement on particle level mainly accounts for the dileptonic decay mode.

One way to still estimate an uncertainty on particle level is to add an additional resolution smearing to the jets and to recompute the missing transverse momentum. Jets are smeared

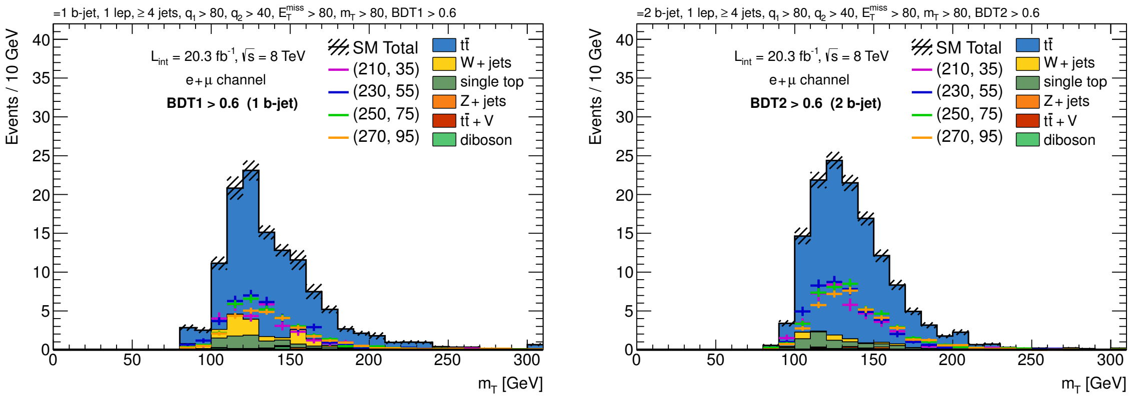

Figure 8.20: The m_T distribution after the BDT1 > 0.6 (1 b-jet, left) and BDT2 > 0.6 (2 b-jet, right) selection. Both distributions are peaked around the $m_T \approx 120$ GeV.

based on equation 3.23, where only the term related to the sampling nature of the calorimeter is kept

$$\frac{\sigma_{p_T}}{p_T} = \frac{a}{\sqrt{p_T}}, \quad a = 1.3\ \sqrt{\text{GeV}}, \tag{8.27}$$

The parameter a is calculated for p_T measured in GeV and estimated from the Figure 3.13, where for jets with $p_T = 25$ GeV the resolution is about 26%, while for $p_T = 200$ GeV is about 9%. In the following, for all uncertainties estimated on a particle level, the jet smearing approach is used.

$t\bar{t}$ production

Parton shower and initial and final state radiation uncertainties on the $t\bar{t}$ production are estimated on detector level, based on samples including the ATLFAST-II fast detector simulation. For these uncertainties, to decrease statistical fluctuations, the number of events is increased by relaxing the selection on the two leading light jets q_1 and q_2 to $p_T(q_1) > 60$ GeV and $p_T(q_2) > 25$ GeV. The factorisation and renormalisation scale uncertainties are estimated on particle level with jet smearing and without relaxing any selection requirements. Since the $t\bar{t}$ process is normalised in the control regions, all uncertainties are estimated on the corresponding transfer factors.

- **Generator uncertainties**
  Following the general one-lepton analysis approach, the uncertainty related to the choice of the generator is not included in the total $t\bar{t}$ uncertainty due to a bad data-MC agreement for the MC@NLO and ALPGEN generators, see details in Section 6.6.3.

- **Scale variations**
  Uncertainties related to the choice of the factorisation and renormalisation scales are estimated on particle level by varying the corresponding scales by factors of 0.5 and 2. The transfer factor uncertainties as a function of the BDT output are shown in Figure 8.21.

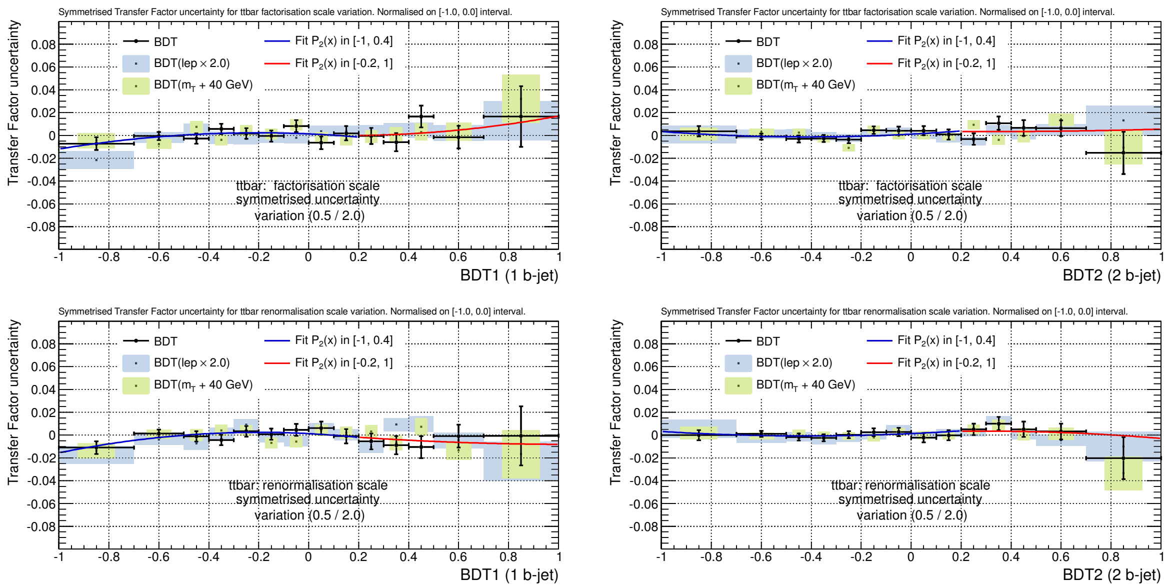

Figure 8.21: Transfer factor uncertainties on the factorisation (top) and renormalisation (bottom) scale variations for the $t\bar{t}$ production as a function of the BDT output for the 1 b-jet (left) and 2 b-jet (right) selections.

– **Parton shower**
Parton shower uncertainties for the BDT1 and BDT2 selections are estimated on the detector level simulation as a symmetrised full difference between the POWHEG+HERWIG and nominal POWHEG+PYTHIA samples. The parton shower uncertainty as a function of the BDT output for the 1 b-jet and 2 b-jet selections is shown in Figure 8.22.

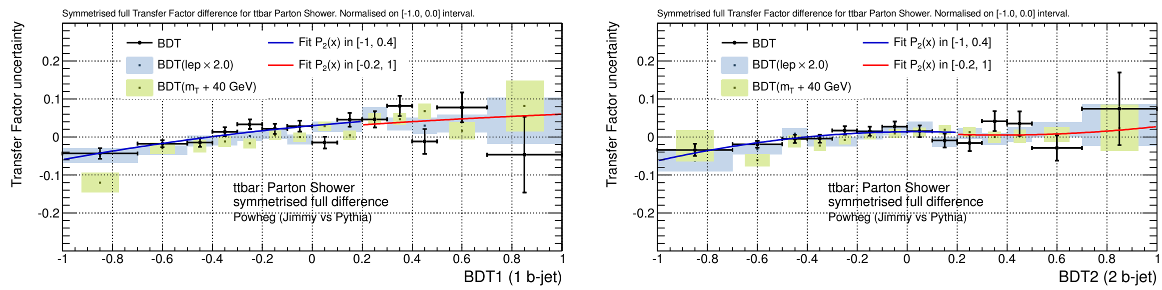

Figure 8.22: Parton shower uncertainty as a function of the BDT output for the $t\bar{t}$ production for the 1 b-jet (left) and 2 b-jet (right) selections.

– **Initial and final state radiation**
The uncertainty is estimated on the detector level simulation as a symmetrised uncertainty of the $t\bar{t}$ production samples generated with ACERMC for higher and lower parton shower activity. The transfer factor uncertainties as a function of the BDT output are shown in Figure 8.23.

All theoretical uncertainties are considered to be uncorrelated. The dominant uncertainty on the $t\bar{t}$ production is the ISR/FSR uncertainty, which is about ±8% for the signal regions. The

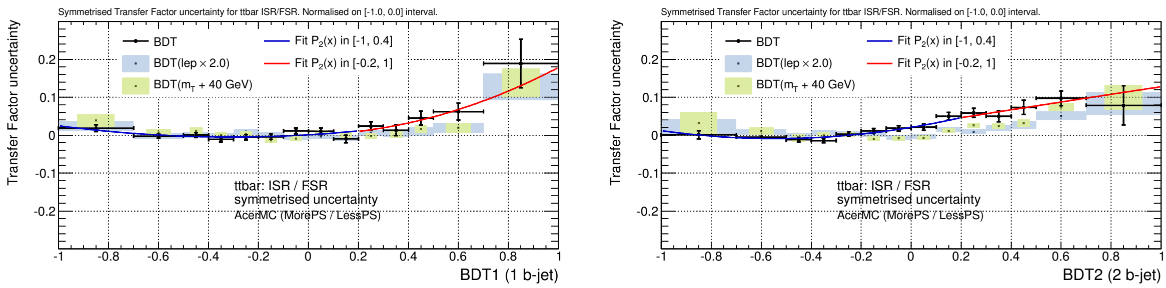

Figure 8.23: Transfer factor uncertainties on the initial and final state radiation as a function of the BDT output for the $t\bar{t}$ production for the 1 b-jet (left) and 2 b-jet (right) selections.

parton shower uncertainty is the sub-dominant uncertainty and is below $\pm 5\%$. The scale variation uncertainties are small, about $\pm 2\%$.

W+jets production

All uncertainties are estimated on particle level. The W+jets process is normalised in the control regions. Therefore all uncertainties are estimated on the corresponding transfer factors.

- **Scale variations**
  Three different scale variations are considered. The systematic uncertainty, related to the matrix element and parton shower matching scheme is estimated by varying the CKKW jet matching parameter from the nominal 20 GeV to 15 GeV and 30 GeV. The factorisation and renormalisation scales are varied by factors of two from the nominal value. Figure 8.24 shows the transfer factor uncertainties as a function of the BDT output.

- **Finite number of partons**
  This uncertainty is related to the number of partons used in the hard scattering. Samples with four and five extra partons generated at matrix element are compared on particle level, see the Figure 8.25.

All uncertainties are considered to be uncorrelated. Due to the low number of events in the last bin $[0.6, 1]$, the estimation of the uncertainty is dominated by the statistical component.

The uncertainties on the W+heavy flavour composition is estimated following the ATLAS SUSY Working Group recommendations. The normalisation of the W+jets background is driven by the 1 b-jet control region (CR1-tN), since the requirement of two b-tagged jets significantly suppresses the W+jets background contribution in the CR2-tN control region. Since the signal and control regions for the 1 b-jet selection (SR1-tN and CR1-tN) have the same number of b-tagged jets, no additional uncertainty related to the W+heavy flavour composition is assigned. Following the recommendations for the 2 b-jet selection an additional uncertainty of $\pm 24\%$ related to the W+heavy flavour composition is assigned for the signal and control regions (SR2-tN and CR2-tN). A contribution of the W+jets background in the SR2-tN signal region is very small (less than 3%), therefore, this uncertainty does not affect the final results.

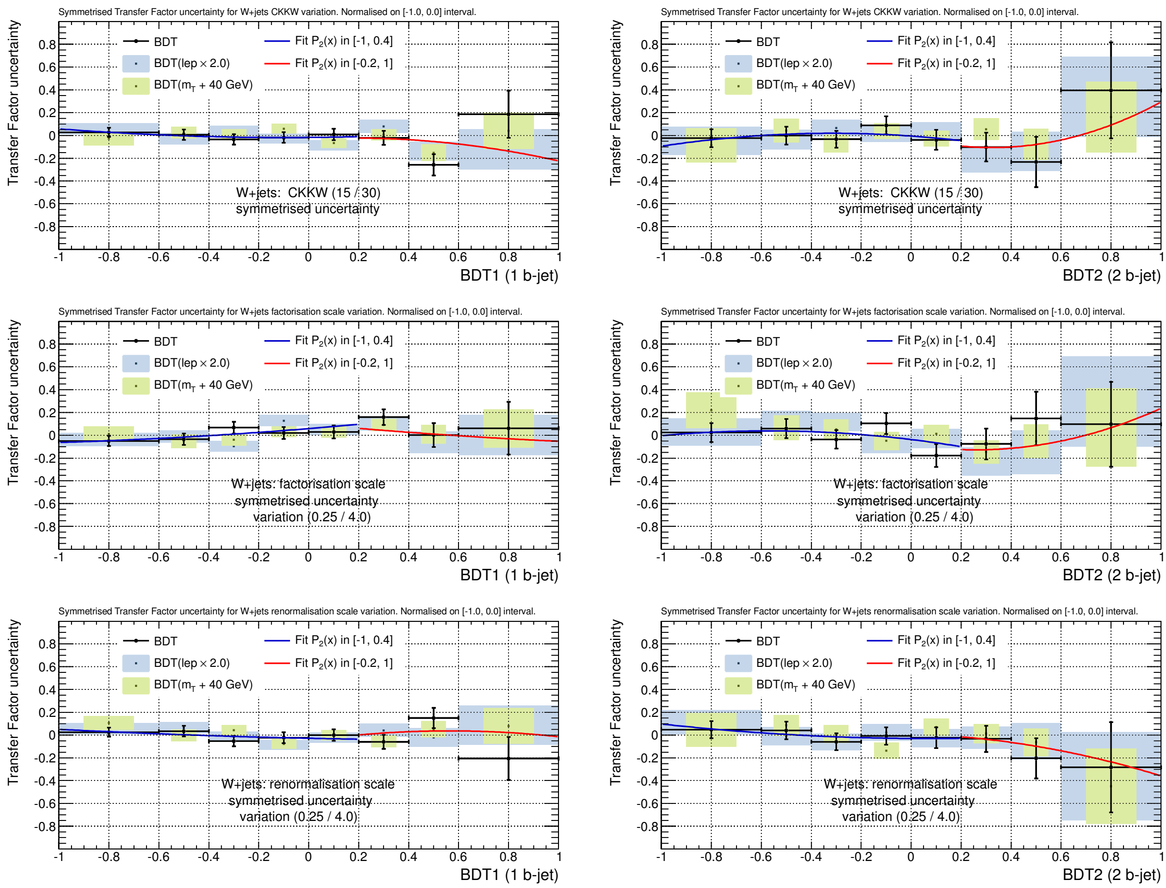

Figure 8.24: Transfer factor uncertainties as a function of the BDT output for the W+jets production.

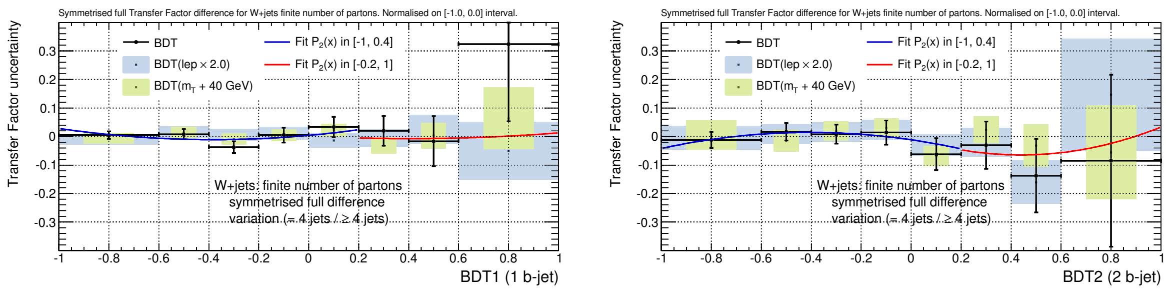

Figure 8.25: Transfer factor uncertainties related to the finite number of partons at matrix element as a function of the BDT output for the W+jets production.

Single top production

All uncertainties on the single top production are estimated on detector level, based on samples generated with the ATLAS full simulation. To decrease the statistical uncertainty, the number of events is increased by relaxing the selection on the two leading light jets q_1 and q_2 to $p_T(q_1) > 60$ GeV and $p_T(q_2) > 25$ GeV.

– **Generator and parton shower**
The generator uncertainties are estimated by a comparison of samples generated with POWHEG and MC@NLO interfaced to HERWIG+JIMMY for parton showering. The parton shower uncertainties are estimated by a comparison to the POWHEG generated events interfaced to PYTHIA or HERWIG+JIMMY for parton showering. Figure 8.26 represents the generator and parton shower uncertainties for the Wt-channel.

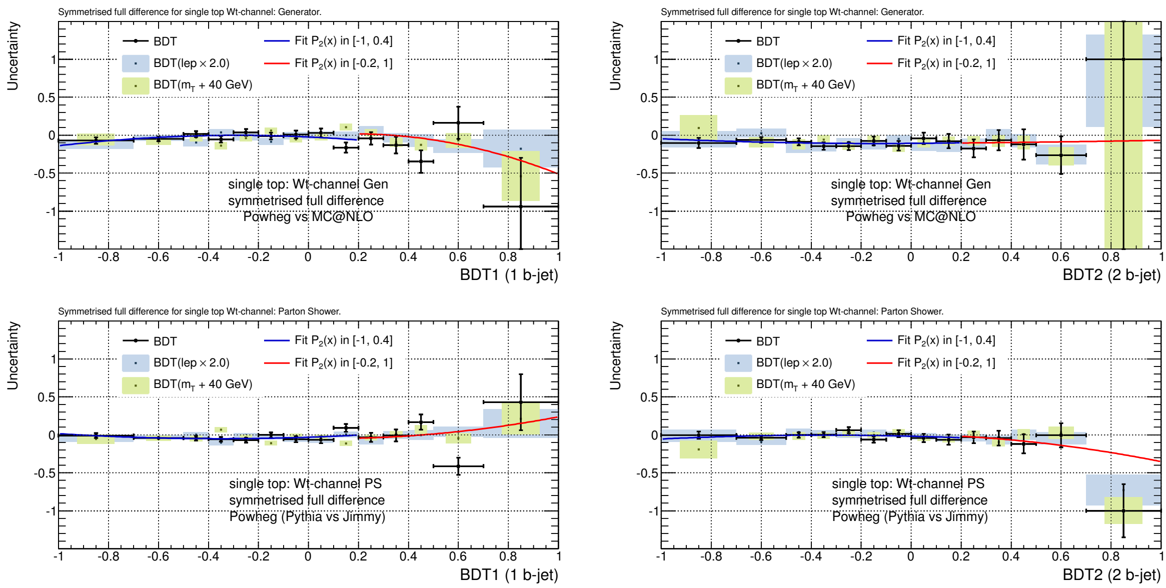

Figure 8.26: The generator (top) and parton shower (bottom) uncertainties for the Wt-channel for the single top production. The uncertainties as a function of the BDT output are shown for the 1 b-jet (left) and 2 b-jet (right) selections.

The combined generator and parton shower uncertainties for the s-channel process are estimated as the difference between POWHEG+PYTHIA and MC@NLO+HERWIG samples, see Figure 8.27.

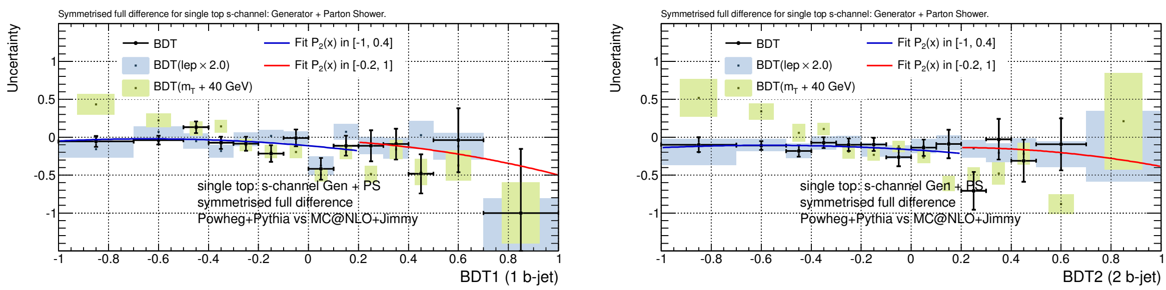

Figure 8.27: The combined generator and parton shower uncertainties for the s-channel for the single top production. The uncertainties are shown as a function of the BDT output for the 1 b-jet (left) and 2 b-jet (right) selections.

– **Interference with ttbar**
Uncertainties related to the single top Wt-channel interference with the next-to-leading

order $t\bar{t}$ production are estimated by comparison of the *diagram removal* (DR) and *diagram subtraction* (DS) samples [96]. The results are shown in Figure 8.28.

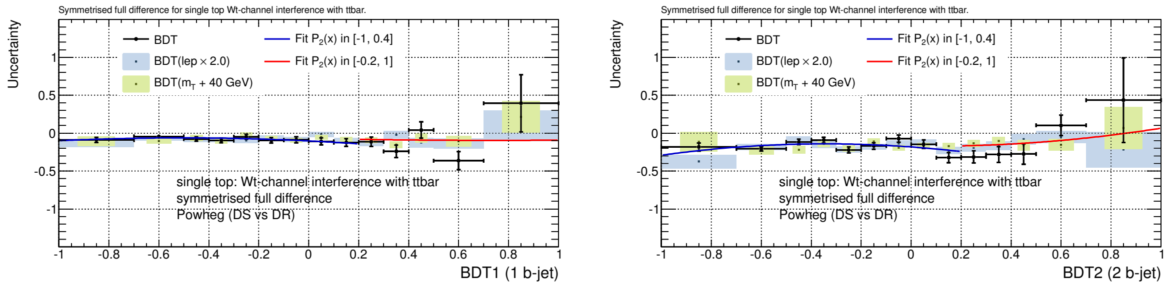

Figure 8.28: Uncertainty on the interference between single top Wt and $t\bar{t}$ production for the 1 b-jet (left) and 2 b-jet (right) selections. A comparison is performed between the diagram removal (DR) and diagram subtraction (DS) samples.

– **Initial and final state radiation**
Initial and final state radiation uncertainties for single top process are presented in Figure 8.29. The uncertainties are estimated as symmetrised uncertainties between the AcerMC with higher and lower parton showering activity.

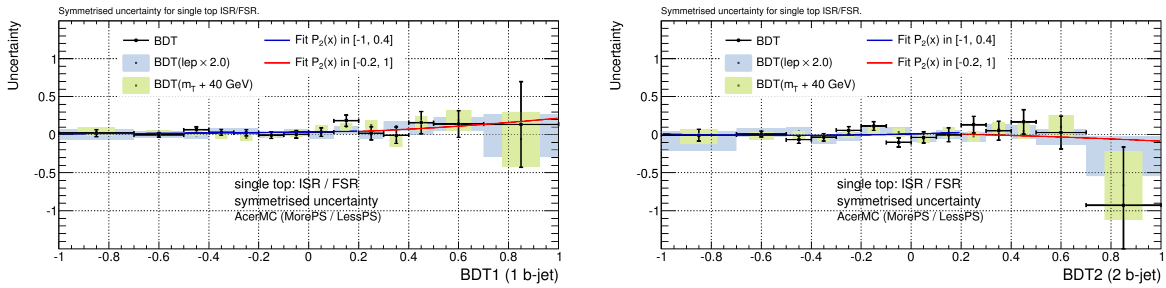

Figure 8.29: Uncertainties resulting from the ISR/FSR modelling as a function of the BDT output for the single top production for the 1 b-jet (left) and 2 b-jet (right) selections.

other background processes

The total contribution of the $t\bar{t}W$ and $t\bar{t}Z$, diboson, and Z+jets production in both signal regions (SR1-tN and SR2-tN) is less than 2% in each bin, while in the CR1-tN and CR2-tN control regions is less than 5% and 1%, respectively.

A detailed study of theoretical uncertainties for the $t\bar{t}W$ and $t\bar{t}Z$, and diboson production is presented in Appendix C. The study shows, that estimate of theoretical systematic uncertainties for the BDT > 0.6 region is mainly dominated by the statistical fluctuations.

Taking into account, that the $t\bar{t}W$ and $t\bar{t}Z$, diboson, and Z+jets background processes are negligible, to decrease a number of fit parameters, and to improve the stability of the fit, the corresponding theoretical uncertainties are not included. Instead, a conservative uncertainty of $\pm 80\%$ is applied to the corresponding Monte Carlo cross sections.

Cross-section uncertainties

The $t\bar{t}$ and W+jets processes are normalised in the TCR1-tN and TCR2-tN control regions. Following the one-lepton analysis, see Section 6.6.3, for the single top production a cross-section uncertainty of $\pm 6.8\%$ is assigned.

As it was mentioned above, the $t\bar{t} + W/Z$, diboson and Z+jets production have a negligible contribution, and due to a high statistical uncertainty on the estimates, the individual theoretical uncertainties are neglected. Instead, for each process a high conservative uncertainty of $\pm 80\%$ is assigned to the cross section.

PDF uncertainties

For the published one-lepton shape-fit analysis (`SRtN1_shape`), which targets the "near the diagonal" region for the $\tilde{t}_1 \to t\tilde{\chi}_1^0$ decay mode, the PDF uncertainties for the $t\bar{t}$ and W+jets processes are estimated to be below $\pm 3\%$, while for the non-dominant backgrounds (single top, diboson, $t\bar{t} + V$ and Z+jets) PDF uncertainties are below $\pm 6\%$.

Taking into account, that for signal regions only the $t\bar{t}$ and W+jets production is relevant, for the current analysis PDF uncertainties are neglected.

8.10.4 Signal uncertainties

Both the published zero- and one-lepton analyses for the $\tilde{t}_1 \to t\tilde{\chi}_1^0$ decay include only cross-section uncertainties for the signal.

To study ISR/FSR and scale variation uncertainties, the corresponding systematic variations were generated for $m(\tilde{t}_1, \tilde{\chi}_1^0) = (180, 1)$ and $(350, 170)$ GeV signal models. Since both are near to the diagonal, where the analyses have no sensitivity, it was decided to estimate the ISR uncertainty based on the difference between the HERWIG++ and MADGRAPH generators.

For both published analyses the difference between the HERWIG++ and MADGRAPH generators were estimated for $m(\tilde{t}_1, \tilde{\chi}_1^0) = (350, 170)$ and $(400, 100)$ GeV signal models. The differences are found to be compatible with zero within 1–2σ for all signal regions. Based on this observation, to avoid double counting of the statistical uncertainty, the ISR systematic uncertainty was not included in the zero- and one-lepton analyses. Some arguments against such an approach are:

- Neglecting the ISR/FSR uncertainties for low $m(\tilde{t}_1)$ masses (below 250 GeV) based on the comparison between two generators for higher masses (350 GeV and 400 GeV) might not be sufficient, especially near to the tN diagonal region, where an ISR/FSR jet significantly improves the signal acceptance.
- The shape-fit approach uses multiple bins and may significantly benefit from applying a variation of 1σ statistical uncertainty of each bin coherently for all bins.
- Even if both generators give similar (within 1σ) results, this does not mean that both are not affected by ISR/FSR uncertainties.

Cross-section uncertainty

The cross-section uncertainty is calculated following the prescriptions in Ref. [110]. Figure 6.18 shows the direct top-squark pair production cross section and the corresponding uncertainty as a function of top-squark mass. The cross-section uncertainty results from α_s, factorisation and renormalisation scale variations and PDF uncertainties.

The analysis is expected to be sensitive to signal models with 180 GeV $< m(\tilde{t}_1) <$ 500 GeV, and for this region the cross-section uncertainty for top-squark pair production is below $\pm$15%. Therefore, this number is used as a conservative estimate for the presented analysis.

PDF uncertainty

The PDF uncertainty related to the total direct top-squark pair production cross section is already included in the signal cross-section uncertainty (see Figure 6.18). An additional PDF uncertainty related to the signal region selection is neglected.

Initial and final state radiation

The presented analysis significantly relies on from the recoil jet signature, and, therefore it is sensitive to the ISR/FSR uncertainties. Following the official recommendations, the uncertainties for each signal model generated with HERWIG++ are estimated by varying parameters in the corresponding samples generated with MADGRAPH+PYTHIA.

The factorisation and renormalisation scales variation, as well as the ISR and FSR modelling uncertainties are estimated on particle level by varying the relevant parameters in the MADGRAPH generator by factors of 0.5 and 2.0 from the nominal. The estimation is based on the officially produced signal variations for the $m(\tilde{t}_1, \tilde{\chi}_1^0) = (180, 1)$ and $(350, 170)$ GeV signal models (about 7 GeV below the tN diagonal) and privately generated ISR and FSR variations with a large number of events for the $m(\tilde{t}_1, \tilde{\chi}_1^0) = (190, 15)$, $(210, 35)$, and $(230, 55)$ GeV signal models (about 2 GeV below the tN diagonal).

Since these variations are already included in the cross-section uncertainty, only uncertainties related to the BDT output are estimated to avoid double-counting. For this, the distributions of the BDT output, used to estimate the uncertainty, are normalised in the $[-1, 1]$ interval. These uncertainties are summed up in quadrature and treated as a signal shape variation in addition to the cross-section uncertainty.

The effect of ISR uncertainties is presented in Figure 8.30, while effect on the BDT output from the FSR uncertainties are shown in Figure 8.31.

The results from the scale variation uncertainties for the $m(\tilde{t}_1, \tilde{\chi}_1^0) = (180, 1)$ and $(350, 170)$ GeV signal models are shown in Figure 8.32. Due to the large statistical fluctuations, it is hard to estimate this uncertainty for the 1 b-jet region. Therefore it is estimated to be below $\pm$5%, based on the 2 b-jet region.

The total uncertainty for the $m(\tilde{t}_1, \tilde{\chi}_1^0) = (180, 5)$ and $(350, 170)$ GeV signal models is estimated by summing up in quadrature the ISR, FSR and scale variation uncertainties. For the private

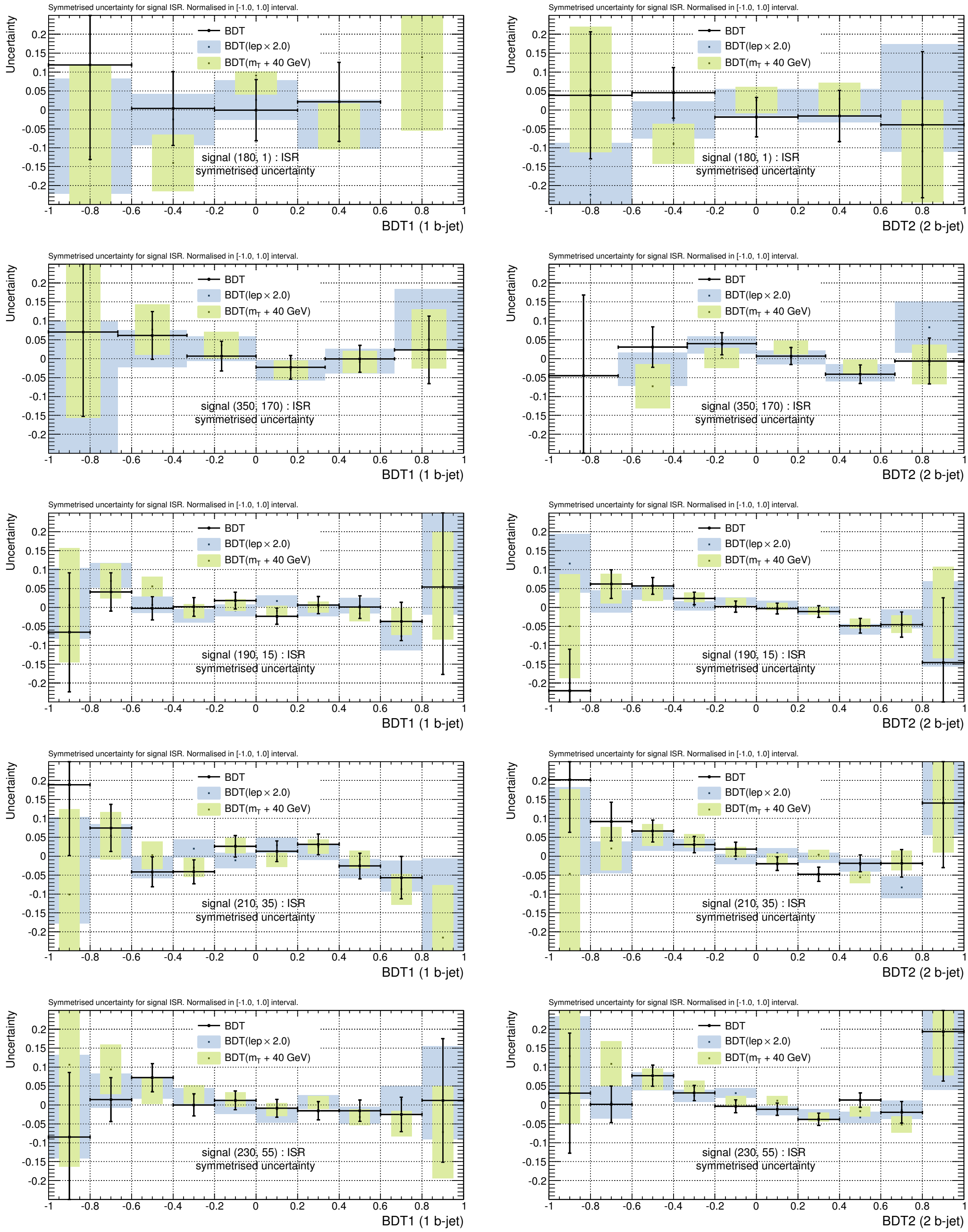

Figure 8.30: Uncertainties on the BDT output resulting from the initial state radiation (ISR) uncertainties for the 1 b-jet (left) and 2 b-jet (right) selections. From top to bottom: the first two rows show the uncertainties for $m(\tilde{t}_1, \tilde{\chi}_1^0) = (180, 1)$ and $(350, 170)$ GeV signal models. Due to a low number of events a large bin size is used. The bottom rows correspond to the $m(\tilde{t}_1, \tilde{\chi}_1^0) = (190, 15)$, $(210, 35)$ and $(230, 55)$ GeV signal models.

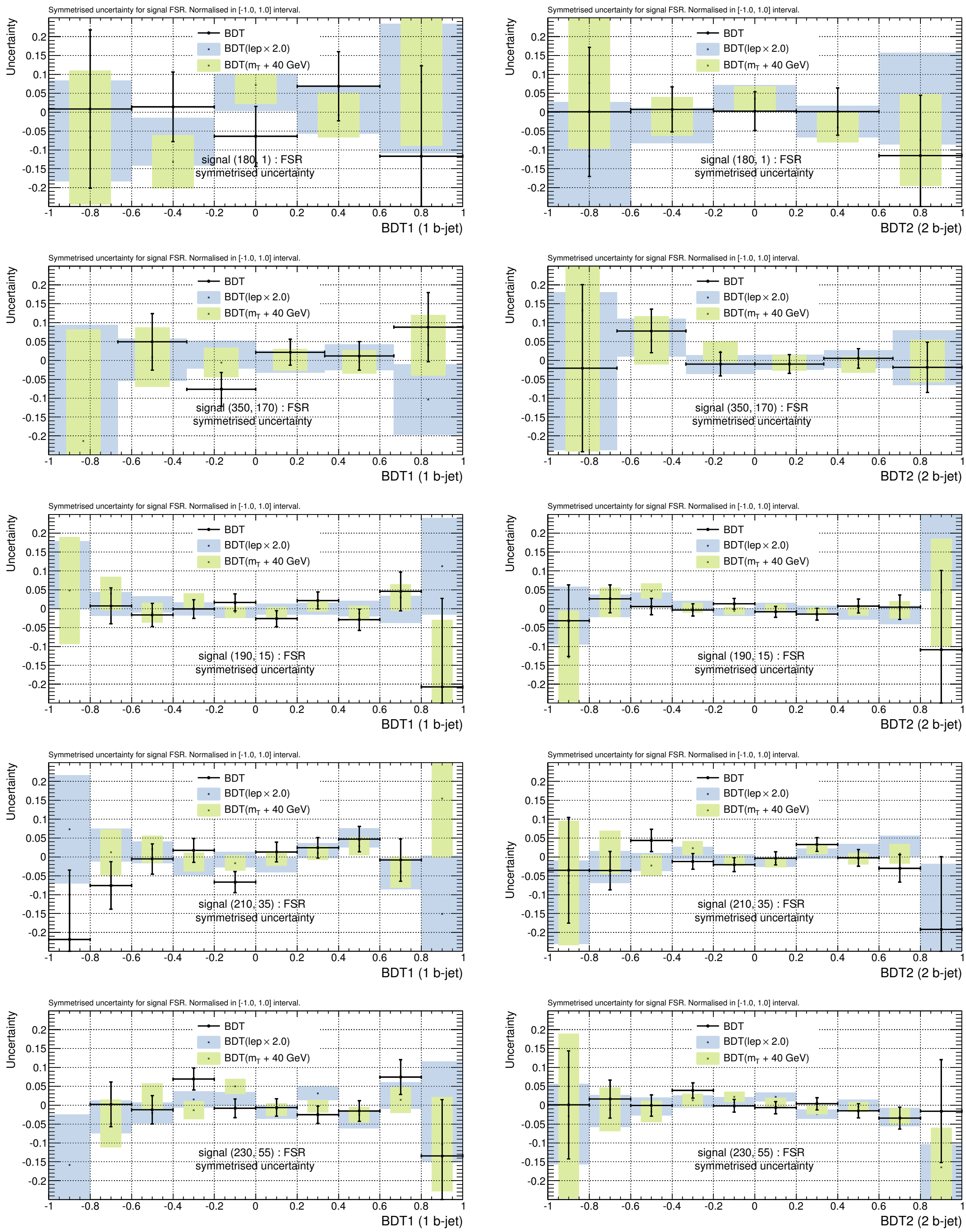

Figure 8.31: Uncertainties on the BDT output resulting from the final state radiation (FSR) uncertainties for the 1 b-jet (left) and 2 b-jet (right) selections. From top to bottom: the first two rows show the uncertainties for $m(\tilde{t}_1, \tilde{\chi}_1^0) = (180, 1)$ and $(350, 170)$ GeV signal models. Due to a low number of events a large bin size is used. The bottom rows correspond to the $m(\tilde{t}_1, \tilde{\chi}_1^0) = (190, 15)$, $(210, 35)$ and $(230, 55)$ GeV signal models.

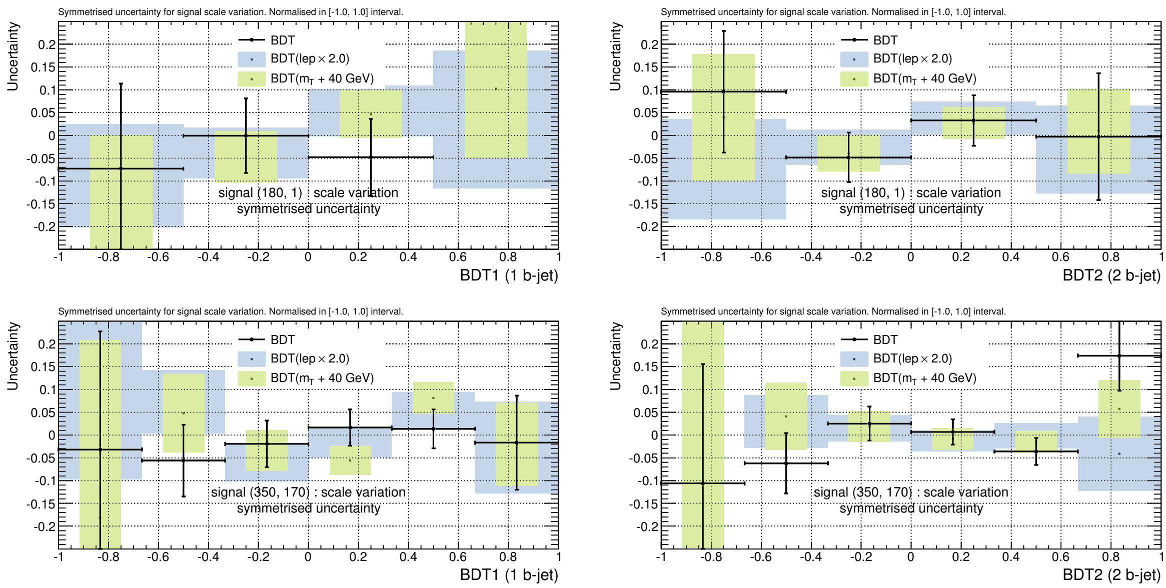

Figure 8.32: Uncertainties on the BDT output resulting from the scale variation uncertainties for the $m(\tilde{t}_1, \tilde{\chi}_1^0) = (180, 1)$ and $(350, 170)$ GeV signal models for the 1 b-jet (left) and 2 b-jet (right) selections. Due to the low number of events, a large bin size is used.

production, the $m(\tilde{t}_1, \tilde{\chi}_1^0) = (190, 15)$, $(210, 35)$ and $(230, 55)$ GeV signal models, the scale variation uncertainties are not generated. Therefore, the total uncertainty includes only the ISR and FSR uncertainties.

Table 8.7 shows the total theoretical uncertainty for the $[0, 0.2]$, $[0.2, 0.4]$, $[0.4, 0.6]$, and $[0.6, 1]$ intervals for different signal models.

In general, the ISR/FSR and scale uncertainties have to be estimated for each signal model separately. Since variations are only available for a few signal models, the same total uncertainty is used for all signal models.

It is assumed, that for the control regions the signal uncertainty can be neglected, while for the signal region (the $[0.4, 1]$ interval) it can be approximated as a linear function of the BDT output $f(x) = \alpha \cdot x + \beta$. Since for the control region the theoretical uncertainty is set to zero, it is assumed that $f(0) = 0$, therefore $\beta = 0$.

To estimate the theoretical uncertainty in the signal region, the uncertainties for each bin are averaged over the $m(\tilde{t}_1, \tilde{\chi}_1^0) = (190, 15)$, $(210, 35)$ and $(230, 55)$ GeV signal models and the 1 b-jet and 2 b-jet selections. For the $[0.4, 0.6]$ and $[0.6, 1]$ intervals the estimated values are about 0.03 and 0.06, respectively. Based on these values the α parameter is conservatively estimated as $\alpha = 0.1$, which corresponds to 4% for BDT = 0.4 and to 8% for BDT = 0.8.

This approach overestimates the total uncertainty for the $m(\tilde{t}_1, \tilde{\chi}_1^0) = (350, 170)$ GeV and is consistent with the total ISR/FSR uncertainties for the $m(\tilde{t}_1, \tilde{\chi}_1^0) = (190, 15)$, $(210, 35)$ and $(230, 55)$ GeV signal models. For the present analysis, the total ISR/FSR uncertainty is accounted for in addition to the signal cross-section uncertainty.

1 b-jet selection

$m(\tilde{t}_1, \tilde{\chi}_1^0)$ [GeV]	$[0, 0.2]$	$[0.2, 0.4]$	$[0.4, 0.6]$	$[0.6, 1]$
$(180, 5)$	0.19 ± 0.08	0.25 ± 0.11	0.26 ± 0.14	0.57 ± 0.30
$(350, 170)$	0.01 ± 0.04	0.06 ± 0.04	0.03 ± 0.05	0.04 ± 0.07
$(190, 15)$	0.03 ± 0.02	0.02 ± 0.02	0.01 ± 0.03	0.02 ± 0.05
$(210, 35)$	0.02 ± 0.02	0.02 ± 0.02	0.06 ± 0.03	0.10 ± 0.05
$(230, 55)$	0.01 ± 0.02	0.03 ± 0.02	0.04 ± 0.03	0.06 ± 0.04

2 b-jet selection

$m(\tilde{t}_1, \tilde{\chi}_1^0)$ [GeV]	$[0, 0.2]$	$[0.2, 0.4]$	$[0.4, 0.6]$	$[0.6, 1]$
$(180, 5)$	0.03 ± 0.06	0.05 ± 0.07	0.14 ± 0.11	0.14 ± 0.18
$(350, 170)$	0.03 ± 0.03	0.05 ± 0.03	0.02 ± 0.03	0.04 ± 0.05
$(190, 15)$	0.01 ± 0.01	0.02 ± 0.01	0.04 ± 0.02	0.06 ± 0.03
$(210, 35)$	0.03 ± 0.01	0.06 ± 0.02	0.02 ± 0.02	0.06 ± 0.04
$(230, 55)$	0.03 ± 0.01	0.04 ± 0.01	0.01 ± 0.02	0.03 ± 0.03

Table 8.7: The total relative uncertainty for signal models for different intervals of the BDT output for the 1 b-jet (top) and 2 b-jet (bottom) selections. The total uncertainty for the $m(\tilde{t}_1, \tilde{\chi}_1^0) = (180, 5)$ and $(350, 170)$ GeV signal models includes scale, ISR and FSR uncertainties, while for the privately produced $m(\tilde{t}_1, \tilde{\chi}_1^0) = (190, 15)$, $(210, 35)$ and $(230, 55)$ GeV signal models only ISR and FSR uncertainties are included.

8.11 Results

The normalisations of the $t\bar{t}$ and $W+$jets backgrounds ($\mu_{t\bar{t}}$ and μ_W, respectively) are considered as floating parameters in the fit. For all other processes fixed cross sections are considered. The uncertainties on cross sections are accounted for as separate nuisance parameters.

Each theoretical uncertainty for $t\bar{t}$, $W+$jets and single top production is considered as an independent shape variation. The contributions from the $t\bar{t}W$ and $t\bar{t}Z$, diboson and $Z+$jets production are negligible. Therefore, to improve the fit stability, instead of accounting for theoretical uncertainty, a cross-section uncertainty of $\pm 80\%$ is assigned for each process (see Section 8.10.3).

Each detector uncertainty enters the fit as an independent shape variation. The jet energy scale uncertainty is considered as one uncertainty and is not broken down into components.

8.11.1 Background-only fit

The background-only fit is performed without a signal model assumption. For the fit only the CR1-tN and CR2-tN control regions are used. The results are extrapolated to the signal and the validation regions. The uncertainties on the nuisance parameters after the fit (pull plot) are shown in Figure 8.33.

There are several nuisance parameters which are constrained, i.e. the uncertainties on the parameters after the fit are smaller than before the fit. The most constrained parameters are

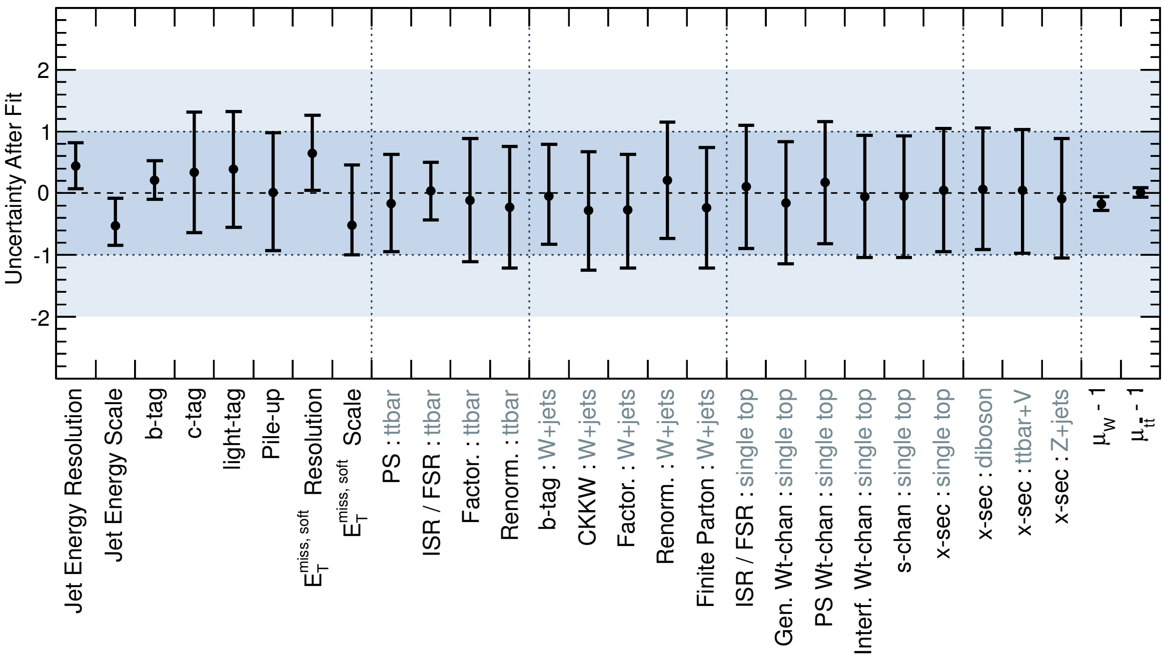

Figure 8.33: Uncertainties of the nuisance parameters after the fit.

related to the jet energy scale and resolution, the b-tagging modelling, and to the ISR/FSR modelling of the dominant $t\bar{t}$ background. Some possible arguments why these parameters are overconstrained are the following:

– For the jet energy scale (JES) the shape variation is estimated based on the total jet energy uncertainty without being broken down into components, i.e. instead of fitting several nuisance parameters, only one parameter is used with the total uncertainty obtained by summing up in quadrature the uncertainties of each component. Some JES parameters may vary a shape simultaneously in different directions. This increases the total uncertainty of the JES, but cannot be followed by one-parametric simplified model. Therefore, the fitted parameter can be constrained. Studies performed in the context of the one-lepton analysis [3] showed that the shape-fit analysis is not very sensitive to the details of the implementation of the JES uncertainty and the obtained CL_s values are similar.

– The same is true for the jet energy resolution (JER). The ATLAS Jet/Etmiss Working Group provides only a total uncertainty, while the resolution effect depends on several parameters. Therefore, the shape variation cannot be modelled perfectly.

– Another constraint of an experimental uncertainty is the b-tagging uncertainty. This uncertainty also cannot be exactly modelled with one nuisance parameter, since it is based on the uncertainties of the measured b-tagging efficiencies and mistag rates. For the 1 b-jet and 2 b-jet selections for $t\bar{t}$ events the relative normalisation is driven by the b-jet tagging efficiency, therefore the uncertainty might be constrained. In addition, the shape variation is affected by the change of the flavour composition due to the Wbb samples. This is especially important for the 1 b-jet selection, since the W+jets composition significantly changes as a function of the BDT output (see Figure 8.34). For the current analysis it is assumed that the relative flavour composition does not change for the 1 b-jet selection. This also may lead to an imperfect estimation of the shape variation.

– For the current analysis, for all theoretical uncertainties the shape variations are approximated with a second order polynomial, which is correct only up to some extent. Therefore, one should expect some constraining of nuisance parameters.

– The most significant theoretical uncertainty for the current analysis is the ISR/FSR uncertainty. It is assumed, that the shape variation due to this uncertainty can be estimated as the difference between the $t\bar{t}$ samples, generated with higher and lower parton shower activity. This approach might overestimate the real ISR/FSR shape variation. Therefore, after the shape-fit the resulting uncertainty on the nuisance parameter might be constrained.

Since these uncertainties have a large impact on the current analysis, a mismodelling of any of them will lead to a shift of other parameters to compensate the variation. This cannot be modelled by the proposed model. In general one can see that regardless of the constraint, the central values of parameters are close to the nominal value.

The normalisation parameters $\mu_{t\bar{t}}$ and μ_W for the $t\bar{t}$ and $W+$jets processes are found to be

$$\mu_{t\bar{t}} = 1.01 \pm 0.08 \qquad \text{and} \qquad \mu_W = 0.82 \pm 0.12. \tag{8.28}$$

The normalisation for $W+$jets production μ_W is a bit low. Nevertheless, the data-MC agreement of the BDT1 variable for the 1 b-jet selection (see Figure 8.34) confirms, that mismodelling mainly affects the normalisation of the $W+$jets process and not the shape.

The numbers of expected events and the fitted results for the CR1-tN and CR2-tN control regions are shown in Tables 8.8 – 8.11. The corresponding distributions of the BDT1 and BDT2 outputs are shown in Figures 8.34 and 8.35. The results for the SR1-tN and SR2-tN signal regions are listed in Tables 8.12 and 8.13. The corresponding distributions for BDT1 and BDT2 outputs are shown in Figures 8.36 and 8.37. The distributions for signal regions show good agreement between data and the Monte Carlo prediction.

The results for the VR1-tN and VR2-tN validation regions are listed in Tables 8.14 and 8.15. The corresponding distributions for the BDT1 and BDT2 outputs are presented in Figures 8.38 and 8.39. The distributions for the VR1-tN validation region for the 1 b-jet selection show some mild discrepancy for the $[0, 0.2]$ interval, which is within 2σ of the expected background. For the $[0.2, 0.4]$ interval, near the signal region, the distributions for both selections show good agreement between data and the Monte Carlo prediction.

Bin's left border	Expected Monte Carlo events for the CR1-tN control region (1 b-jet)						
	SM Total	$t\bar{t}$	W+jets	single top	$t\bar{t}+V$	diboson	Z+jets
−1.00	1156 ± 221	207 ± 30	855 ± 187	39 ± 8	1 ± 1	31 ± 26	23 ± 18
−0.80	589 ± 126	182 ± 25	350 ± 102	27 ± 6	1 ± 1	17 ± 13	12 ± 9
−0.75	699 ± 133	251 ± 35	390 ± 95	33 ± 8	1 ± 1	15 ± 12	9 ± 8
−0.70	794 ± 138	324 ± 47	405 ± 88	40 ± 8	2 ± 1	16 ± 13	9 ± 7
−0.65	845 ± 150	383 ± 60	389 ± 88	42 ± 9	2 ± 2	19 ± 16	11 ± 9
−0.60	917 ± 139	441 ± 65	393 ± 71	52 ± 10	2 ± 2	17 ± 14	12 ± 10
−0.55	935 ± 193	489 ± 75	362 ± 107	52 ± 14	2 ± 2	16 ± 14	15 ± 12
−0.50	981 ± 178	537 ± 88	357 ± 88	56 ± 12	3 ± 2	19 ± 15	11 ± 8
−0.45	973 ± 160	553 ± 88	336 ± 66	55 ± 13	2 ± 2	17 ± 15	10 ± 8
−0.40	997 ± 174	597 ± 99	315 ± 67	59 ± 15	3 ± 2	16 ± 13	7 ± 6
−0.35	972 ± 181	602 ± 100	287 ± 72	57 ± 14	3 ± 2	16 ± 14	7 ± 6
−0.30	950 ± 180	592 ± 98	269 ± 77	58 ± 12	3 ± 2	19 ± 15	10 ± 8
−0.25	902 ± 182	581 ± 102	247 ± 73	53 ± 13	3 ± 2	13 ± 11	5 ± 4
−0.20	867 ± 156	574 ± 96	223 ± 53	49 ± 14	3 ± 3	10 ± 9	6 ± 5
−0.15	817 ± 159	552 ± 98	200 ± 61	46 ± 11	3 ± 3	12 ± 10	4 ± 3
−0.10	787 ± 143	511 ± 97	212 ± 48	46 ± 11	3 ± 2	12 ± 10	3 ± 3
−0.05	703 ± 146	493 ± 90	149 ± 53	41 ± 13	3 ± 2	11 ± 9	6 ± 5

Table 8.8: Expected number of events for the Standard Model processes, predicted from the Monte Carlo simulation for the CR1-tN control region (1 b-jet selection). The numbers in the first column present the left border of each interval. All intervals are $[x, x + 0.05]$. The normalisation is done in the CR1-tN and CR2-tN control regions.

Bin's left border	Expected Monte Carlo events for the CR2-tN control region (2 b-jet)						
	SM Total	$t\bar{t}$	W+jets	single top	$t\bar{t}+V$	diboson	Z+jets
−1.00	162 ± 26	108 ± 14	39 ± 14	11 ± 4	1 ± 1	2 ± 2	1 ± 1
−0.80	157 ± 22	108 ± 15	34 ± 12	9 ± 3	1 ± 1	3 ± 3	3 ± 2
−0.75	206 ± 33	147 ± 23	42 ± 16	13 ± 4	1 ± 1	2 ± 2	1 ± 1
−0.70	277 ± 41	215 ± 30	38 ± 15	20 ± 6	1 ± 1	2 ± 2	1 ± 1
−0.65	337 ± 54	265 ± 38	42 ± 21	25 ± 7	2 ± 1	3 ± 2	1 ± 1
−0.60	415 ± 66	333 ± 51	49 ± 20	27 ± 8	2 ± 1	3 ± 2	2 ± 1
−0.55	486 ± 75	390 ± 54	59 ± 26	29 ± 11	2 ± 2	3 ± 3	1 ± 1
−0.50	540 ± 94	449 ± 71	56 ± 23	29 ± 9	2 ± 2	2 ± 2	2 ± 1
−0.45	577 ± 100	495 ± 78	41 ± 25	34 ± 10	3 ± 2	4 ± 4	1 ± 1
−0.40	611 ± 104	514 ± 83	54 ± 24	35 ± 10	3 ± 2	2 ± 2	4 ± 3
−0.35	620 ± 106	536 ± 91	43 ± 15	35 ± 10	3 ± 3	2 ± 2	1 ± 1
−0.30	629 ± 105	540 ± 92	47 ± 15	33 ± 9	3 ± 3	3 ± 3	2 ± 2
−0.25	619 ± 107	529 ± 89	49 ± 17	33 ± 10	3 ± 3	3 ± 3	1 ± 1
−0.20	591 ± 98	515 ± 86	37 ± 12	31 ± 9	3 ± 3	2 ± 2	2 ± 1
−0.15	582 ± 101	500 ± 84	42 ± 16	32 ± 10	4 ± 3	2 ± 2	3 ± 2
−0.10	526 ± 100	458 ± 86	33 ± 12	27 ± 9	3 ± 3	2 ± 2	1 ± 1
−0.05	504 ± 83	433 ± 75	36 ± 11	28 ± 9	3 ± 2	3 ± 3	1 ± 1

Table 8.9: Expected number of events for the Standard Model processes, predicted from the Monte Carlo simulation for the CR2-tN control region (2 b-jet selection). The numbers in the first column present the left border of each interval. All intervals are $[x, x + 0.05]$. The normalisation is done in the CR1-tN and CR2-tN control regions.

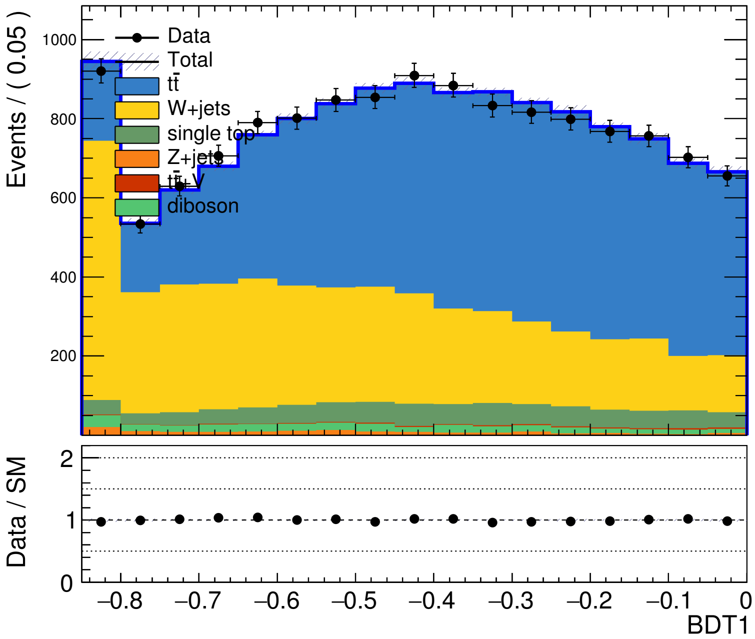

Figure 8.34: The distribution of the BDT1 output for the CR1-tN control region (1 b-jet).

Bin's left border	Observed events	Fitted events of the BDT1 output for the CR1-tN control region (1 b-jet)						
		SM Total	$t\bar{t}$	W+jets	single top	$t\bar{t}+V$	diboson	Z+jets
−1.00	920	944 ± 28	200 ± 17	655 ± 50	37 ± 6	1 ± 1	30 ± 23	21 ± 17
−0.80	534	535 ± 14	173 ± 13	306 ± 25	28 ± 4	1 ± 1	16 ± 13	11 ± 9
−0.75	629	620 ± 10	239 ± 18	323 ± 25	32 ± 5	1 ± 1	16 ± 12	9 ± 7
−0.70	706	680 ± 14	297 ± 20	317 ± 27	37 ± 5	2 ± 1	19 ± 15	8 ± 7
−0.65	790	759 ± 11	363 ± 24	326 ± 29	41 ± 5	2 ± 1	18 ± 14	10 ± 8
−0.60	801	800 ± 16	422 ± 27	301 ± 33	46 ± 7	2 ± 2	18 ± 14	11 ± 9
−0.55	847	838 ± 17	465 ± 28	290 ± 32	50 ± 8	2 ± 2	18 ± 14	13 ± 11
−0.50	854	877 ± 17	501 ± 29	292 ± 31	52 ± 7	2 ± 2	20 ± 15	10 ± 8
−0.45	909	889 ± 14	531 ± 30	279 ± 30	56 ± 7	3 ± 2	12 ± 9	9 ± 7
−0.40	884	866 ± 17	546 ± 29	242 ± 29	50 ± 8	3 ± 2	19 ± 15	7 ± 5
−0.35	833	868 ± 14	554 ± 29	233 ± 29	56 ± 8	3 ± 2	16 ± 13	7 ± 5
−0.30	816	841 ± 16	553 ± 29	209 ± 29	51 ± 9	3 ± 2	16 ± 12	9 ± 8
−0.25	799	817 ± 20	555 ± 28	189 ± 31	51 ± 8	3 ± 2	15 ± 12	5 ± 4
−0.20	768	780 ± 11	537 ± 27	178 ± 25	45 ± 8	3 ± 2	11 ± 9	6 ± 5
−0.15	756	749 ± 16	505 ± 25	182 ± 25	44 ± 7	3 ± 2	11 ± 9	4 ± 3
−0.10	702	687 ± 17	487 ± 23	137 ± 27	46 ± 8	3 ± 2	12 ± 9	3 ± 2
−0.05	655	666 ± 12	463 ± 22	144 ± 21	39 ± 8	3 ± 2	11 ± 8	6 ± 5

Table 8.10: Results for the background-only fit for the CR1-tN control region (1 b-jet selection). The numbers in the first column present the left border of each interval. All intervals are $[x, x + 0.05]$. The normalisation is done in the CR1-tN and CR2-tN control regions.

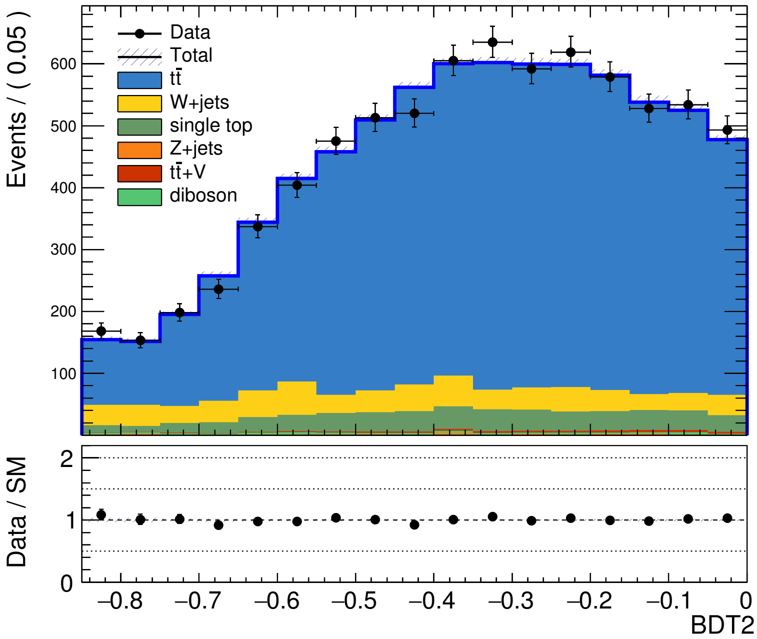

Figure 8.35: The distribution of the BDT2 output for the CR2-tN control region (2 b-jet).

Bin's left border	Observed events	Fitted events of the BDT2 output for the CR2-tN control region (2 b-jet)						
		SM Total	$t\bar{t}$	W+jets	single top	$t\bar{t}+V$	diboson	Z+jets
−1.00	168	155 ± 6	105 ± 6	33 ± 8	12 ± 3	1 ± 1	2 ± 2	1 ± 1
−0.80	153	152 ± 5	103 ± 5	34 ± 8	10 ± 2	1 ± 1	2 ± 2	3 ± 2
−0.75	198	195 ± 5	148 ± 6	28 ± 7	16 ± 3	1 ± 1	2 ± 2	1 ± 1
−0.70	236	258 ± 7	202 ± 9	35 ± 8	17 ± 5	1 ± 1	1 ± 1	1 ± 1
−0.65	337	344 ± 7	271 ± 11	44 ± 10	24 ± 6	1 ± 1	3 ± 3	1 ± 1
−0.60	404	415 ± 8	328 ± 12	54 ± 12	27 ± 6	2 ± 1	3 ± 2	2 ± 1
−0.55	475	458 ± 9	392 ± 16	30 ± 11	29 ± 7	2 ± 2	3 ± 2	1 ± 1
−0.50	513	509 ± 11	437 ± 14	36 ± 11	31 ± 7	2 ± 2	2 ± 2	1 ± 1
−0.45	520	562 ± 10	480 ± 16	43 ± 11	33 ± 8	3 ± 2	3 ± 2	1 ± 1
−0.40	605	600 ± 8	504 ± 17	50 ± 13	37 ± 8	3 ± 2	4 ± 3	3 ± 3
−0.35	635	602 ± 11	529 ± 16	31 ± 8	35 ± 8	3 ± 2	3 ± 2	1 ± 1
−0.30	592	600 ± 10	523 ± 15	36 ± 9	34 ± 8	3 ± 3	2 ± 2	2 ± 2
−0.25	619	599 ± 11	522 ± 15	40 ± 10	31 ± 8	3 ± 3	3 ± 2	1 ± 1
−0.20	579	582 ± 10	509 ± 15	34 ± 8	31 ± 8	3 ± 3	3 ± 2	2 ± 1
−0.15	528	538 ± 13	472 ± 14	26 ± 8	32 ± 8	4 ± 3	2 ± 2	3 ± 2
−0.10	534	525 ± 12	456 ± 14	28 ± 7	32 ± 7	3 ± 2	4 ± 3	1 ± 1
−0.05	493	477 ± 8	412 ± 11	33 ± 8	27 ± 8	3 ± 2	2 ± 1	1 ± 1

Table 8.11: Results for the background-only fit for the CR2-tN control region (2 b-jet selection). The numbers in the first column present the left border of each interval. All intervals are $[x, x + 0.05]$. The normalisation is done in the CR1-tN and CR2-tN control regions.

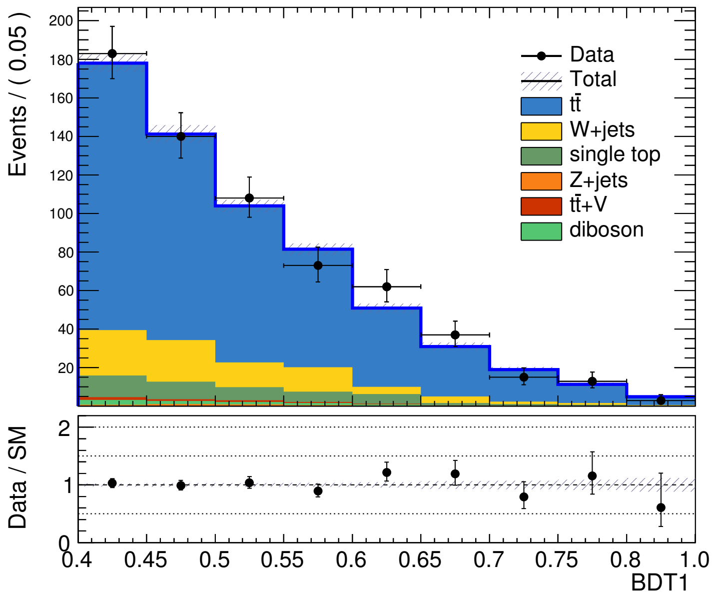

Figure 8.36: The distribution of the BDT1 output for the SR1-tN signal region (1 b-jet).

Bin's left border	Observed events	Fitted events of the BDT1 output for the SR1-tN signal region (1 b-jet)						
		SM Total	$t\bar{t}$	W+jets	single top	$t\bar{t}+V$	diboson	Z+jets
0.40	183	177.9 ± 5.7	138.5 ± 6.5	23.6 ± 4.1	11.2 ± 2.3	1.5 ± 1.2	2.4 ± 1.9	0.8 ± 0.7
0.45	140	141.2 ± 6.2	106.9 ± 5.5	21.7 ± 4.1	9.1 ± 2.4	0.8 ± 0.7	1.5 ± 1.2	1.2 ± 1.0
0.50	108	103.9 ± 4.1	81.1 ± 3.9	12.9 ± 2.7	6.8 ± 2.1	0.9 ± 0.7	1.2 ± 1.1	1.0 ± 0.8
0.55	73	81.5 ± 3.0	61.3 ± 3.0	12.6 ± 2.4	5.3 ± 1.7	0.5 ± 0.4	1.1 ± 0.9	0.6 ± 0.5
0.60	62	50.9 ± 2.4	40.8 ± 2.6	3.8 ± 1.2	5.0 ± 1.3	0.4 ± 0.3	0.8 ± 0.7	0.3 ± 0.2
0.65	37	31.0 ± 2.1	25.9 ± 1.9	3.5 ± 0.7	1.2 ± 1.0	0.2 ± 0.2	0.1 ± 0.1	0.2 ± 0.1
0.70	15	19.0 ± 1.5	16.6 ± 1.4	1.2 ± 0.6	1.0 ± 0.4	0.1 ± 0.1	0.0 ± 0.0	0.0 ± 0.0
0.75	13	11.2 ± 1.0	9.6 ± 0.9	0.7 ± 0.5	0.8 ± 0.3	0.1 ± 0.1	0.0 ± 0.0	0.0 ± 0.0
0.80	3	4.9 ± 0.6	4.3 ± 0.6	0.3 ± 0.1	0.2 ± 0.2	0.0 ± 0.0	0.0 ± 0.0	0.0 ± 0.0

Bin's left border	Monte Carlo expected events for SR1-tN (1 b-jet) signal region						
	SM Total	$t\bar{t}$	W+jets	single top	$t\bar{t}+V$	diboson	Z+jets
0.40	198.5 ± 40.5	148.5 ± 32.1	33.5 ± 8.8	11.5 ± 3.4	1.2 ± 1.0	2.7 ± 2.3	0.9 ± 0.7
0.45	157.6 ± 31.7	115.2 ± 25.1	28.5 ± 6.2	9.2 ± 3.8	1.1 ± 0.9	2.2 ± 2.4	1.3 ± 1.1
0.50	117.5 ± 23.7	87.6 ± 18.1	18.9 ± 4.5	7.9 ± 2.5	0.8 ± 0.7	1.1 ± 1.5	1.1 ± 0.9
0.55	80.7 ± 19.9	64.4 ± 12.6	8.6 ± 8.5	5.5 ± 1.9	0.6 ± 0.5	0.9 ± 0.9	0.7 ± 0.5
0.60	55.2 ± 11.9	43.5 ± 9.2	7.0 ± 3.0	3.6 ± 2.1	0.4 ± 0.3	0.3 ± 0.6	0.3 ± 0.2
0.65	33.8 ± 7.1	27.6 ± 6.6	2.9 ± 1.0	2.6 ± 1.6	0.2 ± 0.2	0.5 ± 0.6	0.2 ± 0.1
0.70	20.5 ± 5.3	17.6 ± 4.0	1.8 ± 1.2	1.0 ± 0.5	0.1 ± 0.1	0.0 ± 0.2	0.0 ± 0.0
0.75	10.8 ± 3.3	9.9 ± 2.4	0.2 ± 1.0	0.5 ± 0.4	0.1 ± 0.1	0.0 ± 0.0	0.0 ± 0.0
0.80	5.7 ± 1.3	5.0 ± 1.2	0.3 ± 0.2	0.3 ± 0.2	0.0 ± 0.0	0.0 ± 0.0	0.0 ± 0.0

Table 8.12: Results for the background-only fit for the SR1-tN signal region for the BDT1 variable (1 b-jet selection). The numbers in the first column present the left border of each bin interval. All intervals, except the last, are $[x, x + 0.05]$, the last interval is $[0.8, 1]$.

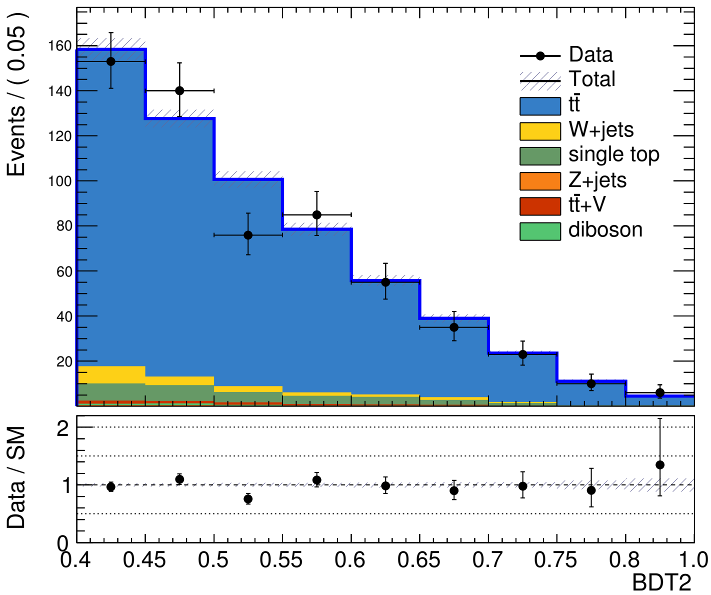

Figure 8.37: The distribution of the BDT2 output for the SR2-tN signal region (2 b-jet).

Bin's left border	Observed events	Fitted events of the BDT2 output for the SR2-tN signal region (2 b-jet)						
		SM Total	$t\bar{t}$	W+jets	single top	$t\bar{t}+V$	diboson	Z+jets
0.40	153	158.4 ± 5.4	140.6 ± 5.8	7.6 ± 2.7	7.8 ± 2.0	1.3 ± 1.1	0.6 ± 0.5	0.5 ± 0.4
0.45	140	127.7 ± 4.1	114.5 ± 4.8	3.7 ± 1.1	7.0 ± 1.8	1.2 ± 0.9	0.8 ± 0.6	0.5 ± 0.4
0.50	76	100.6 ± 3.8	91.7 ± 4.3	2.5 ± 0.8	4.7 ± 1.6	1.0 ± 0.7	0.6 ± 0.4	0.2 ± 0.1
0.55	85	78.5 ± 3.0	72.3 ± 3.3	1.5 ± 0.5	3.7 ± 1.2	0.6 ± 0.5	0.3 ± 0.2	0.1 ± 0.1
0.60	55	55.8 ± 2.6	50.5 ± 2.5	1.1 ± 0.7	3.3 ± 1.1	0.5 ± 0.4	0.3 ± 0.2	0.0 ± 0.0
0.65	35	39.0 ± 1.9	35.0 ± 1.9	1.2 ± 0.4	2.2 ± 0.7	0.3 ± 0.2	0.0 ± 0.0	0.3 ± 0.2
0.70	23	23.6 ± 1.2	21.6 ± 1.2	0.5 ± 0.3	1.3 ± 0.4	0.1 ± 0.1	0.0 ± 0.0	0.0 ± 0.0
0.75	10	11.1 ± 0.9	10.6 ± 0.9	0.0 ± 0.0	0.3 ± 0.2	0.1 ± 0.1	0.0 ± 0.1	0.0 ± 0.0
0.80	6	4.5 ± 0.5	4.1 ± 0.5	0.0 ± 0.0	0.3 ± 0.1	0.0 ± 0.0	0.0 ± 0.0	0.0 ± 0.0

Bin's left border	Monte Carlo expected events for SR2-tN (2 b-jet) signal region						
	SM Total	$t\bar{t}$	W+jets	single top	$t\bar{t}+V$	diboson	Z+jets
0.40	163.1 ± 32.1	145.8 ± 26.0	6.9 ± 6.7	7.3 ± 3.3	1.4 ± 1.1	1.1 ± 1.0	0.6 ± 0.4
0.45	130.7 ± 25.0	118.2 ± 23.1	3.8 ± 1.3	6.4 ± 2.3	1.2 ± 1.0	0.6 ± 0.6	0.5 ± 0.4
0.50	107.6 ± 18.1	97.0 ± 16.3	3.2 ± 1.2	5.6 ± 2.1	0.9 ± 0.7	0.8 ± 0.7	0.2 ± 0.1
0.55	79.5 ± 15.8	72.6 ± 14.5	1.6 ± 1.2	4.3 ± 1.5	0.6 ± 0.5	0.2 ± 0.3	0.1 ± 0.1
0.60	60.5 ± 11.4	54.1 ± 10.7	2.3 ± 1.5	3.5 ± 1.3	0.4 ± 0.3	0.2 ± 0.2	0.0 ± 0.0
0.65	40.4 ± 7.8	36.9 ± 7.2	0.8 ± 0.9	2.0 ± 0.8	0.4 ± 0.3	0.1 ± 0.1	0.3 ± 0.2
0.70	23.0 ± 4.9	22.1 ± 4.2	0.1 ± 0.4	0.7 ± 0.8	0.2 ± 0.1	0.0 ± 0.0	0.0 ± 0.0
0.75	11.3 ± 2.6	10.4 ± 2.5	0.2 ± 0.2	0.5 ± 0.3	0.1 ± 0.1	0.2 ± 0.3	0.0 ± 0.0
0.80	4.5 ± 1.1	4.2 ± 1.1	0.0 ± 0.0	0.2 ± 0.1	0.0 ± 0.0	0.0 ± 0.0	0.0 ± 0.0

Table 8.13: Results for the background-only fit for the SR2-tN signal region for the BDT2 variable (2 b-jet selection). The numbers in the first column present the left border of each bin interval. All intervals, except the last, are $[x, x + 0.05]$, the last interval is $[0.8, 1]$.

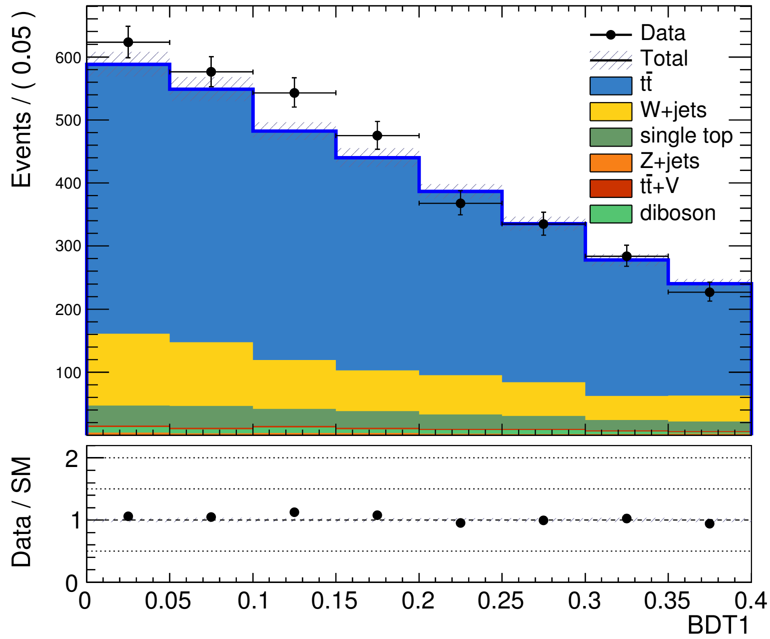

Figure 8.38: The distribution of the BDT1 output for the VR1-tN validation region (1 b-jet).

Bin's left border	Observed events	Fitted events of the BDT1 output for the VR1-tN validation region (1 b-jet)						
		SM Total	$t\bar{t}$	W+jets	single top	$t\bar{t}+V$	diboson	Z+jets
0.00	623	588 ± 24	427 ± 24	113.8 ± 19.4	31.7 ± 4.3	2.4 ± 1.9	9.1 ± 7.1	3.9 ± 3.2
0.05	576	549 ± 23	401 ± 23	101.0 ± 16.2	34.4 ± 3.6	2.7 ± 2.1	6.4 ± 4.9	2.9 ± 2.4
0.10	543	482 ± 15	363 ± 21	78.0 ± 8.8	26.7 ± 3.9	2.5 ± 2.0	8.4 ± 6.7	3.9 ± 3.2
0.15	475	440 ± 17	337 ± 20	64.5 ± 9.0	26.6 ± 3.2	2.2 ± 1.8	5.5 ± 4.3	3.9 ± 3.2
0.20	368	386 ± 14	291 ± 17	62.0 ± 7.3	22.9 ± 2.7	2.1 ± 1.6	5.8 ± 4.6	2.5 ± 2.0
0.25	335	336 ± 12	252 ± 15	53.4 ± 6.8	20.4 ± 2.4	1.9 ± 1.5	6.0 ± 4.7	2.1 ± 1.7
0.30	284	278 ± 11	216 ± 13	37.8 ± 5.3	16.5 ± 1.9	1.7 ± 1.4	4.3 ± 3.3	1.7 ± 1.4
0.35	227	240 ± 8	177 ± 11	41.5 ± 5.2	15.4 ± 1.7	1.5 ± 1.2	2.5 ± 2.1	2.3 ± 1.9

Bin's left border	Monte Carlo expected events for VR1-tN (1 b-jet) validation region						
	SM Total	$t\bar{t}$	W+jets	single top	$t\bar{t}+V$	diboson	Z+jets
0.00	652 ± 140	459 ± 83	140.5 ± 53.9	37.4 ± 9.0	3.0 ± 2.4	8.1 ± 6.6	4.3 ± 3.4
0.05	608 ± 123	428 ± 79	131.3 ± 43.5	33.9 ± 8.3	2.6 ± 2.1	8.7 ± 7.4	3.2 ± 2.5
0.10	536 ± 98	395 ± 68	95.7 ± 24.6	33.4 ± 7.6	2.6 ± 2.1	5.8 ± 5.6	4.2 ± 3.4
0.15	486 ± 88	354 ± 68	90.6 ± 18.0	28.4 ± 6.1	2.4 ± 2.0	6.1 ± 5.1	4.3 ± 3.4
0.20	424 ± 80	314 ± 59	79.1 ± 15.9	22.3 ± 6.4	2.0 ± 1.6	4.4 ± 3.7	2.7 ± 2.1
0.25	361 ± 78	265 ± 55	65.7 ± 18.5	20.6 ± 6.1	1.9 ± 1.6	5.2 ± 4.5	2.3 ± 1.9
0.30	301 ± 62	225 ± 45	47.4 ± 17.3	20.1 ± 3.1	1.8 ± 1.5	4.8 ± 4.1	1.9 ± 1.5
0.35	257 ± 45	190 ± 40	45.6 ± 5.2	14.3 ± 4.3	1.6 ± 1.3	3.3 ± 3.1	2.5 ± 2.0

Table 8.14: Results for the background-only fit for the VR1-tN validation region for the BDT1 variable (1 b-jet selection). Numbers in the first column present the left border of each bin interval. All intervals are $[x, x + 0.05]$.

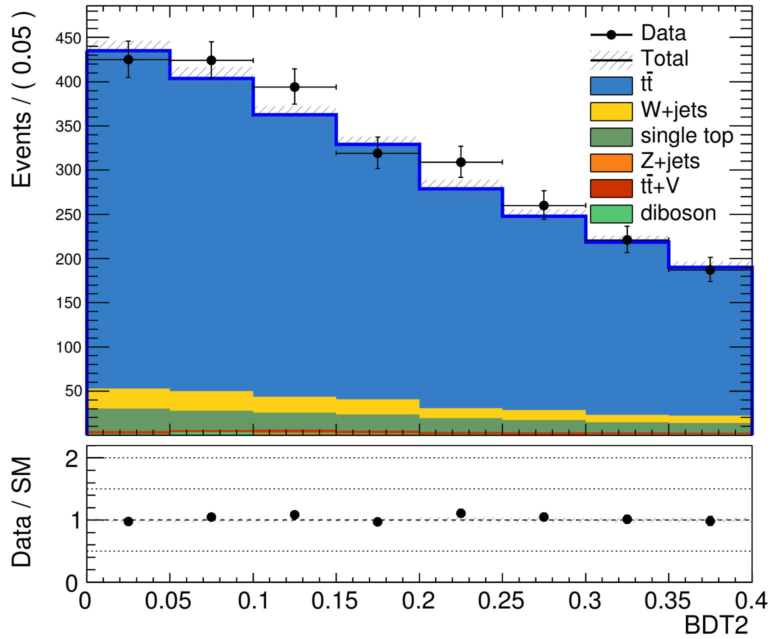

Figure 8.39: The distribution of the BDT2 output for the VR2-tN validation region (2 b-jet).

Bin's left border	Observed events	Fitted events of the BDT2 output for the VR2-tN validation region (2 b-jet)						
		SM Total	$t\bar{t}$	W+jets	single top	$t\bar{t}+V$	diboson	Z+jets
0.00	425	435 ± 12	382 ± 12	22.3 ± 3.5	25.7 ± 2.8	3.1 ± 2.5	1.4 ± 1.1	0.3 ± 0.2
0.05	424	404 ± 16	354 ± 15	22.1 ± 3.3	21.6 ± 3.1	2.9 ± 2.2	3.0 ± 2.5	0.3 ± 0.2
0.10	394	362 ± 11	319 ± 10	18.2 ± 3.0	19.4 ± 2.3	3.0 ± 2.4	1.6 ± 1.3	1.6 ± 1.3
0.15	319	329 ± 10	288 ± 11	17.0 ± 2.1	18.8 ± 1.7	2.7 ± 2.2	1.1 ± 0.9	1.2 ± 0.9
0.20	309	279 ± 13	248 ± 11	11.7 ± 2.9	15.5 ± 1.9	2.5 ± 1.9	0.9 ± 0.7	0.4 ± 0.3
0.25	260	248 ± 9	219 ± 9	11.5 ± 1.8	13.8 ± 2.1	2.3 ± 1.8	0.4 ± 0.3	0.7 ± 0.6
0.30	221	219 ± 8	196 ± 7	8.1 ± 2.6	11.3 ± 1.9	2.1 ± 1.6	1.0 ± 0.9	0.5 ± 0.4
0.35	187	190 ± 7	168 ± 7	8.4 ± 1.8	10.8 ± 1.7	1.6 ± 1.2	0.9 ± 0.8	0.5 ± 0.4

Bin's left border	Monte Carlo expected events for VR2-tN (2 b-jet) validation region						
	SM Total	$t\bar{t}$	W+jets	single top	$t\bar{t}+V$	diboson	Z+jets
0.00	457 ± 88	396 ± 73	32.2 ± 9.7	23.7 ± 6.6	3.1 ± 2.5	1.8 ± 1.6	0.3 ± 0.2
0.05	414 ± 79	365 ± 68	20.5 ± 7.8	24.3 ± 5.1	2.9 ± 2.4	0.7 ± 1.5	0.3 ± 0.3
0.10	372 ± 73	323 ± 63	22.4 ± 6.1	20.6 ± 5.0	2.6 ± 2.1	1.6 ± 1.3	1.7 ± 1.4
0.15	338 ± 64	294 ± 56	18.3 ± 5.6	20.3 ± 3.6	2.8 ± 2.2	1.2 ± 1.0	1.3 ± 1.0
0.20	304 ± 59	264 ± 50	19.2 ± 6.9	16.6 ± 4.1	2.5 ± 2.0	0.9 ± 0.8	0.4 ± 0.3
0.25	256 ± 57	225 ± 47	12.7 ± 6.5	14.6 ± 4.0	2.3 ± 1.8	0.8 ± 0.9	0.8 ± 0.6
0.30	223 ± 45	199 ± 38	9.1 ± 5.9	12.1 ± 2.9	1.8 ± 1.5	0.6 ± 0.6	0.6 ± 0.4
0.35	190 ± 38	167 ± 35	9.0 ± 2.4	10.4 ± 3.4	1.6 ± 1.3	0.7 ± 0.7	0.6 ± 0.4

Table 8.15: Results for the background-only fit for the VR2-tN validation region for the BDT2 variable (2 b-jet selection). Numbers in the first column present the left border of each bin interval. All intervals are $[x, x + 0.05]$.

8.11.2 Interpretation

The background-only fit shows good agreement between data and the expectation from the Monte Carlo simulation, and no excess of events in the high BDT output region is seen. Therefore one can set 95% CL exclusion limits in the $(\tilde{t}_1, \tilde{\chi}_1^0)$ mass plane.

The exclusion limits are determined for two simplified decay modes:

- $\tilde{t}_1 \to t\tilde{\chi}_1^0$, on-shell decay with $\mathcal{BR} = 100\%$;
- $\tilde{t}_1 \to bW\tilde{\chi}_1^0$, off-shell (3-body) decay with $\mathcal{BR} = 100\%$.

The fit to calculate the exclusion limits uses all control and signal regions to calculate the CL_s value. Two different CL_s values are calculated:

- An *expected* CL_s value ($\mathrm{CL}_s^{\mathrm{exp}}$) is calculated under the assumption of no signal, and for the "data" in the signal regions (SR1-tN and SR2-tN) replaced by the total fitted background expectation.
- An *observed* CL_s value ($\mathrm{CL}_s^{\mathrm{obs}}$) is calculated using the data in all signal regions.

The results of the expected and observed CL_s values in percent are shown for different signal models in Figure 8.40. A signal model is considered excluded at 95% CL if the corresponding CL_s is below 5%. For each figure the gray dashed line shows the corresponding exclusion contour at 95% confidence level.

The expected and observed CL_s values for the nominal signal cross section for signal models with a $\Delta m \approx 3$ GeV below the diagonal are listed in Table 8.16.

$m(\tilde{t}_1, \tilde{\chi}_1^0)$ [GeV]	Expected CL_s	Observed CL_s
$(180, 5)$	0.0588	0.0433
$(190, 15)$	0.0467	0.2098
$(210, 35)$	0.0261	0.0180
$(230, 55)$	0.0084	0.0045
$(240, 65)$	0.0071	0.0020
$(250, 75)$	0.0060	0.0025
$(260, 85)$	0.0104	0.0071
$(270, 95)$	0.0092	0.0039
$(300, 125)$	0.0251	0.0203
$(325, 150)$	0.0847	0.0533
$(350, 175)$	0.1797	0.1345
$(375, 200)$	0.2976	0.3023
$(400, 225)$	0.4668	0.3537

Table 8.16: The expected and observed CL_s values for the nominal signal cross section for signal models with a $\Delta m \approx 3$ GeV below the diagonal

The results of the tN diagonal analysis based on data corresponding to an integrated luminosity of $\mathcal{L}_{\mathrm{int}} = 20.3\ \mathrm{fb}^{-1}$ of $\sqrt{s} = 8$ TeV are presented in Figure 8.41. All exclusion limits are

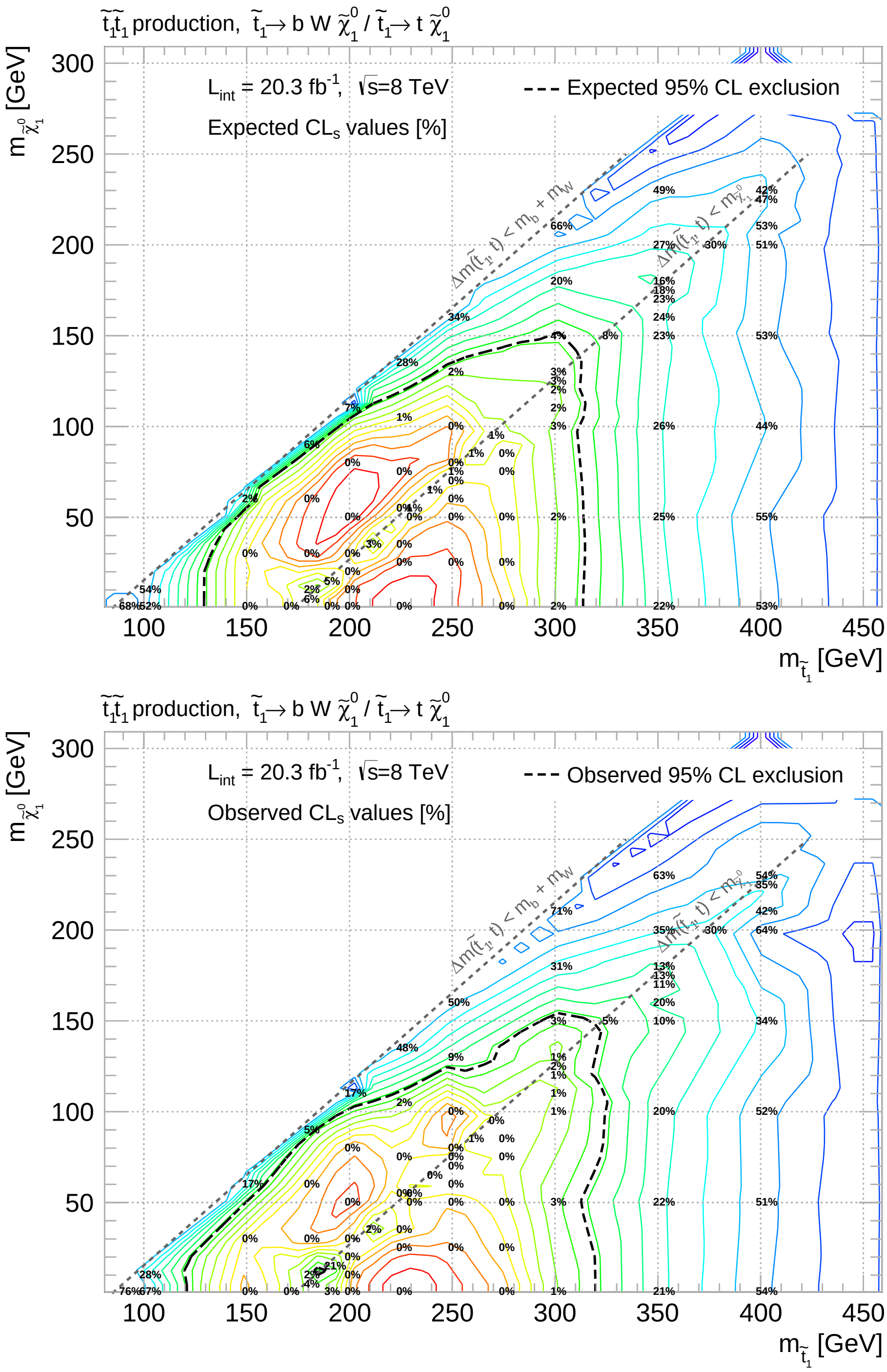

Figure 8.40: Expected limits of the tN diagonal analysis based on data corresponding to an integrated luminosity of $\mathcal{L}_{\text{int}} = 20.3$ fb^{-1} of $\sqrt{s} = 8$ TeV. The $\tilde{t}_1 \to t\tilde{\chi}_1^0$ and $\tilde{t}_1 \to bW\tilde{\chi}_1^0$ (3-body) decay modes are considered. Both decays are assumed to have a $\mathcal{BR}$ of 100%. The expected (top) and observed (bottom) CL_s values are shown for each signal model in percent. The black dashed line shows the corresponding exclusion contour at 95% CL. The limits include all uncertainties except the uncertainty on the signal cross section.

shown at 95% confidence level. The limits include all uncertainties except the uncertainty on the signal cross section (PDF and scale variations).

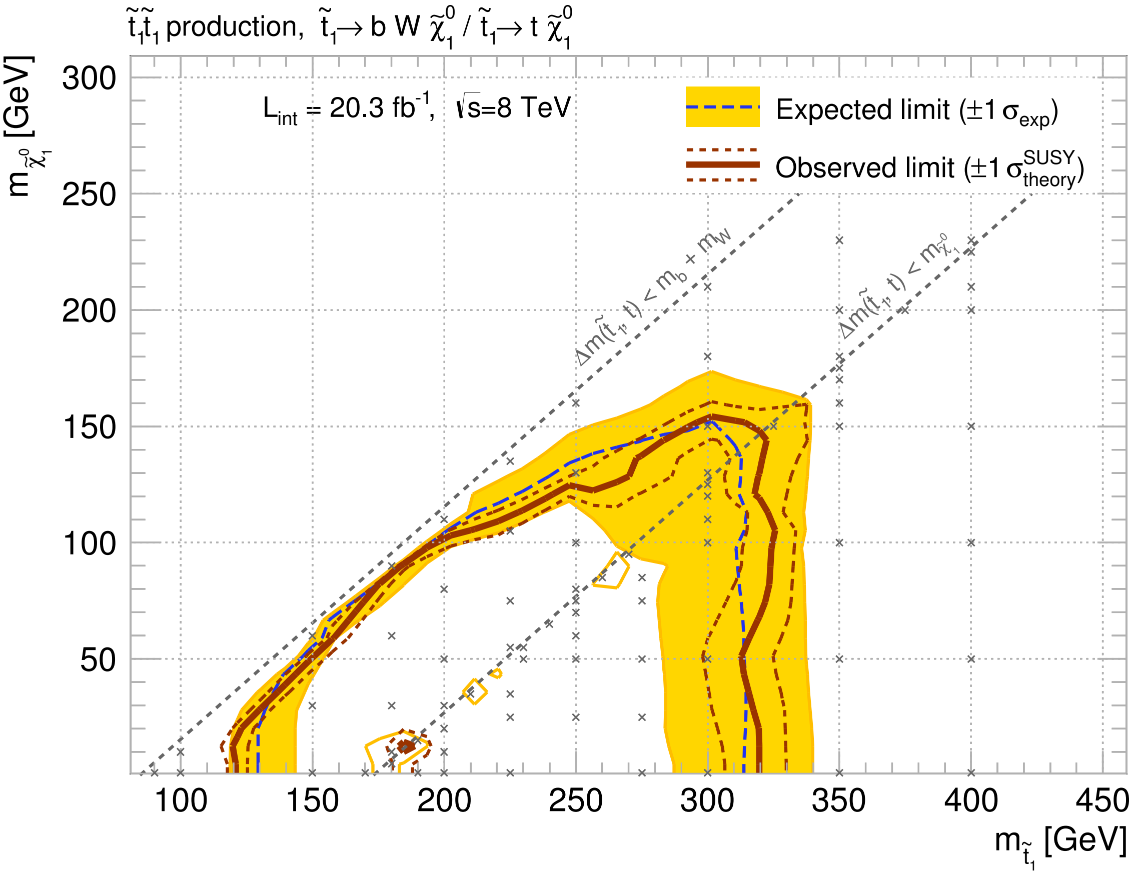

Figure 8.41: Exclusion limits at 95% of the tN diagonal analysis based on data corresponding to an integrated luminosity of $\mathcal{L}_{\text{int}} = 20.3$ fb^{-1} of $\sqrt{s} = 8$ TeV. The $\tilde{t}_1 \rightarrow t\tilde{\chi}^0_1$ and $\tilde{t}_1 \rightarrow bW\tilde{\chi}^0_1$ (3-body) decay modes are considered. Both decays are with $\mathcal{BR} = 100\%$. The dark blue dashed line corresponds to the expected limits. The yellow band includes all uncertainties except the uncertainty on the signal cross section. The red solid line corresponds to the observed limits. The red dashed line represents $\pm1\sigma$ variation of the signal cross-section uncertainty.

Exclusion gap

The analysis leaves a gap around the $m(\tilde{t}_1, \tilde{\chi}^0_1) = (190, 15)$ GeV signal point. There are two different mechanisms involved in the appearance of this gap.

For signal models with lower top-squark masses, the corresponding cross section is getting larger. Under the assumption that along the diagonal the kinematical properties do not change, one should expect an increase of the signal-to-background ratio proportional to the increased cross section.

This is not the case for the current analysis. Figure 8.42 shows the comparison of the signal-to-background ratio as a function of the BDT output for different signal models around the

(190, 15) point of the mass plane. One can see, that when the top-squark mass decreases, the signal-to-background ratio increases in the control region (BDT < 0), but decreases in the signal region (BDT > 0.4). This behaviour is similar for both the 1 b-jet and 2 b-jet selections.

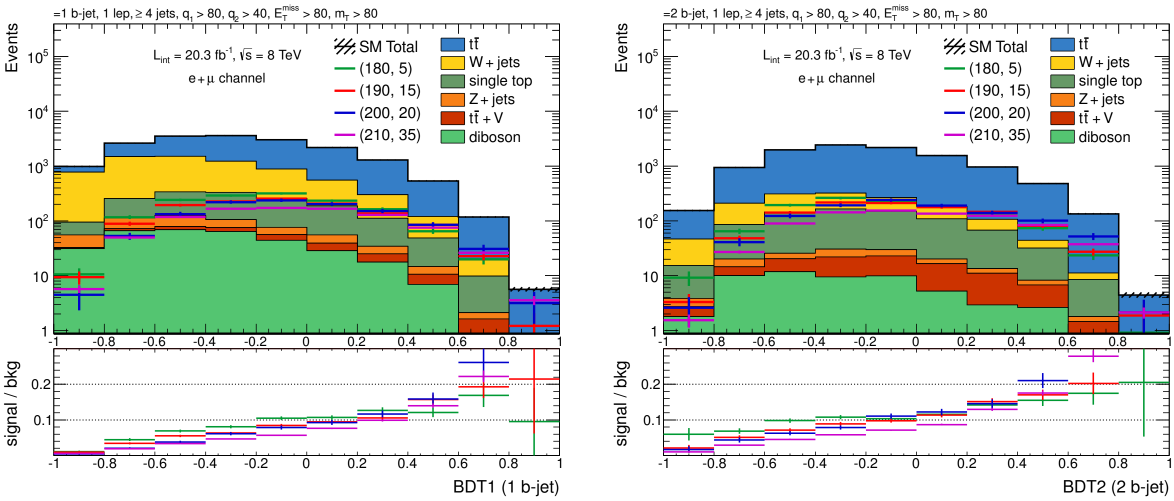

Figure 8.42: Distributions of the BDT1 (1 b-jet selection, left) and BDT2 (2 b-jet selection, right) output. The signal models are for the top-squark masses $m(\tilde{t}_1) = 180, 190, 200, 210$ GeV, for on-shell top decays near the diagonal.

When moving from $m(\tilde{t}_1) = 210$ GeV to 190 GeV along the diagonal, the increase in cross section of the top-squark pair production is not enough to compensate the drop of the acceptance in the signal region due to the change of the kinematical properties. The number of signal events in the control region is increasing, but this is not enough to recover the drop of the separation power, since it is mainly driven by the signal region. Therefore, the exclusion power of the analysis decreases.

With a further decrease of the top-squark mass from $m(\tilde{t}_1) = 190$ GeV to 180 GeV, the signal-to-background ratio decreases further in the signal region, and keeps increasing in the control region, reaching up to 10% in some bins. This allows to increase the separation power due to the shape-fit in the control region. Therefore, for low top-squark masses, $m(\tilde{t}_1) < 180$ GeV, the analysis mainly benefits from the increase of the cross section, rather than from differences in kinematic properties between the signal and $t\bar{t}$ background events.

One can see, that for signal models with a top-squark mass above 200 GeV, the signal contamination in the control region is less than 6%. Therefore a precise modelling of the shape in the control region does not play a significant role, and the shape fit in this region is mainly used to constraint fit parameters, rather than to perform the exclusion.

This is not the case for the signal models for the 180–200 GeV diagonal region. For these signal models the sensitivity in the signal region is decreased and the analysis relies on the precise modelling of the shape, therefore, the results are not reliable to set exclusion limits. To cover the 180–200 GeV diagonal gap, a dedicated analysis has to be developed. In order to estimate the exclusion limits more precisely, additional intermediate signal models for this region would have to be generated.

Default 4-bin reweighting

For a comparison, the exclusion contour using the default 4-bin $t\bar{t}$ reweighting (see Section 7.1) is shown in Figure 8.43. One can see, that an agreement along the diagonal between the expected and observed exclusions is a bit worse, but in general the results are consistent.

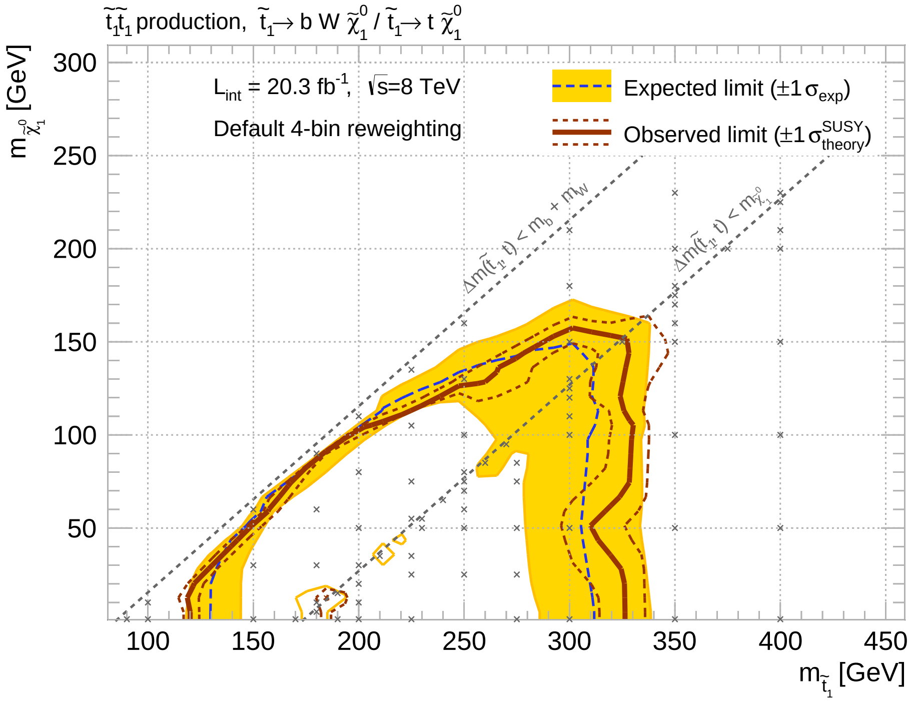

Figure 8.43: Results of the tN diagonal analysis using the default 4-bin reweighting. Results are shown for $\mathcal{L}_{\text{int}} = 20.3\ \text{fb}^{-1}$ data at $\sqrt{s} = 8$ TeV. Exclusion limits are shown at 95% CL. The dashed and solid lines correspond to the expected and observed limits. Limits include all uncertainties except the uncertainty on the signal cross section (PDF and scale). The $\tilde{t}_1 \to t\tilde{\chi}_1^0$ and $\tilde{t}_1 \to bW\tilde{\chi}_1^0$ (3-body) decay modes are considered. Both decays are with $\mathcal{BR} = 100\%$.

Cross-check

A cross-check for the tN diagonal analysis is performed based on the approach proposed in Section 8.10.1. To simplify the cross-check, it is assumed, that the total theoretical uncertainty in the signal region can be estimated by a linear function

$$f(x) = \beta(\alpha \cdot x + 1 - \alpha), \tag{8.29}$$

where x = BDT1 or BDT2, depending to which signal region is used. In this notation the uncertainty for $f(1) = \beta$, while if $\alpha = 1$, the uncertainty for $f(0) = 0$.

For the cross-check, control regions for the 1 b-jet and 2 b-jet selections are defined as corresponding BDT intervals of $[-1, 0]$ with one bin. The same signal regions as for the analysis are used. Theoretical uncertainties are considered only for the $t\bar{t}$, W+jets and single top production. All other processes are neglected, since their contributions are negligible.

The $t\bar{t}$ and W+jets production is normalised in control regions. The total theoretical uncertainty for single top production in control region is set to $\pm 50\%$. Theoretical uncertainties for the $t\bar{t}$, W+jets and single top production in the signal regions are considered as fully correlated shape variations estimated by linear functions with the slope parameter α. In general, since in the signal regions the $t\bar{t}$ production is dominant, there is no significant difference to how the W+jets and single top theoretical uncertainties are included. Nevertheless, treating the uncertainties as uncorrelated may slightly improve the result. Therefore, in a conservative approach, all theoretical uncertainties are considered as fully correlated.

For $t\bar{t}$ production for the 1 b-jet and 2 b-jet signal regions the β parameters for the total theoretical uncertainties are estimated to be $\beta_1 = 15\%$ and $\beta_2 = 13\%$, respectively. This estimation is based on the distributions of the parton shower and ISR/FSR uncertainties, see Figures 8.22 and 8.23. The W+jets and single top contributions in the signal regions are negligible. Therefore, to be conservative, $\beta = 80\%$ is used.

Table 8.17 shows the expected and observed CL$_s$ values for the $m(\tilde{t}_1, \tilde{\chi}_1^0) = (210, 35)$ and $(300, 125)$ GeV signal models for different slope parameters $\alpha = 0.6$, 0.8, 1.0, 1.2, 1.4. For comparison, the results from the tN analysis are shown in the last line.

Slope	$m(\tilde{t}_1, \tilde{\chi}_1^0) = (210, 35)$ GeV		$m(\tilde{t}_1, \tilde{\chi}_1^0) = (300, 125)$ GeV	
α	Expected CL$_s$	Observed CL$_s$	Expected CL$_s$	Observed CL$_s$
0.6	0.019	0.022	0.019	0.018
0.8	0.038	0.043	0.020	0.020
1.0	0.039	0.044	0.021	0.022
1.2	0.018	0.022	0.035	0.039
1.4	0.017	0.020	0.020	0.022
tN Result	0.026	0.018	0.025	0.020

Table 8.17: The expected and observed CL$_s$ values for the $m(\tilde{t}_1, \tilde{\chi}_1^0) = (210, 35)$ and $(300, 125)$ GeV signal models for different slope values α of the total theory systematic uncertainty. For comparison, the results from the tN analysis are shown in the last line.

The worst CL$_s$ value for different signal models may occur for different α parameter. For example, the worst CLs value for the $m(\tilde{t}_1, \tilde{\chi}_1^0) = (210, 35)$ GeV signal model is for $\alpha = 1.0$, while for the $m(\tilde{t}_1, \tilde{\chi}_1^0) = (300, 125)$ GeV signal model it corresponds to $\alpha = 1.2$. One can see a consistency of the results of the tN analysis with both reference models. An improvement of the CL$_s$ for the tN analysis is related to the shape fit in the multibin control regions.

8.11.3 Conclusions

The analysis presented excludes the interval from 200–300 GeV along the diagonal. The dedicated variables, which are developed for the analysis are sensitive in the diagonal region. The sensitivity of the variables increases for higher top-squark masses, therefore, the same variables can be used for $\sqrt{s} = 13$ TeV analyses, where they are expected to have even higher separation power.

The analysis is sensitive to both on- and off-shell decay modes, therefore it can cross the diagonal and signal models can be excluded from both sides. This simplifies the estimate of the significance exactly on the diagonal, where on-shell, off-shell and mixed decay modes are possible. The estimate of the relative branching ratio of these decay modes, which might be quite challenging, is not needed.

The results of the presented analysis have been cross-checked for the $m(\tilde{t}_1, \tilde{\chi}^0_1) = (210, 35)$ and $(300, 125)$ GeV signal models near the diagonal for different assumptions on the shapes of the total systematic uncertainty. The results for both reference signal models are found to be consistent with the results of the tN diagonal analysis.

Top-squark masses above 300 GeV are not excluded due to a too low number of events in the signal region. Therefore, an increase of the integrated luminosity will increase the exclusion limits. An optimisation of the analysis for $\sqrt{s} = 13$ TeV data will also significantly benefit from an increased signal cross section with respect to the $t\bar{t}$ production cross section.

This is not the case for the top-squark masses below the 200 GeV, which are not excluded by this analysis. In this region, even with a higher integrated luminosity, the proposed analysis will have a poor exclusion power.

For the top quark cross-section measurements [121], the observed limit is 177 GeV, while for spin correlation measurements [122] the expected and observed results are 178 GeV and 191 GeV, respectively. This means, that at the moment no analysis exists, which is expected to exclude signal models along the diagonal with top-squark masses around 180–200 GeV.

The exclusion gap for the $m(\tilde{t}_1, \tilde{\chi}^0_1) = (190, 15)$ GeV signal model for $\tilde{t}_1 \to t\tilde{\chi}^0_1$ grid shown in Figure 8.44 (left plot) is consistent with the exclusion gap for $m(\tilde{t}_1, \tilde{\chi}^\pm_1, \tilde{\chi}^0_1) = (190, 120, 60)$ GeV signal model for the ATLAS $\tilde{t}_1 \to b\tilde{\chi}^\pm_1$ gaugino universality grid (right plot). In case of some excess for the $m(\tilde{t}_1, \tilde{\chi}^0_1) = (190, 15)$ GeV signal model, it might be visible as the excess for the

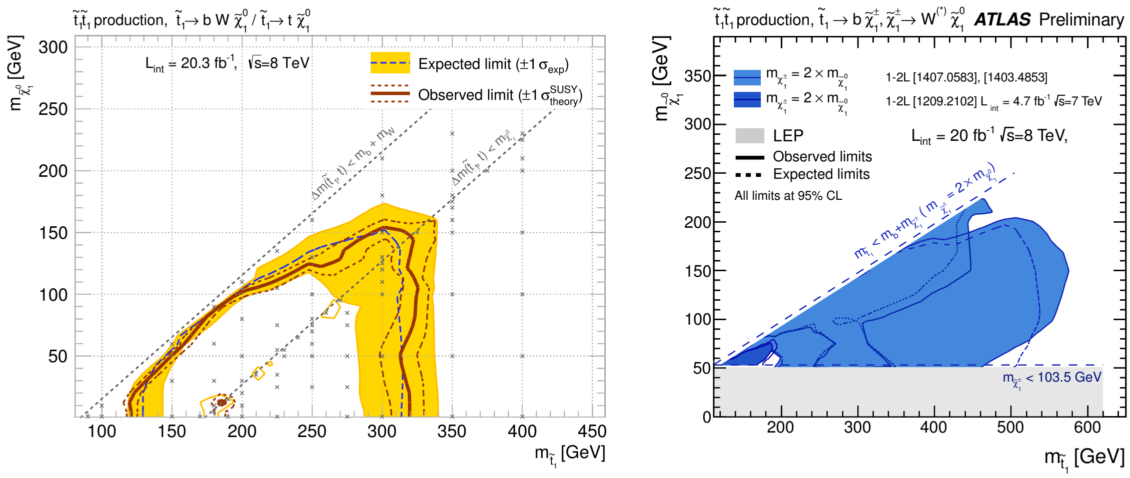

Figure 8.44: Results of the presented $\tilde{t}_1 \to t\tilde{\chi}^0_1$ diagonal analysis (left) and the ATLAS results for the $\tilde{t}_1 \to b\tilde{\chi}^\pm_1$ decay mode for $m(\tilde{\chi}^\pm_1) = 2 \cdot m(\tilde{\chi}^0_1)$ [3, 4, 111] (right) at $\sqrt{s} = 8$ TeV. All exclusion limits are shown at a 95% CL.

$m(\tilde{t}_1, \tilde{\chi}_1^{\pm}, \tilde{\chi}_1^0) = (190, 120, 60)$ GeV, since both signal models have the same $m(\tilde{t}_1)$ and the same final states, including two neutralinos.

On the other side, the gap for both grids might be due to the overlap of two different exclusion mechanisms. For $m(\tilde{t}_1) < 180$ GeV the exclusions for both decay modes may benefit from a high top-squark pair production cross section, while for $m(\tilde{t}_1) > 200$ GeV they might profit from a difference between kinematic properties.

For the intermediate region 180 GeV $< m(\tilde{t}_1) <$ 200 GeV, a decrease of the cross section cannot be compensated by an increase of the separation power due to the difference in kinematic properties. This leads to the gap in the exclusion.

Therefore, it will be necessary to develop dedicated analyses to exclude the 180–200 GeV interval along the diagonal. For further studies, it will be important to generate samples for additional signal models along the diagonal.

CHAPTER 9

Multijet background estimation, an alternative approach

For one-lepton SUSY searches, signal regions with at least one lepton and high $E_{\mathrm{T}}^{\mathrm{miss}}$ are used. This makes it difficult to estimate the *multijet background* (QCD) based on Monte Carlo simulation, since the rejection for QCD background is very high. To have a reasonable estimation of the multijet background, a huge number of multijet events has to be simulated. On the other hand, due to a high rejection of the multijet background, the contribution in the signal regions is small and it is often sufficient to estimate an upper limit.

A multijet event can pass the lepton filter if:

– A jet is misidentified as a lepton (mainly as an electron), so-called *misidentified lepton*;

– A real lepton is produced from a weakly decaying b or c hadron, referred to as a *lepton from heavy flavour decays*;

– An electron is produced in a photon conversion, referred to as a *photon conversion electron*.

All these types of leptons are collectively referred to as *fake leptons*.

To estimate the multijet background, data-driven approaches are used. One such approach, which is used in the one-lepton SUSY searches, is the so-called *Matrix Method* approach [124]. It is briefly described below. The typical limitations of the method are also highlighted.

An alternative data-driven *Exponential Extrapolation* approach for the estimation of the fake lepton background is proposed in this chapter. Various aspects of this approach are discussed in the following. A verification and cross-check with the Matrix Method is also performed.

9.1 Matrix Method

This data driven approach for the fake electron estimation uses two definitions of electrons: *loose* and *tight* with probability coefficients, that the loose electron satisfies the tight criteria $\varepsilon_{\text{real}}, \varepsilon_{\text{fake}}$ separately for *real* and *fake* electrons. The real and fake electron contamination is evaluated according to the following equations:

$$\begin{aligned} N^{\text{loose}} &= N^{\text{loose}}_{\text{real}} + N^{\text{loose}}_{\text{fake}}, \\ N^{\text{tight}} &= N^{\text{tight}}_{\text{real}} + N^{\text{tight}}_{\text{fake}} = \varepsilon_{\text{real}} N^{\text{loose}}_{\text{real}} + \varepsilon_{\text{fake}} N^{\text{loose}}_{\text{fake}}, \end{aligned} \tag{9.1}$$

where N^{loose} and N^{tight} are a number of loose and tight electrons in the signal region, respectively. These numbers can be directly measured from the data.

The goal is to evaluate the number of fake electrons $N^{\text{tight}}_{\text{fake}}$. The method consists of the following steps:

- Evaluate $\varepsilon_{\text{real}}$ and $\varepsilon_{\text{fake}}$ in some control region CR;
- Transfer these coefficients to the signal region SR;
- Solve the linear equations 9.1.

Solving equations 9.1 gives the following solution:

$$N^{\text{tight}}_{\text{fake}} = \frac{\varepsilon_{\text{fake}}}{\varepsilon_{\text{real}} - \varepsilon_{\text{fake}}} (\varepsilon_{\text{real}} N^{\text{loose}} - N^{\text{tight}}). \tag{9.2}$$

It should be noted that the signal region is involved in the evaluation of a number of fake electrons $N^{\text{tight}}_{\text{fake}}$, via a number of tight electrons in the signal region N^{tight}.

The main challenges of the Matrix Method are to determine:

- Appropriate control region CR;
- Correct transfer of coefficients from CR to SR;
- Reliable scheme for cross-checking the results.

The coefficients $\varepsilon_{\text{real}}$ and $\varepsilon_{\text{fake}}$ may depend on the electron parameters (p_{T}, η) as well as on other factors, related to the whole event ($E_{\text{T}}^{\text{miss}}$, jets p_{T}, etc.). Therefore, it is not easy to prove that the coefficients evaluated from control regions are applicable for the signal region, since this always involves some additional assumptions about the transfer mechanism.

9.2 Estimation of fake electrons

The *Exponential Extrapolation* approach solves some of the challenges mentioned above.

9.2.1 Exponential Extrapolation

In the following example the *isolation variable* ξ is defined as $\xi = p_{\mathrm{T}}^{\mathrm{cone}\,0.2}/p_{\mathrm{T}}$, and *signal electrons* are defined to be isolated with $\xi < 0.1$.

The distribution of the isolation variable ξ, which is referred to as $h(\xi)$, can be splitted in two part, for real and fake electrons, $h(\xi) = h_{\mathrm{real}}(\xi) + h_{\mathrm{fake}}(\xi)$. Figure 9.1 shows the distribution of the isolation variable ξ for data.

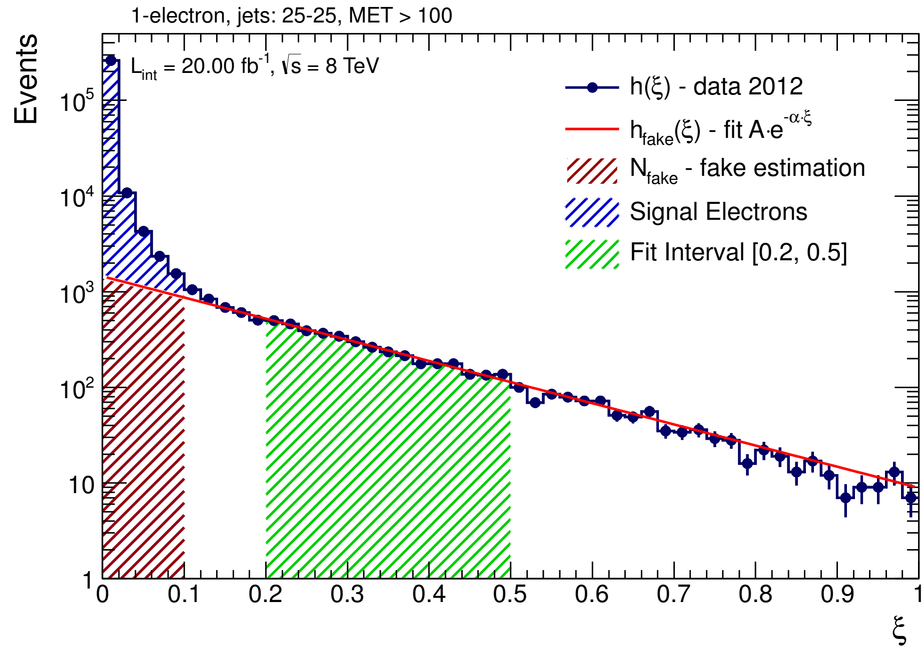

Figure 9.1: Distribution of the isolation variable ξ for data.

The examination of this and related plots suggests the following assumptions:

- The $h_{\mathrm{fake}}(\xi)$ can be described by an exponential function $A \cdot e^{-\alpha\xi}$;
- Fake electrons dominate in the region $\xi > 0.2$.

Based on these assumptions the following steps for fake electron estimation are defined:

- Fit $A \cdot e^{-\alpha\xi}$ to the data in the $[0.2, 0.5]$ interval;
- Extrapolate the exponential function to the $[0, 0.2]$ interval;
- Estimate the number of fake electrons:

$$N_{\mathrm{fake}} = \int_0^{0.1} h_{\mathrm{fake}}(\xi) d\xi. \tag{9.3}$$

In the following sections, the correctness of these assumptions is verified and cross-checked with the multijet Monte Carlo samples in regions with sufficient data, such that statistical uncertainties are small. In the following, various aspects of this approach are discussed and illustrated with examples.

The $h^{\text{loose}}(\xi)$ and $h^{\text{tight}}(\xi)$ distribution functions

As an example, the following region is considered:

- Exactly one electron with $p_{\text{T}}(e) > 25$ GeV (no isolation requirement);
- At least two jets with $p_{\text{T}}(j_1) > 25$ GeV and $p_{\text{T}}(j_2) > 25$ GeV;
- $E_{\text{T}}^{\text{miss}} > 100$ GeV.

In the following all distributions are shown for data taken at $\sqrt{s} = 8$ TeV and corresponding to an integrated luminosity of $\mathcal{L}_{\text{int}} = 20.3\ \text{fb}^{-1}$.

Two electron definitions *loose* and *tight*, with no isolation requirement on ξ, are used. A *signal electron* is defined as a tight electron with isolation $\xi < 0.1$. In the current analysis, loose electrons are defined as baseline electrons, while tight electrons are defined as signal electrons without fulfilling the $p_{\text{T}}^{\text{cone}\,0.2}/p_{\text{T}} < 0.1$ isolation requirement (see Section 6.2.1).

Figure 9.2 shows the distributions of the isolation variable ξ for loose and tight electrons for data and Monte Carlo samples. In all following plots, the curve labeled "SM Total" (for the total Standard Model contribution) does not contain multijet (QCD) contribution, unless stated otherwise.

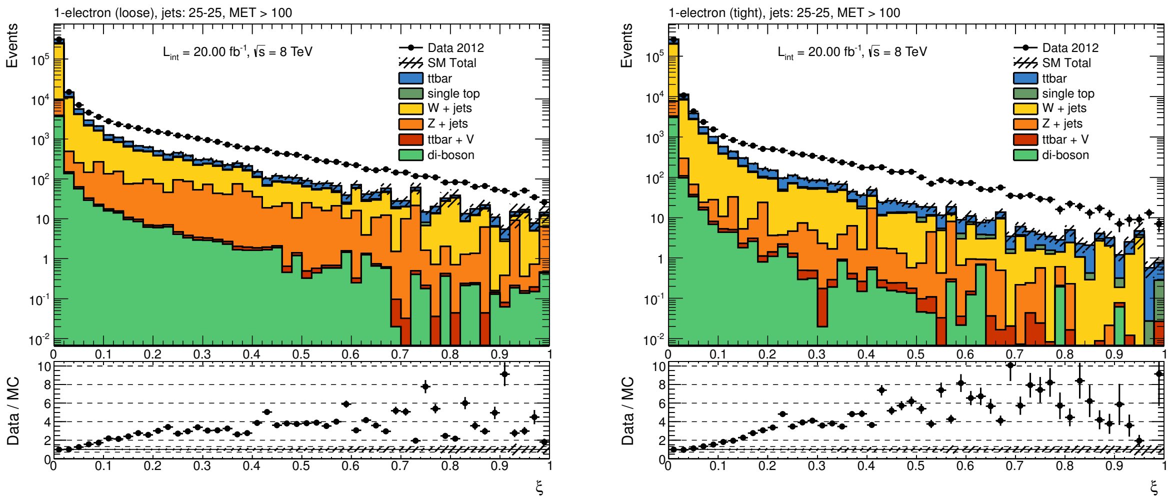

loose electrons, no isolation requirement   tight electrons, no isolation requirement

Figure 9.2: Distributions of the isolation variable ξ for loose (left) and tight (right) electrons.

Evaluation of $\varepsilon_{\text{fake}}$

From the data one can directly calculate the ratio

$$\frac{h^{\text{tight}}(\xi)}{h^{\text{loose}}(\xi)} = \frac{h_{\text{real}}^{\text{tight}}(\xi) + h_{\text{fake}}^{\text{tight}}(\xi)}{h_{\text{real}}^{\text{loose}}(\xi) + h_{\text{fake}}^{\text{loose}}(\xi)} = \frac{\varepsilon_{\text{real}} \cdot h_{\text{real}}^{\text{loose}}(\xi) + \varepsilon_{\text{fake}} \cdot h_{\text{fake}}^{\text{loose}}(\xi)}{h_{\text{real}}^{\text{loose}}(\xi) + h_{\text{fake}}^{\text{loose}}(\xi)} \tag{9.4}$$

The same ratio, but without the QCD contribution, is also available for Monte Carlo. Figure 9.3 shows the distribution of the $h^{\text{tight}}(\xi)/h^{\text{loose}}(\xi)$ ratio from data and Monte Cralo. The ratio calculated for Monte Carlo does not include the QCD samples. From the figure one can see that $h^{\text{tight}}(\xi)/h^{\text{loose}}(\xi)$ is flat in the $[0.2, 0.5]$ interval for both data and Monte Carlo.

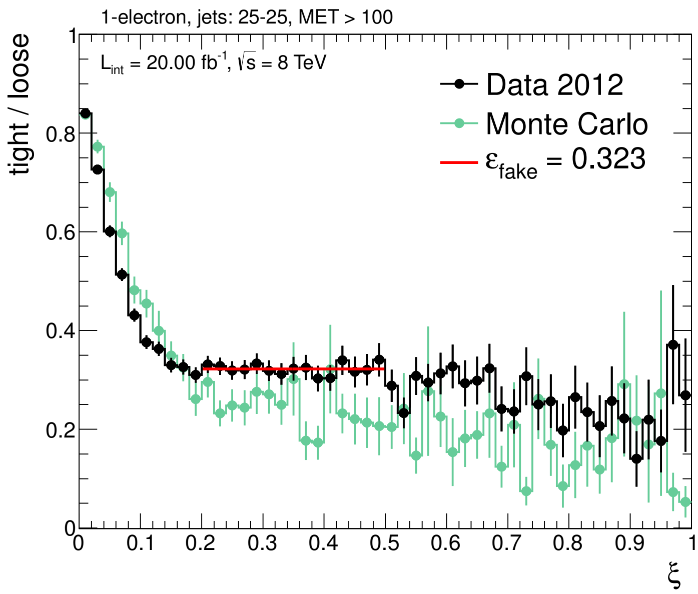

Figure 9.3: Distribution of the ratio $h^{\text{tight}}(\xi)/h^{\text{loose}}(\xi)$ from data and Monte Carlo samples (the Monte Carlo does not include QCD contributions)

Under the assumption, that $h_{\text{real}}(\xi)$ and $h_{\text{fake}}(\xi)$ do not have exactly the same shape in this region, one can conclude, that here the fake electrons dominate and one can evaluate

$$\varepsilon_{\text{fake}} = 0.323 \pm 0.006. \tag{9.5}$$

Evaluation of $h_{\text{real}}(\xi)$, $h_{\text{fake}}(\xi)$ and $\varepsilon_{\text{real}}(\xi)$

Using $\varepsilon_{\text{fake}}$, one can reconstruct the shape of $h_{\text{real}}(\xi) \sim h^{\text{tight}}(\xi) - \varepsilon_{\text{fake}} \cdot h^{\text{loose}}(\xi)$. Figure 9.4 shows the $h^{\text{loose}}(\xi)$, $h^{\text{tight}}(\xi)$ and $h_{\text{real}}(\xi)$ distribution functions in logarithmic and linear scales. As one can see, that the contribution of real electrons for the $\xi > 0.2$ region is negligible.

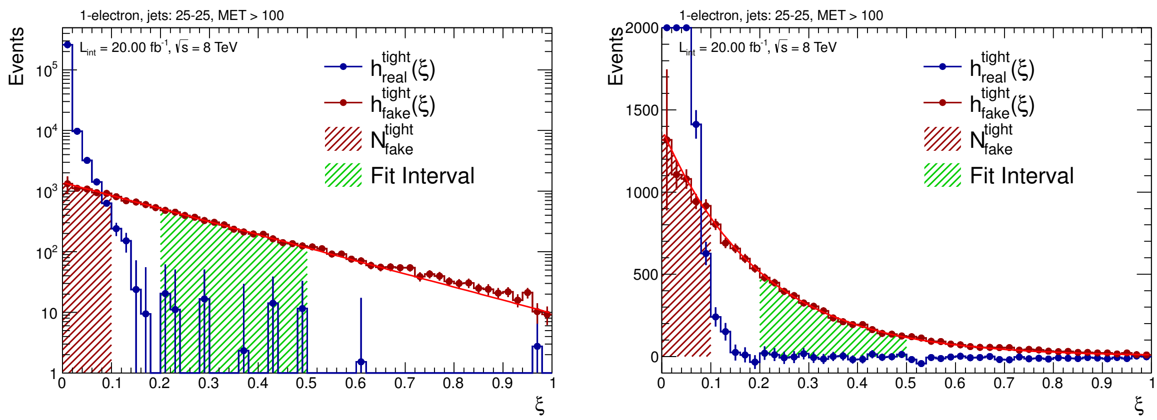

Figure 9.4: Reconstruction of $h_{\text{real}}(\xi)$ and $h_{\text{fake}}(\xi)$ in log scale (left) and linear scale (right).

Using this observation, $h^{\text{tight}}_{\text{fake}}(\xi)$ is calculated by fitting $A \cdot e^{-\alpha\xi}$ to the $h^{tight}(\xi)$ in the $[0.2, 0.5]$ and extrapolating the result to the interval $[0, 0.2]$. Now, one can evaluate $\varepsilon_{\text{real}}$ as a function of ξ, at least in the $[0, 0.2]$ interval, where a sufficient number of events is available. Figure 9.5 shows the estimated values with uncertainties for $\varepsilon_{\text{real}}(\xi)$. They are found to be constant in the $[0, 0.2]$ interval.

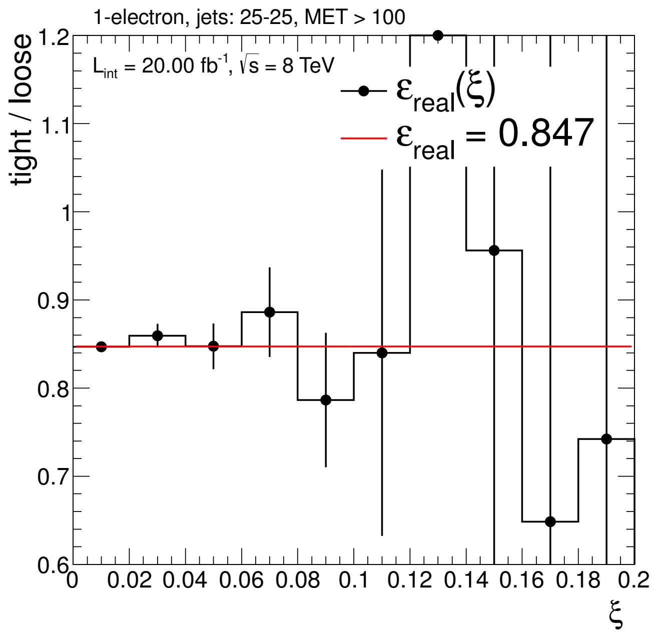

Figure 9.5: Estimated values of $\varepsilon_{\text{real}}$ as a function of ξ.

Fitting a constant in the $[0, 0.2]$ interval, one can obtain

$$\varepsilon_{\text{real}} = 0.847 \pm 0.002. \tag{9.6}$$

The evaluation for $t\bar{t}$ events, generated by POWHEG+PYTHIA, gives

$$\varepsilon^{\text{MC}}_{\text{real}} = 0.846 \pm 0.002. \tag{9.7}$$

These results are consistent within the statistical uncertainties. Just for comparison, one can check to how significant is the fake electrons contribution. Assuming, that there are no fakes among signal electrons, one can estimate the corresponding $\varepsilon_{\text{real}}$ as the value of the tight-to-loose ratio in the first bin

$$h^{\text{tight}}(0)/h^{\text{loose}}(0) = 0.840 \pm 0.002. \tag{9.8}$$

One can see, that result is outside of 3σ from the both $\varepsilon_{\text{real}}$ and $\varepsilon^{\text{MC}}_{\text{real}}$ estimates.

Base on these findings, one can use the following assumptions:

- Estimation of the $\varepsilon_{\text{fake}}$ coefficient does not involve any assumption about the $\varepsilon_{\text{real}}$;
- The $\varepsilon_{\text{fake}}$ does not depend on ξ;
- The $h_{\text{fake}}(\xi)$ remains linear in logarithmic scale for all ξ;
- The area, where $h_{\text{real}}(\xi)$ has non-zero values is small with respect to $h_{\text{fake}}(\xi)$.

The last two assumptions are verified in the following with Monte Carlo simulation. It should be noted, that in the current case the contribution of the $h_{\mathrm{real}}(\xi)$ for the $\xi > 0.2$ region is negligible (see Figure 9.4).

Estimation of fake electrons

Based on above observations, the number of fake electrons can be estimated by fitting the function $A \cdot e^{-\alpha\xi}$ to the $h^{\mathrm{tight}}(\xi)$ distribution function in the $[0.2, 0.5]$ interval, where $h_{\mathrm{real}}(\xi)$ is negligible, and extrapolating it to $[0, 0.1]$, where $h_{\mathrm{real}}(\xi)$ dominates.

Figure 9.6 shows the distribution of the isolation variable ξ for loose and tight electrons in the

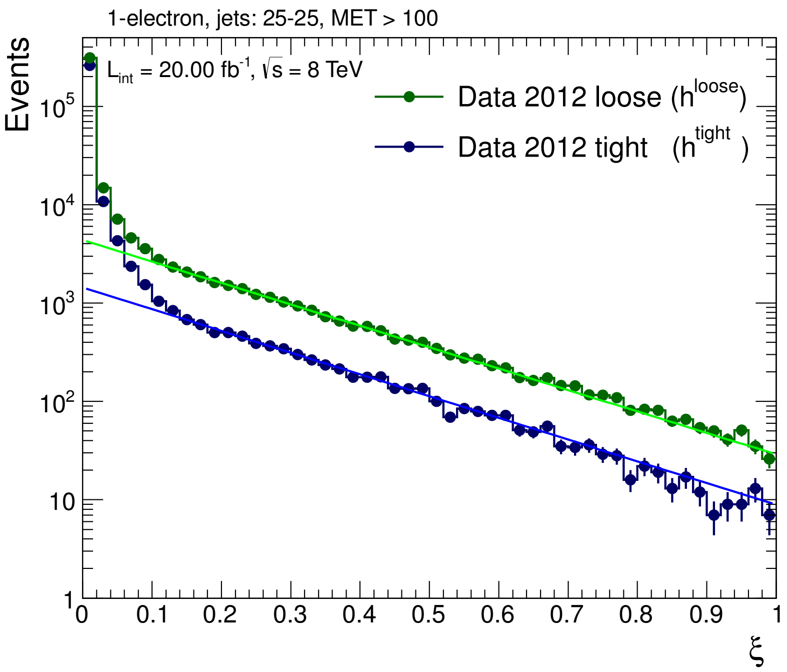

Figure 9.6: Distribution of the isolation variable ξ for loose and tight electrons in the data.

data. The results of the exponential fits to the data are:

$$\begin{aligned} A^{\mathrm{loose}} &= (4.36 \pm 0.16) \cdot 10^3, \quad & \alpha^{\mathrm{loose}} &= 5.01 \pm 0.11, \\ A^{\mathrm{tight}} &= (1.44 \pm 0.09) \cdot 10^3, \quad & \alpha^{\mathrm{tight}} &= 5.11 \pm 0.20. \end{aligned} \tag{9.9}$$

Integration in the $[0, 0.1]$ interval gives the fake electron estimation

$$N_{\mathrm{fake}}^{\mathrm{tight}} = (5.64 \pm 0.05) \cdot 10^3. \tag{9.10}$$

One can see, that the slopes α^{loose} and α^{tight} are in agreement. Based on these fit results one can calculate

$$\varepsilon_{\mathrm{fake}} = A^{\mathrm{tight}} / A^{\mathrm{loose}} = 0.330 \pm 0.024, \tag{9.11}$$

which is also in agreement with the value estimated from the $h^{\mathrm{tight}}(\xi)/h^{\mathrm{loose}}(\xi)$ ratio.

Combined fit

In case enough tight electrons are available in the fit interval, one can directly fit an exponential function $e^{-\alpha\xi+\beta}$ to the distribution of the isolation variable ξ for tight electrons $h^{\text{tight}}(\xi)$. When the number of available tight electrons is limited, a *Combined Fit* approach can be used. This approach benefits from the simultaneous fit of both the distributions for loose and tight electrons with the same α slope.

The $h^{\text{loose}}(\xi)$ and $h^{\text{tight}}(\xi)$ are statistically dependent, since all tight electrons fulfil loose criteria. To make the fit statistically independent, the $h^{\text{diff}}(\xi) = h^{\text{loose}}(\xi) - h^{\text{tight}}(\xi)$ is considered, i.e. distribution of the isolation variable ξ for loose electrons, which do not fulfil the tight selection criteria. These electrons, in the following, are referred to as *loose-not-tight electrons*.

In a combined fit approach exponential functions $e^{-\alpha\xi+\beta}$ and $e^{-\alpha\xi+\beta'}$ are fitted to the $h^{\text{tight}}(\xi)$ and $h^{\text{diff}}(\xi)$ distribution functions, respectively. Uncertainties related to the use of the same slope α can be estimated as the relative difference between α^{loose} and α^{tight}, which is about 2% for the example shown in Figure 9.6, while for some other examples shown in the following, it can reach up to 10%, see Table 9.2.

Usually, a combined fit approach is useful for regions where the statistical uncertainty of the exponential fit is dominant. Therefore, for these regions, the systematic uncertainty related to the difference between the slopes can be safely neglected.

The number of fake signal electrons for the combined fit is estimated as

$$N_{\text{fake}} = \int_0^{0.1} e^{-\alpha\xi+\beta} d\xi. \tag{9.12}$$

As an example of the combined fit approach one can see the estimation of fake electrons background for the SR-bC signal region of the bC analysis, see Section 6.5.2.

9.2.2 Validation

The validation of the method is done in two different ways: the main assumptions and results are validated using both multijet simulated samples and multijet enriched regions in data.

Linearity validation with data

The goal of this validation is to cross-check the assumption that the distribution of the isolation variable can be approximated by an exponential function.

To this extent, a QCD enriched region is chosen with the following preselection:

– Exactly one electron with $p_{\text{T}}(e) > 25$ GeV (no isolation requirement);

– At least three leading jets with $p_{\text{T}}(j_{1,2,3}) > 80, 40, 30$ GeV;

– Veto on b-tagged jets.

To avoid distortions of the distribution of the isolation variable, electron and missing transverse momentum triggers without isolation requirements are used.

The distributions of the isolation variable ξ for loose and tight electrons after the application of preselection requirements are shown in Figure 9.7. The Monte Carlo does not contains any multijet contributions. As one can see, for $\xi > 0.2$ the contamination of processes other than multijet production is less than 1%. The multijet background can therefore be estimated as

$$h_{\mathrm{QCD}}(\xi) = h_{\mathrm{data}}(\xi) - h_{\mathrm{MC}}(\xi). \tag{9.13}$$

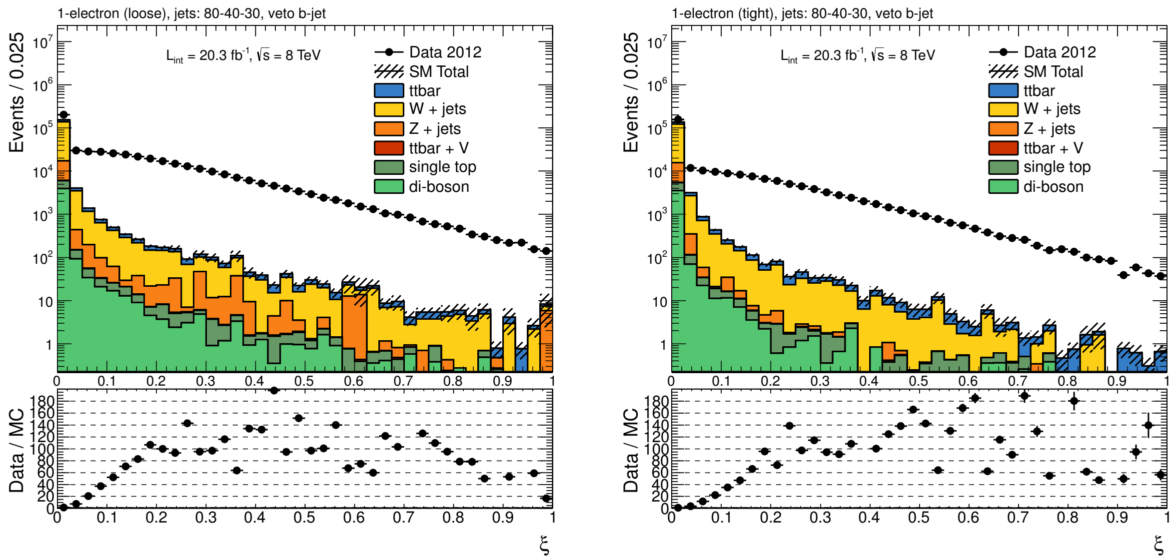

loose electrons, no isolation requirement

tight electrons, no isolation requirement

Figure 9.7: Distributions of the isolation variable ξ for loose (left) and tight (right) electrons. No QCD samples are included in the Monte Carlo.

The distributions of $E_{\mathrm{T}}^{\mathrm{miss}}$ for loose and tight electrons after the preselection without applying the requirements on the isolation variable are shown in Figure 9.8.

The region with $E_{\mathrm{T}}^{\mathrm{miss}} < 30$ GeV is enriched with fake electrons. Figure 9.9 shows the $h_{\mathrm{QCD}}^{\mathrm{loose}}(\xi)$ and $h_{\mathrm{QCD}}^{\mathrm{tight}}(\xi)$ distribution functions for preselected events with $E_{\mathrm{T}}^{\mathrm{miss}} < 30$ GeV. One can see, that distributions can be estimated by an exponential function and have similar slopes for loose and tight electrons.

To be more precise, an exponential function slightly overestimates the real distribution near zero. This may cause some problems, if one wants to exactly estimate the multijet contribution, but if one can prove with an exponential assumption, that the multijet contribution is negligible, the results stay valid for real multijet contributions too.

For all checks performed in the following, the main goal is to validate, that an exponential approach never underestimates the real multijet distribution. Therefore it can be used to set upper limits on the multijet contamination.

The validation is performed in the following way. The distribution function $h_{\mathrm{QCD}}(\xi)$ is fitted by an exponential function $e^{-\alpha\xi+\beta}$ in the $[0.2, 1]$ interval. A number of fake signal electrons (i.e.

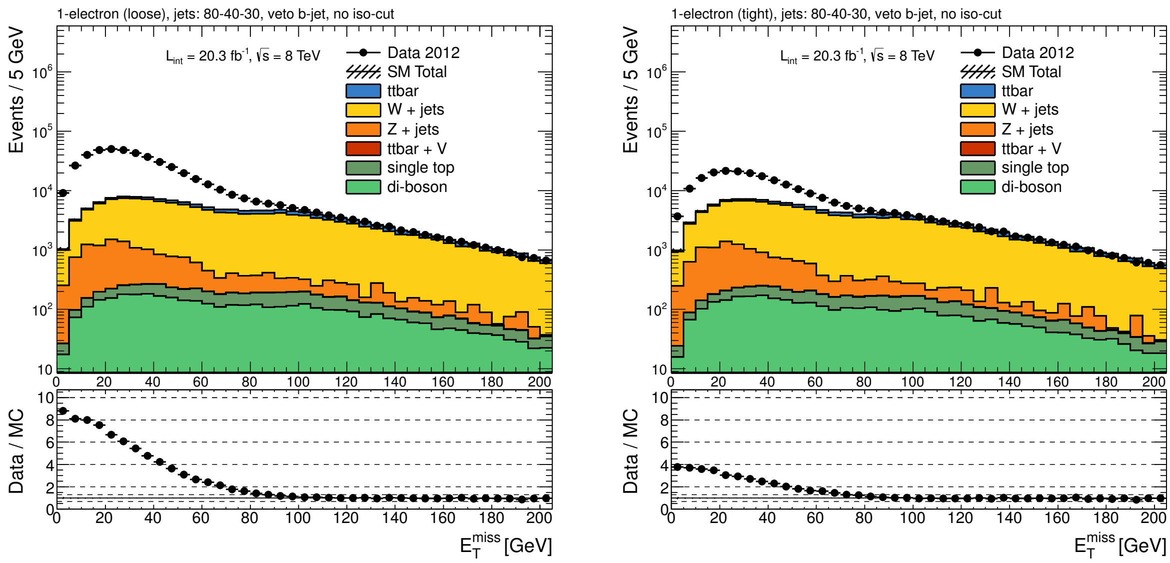

loose electrons, no isolation requirement | tight electrons, no isolation requirement

Figure 9.8: Distributions of $E_{\mathrm{T}}^{\mathrm{miss}}$ for loose (left) and tight (right) electrons. No selection on the isolation variable is applied. No QCD samples are included in the Monte Carlo.

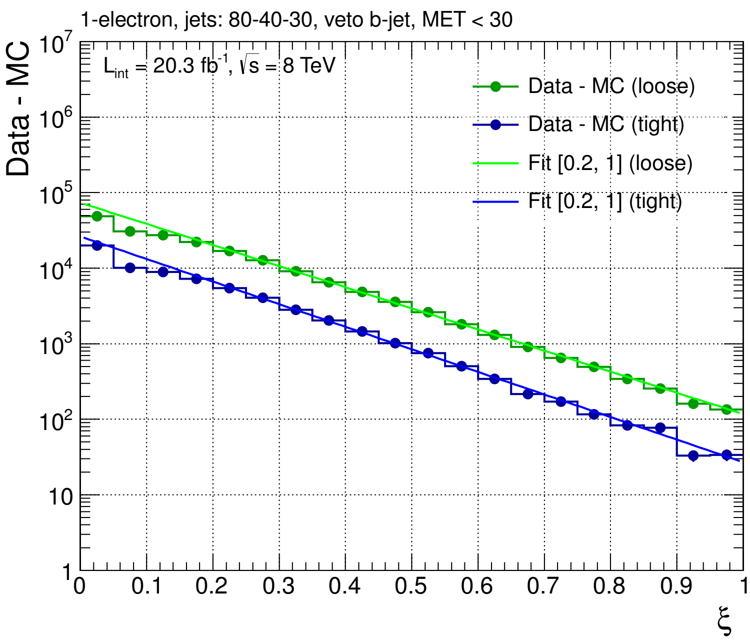

Figure 9.9: Distribution functions for the QCD estimate for loose and tight electrons, the $h_{\mathrm{QCD}}^{\mathrm{loose}}(\xi)$ and $h_{\mathrm{QCD}}^{\mathrm{tight}}(\xi)$, respectively, for preselected events with $E_{\mathrm{T}}^{\mathrm{miss}} < 30$ GeV. Both distributions are fitted with the corresponding exponential fit in the $[0.2, 1]$ interval.

fake electrons with $\xi < 0.1$) is estimated separately based on the $h_{\mathrm{QCD}}(\xi)$ and and the fitted exponential function as

$$N_{\text{QCD}} = \int_0^{0.1} h_{\text{QCD}}(\xi) d\xi \quad \text{and} \quad N_{\text{Fit}} = \int_0^{0.1} e^{-\alpha\xi+\beta} d\xi. \tag{9.14}$$

The statistical uncertainty is estimated for N_{Fit} and presented in the column "Stat.", while the systematic uncertainty is estimated as a relative difference $(N_{\text{QCD}} - N_{\text{Fit}})/N_{\text{Fit}}$ and presented in the column "Syst.". A negative systematic uncertainty indicate, that the exponential approach overestimates the $h_{\text{QCD}}(\xi)$, therefore it fulfils the validation. The multijet background for loose and tight electrons can be estimated as

$$h^{\text{loose}}_{\text{QCD}}(\xi) = h^{\text{loose}}_{\text{data}}(\xi) - h^{\text{loose}}_{\text{MC}}(\xi) \quad \text{and} \quad h^{\text{tight}}_{\text{QCD}}(\xi) = h^{\text{tight}}_{\text{data}}(\xi) - h^{\text{tight}}_{\text{MC}}(\xi). \tag{9.15}$$

The validation is performed for various selections on $E_{\text{T}}^{\text{miss}}$, m_{T} and $p_{\text{T}}(e)$ variables.

Validation for m_{T} bins

To further enrich region with multijet events an additional $E_{\text{T}}^{\text{miss}} < 30$ GeV selection is applied on top of the preselection requirements. Figure 9.10 shows the distribution of m_{T} for loose and tight electrons. No selection on the isolation variable is applied. The multijet Monte Carlo

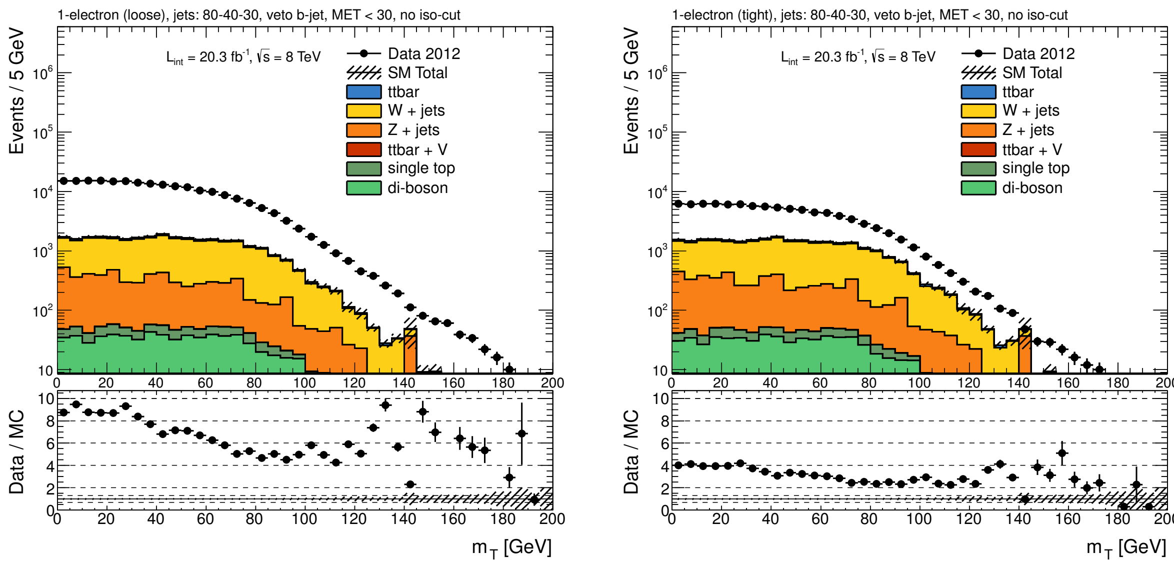

loose electrons, no isolation requirement | tight electrons, no isolation requirement

Figure 9.10: Distribution of m_{T} for loose (left) and tight (right) electrons. No selection on the isolation variable is applied. No QCD samples are included in the Monte Carlo.

samples are not included in the background processes. From the distributions one can see, that the contribution from non-multijet processes for loose electrons is about 10%, while for tight electrons it is about 25%.

Figure 9.11 shows the linearity validation of $h^{\text{loose}}_{\text{QCD}}(\xi)$ and $h^{\text{tight}}_{\text{QCD}}(\xi)$ for different m_{T} bins for the preselection region with an additional $E_{\text{T}}^{\text{miss}} < 30$ GeV requirement.

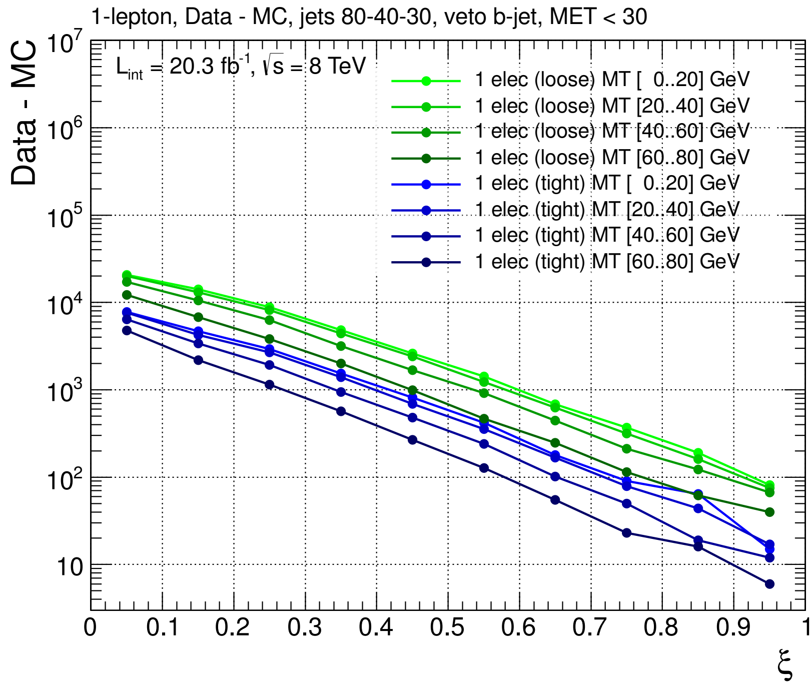

Figure 9.11: Distribution functions for the QCD estimate for loose and tight electrons, the $h_{\mathrm{QCD}}^{\mathrm{loose}}(\xi)$ and $h_{\mathrm{QCD}}^{\mathrm{tight}}(\xi)$, respectively, for preselected events with an additional $E_{\mathrm{T}}^{\mathrm{miss}} < 30$ GeV requirement. Distributions are shown for the following m_{T} bins: $[0, 20]$, $[20, 40]$, $[40, 60]$, $[60, 80]$ GeV.

The results of the fit of an exponential function $e^{-\alpha\xi+\beta}$ to the $h_{\mathrm{QCD}}^{\mathrm{loose}}(\xi)$ and $h_{\mathrm{QCD}}^{\mathrm{tight}}(\xi)$ for the region with preselection and $E_{\mathrm{T}}^{\mathrm{miss}} < 30$ GeV requirements are shown in Table 9.1.

	Loose electrons				Tight electrons			
m_{T} [GeV]	α	β	Stat.	Syst.	α	β	Stat.	Syst.
$[0, 20]$	6.3 ± 0.05	9.9 ± 0.02	2%	−54%	6.7 ± 0.09	9.0 ± 0.03	3%	−48%
$[20, 40]$	6.4 ± 0.05	9.9 ± 0.03	2%	−48%	6.8 ± 0.10	8.9 ± 0.04	3%	−40%
$[40, 60]$	6.6 ± 0.06	9.7 ± 0.02	2%	−35%	7.2 ± 0.12	8.6 ± 0.05	4%	−27%
$[60, 80]$	6.9 ± 0.08	9.3 ± 0.03	3%	−24%	7.4 ± 0.17	8.2 ± 0.06	5%	−8%

Table 9.1: Results of the fit of an exponential function $e^{-\alpha\xi+\beta}$ to the $h_{\mathrm{QCD}}^{\mathrm{loose}}(\xi)$ and $h_{\mathrm{QCD}}^{\mathrm{tight}}(\xi)$ in the $[0.2, 1.0]$ interval. The results are shown for preselected events with an additional $E_{\mathrm{T}}^{\mathrm{miss}} < 30$ GeV requirement, for the following m_{T} bins: $[0, 20]$, $[20, 40]$, $[40, 60]$, $[60, 80]$ GeV.

Figure 9.12 shows the linearity validation of $h_{\mathrm{QCD}}^{\mathrm{loose}}$ and $h_{\mathrm{QCD}}^{\mathrm{tight}}$ for different m_{T} bins for the preselection region with an additional 30 GeV $< E_{\mathrm{T}}^{\mathrm{miss}} < 60$ GeV requirement.

The results of the fit of an exponential function $e^{-\alpha\xi+\beta}$ to the $h_{\mathrm{QCD}}^{\mathrm{loose}}(\xi)$ and $h_{\mathrm{QCD}}^{\mathrm{tight}}(\xi)$ for the region with preselection and 30 GeV $< E_{\mathrm{T}}^{\mathrm{miss}} < 60$ GeV requirements are shown in Table 9.2.

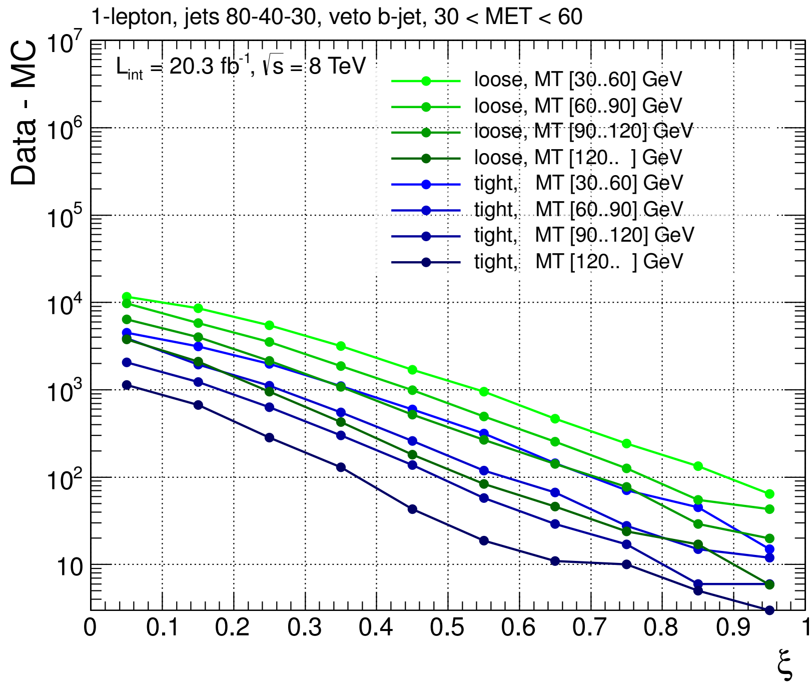

Figure 9.12: Distribution functions for the QCD estimate for loose and tight electrons, the $h_{\mathrm{QCD}}^{\mathrm{loose}}(\xi)$ and $h_{\mathrm{QCD}}^{\mathrm{tight}}(\xi)$, respectively, for preselection events with an additional 30 GeV $< E_{\mathrm{T}}^{\mathrm{miss}} <$ 60 GeV requirement. Distributions are shown for the following m_{T} bins: $[30, 60]$, $[60, 90]$, $[90, 120]$, $[120, \infty)$ GeV.

	Loose electrons				Tight electrons			
m_{T} [GeV]	α	β	Stat.	Syst.	α	β	Stat.	Syst.
$[30, 60]$	5.7 ± 0.04	10.0 ± 0.01	1%	−41%	5.9 ± 0.08	9.0 ± 0.02	2%	−36%
$[60, 90]$	6.2 ± 0.06	9.6 ± 0.02	2%	−18%	6.8 ± 0.11	8.6 ± 0.03	3%	−4%
$[90, 120]$	6.7 ± 0.08	9.3 ± 0.02	2%	−27%	7.3 ± 0.16	8.2 ± 0.04	4%	−29%
$[120, \infty)$	7.8 ± 0.13	8.8 ± 0.03	3%	−22%	8.2 ± 0.25	7.7 ± 0.06	5%	−34%

Table 9.2: Results of the fit of an exponential function $e^{-\alpha\xi+\beta}$ to the $h_{\mathrm{QCD}}^{\mathrm{loose}}(\xi)$ and $h_{\mathrm{QCD}}^{\mathrm{tight}}(\xi)$ in the $[0.2, 1.0]$ interval. The results are shown for preselected events with an additional 30 GeV $< E_{\mathrm{T}}^{\mathrm{miss}} <$ 60 GeV requirement, for the following m_{T} bins: $[30, 60]$, $[60, 90]$, $[90, 120]$, $[120, \infty)$ GeV.

Validation for $p_{\mathrm{T}}(e)$ bins

Figure 9.13 shows the $h_{\mathrm{QCD}}^{\mathrm{loose}}(\xi)$ and $h_{\mathrm{QCD}}^{\mathrm{tight}}(\xi)$ distribution functions for preselected events, with an additional $E_{\mathrm{T}}^{\mathrm{miss}} <$ 60 GeV requirement, for different $p_{\mathrm{T}}(e)$ bins: $[60, 100]$, $[100, 140]$, $[140, 180]$, $[180, 220]$ GeV. The corresponding fit results are shown in Table 9.3.

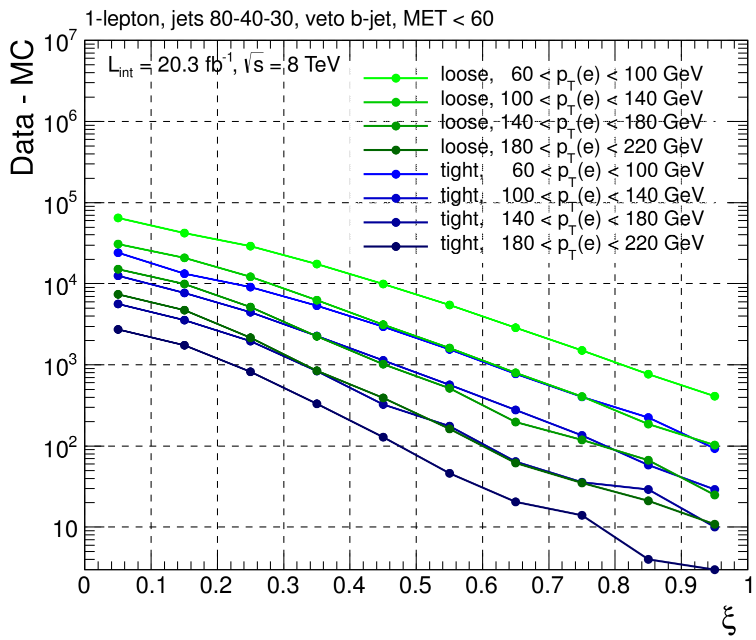

Figure 9.13: Distribution functions for the QCD estimate for loose and tight electrons, the $h^{\text{loose}}_{\text{QCD}}(\xi)$ and $h^{\text{tight}}_{\text{QCD}}(\xi)$, respectively, for preselection events with an additional $E_{\text{T}}^{\text{miss}} < 60$ GeV requirement. Distributions are shown for the following $p_{\text{T}}(e)$ bins: [60, 100], [100, 140], [140, 180], [180, 220] GeV.

	Loose electrons				Tight electrons			
$p_{\text{T}}(e)$ [GeV]	α	β	Stat.	Syst.	α	β	Stat.	Syst.
[60, 100]	5.3 ± 0.02	11.5 ± 0.01	1%	−22%	5.5 ± 0.03	10.4 ± 0.01	1%	−5%
[100, 140]	6.4 ± 0.03	10.9 ± 0.01	1%	−36%	6.6 ± 0.05	10.0 ± 0.02	1%	−26%
[140, 180]	7.5 ± 0.06	10.4 ± 0.02	1%	−46%	7.6 ± 0.09	9.4 ± 0.03	2%	−44%
[180, 220]	8.3 ± 0.09	9.7 ± 0.02	2%	−52%	8.5 ± 0.16	8.8 ± 0.04	3%	−58%

Table 9.3: Results of the fit of an exponential function $e^{-\alpha\xi+\beta}$ to the $h^{\text{loose}}_{\text{QCD}}(\xi)$ and $h^{\text{tight}}_{\text{QCD}}(\xi)$ in the [0.2, 1.0] interval. The results are shown for preselected events with an additional $E_{\text{T}}^{\text{miss}} < 60$ GeV requirement, for the following $p_{\text{T}}(e)$ bins: [60, 100], [100, 140], [140, 180], [180, 220] GeV.

Validation for high $E_{\text{T}}^{\text{miss}}$

All checks done so far, used multijet enriched regions with $E_{\text{T}}^{\text{miss}} < 60$ GeV. Checking in regions with high $E_{\text{T}}^{\text{miss}}$ are quite challenging. The following example validates the linearity for selection with high $E_{\text{T}}^{\text{miss}}$:

- Exactly one electron with $p_{\text{T}}(e) > 25$ GeV (no isolation requirement);
- At least two jets with $p_{\text{T}}(j_1) > 25$ GeV, $p_{\text{T}}(j_2) > 25$ GeV;
- 100 GeV $< E_{\text{T}}^{\text{miss}} <$ 140 GeV;
- $m_{\text{T}} > 360$ GeV.

The distributions of the m_T for loose and tight electrons without the isolation requirement is applied for the selection above without the m_T requirement are shown in Figure 9.14. One can see, that the $m_T > 360$ GeV region dominate by multijet events.

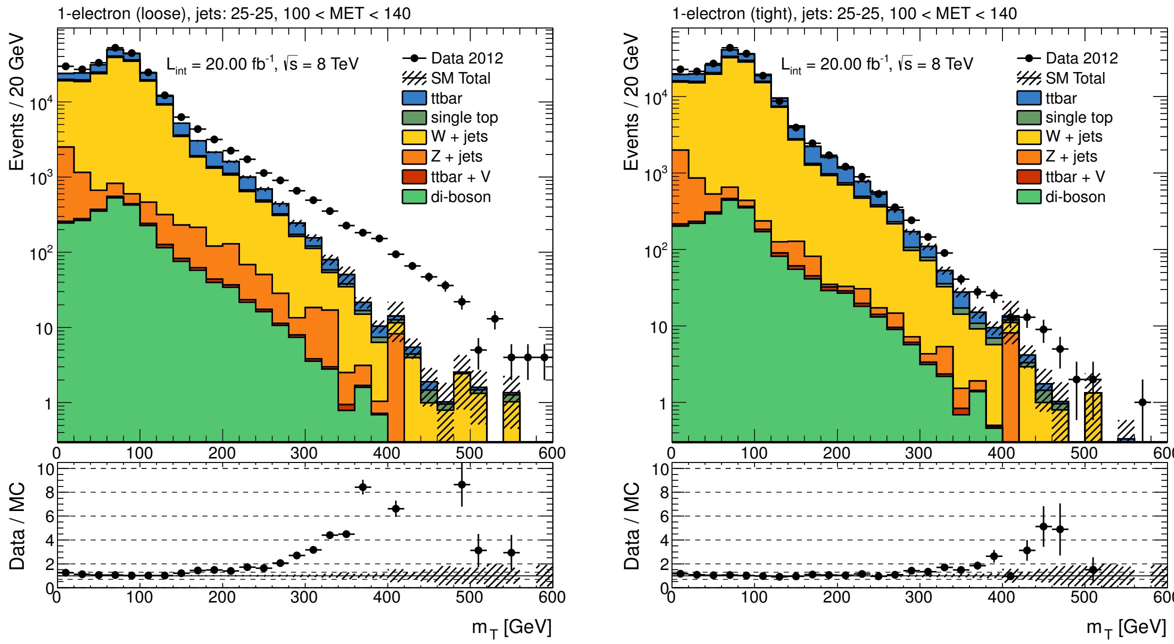

loose electrons, no isolation requirement

tight electrons, no isolation requirement

Figure 9.14: Distribution of m_T for loose (left) and tight (right) electrons. No selection on isolation variable ξ is applied.

The distributions of the isolation variable ξ for the data and QCD estimate for loose and tight electrons, and the ratio $h^{\text{tight}}_{\text{QCD}}(\xi)/h^{\text{loose}}_{\text{QCD}}(\xi)$ are shown in Figure 9.15. One can see, that in the signal region ($\xi < 0.1$) the exponential fit overestimates the QCD estimate.

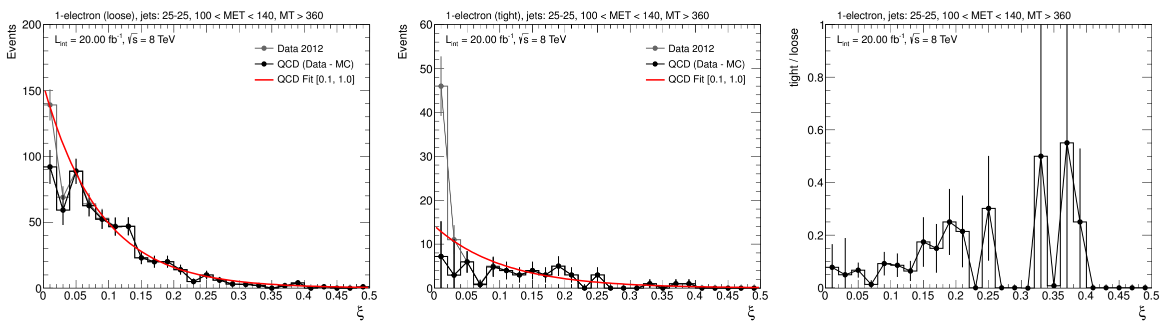

loose electrons

tight electrons

ratio

Figure 9.15: Distributions of the isolation variable ξ for the data and QCD estimate for loose (left) and tight (middle) electrons, and the ratio $h^{\text{tight}}_{\text{QCD}}(\xi)/h^{\text{loose}}_{\text{QCD}}(\xi)$ (right).

Linearity validation with Monte Carlo

The validation of the linearity assumption for the multijet background is done with PYTHIA8 dijet samples. The samples are generated for different slices depending on the transverse momentum of the $2 \to 2$ process, see Table 9.4.

Sample	JZ0	JZ1	JZ2	JZ3	JZ4	JZ5	JZ6	JZ7
p_T [GeV]	$[0, 20]$	$[20, 80]$	$[80, 200]$	$[200, 500]$	$[500, 1000]$	$[1000, 1500]$	$[1500, 2000]$	$[2000, \infty)$

Table 9.4: The p_T slices for dijet Monte Carlo samples.

Due to the high cross section of the dijet process for low p_T slices, the equivalent number of events per unit luminosity is very low. The requirement of one electron, significantly suppresses the multijet background, therefore no event from the first three slices JZ0-JZ2 passes even a loose selection. This makes it very difficult to properly estimate their contribution. A proper estimation introduces very high statistical uncertainties even if no event passes the selection from these slices. The number of multijet events has to be estimated using the Poisson distribution. If no event passes the selection, with 95% probability the estimation gives 5% of the generated event weight. Therefore the estimation of any value, for example $\varepsilon_{\text{fake}}$, becomes completely impossible.

One approach is to neglect the contribution from the low p_T slices and take into account only higher p_T slices to estimate properties for each slice separately. For the linearity validation, each slice is studied separately. This implicitly assumes that the results can be extrapolated to lower p_T slices. Figure 9.16 shows distributions of the isolation variable for loose (left) and tight (right) electrons for the following selection:

- Exactly one electron with $p_T(e) > 25$ GeV (no isolation requirement);
- At least two jets with $p_T(j_1) > 80$ GeV and $p_T(j_2) > 25$ GeV.

No events from JZ0 and JZ1 survive the selection. For both types of electrons the distribution near to $\xi = 0$ does not have any peak and can be estimated by an exponential function.

The plots in Figure 9.17 are showing the case where a selection on E_T^{miss} is applied:

- Exactly one electron with $p_T(e) > 25$ GeV (no isolation requirement);
- At least two jets with $p_T > 25$ GeV;
- $E_T^{\text{miss}} > 100$ GeV.

One can see, that for this selection, due to the low number of available Monte Carlo events, it is difficult to make any conclusion about the behaviour of the JZ3 sample. For the JZ4 validation shows that there is no peak near to zero.

The estimation of $\varepsilon_{\text{fake}}$ (tight to loose ratio) for the selections described above are shown in Figure 9.18. The left plot represents the selection without the E_T^{miss} requirement, while the right plot corresponds to the high E_T^{miss} selection. For the first selection the $\varepsilon_{\text{fake}}$ (tight to loose ratio) is below 0.2, while for region with high E_T^{miss} no conclusion can be made.

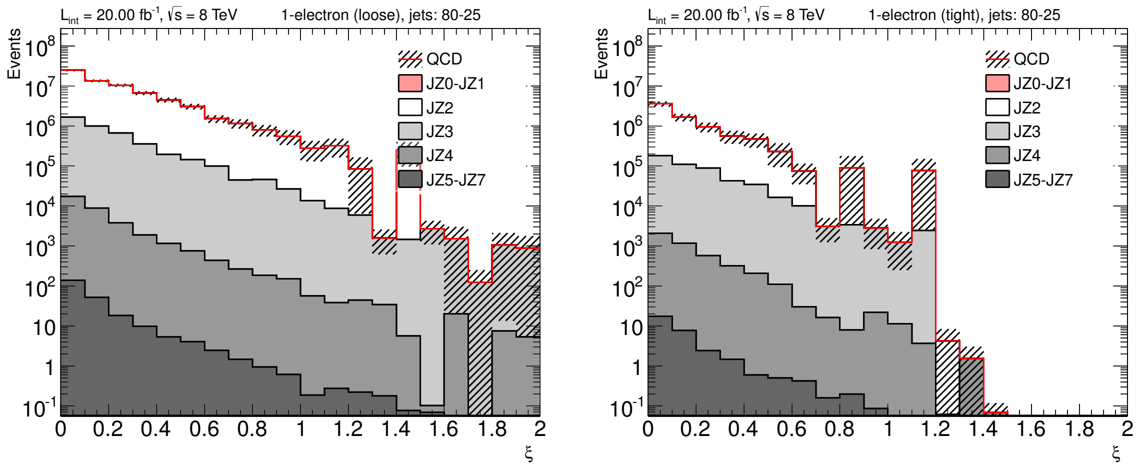

Figure 9.16: Distribution of the isolation variable ξ for dijet samples for loose (left) and tight (right) electrons. Selection: one electron with $p_{\mathrm{T}}(e) > 25$ GeV and at least two jets with $p_{\mathrm{T}}(j_{1,2}) > 80, 25$ GeV.

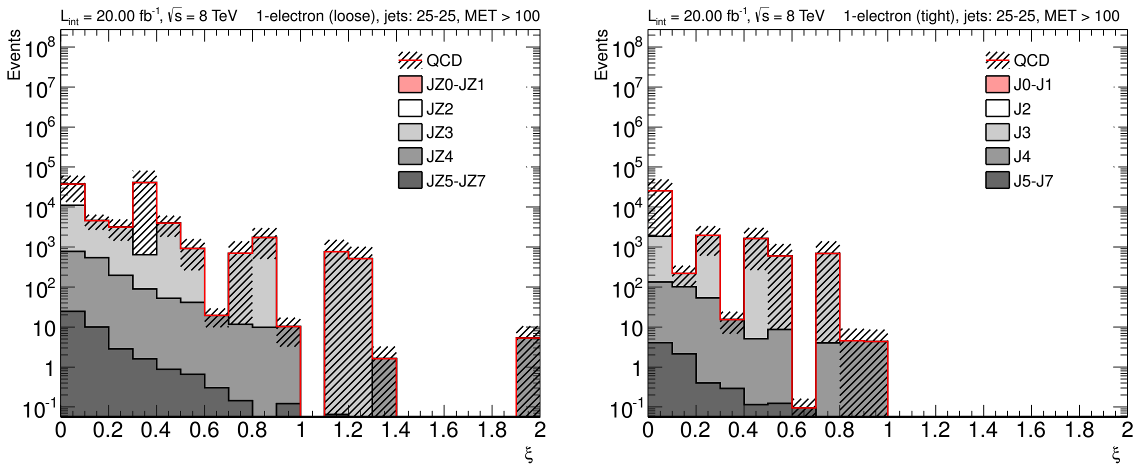

Figure 9.17: Distribution of the isolation variable ξ for dijet samples for loose (left) and tight (right) electrons. Selection: one electron with $p_{\mathrm{T}}(e) > 25$ GeV, at least two jets with $p_{\mathrm{T}}(j_{1,2}) > 80, 25$ GeV and $E_{\mathrm{T}}^{\mathrm{miss}} > 100$ GeV.

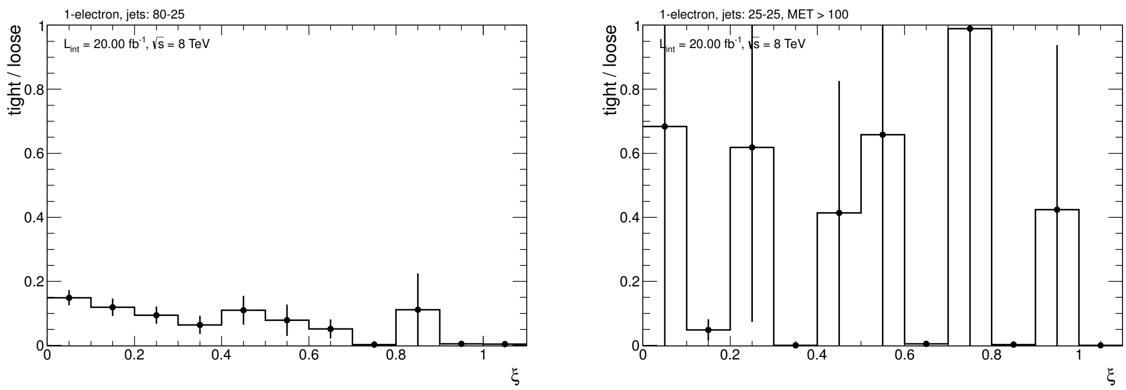

Figure 9.18: Distribution of the isolation variable ξ for multijet samples for one electron with $p_{\mathrm{T}}(e) > 25$ GeV and at least two jets with $p_{\mathrm{T}}(j_{1,2}) > 80, 25$ GeV (left) and for one electron with $p_{\mathrm{T}}(e) > 25$ GeV, at least two jets with $p_{\mathrm{T}}(j_{1,2}) > 25, 25$ GeV and $E_{\mathrm{T}}^{\mathrm{miss}} > 100$ GeV (right).

Linearity uncertainty

The uncertainty on the exponential extrapolation can be defined using the following approach. The isolation variable distribution $h(\xi)$ is fitted with an exponential function $e^{-\alpha\xi+\beta}$ in the fit region $[0.1, 0.4]$. The number of multijet events (fake electrons) in the signal region N_{sig} and the number of events estimated from an exponential extrapolation N_{exp} are defined as

$$N_{\text{sig}} = \int_0^{0.1} h(\xi)d\xi \qquad \text{and} \qquad N_{\text{exp}} = \int_0^{0.1} e^{-\alpha\xi+\beta}(\xi)d\xi. \tag{9.16}$$

A systematic uncertainty is estimated as $(N_{\text{sig}} - N_{\text{exp}})/N_{\text{exp}}$. An uncertainty on the exponential extrapolation $\sigma_{N_{\text{exp}}}$ includes α and β uncertainties. The uncertainties are estimated for different multijet slices for events passing the following selection:

- Exactly one electron with $p_{\text{T}}(e) > 25$ GeV (no isolation requirement);
- At least three jets with $p_{\text{T}}(j_{1,2,3}) > 80, 40, 30$ GeV;
- $E_{\text{T}}^{\text{miss}} > 20$ GeV.

The distributions of the isolation variable ξ for different multijet slices are shown in Figure 9.19, and the corresponding results are shown in Table 9.5. The results show that for the JZ3-JZ5 slices the exponential approach overestimates N_{sig}. The total contribution from JZ6 and JZ7 is negligible (less than one event) and can be neglected.

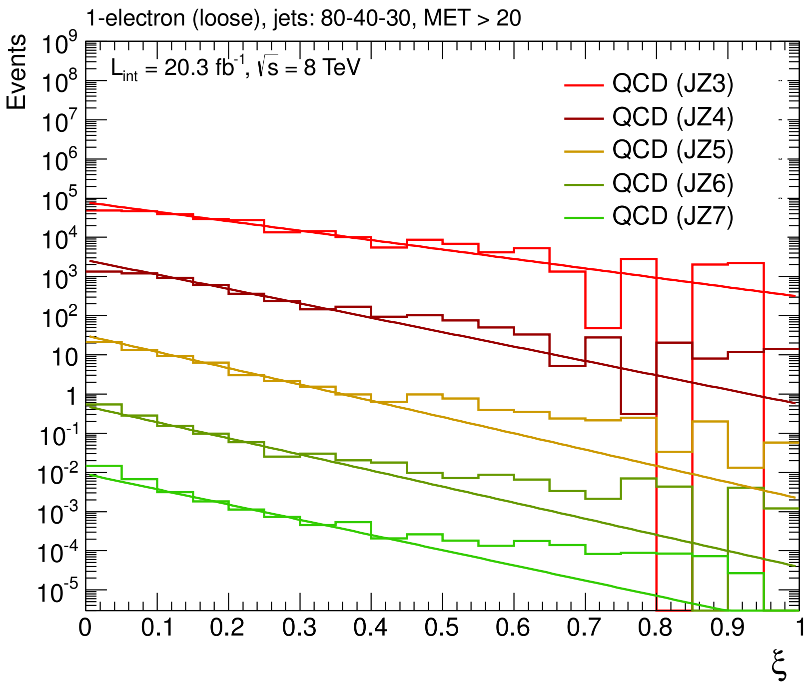

Figure 9.19: Distributions of the isolation variable ξ for different multijet slices JZ3-JZ7. Selection: one electron with $p_{\text{T}}(e) > 25$ GeV, at least three jets with $p_{\text{T}}(j_{1,2,3}) > 80, 40, 30$ GeV and $E_{\text{T}}^{\text{miss}} > 20$ GeV.

Sample	α	β	$\sigma_{N_{exp}}$	Syst.
QCD JZ3	5.5 ± 1.0	11.2 ± 0.2	20%	−21%
QCD JZ4	8.4 ± 0.7	7.8 ± 0.1	11%	−28%
QCD JZ5	9.6 ± 0.6	3.4 ± 0.1	10%	−13%
QCD JZ6	9.4 ± 0.7	-7.1 ± 0.1	11%	29%
QCD JZ7	8.9 ± 0.7	-4.7 ± 0.2	12%	79%

Table 9.5: Fit results for different dijet slices JZ3-JZ7. Selection: one electron with $p_{\mathrm{T}}(e) > 25$ GeV, at least three jets with $p_{\mathrm{T}}(j_{1,2,3}) > 80, 40, 30$ GeV and $E_{\mathrm{T}}^{\mathrm{miss}} > 20$ GeV.

Validation with $W \to \mu\nu, \tau\nu$ samples

Another possible check of linearity can be done with the $W \to \mu\nu$ and $W \to \tau\nu$ samples. The comparison is performed on the QCD JZ4-JZ6 slices and W+jets samples for the $W \to \mu\nu$ decay, where only fake electrons are expected. A comparison is done for the following event selection region, which targets the SR-bC signal selection:

– Exactly one electron with $p_{\mathrm{T}}(e) > 25$ GeV (no isolation requirement);

– At least three jets with $p_{\mathrm{T}}(j_{1,2,3}) > 80, 40, 30$ GeV;

– $E_{\mathrm{T}}^{\mathrm{miss}} > 110$ GeV.

The validation is shown in Figure 9.20, and the corresponding results are given in Table 9.6.

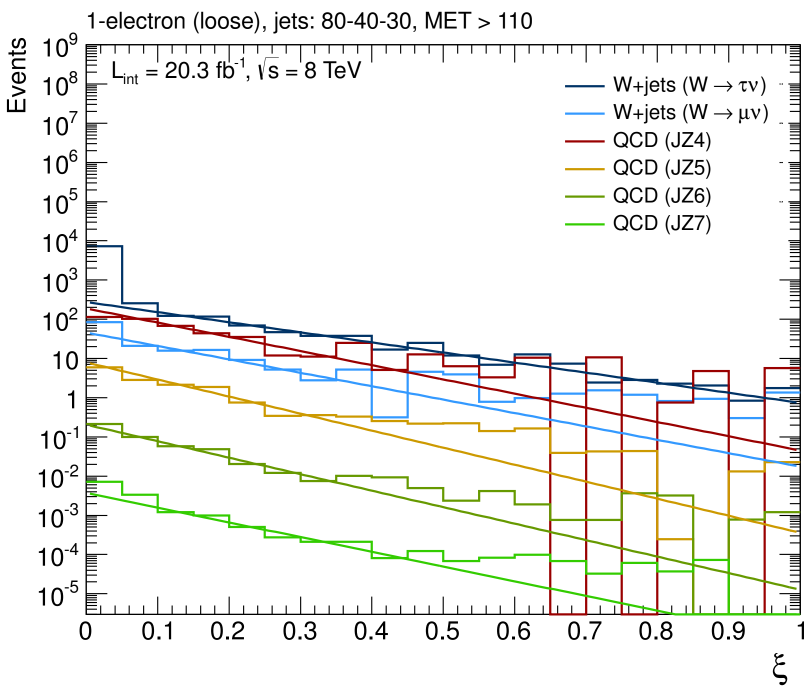

Figure 9.20: Validation with the $W \to \mu\nu$ and $W \to \tau\nu$ processes and with different dijet slices JZ4-JZ7. Selection: one electron with $p_{\mathrm{T}}(e) > 25$ GeV, at least three jets with $p_{\mathrm{T}}(j_{1,2,3}) > 80, 40, 30$ GeV and $E_{\mathrm{T}}^{\mathrm{miss}} > 110$ GeV.

Sample	α	β	$\sigma_{N_{\text{exp}}}$	Syst.
$W \to \tau\nu$	5.9 ± 1.0	5.6 ± 0.2	16%	1725%
$W \to \mu\nu$	7.9 ± 1.8	3.8 ± 0.4	33%	65%
QCD JZ4	8.3 ± 2.7	5.2 ± 0.6	44%	−15%
QCD JZ5	10.0 ± 1.3	2.1 ± 0.3	20%	−12%
QCD JZ6	9.7 ± 1.0	1.6 ± 0.2	16%	19%
QCD JZ7	8.6 ± 1.0	-5.6 ± 0.2	17%	111%

Table 9.6: Fit results for the $W \to \mu\nu$ and $W \to \tau\nu$ processes and for different dijet slices JZ4-JZ7. Selection: one electron with $p_{\text{T}}(e) > 25$ GeV, at least three jets with $p_{\text{T}}(j_{1,2,3}) > 80, 40, 30$ GeV and $E_{\text{T}}^{\text{miss}} > 110$ GeV.

The slopes from the $W \to \mu\nu$ and $W \to \tau\nu$ decays for $\xi > 0.1$ are similar to the multijet slices JZ4-JZ6. The peak in the first bin for W samples does not exist for the multijet slices.

Isolated electrons

Electrons produced from the W-boson decay on the generator level are referred to as *isolated electrons*. The proposed Exponential Extrapolation approach assumes that a contamination of isolated electrons for $\xi > 0.1$ region is negligible. As an example, distributions of the isolation variable ξ for isolated electrons for the WCR-bC and TCR-bC control regions of the bC diagonal analysis (see Section 6.5.1) are shown in Figure 9.21. The distributions confirm, that for the $\xi > 0.1$ region the contamination of isolated electrons is negligible.

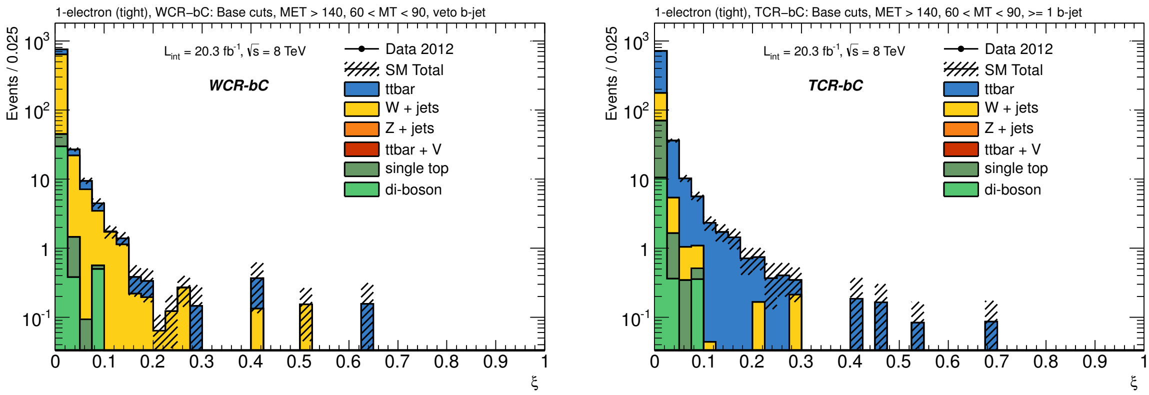

Figure 9.21: Distributions of the isolation variable ξ for tight isolated electrons for the WCR-bC (b-jet veto, left) and TCR-bC (at least 1 b-jet, right) control regions of the bC analysis. The distributions confirm, that for the $\xi > 0.1$ region the contamination of isolated electrons is negligible.

Summary

Validation studies show that for all verified regions, an exponential fit overestimates the distribution of the isolation parameter ξ for fake electrons. The overestimation may vary depending on the selections applied. Therefore, the exponential fit can be used to prove, that the contribution from the fake electron background is negligible. For a more precise estimation of $h_{\mathrm{QCD}}(\xi)$ further studies are needed.

The contribution of isolated electrons in the region $\xi > 0.1$ is negligible. For all considered examples, this contribution as a function of the isolation parameter ξ is rapidly decreasing with a very steep slope, which is much bigger than the α slope for the distribution of fake electrons for $\xi > 0.1$. Therefore, the contamination of the fit region with isolated electrons can only increase the fake electrons estimate. Due to this, uncertainties related to the contamination of the fit region with real electrons, can be safely neglected.

A systematic uncertainty of the combined fit approach, related to use of the same slope α for the loose and tight electron distributions can reach up to 10%. To state a lower uncertainty, the corresponding study has to be performed separately for each region.

As a cross-check between the exponential extrapolation approach and the matrix method, one can compare the fake electrons estimation for the bC and tN analyses, see Sections 6.5.2 and 8.9.2. The cross-check shows that the results are consistent.

9.3 Estimation of fake muons

An estimation of fake muons background based on a slightly modified Exponential Extrapolation approach.

9.3.1 Exponential Extrapolation

In the following it is assumed that an *isolation variable* ξ for muons is defined as $p_{\mathrm{T}}^{\mathrm{cone}\,0.2}$. The *signal muons* are defined to be isolated with $\xi < 1.8$ GeV. The distribution of the isolation variable ξ, which is referred to in the following as $h(\xi)$, can be splitted in two part, for real and fake muons $h(\xi) = h_{\mathrm{real}}(\xi) + h_{\mathrm{fake}}(\xi)$.

Two definitions of muons are used. A *loose muon* is defined as a signal muon without the isolation requirement and with the relaxed overlap removal requirement $\Delta R(\mu, \mathrm{jet})$ from 0.4 to 0.2, see Section 6.2.2. A *tight muon* is defined as a signal muons without the isolation requirement. In the following, the distribution of the isolation variable ξ for loose and tight muons is denoted as $h^{\mathrm{loose}}(\xi)$ and $h^{\mathrm{tight}}(\xi)$, respectively.

The difference between these distributions $h^{\mathrm{diff}}(\xi) = h^{\mathrm{loose}}(\xi) - h^{\mathrm{tight}}(\xi)$ can be defined as the distribution of the isolation variable ξ for loose muons which do not pass the tight criteria. In the following these muons are referred to as *loose-not-tight muons*. The equivalent definition for the loose-not-tight muon is a loose muons with the $0.2 < \Delta R(\mu, \mathrm{jet}) < 0.4$ requirement.

As an example, in this section the following preselection region is considered:

- Exactly one muon with $p_{\mathrm{T}}(\mu) > 25$ GeV (no isolation requirement);
- At least three jets with $p_{\mathrm{T}}(j_{1,2,3}) > 40, 25, 25$ GeV;
- Exactly one b-tagged jet;
- $E_{\mathrm{T}}^{\mathrm{miss}} > 80$ GeV.

The selection uses a missing transverse momentum trigger with 80 GeV requirement on the trigger level without any isolation requirement. This trigger is fully efficient (efficiency is above 99%) for offline-reconstructed $E_{\mathrm{T}}^{\mathrm{miss}}$ values above 150 GeV. In order to correct the trigger inefficiencies below 150 GeV, the corresponding correction factors are applied.

In the following all distributions are shown for data taken at $\sqrt{s} = 8$ TeV and corresponding to an integrated luminosity of $\mathcal{L}_{\mathrm{int}} = 20.3\ \mathrm{fb}^{-1}$.

Figure 9.22 shows the distributions of the isolation variable ζ for the loose, tight and loose-not-tight muons, which are denoted as $h^{\mathrm{loose}}(\xi)$, $h^{\mathrm{tight}}(\xi)$ and $h^{\mathrm{diff}}(\xi)$, respectively. The distributions are shown for data for the preselection region. It is assumed, that $h^{\mathrm{diff}}(\xi)$ is dominated by fake and non-prompt muons produced within jets.

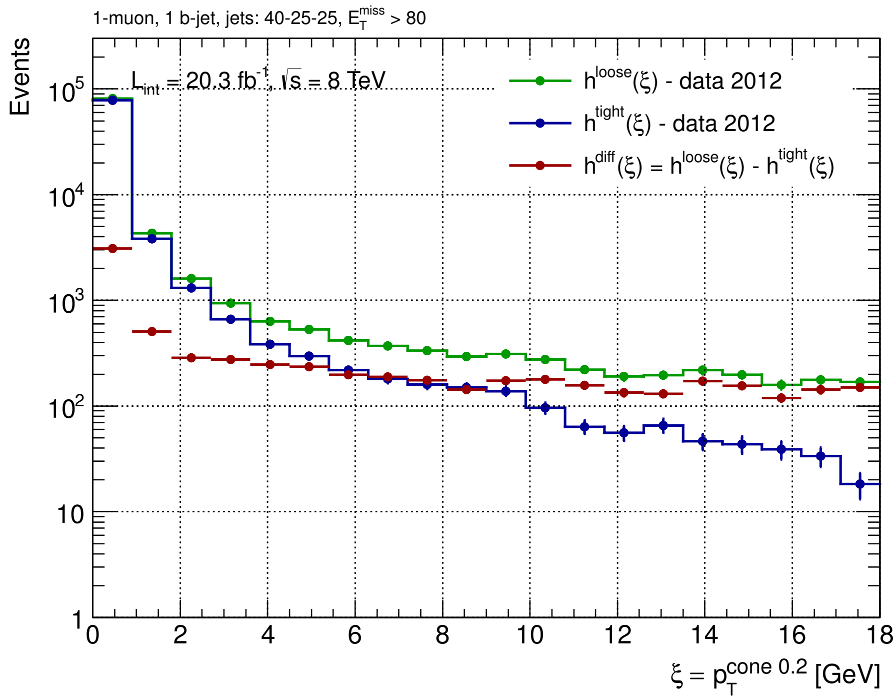

Figure 9.22: Distributions of the isolation variable ξ for loose, tight and loose-not-tight muons for data for the preselection region, are denoted as the $h^{\mathrm{loose}}(\xi)$, $h^{\mathrm{tight}}(\xi)$ and $h^{\mathrm{diff}}(\xi)$, respectively.

One can see that for the isolation variable ξ an exponential extrapolation approach as used for the electrons is not applicable. The problem is caused by two properties:

- The $h^{\mathrm{loose}}(\xi)$ and $h^{\mathrm{tight}}(\xi)$ distribution functions have different slopes, which means that either this region is not dominated by fake muons, or the ratio of tight-to-loose muons depends on the isolation variable ξ;
- The $h^{\mathrm{diff}}(\xi)$ distribution function, which is assumed to be composed dominantly by fake muons, cannot be estimated by an exponential function.

Therefore, to apply an exponential approach, a different variable, which has an exponential behaviour for fake muons has to be found.

The fake muons produced within jets have a higher track activity in the $0.2 < \Delta R < 0.4$ region around the muon. Therefore, for a fake muon estimation, a $\zeta = p_T^{\text{cone}\,0.4} - p_T^{\text{cone}\,0.2}$ variable is considered. It was found, that the ζ variable has an exponential distribution in regions dominated by fake muons. An additional advantage is that the ζ and ξ variables are statistically independent.

Distributions of the ζ variable for loose and signal muons, denoted as $h^{\text{loose}}(\zeta)$ and $h^{\text{signal}}(\zeta)$, respectively, are presented in Figure 9.23. The signal muons are tight muons with $\xi < 1.8$ GeV.

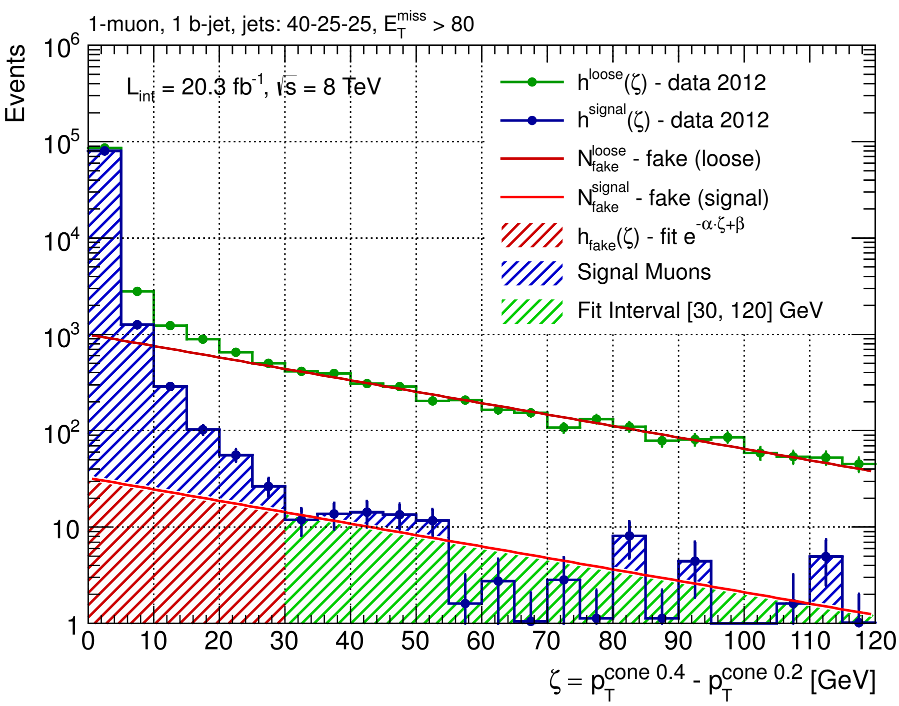

Figure 9.23: Distributions of the variable ζ for loose and signal muons for the preselection region for data, denoted as the $h^{\text{loose}}(\zeta)$ and $h^{\text{signal}}(\zeta)$, respectively.

For the fake muons background estimation, the following assumptions are used:

- The slopes in the $[30, 120]$ GeV region for the $h^{\text{loose}}(\zeta)$ and $h^{\text{signal}}(\zeta)$ distribution functions are considered similar;
- The distribution of the variable ζ for fake muons, whith a good approximation can be estimated by an exponential function.

The lower enge of the $[30, 120]$ GeV interval is selected to suppress the contribution of the real muons in the region. The slope α is estimated for loose muons by fitting the exponential function $e^{-\alpha\zeta+\beta'}$ to the $h^{\text{loose}}(\zeta)$. For signal muons the $h^{\text{signal}}(\zeta)$ distribution function is fitted by the $e^{-\alpha\zeta+\beta}$ function, where α parameter is fixed.

The number of fake muons is estimated as

$$N_{\text{fake}}^{\text{signal}} = \int_0^\infty e^{-\alpha\zeta+\beta} d\zeta. \tag{9.17}$$

In general, one can also cut out the region $\zeta > 30$ GeV from the signal muons definition, since it is dominated by fakes.

9.3.2 Validation

Two validations are performed for the preselection region mentioned above. The first is a linearity validation, which checks to what extent the distribution of the ζ for fake muons can be approximated by an exponential function. Another is a slope validation, which tests the assumption, that the slope α estimated for the distribution of the ζ for loose muons, is applicable for the tight muons.

Linearity validation

Figure 9.24 shows the distributions of the variable ζ for loose, tight and loose-not-tight muons, the $h^{\text{loose}}(\zeta)$, $h^{\text{tight}}(\zeta)$ and $h^{\text{diff}}(\zeta) = h^{\text{loose}}(\zeta) - h^{\text{tight}}(\zeta)$, respectively. An exponential function $e^{-\alpha\zeta+\beta}$ (red line) is fitted to the $h^{\text{loose}}(\zeta)$ distribution function in the $[30, 120]$ GeV region.

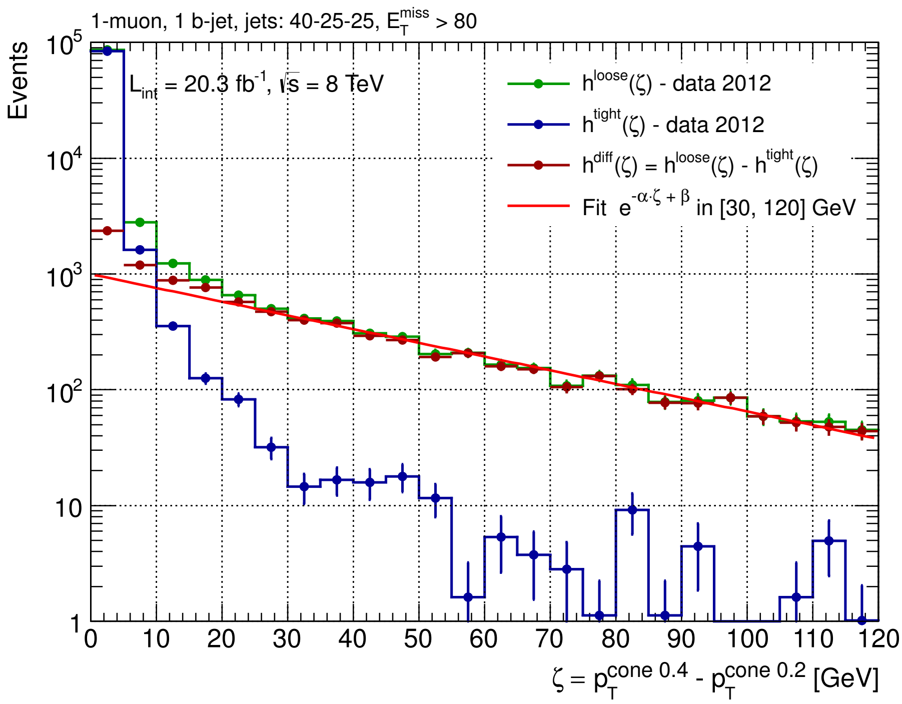

Figure 9.24: Distributions of the variable ζ for loose, tight and loose-not-tight muons, referred to as the $h^{\text{loose}}(\zeta)$, $h^{\text{tight}}(\zeta)$ and $h^{\text{diff}}(\zeta)$, respectively, are shown for the preselection region. An exponential function $e^{-\alpha\zeta+\beta}$ (red line) is fitted to the $h^{\text{loose}}(\zeta)$ distribution function in the $[30, 120]$ GeV region.

The results of the fit are:

$$\alpha = 0.027 \pm 0.001, \quad \beta = 6.90 \pm 0.03. \tag{9.18}$$

One can see that an exponential function with a good approximation describes the difference

$h^{\text{diff}}(\zeta)$ with the exception of the two lowermost bins. These bins have some excess caused by a real muon contribution, as outlined in the following.

To study exponentiality of a fake muons distribution, one has to suppress a contribution from real muons. This is done by inverting the requirement on the isolation variable ξ. Figure 9.25 shows the distributions of the variable ζ for loose, tight and loose-not-tight muons for the inverted isolation requirement $\xi > 1.8$ GeV. One can see, that the peak in the two lowermost bins significantly decreased. An exponential function $e^{-\alpha\zeta+\beta}$ is fitted to the $h^{\text{diff}}(\zeta)$ in the $[30, 120]$ GeV interval.

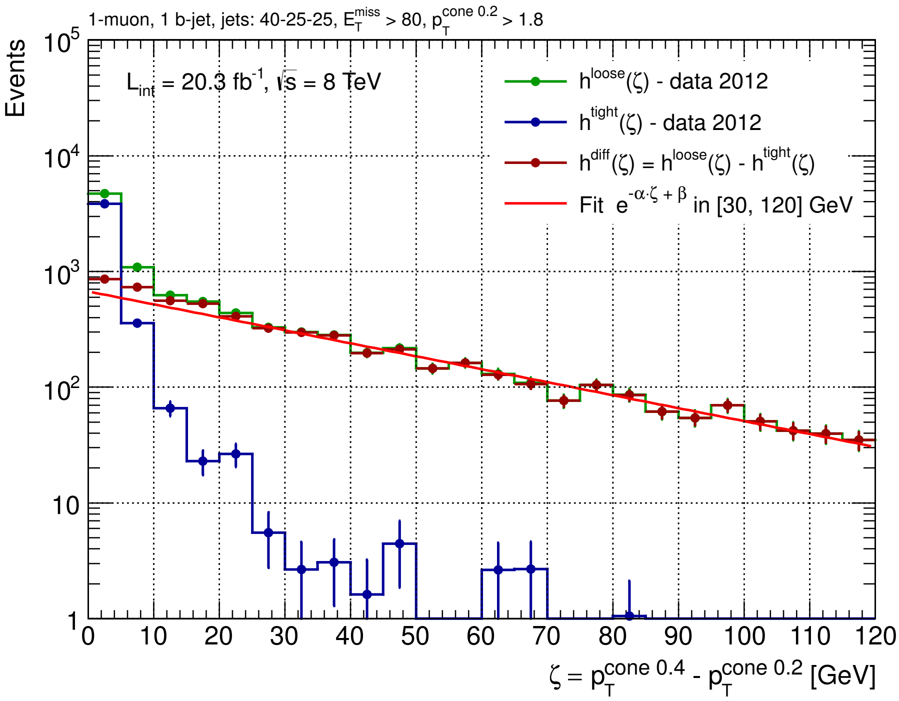

Figure 9.25: Distributions of the variable ζ for preselected events with an inverted isolation requirement $\xi > 1.8$ GeV for loose, tight and loose-not-tight muons, referred to as the $h^{\text{loose}}(\zeta)$, $h^{\text{tight}}(\zeta)$ and $h^{\text{diff}}(\zeta)$, respectively. An exponential function $e^{-\alpha\zeta+\beta}$ (red line) is fitted to the $h^{\text{loose}}(\zeta)$ distribution function in the $[30, 120]$ GeV region.

The results of the fit are:

$$\alpha = 0.026 \pm 0.001, \qquad \beta = 6.51 \pm 0.04. \tag{9.19}$$

The estimate of the slope α is consistent with the fit result without any isolation requirements. Under the assumption, that the $h^{\text{diff}}(\zeta)$ distribution function does not distorted by real muons, one can estimate the uncertainty on this approach as a relative difference between the number of fake muons N_{diff} and N_{fake}, estimated for the $h^{\text{diff}}(\zeta)$ and fitted exponential function, respectively.

The numbers are estimated as:

$$N_{\text{diff}} = \int_0^\infty h^{\text{diff}}(\zeta)d\zeta \qquad \text{and} \qquad N_{\text{fake}} = \int_0^\infty e^{-\alpha\zeta+\beta}d\zeta. \tag{9.20}$$

The systematic uncertainty is estimated as

$$\text{Syst} = \frac{N_{\text{diff}} - N_{\text{fake}}}{N_{\text{fake}}}. \tag{9.21}$$

For the current case, this uncertainty is estimated as about of $\pm 7\%$.

A contamination of signal muons in a fit region leads to an overestimation of a number of fake muons, therefore no additional systematic uncertainty is assigned to the choice of the fit interval.

Validation of the slope

The next step is to validate the assumption, that the α slope estimated for loose muons is applicable to the tight muons distribution.

Figure 9.26 shows the distribution of the variable ζ for loose muons with different $\Delta R(\mu, \text{jet})$ overlap removal requirements, referred to as $h^{\Delta R}(\zeta)$. The $\Delta R > 0.2$ requirement corresponds to the $h^{\text{loose}}(\zeta)$, while the case $\Delta R > 0.4$ represents the $h^{\text{tight}}(\zeta)$. Additionally, two intermediate distributions for $\Delta R = 0.28$ and $\Delta R = 0.35$ are also shown.

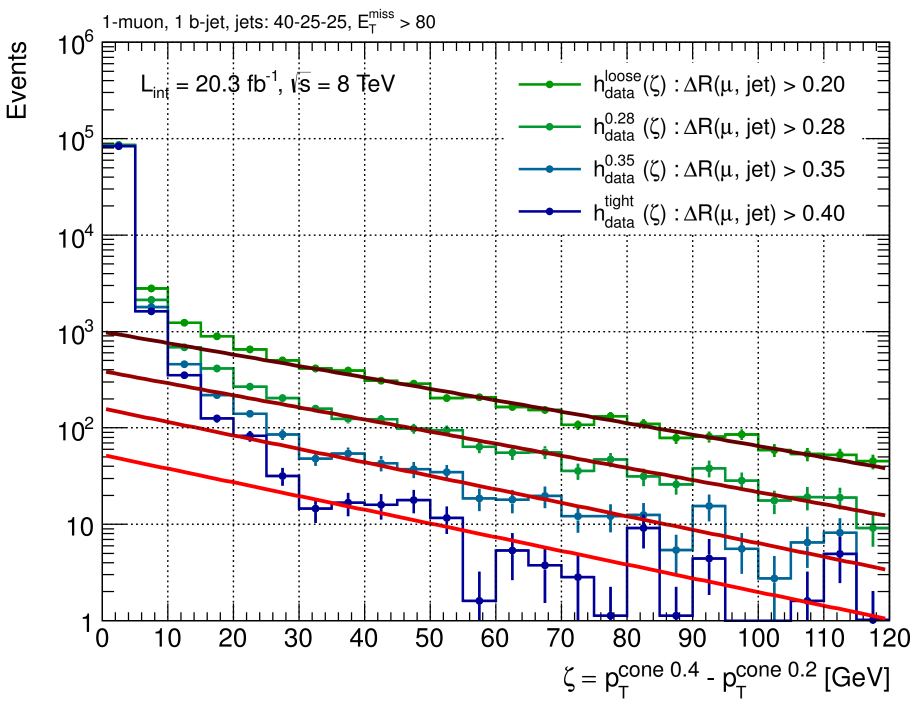

Figure 9.26: Distributions of the variable ζ for loose muons for preselected events with different $\Delta R(\mu, \text{jet})$ overlap removal requirements. The $h^{\text{loose}}(\zeta)$ and $h^{\text{tight}}(\zeta)$ distribution functions correspond to the $\Delta R = 0.2$ and $\Delta R = 0.4$, respectively. For each distribution, an exponential function $e^{-\alpha\zeta+\beta}$ is fitted in the $[30, 120]$ GeV interval.

The results for the exponential fit in the $[30, 120]$ GeV interval are shown in Table 9.7. One can see, that the α slope is increasing as a function of ΔR, which might be due to a relative increase of a real muon contamination in the $[30, 120]$ GeV fit region.

Distribution	$\Delta R(\mu, \text{jet})$	α	β
$h^{\text{loose}}_{\text{data}}(\zeta)$	> 0.20	0.027 ± 0.001	6.90 ± 0.04
$h^{0.28}_{\text{data}}(\zeta)$	> 0.28	0.029 ± 0.001	5.96 ± 0.06
$h^{0.35}_{\text{data}}(\zeta)$	> 0.35	0.032 ± 0.002	5.07 ± 0.12
$h^{\text{tight}}_{\text{data}}(\zeta)$	> 0.40	0.033 ± 0.004	3.96 ± 0.22

Table 9.7: Fit results for distributions presented in Figure 9.26. For each distribution an exponential function $e^{-\alpha\zeta+\beta}$ is fitted in the $[30, 120]$ GeV interval.

The slopes α for different ΔR are consistent within 1.5σ of the statistical uncertainty. From the difference between the α for loose and tight distributions a systematic uncertainty can be estimated as about $\pm 20\%$.

Summary

The validation of the current example shows, that one can expect the uncertainty related to the difference between the α slope estimate for the loose and tight muon distributions to be about $\pm 20\%$. The approximation of the distribution for loose muons by an exponential function (linearity validation) has an uncertainty of $\pm 7\%$. It is assumed, that the same uncertainty is applicable to the distribution of tight muons.

In general, for each analysis, the estimate of these two uncertainties has to be performed for each region individually.

9.4 Conclusions

The exponential extrapolation approach can be used to estimate the fake lepton background in the one-lepton analyses. Some features and advantages of the approach are highlighted:

– ***Fully data driven approach***
  There is no need to estimate $\varepsilon_{\text{real}}$ and $\varepsilon_{\text{fake}}$ from the multijet samples, which usually do not have enough amount of events, especially after tight analysis requirements.

– ***The same event topology***
  For the exponential extrapolation approach the estimation of fake leptons is based on events with signal, tight and loose leptons (electrons or muons) which have the same event topology (selection requirement related to the kinematics of objects). The selection differs only in ξ for electrons, and in ξ and ζ for muons.

  This is not the case for the matrix method approach used in the one-lepton analysis [3], where the $\varepsilon_{\text{real}}$ and $\varepsilon_{\text{fake}}$ coefficients are estimated for regions with a different topology.

- ***Estimate only with tight leptons***
  In case of a sufficient number of events in the fit region, the contribution of fake leptons can be estimated based only on tight leptons, i.e. the proposed approach does not need loose leptons at all.

- ***Statistical independence***
  The fake electrons estimate uses events from the *fake* region ($\xi > 0.1$), which are statistically uncorrelated with events from the *signal* region ($\xi < 0.1$).

  For the estimate of fake muons, loose muons with $\zeta > 30$ GeV are used. The overlap with signal muons is negligible, therefore events are almost statistically uncorrelated. Additionally, one can use only signal muons with $\zeta < 30$ GeV to make the estimate statistically uncorrelated.

- ***Accuracy of the estimate***
  The estimation of fake electrons for the bC and tN analyses shows that the results for the exponential extrapolation approach and the matrix method are consistent within the statistical uncertainties (see Sections 6.5.2 and 8.9.2).

  The precision of the matrix method depends on the number of events in the signal region, since this number is involved in the fake leptons estimation, see equation 9.2. The exponential extrapolation approach does use the signal region. Therefore, the accuracy of the approach is independent of the amount of events in the signal region.

In addition, a difference between the estimation approach for the exponential extrapolation and the Matrix Method can be used for a cross-check.

CHAPTER 10

Summary and Outlook

During the Run-1 data taking period, the LHC delivered proton-proton collision data corresponding to an integrated luminosity of about 5 fb^{-1} at $\sqrt{s} = 7$ TeV and 23 fb^{-1} at $\sqrt{s} = 8$ TeV for physics analysis.

The last missing particle predicted by the Standard Model, the Higgs boson, was discovered by both the ATLAS and CMS experiments, with a mass of about 125 GeV. After this discovery there are no other predictions from the Standard Model, which may hint in the direction of new physics.

Independently from the big success of the Standard Model, it is not the ultimate theory. The dark matter problem motivates searches for heavy weakly interacting particles which are predicted in many physics scenarios beyond the Standard Model. Supersymmetry, if it is found, may provide a solution to this problem, as well as to the hierarchy problem. Wide searches for supersymmetry are performed in the ATLAS and CMS experiments, among which searches for the top squark are important ones.

If supersymmetry is expected to solve the hierarchy problem, new particles should be found in the 1 TeV mass range. In this context, it is important to cover all regions, where a light top squark could be found.

The searches for a light top squark in the $\tilde{t}_1 \to b\tilde{\chi}_1^{\pm} \to bW^{\pm(*)}\tilde{\chi}_1^0$ decay mode were performed on data recorded at $\sqrt{s} = 7$ TeV with an integrated luminosity of 4.7 fb^{-1}. The developed analysis shows a better sensitivity to the compressed scenario for $\Delta m(\tilde{t}_1, \tilde{\chi}_1^{\pm}) \approx 20$ GeV with respect to published ATLAS SUSY analyses. This analysis was re-optimised and performed on $\sqrt{s} = 8$ TeV data.

The presented one-lepton analysis for the $\tilde{t}_1 \to b\tilde{\chi}_1^{\pm} \to bW^{\pm(*)}\tilde{\chi}_1^0$ decay mode was developed for the compressed scenario $\Delta m(\tilde{t}_1, \tilde{\chi}_1^{\pm}) \approx m(b)$ and was performed based on data corresponding to an integrated luminosity of 20.3 fb^{-1} recorded at $\sqrt{s} = 8$ TeV. The analysis is published as part of the ATLAS SUSY searches for top-squark pair production in final states with one lepton, jets and missing transverse momentum [3]. This analysis covers top-squark masses for the diagonal region from 125 GeV to 350 GeV.

The key difference of this analysis from other one-lepton analyses is the change of the dominant background. Instead of attempts to increase the sensitivity for the compressed scenario, while keeping the $t\bar{t}$ process as the dominant background, in the analysis events with b-tagged jets are vetoed. This allows to significantly suppress the $t\bar{t}$ background, but makes the $W+$jets background the dominant one. In this case the main challenge is to suppress $W+$jets events, which, however, have less kinematical properties that can be exploited. The suppression of the $W+$jets background in the analysis is based on the existence of a hard ISR/FSR jet and on signal model related kinematical properties. This analysis is the only SUSY analysis of the ATLAS Collaboration covering the low top-squark mass diagonal region from 125 GeV to 175 GeV.

The one-lepton analysis developed in this thesis for the $\tilde{t}_1 \to t\tilde{\chi}_1^0$ decay mode targets the very challenging compressed scenario $\Delta m(\tilde{t}, \tilde{\chi}_1^0) \approx m(t)$. This diagonal region stayed uncovered by the SUSY searches of the ATLAS and CMS experiments at $\sqrt{s} = 8$ TeV data. The only progress made in this area by the ATLAS experiment relies on analyses based on measurements of the top-quark production cross section [121] and spin correlation [122], from which limits of 177 GeV and 191 GeV have been determined, respectively.

The presented analysis is based on an integrated luminosity of 20.3 fb^{-1} of data recorded at $\sqrt{s} = 8$ TeV and covers on- and off-shell decays of the $\tilde{t}_1 \to t\tilde{\chi}_1^0$ decay mode for the compressed scenario for top-squark masses in the 200 GeV to 300 GeV interval. A gap from 190 GeV to 200 GeV remains uncovered. Nevertheless, the analysis has a significant reach for higher top-squark masses, which was not reachable by any other ATLAS and CMS analysis so far. For top-squark masses above 300 GeV the exclusion is mainly limited by the statistical uncertainty on the number of expected events. Therefore, for a higher luminosity or with an increased centre-of-mass energy, the presented analysis can increase the exclusion limits.

The strategy and new kinematic variables developed for this compressed scenario can also be applied for searches of top-squark pair production for fully hadronic and dileptonic final states.

The increase of the LHC centre-of-mass energy to $\sqrt{s} = 13$ TeV significantly increases the signal cross section for large top-squark masses. Even with an integrated luminosity of 3 fb^{-1} results may be comparable with the one based on data recorded at $\sqrt{s} = 8$ TeV.

It is important to mention, that searches in the region with low top-squark masses (below 250 GeV) are not strongly affected. In this mass range, the relative gain between the signal and the $t\bar{t}$ production cross sections is small. Therefore, the exclusion limits are mainly driven by the amount of the integrated luminosity. Since during this year it is expected to collect an integrated luminosity of about 20 fb^{-1} of data at $\sqrt{s} = 13$ TeV, the analyses based on the $\sqrt{s} = 8$ TeV data will still play an important role for this region of phase space.

The LHC has started data taking at a centre-of-mass energy of $\sqrt{s} = 13$ TeV. The data that are planned to be collected during the next few years, will be sufficient to discover or exclude top squarks with masses up to about 1 TeV. Therefore, these years will be crucial for searches for Supersymmetry, at least, for models motivated by the hierarchy problem.

Appendix

APPENDIX A

Background reweighting

In some analyses a mismodelling of a multijet distribution (N_{jets}) is observed. One can attempt to fix this disagreement by applying reweighting coefficients evaluated from a control region. This approach may introduce even more mismodelling in a signal region. The following selection represents an example, where fixing the slope of the multijet distribution for a control region introduces an opposite slope for a signal region.

To decrease the multijet (QCD) contamination in this example only the muon channel is considered. To avoid a distortion of distributions due to a possible b-tagging scale factors mismodelling, no b-jet requirement is applied.

For this example, the following selection is used:

- Exactly one muon with $p_{\text{T}}(\mu) > 25$ GeV;
- At least three jets with $p_{\text{T}}(j_{1,2,3}) > 80, 40, 30$ GeV, others with $p_{\text{T}} > 25$ GeV;
- $E_{\text{T}}^{\text{miss}} > 120$ GeV;
- $m_{\text{T}} > 120$ GeV;
- $H_{\text{T}} > 300$ GeV – Control Region (CR);
- $E_{\text{T}}^{\text{miss}}/\sqrt{H_{\text{T}}} > 7.0\ \sqrt{\text{GeV}}$ – Signal Region (SR).

The jet multiplicity (N_{jets}) and $E_{\text{T}}^{\text{miss}}/\sqrt{H_{\text{T}}}$ distributions for the CR are shown in Figure A.1, left and right plots, respectively. Using the CR one can introduce a bin-by-bin reweighting for the jet multiplicity N_{jets}, see Table A.1. In this example, the same reweighting is applied for both $t\bar{t}$ and $W+$jets production.

N_{jets}	3	4	5	6	7	8	9	10
Weight	1.01	0.93	0.83	0.79	0.79	0.85	0.54	0.65

Table A.1: Reweighting coefficients for jet multiplicity N_{jets} estimated for the CR.

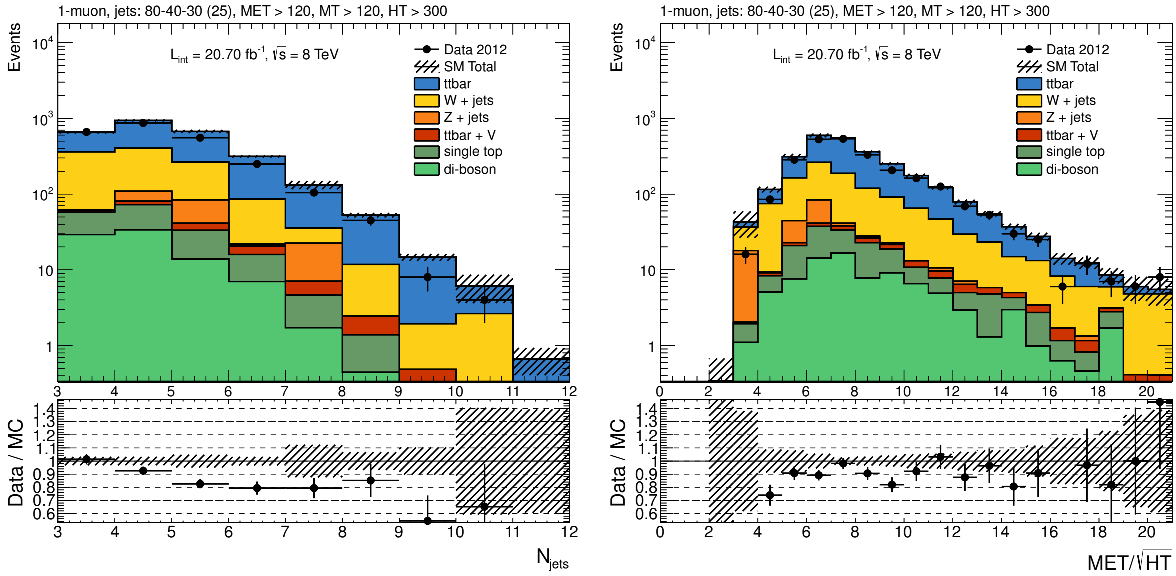

Figure A.1: Distributions of the jet multiplicity (left) and $E_{\mathrm{T}}^{\mathrm{miss}}/\sqrt{H_{\mathrm{T}}}$ (right) for the CR.

Figure A.2 shows the jet multiplicity distributions for signal region SR, before any reweighting is applied and after the jet multiplicity reweighting.

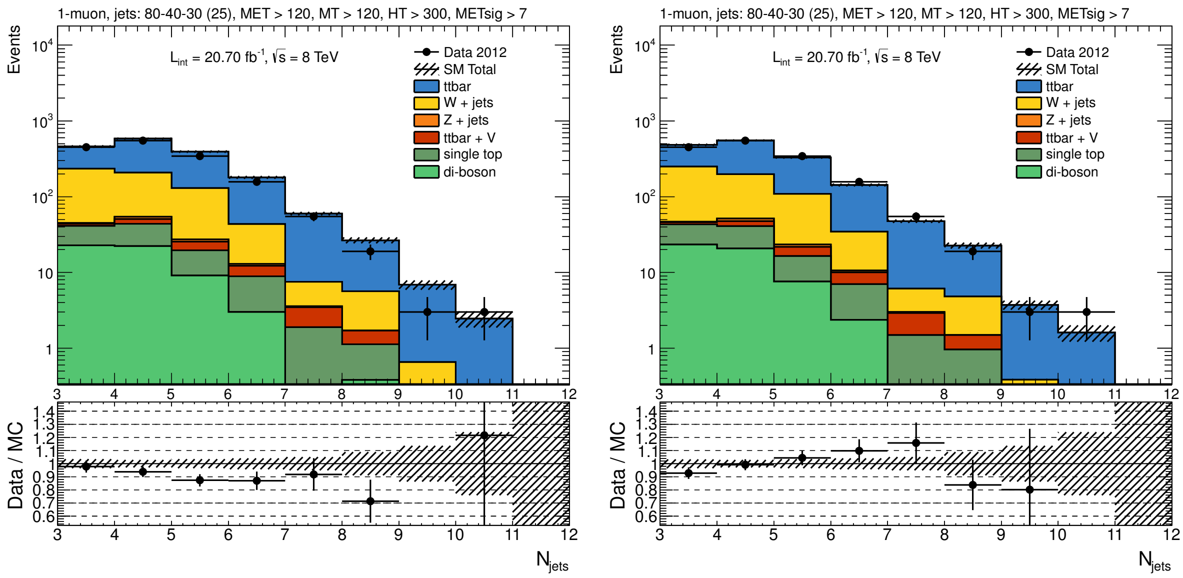

Figure A.2: Distributions of the jet multiplicity before (left) and after (right) reweighting for the SR.

One can see, that after the reweighting in the CR the jet multiplicity distribution (right plot) has an opposite slope in the signal region SR, while the same distribution without any reweighting (left plot) still have mismodelling, but within 10%. Hence, for this analysis a jet multiplicity based reweighting is considered unacceptable.

APPENDIX B

Data-MC comparison for $\tilde{t}_1 \rightarrow b\tilde{\chi}_1^{\pm}$ analysis

In this section a comparison between the data and Monte Carlo is presented for the bC diagonal analysis at $\sqrt{s} = 8$ TeV. The Monte Carlo samples do not include multijet events. Error bounds for all plots presents only the Monte Carlo statistical uncertainty. The normalisation factors for the $t\bar{t}$ and $W+$jets productions are applied according to the results of the background-only fit.

Figures B.1 – B.7 shows data vs Monte Carlo comparison for control and verification regions of the bC diagonal analysis. Distributions for the following kinematic variable are shown:

- Distributions of the jet multiplicity (N_{jet}) for the $t\bar{t}$ and $W+$jets regions and number of b-tagged jets ($N_{b\text{-jet}}$) for the $t\bar{t}$ regions for jets with $p_{\text{T}} > 25$ GeV requirement, are shown in Figure B.1.
- Distributions of the p_{T} of the leading jet ($p_{\text{T}}(j_1)$), sub-leading jet ($p_{\text{T}}(j_2)$) and lepton ($p_{\text{T}}(\ell)$) are shown for the $W+$jets and $t\bar{t}$ regions in Figures B.2 and B.3, respectively.
- Distributions of the $E_{\text{T}}^{\text{miss}}$, m_{T} and H_{T} are shown for $W+$jets and $t\bar{t}$ regions in Figures B.4 and B.5, respectively.
- Distributions of the $\Delta\phi(j_1, p_{\text{T}}^{\text{miss}})$ between the leading jet and $p_{\text{T}}^{\text{miss}}$, the $\Delta R(j_1, \ell)$ between the jeading jet and lepton and absolute value of the lepton pseudorapidity $|\eta(\ell)|$ are shown for $W+$jets and $t\bar{t}$ regions in Figures B.6 and B.7, respectively.

The $(180, 174, 87)$, $(250, 240, 120)$ and $(350, 340, 170)$ signal models for the $(\tilde{t}_1, \tilde{\chi}_1^{\pm}, \tilde{\chi}_1^0)$ mass plane are shown for comparison. The masses of $\tilde{t}_1$, $\tilde{\chi}_1^{\pm}$ and $\tilde{\chi}_1^0$ are given in GeV.

As one can see, for WCR-bC and TCR-bC control regions (especially for TCR-bC) some distributions have a slope, which is not a case for verification regions WVR-bC and TVR-bC. Distributions in verification regions are consistent with data within systematical uncertainties.

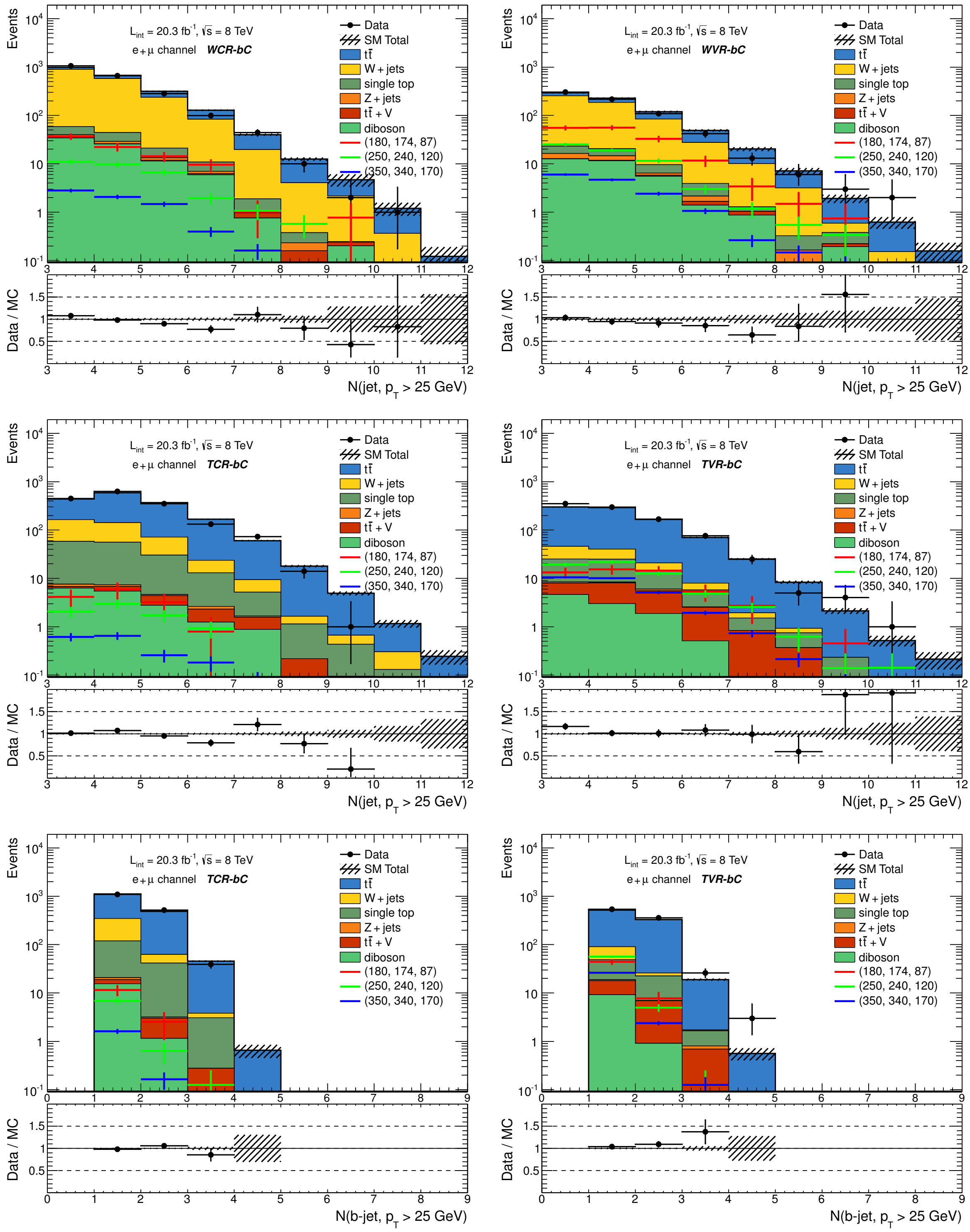

Figure B.1: Distribution of the number of selected jets (N_{jet}) for the WCR-bC (top left), WVR-bC (top right), TCR-bC (middle left), and TVR-bC (middle right). The distribution of the number of b-tagged jets ($N_{b\text{-jet}}$) for the TCR-bC (bottom left) and TVR-bC (bottom right). The error bars on data and data/MC ratio points represent the 68% confidence interval.

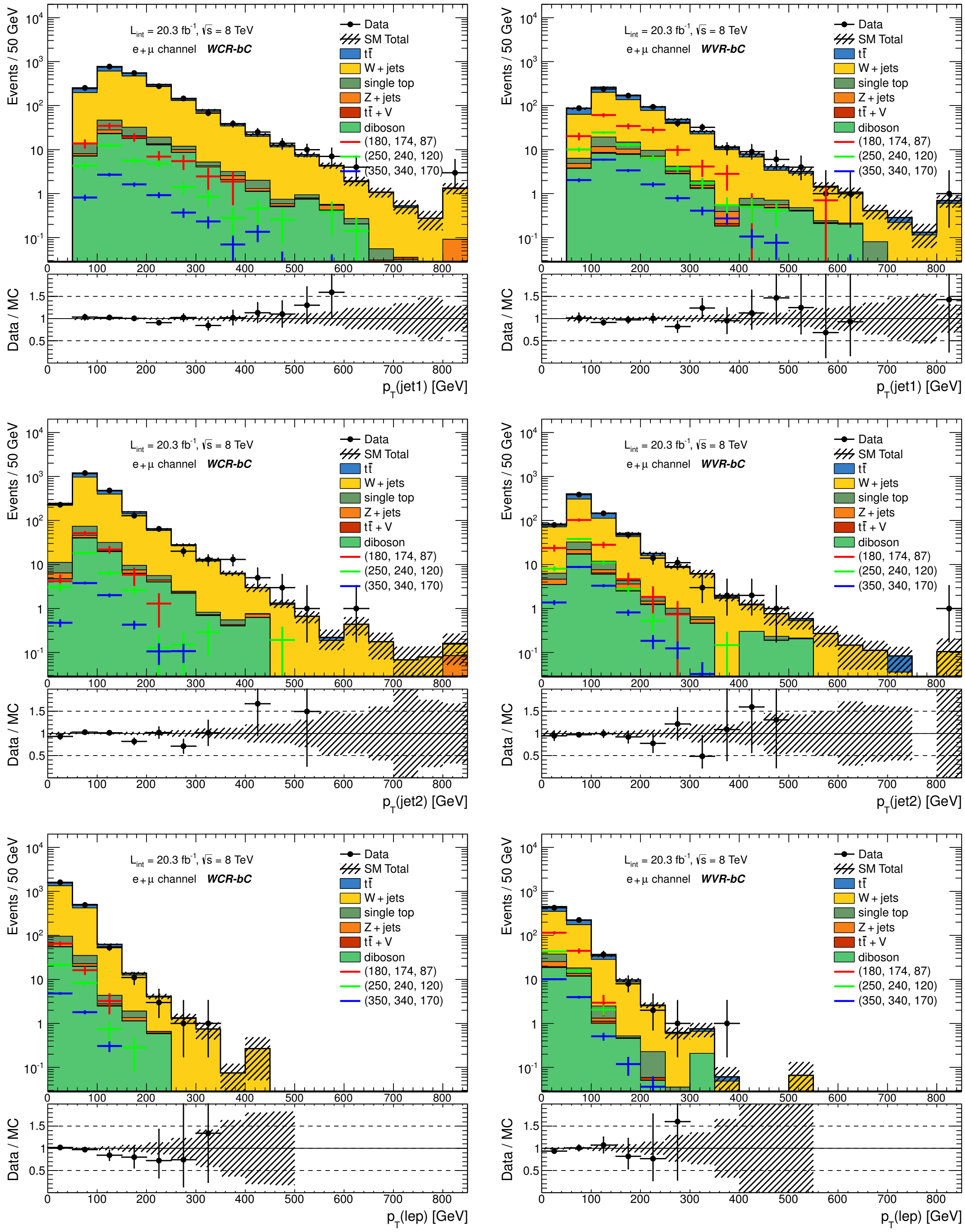

Figure B.2: Distributions of the leading jet p_T (top), sub-leading jet p_T (middle), and lepton p_T (bottom) for the WCR-bC (left) and WVR-bC (right). The error bars on data and data/MC ratio points represent the 68% confidence interval.

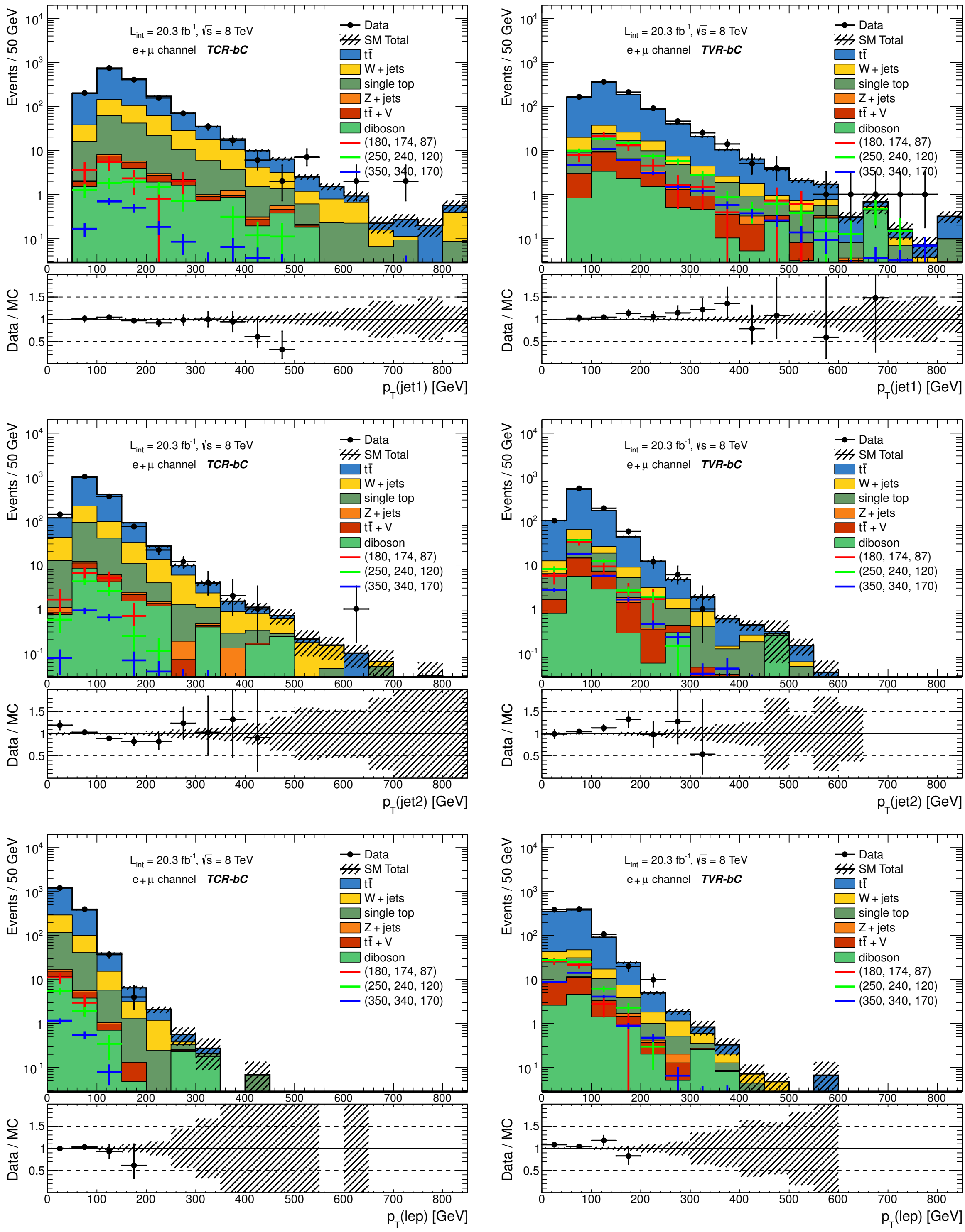

Figure B.3: Distributions of the leading jet p_{T} (top), sub-leading jet p_{T} (middle), and lepton p_{T} (bottom) for the TCR-bC (left) and TVR-bC (right). The error bars on data and data/MC ratio points represent the 68% confidence interval.

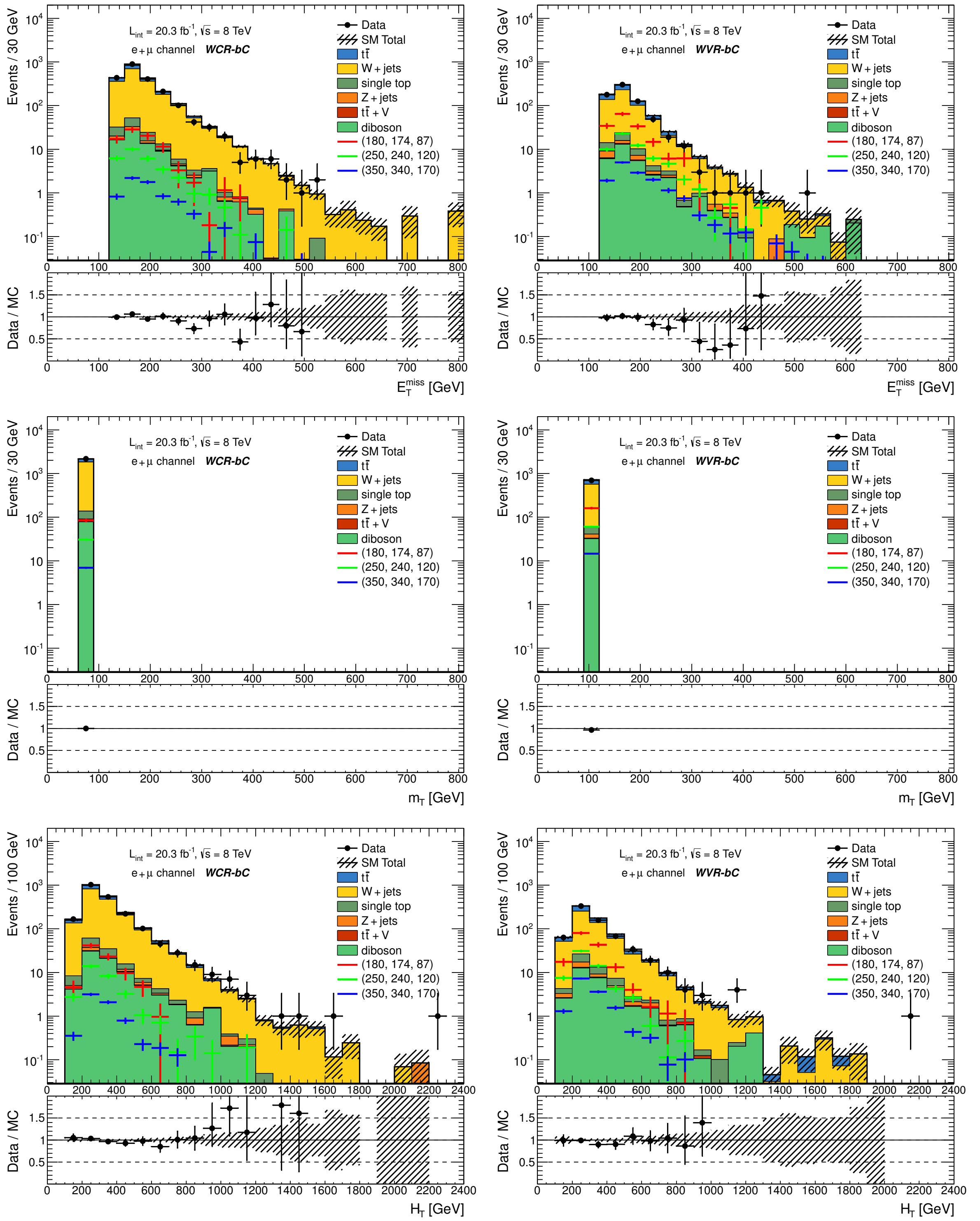

Figure B.4: Distributions of the $E_{\mathrm{T}}^{\mathrm{miss}}$ (top), m_{T} (middle), and H_{T} (bottom) for the WCR-bC (left) and WVR-bC (right). The error bars on data and data/MC ratio points represent the 68% confidence interval.

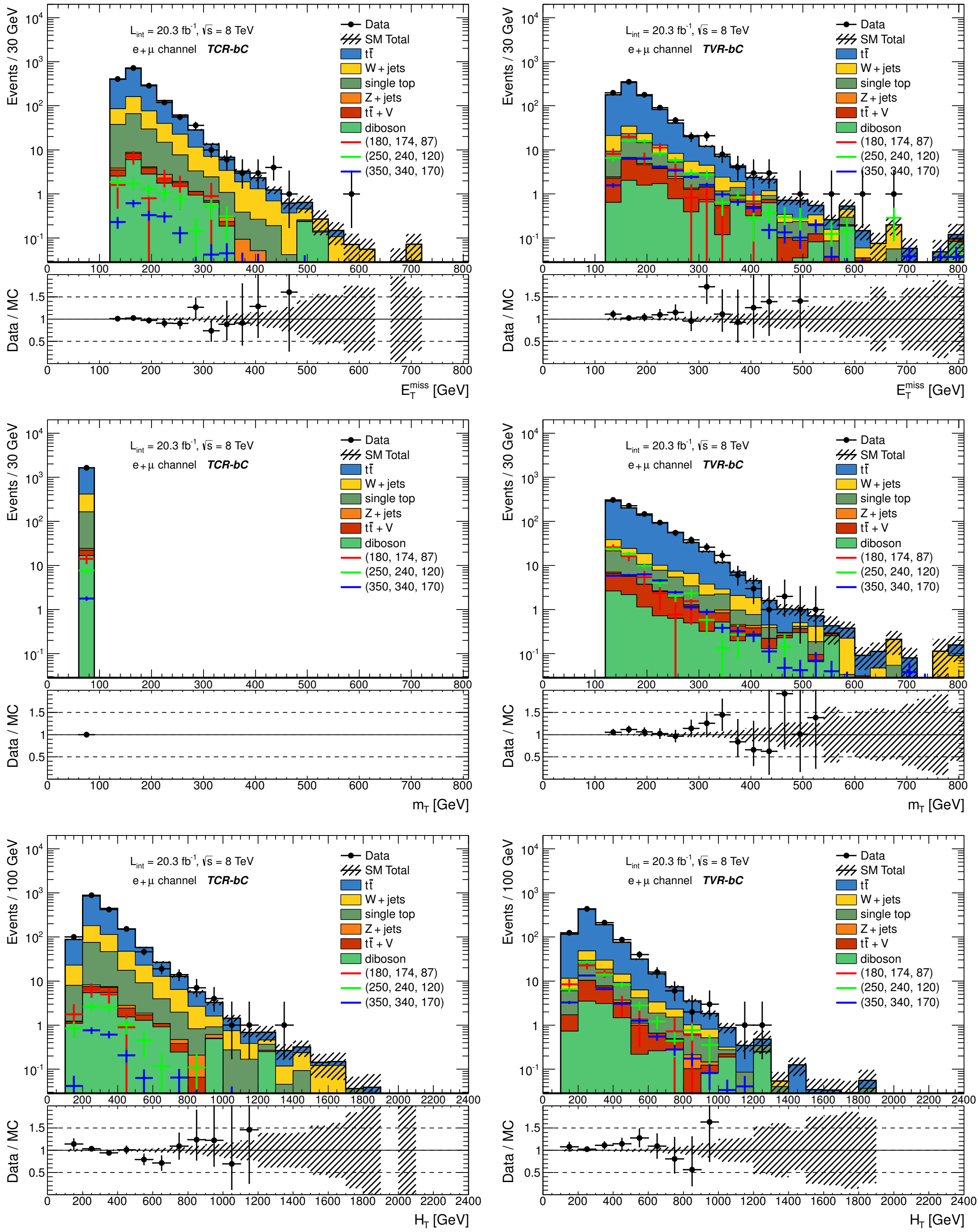

Figure B.5: Distributions of the $E_{\mathrm{T}}^{\mathrm{miss}}$ (top), m_{T} (middle), and H_{T} (bottom) for the TCR-bC (left) and TVR-bC (right). The error bars on data and data/MC ratio points represent the 68% confidence interval.

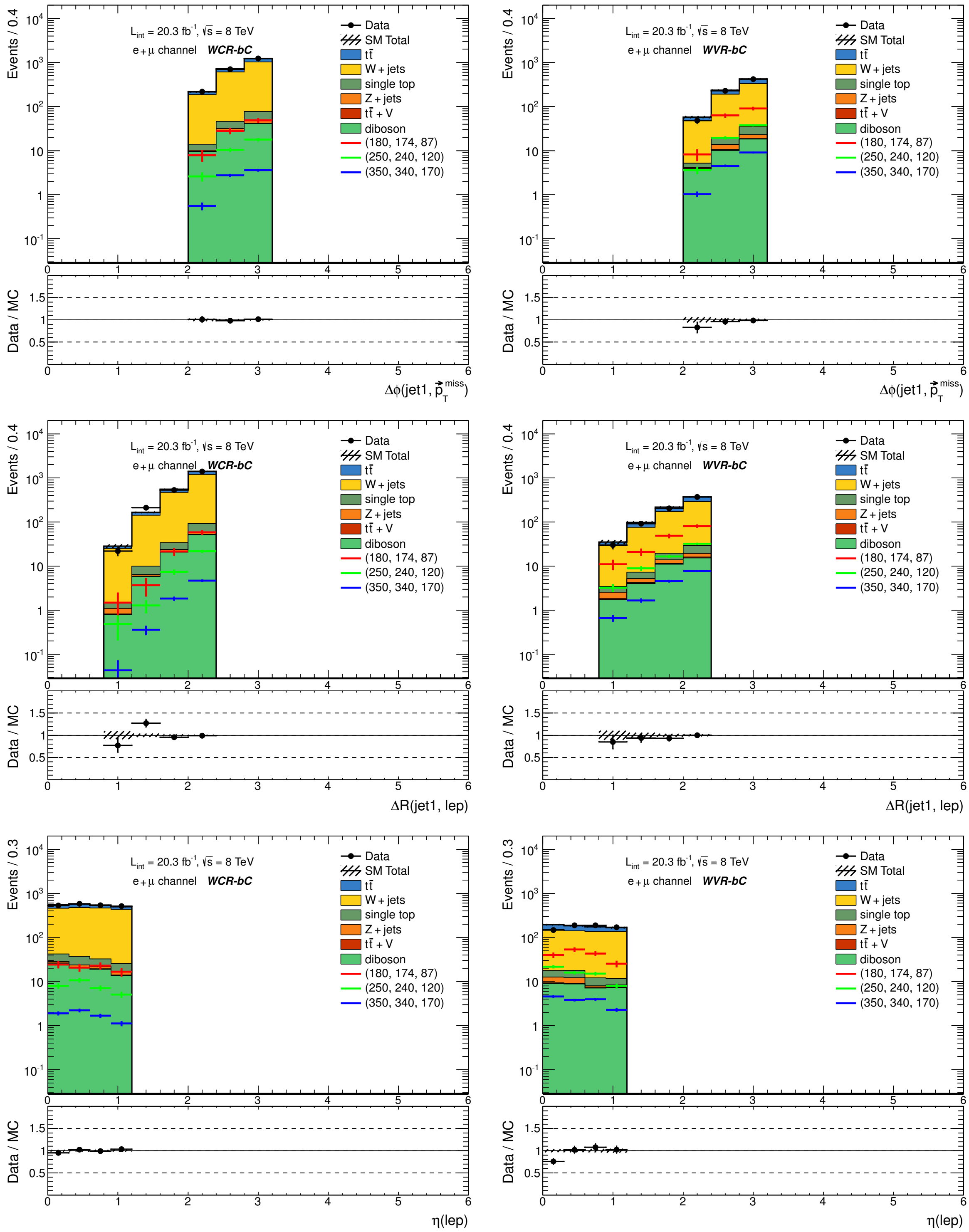

Figure B.6: Distributions for the $\Delta\phi(j_1, E_{\mathrm{T}}^{\mathrm{miss}})$ (top), $\Delta\phi(j_1, \ell)$ (middle), and $\eta(\ell)$ (bottom) for the WCR-bC (left) and WVR-bC (right). The error bars on data and data/MC ratio points represent the 68% confidence interval.

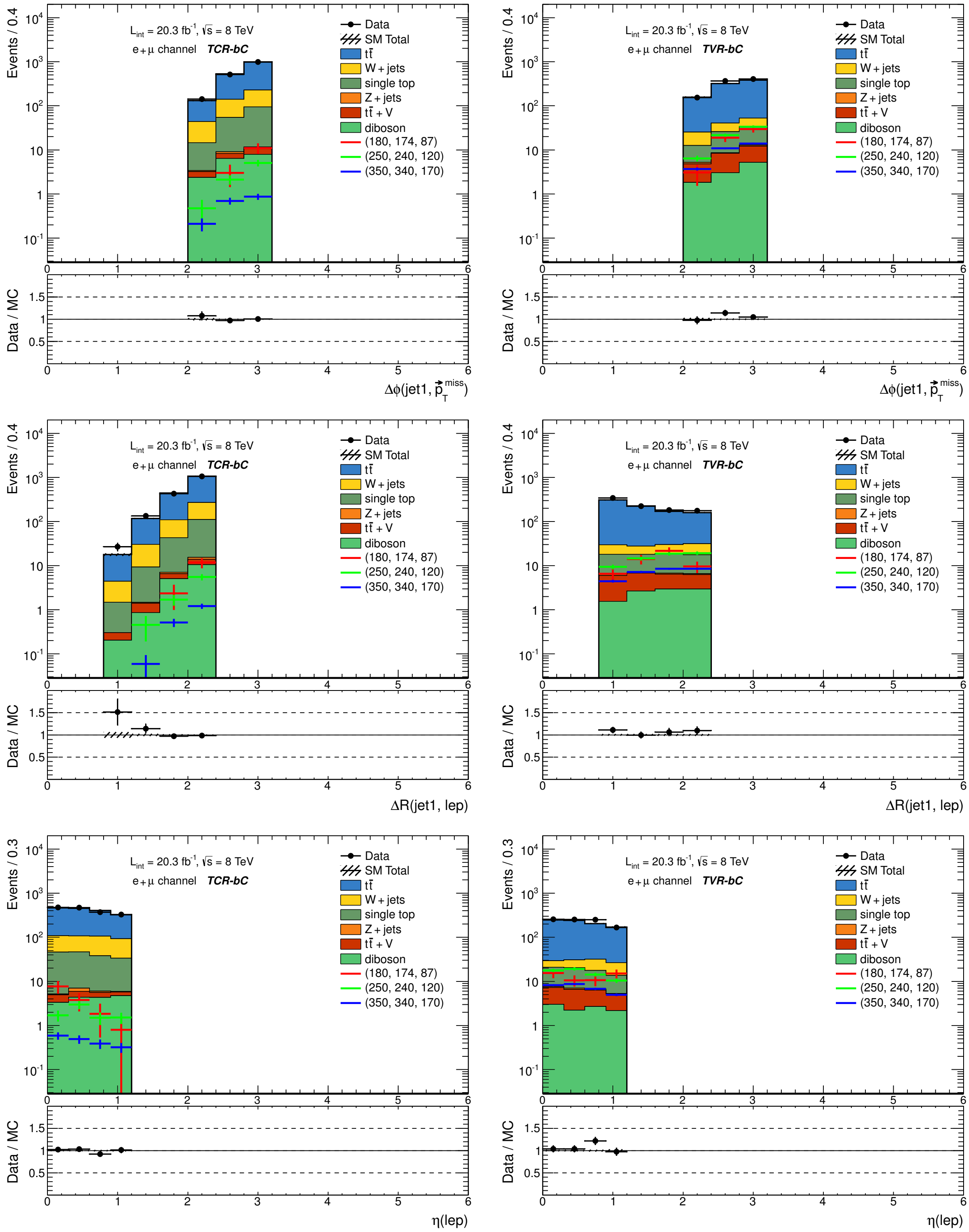

Figure B.7: Distributions for the $\Delta\phi(j_1, E_{\mathrm{T}}^{\mathrm{miss}})$ (top), $\Delta\phi(j_1, \ell)$ (middle), and $\eta(\ell)$ (bottom) for the TCR-bC (left) and TVR-bC (right). The error bars on data and data/MC ratio points represent the 68% confidence interval.

APPENDIX C

Additional studies for $\tilde{t}_1 \rightarrow t\tilde{\chi}_1^0$ analysis

The $t\bar{t}W$, $t\bar{t}Z$, and diboson processes have negligible contribution for the tN diagonal analysis. Therefore, instead of including theoretical uncertainties, a conservative uncertainty of 80% is assigned to the cross sections of these processes.

The estimate of theoretical uncertainties for the $t\bar{t}W$, $t\bar{t}Z$, and diboson processes presented in the following confirms, that for the current case this approach is applicable.

$t\bar{t}W$ and $t\bar{t}Z$ production

The scale variation uncertainties for $t\bar{t}W$ and $t\bar{t}Z$ process are estimated on particle level, while the uncertainty on the finite number of partons in the matrix element is estimated using samples with ATLAS full simulation.

- **Scale variations**
  For the scale variations the following uncertainties are considered: the renormalisation and factorisation scales are varied coherently by factor of 0.5 and 2.0 from the nominal; the ISR and FSR uncertainties are estimated by varying of the α_s parameter and relevant parameter in PYTHIA showering model, respectively; and the matrix element to parton shower matching scale for jets.
- **Finite number of partons**
  This uncertainty is estimated as the difference between one-jet inclusive and two-jet inclusive samples.

Figure C.1 shows the renormalisation and factorisation scale, ISR, FSR, jet matching scale, and the finite number of partons uncertainties, as a function of the BDT output.

One can see, that for the last bin $[0.7, 1]$, for all sources of uncertainties the uncertainty estimate does not exceed 20%. Therefore, the uncertainty estimate of 80% on the cross section can be considered as a conservative approach.

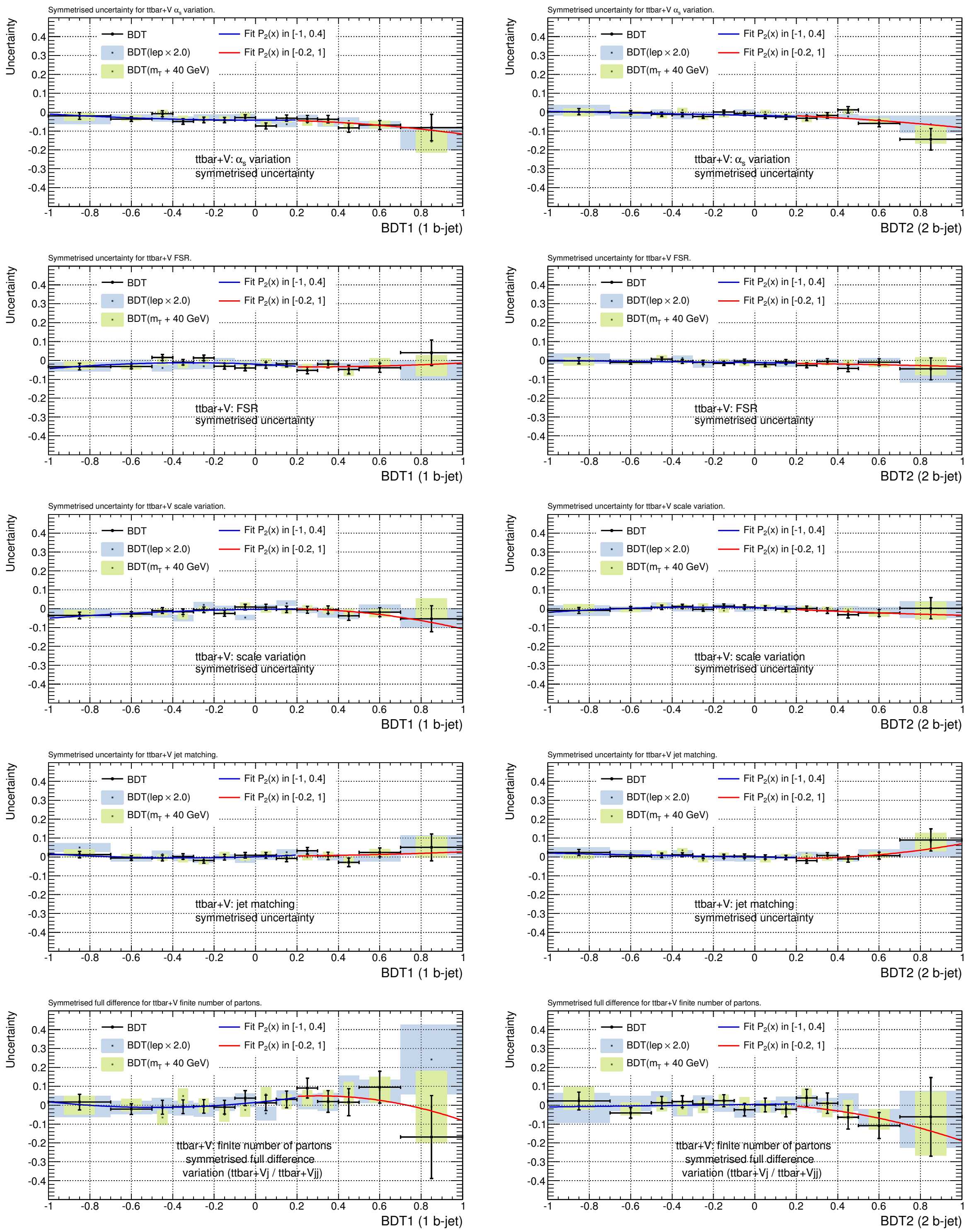

Figure C.1: Uncertainties of the $t\bar{t}W$ and $t\bar{t}Z$ production for the 1 b-jet (left) and 2 b-jet (right) selections. From top to bottom: the renormalisation and factorisation scale, ISR, FSR, jet matching scale, and the finite number of partons uncertainties.

Diboson production

All uncertainties for the diboson production are estimated on particle level.

- **Scale variations**
  Three different scale variations are considered. The CKKW uncertainty is estimated by varying the corresponding matching parameter. The factorisation and renormalisation scales are varied by factor of 0.5 and 2.0 from the nominal value.

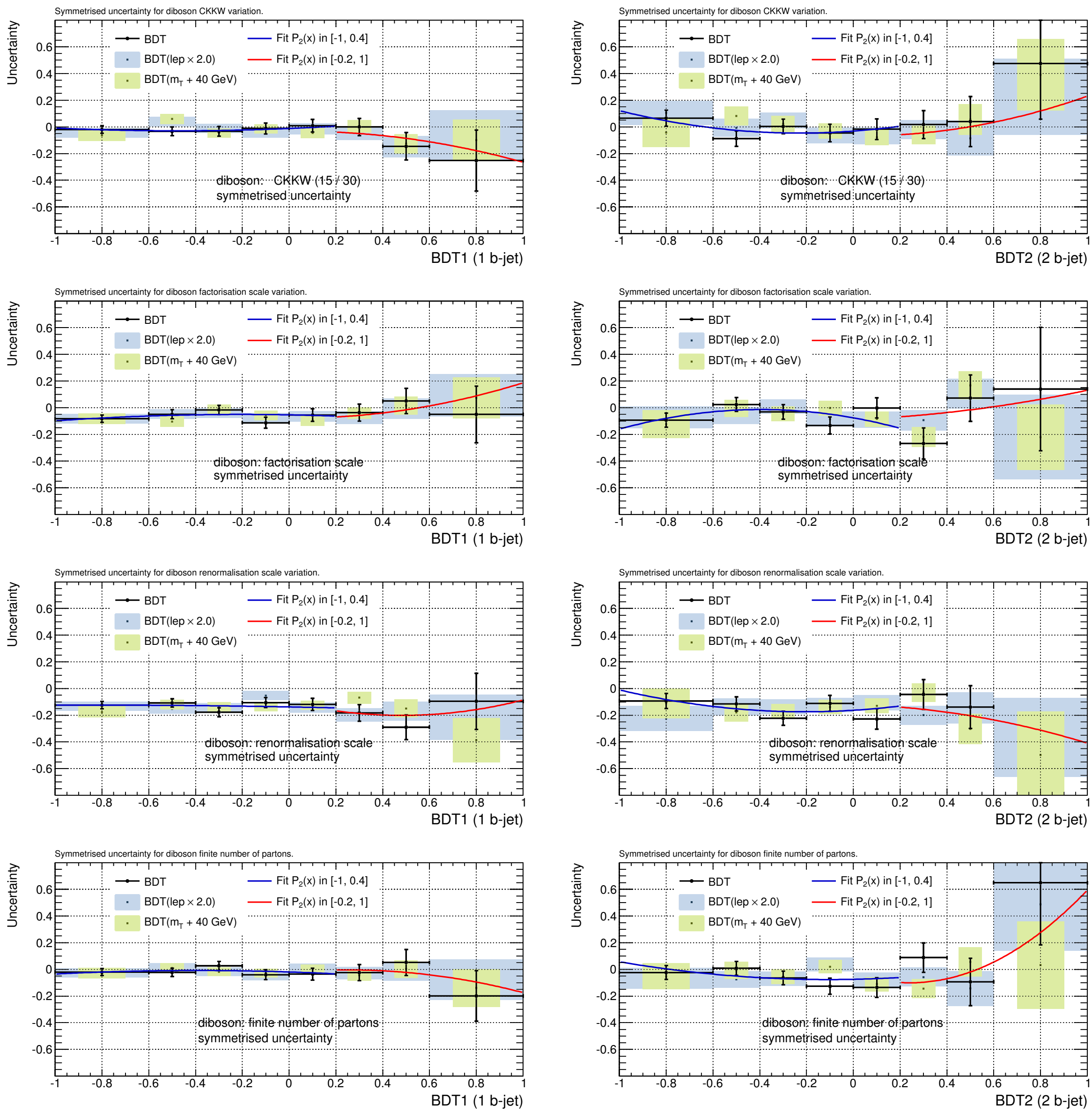

Figure C.2: Uncertainties of the diboson production for the 1 *b*-jet (left) and 2 *b*-jet (right) selections. From top to bottom: the CKKW matching parameter, factorisation scale, renormalisation scale, and the finite number of partons uncertainties.

- **Finite number of partons**
  Finite number of partons uncertainty is estimated as a symmetrised full difference between the samples with two extra partons and the nominal samples with three extra partons included in the matrix element calculations.

The uncertainties as a function of the BDT output are shown for both selections in Figure C.2. One can see, that for the last bin $[0.6, 1]$, for the 1 b-jet selection uncertainty estimate for all sources of uncertainty is less than 20%, therefore, the total uncertainty can be conservatively estimated as below 80%. For the 2 b-jet selection the uncertainty dominates by the statistical component (about 40%). Therefore, to estimate uncertainty one can use uncertainty values from the $[0.4, 0.6]$ bin. The uncertainty values in this bin are found to be below 20%. Therefore, for both selections, a conservative total uncertainty estimate of 80% on the cross section can be used.

Bibliography

[1] ATLAS Collaboration, *Observation of a new particle in the search for the Standard Model Higgs boson with the ATLAS detector at the LHC*, Phys.Lett. **B716** (2012) 1–29, `arXiv:1207.7214 [hep-ex]`.

[2] CMS Collaboration, *Observation of a new boson at a mass of 125 GeV with the CMS experiment at the LHC*, Phys.Lett. **B716** (2012) 30–61, `arXiv:1207.7235 [hep-ex]`.

[3] ATLAS Collaboration, *Search for top squark pair production in final states with one isolated lepton, jets, and missing transverse momentum in $\sqrt{s} = 8$ TeV pp collisions with the ATLAS detector*, JHEP **1411** (2014) 118, `arXiv:1407.0583 [hep-ex]`.

[4] ATLAS Collaboration, *Search for light top squark pair production in final states with leptons and b^- jets with the ATLAS detector in $\sqrt{s} = 7$ TeV proton-proton collisions*, Phys.Lett. **B720** (2013) 13–31, `arXiv:1209.2102 [hep-ex]`.

[5] J. Donoghue, E. Golowich, and B. Holstein, *Dynamics of the Standard Model*, Cambridge University Press, second ed., 2014.

[6] D. Gross, D. Politzer, and F. Wilczek, "Unification of the electromagnetic, weak and strong coupling constants." Nobel lecture, 2004. `http://www.nobelprize.org/nobel_prizes/physics/laureates/2004/popular.html`.

[7] V. Varadarajan, *Supersymmetry for Mathematicians: An Introduction*, American Mathematical Soc. `https://books.google.de/books?id=sZ1-G4hQgIIC`.

[8] A. B. Galajinsky, *Introduction to Supersymmetry*, Tomsk Polytechnic University, 2008.

[9] S. R. Coleman and J. Mandula, *All Possible Symmetries of the S Matrix*, Phys. Rev. **159** (1967) 1251–1256.

[10] S. P. Martin, *A Supersymmetry Primer*, `arXiv:9709356v6 [hep-ph]`.

[11] R. K. Ellis, W. J. Stirling, and B. Webber, *QCD and Collider Physics*, 1996.

[12] J. M. Campbell, J. Huston, and W. Stirling, *Hard Interactions of Quarks and Gluons: A Primer for LHC Physics*, Rept.Prog.Phys. **70** (2007) 89, `arXiv:hep-ph/0611148 [hep-ph]`.

[13] A. Buckley, J. Butterworth, S. Gieseke, D. Grellscheid, S. Hoche, et al., *General-purpose event generators for LHC physics*, Phys.Rept. **504** (2011) 145–233, `arXiv:1101.2599 [hep-ph]`.

[14] M. Dobbs, S. Frixione, E. Laenen, K. Tollefson, H. Baer, et al., *Les Houches guidebook to Monte Carlo generators for hadron collider physics*, arXiv:hep-ph/0403045 [hep-ph].

[15] Y. L. Dokshitzer, *Calculation of the Structure Functions for Deep Inelastic Scattering and e+ e- Annihilation by Perturbation Theory in Quantum Chromodynamics.*, Sov.Phys.JETP **46** (1977) 641–653.

[16] V. Gribov and L. Lipatov, *Deep inelastic e p scattering in perturbation theory*, Sov.J.Nucl.Phys. **15** (1972) 438–450.

[17] G. Altarelli and G. Parisi, *Asymptotic Freedom in Parton Language*, Nucl.Phys. **B126** (1977) 298.

[18] H.-L. Lai, M. Guzzi, J. Huston, Z. Li, P. M. Nadolsky, et al., *New parton distributions for collider physics*, Phys.Rev. **D82** (2010) 074024, arXiv:1007.2241 [hep-ph].

[19] J. Pumplin et al., *New generation of parton distributions with uncertainties from global QCD analysis*, JHEP **07** (2002) 012, arXiv:hep-ph/0201195.

[20] A. Martin, W. Stirling, R. Thorne, and G. Watt, *Parton distributions for the LHC*, Eur.Phys.J. **C63** (2009) 189–285, arXiv:0901.0002 [hep-ph].

[21] R. D. Ball, L. Del Debbio, S. Forte, A. Guffanti, J. I. Latorre, et al., *A first unbiased global NLO determination of parton distributions and their uncertainties*, Nucl.Phys. **B838** (2010) 136–206, arXiv:1002.4407 [hep-ph].

[22] NNPDF Collaboration, R. D. Ball et al., *Unbiased global determination of parton distributions and their uncertainties at NNLO and at LO*, Nucl.Phys. **B855** (2012) 153–221, arXiv:1107.2652 [hep-ph].

[23] M. Whalley, D. Bourilkov, and R. Group, *The Les Houches accord PDFs (LHAPDF) and LHAGLUE*, arXiv:hep-ph/0508110 [hep-ph].

[24] NNPDF Collaboration, "NNPDF web site." https://nnpdf.hepforge.org/.

[25] S. Hoche, *Introduction to parton-shower event generators*, in *Theoretical Advanced Study Institute in Elementary Particle Physics: Journeys Through the Precision Frontier: Amplitudes for Colliders (TASI 2014) Boulder, Colorado, June 2-27, 2014.* 2014. arXiv:1411.4085 [hep-ph]. https://inspirehep.net/record/1328513/files/arXiv:1411.4085.pdf.

[26] S. Catani, F. Krauss, R. Kuhn, and B. R. Webber, *QCD matrix elements + parton showers*, JHEP **11** (2001) 063, arXiv:hep-ph/0109231 [hep-ph].

[27] M. L. Mangano, M. Moretti, F. Piccinini, and M. Treccani, *Matching matrix elements and shower evolution for top-quark production in hadronic collisions*, JHEP **01** (2007) 013, arXiv:hep-ph/0611129 [hep-ph].

[28] Webber, B., *Parton shower Monte Carlo event generators*, Scholarpedia **6** no. 12, (2011) 10662.

[29] Particle Data Group Collaboration, K. Olive et al., *Review of Particle Physics*, Chin. Phys. **C38** (2014) 090001, arXiv:1412.1408.

[30] ATLAS Collaboration, *New ATLAS event generator tunes to 2010 data*, Tech. Rep. ATL-PHYS-PUB-2011-008, 2011.

[31] ATLAS Collaboration, *Summary of ATLAS Pythia 8 tunes*, Tech. Rep. ATL-PHYS-PUB-2012-003, 2012.

[32] T. Sjostrand, S. Mrenna, and P. Z. Skands, *PYTHIA 6.4 Physics and Manual*, JHEP **0605** (2006) 026, `arXiv:hep-ph/0603175 [hep-ph]`.

[33] T. Sjostrand, S. Mrenna, and P. Z. Skands, *A Brief Introduction to PYTHIA 8.1*, Comput.Phys.Commun. **178** (2008) 852–867, `arXiv:0710.3820 [hep-ph]`.

[34] M. Bahr, S. Gieseke, M. Gigg, D. Grellscheid, K. Hamilton, et al., *Herwig++ Physics and Manual*, Eur.Phys.J. **C58** (2008) 639–707, `arXiv:0803.0883 [hep-ph]`.

[35] T. Gleisberg, S. Hoeche, F. Krauss, M. Schonherr, S. Schumann, et al., *Event generation with SHERPA 1.1*, JHEP **0902** (2009) 007, `arXiv:0811.4622 [hep-ph]`.

[36] M. L. Mangano, M. Moretti, F. Piccinini, R. Pittau, and A. D. Polosa, *ALPGEN, a generator for hard multiparton processes in hadronic collisions*, JHEP **0307** (2003) 001, `arXiv:hep-ph/0206293 [hep-ph]`.

[37] B. P. Kersevan and E. Richter-Was, *The Monte Carlo event generator AcerMC versions 2.0 to 3.8 with interfaces to PYTHIA 6.4, HERWIG 6.5 and ARIADNE 4.1*, Comput.Phys.Commun. **184** (2013) 919–985, `arXiv:hep-ph/0405247 [hep-ph]`.

[38] J. Alwall, M. Herquet, F. Maltoni, O. Mattelaer, and T. Stelzer, *MadGraph 5 : Going Beyond*, JHEP **1106** (2011) 128, `arXiv:1106.0522 [hep-ph]`.

[39] P. Nason and B. Webber, *Next-to-Leading-Order Event Generators*, Ann. Rev. Nucl. Part. Sci. **62** (2012) 187–213, `arXiv:1202.1251 [hep-ph]`.

[40] S. Frixione and B. R. Webber, *Matching NLO QCD computations and parton shower simulations*, JHEP **06** (2002) 029, `arXiv:hep-ph/0204244`.

[41] S. Frixione, P. Nason, and C. Oleari, *Matching NLO QCD computations with Parton Shower simulations: the POWHEG method*, JHEP **0711** (2007) 070, `arXiv:0709.2092 [hep-ph]`.

[42] L. Evans and P. Bryant, *LHC Machine*, JINST **3** (2008) S08001.

[43] TE-EPC CERN group, "Machines Operation and Mantainace." `http://te-dep-epc.web.cern.ch/te-dep-epc/nw_general/welcome.stm`.

[44] ATLAS Collaboration, *The ATLAS Experiment at the CERN Large Hadron Collider*, JINST **3** (2008) S08003.

[45] ATLAS Collaboration, *ATLAS level-1 trigger: Technical Design Report*, Technical Design Report ATLAS, CERN, Geneva, 1998.

[46] ATLAS Collaboration, *Expected Performance of the ATLAS Experiment - Detector, Trigger and Physics*, `arXiv:0901.0512 [hep-ex]`.

[47] ATLAS Collaboration, *Performance of the ATLAS Inner Detector Track and Vertex Reconstruction in the High Pile-Up LHC Environment*, Tech. Rep. ATLAS-CONF-2012-042, CERN, Geneva, Mar, 2012.

[48] T. Cornelissen, M. Elsing, S. Fleischmann, W. Liebig, E. Moyse, and A. Salzburger, *Concepts, Design and Implementation of the ATLAS New Tracking (NEWT)*, Tech. Rep. ATL-SOFT-PUB-2007-007, CERN, Geneva, Mar, 2007. `https://cds.cern.ch/record/1020106`.

[49] ATLAS Collaboration, *Performance of primary vertex reconstruction in proton-proton collisions at $\sqrt{s} = 7$ TeV in the ATLAS experiment*, Tech. Rep. ATLAS-CONF-2010-069, CERN, Geneva, Jul, 2010.

[50] R. Fruhwirth, W. Waltenberger, and P. Vanlaer, *Adaptive vertex fitting*, J. Phys. **G34** (2007) N343.

[51] ATLAS Collaboration, *Performance of the ATLAS Electron and Photon Trigger in p-p Collisions at $\sqrt{s} = 7$ TeV in 2011*, Tech. Rep. ATLAS-CONF-2012-048, CERN, Geneva, May, 2012.

[52] W. Lampl, S. Laplace, D. Lelas, P. Loch, H. Ma, S. Menke, S. Rajagopalan, D. Rousseau, S. Snyder, and G. Unal, *Calorimeter clustering algorithms: Description and performance*,.

[53] *Electron efficiency measurements with the ATLAS detector using the 2012 LHC proton-proton collision data*, Tech. Rep. ATLAS-CONF-2014-032, CERN, Geneva, Jun, 2014.

[54] ATLAS Collaboration, *Electron and photon energy calibration with the ATLAS detector using LHC Run 1 data*, `arXiv:1407.5063 [hep-ex]`.

[55] ATLAS, *Measurement of the muon reconstruction performance of the ATLAS detector using 2011 and 2012 LHC proton-proton collision data*, `arXiv:1407.3935`. `http://atlas.web.cern.ch/Atlas/GROUPS/PHYSICS/PAPERS/PERF-2014-05/`.

[56] ATLAS Collaboration, *Performance of the ATLAS muon trigger in pp collisions at $\sqrt{s} = 8$ TeV*, `arXiv:1408.3179 [hep-ex]`.

[57] M. Cacciari, G. P. Salam, and G. Soyez, *The Anti-k_t jet clustering algorithm*, JHEP **0804** (2008) 063, `arXiv:0802.1189 [hep-ph]`.

[58] S. D. Ellis and D. E. Soper, *Successive combination jet algorithm for hadron collisions*, Phys. Rev. **D48** (1993) 3160–3166, `arXiv:hep-ph/9305266 [hep-ph]`.

[59] Y. L. Dokshitzer, G. Leder, S. Moretti, and B. Webber, *Better jet clustering algorithms*, JHEP **9708** (1997) 001, `arXiv:hep-ph/9707323 [hep-ph]`.

[60] M. Cacciari, G. P. Salam, and G. Soyez, *The Catchment Area of Jets*, JHEP **0804** (2008) 005, `arXiv:0802.1188 [hep-ph]`.

[61] M. Cacciari and G. P. Salam, *Pileup subtraction using jet areas*, Phys.Lett. **B659** (2008) 119–126, `arXiv:0707.1378 [hep-ph]`.

[62] *Pile-up subtraction and suppression for jets in ATLAS*, Tech. Rep. ATLAS-CONF-2013-083, CERN, Geneva, Aug, 2013.

[63] ATLAS Collaboration, *Jet energy measurement with the ATLAS detector in proton-proton collisions at $\sqrt{s} = 7$ TeV*, Eur.Phys.J. **C73** (2013) 2304, `arXiv:1112.6426 [hep-ex]`.

[64] *Jet global sequential corrections with the ATLAS detector in proton-proton collisions at $\sqrt{s} = 8$ TeV*, Tech. Rep. ATLAS-CONF-2015-002, CERN, Geneva, Mar, 2015.

[65] ATLAS Collaboration, *Monte Carlo Calibration and Combination of In-situ Measurements of Jet Energy Scale, Jet Energy Resolution and Jet Mass in ATLAS*, Tech. Rep. ATLAS-CONF-2015-037, CERN, Geneva, Aug, 2015.

[66] *Determination of the jet energy scale and resolution at ATLAS using Z/γ–jet events in data at $\sqrt{s} = 8$ TeV*, Tech. Rep. ATLAS-CONF-2015-057, CERN, Geneva, Oct, 2015.

[67] ATLAS Collaboration, *Data-driven determination of the energy scale and resolution of jets reconstructed in the ATLAS calorimeters using dijet and multijet events at $\sqrt{s} = 8$ TeV*, Tech. Rep. ATLAS-CONF-2015-017, CERN, Geneva, Apr, 2015.

[68] *b-tagging in dense environments*, Tech. Rep. ATL-PHYS-PUB-2014-014, CERN, Geneva, Aug, 2014. `https://cds.cern.ch/record/1750682`.

[69] ATLAS Collaboration, *Commissioning of the ATLAS high-performance b-tagging algorithms in the 7 TeV collision data*, Tech. Rep. ATLAS-CONF-2011-102, CERN, Geneva, Jul, 2011.

[70] ATLAS Collaboration, *Measurement of the b-tag Efficiency in a Sample of Jets Containing Muons with 5 fb^{-1} of Data from the ATLAS Detector*, Tech. Rep. ATLAS-CONF-2012-043, CERN, Geneva, Mar, 2012.

[71] *Calibration of the performance of b-tagging for c and light-flavour jets in the 2012 ATLAS data*, Tech. Rep. ATLAS-CONF-2014-046, CERN, Geneva, Jul, 2014.

[72] ATLAS Collaboration, *Performance of Missing Transverse Momentum Reconstruction in Proton-Proton Collisions at 7 TeV with ATLAS*, Eur.Phys.J. **C72** (2012) 1844, `arXiv:1108.5602 [hep-ex]`.

[73] *Performance of the ATLAS missing E_T trigger with first $\sqrt{s} = 7$ TeV data*, Tech. Rep. ATL-DAQ-PROC-2010-024, CERN, Geneva, Aug, 2010. `https://cds.cern.ch/record/1282366`.

[74] *The ATLAS transverse-momentum trigger performance at the LHC in 2011*, Tech. Rep. ATLAS-CONF-2014-002, CERN, Geneva, Feb, 2014.

[75] ATLAS Collaboration, *Performance of Missing Transverse Momentum Reconstruction in ATLAS with 2011 Proton-Proton Collisions at $\sqrt{s} = 7$ TeV*, Tech. Rep. ATLAS-CONF-2012-101, CERN, Geneva, Jul, 2012.

[76] *Performance of Missing Transverse Momentum Reconstruction in ATLAS studied in Proton-Proton Collisions recorded in 2012 at 8 TeV*, Tech. Rep. ATLAS-CONF-2013-082, CERN, Geneva, Aug, 2013.

[77] A. Hoecker, P. Speckmayer, J. Stelzer, J. Therhaag, E. von Toerne, and H. Voss, *TMVA: Toolkit for Multivariate Data Analysis*, PoS **ACAT** (2007) 040, `arXiv:physics/0703039`.

[78] R. Brun and F. Rademakers, *ROOT: An object oriented data analysis framework*, Nucl.Instrum.Meth. **A389** (1997) 81–86.

[79] M. Baak, G. Besjes, D. Cote, A. Koutsman, J. Lorenz, et al., *HistFitter software framework for statistical data analysis*, `arXiv:1410.1280 [hep-ex]`.

[80] A. L. Read, *Presentation of search results: The CL_s technique*, J.Phys. **G28** (2002) 2693–2704.

[81] G. Cowan, *Statistics for Searches at the LHC*, arXiv:1307.2487 [hep-ex]. http://inspirehep.net/record/1242009/files/arXiv:1307.2487.pdf.

[82] P. Konar, K. Kong, K. T. Matchev, and M. Park, *RECO level $\sqrt{s}_{min}$ and subsystem $\sqrt{s}_{min}$: Improved global inclusive variables for measuring the new physics mass scale in $E_{\mathrm{T}}^{\mathrm{miss}}$ events at hadron colliders*, JHEP **1106** (2011) 041, arXiv:1006.0653 [hep-ph].

[83] ATLAS Collaboration, *The ATLAS Simulation Infrastructure*, Eur.Phys.J. **C70** (2010) 823–874, arXiv:1005.4568 [physics.ins-det].

[84] GEANT4 Collaboration, S. Agostinelli et al., *GEANT4: A Simulation toolkit*, Nucl.Instrum.Meth. **A506** (2003) 250–303.

[85] E. Richter-Was, D. Froidevaux, and L. Poggioli, *ATLFAST 2.0 a fast simulation package for ATLAS*, Tech. Rep. ATL-PHYS-98-131, 1998.

[86] P. M. Nadolsky, H.-L. Lai, Q.-H. Cao, J. Huston, J. Pumplin, D. Stump, W.-K. Tung, and C. P. Yuan, *Implications of CTEQ global analysis for collider observables*, Phys. Rev. **D78** (2008) 013004, arXiv:0802.0007 [hep-ph].

[87] G. Corcella, I. Knowles, G. Marchesini, S. Moretti, K. Odagiri, et al., *HERWIG 6: An Event generator for hadron emission reactions with interfering gluons (including supersymmetric processes)*, JHEP **0101** (2001) 010, arXiv:hep-ph/0011363 [hep-ph].

[88] A. Sherstnev and R. Thorne, *Parton Distributions for LO Generators*, Eur.Phys.J. **C55** (2008) 553–575, arXiv:0711.2473 [hep-ph].

[89] ATLAS Collaboration, *Electron performance measurements with the ATLAS detector using the 2010 LHC proton-proton collision data*, Eur.Phys.J. **C72** (2012) 1909, arXiv:1110.3174 [hep-ex].

[90] ATLAS Collaboration, *Further search for supersymmetry at $\sqrt{s} = 7$ TeV in final states with jets, missing transverse momentum and isolated leptons with the ATLAS detector*, Phys.Rev. **D86** (2012) 092002, arXiv:1208.4688 [hep-ex].

[91] ATLAS Collaboration Collaboration, *Search for direct top squark pair production in final states with one isolated lepton, jets, and missing transverse momentum in sqrts $= 8$,TeV pp collisions using 21 fb^{-1} of ATLAS data*, Tech. Rep. ATLAS-CONF-2013-037, CERN, Geneva, Mar, 2013. https://cds.cern.ch/record/1532431.

[92] ATLAS Collaboration, *Luminosity Determination in pp Collisions at $\sqrt{s} = 7$ TeV Using the ATLAS Detector at the LHC*, Eur.Phys.J. **C71** (2011) 1630, arXiv:1101.2185 [hep-ex].

[93] ATLAS Collaboration, "Atlas luminosity public page." https://twiki.cern.ch/twiki/bin/view/AtlasPublic/LuminosityPublicResults.

[94] M. Czakon and A. Mitov, *NNLO corrections to top pair production at hadron colliders: the quark-gluon reaction*, JHEP **01** (2013) 080, arXiv:1210.6832 [hep-ph].

[95] M. Cacciari, M. Czakon, M. Mangano, A. Mitov, and P. Nason, *Top-pair production at hadron colliders with next-to-next-to-leading logarithmic soft-gluon resummation*, Phys. Lett. **B710** (2012) 612–622, arXiv:1111.5869 [hep-ph].

[96] S. Frixione, E. Laenen, P. Motylinski, B. R. Webber, and C. D. White, *Single-top hadroproduction in association with a W boson*, JHEP **07** (2008) 029, `arXiv:0805.3067 [hep-ph]`.

[97] N. Kidonakis, *Next-to-next-to-leading-order collinear and soft gluon corrections for t-channel single top quark production*, Phys. Rev. **D83** (2011) 091503, `arXiv:1103.2792 [hep-ph]`.

[98] N. Kidonakis, *NNLL resummation for s-channel single top quark production*, Phys. Rev. **D81** (2010) 054028, `arXiv:1001.5034 [hep-ph]`.

[99] S. Catani, L. Cieri, G. Ferrera, D. de Florian, and M. Grazzini, *Vector boson production at hadron colliders: a fully exclusive QCD calculation at NNLO*, Phys. Rev. Lett. **103** (2009) 082001, `arXiv:0903.2120 [hep-ph]`.

[100] J. M. Campbell and R. K. Ellis, *$t\bar{t}W^{+-}$ production and decay at NLO*, JHEP **07** (2012) 052, `arXiv:1204.5678 [hep-ph]`.

[101] M. V. Garzelli, A. Kardos, C. G. Papadopoulos, and Z. Trocsanyi, *$t\,\bar{t}\,W^{+-}$ and $t\,\bar{t}\,Z$ Hadroproduction at NLO accuracy in QCD with Parton Shower and Hadronization effects*, JHEP **11** (2012) 056, `arXiv:1208.2665 [hep-ph]`.

[102] J. Campbell, R. K. Ellis, and R. Röntsch, *Single top production in association with a Z boson at the LHC*, Phys. Rev. **D87** (2013) 114006, `arXiv:1302.3856 [hep-ph]`.

[103] J. M. Campbell, R. K. Ellis, and C. Williams, *Vector boson pair production at the LHC*, JHEP **07** (2011) 018, `arXiv:1105.0020 [hep-ph]`.

[104] *Measurement of top-quark pair differential cross-sections in the l+jets channel in pp collisions at $\sqrt{s} = 7$ TeV using the ATLAS detector*, Tech. Rep. ATLAS-CONF-2013-099, CERN, Geneva, Sep, 2013. `https://cds.cern.ch/record/1600778`.

[105] ATLAS Collaboration, *Measurement of the cross-section for W boson production in association with b-jets in pp collisions at $\sqrt{s}$ = 7 TeV with the ATLAS detector*, JHEP **1306** (2013) 084, `arXiv:1302.2929 [hep-ex]`.

[106] N. Kidonakis, *Two-loop soft anomalous dimensions for single top quark associated production with a W or H*, Phys.Rev. **D82** (2010) 054018, `arXiv:1005.4451 [hep-ph]`.

[107] J. Butterworth, E. Dobson, U. Klein, B. Mellado Garcia, T. Nunnemann, J. Qian, D. Rebuzzi, and R. Tanaka, *Single Boson and Diboson Production Cross Sections in pp Collisions at $\sqrt{s} = 7$ TeV*, Tech. Rep. ATL-COM-PHYS-2010-695, CERN, Geneva, Aug, 2010. `https://cds.cern.ch/record/1287902`.

[108] M. Botje et al., *The PDF4LHC Working Group Interim Recommendations*, `arXiv:1101.0538 [hep-ph]`.

[109] R. D. Ball et al., *Parton distributions with LHC data*, Nucl. Phys. **B867** (2013) 244–289, `arXiv:1207.1303 [hep-ph]`.

[110] M. Kramer, A. Kulesza, R. van der Leeuw, M. Mangano, S. Padhi, T. Plehn, and X. Portell, *Supersymmetry production cross sections in pp collisions at $\sqrt{s} = 7$ TeV*, `arXiv:1206.2892 [hep-ph]`.

[111] ATLAS Collaboration, *Search for direct top-squark pair production in final states with two leptons in pp collisions at $\sqrt{s} = 8$ TeV with the ATLAS detector*, JHEP **1406** (2014) 124, `arXiv:1403.4853 [hep-ex]`.

[112] ATLAS Collaboration, *ATLAS Run 1 searches for direct pair production of third-generation squarks at the Large Hadron Collider*, Eur. Phys. J. **C75** no. 10, (2015) 510, `arXiv:1506.08616 [hep-ex]`.

[113] ATLAS Collaboration, *Search for direct third-generation squark pair production in final states with missing transverse momentum and two b-jets in $\sqrt{s} = 8$ TeV pp collisions with the ATLAS detector*, JHEP **1310** (2013) 189, `arXiv:1308.2631 [hep-ex]`.

[114] ATLAS Collaboration, *Search for light scalar top quark pair production in final states with two leptons with the ATLAS detector in $\sqrt{s} = 7$ TeV proton-proton collisions*, Eur.Phys.J. **C72** (2012) 2237, `arXiv:1208.4305 [hep-ex]`.

[115] CMS Collaboration, *Search for top-squark pair production in the single-lepton final state in pp collisions at $\sqrt{s} = 8$ TeV*, Eur. Phys. J. **C73** no. 12, (2013) 2677, `arXiv:1308.1586 [hep-ex]`.

[116] CMS Collaboration, *A Search for Scalar Top Quark Production and Decay to All Hadronic Final States in pp Collisions at $\sqrt{s} = 8$ TeV*, Tech. Rep. CMS-PAS-SUS-13-023, 2015.

[117] CMS Collaboration, *Searches for third-generation squark production in fully hadronic final states in proton-proton collisions at $\sqrt{s} = 8$ TeV*, JHEP **06** (2015) 116, `arXiv:1503.08037 [hep-ex]`.

[118] CMS Collaboration, *Exclusion limits on gluino and top-squark pair production in natural SUSY scenarios with inclusive razor and exclusive single-lepton searches at 8 TeV*, Tech. Rep. CMS-PAS-SUS-14-011, 2014.

[119] CMS Collaboration, *Search for direct pair production of scalar top quarks in the single- and dilepton channels in proton-proton collisions at $\sqrt{s} = 8$ TeV*, `arXiv:1602.03169 [hep-ex]`.

[120] CMS Collaboration, *Search for supersymmetry in events with soft leptons, low jet multiplicity, and missing transverse momentum in proton-proton collisions at $\sqrt{s} = 8$ TeV*, Tech. Rep. CMS-PAS-SUS-14-021, CERN, Geneva, 2015. `https://cds.cern.ch/record/2010110`.

[121] ATLAS Collaboration, *Measurement of the $t\bar{t}$ production cross-section using $e\mu$ events with b -tagged jets in pp collisions at $\sqrt{s} = 7$ and 8 TeV with the ATLAS detector*, Eur. Phys. J. **C74** no. 10, (2014) 3109, `arXiv:1406.5375 [hep-ex]`.

[122] ATLAS Collaboration, *Measurement of Spin Correlation in Top-Antitop Quark Events and Search for Top Squark Pair Production in pp Collisions at $\sqrt{s} = 8$ TeV Using the ATLAS Detector*, Phys. Rev. Lett. **114** no. 14, (2015) 142001, `arXiv:1412.4742 [hep-ex]`.

[123] A. Mayr, H. Binder, O. Gefeller, and M. Schmid, *The Evolution of Boosting Algorithms - From Machine Learning to Statistical Modelling*, ArXiv e-prints (2014), `arXiv:1403.1452`.

[124] ATLAS Collaboration, *Further search for supersymmetry at $\sqrt{s} = 7$ TeV in final states with jets, missing transverse momentum and isolated leptons with the ATLAS detector*, Phys.Rev. **D86** (2012) 092002, `arXiv:1208.4688 [hep-ex]`.

Acknowledgements

I would like to start my acknowledgments with thanks to Prof. Vakhtang Garsevanishvili from Tbilisi State University, who advised me to switch to High Energy Physics.

Special thanks to Bob Stanek, former project leader of the ATLAS Tile Calorimeter group who invited me to CERN and was supporting and cheering me up during the whole period of my stay in the ATLAS Tile Calorimeter group. He strongly supported my PhD application and, as I discovered recently, have played a definite role that I was accepted to this PhD position.

Thanks to Iacopo Vivarelli, my first supervisor, who actually advised me to apply to this PhD position and who played important role at the first stage of my PhD research.

Special thanks to Priscilla Pani and Sopho Pataraia, for their constant support in the ATLAS SUSY one-lepton group.

Thanks to Claudia, Francesca, Phuong and all other members of our group. I would also like to thank all the people from the Schumacher group for beeng good neighbours.

Special IT thanks to the BFG team and especially to the Michael and Anton. Exclusive amount of storage and computing power which was available for me was playing an important role at all stages of this work.

I would also like to say thanks to all people who gave their corrections and advices for this thesis.

Special thanks to Christian Weiser for helpful discussions related to different topics and approaches used in the analysis, for all corrections and improvements related to this work.

Big thanks to Frederik Rühr, my second supervisor, for constant attention and important discussions related to my work and for his help in pushing the analysis for publishing during heated discussions in the ATLAS SUSY one-lepton group.

And, at last, I would like to express my deepest gratitude to Prof. Karl Jakobs for accepting me as a PhD student in his group, for his belief in me and immence support, especially during the last phase of this work, for guiding and fruitful discussions around the key problems, for his patience and tolerance while thoroughly reading my ugly written text and giving notes and corrections to almost all the pages, for finding needed time in his tight schedule, all of which made it possible to successfully finalize the analysis and to significantly improve the overall thesis appearance, for his excepional human qualities, and … for being for us much more than just a group leader.

I am particularly grateful to our secretary Christina Skorek. It was always a pleasure to talk with her on any topic. Thanks for her help with all formalities, bureaucracy and various problems, which, I think, I could never have managed to solve by myself. Thanks for her corrections to make my writings more human readable. And, especially, for finding time to help to each of us, independently to how busy she was.

And, of course, I am very thankful to Frau Gisela Morgenstern who was hosting me all these years for her cordiality and moral support and help. During the whole my stay in Freiburg she was my “oma”, and here, far away from my native counrty, I was always feeling myself as at home.

I want to say thanks to my family, my four brothers and sisters and especially to my parents, for their constant support during the whole my life, for giving me competitive education with a strong mathematical background, which was always helping me in whatever field I was working.